

Generation of Titanium Oxide Nanostructures via Electron Beam Induced Deposition in UHV

Herstellung von Titanoxid Nanostrukturen mittels
elektronenstrahlinduzierter Abscheidung im UHV

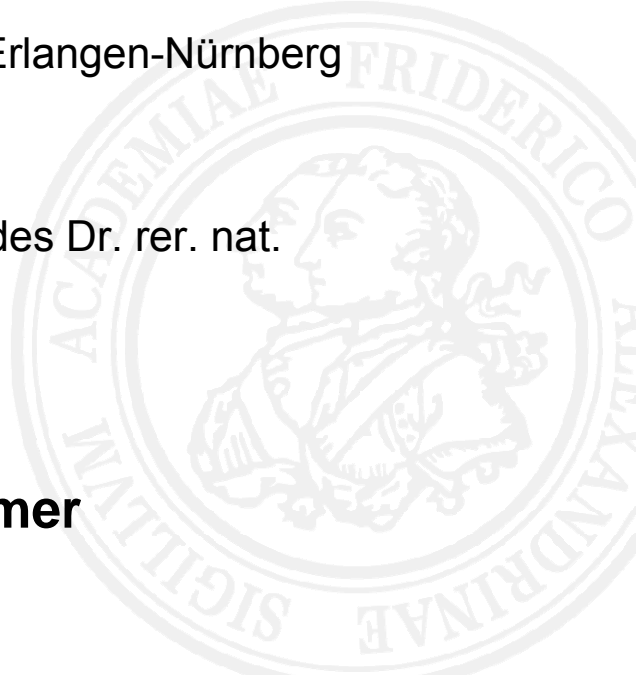
Der Naturwissenschaftlichen Fakultät der
Friedrich-Alexander-Universität Erlangen-Nürnberg

zur Erlangung des Doktorgrades Dr. rer. nat.

vorgelegt von

Michael Schirmer

aus Forchheim



Als Dissertation genehmigt
durch die Naturwissenschaftliche Fakultät
der Friedrich-Alexander-Universität Erlangen-Nürnberg

Tag der mündlichen Prüfung: 10.05.2012

Vorsitzender der Promotionskommission: Prof. Dr. Rainer Fink

Erstberichterstatter: Prof. Dr. Hans-Peter Steinrück

Zweitberichterstatter: Prof. Dr. Oliver Diwald

Gewidmet meiner Familie:
meiner Ehefrau Nicole, meinen Eltern Hermann und Sigrid,
meinem Bruder Markus und meinen Großeltern Jakob, Anna,
Andreas und Margareta.

Table of contents

1	Introduction	1
2	Fundamentals, techniques and ingredients	5
2.1	Electron beam induced deposition (EBID).....	5
2.2	Scanning electron microscopy (SEM).....	7
2.3	Auger spectroscopy and spectromicroscopy (AES, AELS and SAM).....	11
2.4	Atomic force microscopy (AFM).....	15
2.5	Quadrupole mass spectrometry (QMS)	17
2.6	Low energy electron diffraction (LEED)	19
2.7	Sputtering	21
2.8	Ingredients	26
2.8.1	The substrate silicon.....	26
2.8.2	The substrate silicon oxide (on silicon).....	26
2.8.3	The substrate gold.....	27
2.8.4	The precursor titanium(IV) tetraisopropoxide (TTIP)	27
2.8.5	The precursor iron pentacarbonyl.....	31
3	Experimental	33
3.1	The UHV instrument	33
3.1.1	The preparation chamber	33
3.1.2	The analysis chamber	35
3.1.3	The self-constructed gas dosage and gas injection system	36
3.1.4	Precursor storage.....	39
3.2	Control of the electron beam	40
3.2.1	The SmartSEM imaging software (Zeiss).....	40
3.2.2	The lithographic attachment ELPHY Quantum (Raith)	42
3.2.3	Waveform generators (Hewlett-Packard)	43
3.3	Sample preparation	46
3.3.1	Preparation of Si(100) samples	46
3.3.2	Preparation of SiO _x (300 nm) / Si(100) samples.....	47

3.3.3	Preparation of the Au(111) sample	47
3.4	Gas handling and preparation of the TTIP precursor	48
3.5	Materials	49
3.6	Experimental details, data acquisition and data processing	50
3.6.1	Pressure values	50
3.6.2	Temperature values	51
3.6.3	EBID experiments	52
3.6.4	SEM measurements	54
3.6.5	AES, AELS and SAM measurements	54
3.6.6	AFM measurements	57
3.6.7	Sputtering	58
3.6.8	Quantitative analyses	59
4	Literature review	69
4.1	Electron beam induced deposition (EBID)	69
4.2	Proximity effects in EBID	73
4.3	Fabrication of clean deposits via EBID	75
4.4	Application of titanium(IV) tetraisopropoxide (TTIP)	77
4.5	EBID with titanium(IV) tetraisopropoxide (TTIP)	80
4.6	Titanium oxides and titanium dioxide	81
5	Purification of the precursor gas titanium(IV) tetraisopropoxide (TTIP)	89
5.1	Introduction	89
5.2	Purification of the precursor gas TTIP	90
5.3	Summary and conclusion	104
5.4	Outlook	105
6	Flux distribution of TTIP in the applied setup	107
6.1	Introduction	107
6.2	Fundamentals	109
6.2.1	Flow and rarefied gas flow	109
6.2.2	Gas flow and throughput	113

6.2.3	Flux.....	114
6.2.4	Pumping speed and throughput of a vacuum pump	115
6.3	Determination of precursor flux and pressure at the nozzle exit	115
6.4	Determination of flux distribution, precursor flux and pressure directly at the sample surface	118
6.4.1	The GIS Simulator	118
6.4.2	Simulation of flux distribution, precursor flux and pressure at the sample surface for the applied instrumental setup	120
6.5	Summary and conclusions.....	125
7	Nanostructure fabrication with TTIP	127
7.1	Deposition with arbitrary shape on the nanometer scale	127
7.2	Chemical composition of EBID deposits with TTIP	131
7.2.1	Literature overview on the chemical compositions for CVD and EBID	131
7.2.2	Chemical composition of area structures.....	132
7.2.3	Variation of lithographic parameters	137
7.2.4	Chemical composition of line and dot structures	142
7.2.5	Strategies for carbon reduction in the deposits	145
7.2.6	The oxidation state of titanium in the deposited material.....	146
7.3	Contrast on Si(100) and Au(111).....	154
7.4	Summary and conclusions.....	160
8	Proximity effects in EBID	163
8.1	Proximity effects on silicon	163
8.2	Monte Carlo simulation of the electron substrate interaction	170
8.3	Proximity effects on gold.....	177
8.4	Summary and conclusions.....	182
9	Post-treatment procedures	185
9.1	Sputtering	185
9.1.1	Sputtering as a tool for the reduction of lateral size.....	185

9.1.2	Sputtering as a tool to elucidate structure morphologies	199
9.1.3	Sputtering for depth ion profiling	199
9.2	Annealing in oxygen	201
9.3	Two-step post-treatment procedure for clean localized nanostructures	222
9.4	Summary and conclusions	232
10	Morphology of EBID deposits	235
10.1	Influence of the process regime	235
10.2	Influence of lithographic parameters	245
10.3	Topography of EBID deposits	255
10.3.1	Topography investigation of dot deposits	255
10.3.2	Topography investigation of line deposits	262
10.3.3	Topography investigation of area deposits	269
10.3.4	Summary	276
11	Stability of fabricated nanostructures	279
12	Investigation of catalytic effects	281
12.1	Motivation	281
12.2	Exclusion of autocatalytic growth for TTIP at RT	283
12.3	Exclusion of EBISA for catalytic decomposition of TTIP	286
12.4	Summary and conclusions	289
13	EBID with TTIP as a tool for local protective capping of nanostructures	291
13.1	Motivation for capping nanostructures	291
13.2	Local capping of iron nanostructures	293
13.3	Protection of capped iron nanostructures from oxidation upon exposure to ambient conditions	300
13.4	Summary and conclusions	303
14	Summary	305
15	Zusammenfassung	309

16	Appendixes	313
16.1	Chapter 3 – Experimental	313
16.1.1	Precursor storage devices	313
16.1.2	Lithographic parameters of the SmartSEM imaging software.....	314
16.1.3	Experimental parameters	316
16.1.4	Normalization and quantitative analysis of Auger spectra	319
16.1.5	Reference AE spectra	322
16.1.6	Attenuation lengths.....	323
16.2	Chapter 5 – Purification of TTIP.....	325
16.2.1	Reference mass spectra of isopropanol and acetone.....	325
16.2.2	Hydrocarbon precursor fragments.....	325
16.2.3	Experimental details for an exemplary precursor purification	327
16.2.4	Titanium containing precursor fragments	328
16.3	Chapter 6 – Flux distribution of TTIP	331
16.4	Chapter 9 – Post-treatment procedures.....	332
16.5	Chapter 10 – Morphology of EBID deposits.....	334
16.6	Chapter 11 – Stability of fabricated nanostructures.....	336
16.7	Chapter 13 – Local protective capping of nanostructures.....	338
17	References	339

List of abbreviations

AE	Auger electron
AELS	Auger electron line scan
AES	Auger electron spectroscopy
AFM	Atomic force microscopy
ALD	Atomic layer deposition
ALE	Atomic layer epitaxy
ASCII	American standard code for information interchange
BSE	Backscattered electron
CL	Cathodoluminescence
COST	Coopération européenne dans le domaine de la recherche scientifique et technique / European cooperation in science and technology
CRR	Constant retard ratio
C-SEM	Continuous secondary electron multiplier
CVD	Chemical vapor deposition
DAC	Digital to analog converter
DCI-MS	Desorption chemical ionization mass spectrometry
EBID	Electron beam induced deposition
EBIE	Electron beam induced etching
EBIH	Electron beam induced heating
EBISA	Electron beam induced surface activation
EBL	Electron beam lithography
ECCL	Electron controlled chemical lithography
EDX	Energy dispersive X-ray spectroscopy
ESD	Electron stimulated desorption
ESF	European science foundation
EUV	Extreme ultraviolet
EUVL	Extreme ultraviolet lithography
FEB	Focused electron beam
FEBID	Focused electron beam induced deposition
FEBIP	Focused electron beam induced processing
FIB	Focused ion beam
FIBID	Focused ion beam induced deposition

FSE	Forward scattered electron
FWHM	Full width at half maximum
GIS	Gas injection system
IGP	Ion getter pump
LEED	Low energy electron diffraction
MC	Monte Carlo
MOCVD	Metal-organic chemical vapor deposition
MOSFET	Metal-oxide-semiconductor field-effect transistor
PBN	Pyrolytic boron nitride
PCI	Peripheral component interconnect
PE	Primary electron
PECVD	Plasma enhanced chemical vapor deposition
PEEM	Photoelectron emission microscopy
PET	Polyethylene terephthalate
QMS	Quadrupole mass spectrometry
RT	Room temperature
SAM	Scanning Auger electron microscopy
SE	Secondary electron
SE1	SE excited by a PE
SE2	SE excited by a BSE
SE3	SE excited by a BSE that impinged parts of the specimen chamber
SEM	Scanning electron microscopy
SIMS	Secondary ion mass spectroscopy
SQUID	Superconducting quantum interference device
STM	Scanning tunneling microscopy
TE	Transmitted electron
TEM	Transmission electron microscopy
TMP	Turbo molecular pump
TPMC	Test-particle Monte Carlo method
TSP	Titanium sublimation pump
TTIP	Titanium(IV) tetraisopropoxide
TTL	Transistor-transistor-logic
UHV	Ultra high vacuum
UV	Ultraviolet

XAS	X-ray absorption spectroscopy
X-PEEM	X-ray photoelectron emission microscopy
XPS	X-ray photoelectron spectroscopy

List of symbols

I LATIN SYMBOLS

a	Lattice parameter of an overlayer matrix A
A	Area
\bar{c}	Mean particle velocity
d	Diameter or
d	Layer thickness of the overlayer material A
d_A	Area dose
d_D	Dot dose
d_L	Line dose
D	Diffusion constant on a surface
E	Energy
E_A	Auger electron energy
E_{Bg}	Background energy applied in an AELS or SAM measurement
E_F	Fermi level
E_g	Band gap
E_{kin}	Kinetic energy
E_P	Primary energy
E_{Peak}	Peak energy applied in an AELS or SAM measurement
E_{VAC}	Vacuum level
g	Sticking probability of the precursor molecule on the surface
I_A	Intensity of electrons from the overlayer A for the layer thickness d
I_A^∞	Intensity acquired from a specimen of pure material A
I_B	Electron beam current or
I_B	Intensity of electrons from the substrate B below the overlayer A
I_B^∞	Intensity acquired from a specimen of pure material B
I_{BSE}	Current caused by BSEs
I_{PE}	Current caused by PEs
I_{SE}	Current caused by SEs
I_{SE1}	Current caused by SE1
I_{SE2}	Current caused by SE2

J	Particle flux
J_{tot}	Total particle flux
k	Boltzmann constant ($k = 1.38 \cdot 10^{-23} \text{ J K}^{-1}$)
Kn	Knudsen number
L_r	Reduced tube length
m	Mass
M	Molar mass
n	Amount of substance
N	Number of particles
N_A	Avogadro constant ($N_A = 6.022 \cdot 10^{23} \text{ mol}^{-1}$)
N_P	Number of points
N_S	Number of sweeps
p	Pressure
q_m	Mass throughput
q_n	Amount of substance throughput
q_N	Number of particles throughput
q_{pV}	pV-Throughput
q_V	Volume throughput
\dot{Q}	Throughput of a vacuum pump
R	Universal gas constant ($R = 8.31451 \text{ J mol}^{-1} \text{ K}^{-1}$)
s	Scan speed
s_A	Area step size
s_L	Line step size
S	Pumping speed of a vacuum pump
S°	Standard molar entropy
t	Time
t_{add}	Additional gas dosage time
t_{ALD}	Active line duration
t_D	Dwell time (pixel time)
t_{exp}	Exposure time
t_{repl}	Replenishment time
t_{TLD}	Total line duration
t_{wait}	Waiting time
T	Temperature

T_{\max}	Maximum temperature
U	Voltage
U_B	Beam voltage
U_C	Cathode voltage of the QMS
U_{SEM}	Secondary electron multiplier voltage of the QMS
v_B	Electron beam velocity
V	Volume
x_{LT}	Position of the linear translator actuating the dosing nozzle
Z	Atomic number or
Z	Averaged atomic number of the overlayer matrix A
1Z_W	Number of particle collisions per time unit onto the unit area of a wall

II GREEK SYMBOLS

δ	Diameter of a particle (in Chapter 6)
δ	Secondary electron yield
δ_{BSE}	Secondary electron yield for SE2
δ_{PE}	Secondary electron yield for SE1
Δr	Increment of the radius
ΔG_f°	Standard molar formation free enthalpy
ΔH_f°	Standard molar formation enthalpy
ΔS_f°	Standard molar formation entropy
η	Viscosity (in Chapter 6)
η	Backscattering coefficient
θ	Angle between surface normal and electron spectrometer
λ	Mean free path
λ_{AL}	Attenuation length
$\lambda_{\text{AL}}^A(E_A)$	Attenuation length of electrons with energy E_A in the overlayer A
$\lambda_{\text{AL}}^A(E_B)$	Attenuation length of electrons with energy E_B in the overlayer A
λ_{IMFP}	Inelastic mean free path
μ	Average atomic mass per mol of the overlayer matrix A

ν	Frequency of a photon
π	Archimedes' constant ($\pi = 3.14159$)
ρ	Density
σ	Cross-section
τ	Residence time of the precursor molecule on the surface
Φ	Work function

1 Introduction

Driven by the steady demand for continuing miniaturization and triggered by the finding that physical and chemical properties of materials drastically change when particle size or film thickness are reduced down to the nanometer scale, a new technology developed since the end of last century. This technology, today generally denoted as “nanotechnology”, deals with objects that have a size of less than 100 nm at least in one dimension [1]. In the last decades, increasing efforts were made to enable the controlled fabrication of well-defined nanostructures and to understand in particular phenomena related to the size. In addition, numerous techniques were developed that allow for the synthesis, manipulation and characterization of materials on the nanometer and sub-nanometer scale [1]. Today, nanotechnology is regarded as one of the most important technologies for the generation of novel materials and for applications that find entrance into daily life, covering the fields of communication, energy generation, health, leisure, traffic and environment [1].

One nanofabrication technique is electron beam induced deposition (EBID) [2-5]. In this mask-less, “direct-write” method, an electron beam is used to locally fabricate nanostructures by the dissociation of adsorbed precursor molecules. The technique features outstanding advantages compared to other techniques. These are e.g. the generation of structures on the very low nanometer scale, the precise position control during fabrication, the realization of arbitrary shapes and the large variety of applicable precursors for the deposition of various materials [5].

A highly interesting and fascinating material, which is used in many applications in industry, science and everyday life, is titanium dioxide (titania, TiO_2) [6]. Important applications are, e.g., the use as heterogeneous catalyst, as photocatalyst, in solar cells, as gas sensor, as white pigment, as coating, in ceramics, in diverse electric, electronic and electrochromic devices, in Li-based batteries and for the photo-assisted degradation of organic molecules [6]. Additionally, in the last decades, an increasing interest and progress in the fabrication of titania nanostructures could be observed [6, 7]. Many techniques have been developed for the generation of TiO_2 nanostructures, and the investigation of their properties, possibilities for nanomaterial modifications (e.g. by doping or sensitization) and various applications in the fields of photocatalysis, photovoltaics, photocatalytic water splitting, electrochromic devices,

hydrogen storage and sensing are reported in a large number of publications (see review article [7]).

In this work, the technique EBID was applied to locally fabricate well-defined titanium oxide nanostructures on Si(100) and Au(111) surfaces with the precursor titanium(IV) tetraisopropoxide (TTIP) under ultra high vacuum (UHV) conditions. Silicon was the substrate of choice since it is a standard material in semiconductor industry. In addition, a gold single crystal was used for EBID because the system gold / titanium dioxide has attracted significant attention after the discovery of CO oxidation at low temperature by finely dispersed Au nanoparticles supported on TiO₂ [6, 8, 9]. Therefore, the fabrication of well-defined titanium oxide nanostructures on a gold support, which might feature promising catalytic properties, was further motivation for this work. The compound TTIP is a well-known and frequently used precursor in chemical vapor deposition (CVD), generally applied for the direct fabrication of titanium dioxide films [10-15]. However, in EBID the use of TTIP as precursor is rare, up to now [16-18].

An important aspect of the thesis at hand was to perform EBID under ultra clean conditions, i.e. UHV conditions. In this 'surface science approach' to EBID a clean and well-defined sample surface can be prepared and maintained. Secondly, it enables to study the EBID process with a negligible influence of residual gases (e.g. water and hydrocarbons). By this approach, the generation of well-defined and "clean" deposits, i.e. here titanium oxide nanostructures, was envisaged.

In this work, two main challenges of EBID were addressed. The first task was the fabrication of deposits with defined chemical composition. This is often difficult since EBID deposits are typically contaminated with carbon and oxygen stemming either from the precursor itself or from residual gases. Secondly, material deposition by an unwanted side effect of EBID, the so-called proximity effects, was investigated. Both challenges of EBID were addressed with certain post-treatment procedures.

When getting started, it was important to characterize and purify the dosed precursor gas TTIP since the compound tends to decompose. In order to clean the gas, a purification procedure was developed, which led to a gas composition enabling the deposition of titanium and oxygen containing structures (see Chapter 5).

Important parameters of EBID are the flux distribution, the precursor flux and the actual precursor pressure directly at the sample surface during EBID. To estimate

these parameters in the applied setup, Monte Carlo (MC) simulations were performed with the software 'GIS Simulator' [19] (see Chapter 6).

The structure, shape and chemical composition of EBID deposits from TTIP were studied thoroughly via scanning electron microscopy (SEM) and local Auger electron spectroscopy (AES). In addition, the contrast mechanisms in SEM in dependence of the substrate material were investigated (Chapter 7). To study the consequences of the proximity effects in EBID, deposits and their close surrounding on silicon and gold were characterized via SEM and AES. MC simulations of the electron/substrate interaction in both specimens via the software 'CASINO' [20] helped to understand the experimental results (see Chapter 8).

Post-treatment procedures, developed to remove unintended deposits caused by proximity effects, to reduce the lateral size of EBID structures and to possibly reduce their carbon content are presented in Chapter 9. These are (moderate) sputtering, annealing in oxygen and as a novel two-step post-treatment procedure a combination of both, which enables the generation of clean localized nanostructures.

In Chapter 10, the morphology of EBID deposits was investigated, and particularly the influence of the process regime and the lithographic parameters was considered. An extensive topography investigation, including both the lateral and vertical size of dot, line and area structures, allowed to estimate the number of primary electrons needed to deposit one atom via EBID with TTIP on silicon.

While the stability of fabricated titanium oxide nanostructures is briefly addressed in Chapter 11, catalytic effects with the precursor TTIP were investigated in Chapter 12. Here, the possibility of autocatalytic growth of EBID deposits at room temperature (RT) upon additional gas dosage and the possibility of surface activation for the catalytic decomposition of TTIP were studied.

Finally, an application for EBID with the precursor TTIP was investigated. The local generation of a thin titanium and oxygen containing capping layer on an iron line structure by successive EBID with the two precursors $\text{Fe}(\text{CO})_5$ and TTIP was studied. The intention of this project was to protect the metallic iron structures and to avoid oxidation of the latter upon exposure to ambient conditions (see Chapter 13).

To summarize, in this work the local fabrication of well-defined titanium oxide nanostructures on Si(100) and Au(111) surfaces via EBID with the precursor TTIP under UHV conditions is reported. Two main challenges of the EBID technique were

successfully addressed via post-treatment processing, namely a well-defined chemical composition and the unintentional broadening of the structures due to proximity effects.

2 Fundamentals, techniques and ingredients

In this chapter, fundamentals and the applied techniques are described. The latter are the nanofabrication technique of electron beam induced deposition (EBID) and the surface science and analysis techniques scanning electron microscopy (SEM), Auger spectroscopy and spectromicroscopy (AES, AELS and SAM), atomic force microscopy (AFM), quadrupole mass spectrometry (QMS), low energy electron diffraction (LEED) and sputtering (Chapters 2.1 - 2.7). In addition, the ingredients used in this work, namely the substrates silicon, silicon oxide (on silicon) and gold, and the precursors titanium(IV) tetraisopropoxide (TTIP) and iron pentacarbonyl ($\text{Fe}(\text{CO})_5$), are briefly described (Chapter 2.8).

2.1 Electron beam induced deposition (EBID)

Electron beam induced deposition (EBID) is a mask-less, “direct-write” technique, which enables the local fabrication of structures on the micro- or nanometer scale [2-5]. Generally, a highly focused electron beam from a scanning electron microscope (SEM) or a transmission electron microscope (TEM) is used to locally decompose adsorbed precursor molecules. The latter are dissociated into non-volatile and volatile fragments by the interaction with primary electrons (PEs) from the microscope, surface released secondary electrons (SEs) and backscattered electrons (BSEs) with different cross-sections. While the non-volatile fragments stay on the surface and locally form the intended deposit, the volatile fragments and unexposed, intact precursor molecules desorb and are pumped off the vacuum chamber. A schematic drawing of the ideal EBID process with an arbitrary precursor molecule is depicted in Figure 2.1.

The nature of the deposit depends on the used precursor compound. Choosing a suitable precursor enables the fabrication of deposits containing metals, metal oxides, or “just” carbon [2-5]. In practice, a large variety of precursors has already been used for EBID and the generation of deposits consisting of a multitude of materials has been targeted up to now. A brief overview for used precursors and targeted materials is given in Chapter 4.1.

Methodologically, EBID belongs to the “family” of focused electron beam induced processing (FEBIP) [5]. The latter also comprises, for instance, the techniques of

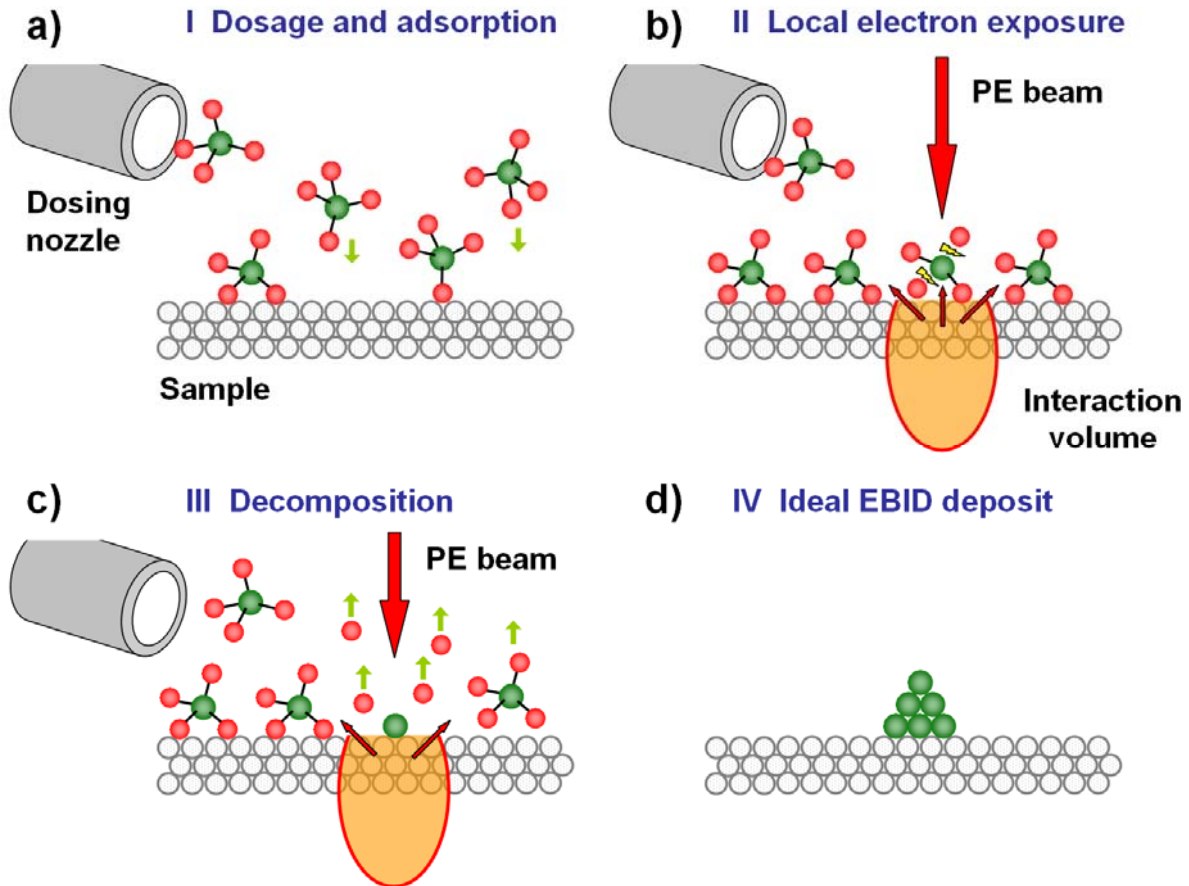


Figure 2.1: Schematic drawing of the ideal EBID process with an arbitrary precursor molecule. a) Dosage of the precursor and adsorption on the sample surface. b) Local exposure of the surface with an electron beam. c) Local decomposition of precursor molecules by PEs, SEs and BSEs and desorption of volatile fragments and unexposed precursor molecules. d) Ideal EBID deposit composed of the pure target material at the intended position.

electron beam induced etching (EBIE) [2], electron beam induced heating (EBIH) [21] and electron beam induced surface activation (EBISA) [22, 23].

Further information concerning EBID, including “discovery”, advantages and disadvantages, precursor molecules, achievable materials and possible applications, are given in Chapter 4.1. In addition, significant aspects concerning EBID, namely proximity effects and strategies for generating materials of high purity, which are both relevant for this work, are described in the Chapters 4.2 and 4.3. The interested

reader is further referred to the comprehensive review articles of Randolph *et al.* [2], Silvis-Cividjian and Hagen [3], Utke *et al.* [4] and van Dorp and Hagen [5].

2.2 Scanning electron microscopy (SEM)

Scanning electron microscopy (SEM) is an imaging technique, which enables the investigation of specimen surfaces with a resolution down to the sub-nanometer scale. Generally, a focused electron beam is scanned across the sample surface and signals released from the surface are detected and used for image generation. Compared to optical microscopy with a resolution limit of $\approx 0.2 \mu\text{m}$ and a depth of focus of $\approx 0.1 \mu\text{m}$ [24], scanning electron microscopy has a much better performance. In modern SEM instruments, the lateral resolution is typically in the sub-nanometer or very low nanometer range, high depths of focus can be realized [24] and images with high contrasts can be acquired. Beside the outstanding lateral resolution and depth of focus a major advantage of SEM is that a large variety of electron-specimen interactions can be used to generate the image and to acquire qualitative and quantitative information [25]. The applied signals are secondary electrons (SEs), backscattered electrons (BSEs), Auger electrons (AEs), transmitted electrons, the specimen current, characteristic X-rays and ultraviolet, visible and infrared light (cathodoluminescence). Figure 2.2 a) sketches the interaction volume of the impinging primary electron beam with the specimen and the regions from which the different signals originate [25] while in Figure 2.2 b) the applicable signals are schematically depicted [24]. The electron escape depths noted in Figure 2.2 a) are taken from reference [26].

The principle setup of an SEM is sketched in Figure 2.3. Generally, an SEM consists of a vacuum system, an electron-optical column, a deflection system and one or several detector systems [27]. An important requirement for SEM operation is that vacuum conditions exist. Concerning the vacuum system one can distinguish between SEMs operating at low vacuum (environmental SEMs), at high vacuum conditions and in ultra high vacuum. In the electron-optical column, the primary electron beam is generated and focused by several lenses. For electron emission several cathode systems are available, i.e. thermal electron sources (W ($\approx 2,800 \text{ K}$), LaB₆ ($\approx 1,800 \text{ K}$), CeB₆ ($\approx 1,800 \text{ K}$)), field emission sources (working at RT), Schottky

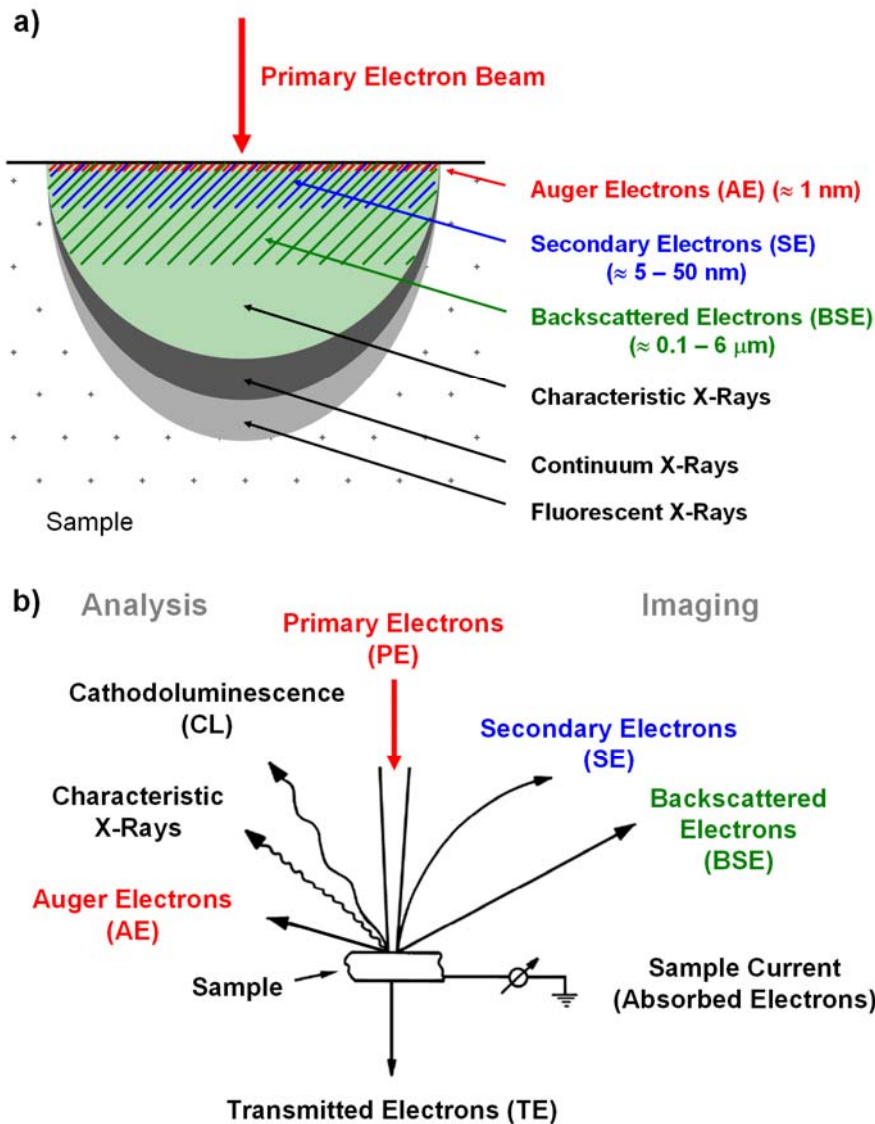


Figure 2.2: a) Interaction volume of the impinging primary electron beam with the specimen and regions from which the different signals originate [25]. The electron escape depths are taken from reference [26]. b) Usable signals for imaging and qualitative and quantitative surface analysis [24].

field emission sources ($\approx 1,800$ K) and thermal field emission sources ($\approx 1,800$ K) [27]. The first step of focusing is realized by a Wehnelt cylinder surrounding the filament, which is kept at a negative potential (bias voltage). The emitting primary electrons are then accelerated by an anode, typically to primary beam energies between 0.1 and 50 keV [25]. Via one or two condenser lenses the electron beam is further focused and downscaled to the final electron beam diameter and via an objective lens the beam is focused onto the specimen surface. The electron beam

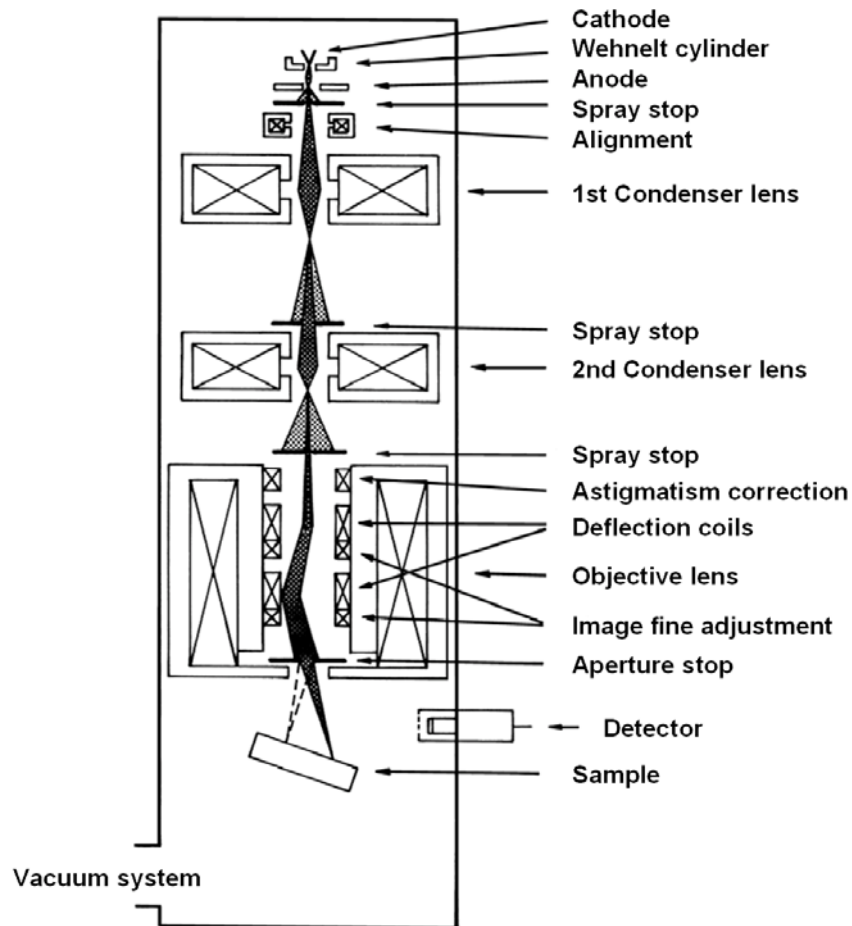


Figure 2.3: General setup of a scanning electron microscope [27].

quality is optimized by the aperture stop, which also determines the depth of focus. For beam deflection during the scan process two deflection coils are used, each for one lateral direction. Finally, the released signals from the substrate surface are detected via a detector system. Depending on the information to be acquired a large variety of detectors is available. The most important ones for imaging are detectors for SEs and BSEs while for chemical analysis detectors for AEs and characteristic X-rays are most widely used [27].

For imaging in SEM, a large variety of different contrasts can be used. They depend on several parameters like the detected signal (e.g. SE or BSE), the applied primary electron energy, the specimen tilt, the specimen structure, the collected angular range of emitted electrons and the detector configuration [25, 28]. A comprehensive description and explanation of the different contrasts in SEM is particularly given in the reference book from Reimer [25]. Generally, the following types of image

contrasts are distinguished: topographic contrast, material contrast, crystal orientation and channeling contrast, magnetic contrast, voltage or potential contrast and charging contrast [25]. Some of these contrast types are signal specific, i.e. peculiar for SE or BSE, but some types can also occur for both signals. A common complication of data interpretation is that different types of contrast can be superimposed in SEM images.

In this work, exclusively the 'secondary electron imaging mode' was applied with an 'in-lens detector' located in the electron column of the SEM instrument. For this mode, the 'topographic contrast' and the 'material contrast' are the most important contrasts [25]. They are briefly described in the following.

The topographic contrast in SE images is generally caused by several contrast mechanisms [25], which can also be superimposed. The latter are the surface-tilt contrast, the shadowing contrast, the BSE diffusion contrast, the SE diffusion contrast and the mass-thickness contrast. The surface-tilt contrast results from the dependence of the secondary electron yield δ on the angle between the incident beam and the surface normal either of the sample or the investigated structures on the sample. Generally, this contrast mechanism causes enhanced emission of SEs from edges ('edge effect') and small particles. The shadowing contrast, which is generally superimposed on the surface-tilt contrast, results from the fact that less SEs are detected from sides pointing into the opposite direction of the detector since electrons released from there "simply" do not reach the detector. The BSE and SE diffusion contrasts are based on electron scattering events at edges, which also cause increased signal intensity at edges ('edge effect') and small particles. The mass-thickness contrast appears in films of certain thickness coating the specimen surface and also influences the topographic contrast [25].

The material contrast in SE images is caused by local variations of the secondary electron yield δ due to different materials being present in the investigated section of the sample. Two reasons can be stated for this effect. First, the yield of SEs excited by high energetic PEs (SE1) increases monotonically with the atomic number Z . Secondly, also the yield of SEs released by BSEs (SE2) strongly increases with increasing atomic number, since the backscattering coefficient η shows this behavior. The latter is clearly the main contribution for the described effect [25].

For further details about scanning electron microscopy the interested reader is referred to the excellent reference book from Reimer [25] and to the references [24,

26-28]. Detailed information concerning the energy distribution, the angular distribution, the yield and the escape depth of SEs from metals and insulators and more information about SEs in the SEM, e.g. SE detectors, SE contrast mechanisms and lateral resolution, is further given in the article from Seiler [29]. In addition, the basics of SEM were recently described in detail by Thomas Lukasczyk [30].

2.3 Auger spectroscopy and spectromicroscopy (AES, AELS and SAM)

Auger electron spectroscopy (AES) is a standard technique in surface science for the qualitative and quantitative chemical analysis of specimen surfaces. The technique is characterized by a very high surface sensitivity, a high sensitivity for chemical elements with low atomic number (like e.g. carbon or oxygen) and the possibility to perform it locally with high spatial resolution.

The basic process of AES is the Auger electron process, which was first described by Lise Meitner in 1922 [31] and by Pierre Auger in 1925 [32, 33]. It is schematically depicted in Figure 2.4 [34]. Figure 2.4 a) shows the energy level diagram of the ground state of an atom, Figure 2.4 b) the excitation and relaxation of the atom and Figure 2.4 c) the doubly ionized final state. In the initial step of the Auger process, a core hole is created in the target atom by ionization (here in the K level). This process can be initiated either by impinging electrons, ions or X-rays with a primary energy E_P . In the following of this chapter, only ionization caused by electrons is considered. Core hole generation occurs efficiently when the primary energy E_P of the incident electron is at least 5 times higher than the binding energy of the core hole electron (here denoted as E_K) [34]. The ionized, excited atom relaxes by filling the core hole with an electron from an outer shell and thus higher energy level (here from the L_1 level). Consequently, as a result of this transition, energy becomes available, which corresponds to the energy difference of both levels, i.e. $E_K - E_{L_1}$ in Figure 2.4. This energy can either be released in the form of a characteristic X-ray photon of energy $h\nu = E_K - E_{L_1}$ (X-ray fluorescence) or it can be transferred radiationless to another electron either from the same (L_1) or from another level (e.g. $L_{2,3}^*$ in Figure 2.4), which is then ejected from the atom (Auger electron emission). Its characteristic kinetic energy is $E_{kin} = E_K - E_{L_1} - E_{L_{2,3}^*}$ (in relation to the reference

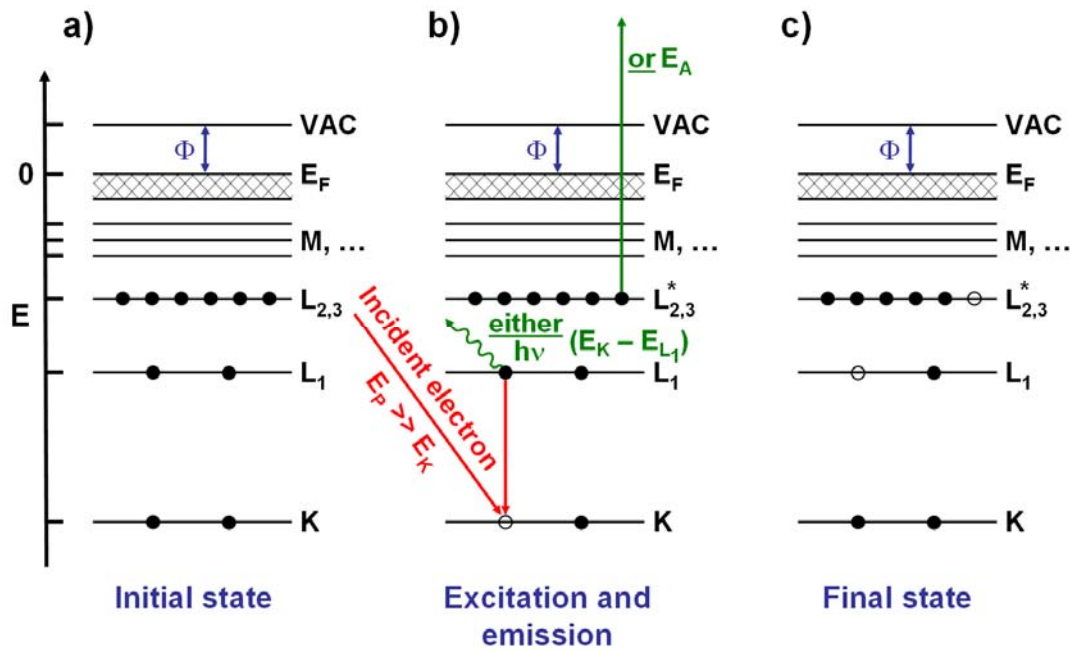


Figure 2.4: Schematic description of the Auger process showing the energy level diagram of a) the ground state, b) the ionized, excited state and c) the doubly ionized final state (adapted from reference [34]). Φ is the work function of the atom ($\Phi = E_{VAC} - E_F$). The reference level is E_F (0 eV).

level E_F). The released electron in that case is denoted ‘Auger electron’ and its kinetic energy ‘Auger electron energy’ E_A . Finally, a doubly ionized atom is left, which corresponds to the final state of the Auger process (see Figure 2.4 c)). The energy level $L_{2,3}^*$ is starred because it is not the binding energy of $L_{2,3}$ in the ground state but the binding energy of $L_{2,3}$ in an excited state with the presence of a core hole in L_1 [34]. In Figure 2.4 b), both possible processes, i.e. X-ray fluorescence and Auger electron emission, are indicated in green.

After initial core hole generation in an atom, only one of the described processes can occur. Thus, X-ray fluorescence and Auger electron emission are competing processes with certain process probabilities. The relative probability of relaxation for each process strongly depends on the atomic number Z and the shell, in which the initial core hole is generated. Generally, the relaxation probability by Auger emission is strongly favored over that of X-ray fluorescence “for relatively shallow core levels, i.e. with binding energies below about 2 keV” [34]. This holds for K shell ionization, but for L, M, N, ... atomic levels, as well. Figure 2.5 depicts e.g. the relative probability of relaxation after the initial generation of a core hole in the K shell [34].

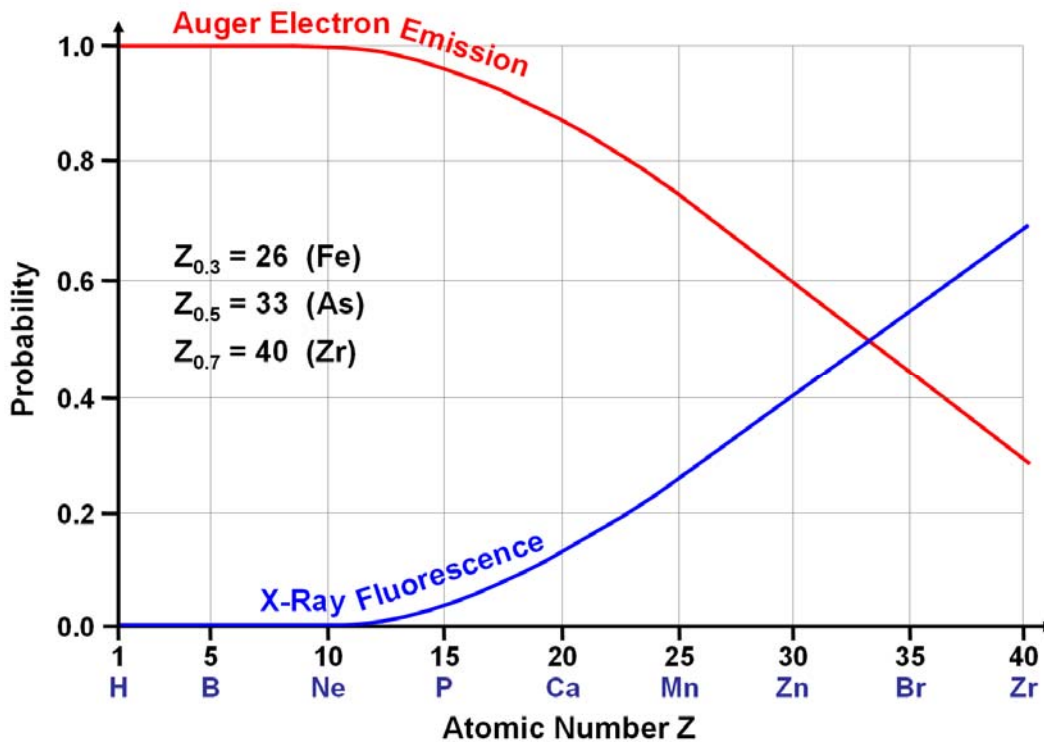


Figure 2.5: Relative probabilities of relaxation by Auger electron emission or X-ray fluorescence after the initial generation of a core hole in the K shell (adapted from reference [34]).

The Auger process is a process in which three electrons are involved. Therefore, three characters are used to describe it. The first one represents the generated core hole level, the second one the level of the electron filling up the hole and the third one represents the level from which the Auger electron is ejected. Consequently, the process depicted in Figure 2.4 is denoted as $KL_1L_{2,3}$ Auger process [34, 35].

Considering the kinetic energy of the emitted Auger electron, i.e. $E_K - E_{L_1} - E_{L_{2,3}^*}$ for the process shown in Figure 2.4, one finds that it is only depending on the binding energies of the involved electrons from the target atom and independent from the primary energy E_P . This means that for each element with $Z > 2$ there is a distinct series of Auger electron energies, which are characteristic for this chemical element. Thus, chemical analysis is possible by elemental identification via the measured Auger energies [34, 35].

With modern SEMs in combination with an electron energy analyzer and the use of highly focused electron beam sources for AES, local Auger electron spectroscopy becomes possible.

However, when performing local AES one has to keep in mind that inevitably a phenomenon called 'background contribution' occurs. It means that Auger electrons are always released from a wider area than the one that is irradiated by the primary electron beam, i.e. also from the close surrounding. The reason for that is the excitation of Auger electrons by backscattered, high energy primary electrons stemming from the interaction volume of the impinging PE beam with the specimen (see Figure 2.2 a)) [36-38]. Therefore, the maximum range from which 'background contribution' is to be expected is given by the size of the area from which BSEs leave the surface, which is generally called 'BSE exit area' and depends on the substrate material and the PE energy. When performing local AES on very small structures (i.e. on the nanometer scale) the consequence of the phenomenon of 'background contribution' is that Auger signals from elements present in the surrounding of the structure can appear in the spectrum although the focused PE beam was directed only on the structure itself. This generally unwanted effect is well-known in the characterization of nanostructures and nanoparticles via Auger based analysis tools (AES, SAM) and is also reported in literature [36-38]. The lateral area of the sample surface from which the analytical signal is detected and the lateral resolution for AES can be determined from an ISO standard [39].

In this work, the effect of 'background contribution' was observed and examples can be found in the Chapters 9.2, 9.3 and 13.2.

For the local, chemical analysis of surfaces, particles and structures also the spectromicroscopic techniques of Auger electron line scans (AELS) and of scanning Auger electron microscopy (SAM) can be applied. Both techniques allow for elemental mapping either along the path of a line (in AELS) or in a certain region of the surface (in SAM).

To acquire locally resolved element-specific information, the electron energy analyzer is used to detect the intensity of electrons of one specific, pre-defined kinetic energy which is characteristic for the element of interest, while the PE beam is scanned. Typically, the kinetic energy of an Auger peak is used (E_{Peak}) here. Additionally, at each point of the scan the intensity of electrons of an energy characterizing the

background of a signal in a characteristic Auger spectrum (E_{Bg}) is detected. By intensity subtraction (intensity at E_{Peak} minus the intensity at E_{Bg}) an intensity value is acquired at each point of the scan which is characteristic for the element of interest. This means that the acquired profile in AELS and the acquired gray scale micrograph in SAM show directly the distribution of the element along the scanned path or in the scanned region.

For further details concerning the technique of Auger electron spectroscopy the interested reader is referred to the excellent reference book from Briggs and Seah [34]. In addition, a very useful collection of Auger spectra for most of the elements of the periodic table is given in the 'Handbook of Auger Electron Spectroscopy' from Davis *et al.* [40].

2.4 Atomic force microscopy (AFM)

Atomic force microscopy (AFM) is a scanning probe microscopy technique that enables to map the surface topography on the very low nanometer or even atomic scale. It was invented by Binnig, Quate and Gerber in 1986 [41] and finds wide application in science today.

The basic principle of AFM operation is similar to that of scanning tunneling microscopy (STM), which was introduced some years before [42]. A sharp tip, located at the very end of the so-called cantilever, is used to scan a surface in a point-by-point fashion. At each position of the surface, the AFM senses the forces between tip and sample [43]. Relevant short range forces are dipole-dipole interaction forces and friction forces while van der Waals forces, capillary forces (only in air) and electrostatic forces are the ones with long range [44]. These interatomic forces cause the cantilever to deflect and the vertical cantilever displacement is measured by a deflection sensor [43] and exploited to generate an image of the surface topography. Different detection schemes can be used to sense the small cantilever deflections with a typical accuracy of 1 pm. They range from measuring the tunneling current between an STM tip and the conductive rear side of the cantilever, measuring the reflection of a laser beam from the cantilever rear side, using optical interferometry, measuring the capacitance between the cantilever and an electrode

close to its rear side or using piezoresistance or piezoelectricity [43, 44]. The setup of a typical atomic force microscope, using laser beam deflection as detection scheme, is schematically depicted in Figure 2.6.

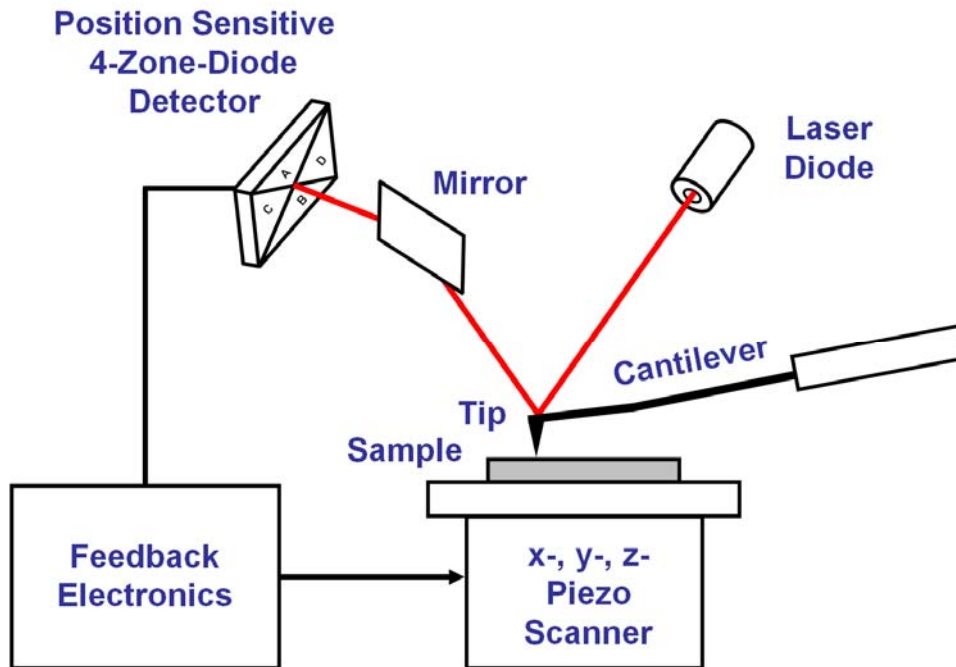


Figure 2.6: Schematic setup of a typical atomic force microscope (AFM) using laser beam deflection as detection scheme (image adapted from references [43-46]). The beam is reflected from the cantilever rear side, deflected by a mirror and usually detected by a position sensitive 4-zone-diode detector.

The main advantage of AFM is that the method provides accurate height information of the surface and supported structures. In addition, further advantages are the outstanding lateral resolution (atomic resolution possible) and the fact that AFM operation is not restricted to conductive samples (like STM) but is applicable for all types of samples, no matter whether they are conducting, semiconducting or insulating [43]. The AFM sensitivity is in the order of $10^{-13} - 10^{-8}$ N. This enables the direct measurement of van der Waals interactions [45]. Operation is also possible at ambient conditions and in a liquid environment.

For AFM, a large variety of different modes of operation can be used, and the choice of the operating mode typically depends on the substrate material and the information to be acquired from the sample. Generally, one distinguishes between static and dynamic AFM modes. The most important modes of operation are the contact mode (static mode, either in the constant-height or constant-force mode), the non-contact mode (dynamic mode) and the tapping mode (dynamic mode, also denoted as intermittent mode).

Since in this work only one mode of operation was applied, i.e. the dynamic force mode, only this one is briefly described in the following. For details concerning the other operating modes the interested reader is referred to the comprehensive AFM literature (see below).

In the dynamic force mode, the stiff AFM cantilever is vibrated close to its resonance frequency and scanned at a certain distance to the sample surface. During the scan, the oscillation amplitude of the cantilever is influenced by the forces occurring between tip and sample surface. This is exploited for image generation. A control unit is used to keep the oscillation amplitude constant by changing the distance between cantilever and surface. The topographical image is then generated from the vertical displacement of the cantilever by the control unit. The advantages of the dynamic force mode compared to the contact mode are that lateral forces (like friction forces) do not occur and that less mechanical damage is done both to the sample surface and to the AFM tip.

For a comprehensive description and further details concerning atomic force microscopy the interested reader is referred to the reference books from Meyer *et al.* [47] and Wiesendanger [48] and the review articles from García and Pérez [49] and Giessibl [50].

2.5 Quadrupole mass spectrometry (QMS)

Mass spectrometry is a technique for the analysis of chemical compounds in the gas phase. When a substance is analyzed, the relative molecule mass and elemental composition can be determined [51]. Further, the obtained fragmentation pattern of a compound provides information concerning its structure [51].

Generally, a mass spectrometer consists of four different functional devices. These are the substance supply, the ion generation, the mass separation and the ion detection. Except for the substance supply, at least high vacuum conditions are necessary. Analysis is performed by the ionization of atoms or molecules, typically by electron impact ionization. The ions are then accelerated by a high voltage towards a mass filtering device which allows for separation of the ions according to their mass to charge ratio (m/z). For a specific adjustment of the filter device only ions with one specific m/z ratio can pass the filter and reach the detector. A complete mass spectrum is taken by changing the filter adjustments such that ions of all possible m/z ratios can successively pass the device. For each m/z ratio the number of detected ions results in a signal and the plot of all signal intensities vs. the corresponding m/z ratio leads to the complete QM spectrum [30].

In the work at hand, a quadrupole mass spectrometer (QMS) was applied with a specific mass filtering device. Ions in a QMS are generated by the bombardment of atoms and molecules in the gas phase with low energetic electrons (typically 70 - 100 eV) [52]. In this process, a small amount of atoms and molecules is ionized whereby singly and multiply charged ions are formed. Separation of the generated ions is realized by deflection in electric fields. For this purpose, four parallel aligned metal rods are used (quadrupole). Two rods lying at opposite side to each other are electrically connected, respectively, and to each pair of rods a direct current voltage (U) is applied with a superimposed alternating current voltage ($V \cos(\omega t)$) which is modulated by a radio frequency. Thereby, an alternating electric quadrupole field is generated enabling the ion separation according to their m/z ratio. Passing the filter device is only possible when the oscillating ions are in resonance with the electric field and gain a stable path through the filter. The other ions move on unstable paths and are deflected out of the four-pole-system [30]. At the end of the filter, the ions which passed are detected. For this purpose, e.g. a Faraday cup or a secondary electron multiplier (continuous (C-SEM) or discontinuous) can be used. Typically, channeltrons are applied [51, 52].

The main advantages of QMS instruments are the small, simple and lightweight setup and the user-friendly operation [51]. Therefore, they are frequently used. The characteristic setup of a QMS is schematically shown in Figure 2.7.

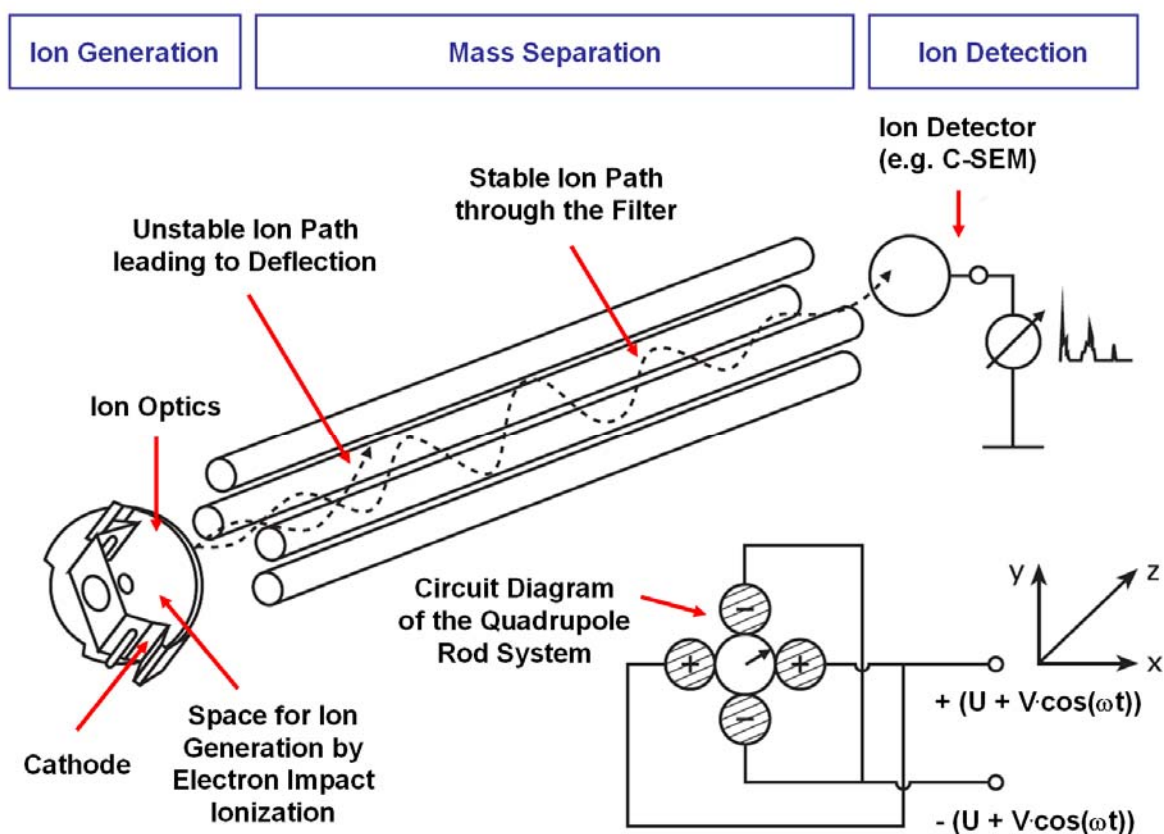


Figure 2.7: Schematic drawing of the characteristic setup of a quadrupole mass spectrometer (QMS) [52].

In the work at hand, QMS was applied to analyze the composition of the residual gas inside the chambers of the UHV instrument and to analyze the purity of applied gases in all experiments. Moreover, QMS was used for *in situ* monitoring of the purification process of the precursor TTIP.

2.6 Low energy electron diffraction (LEED)

Low energy electron diffraction (LEED) is a standard technique in surface science. It allows for the determination of the long range atomic order of a sample surface and makes use of the wave properties of electrons (wave-particle dualism). Low energetic electrons with a kinetic energy typically between 20 and 500 eV are used [53]. Via the de Broglie relation the corresponding wavelength can be determined. It lies between 0.5 and 2.7 Å and is therefore in the range of atomic distances [53]. The

applied low energetic electrons have a small mean free path resulting in a high surface sensitivity of the technique. Constructive interference is observed when the diffracted electron waves are 'in phase' and Bragg's diffraction condition is fulfilled. For this condition, the wavelength of the diffracted electrons corresponds to the lattice distance [46]. A schematic drawing of a typical LEED display system is given in Figure 2.8.

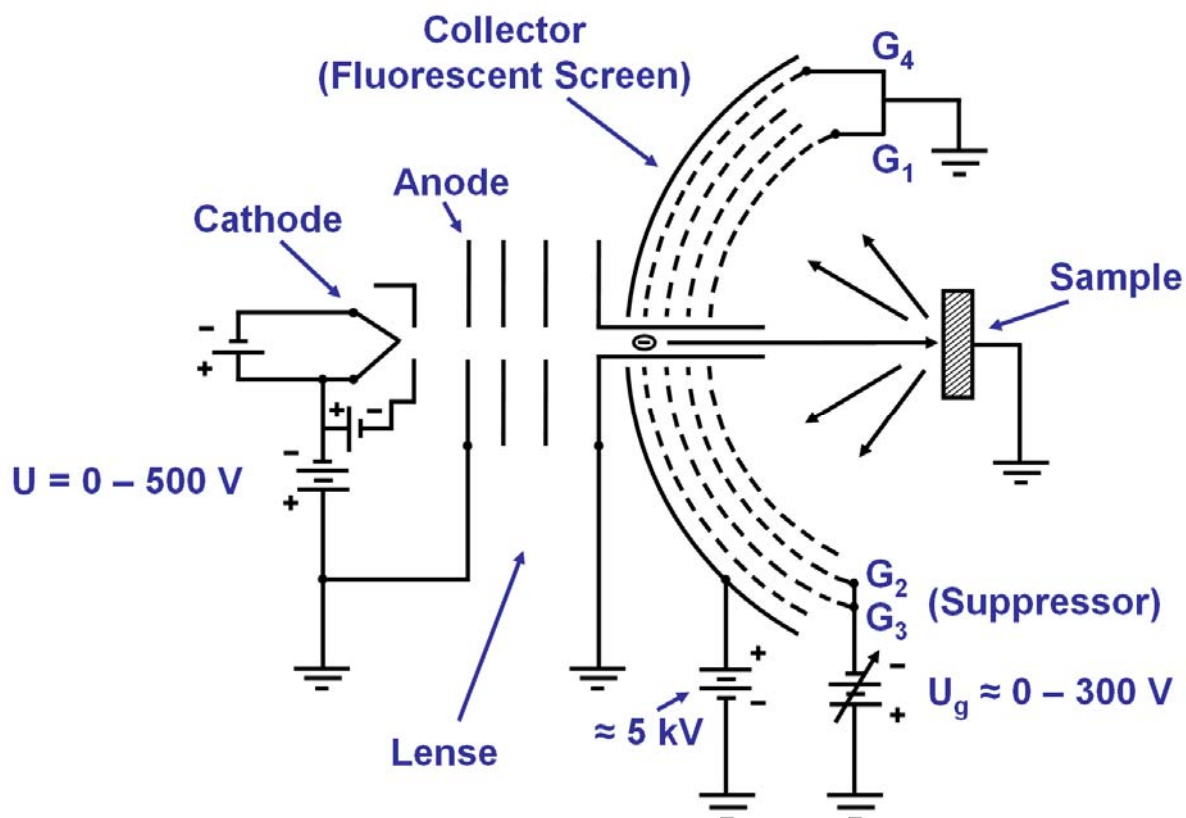


Figure 2.8: Schematic drawing of a typical LEED display system [53].

The low energetic electrons are first accelerated towards the sample and pass a field-free drift tube. After the diffraction process at the sample surface the electrons are accelerated towards a spherical fluorescent screen where they show a diffraction pattern [53]. The latter is a reciprocal representation of the surface lattice [30]. It provides information of the long range order of surface atoms and / or adsorbed molecules. A good long range order is represented by narrow and well-defined diffraction spots. Small spot distances on the screen correspond to large atomic distances on the surface and vice versa [30], and the spot positions with respect to

the central reflection spot of the primary electron beam ((00)-spot) provide the size and form both of the reciprocal and the surface unit cell [54].

In contrast to the unit cell, the surface structure, i.e. the atomic positions in the unit cell, can be derived from the analysis of the diffraction spot intensities as a function of the electron energy. This technique is called LEED I(V) [46, 53, 54]. For further details concerning the techniques LEED and LEED I(V) the interested reader is referred to the references [46, 53, 54].

In the work at hand, LEED was used to verify the quality of the surface before an EBID experiment was performed. LEED measurements were conducted with Si(100) samples and the Au(111) sample.

2.7 Sputtering

Sputtering, or 'ion sputtering', is the process of material removal from a sample surface by its bombardment with energetic (noble gas) ions. In surface science, it is a standard technique for the *in situ* cleaning of samples and the preparation of atomically clean surfaces [43].

A schematic drawing of the setup of a typical 'ion sputter gun' is depicted in Figure 2.9.

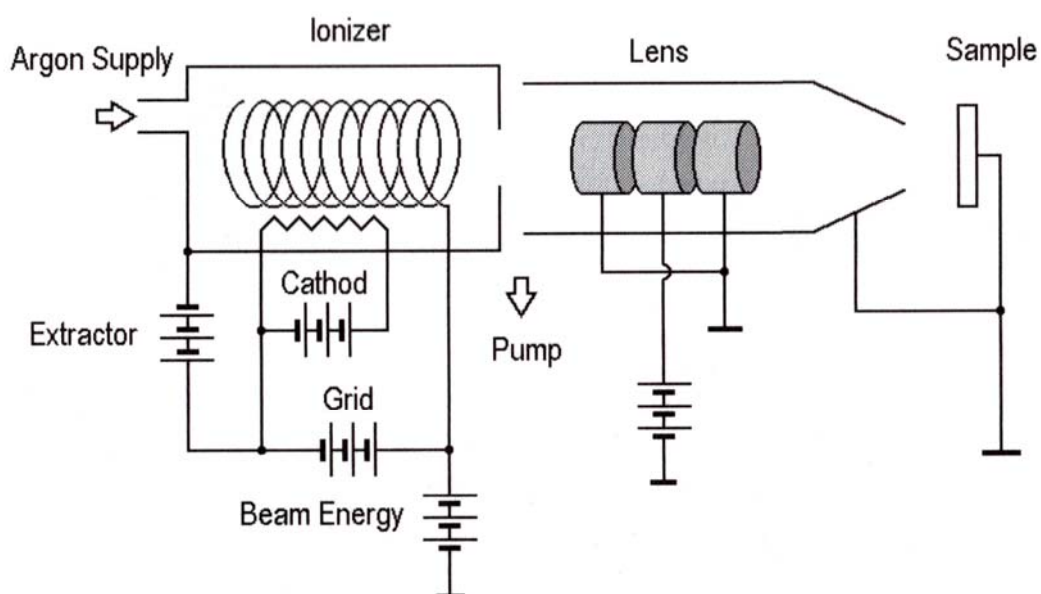


Figure 2.9: Schematic drawing of a typical 'ion sputter gun' [43].

Such a sputter gun typically consists of two parts, i.e. the ionizer and several lenses, and optionally can be equipped with a deflection unit. The ions are generated in the ‘ionizer’ of the gun by electron impact ionization of admitted noble gas atoms. Argon is typically the noble gas of choice, but alternatively also neon, xenon and other gases are used. The electrons used for ionization are produced at the cathode. Then, the generated ions are extracted, accelerated to a defined kinetic energy and finally directed towards the sample surface [43]. Typically, the range of acceleration voltages is 0.5 – 5.0 keV.

When the energetic noble gas ions impinge on the sample surface, they can penetrate into the bulk and undergo numerous inelastic collisions with sample atoms. Each collision results in the loss of kinetic energy until the ions finally come to rest. In contrast, numerous sample atoms in the bulk take up sufficient energy in these collision events to displace from their original site. Therefore, so-called “recoil cascades” are triggered [43]. Several cascades end at the surface and eventually a surface atom leaves the surface. These processes result in the implantation of noble gas ions in the bulk and the loss of atoms or positively or negatively charged ions from the surface. An overview of the cascade of collisions after ion impingement is depicted in Figure 2.10. The numerical values indicate the magnitude of the ion penetration depth (for a primary ion energy of ≈ 10 keV), the escape depth of sputtered atoms / ions and the energy of the latter particles [43].

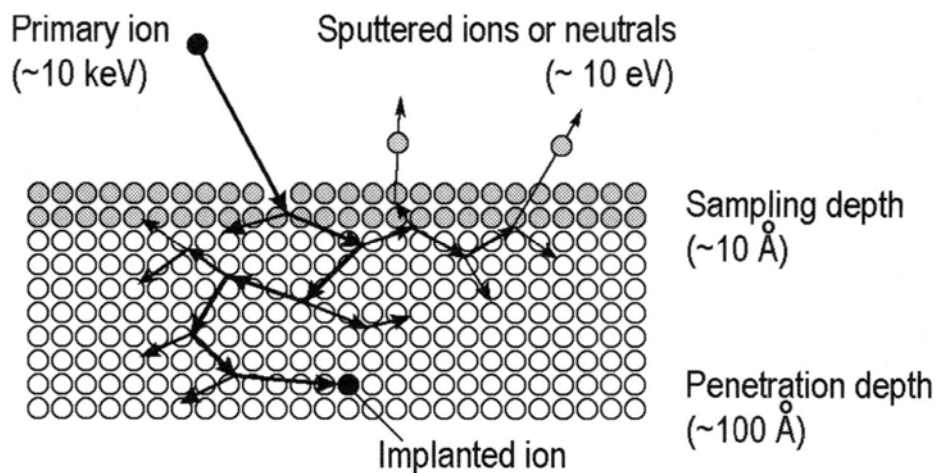


Figure 2.10: Overview of the processes after the penetration of an energetic noble gas ion into the bulk of a sample [43].

By this process, the removal of surface contaminants can be achieved leading to a clean surface. However, the described processes also cause a roughening of the sample surface. Therefore, when sputtering is used for sample preparation, a successive heating step is necessary in order to restore the atomic order at the surface and to remove adsorbed and embedded argon atoms from the sample [43].

A quantity characterizing the sputtering process is the “sputtering yield”. It is defined by the number of sputtered atoms, i.e. atoms which have left the sample surface, per incident ion [43]. This quantity depends on a number of parameters which are listed in the following [43, 55, 56]:

- Bombarding ions:
 - a) Kinetic energy
 - b) Mass
 - c) Electronic configuration
 - d) Angle of incidence
- Surface atoms:
 - a) Atomic mass
 - b) Electronic structure
 - c) Crystal structure
 - d) Surface orientation
 - e) Binding energy
- Sample:
 - a) Chemical composition
 - b) Surface roughness

Figure 2.11 depicts the sputtering yield in dependence on the incident ion energy for different ions. Data is shown for hydrogen (H_2), deuterium (D_2) and the four noble gases helium (He), neon (Ne), argon (Ar) and xenon (Xe) as sputter gas and a polycrystalline Ni sample as substrate material. The general tendency for all ions is that the sputtering yield increases strongly with increasing ion energy, reaches a flat maximum and finally slightly decreases again [55]. For low incident ion energies a threshold exists for the sputtering yield determined by the binding energy. Moreover, the sputtering efficiency scales with the mass of the applied ions, i.e. the heavier the

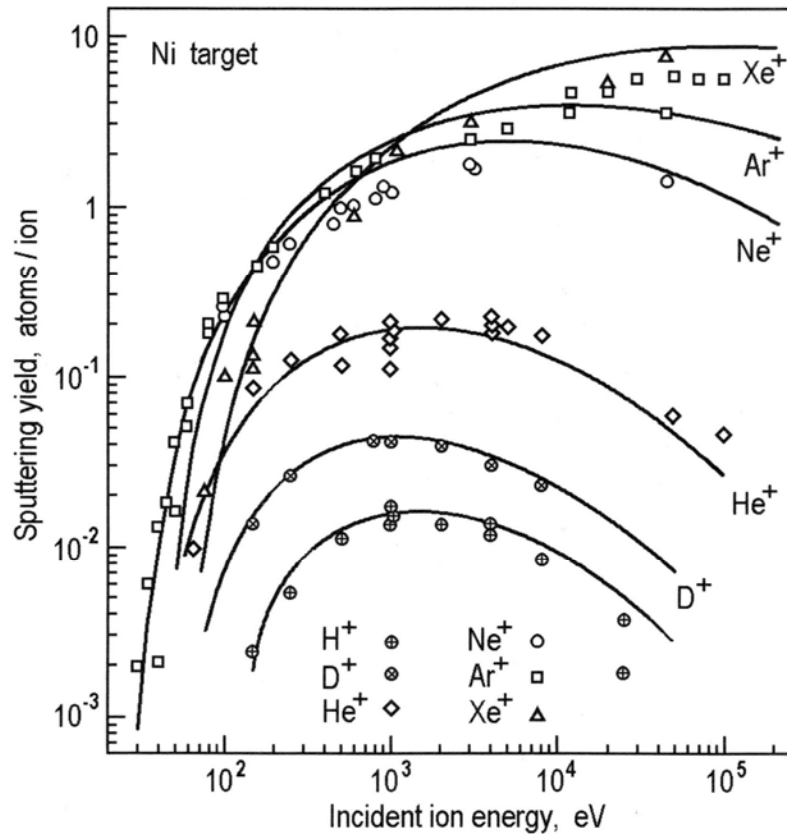


Figure 2.11: Sputtering yield as a function of the incident ion energy for a polycrystalline Ni sample bombarded with different ions at normal incidence [43, 57].

gas atom used for sputtering the higher the sputtering yield [43]. In this work, exclusively argon was used as sputtering gas with an incident ion energy of 1 keV.

Upon sputtering, not all chemical elements are sputtered off with the same probability [53, 55, 58] resulting in a different sputtering yield. This phenomenon can be described by the term “selective sputtering”. Consequently, a different chemical composition of the sample surface after sputtering is possible and in the extreme case some elements can not be sputtered off [53].

In Table 2.1 the yields for sputtering with argon ions of different primary energy are depicted for the elements relevant in this work (C, Si, Ti and Au) [53, 55, 58]. The yields specified in reference [58] are calculated values based on a semi-empirical equation introduced by Seah *et al.* [59-61].

Element	Ref.	Symbol	Z	0.5 keV	1 keV	10 keV
Carbon	[53, 55]	C	6	0.12	-	-
Silicon	[53, 55]	Si	14	0.5	0.6	-
Titanium	[53, 55]	Ti	22	0.5	-	2.1
Gold	[53, 55]	Au	79	2.4	3.6	8.4
Carbon	[58]	C	6	0.197	0.449	1.411
Silicon	[58]	Si	14	0.538	0.874	2.020
Titanium	[58]	Ti	22	0.577	0.901	2.025
Gold	[58]	Au	79	2.008	3.032	7.189

Table 2.1: Sputtering yields in ‘atoms per ion’ for different elements and different primary ion energies when sputtering with argon [53, 55, 58].

The sputtering yields show characteristic periodicities depending on the position of the impinging ions and target atoms in the periodic table of elements [55]. The highest yields are observed for ions and atoms which behave most closely like hard spheres [55]. This is valid both for the bombarding noble gas ions and surface atoms.

Generally, ion sputtering is applied in surface analysis in two major areas [43]. One application is secondary ion mass spectroscopy (SIMS), a technique in which the particles sputtered from a surface are detected and identified to gain information about the elemental composition of a sample. The other application is depth ion profiling. Here, sputtering is used for controlled etching of a sample surface in order to uncover underlying layers. Via surface science techniques for chemical analysis (e.g. AES or X-ray photoelectron spectroscopy (XPS)) it is then possible to analyze the subsurface composition as a function of depth [43].

In this work, sputtering was used for the preparation of a Au(111) single crystal according to a standard procedure (see Chapter 3.3.3). Moreover, it was used as a post-treatment tool in the fabrication of defined nanostructures. It allowed for the downsizing of generated nanostructures and for the removal of unintentionally deposited material (see Chapter 9.1.1). In addition, sputtering was applied to elucidate structure morphologies of EBID deposits (see Chapter 10).

2.8 Ingredients

2.8.1 The substrate silicon

Silicon ($^{28.086}_{14}\text{Si}$) belongs to the fourth main group of the periodic table of elements and is after oxygen the second most abundant element of the earth crust [62]. In its pure, crystalline form (α -silicon) it is a dark gray, nontransparent, strongly gleaming material with a density of 2.328 g/cm^3 , a melting point of 1683 K and a boiling point of 2750 K [62]. The crystal structure is practically the same as that of cubic diamond with a tetrahedral surrounding of the silicon atoms in the lattice [62].

In industry, high-purity silicon has gained a very high importance due to its excellent properties as semiconductor (band gap E_g of 1.09 eV). It is the standard material of semiconductor industry and is used in electronic (e.g. in transistors, integrated circuits, rectifier diodes and light-emitting diodes) and photovoltaic devices [62].

In this work, silicon samples with the surface orientation (100) were used for EBID experiments due to the high relevance of the material in semiconductor industry. The (100) planes of this surface have a square unit cell and the surface atoms have two dangling bonds. Consequently, the surface shows a (2x1) reconstruction by the formation of rows of dimers [63]. Further details concerning silicon can be found in the references [30, 62, 64]. In addition, the surface chemistry of silicon is nicely reviewed in reference [63].

2.8.2 The substrate silicon oxide (on silicon)

Silicon has a strong affinity towards oxygen and forms two stoichiometric oxides, i.e. silicon monoxide (SiO) and silicon dioxide (SiO₂) [62]. Silicon dioxide is a widely spread material in nature and appears both in amorphous and in crystalline form. There are in total eight different crystalline modifications of SiO₂ with densities between 1.970 and 4.387 g/cm^3 and quartz being the most abundant form ($\rho = 2.648 \text{ g/cm}^3$) [62]. Upon heating, quartz incurs several transformations, melts at 1978 K and boils at $\approx 3073 \text{ K}$ by silicon monoxide and oxygen formation [62]. The average atomic number of silicon dioxide is 10.

In this work, SiO_x(300 nm) / Si(100) samples were used for EBID experiments with x being most presumably close to 2. Concerning the interaction with a focused electron

beam, which is relevant for the work at hand, a very similar behavior to that of silicon is expected due to the similar density and the similar average atomic number.

2.8.3 The substrate gold

Gold ($^{196.967}_{79}\text{Au}$) is a transition metal and belongs to the first subgroup of the periodic table of elements [62]. In its pure form, it is a reddish-yellow, soft metal with cubic close-packed arrangement of atoms and high density ($\rho = 19.32 \text{ g/cm}^3$). It melts at 1338 K to a green shining liquid and boils at 2933 K [62]. An important property of gold is its very noble character, which makes the metal extremely stable and inert against air, sulfur and the vast majority of solvents [62].

In industry, gold typically finds application in the fabrication of jewelry, items of luxury and mintage, in dental technology and in the glass and ceramic industry. However, also an increasing use in electrical engineering (e.g. conductive coatings), in electronic engineering (e.g. metal support for dopants or electrical contacts for semiconductors) and in optics (e.g. high grade mirrors, zone plates or in UV spectrometers) is observed [62].

In this work, a Au(111) single crystal was used for EBID experiments. Further details concerning gold can be found in reference [62]. In addition, detailed information about the topography and reconstruction of the Au(111) surface, a well-known, long range superstructure (zigzag or herringbone pattern) and the local reactivity of the reconstructed Au(111) surface is reported in the references [65-71]. Concerning the interaction with a focused electron beam, which is relevant for the work at hand, a strongly different behavior to that of silicon is expected due to the much higher density and atomic number of gold.

2.8.4 The precursor titanium(IV) tetraisopropoxide (TTIP)

The precursor applied in the work at hand is titanium(IV) tetraisopropoxide ($\text{Ti}(\text{OCH}(\text{CH}_3)_2)_4$, $\text{Ti}(\text{O}^i\text{Pr})_4$, TTIP). The structural formula (valence-dash formula) and an illustration in the “balls and sticks model” are depicted in Figure 2.12. Both drawings show the tetrahedral structure of the molecule.

At first glance, one might be apt to count this substance to the class of organometallic compounds since the center of the molecule is a metal atom and the four ligands are of organic nature. But, due to the lack of a direct metal-carbon bond within the molecule, which is the prerequisite for an organometallic species [62, 72], this assignment is not correct. In fact, TTIP belongs to the class of metal alkoxide complexes, $[M(OR)_m]_n$ ($R = \text{Me, Et, } ^n\text{Pr, } ^i\text{Pr, } ^n\text{Bu, etc., } m, n = 1, 2, \text{ etc.}$).

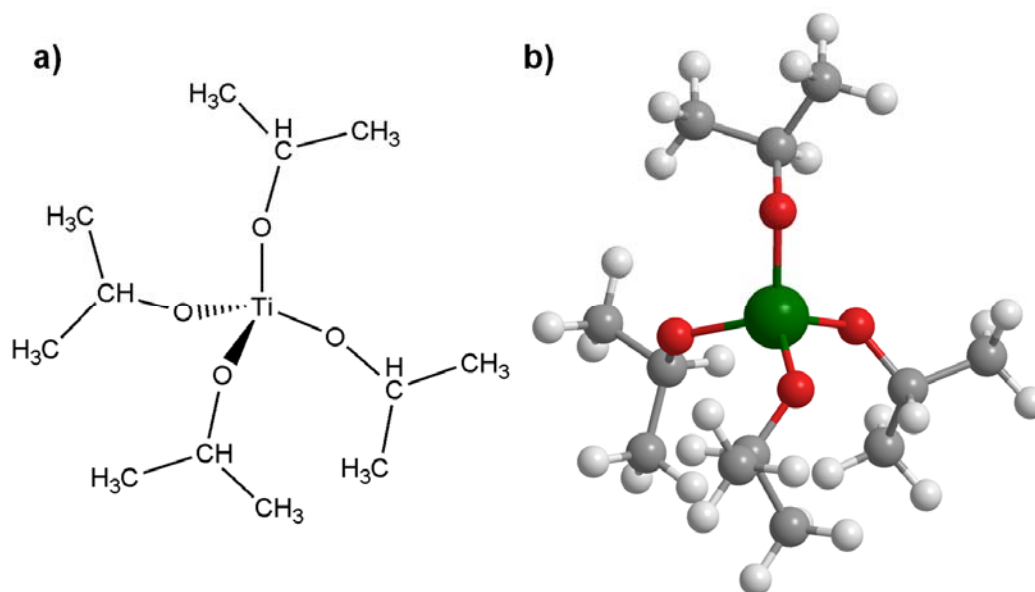
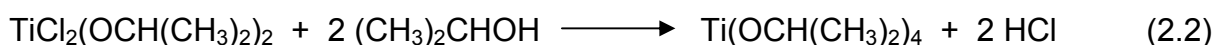


Figure 2.12: a) Structural formula (valence-dash formula) and b) "balls and sticks model" of titanium(IV) tetraisopropoxide (TTIP).

Synthesis:

The synthesis of titanium(IV) tetraisopropoxide is realized with the starting materials titanium tetrachloride (TiCl_4) and the alcohol isopropanol ($(\text{CH}_3)_2\text{CHOH}$). According to the following chemical reactions TTIP and the byproduct hydrogen chloride (HCl) are formed [62]:



Physical and chemical properties:

At ambient conditions, i.e. room temperature and standard pressure, the compound is a transparent, light yellow liquid. The substance is flammable and the vapor is irritating to the eyes. The melting point is closely below 293 K while the liquid starts to boil at 505 K at atmospheric pressure.

Among the titanium alkoxide complexes TTIP is one of the most volatile substances [73-75]. On the one hand, this property is based on the low molecular weight ($M = 284.216 \text{ g/mol}$), on the other, the increased volatility derives from steric effects of the four isopropoxy ligands which restrict the nuclearity of the complex (see subchapter "Structure of TTIP", below) [73, 75]. The increased volatility in comparison to the other, simpler titanium alkoxides, like titanium methoxide or titanium ethoxide, is the most important reason for using TTIP in this work for EBID.

The manufacturers advise to handle and store the compound under dry inert gas because TTIP is moisture sensitive [76, 77]. Therefore, it is also packaged and delivered under nitrogen or argon atmosphere. In contact with water, the substance hydrolyzes readily upon the formation of titanium dioxide (TiO_2) and isopropanol ($(\text{CH}_3)_2\text{CHOH}$) already at RT (see Equation 2.3).



Apart from this complete hydrolysis reaction, also incomplete hydrolysis of TTIP can occur, leading to the formation of alcoholic species of the composition $\text{Ti}(\text{O}^i\text{Pr})_a(\text{OH})_b$ (with $a + b = 4$). The latter compounds have hydroxyl groups directly attached to titanium atoms. They typically undergo condensation reactions and result in very low volatile and sticky oligomers that have the potential to strongly contaminate vacuum systems [4]. Due to this property of TTIP, any contact to air and moisture was avoided in this work (see Chapter 3.4).

An overview of the physical properties of the compound TTIP is given in Table 2.2 [4, 74, 76-78].

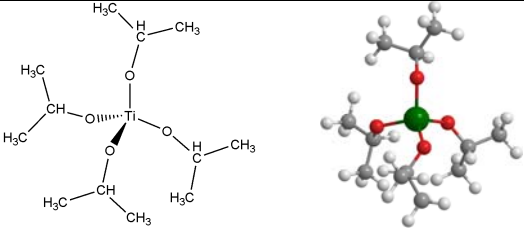
TTIP	
Molecular formula:	Ti(OCH(CH ₃) ₂) ₄ , Ti(O ⁱ Pr) ₄
Empirical Formula:	TiC ₁₂ H ₂₈ O ₄
Compound:	titanium(IV) tetraisopropoxide (TTIP)
Synonyms:	titanium(IV) isopropoxide, tetraisopropyl orthotitanate
CAS number:	546-68-9
Molar Mass:	284.216 g/mol
Molecular shape:	tetrahedral
Appearance:	transparent, slightly yellow liquid
Melting point:	289 – 293 K [76], 287 – 290 K [77]
Boiling point:	505 K [76, 77]
Flash point:	319 K [76], 318 K [77]
Vapor pressure:	0.27 mbar at 303 K (according to ref. [4]) 0.13 mbar at 322 K (according to ref. [74])
Density (at 293 K):	0.955 g/cm ³ [76], 0.96 g/cm ³ [77]
Viscosity (at 293 K):	3 – 4 mPas [76]
Bond length Ti-O:	176 pm [78]
Water solubility:	hydrolyzes
Properties:	flammable, irritating to eyes
R-phrases:	10-20-36
S-phrases:	16-26-36/37/39

Table 2.2: Physical properties of TTIP [4, 74, 76-78].

Structure of TTIP:

For titanium alkoxide complexes it is well-known that these compounds exhibit an oligomeric nature [62, 74, 75], which usually depends on the state of the substance (solid, liquid, gaseous), on the steric constraints of the ligands [74, 79] and possibly

also on the solvent. The appearance of associated species is the response to the electron-deficient nature of the titanium atom in the fourfold coordinated titanium alkoxides [79]. The metal atom tends to expand its coordination number from the own covalence number of '4' to a higher value, e.g. to '6' to form an octahedral complex [74]. For titanium methoxide and titanium ethoxide, for instance, a tetrameric structure is reported in the solid state and for titanium ethoxide a trimeric one in the liquid state and in benzene solution [62, 75].

However, concerning the structure of TTIP no definite specification is found in literature. Instead, different structures are discussed and it is stated that TTIP appears monomeric [78, 80, 81], as a dimer [75] and as a mixture of monomeric and different associated species [73, 79].

Due to the inconsistency in literature concerning the structure of the precursor molecule TTIP, in this work no determination concerning the degree of association is made. For the determination of the precursor flux and pressure at the nozzle exit (Chapter 6.3), TTIP was considered to be monomeric with the acquired results being just marginally touched by this assumption.

For simplicity reasons, in the following, the used precursor is exclusively addressed with the acronym TTIP.

2.8.5 The precursor iron pentacarbonyl

The second precursor applied in this work is iron pentacarbonyl ($\text{Fe}(\text{CO})_5$). This organometallic compound belongs to the class of metal carbonyls, generally characterized by the molecular formula $\text{M}_n(\text{CO})_m$ [62]. Figure 2.13 shows the structural formula (valence-dash formula) and an illustration in the "balls and sticks model", demonstrating the trigonal bipyramidal structure of $\text{Fe}(\text{CO})_5$.

Iron pentacarbonyl is a comparably small molecule with regard to TTIP and has a molar mass of 195.897 g/mol and a density of 1.49 g/cm³ at 298 K [82, 83]. It has a melting point of 253 K and an (initial) boiling point of 376 K and is thus a liquid at RT [82, 83]. The vapor pressure of the compound is 47 mbar at 298 K [82] and 53 mbar at 303 K [82, 83]. Compared to the precursor TTIP, this means a \approx 200 times higher vapor pressure.

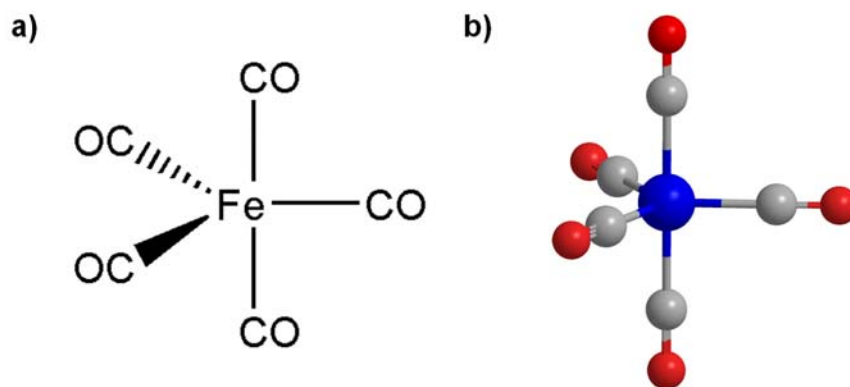


Figure 2.13: a) Structural formula (valence-dash formula) and b) “balls and sticks model” of iron pentacarbonyl ($\text{Fe}(\text{CO})_5$).

The compound $\text{Fe}(\text{CO})_5$ was described in detail in previous theses in our group [30, 64, 84]. The interested reader is referred to these references and to [62, 72] for further details.

3 Experimental

In this chapter, the experimental details, data acquisition and data processing are described. First, the UHV instrument is briefly introduced in Chapter 3.1, and the different possibilities to control the electron beam for patterning are presented in Chapter 3.2. In addition, details concerning sample preparation in UHV and the gas handling and preparation of the titanium(IV) tetraisopropoxide precursor are given in the Chapters 3.3 and 3.4. The applied materials are specified in Chapter 3.5 and experimental details concerning data acquisition and data processing are given in Chapter 3.6.

3.1 The UHV instrument

All experiments (except for the ambient AFM measurements) were performed in an ultra high vacuum (UHV) instrument (Multiscan Lab, Omicron NanoTechnology, Taunusstein, Germany). It is a stainless steel instrument that consists of two main chambers, i.e. a preparation chamber and an analysis chamber, with the base pressure in the low 10^{-10} mbar regime. The vacuum system, the equipment for sample preparation and the surface science analysis tools were recently described in detail by Thomas Lukasczyk [30]. Therefore, in the following chapter, only a brief overview of the Multiscan Lab instrument is given. For detailed information, the interested reader is referred to reference [30].

In the following subchapters the preparation chamber, the analysis chamber, the self-constructed gas dosage and gas injection system and the precursor storage are described.

3.1.1 The preparation chamber

The preparation chamber of the UHV instrument houses the equipment necessary for sample preparation in UHV and for investigating the chemical composition of reactive and precursor gases. Two images of the preparation chamber, taken from different perspectives, are depicted in Figure 3.1. The attached components are labeled correspondingly.

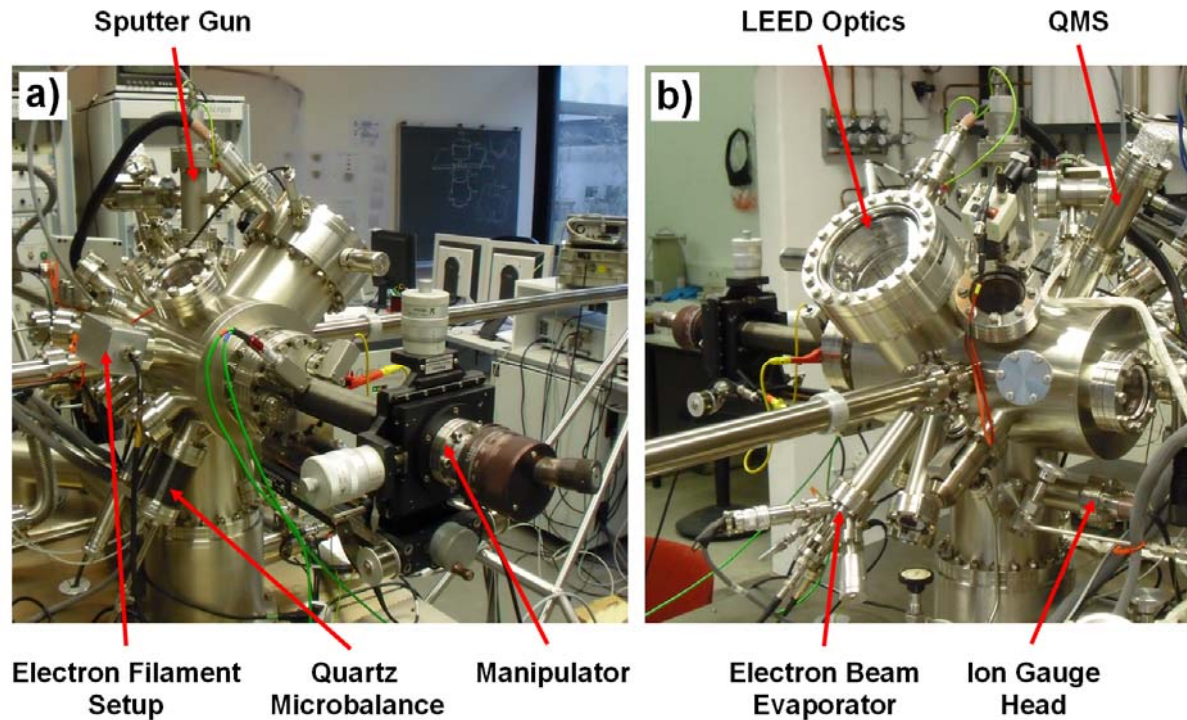


Figure 3.1: Two images of the preparation chamber of the applied UHV instrument with the attached components labeled correspondingly (images adapted from [30]).

The sample is mounted on a fully rotatable, long travel manipulator (Omicron NanoTechnology, RX1515). It can be heated on the manipulator either via resistive, radiative or electron beam heating, temperature readout is realized via type K thermocouples. An ion gun (Omicron NanoTechnology, ISE 10) is attached to the preparation chamber to enable sputtering for sample preparation. Moreover, the evaporation of metals onto the sample surface can be realized by an electron beam evaporator (Focus, IBAD evaporator, EFM 3i). The evaporation rate can be controlled via a quartz microbalance (Syscon, OSC-100A). To control the long range atomic order of the sample surface the chamber is further equipped with a retractable LEED optics (Omicron NanoTechnology, Spectaleed, rear view LEED optics). Additionally, a quadrupole mass spectrometer (Pfeiffer Vacuum, Prisma QMS 200 M2) can be used to monitor the chemical composition of reactive and precursor gases. The large area bombardment of the sample surface with electrons can be realized by a self-constructed electron filament setup with two thoriated tungsten filaments. Moreover, the sample can be cooled using a cryostat.

The fast transfer of samples into and out of the UHV system is realized via the so-called “fast entry lock” or “load-lock” chamber, which is attached to the preparation chamber. The quick and easy transfer of samples within the instrument can be performed by two linear translators.

3.1.2 The analysis chamber

The analysis chamber of the UHV instrument houses the surface science analysis tools used for nanostructure fabrication and characterization. Two images of the analysis chamber are depicted in Figure 3.2. The attached surface science components are labeled correspondingly.

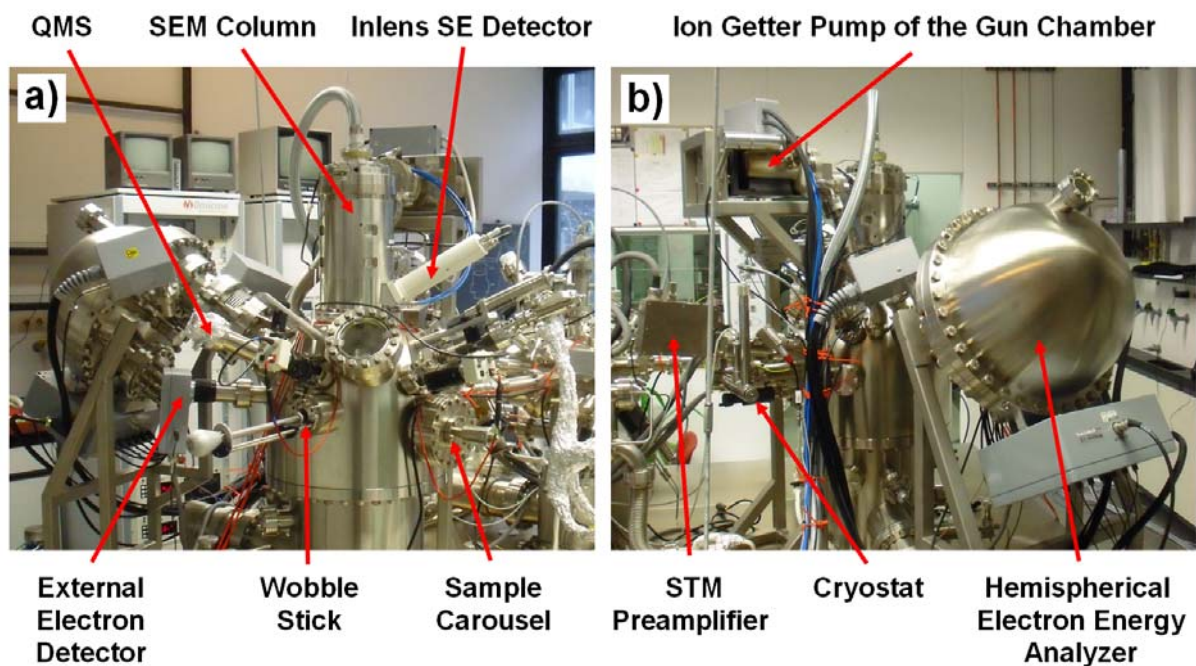


Figure 3.2: Two images of the analysis chamber of the applied UHV instrument with the attached components labeled correspondingly (images adapted from [30]).

The analysis chamber houses a UHV compatible electron column (Zeiss, UHV Gemini), which is the electron source for SEM, AES and SAM. The UHV Gemini

column enables SEM imaging with a high lateral resolution. For a wide range of beam energies (from 0.1 keV up to 30 keV) small spot diameters on the low nanometer scale can be realized with an ultimate spot size of less than 3 nm at a beam energy of 15 keV and a beam current of 400 pA. The instrument also enables laterally resolved AES and SAM measurements with a resolution of less than 10 nm at 15 keV and 3 nA. The 'in-lens detector' (for secondary electron detection), which is located in the UHV Gemini column, is characterized by a wide acceptance angle and a high detection efficiency [85]. Additionally to the 'in-lens detector' an external electron detector can be used for SEM imaging.

Sample and STM tip holder transfers within the analysis chamber are performed via a 'wobble stick' and a sample carousel allows for the storage of up to twelve samples and tip holders. The goniometer-mounted sample stage can be rotated up to $\approx 25^\circ$ into the direction of the hemispherical electron energy analyzer. Electric contacting of the sample holders and a flow cryostat at the sample stage enable variable temperature measurements. Both heating and cooling (with gaseous or liquid nitrogen or helium) of the specimens is possible. The analysis chamber is further equipped with an STM. The flat STM scanner design allows for operation in between of the electron column and the sample holder and thus for controlling the position of the STM tip *in situ* with the SEM. A hemispherical electron energy analyzer (Omicron NanoTechnology, NanoSAM EA U7 analyzer, 125 mm mean radius, 180° double focusing geometry) enables AES and SAM applications (see Figure 3.2 b)). The chemical composition of reactive and precursor gases can be monitored with a quadrupole mass spectrometer (Pfeiffer Vacuum, Prisma QMS 200), which is attached to the analysis chamber.

3.1.3 The self-constructed gas dosage and gas injection system

A self-constructed gas dosage system was applied to enable the dosage of gases into both instrument chambers. A complete description of the latter and all details concerning the construction of self-made components are given in the PhD thesis of Thomas Lukasczyk [30].

The gas dosage system consists of two separate gas lines. Dosage into the UHV chambers is realized by leak dosage valves whereby both reactive and / or precursor

gases can be supplied simultaneously. Via the TMP and the rotary vane pump of the preparation chamber the gas handling system can be evacuated [30]. Moreover, the gas lines can be heated after the usage of precursors to “clean” the pipes. For the same reason the TMP of the preparation chamber can be heated. Heating of the gas dosage system was usually performed to a temperature of ≈ 413 K, the TMP of the preparation chamber was heated to approximately 323 - 333 K.

The gas injection system (GIS) of the analysis chamber, which is used to dose the precursor in the EBID experiments, consists of a self-constructed gas dosing nozzle. A complete description of the GIS is given in the PhD thesis of Thomas Lukasczyk [30]. It can be approached to the sample by a linear translator. In the “home position” (upon normal operation) the dosing nozzle has a distance of ≈ 42 mm to the sample surface to minimize a possible influence on the measurement techniques [30]. During the EBID experiments the nozzle was brought closer to the surface until a distance of ≈ 12 mm to the sample surface was reached. The inner tube diameter at the nozzle exit is 3.0 mm given by a tube with an outer diameter of 4.0 mm and a wall thickness of 0.5 mm. Figure 3.3 shows the sample stage and the dosing nozzle in the analysis chamber in front view (images a) and b)) and side view (images c) and d)). In Figure 3.3 a) and c) the dosing nozzle is retracted from the sample stage (position of the linear translator is set to ‘55’) while in Figure 3.3 b) and d) the nozzle is approached (position of the linear translator set to ‘85’).

The distance of ≈ 12 mm was applied for almost all experiments described in this work. Only in one experiment (see Chapter 9.2) the dosing nozzle was approached 4 mm closer to a distance of ≈ 8 mm (labeled in the figure captions). The adjustment of this distance was possible until 2007, when a heating wire (Thermocoax, NcAc10) was wrapped around the tubes of the dosing nozzle. The latter was added to the tubes to remove contaminants. For details see reference [30].

In the EBID experiments, the precursor was supplied via the GIS in the form of a molecular flux which is effusing from the nozzle exit onto the substrate. Since the nozzle was approached close to the sample stage during EBID, a significantly higher local pressure was realized directly at the sample surface in comparison to the background pressure. The actual pressure and thus the actual precursor molecule flux directly at the sample surface are significant parameters for EBID. Therefore, in

this work an estimation of these parameters is given based on Monte Carlo simulations (see Chapter 6). Both dosing geometries, i.e. with a distance of the nozzle to the sample surface of ≈ 12 mm and of ≈ 8 mm, were considered.

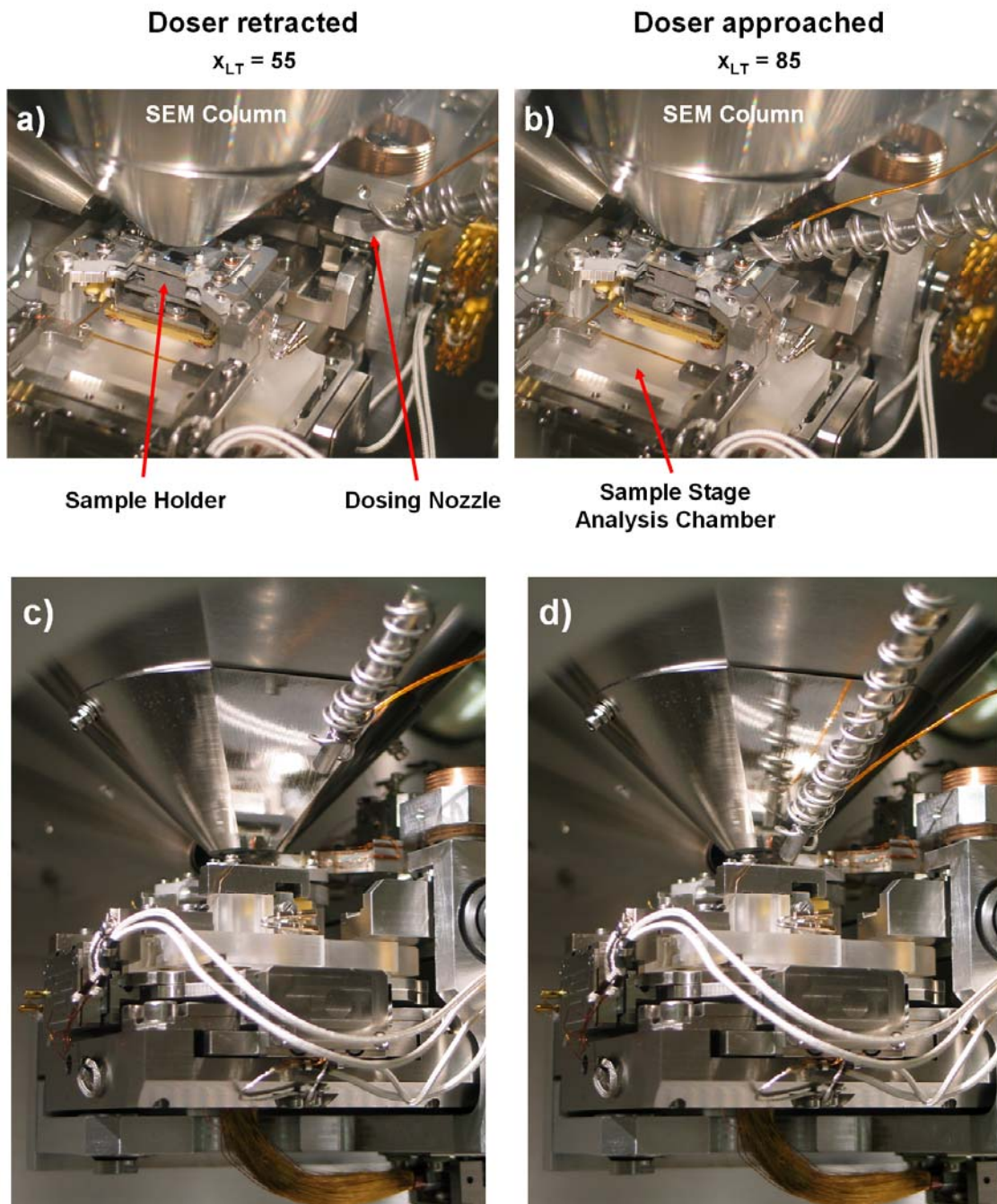


Figure 3.3: Sample stage and dosing nozzle in the analysis chamber, depicted in front view (see a) and b)) and side view (see c) and d)). In the images a) and c) the dosing nozzle is retracted ($x_{LT} = 55$), while in the images b) and d) the nozzle is approached to the sample stage ($x_{LT} = 85$).

3.1.4 Precursor storage

For the storage of the precursor compounds a stainless steel storage device was constructed which is compatible to the gas dosage system and can thus be attached to the UHV instrument [30]. An image of a TTIP precursor storage device “in use” is shown in Figure 3.4.

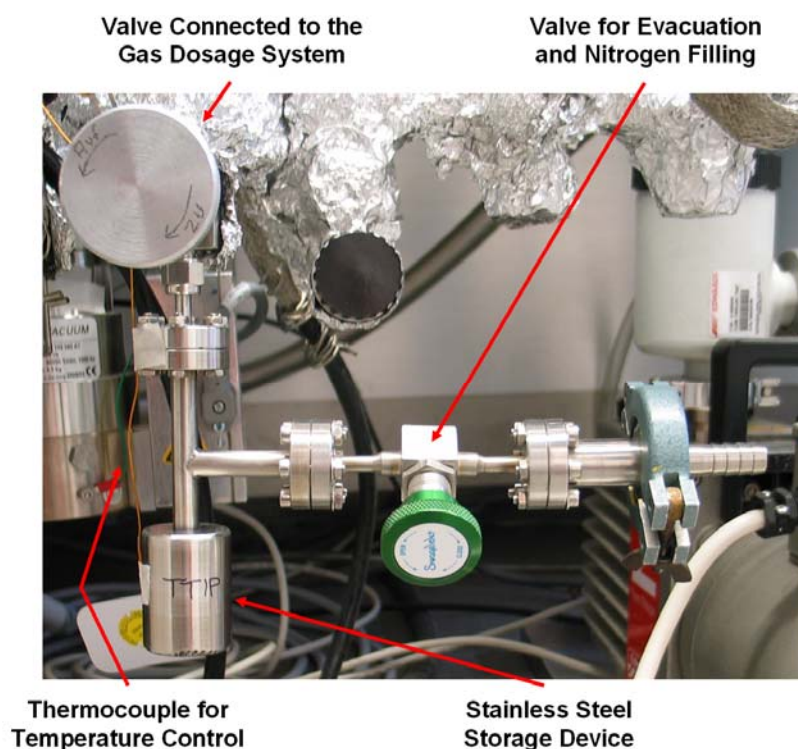


Figure 3.4: TTIP precursor storage device connected to the gas dosage system of the instrument, using the “Type II” bottom part (see Chapter 16.1.1).

The precursor compound is stored in a cylindrical vessel, which is connected to two full metal valves (see Figure 3.4). The valve mounted on top separates the storage device from the gas lines to the vacuum chambers. The other valve is needed for filling the precursor TTIP [30]. For precursors with a low vapor pressure the possibility of heating the cylindrical vessel at the bottom with an external heating device is given (see Chapter 3.4). To monitor the temperature a pair of thermocouples was fitted directly to the precursor vessel (see Figure 3.4). Further details concerning the bottom parts of the precursor storage devices are given in the Appendix of this work (see Chapter 16.1.1).

3.2 Control of the electron beam

For the fabrication of deposits with defined shape (e.g. dot, line or area structures) and size it is necessary to control the position of the electron beam on the substrate surface. The latter can be realized in different ways, and for the irradiation process a large amount of lithographic parameters is accessible like dwell times, waiting times, step sizes and electron doses.

In the following subchapters, three different possibilities of controlling the electron beam are presented which are relevant for the work at hand. It turned out that each of them shows certain restrictions. To overcome the tool specific limitations new methods were applied and the tools were developed further. The main advantages and disadvantages of each method are briefly discussed.

3.2.1 The SmartSEM imaging software (Zeiss)

An obvious way to control the electron beam in EBID experiments is to use the SEM imaging software delivered with the microscope, i.e. here the “SmartSEM” software from Zeiss (version V05.00.08 from 17.01.2005). For EBID, different tools of this software can be used to fabricate dot, line and area deposits. However, since “SmartSEM” is an imaging software, which is not designed for lithography, several limitations turned out when using it for this purpose. The most serious restriction is that the lithographic parameters can not be adjusted separately from each other. Instead, the software enables to adjust only certain, independent parameters, which are the ones necessary for SEM image acquisition. Many other ones do then result from the performed adjustments, i.e. they are dependent parameters, which can not be adjusted freely. In the following, the independent and dependent parameters are discussed for the different tools to generate dot, line and area structures.

For the deposition of a single dot the “spot mode” of the software can be used. In this mode the electron beam rests at a defined position. The time the beam is activated, i.e. the exposure time t_{exp} , determines the dot dose d_D .

For the fabrication of line deposits, a “line scan mode” is available in the software. The independent parameters of this mode are the image magnification, the scan speed s , the image store resolution and the exposure time t_{exp} . While the image

magnification determines the length of the line, the scan speed s determines the dwell time t_D , the active line duration t_{ALD} , the waiting time t_{wait} at the line starting point (for beam stabilization) and the total line duration t_{TLD} , which is the sum of t_{ALD} and t_{wait} . The line step size s_L is determined by the magnification and the image store resolution. The exposure time t_{exp} determines the line dose d_L and the number of sweeps N_S , which is the quotient of t_{exp} and t_{TLD} . Two characteristics of the “line scan mode” have to be noted. First, the waiting time at the line starting point causes the growth of an additional circular deposit in EBID experiments. In the following chapters of this work, this additional, unintended deposit is addressed as ‘waiting time deposit’, abbreviated as ‘WT deposit’. Secondly, an important feature of the “line scan mode” is that waiting times and thus total line durations are applied which deviate from the specified values [86] for the “full image scan mode” (see Table 16.1 in the Appendix). The parameters valid for the “line scan mode” are listed in Table 16.2 in the Appendix for the scan speeds applied in this work.

For the deposition of area deposits the “full image scan mode” of the software can be used. The independent parameters of this mode are again the image magnification, the scan speed s , the image store resolution and the exposure time t_{exp} . The image magnification determines the size of the rectangular area deposits with a side length ratio of ‘4:3’. The scan speed s determines the dwell time t_D , the active line duration t_{ALD} , the waiting times t_{wait} (at the line starting points and in the upper left corner after each image scan; for beam stabilization), the total line duration t_{TLD} and the total frame duration (see Table 16.1 in the Appendix of this work). The area step size s_A is determined by the magnification and the image store resolution, while the number of sweeps N_S is either adjusted by the number of image scans or results from the exposure time t_{exp} . The number of sweeps and the exposure time determine the area dose d_A . Analog to the fabrication of lines, the waiting times cause additional ‘waiting time deposits’ (‘WT deposits’) in EBID. More material is deposited at the left edge and in the upper left corner of the area deposits.

The most important advantages of using the “SmartSEM” software to control the position of the electron beam for EBID are the easy and convenient use and the instant availability. As mentioned above, the main drawback is that only few parameters can be adjusted independently, while the vast majority of parameters results from their adjustment. In addition, unintended waiting times influence the

fabricated structures ('WT deposit' formation) and no arbitrarily shaped patterns can be realized.

3.2.2 The lithographic attachment ELPHY Quantum (Raith)

Another way to control the electron beam for lithography in EBID experiments is to use a commercial EBL attachment. In the applied setup the lithographic attachment ELPHY Quantum from Raith was used. The system comprises a computer with integrated 'PCI 16 bit DAC board' [87] and the ELPHY Quantum software (version 4.0, SP 8.0, 07.07.2006). Additionally, the remote control program REMCON (Zeiss) realizes the communication between ELPHY Quantum and SmartSEM software [30].

The beam deflection in the electron column and the control by an analog external scan interface is described in detail by Thomas Lukasczyk [30]. Generally, the irradiation of the surface via the electron beam is carried out within a square area, the so-called "write field", and is performed point by point (for line and area structures). Within this pre-defined field any position can be addressed by actuating the x- and y- direction ports correspondingly [30]. The write field size is adjusted by the image magnification, and for each size once a calibration has to be performed with a reference sample. The minimum distance between two separately irradiated points is 0.8 nm [30] and the maximum pixel to pixel frequency that can be realized by the ELPHY Quantum vector scan beam deflection board is 2.5 MHz [87]. This corresponds to a minimum pixel time of 0.4 μ s which can be increased to several seconds [30].

Using ELPHY Quantum the fabrication of dot, line and area deposits is possible. As a dedicated lithography package the system enables the precise control of the lithographic parameters. By specification of the electron beam current (I_B), the step sizes for area and line structures and the dwell times for area, line and dot structures, the corresponding doses of each structure can be adjusted. The patterns can be generated in a graphical user interface of the software. The latter also enables the generation of structures with arbitrary shape or superimposing features. Logos, emblems and images can be converted to ASCII files (Raith, 'Image 2 ASCII converter'), integrated in the ELPHY Quantum software and then be handled and manipulated independently. Moreover, the software enables the use of different

layers for each feature of a pattern, which allows for the fabrication of sophisticated, three-dimensional structures [30, 88].

Since the applied Gemini column in the instrument is not equipped with an electron beam blander, the ELPHY quantum software cannot blank the beam automatically after the irradiation of a pattern. Therefore, the software is “parking” the electron beam after pattern exposure in the upper left corner of the write field in order to avoid unintended additional structure irradiation. The beam must then be blanked manually by the user. However, the time between finished structure irradiation and manual beam blanking leads to an additional, unintended deposit in the upper left corner of the write field, which is a drawback of applying ELPHY Quantum without a beam blander. In the following chapters of this work, this additional, unintended deposit is addressed as ‘parking time deposit’, abbreviated as ‘PT deposit’.

The most serious drawback of ELPHY Quantum is that it is designed and optimized for single sweep exposures. When it is used for multiple sweep experiments, undefined, additional waiting times occur during irradiation within the intended structure (presumably for reloading the pattern). The latter cause unintended deposits, change the electron dose, and the replenishment time becomes uncontrolled.

3.2.3 Waveform generators (Hewlett-Packard)

To address the limitations of the latter two systems for controlling the electron beam, a new method was developed in our group, in which waveform generators are used for lithography. The main advantage of applying waveform generators in comparison to ELPHY Quantum is that multiple sweep exposures can be realized in a well-defined way. Moreover, the beam exposure can be accomplished without unintended waiting times while precise control of the lithographic parameters is given.

Two waveform generators (Hewlett-Packard, ‘Arbitrary waveform generator’, HP 33120A) are applied. Each is used for the control of one coordinate of the data points of a pattern. Since the actuation of the analog x- and y- direction ports of the control electronics is performed separately, external synchronization of both waveform generators is necessary. This was implemented by using an external

trigger device (ELV, Universal-Pulse-Generator, UPG 100, 9 V - 15 V (DC), 250 mA) providing rising edge pulses (10 μ s, 5 V, TTL).

The waveform generators feature ten standard signal forms and have an integrated function for the realization of arbitrary signal shapes. The latter can be generated with a signal form length in the range of 8 to 16,000 points and an amplitude resolution of 12 bit (4096 steps). The sampling frequency is 40 MSa/s and the generated patterns can be stored in four permanent memory capacities [89]. For the construction of arbitrarily shaped voltage patterns a graphical user interface is available (Agilent Technologies, 'Agilent IntuiLink Waveform Editor', version 1.6.0, 2008). By the generation of patterns for the x- and the y- direction port the realization of dot, line and area structures is possible. However, the use for area structures is limited due to the limited waveform length and due to synchronization issues.

The size of lines and areas is defined by the magnification of the microscope and the lithographic parameters can be controlled independently by the user settings. Table 3.1 illustrates the dependence of the lithographic parameters on adjustable waveform generator settings which provide precise control to the user. The waveform frequency is the frequency that is used for sending the patterns from the graphical user interface to the x- and y- input ports of the control electronics. The number of sweeps depends on the total exposure time, i.e. the time the beam is activated. It can be adjusted manually, either via the waveform generators or via the external trigger device.

	Magnification of the SEM	Waveform shapes	Waveform frequencies	Number of sweeps
Step size	X	X		
Pixel time		X	X	
Waiting time		X	X	
Replenishment time		X	X	
Electron dose	X	X		X

Table 3.1: Dependence of the lithographic parameters on adjustable waveform generator settings.

Additionally to dot, line and area structures, the waveform generators enable the fabrication of arbitrarily shaped deposits. Logos, emblems and images can be applied in lithography experiments after file conversion and generation of the necessary voltage patterns. The latter was performed by a self-programmed script (implemented by Florian Vollnhals via the programming language 'python'). It converts the original file into an ASCII file containing all points of the original pattern in the form of x- and y- coordinates. After these coordinate pairs have been separated into two independent lists (one for each coordinate), they are transferred from "real space" to the "voltage space" (with a range from -10 V to +10 V corresponding to the full axis of the area at a certain SEM magnification) [90]. Then, the obtained voltage patterns can be transferred to the analog x- and y- direction ports of the control electronics.

The most serious drawback of using waveform generators to control the electron beam is the need for external synchronization. It is not possible to synchronize the sampling rate but only the pattern frequency. Therefore, it is not guaranteed that all coordinate pairs are perfectly synchronized. Small time delays can cause the irradiation of points with dislocated coordinates that do not belong to the pattern. The consequence is that synchronization artifacts can appear in the deposits.

3.3 Sample preparation

In this chapter, the preparation of the Si(100) samples, the SiO_x(300 nm) / Si(100) samples and the Au(111) single crystal is described.

3.3.1 Preparation of Si(100) samples

The Si(100) samples were prepared in UHV according to a standardized procedure, which is described in Table 3.2.

	Time [s]	Current [A]	Frequency	Procedure	T [K]
1	over night	0.8	1 x	Resistive heating of the sample in UHV	≈ 1,010
2	5	1.5	5 x	Flashing of the sample	≈ 1,200
3	5	2.4	5 x	Flashing of the sample	≈ 1,330
4	5	3.5	5 x	Flashing of the sample	≈ 1,430
5	5	4.2	5 x	Flashing of the sample	≈ 1,500
6	-	1.5	1 x	Fast adjustment of a heating current of 1.5 A	-
7	150	1.5 – 0	1 x	Stepwise, slow reduction of the heating current by 0.1 A every 10 s	≈ 1,180 - ≈ 600

Table 3.2: Preparation procedure for the applied Si(100) samples.

The temperatures during the preparation procedure were measured via a pyrometer in the preparation chamber (see Chapter 3.6.2). After cooling down of the samples, the quality of the Si(100) surfaces was controlled by LEED (long range atomic order), AES (chemical purity) and SEM (topography).

3.3.2 Preparation of SiO_x(300 nm) / Si(100) samples

The SiO_x(300 nm) / Si(100) samples were freed from the organic protective coating layer (Illmar P4, Pieplow & Brandt GmbH) by sonicating them in acetone, isopropanol and distilled water for at least ≈ 5 min, respectively. After cleaning of the samples, they were mounted below a tantalum standard sample plate and introduced into the UHV instrument. In UHV, they were not further cleaned.

3.3.3 Preparation of the Au(111) sample

The Au(111) single crystal was prepared in UHV by a repeated procedure, which is described in the following:

- 1.) Ar⁺ ion sputtering

Ar background pressure:	$p(\text{Ar}) = 4.0 \cdot 10^{-6}$ mbar
Ar ion energy:	$E = 1$ keV
Temperature:	$T = \text{RT}$
Time:	$t = 30 - 60$ min

- 2.) Annealing

Temperature:	$T = 873$ K
Time:	$t = 10 - 30$ min

- 3.) Cooling down

The sample was cooled down by two different cooling procedures. The heating power was reduced stepwise either by decreasing the heating current (by -0.1 A every 1.5 min in ≈ 40 min) or by decreasing the heating voltage (by -0.1 V every 1.5 min in ≈ 150 min).

The temperatures during the preparation procedure were measured via a pair of thermocouples directly attached to the gold sample and via a pyrometer in the preparation chamber (see Chapter 3.6.2). Before an EBID experiment the surface quality was controlled via LEED, AES and SEM.

3.4 Gas handling and preparation of the TTIP precursor

The precursor molecule TTIP is highly sensitive to air and especially to moisture (see Chapter 2.8.4) [76, 77]. Contact with moisture leads to the decomposition of the compound (see Equation 2.3) and to the formation of very low volatile and sticky oligomers that potentially strongly contaminate vacuum systems [4]. Due to this property, any contact with air or water had strictly to be avoided.

The compound TTIP was filled into UHV compatible stainless steel storage devices (see Figure 3.4). To avoid contact with water, filling was performed according to the “Schlenk technique”. The latter is a working technique applied in chemistry, which enables to process air or water sensitive compounds without exposing them to ambient conditions. Instead they are kept and treated in a dry inert gas (nitrogen) atmosphere.

TTIP has a comparably low vapor pressure at RT (see Chapter 2.8.4). To increase the vapor pressure the precursor storage device was heated via an external heating device, i.e. an oven. Via a pair of thermocouples the temperature was measured directly at the precursor vessel (see Figure 3.4), and an electronic control unit was applied to keep the temperature of the precursor vessel constant at 413 K. Heating of the precursor vessel was performed both during the purification of TTIP and during the EBID experiments with it.

Before the precursor is dosed, it is necessary to clean the gas dosage system from residues and adsorbents. For this purpose, it was baked and simultaneously evacuated via a TMP and rotary vane pump. It is advisable to bake over night at a temperature of ≈ 413 K.

A crucial step was to purify the precursor TTIP before its use since it tends to decompose. In this work, a procedure comprising several purification steps was applied. It is described in detail in Chapter 5.2. For an exemplary purification of freshly filled TTIP all parameters are specified in the Appendix of this work (see Chapter 16.2.3). Monitoring of the gas composition *in situ* via QMS is strongly recommended during the whole process. Purification was performed until a QM spectrum similar to a QMS reference spectrum was observed, which was obtained in the exemplary TTIP purification (see Chapter 5.2).

3.5 Materials

The precursor compounds TTIP and $\text{Fe}(\text{CO})_5$ and the gases that were used in this work are listed in Table 3.3 with the corresponding supplier and the specified purities.

Compound	Formula	Supplier	Purity
TTIP	$\text{Ti}(\text{OCH}(\text{CH}_3)_2)_4$	Alfa Aesar (Karlsruhe, Germany)	$\geq 99.995\%$ (metals basis)
		Sigma-Aldrich (Steinheim, Germany)	$\geq 99.999\%$ (trace metals basis)
Iron pentacarbonyl	$\text{Fe}(\text{CO})_5$	Acros Organics (Geel, Belgium)	99.5 %
Oxygen	O_2	Linde (Unterschleißheim, Germany)	$\geq 99.995\%$
		Air Liquide (Düsseldorf, Germany)	$\geq 99.998\%$
Argon	Ar	Linde (Unterschleißheim, Germany)	$\geq 99.999\%$
		Air Liquide (Düsseldorf, Germany)	$\geq 99.999\%$

Table 3.3: Applied precursor compounds and gases.

Oxygen and argon were provided in the form of 12 liter lecture bottles. They were attached to the instrument at the “reactive gas storage” part of the gas dosage system (see Figure 3.2 in reference [30] from Thomas Lukasczyk). Before the use of these gases, the gas dosage system was evacuated via a turbo molecular pump and afterwards the attached gas pipes were alternately purged and pumped for several times. Additionally, the purity of the dosed gases was controlled via QMS.

The applied samples are listed in Table 3.4. The table shows the supplier and significant properties of each sample.

Sample	Supplier	Properties
Si(100)	Institute of Electronic Materials Technology (Warsaw, Poland)	<ul style="list-style-type: none"> - Laser cut 2 inch wafer - Both sides polished - Sample size: 10 mm x 1 mm x 0.5 mm - Boron doping: $4.5 \cdot 10^{17} - 5.4 \cdot 10^{17}$ at/cm³ - Resistivity: 0.065 – 0.074 Ω cm
SiO _x (300 nm)/ Si(100)	CrysTec (Berlin, Germany)	<ul style="list-style-type: none"> - Laser cut 3 inch wafer, Si(100) - Upper side polished and thermally oxidized - SiO_x layer thickness 300 nm - Protective coating: Illmar P4 - Sample size: 7 mm x 2 mm x 0.38 mm - p-type, boron doped - Resistivity: 1 – 20 Ω cm
Au(111)	MaTeck (Jülich, Germany)	<ul style="list-style-type: none"> - Au single crystal - One 9 x 2 mm² side polished with a roughness < 30 nm - Accuracy of surface orientation: < 0.1° - Sample size: 9 mm x 2 mm x 1.3 mm - Drill hole in the center of one 9 x 1.3 mm² side for a pair of thermocouples for temperature readout

Table 3.4: Applied samples.

Details concerning sample mounting and heating are given in the Appendix of this work (see Chapter 16.1.3).

3.6 Experimental details, data acquisition and data processing

3.6.1 Pressure values

The gas pressures given in this work were measured via a 'hot cathode ionization gauge' (Bayard-Alpert gauge), which is available in both chambers of the instrument. Therefore, the pressure measurement is an indirect measurement, which depends on

the nature of the gas [53, 91]. If not stated otherwise (Chapter 6), the denoted pressure values in this work correspond to the background pressure in the chamber. Without exception uncorrected pressure values are given.

3.6.2 Temperature values

The temperature of the Si(100) samples upon resistive heating was calibrated via pyrometer measurements (Impac Elektronik GmbH / IP 120) with the sample located on the manipulator of the preparation chamber. Further details concerning the pyrometer measurements are given in the Appendix of this work (see Chapter 16.1.3) and in the PhD thesis of Thomas Lukasczyk [30]. Figure 3.5 shows the acquired temperature curve in dependence of the heating current.

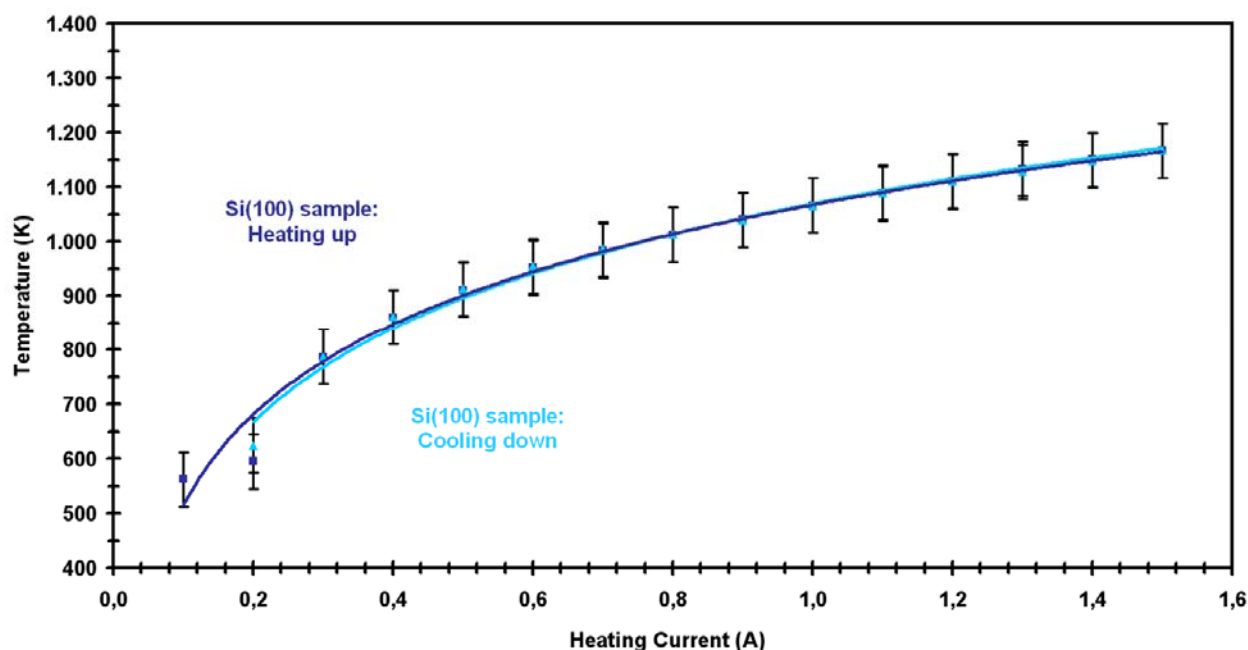


Figure 3.5: Temperature of a Si(100) sample vs. the heating current. The temperature values were measured via a pyrometer through a quartz window.

The heating curve (dark blue) and the cooling curve (light blue) lie very close to each other, which indicates a high reproducibility of the measurement. The error bars in Figure 3.5 correspond to the maximum absolute pyrometer error of ± 50 K.

The temperature of the Au(111) single crystal upon radiative heating was calibrated via a pair of thermocouples (type K), which was mounted directly at the single crystal (see Chapters 3.5 and 16.1.3). Additionally, the temperature of the baseplate of the manipulator was determined, also via thermocouple temperature readout (contact point see Figure 3.5 a) of reference [30]). Figure 3.6 shows the acquired temperature curves of the crystal and the manipulator baseplate in dependence of the PBN heating power.

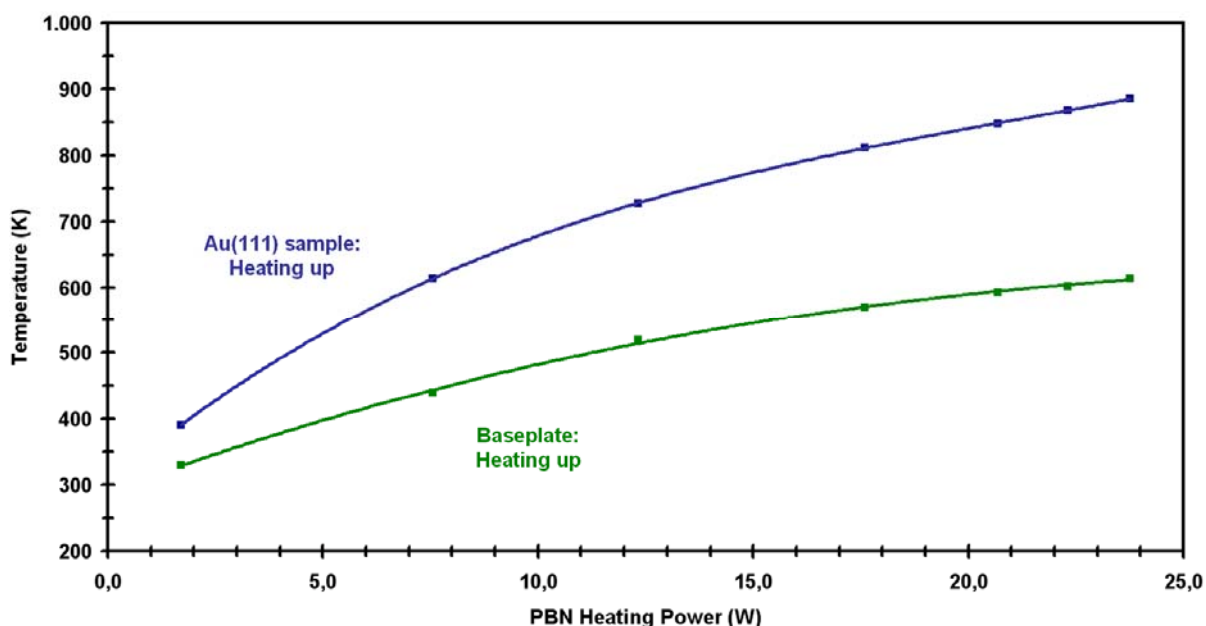


Figure 3.6: Temperature of the Au(111) single crystal and of the manipulator baseplate vs. the PBN heating power. Both temperature data were measured via a pair of thermocouples, respectively.

The temperature of the Au(111) single crystal was further confirmed via pyrometer measurements (see Chapter 16.1.3).

3.6.3 EBID experiments

All EBID experiments presented in this work were carried out at RT with a primary electron beam energy of 15 keV and an electron beam current of 400 pA. For the latter parameters the maximum resolution in SEM, i.e. the smallest spot size with an

electron beam diameter of less than 3 nm, is specified. The beam current of 400 pA corresponds to $2.5 \cdot 10^9$ electrons per second.

In all EBID experiments with the precursor TTIP, the storage device was heated to 413 K to increase the TTIP vapor pressure (see Chapter 3.4). For the $\text{Fe}(\text{CO})_5$ precursor heating was not necessary and the corresponding storage device was kept at RT.

During the EBID experiments the dosing nozzle was approached to the sample surface (see Chapter 3.1.3) and the precursor (TTIP or $\text{Fe}(\text{CO})_5$) was dosed to a background pressure of $3.0 \cdot 10^{-7}$ mbar. An estimation of the flux, the flux distribution and the pressure directly at the sample surface, which is significantly higher than the background pressure, is given in Chapter 6 for TTIP. During the EBID experiments the turbo molecular pumps (TMPs) and titanium sublimation pumps (TSPs) were switched off with only the ion getter pumps (IGPs) maintaining the vacuum in both chambers.

For all deposits from TTIP which were fabricated with the SmartSEM software (Chapter 3.2.1) the image store resolution was set to 1024 x 768 pixels. Since line deposits were exclusively engineered in horizontal direction and vertical lines by rotating the sampling direction by 90° , all lines were fabricated with 1024 pixels. For area deposits the image store resolution of 1024 x 768 pixels yields one area step size for both directions. When the lithographic attachment ELPHY Quantum (Chapter 3.2.2) was used for EBID, a fixed set of lithographic parameters was applied, which was adjusted in the graphical user interface. The write field size was $2 \mu\text{m} \times 2 \mu\text{m}$ for all experiments. Arbitrarily shaped patterns that were generated from external files (logos, emblems or images) and realized via waveform generators (Chapter 3.2.3) were monitored via an oscilloscope before they were irradiated.

In the following chapters, for each depicted EBID deposit the applied electron dose is specified. Further lithographic parameters are only specified if they are substantially important for the understanding of the corresponding section.

3.6.4 SEM measurements

All SEM images depicted in this work were acquired using the 'in-lens detector' of the instrument detecting in the 'secondary electron imaging mode'. For image acquisition the software SmartSEM (Zeiss, version V05.00.08 from 17.01.2005, see Chapter 3.2.1) was used. To enhance image visibility minor brightness and contrast adjustments were performed.

The beam voltage was exclusively 15 kV and the working distance between pole shoe of the SEM and sample surface was ≈ 9 mm. If not stated otherwise, the beam current was 400 pA and the sample surface normal was parallel to the primary electron beam. For some images a beam current of 3 nA was used and the sample was tilted with respect to the electron column ($\approx 25^\circ$ between surface normal and primary electron beam). For the corresponding SEM images the parameters are denoted in the respective figure captions.

The SEM images were typically acquired and stored with a resolution of 1024 x 768 pixels and a dwell time of 204.8 μ s (image acquisition time 2 min 49.5 s). For *in situ* observations of fast processes (e.g. the nanocrystal growth in Chapter 9) a shorter dwell time of 51.2 μ s was used (image acquisition time 48.7 s). The corresponding SEM images exhibit a slightly reduced signal-to-noise ratio.

3.6.5 AES, AELS and SAM measurements

For all Auger measurements the sample was tilted by an angle of $\approx 25^\circ$ between surface normal and primary electron beam of the SEM. Under these conditions, the angle between inlet port of the hemispherical electron energy analyzer and surface normal is decreased from 60° to 35° , which significantly increases the intensity of detected electrons in the analyzer. All Auger measurements were performed with a primary beam energy of 15 keV and a beam current of 3 nA (minimum spot size < 10 nm).

AES measurements

Local AE spectra were recorded using the software EIS (Omicron Nanotechnology, version 2.4.16.37, 2004). Surface irradiation for spectrum acquisition was performed

with different scan parameters which are specified in the corresponding chapters of this work. One way was to irradiate one spot on the surface ('spot mode') at a pre-defined position, which was either adjusted via the SmartSEM software (Zeiss) or via the software ISEM (Omicron Nanotechnology, version 1.0.2.2, 2004). A modified scan strategy for AE spectrum acquisition ('area mode') is to scan repeatedly a defined small area ('scan window') instead of irradiating only one spot. This scan strategy has two advantages: first, it allows tracking the position, from which the spectroscopic information originates *in situ*; second, the 'accumulated charge' upon electron irradiation is distributed over the whole 'scan window', which lowers the local electron dose. Thus, electron-induced effects like electron stimulated desorption (ESD) or electron beam induced heating (EBIH) are reduced.

For the AE spectra presented in this work, typically the scan strategy of repeatedly scanning a small area was applied. For the characterization of area deposits and unexposed surfaces the 'scan window' usually had a size of 200 x 200 nm² while for the characterization of line and dot structures on the very low nanometer scale it was set to 20 x 20 nm² or 18 x 18 nm². The SEM pixel time during the scan process was exclusively set to 1.6 μs. The experimental parameters that were adjusted in the EIS software are given in the Appendix of this work (see Chapter 16.1.3).

Processing and reproduction of AE spectra

The AES data was processed with the software 'Igor Pro' (WaveMetrics, version 5.0.2.0, 2004).

All AE spectra displayed in this work are shown with normalized intensity (details concerning the normalization see Chapters 3.6.8 and 16.1.4) and without data smoothing. For very few spectra, additionally to the normalized raw data also the smoothed data is depicted (see e.g. Figure 7.5). In this case, the smoothing algorithm 'binomial smoothing' was applied for ten times. The algorithm is a Gaussian filter and is based on reference [92].

When several AE spectra are plotted in one frame, an offset on the intensity axis was applied to each spectrum to improve visibility [30]. AE spectra acquired on the Au(111) surface with high kinetic energies (in the range of 1000 – 1987 eV) are displayed with an intensity scaling factor of 2 to enhance the intensity of the small gold Auger signals in this kinetic energy range (see e.g. Figure 7.2 d)).

AE line scan (AELS) measurements

Auger line scans were measured via the software ISEM (Omicron Nanotechnology, version 1.0.2.2, 2004). The position of the measurement and the lateral size of a line scan were adjusted in ISEM in an imported SEM image that was taken before with the SEM software. The lateral step size was defined by the adjusted number of points. During the measurement, a background signal was subtracted from the signal of interest. Both signals were measured alternatively at each point of the line in a point by point “fashion”. The parameters for each AE line scan (peak energy, background energy, step size and dwell time) are specified in the corresponding chapters of this work. In addition, the parameters that were adjusted in the ISEM software are given in the Appendix (see Chapter 16.1.3).

Processing and reproduction of AE line scans

The AE line scan data was exported from ISEM, converted and then processed with the software ‘Igor Pro’ (WaveMetrics, version 5.0.2.0, 2004). If more than one line scan is shown in one figure, an offset on the intensity axis was applied to each line scan to improve visibility. If necessary, a minor manual shift of the line scan curves on the abscissa (lateral position) was carried out to compensate drift effects.

SAM measurements

SAM images were acquired via the software ISEM (Omicron Nanotechnology, version 1.0.2.2, 2004). The position of the measurement and the lateral size of a SAM image were adjusted in the SEM software. The lateral step size was defined by the resolution, i.e. the number of points in each row and column. During the measurement, a background signal was subtracted from the signal of interest. Both signals were measured alternatively in a line by line “fashion”. The SAM parameters (peak energy, background energy, resolution and dwell time) are specified in the corresponding chapters of this work. Additionally, the parameters that were adjusted in the ISEM software are given in the Appendix (see Chapter 16.1.3).

Reproduction of SAM images

SAM images are displayed with modified brightness and contrast settings in order to enhance the observed chemical contrast and to increase the force of expression of the image.

3.6.6 AFM measurements

The characterization of EBID deposits via atomic force microscopy (AFM) was done with an easyScan DFM system (Nanosurf AG, Switzerland) at ambient conditions. Figure 3.7 shows the applied AFM instrument.

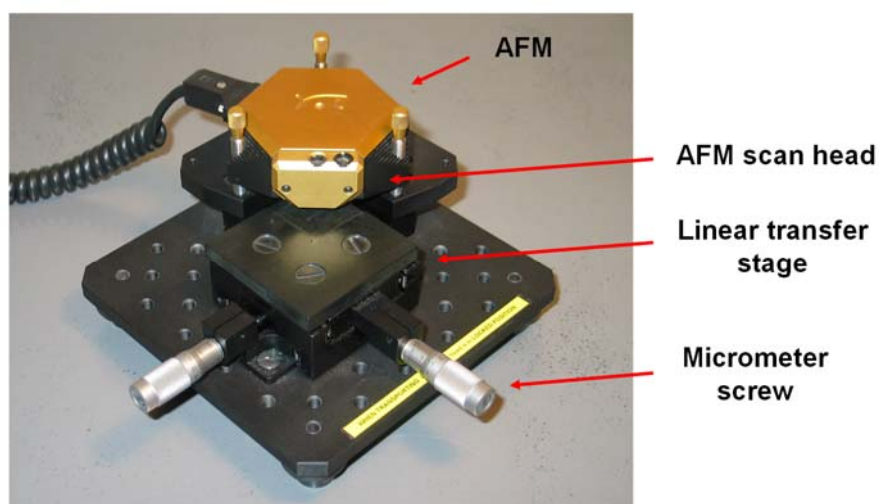


Figure 3.7: Atomic force microscope (easyScan DFM system, Nanosurf AG, Switzerland) working at ambient conditions.

To minimize the influence of external vibrations on the AFM measurements the instrument is located on a vibration isolation table-top system ('Table Stable TS-150', HWL Scientific Instruments GmbH, Germany) isolating dynamically in the frequency range from 0.7 Hz to 1 kHz [93]. For precise position control during the AFM measurements a linear transfer stage (M-460A-XY, Newport Corporation) with two micrometer screws (type SM-13) for the X- and Y- direction, respectively, was applied. The travel of the stage and the screws is 13 mm with an accuracy of 1 μm [94].

The instrument is equipped with the “large scan head” with a maximum XY scan range of 110 μm , a maximum Z range of 22 μm and scan step resolutions of 1.7 nm in XY and 0.34 nm in Z direction [95]. Silicon cantilevers of the type ‘PPP-NCLR-50’ (Nanosensors, NanoWorld AG, Switzerland) were used with a resonance frequency range from 146 to 236 kHz and a force constant range from 21 to 98 N/m.

All measurements were conducted in the dynamic force mode. In this mode, the cantilever is mechanically excited close to its resonance frequency and during the scan process a constant oscillation amplitude is maintained (see Chapter 2.4). According to reference [96], the vibrating cantilever contacts the surface only intermittently, which eliminates potentially damaging lateral forces. In the work at hand, the oscillation amplitude was set to a value between 50 and 60 % of the free and undamped amplitude. Each AFM image was acquired with a minimum resolution of 512 x 512 pixels and a minimum scan time of 0.500 s per line. Typically, both the forward and the backward scan image were recorded.

Data processing was performed with the software WSxM (version 5.0, Develop 3.2, 2011) [97]. The AFM images were processed via the filter “Flatten”, which subtracts a selectable function from each single line of the unprocessed image [97]. As function to subtract, typically the averaged line profile of each line scan of the image was chosen. All specified height values were determined via the software WSxM, as well, applying the corresponding “Profile” function.

3.6.7 Sputtering

Sputtering was performed with the grounded sample located on the manipulator of the preparation chamber, exclusively under normal incidence. The sputter gas was argon with a background pressure in the chamber of $4.0 \cdot 10^{-6}$ mbar. The kinetic energy of the Ar^+ ions was 1 keV and the emission current was 10 mA. The ion gun was set such that the ion beam had a lateral dimension of 16 mm (details see Chapter 16.1.3 in the Appendix). Thus, it was guaranteed that the whole sample surface was sputtered [98]. Before sputtering, the purity of the argon gas was verified via QMS [99]. The sputtering current was measured to be 0.3 μA (details see Chapter 16.1.3 in the Appendix).

3.6.8 Quantitative analyses

Normalization of Auger spectra

It was found that the measured signal intensity for Auger electrons depends on several factors. These are the sample holder geometry, performed sample holder modifications, the sample geometry, the surface roughness and topography, the position of the measurement on the sample and electric and magnetic fields (for more details see Chapter 16.1.4 in the Appendix). Influenced by these parameters varying intensities are measured despite investigating identically fabricated structures or samples of the same material and surface orientation, for which an identical intensity was expected. This effect is no background effect since the total number of detected Auger electrons is different.

Generally, for high detection efficiency of electrons in the hemispherical electron energy analyzer a control of the octopole deflector electrodes is necessary. For this purpose, a so-called “octopole correction table” is generated with a test sample (details see reference [30]). To handle the influence of the vast majority of the above stated parameters, one would have to generate an own “octopole correction table” for each sample holder and sample geometry. However, the latter is strongly time-consuming (several days for each table), and thus this procedure is not practicable.

Therefore, to make AE spectra comparable and to enable quantitative analyses, the intensity of all AE spectra displayed and analyzed in this work was normalized. The proceeding applied for normalization is briefly described in the following.

Normalization was done by scaling the whole spectrum with a factor such that the spectrum features at a reference energy the intensity of a reference spectrum (or a constant intensity value). The factor is the quotient of the intensity of the reference spectrum (or the constant intensity value) and the intensity of the spectrum to be normalized at the reference energy. Since each Auger signal in an AE spectrum generally contributes to the intensity of the Auger signals which appear at lower kinetic energy, for all spectra a reference energy higher than the kinetic energy of the Auger signal with the highest kinetic energy in the corresponding energy range was used. Consequently, intensity contributions from Auger signals of higher kinetic energy can be minimized. Since low (0 – 990 eV) and high energy range (1000 – 1987 eV) AE spectra had to be measured with different settings for the hemispherical electron energy analyzer (CRR value, see Chapter 16.1.3),

normalization of these spectra was done separately. For further details concerning the normalization, the interested reader is referred to Chapter 16.1.4 in the Appendix of this work. Here, the used reference spectra, reference energies and technical parameters are specified.

A very similar normalization of Auger spectra acquired in the non-derivative form was recently reported by Wu *et al.* who normalize their spectra by scaling the intensity such that it is 1,000 counts at the energy of 535 eV [100]. The authors argue as well that normalizing the spectra allows for quantitative comparisons of Auger peak heights [100].

Quantitative analysis of Auger spectra

For the quantitative analysis of Auger spectra and the determination of the chemical composition of EBID deposits with TTIP, self-measured reference AE spectra for titanium dioxide and carbon were used (see Chapter 16.1.5 in the Appendix). This procedure has several advantages compared to the use of reference spectra from literature. First, the measured intensity in an AE spectrum is always dependent on the analyzer of the instrument, i.e. on its transmission function. Since the latter is specific for each analyzer and thus varies in dependence of the instrument, the use of self-measured reference spectra is generally preferable compared to the use of data measured in a different setup. Secondly, the Auger electron yield strongly depends on the atomic number of the detected elements (see Figure 2.5), the used PE beam energy for excitation and the particular transition. Therefore, energy and transition specific sensitivity factors are generally used for the quantitative analysis of Auger spectra [34]. Measuring reference AE spectra for the elements of interest (with identical measurement parameters and in the same instrument) enables to determine directly the amount of each element in the investigated structure without the need for sensitivity factors. Thirdly, the vast majority of Auger spectra which are specified in literature were acquired in the derivative form (see e.g. [40]). Since in this work non-derivative Auger spectra were measured, the latter can not be used as reference. Fourthly, published Auger spectra can only be used as reference when they were acquired with the same parameters. It was found that the latter are often incompletely specified in literature.

For the determination of the titanium and oxygen content of EBID deposits, reference AE spectra were measured on a clean rutile $\text{TiO}_2(110)$ single crystal. Additionally, these spectra were used to prove the oxidized chemical nature of titanium in the deposit. This procedure, applying a rutile $\text{TiO}_2(110)$ crystal as a reference, was recently also reported by Wu *et al.* [100].

It is well-known from literature that the rutile $\text{TiO}_2(110)$ surface features point defects after heating in UHV, which can be attributed to oxygen vacancies [6, 101-103]. Thermal oxygen loss is accompanied by the formation of Ti^{n+} interstitials, which diffuse into the bulk of the crystal [101]. However, the density of oxygen vacancies at the surface and in the crystal is regarded to be rather low. While Bowker *et al.* [101] and Bennett *et al.* [102, 103] report of a bulk stoichiometry of TiO_{2-x} with x being in the range of 10^{-4} to 10^{-3} (depending on the applied temperature and the number of sputter / anneal cycles), Diebold [6] reports of a density of $7\% \pm 3\%$ per surface unit cell. Analogously to [100], in this work the slightly reduced, UHV prepared rutile $\text{TiO}_2(110)$ sample is regarded as reference for “ TiO_2 ” with a maximum error of $7\% \pm 3\%$ [6].

Further, it has to be noted that upon electron irradiation of TiO_2 inevitably electron stimulated desorption (ESD) of oxygen occurs [6, 104-107], which has to be considered for the quantitative analysis of titanium and oxygen containing EBID structures. The amount of oxygen that desorbs from the surface depends on the measurement parameters, i.e. on the local electron dose. Consequently, the use of reference spectra is only valid if they are measured with the same acquisition parameters as the spectra they are compared to, which was considered in this work. By this approach, references were generated for the scan strategies and acquisition parameters used for the measurement of AES data.

For the determination of the carbon content, a reference AE spectra was used which was acquired on a thick carbon layer on an $\text{SiO}_x(300\text{ nm}) / \text{Si}(100)$ sample. In this spectrum the large carbon KLL signal was the only detected signal and the Auger electrons of the SiO_x support were completely damped.

For quantitative analysis, the Auger signal intensities, i.e. the areas of the Auger peaks, were determined by linear background subtraction in the normalized spectra (normalization see above and in Chapter 16.1.4 in the Appendix). The determination

of the chemical composition of EBID deposits was then performed by dividing the C, Ti and O peak areas by the ones deduced from the corresponding normalized carbon and titanium dioxide reference spectra (reference values for C, Ti and O) which were acquired with identical or very similar scan parameters. This proceeding enables to specify the chemical composition in atomic percent (at. %).

In the case of incomplete substrate signal damping in an AE spectrum acquired on an EBID deposit, the reference values for C, Ti and O (deduced from the normalized reference spectra) had to be adjusted with respect to the corresponding layer thickness. This adjustment was done applying the straight-line approximation model and considering the peak intensity from an overlayer material A (carbon or titanium dioxide) as a function of the layer thickness d (see Equation 3.1) [30, 108].

$$I_A = I_A^\infty \left[1 - \exp\left(-\frac{d}{\lambda_{AL}^A(E_A) \cdot \cos \theta}\right) \right] \quad (3.1)$$

I_A	Intensity of electrons from the overlayer material A for the layer thickness d
I_A^∞	Intensity of electrons from a specimen of the pure material A
d	Layer thickness of the overlayer material A
$\lambda_{AL}^A(E_A)$	Attenuation length of electrons with energy E_A in the overlayer material A
θ	Angle between surface normal and electron spectrometer (35° for the applied instrumental setup) [30, 108]

The attenuation lengths for carbon ($\lambda_{AL}^C(E_C)$), titanium ($\lambda_{AL}^{TiO_2}(E_{Ti})$) and oxygen ($\lambda_{AL}^{TiO_2}(E_O)$) were calculated using equations 13 and 15 of reference [108] (for details see subchapter 'Attenuation lengths' below), and for I_A^∞ the reference values for C, Ti and O, deduced from the normalized reference spectra, were used. By this procedure (normalized Auger peak area) reference values for C, Ti and O were calculated for a pure overlayer material A (carbon or titanium dioxide) with the corresponding layer thickness d .

For the quantitative analyses of this work it was found that the sum of the calculated carbon, titanium and oxygen content of EBID deposits lies below 100 %. Possible explanations for this finding are listed in Chapter 16.1.4 in the Appendix of this work. As main reason it is considered that the fabricated EBID deposits probably feature an inhomogeneous element distribution with an increased amount of carbon at the surface (see results presented in Chapter 9.1.1) while the performed analysis is based on a homogeneous distribution of all elements in the deposits. To address the observed deviation, the initially calculated values for C, Ti and O were uniformly scaled with a factor such that they sum to 100 %.

In Chapter 13 AE spectra are shown that were measured on EBID deposits which were fabricated with the precursor iron pentacarbonyl and consist mainly of iron with a small carbon and oxygen contamination. For the quantitative analysis of these spectra they were normalized as described above and in Chapter 16.1.4 in the Appendix. The amount of carbon was estimated via the normalized reference AE spectrum for carbon (see above). Since no reference AE spectrum for the element oxygen, i.e. an AE spectrum measured on a pure and thick oxygen layer depicting solely oxygen KLL signals, is available, the amount of oxygen was estimated by a self-determined reference value of Thomas Lukasczyk (details see Chapter 9.1.11 in reference [30]).

Considering all different sources which influence the quantitative determination of the chemical composition an accuracy of ± 5 at. % is assumed.

Determination of layer thicknesses

Layer thicknesses of EBID deposits were determined by applying the modified straight-line approximation model using Equation 3.2 (equation 2 of Cumpson and Seah [108]).

$$I_B = I_B^\infty \cdot \exp\left(-\frac{d}{\lambda_{AL}^A(E_B) \cdot \cos \theta}\right) \quad (3.2)$$

I_B Intensity of electrons from the substrate material B below

	the overlayer material A of the layer thickness d
I_B^∞	Intensity of electrons from a specimen of the pure material B
d	Layer thickness of the overlayer material A
$\lambda_{AL}^A(E_B)$	Attenuation length of electrons with energy E_B in the overlayer material A
θ	Angle between surface normal and electron spectrometer (35° for the applied instrumental setup) [30, 108]

The relevant substrate intensities of Si KLL, Au MNN and Fe LMM Auger signals were determined via linear background subtraction (see above). The I_B^∞ values for Si, Au and Fe were deduced from the clean Si(100), SiO_x(300 nm) / Si(100) and Au(111) surfaces before the EBID experiments ($E_{kin}(Si) \approx 1615$ eV, $E_{kin}(Si \text{ in } SiO_x) \approx 1604 - 1606$ eV, $E_{kin}(Au) \approx 1743$ eV and ≈ 1765 eV) and from a large EBID iron line deposit with complete substrate signal damping ($E_{kin}(Fe) \approx 645$ eV). The inelastic mean free paths specified in equation 2 of Cumpson and Seah [108] were approximated with the corresponding attenuation lengths (for details see subchapter ‘Attenuation lengths’ below).

The determination of layer thicknesses via this model and Equation 3.2 yields reliable results for thicknesses $d > 0.2$ nm, i.e. more than fractional monolayer coverages [108], and when the damped substrate signal intensity I_B can still be measured with sufficient accuracy. For the latter, the authors Cumpson and Seah propose that I_B should be at least 5 % of I_A [108].

Attenuation lengths

The attenuation lengths λ_{AL} used in Equation 3.1 and 3.2 were calculated applying the semi-empirical Equations 3.3 and 3.4 specified in reference [108].

$$a = 10^8 \cdot \left(\frac{\mu}{\rho \cdot N_A} \right)^{1/3} \quad (3.3)$$

a “Lattice parameter” of an overlayer matrix A

	(defined by Cumpson and Seah in reference [108])
μ	Average atomic mass per mol of the overlayer matrix A (in g)
ρ	Density of the overlayer matrix A (in kg m ⁻³)
N_A	Avogadro constant

$$\lambda_{AL} = 0.316 \cdot a^{3/2} \cdot \left\{ \frac{E}{Z^{0.45} \cdot [\ln(E/27) + 3]} + 4 \right\} \quad (3.4)$$

λ_{AL}	Attenuation length (in nm) of electrons with energy E in an overlayer matrix A characterized by a
a	“Lattice parameter” of an overlayer matrix A (defined by Cumpson and Seah in reference [108])
E	Electron energy (in eV)
Z	Averaged atomic number Z of the overlayer matrix A

In the work at hand, these equations were used to account for the chemical composition of the deposited material. The composition was determined from the experiment and the stoichiometric coefficients of C, Ti and O were used to determine the average atomic mass per mol μ and the average atomic number Z tailored for the actually deposited material. For the density ρ of the overlayer matrix an averaged density value deduced from the different titanium dioxide mineral forms was applied (4,070 kg m⁻³). Plots for λ_{AL} in dependence of the electron energy E and the applied values for layer thickness calculations are specified in the Appendix of this work (see Chapter 16.1.6).

Determination of lateral sizes from SEM images

All measurements of lateral structure sizes from SEM images were performed with the software WSxM (version 5.0, Develop 3.2, 2011) [97].

Since there is no definite criterion to determine the lateral size of structures, standard criterions were introduced and used in this work. Figure 3.8 depicts the two procedures applied for the estimation of lateral sizes of EBID deposits.

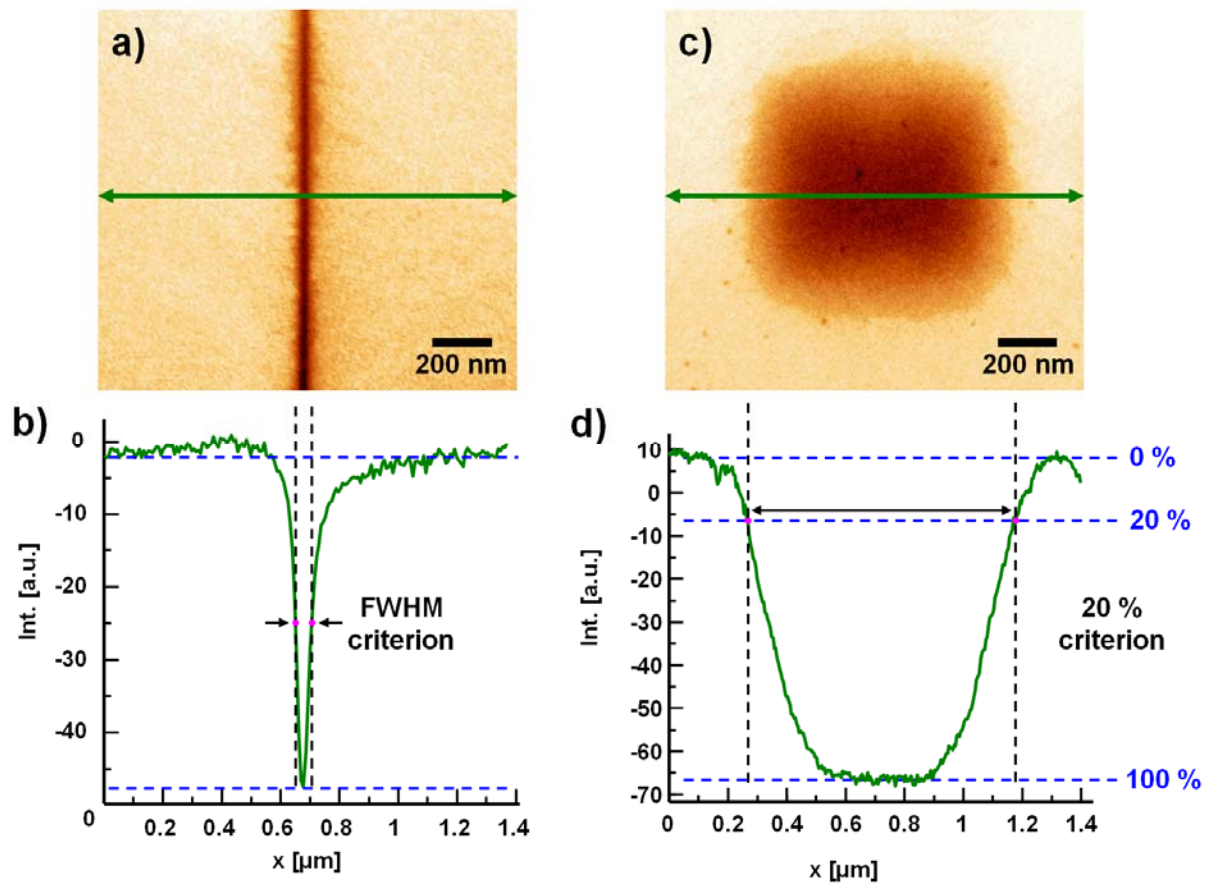


Figure 3.8: Two procedures applied for the estimation of lateral sizes of EBID structures, both performed with WSxM [97]. a) and b) Estimation of the width of a line structure according to the 'FWHM criterion'. c) and d) Estimation of the width of a square structure according to the '20 % criterion'.

The vast majority of lateral sizes of EBID deposits was determined according to the 'FWHM criterion' (full width at half maximum). This criterion is a widely applied criterion for the determination of lateral structure sizes (see e.g. reference [109]). In Figure 3.8 a) and b) the determination of a line width according to the 'FWHM criterion' is shown exemplarily. The estimated lateral size is the distance between a left and a right border, at which the gray scale value in the SEM image is half of the two extreme gray scale values, i.e. the value of the surface and the value of the center of the line deposit.

Some EBID deposits depicted in this work show a comparably broad fading at the structure edges in SEM, i.e. a comparably flat increase or decrease of the gray scale intensity (see the halos around dot deposits in Figure 7.1 a) and the area deposits in Figure 7.1 c)). It was found that the lateral size of these deposits appears to be underestimated when applying the 'FWHM criterion'. Therefore, a second criterion was introduced in this work, the so-called '20 % criterion'. It was applied when the fading at the structure edge was larger than ≈ 50 nm. Figure 3.8 c) and d) shows the determination of the width of a square deposit according to the '20 % criterion'. The estimated lateral size is the distance between two borders, at which the gray scale value in the SEM image has decreased to 20 % of the difference of the two extreme gray scale values, i.e. of the surface and the center of the structure. In the latter, the 100 % value is always set to the deposit center (not to the surface).

To enhance the signal-to-noise ratio, it was typically averaged over 5 or 10 profile lines in both procedures, with the number of profile lines being specified in the corresponding section of this work.

The '20 % criterion' was also applied for the estimation of the diameter of statically irradiated dot deposits (see Chapter 10.3.1). However, due to the asymmetric shape of the acquired profiles (see Figure 3.9 a)) and due to the appearance of a central area of strongly different gray scale compared to the rest of the structure (see Figure 3.9 b)), the '20 % criterion' was applied in a slightly modified way, which is described in the following.

The center of the dot structures was determined optically and the radius was determined exclusively at the right side, i.e. into the direction of the dosing nozzle in the EBID experiment. The right end of the radius was defined as the exterior point at which the gray scale value has decreased to 20 % of the maximum gray scale value of the deposit (see Figure 3.9) [110]. The doubled radius was considered as the (average) width of the dot deposits.

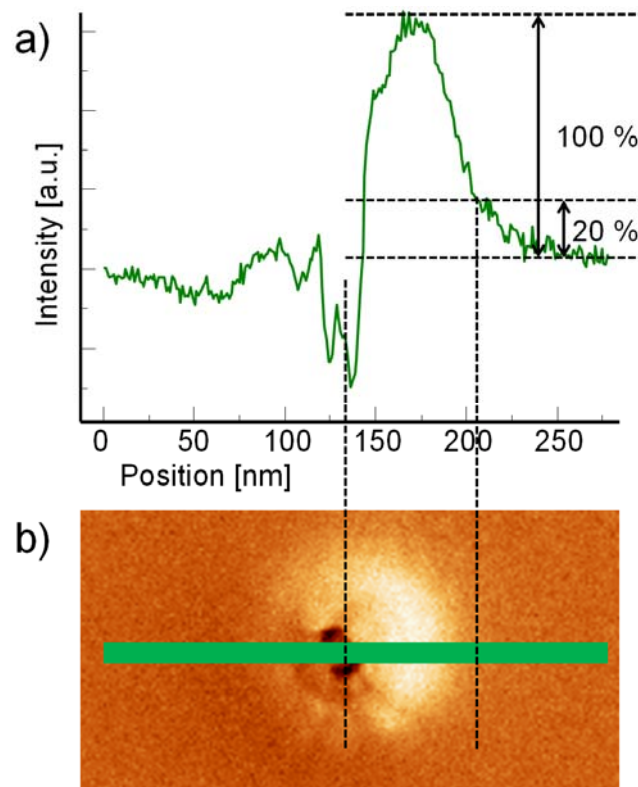


Figure 3.9: Exemplary determination of the lateral size of a statically irradiated dot deposit. The dot radius was determined in the SEM image from the optically determined center to an exterior point at the right side where the gray scale has reached 20 % of the maximum gray scale value of the deposit. Please note that this figure is reproduced from reference [110].

Determination of structure heights from AFM images

All measurements of structure heights from AFM images were performed with the software WSxM (version 5.0, Develop 3.2, 2011) [97]. To enhance the signal-to-noise ratio, it was averaged over several profile lines. The number of profile lines was either 5 or 10, depending on the shape of the investigated structure. The latter is specified in the respective chapters of this work.

4 Literature review

In this chapter, a brief literature review of EBID is given (Chapter 4.1). Emphasis is further put on proximity effects in EBID (Chapter 4.2) and on strategies for the fabrication of clean deposits via EBID (Chapter 4.3), which is a major challenge of this technique. In addition, present applications for the compound titanium(IV) tetraisopropoxide (TTIP) are reviewed (Chapter 4.4) and the use of TTIP in EBID is reported (Chapter 4.5). Finally, the target material of this work, i.e. titanium dioxide, is briefly reviewed including properties and applications (Chapter 4.6).

4.1 Electron beam induced deposition (EBID)

The technique of electron beam induced deposition, as it is known today, was not “discovered” in the classical meaning. It is historically derived from a carbon contamination effect in particle beam systems. In 1934, Stewart [111] reported on the already at that time well-known phenomenon of the formation of insulating, carbonaceous films upon electron and ion bombardment and refers to numerous examples, where the deposits vitiate scientific results. The author denoted these deposits as a “very insidious and prevalent source of error” [111]. In 1953, Ennos [112] and Poole [113] described that electron induced specimen and electrode contamination occur in electron microscopes and electron optical systems. The authors traced the contamination back to the electron induced dissociation of organic molecules, which are adsorbed on the bombarded surfaces and are replenished from the “vapor phase” of the vacuum system.

Initially an unwanted side effect, the first intentional use for the well-directed fabrication of films on surfaces is reported by Christy [114] in 1960 and Baker and Morris [115] in 1961. While Christy generated thin, insulating films from silicone oil vapor, Baker and Morris deposited metallic films by the decomposition of organometallic tin and lead vapors [114, 115]. These works can be considered as the starting point of the EBID technique and in the following years numerous efforts have been made for the fabrication of spatially and chemically well-defined structures (see review articles [2-5]).

EBID features several advantages compared to other lithography techniques. One of the most important advantages is the generation of structures on the very low nanometer scale. This is possible since in modern instruments electron beams can be focused to beam diameters even in the sub-nm range. In 2005, the fabrication of tungsten containing dot structures with a lateral size of less than 1 nm (FWHM) on 30 nm thick Si_3N_4 membranes was reported by van Dorp *et al.* [109]. This is the smallest size of EBID structures published in literature so far and demonstrates that EBID is a promising technique for high resolution, resist-less lithography [109]. Secondly, EBID allows for the local generation of nanostructures by the precise position control during fabrication. Another advantage is the generation of structures of arbitrary shape and in particular of three-dimensional structures by controlling the electron beam and applying a predefined scan pattern [116]. The large variety of applicable precursors and thus the diversity of achievable deposits (see below) [3, 4] is another benefit of the EBID technique. In addition, the latter is a “direct-write”, i.e. mask-less and resist-less, technique, which allows for the generation of structures with less process steps compared to other techniques [117]. Last but not least, the fabrication of nanostructures via EBID is possible both on flat and on “topographical”, i.e. pre-structured or rough, surfaces (e.g. on an STM tip [118] or AFM tip [119]).

However, the EBID technique also has some disadvantages, which are subject of further studies. One important challenge of EBID is the phenomenon of proximity effects (see Chapter 4.2). These effects, usually occurring due to electron scattering events, lead to additional, unintended deposits off the targeted structure and thus cause structure broadening. Apart from that, another important challenge is the fabrication of deposits with defined chemical composition, i.e. without the typical contaminants carbon and oxygen. Deposits generated from organometallic precursors typically have a rather low metal content and consist of a nanocomposite material with metal crystals embedded in a matrix of amorphous carbon [5, 120]. Van Dorp specifies a usual metal content of 10 % while the remaining 90 % are carbon and other elements stemming from the precursor molecule [5] or from the residual gas. Also higher metal contents are reported in literature, which are typically in the range of 10 to ≈ 60 at. % [119, 121-133]. Only rarely, metal contents higher than 60 % are documented, mostly acquired by the use of special precursors, specific lithographic parameters or better vacuum conditions (see Chapter 4.3). Furthermore, EBID is a comparably slow technique and features low growth rates compared to

other lithography techniques like electron beam lithography (EBL) [5]. The reason for this is that structure generation occurs by sequential processing in EBID while parallel processing is conducted in EBL.

A very important factor is the choice of the precursor for EBID since it determines the composition of the deposited material [2-5]. The precursor should meet several requirements. First of all, it must be volatile so that it can be dosed into the instrument chamber. Therefore, the use of gaseous compounds or liquids with a considerable vapor pressure is preferable. The precursor molecules must stick to the surface, should temporarily reside on it and upon electron beam irradiation they should decompose to the desired product [4]. Another requirement for a suitable precursor is that the generated non-desired fragments of the EBID process are volatile and desorb readily without being embedded in the deposit or being decomposed themselves by electron irradiation [4]. Further, the precursor should exhibit a certain stability both during storage and dosage [4, 5] and should not cause a persistent vacuum contamination after the experiment.

Utke *et al.* [4] indicate that precursor transformation and / or degradation might take place in the storage device and in the gas dosage system. The degree of degradation depends on several factors like container material, storage time and temperature. Many precursor molecules are sensitive to air and especially to oxygen or water. Therefore, they have to be filled into the storage device under inert gas atmosphere (typically nitrogen or argon). This necessitates the purification of the filled precursor to remove the inert gas before the experiments. The chemical composition of the substance can be changed by pumping at room temperature on the precursor [4]. A slow but constant ligand loss can occur, which may induce higher clustering of the compound. The phenomenon of precursor clustering is assumed for several precursors. However, the experimental verification is difficult [4].

When a liquid or solid precursor has a low vapor pressure, heating of the storage device is a suitable way to increase the precursor volatility. However, for some compounds (e.g., $\text{Fe}(\text{CO})_5$ [4]) thermal decomposition of the precursor is reported and also transformations like clustering are supposable. This emphasizes the importance of the precursor volatility, i.e. the vapor pressure, for the use in EBID experiments.

In the review articles from Silvis-Cividjian and Hagen [3] and particularly from Utke *et al.* [4] a detailed overview of hitherto applied precursor molecules is given. The precursors range from organic compounds to metal hydrides, halides, carbonyls, phosphines, halogenophosphines, organometallic compounds, acetylacetonates, alkoxides, nitrates and amides [4]. By this large precursor variety also a large variety of target materials has been realized up to now. The latter were, for instance, of carbonaceous nature (e.g. [134, 135]), contained metals (e.g. chromium [122, 136], iron [136-143], cobalt [119, 125, 144, 145], nickel [127], copper [123, 132, 146], molybdenum [116, 123], rhodium [126, 147], tungsten [109, 121, 122, 148-151], platinum [123, 124, 152, 153] and gold [116, 121, 123, 124, 154-156]) or consisted of a metal oxide material (e.g. [16-18, 133, 157]).

Many applications have been developed for EBID and presently there are three industrial applications. First of all, EBID is commercially used for the repair of photomasks and EUV masks in semiconductor industry [4], where it is applied in the 65 nm node [4], 45 nm node [30] and 32 nm node [158] technology. While this field of application was initially covered by the technique of focused ion beam (FIB) processing, meanwhile EBID is the state-of-the-art mask repair tool [159, 160]. Another commercial application of EBID is the fabrication of high-aspect-ratio tips, which are used in scanning probe microscopy (AFM and STM, see e.g. references [118, 119, 125, 161]) and for local conductivity measurements. Thirdly, EBID is used for circuit editing of multilevel architectures [4]. The repair of a metal-semiconductor field-effect transistor gate by fabricating deposits from $W(CO)_6$ on a doped GaAs substrate to form a Schottky contact was e.g. reported by Hoyle *et al.* [162].

Further applications of the EBID technique are the generation of nanophotonic structures, the use in micro- and nanoelectronics (i.e. the fabrication of insulators, resistors, electrical contacts, conducting wires, diodes and laboratory prototype devices), the generation of field emitters and masks, diverse mechanical applications and also applications in biology (see Utke *et al.* [4]). Additionally to these applications, van Dorp and Hagen mention the fabrication of electron sources, micro-Hall devices, micrometer scaled superconducting quantum interference devices (SQUIDs), nanotweezers, gripping devices and the use of EBID structures as seeds for nanotube growth [5].

For further details concerning the EBID technique, the interested reader is referred to the comprehensive review articles of Randolph *et al.* [2], Silvis-Cividjian and Hagen [3], Utke *et al.* [4] and van Dorp and Hagen [5].

4.2 Proximity effects in EBID

A typically unintended phenomenon in EBID is the occurrence of so-called proximity effects. These effects are mainly due to electron scattering events and can significantly influence the final deposit shape or the material distribution on the surface [5]. Generally, they cause an unintentional structure broadening in EBID due to additional, unintended deposits in close vicinity or lead to structure bending. The term 'proximity effect' originates from the resist based technique of electron beam lithography (EBL) and is defined as the "extra and unintentional exposure (...) surrounding the irradiated areas" [5].

Up to now, several types of EBID proximity effects have been described in literature (see e.g. in the review article [5]). They are listed in the following and the proximity effects that are relevant for this work are briefly explained below.

- BSE proximity effect
- FSE proximity effect
- SE proximity effect
- Slope dependent proximity effect
- Surface plasmon proximity effect
- Bending proximity effect

The 'BSE proximity effect' is caused by high energetic backscattered electrons (BSEs), which leave the sample surface within the 'BSE exit area' surrounding the point of irradiation. Both the emitted BSEs and thereby released SEs (SE2) cause the formation of an additional, unintended deposit in EBID that typically covers the 'BSE exit area'. The latter can be observed as a halo in the surrounding of the targeted structure. In literature, this effect was reported e.g. by Lau *et al.* [119], Boero *et al.* [163] and Edinger *et al.* [159]. Since the size of the 'BSE exit area' depends, for instance, on the primary beam energy, choosing low beam energies is a suitable way to reduce the lateral size of the caused deposit [5].

The 'FSE proximity effect' is caused by high energetic forward scattered electrons (FSEs), which escape from the side faces of growing EBID structures. While the result is similar to that of the 'BSE proximity effect', i.e. an additional, unintended deposit in the surrounding, a significant difference is that unintended deposition occurs on a larger length scale, i.e. going beyond the range of the 'BSE exit area' [5]. Evidence that this proximity effect is actually caused by forward scattered and not by backscattered electrons was given e.g. by Bret *et al.* [164] who fabricated a tall tip on a substrate covered with small silicon particles. Since the unintended deposit was found in the complete surrounding of the tip but not directly behind the silicon particles, the 'BSE proximity effect' could be excluded [5]. The affected lateral area of the 'FSE proximity effect' strongly depends on the height of the targeted structures. Therefore, it is typically observed for tall deposits.

The 'SE proximity effect' is caused by spraying of secondary electrons (SEs) from the currently fabricated deposit, which leads to additional material deposition on already existing structures in close vicinity [5]. This effect was e.g. described by Aristov *et al.* [165] and Lau *et al.* [119] for self-standing rod and dot structures. However, one aspect has to be noted for this proximity effect. Per definition, SEs are electrons with an energy ≤ 50 eV and, in principle, the described unintended additional deposits can also be caused by higher energetic scattered or generated electrons. Consequently, the FSE and SE proximity effect might be without fundamental difference [5].

Since the slope dependent, surface plasmon and bending proximity effect are not relevant for this work, they are not described in this chapter. The interested reader is referred to the review article of van Dorp and Hagen [5] and to the articles quoted there.

Finally, it is pointed out that the targeted structures and the unintended additional deposits caused by proximity effects can feature a different chemical composition and thus different properties. Possible reasons for this finding are e.g. the different time the dissociated molecules have to rearrange, the different current densities and the different electron energy distributions in the PE irradiated area and in the surrounding regions. Additionally, electron beam induced heating (EBIH) in the central, PE irradiated area could play a role [5].

4.3 Fabrication of clean deposits via EBID

One of the most important challenges of EBID is the generation of structures with defined chemical composition. However, the low purity level of the deposits has been a significant drawback of the technique to date [166] and carbon and oxygen are typically found as contaminants. Generally, two reasons are denoted for contamination. First, partial or incomplete decomposition of the precursor molecules can cause the inclusion of contaminants into the deposit. Secondly, contaminations can stem from the residual gas in the chamber, which contains e.g. hydrocarbons nitrogen, oxygen and water [166].

Since contaminants in the EBID structures typically limit their functionality, considerable effort has been made either to avoid / reduce deposit contamination or to purify the as-deposited, impure structures. Recently, a review article was published by Botman *et al.* [166] giving a comprehensive review of the techniques to generate high purity materials via EBID. The authors found some general trends. First, the application of heat, either during or after EBID, is commonly favorable to some extent. Secondly, working in an instrument with favorable residual gas is strongly recommended. The latter can be realized by ultra high vacuum systems or by plasma cleaning the chamber before EBID. Thirdly, the use of carbon free precursors was found to be a promising way although it tends to chemical compositions with oxygen being the dominant contaminant instead of carbon. Finally, gas mixing approaches are reported but it was found that the results are variable and not always reproducible between different scientific groups [166].

Botman *et al.* categorize the existing purification methods in literature into the following seven techniques to acquire higher purity EBID materials [166]:

- 1.) Annealing deposits or deposition onto a hot substrate
- 2.) Variation of beam parameters or deposition conditions
- 3.) *Ex situ* post-treatment procedures
- 4.) *In situ* post-treatment procedures
- 5.) Reactive gas mixing (H₂, O₂, H₂O)
- 6.) Use of carbon free precursors
- 7.) UHV set-ups or working under clean conditions

In this list and in reference [166], the term '*in situ*' describes purification methods and steps which were conducted in the same instrument than that in which EBID was performed. The corresponding experiments have the advantage that no breaking of the vacuum is necessary between deposition and post-treatment, which causes an additional contamination. Analogously, the term '*ex situ*' describes purification methods which were conducted in a different instrument, i.e. breaking the vacuum conditions took place.

Targeting the fabrication of high purity EBID structures, the authors of reference [166] suggest to apply a combination of the techniques shown in Figure 4.1.

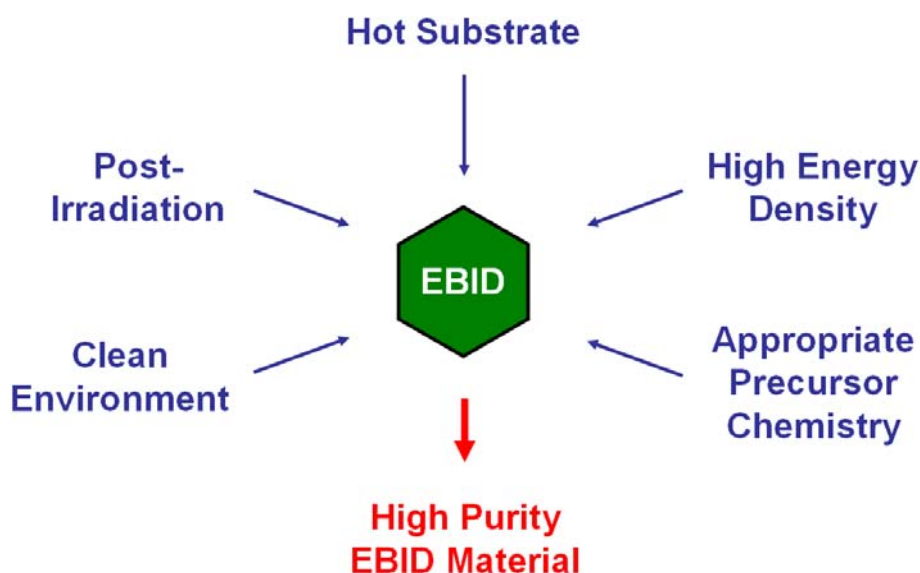


Figure 4.1: Schematic drawing, which illustrates the main strategies for the generation of higher purity EBID materials (adapted from reference [166]).

The vast majority of EBID studies reported in literature up to now was performed under HV conditions, i.e. with an undefined state of residual gas and substrate surface. However, applying a 'clean environment' and thus well-defined conditions is considered to play a key role for future EBID studies out of two reasons. First, it is beneficial for the fabrication of high purity nanostructures since the deposition of material stemming from the residual gas and chemical reactions of residual species like O_2 or H_2O with the precursor or precursor fragments are strongly minimized. In addition, such an atmosphere provides the possibility to considerably extend the

understanding of the ongoing fundamental (physical and chemical) processes. Therefore, in this work a 'surface science approach' to EBID was applied and the experiments were performed under well-defined, ultra clean UHV conditions.

Two successful approaches to increase the metal content of EBID structures by applying heat and dosing the reactive gas oxygen, which are relevant for this work, are reported in the review article [166]: Botman *et al.* [167] could increase the platinum and gold content of their deposits from 15 to ≈ 70 and from 8 to ≈ 60 at. %, respectively, by a post-treatment step of heating (up to ≈ 770 K) in a reactive atmosphere of oxygen (after having stored the samples for several days in air). The post-treatment enabled to reduce the electrical resistivity of the noble metal structures to three (one) orders of magnitude lower values for Pt (Au). However, the authors found void formation in the EBID structures induced by the loss of carbon. They mention that the structural integrity of the deposits is "uncertain" and report resistivity values still being significantly higher than the bulk values [167]. Wang *et al.* [168] successfully improved the chemical composition of fabricated platinum deposits from $\text{Pt}(\text{PF}_3)_4$ via two different approaches. By the co-dosage of O_2 during EBID they were able to increase the Pt content in the deposit from 15 to ≈ 24 at. % and thus to increase the Pt / P ratio from 0.26 to 0.63. Heating the substrate during EBID from RT to ≈ 350 K increased the Pt / (Pt + P) ratio of the structures from 0.26 to 0.60 [168].

In this work, an *in situ* post-treatment procedure based on heating and simultaneously dosing oxygen was developed with the intention of increasing the deposit purity by reducing the carbon content (see Chapter 9).

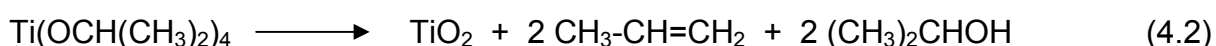
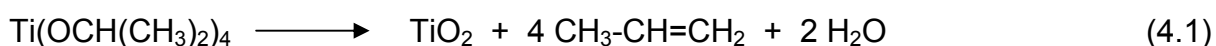
4.4 Application of titanium(IV) tetraisopropoxide (TTIP)

The precursor applied in this work, titanium(IV) tetraisopropoxide (TTIP), is widely used in many different applications. The following list gives a short overview for the fields of applications, covering 'organic synthesis', 'medicine' and 'materials science':

- Enantioselective chemical reactions (organic synthesis) (see e.g. [169-173] and reference [174] with the most prominent reaction being the so-called Sharpless epoxidation)
- Special syntheses and synthesis of special chemicals (organic synthesis) (see e.g. [175-178])
- Fabrication of coatings for medical applications (medicine) (see e.g. [179, 180])
- Use in the sol-gel technique for the deposition of titanium oxide and titania (materials science) (see e.g. [74, 181-183])
- Use in chemical vapor deposition (CVD) and atomic layer deposition (ALD) for the deposition of titanium oxide and titania (materials science) (references see below)

The most important application for TTIP with regard to this work is the use in chemical vapor deposition (CVD) and atomic layer deposition (ALD) with the target to deposit titanium dioxide.

CVD is a technique for the fabrication of thin films on surfaces. In this technique, the substrate surface is exposed to the vapor of a precursor compound and a chemical reaction is induced, which causes the decomposition of the precursor and material deposition on the surface. A large variety of different CVD techniques is known, which differ e.g. in the way how the chemical process is induced. CVD of titanium dioxide has been practiced for several decades and the beginnings go back to the year 1952 [184]. The most frequently used precursor for titanium dioxide deposition is TTIP [185]. This fact is attributed to the high volatility of the compound on the one hand and the ease of removal of the isopropoxy ligands on the other [74]. The direct thermolysis in the CVD process can be described by the following two equations [14, 15, 185]:



Both reactions can take place and realize the deposition of titanium dioxide on the surface. It was shown that the reactions expressed in Equations 4.1 and 4.2 must occur independently in different reaction pathways [15]. The decomposition of TTIP

to titanium dioxide, propene and water (Equation 4.1) is favored at higher temperatures (650 - 800 K) because lower surface coverages of adsorbed isopropoxide ligands support a dehydration reaction. In contrast to this, the thermolysis of TTIP to titanium dioxide, propene and isopropanol (Equation 4.2) occurs at lower temperatures (550 – 650 K) as the increased proximity of the isopropoxide ligands of adsorbed TTIP favors a concerted elimination reaction. At temperatures above 800 K the dehydrogenation of the isopropoxide ligands occurs and acetone is formed [15].

In literature, a large variety of articles exists concerning titanium oxide deposition via CVD. In this work, some selected examples are referred to [10-15, 74, 185, 186] with further references therein. While CVD was performed by most of the groups via thermal CVD, i.e. directing the precursor gas with or without a carrier gas along the surface of a heated sample [10, 12, 15, 74, 185], also the successful deposition of titanium dioxide via plasma enhanced CVD (PECVD) and remote plasma enhanced CVD (remote-PECVD) was reported [14]. Interesting approaches are further the deposition of titanium oxide films via the technique of krypton fluoride laser CVD (KrF laser CVD) by Watanabe *et al.* [11, 186] and liquid injection CVD reported by Simcock *et al.* [13].

A technique related to CVD is atomic layer deposition (ALD), which is also known by the name atomic layer epitaxy (ALE). It is a vapor phase deposition technique that allows for the fabrication of ultra thin films on surfaces, typically with thicknesses on the atomic scale [187]. Characteristic for ALD is the sequential use of precursor compounds (by repeating two subsequently executed half-cycles) and the film generation sub-monolayer by sub-monolayer (for a schematic illustration of ALD see reference [187]). After each precursor dose step, a purge or evacuation step is executed to remove the residual precursor or reactant species. This guarantees a self-limiting, well controlled film growth [187]. Recently, Profijt *et al.* gave a review of plasma-assisted ALD including basics, opportunities and challenges [187]. In this article, the use of TTIP as widely employed, suitable precursor for the deposition of TiO₂ films via ALD techniques was specified. Potts *et al.* demonstrated e.g. the plasma-enhanced ALD of TiO₂ at 298 -673 K using TTIP as precursor in combination with an O₂ plasma [188] and Xie *et al.* have shown the thermal ALD of TiO₂ thin films with TTIP and H₂O as second reactant [189].

In the work at hand, the chemical compound TTIP was applied as precursor for electron beam induced deposition (EBID). Analog to the use of TTIP in the sol-gel technique, in CVD and in ALD, also in EBID the target was the fabrication of titanium oxide deposits and in the ideal case of titanium dioxide structures.

4.5 EBID with titanium(IV) tetraisopropoxide (TTIP)

Despite being frequently used in the sol-gel technique [181-183], in CVD [10-15, 74, 185, 186] and in ALD [187-189] for the fabrication of titanium dioxide films (see previous chapter), the precursor TTIP has up to now only rarely been used for EBID. One possible explanation might be that residues of water in the precursor storage device, in the gas dosing pipes or in the vacuum instrument lead to the hydrolysis of TTIP and consequently to the formation of very low volatile and sticky oligomers that have the potential to “eternally” contaminate vacuum systems [4] (see also Chapter 2.8.4).

Before this work, only three articles concerning EBID with TTIP were known from literature. In 1999, Mitchell and Hu reported the fabrication of thin titanium oxide films on a GaAs substrate under UHV conditions [16, 17]. For this purpose, the authors used a procedure deviating from the “conventional” EBID technique, in which the precursor is dosed during pattern irradiation. Instead, Mitchell and Hu report of a three-step lithography process [16]. In the first step, they condensed multilayers of TTIP on the GaAs surface, which was cooled to 213 K. Then, selected areas of the precursor covered surface were irradiated by the focused electron beam of a scanning Auger microscope in order to generate the titanium oxide deposits. Finally, in the third step the substrate was warmed up to RT which enabled desorption of the intact precursor molecules from the unexposed surface [16]. To address the water sensitivity of TTIP, the authors used a N₂ purged glove box, a valved glass bulb and an “HV gas manifold system” pumped by a TMP to handle the precursor [16]. Purification was done by “repeated freeze-pump-thaw cycles under vacuum” [16]. Interestingly, the authors give a temperature for TTIP desorption of 253 K. Mitchell and Hu found that their deposition process is “selective”, i.e. that there is no deposition off the intended structures. Moreover, they specified a high deposition rate which they traced back to a high sensitivity of TTIP to electron irradiation. All deposits

fabricated with a beam current of 0.2 nA feature the incorporation of carbon [16]. For the higher beam current of 2 nA and low electron doses ($\leq 1.8 \text{ mC/cm}^2$) no carbon contamination was detected via AELS, but when increasing the electron dose the deposits showed a distinct carbon contamination, as well [17]. Furthermore, Mitchell and Hu investigated the etch resistance of the fabricated titanium oxide deposits by *ex situ* etching in chlorine atmosphere ($2 \cdot 10^{-4}$ Torr) at elevated temperature (453 K [17], 523 K [16]). They found that the titanium oxide films are resistant to etching in Cl_2 and demonstrate an efficient transfer of the generated patterns to the underlying GaAs substrate [16, 17]. Consequently, they specified TTIP to be an “excellent candidate for a negative-type resist” [16] in electron beam lithography.

The third publication concerning EBID with TTIP is an article from Hoffmann *et al.* published in 2005 [18]. The authors used TTIP in an HV system to generate structures via EBID and investigated their refractive index. The target was the generation of ‘high refractive index materials’ for ‘photonic band gap structures’ [18]. In the deposition process, they applied a beam voltage of 25 kV and comparably high beam currents of 10 – 250 nA. Hoffmann *et al.* found that the fabricated structures have a chemical composition of 34 at. % titanium, 51 at. % oxygen and 15 at. % carbon and e.g. an index of refraction of 3.3 for light with a wavelength of 500 nm as specified in reference [4].

4.6 Titanium oxides and titanium dioxide

The target material of this work was titanium oxide, in the ideal case with the stoichiometry of titanium dioxide (TiO_2), locally fabricated via EBID on the low nanometer scale.

Titanium oxide species:

For the material titanium oxide, a large variety of different compounds exists. There are not only the oxides with whole-number stoichiometries, like titanium(II) oxide, TiO , titanium(III) oxide, Ti_2O_3 , and titanium(IV) oxide, TiO_2 , but also a large number of stable substoichiometric species, best described by Ti_mO_n [190]. For this reason, the system ‘titanium / oxygen’ generally is subject to the study of nonstoichiometry [191]. Figure 4.2 depicts the phase diagram for the system ‘titanium / oxygen’ [192].

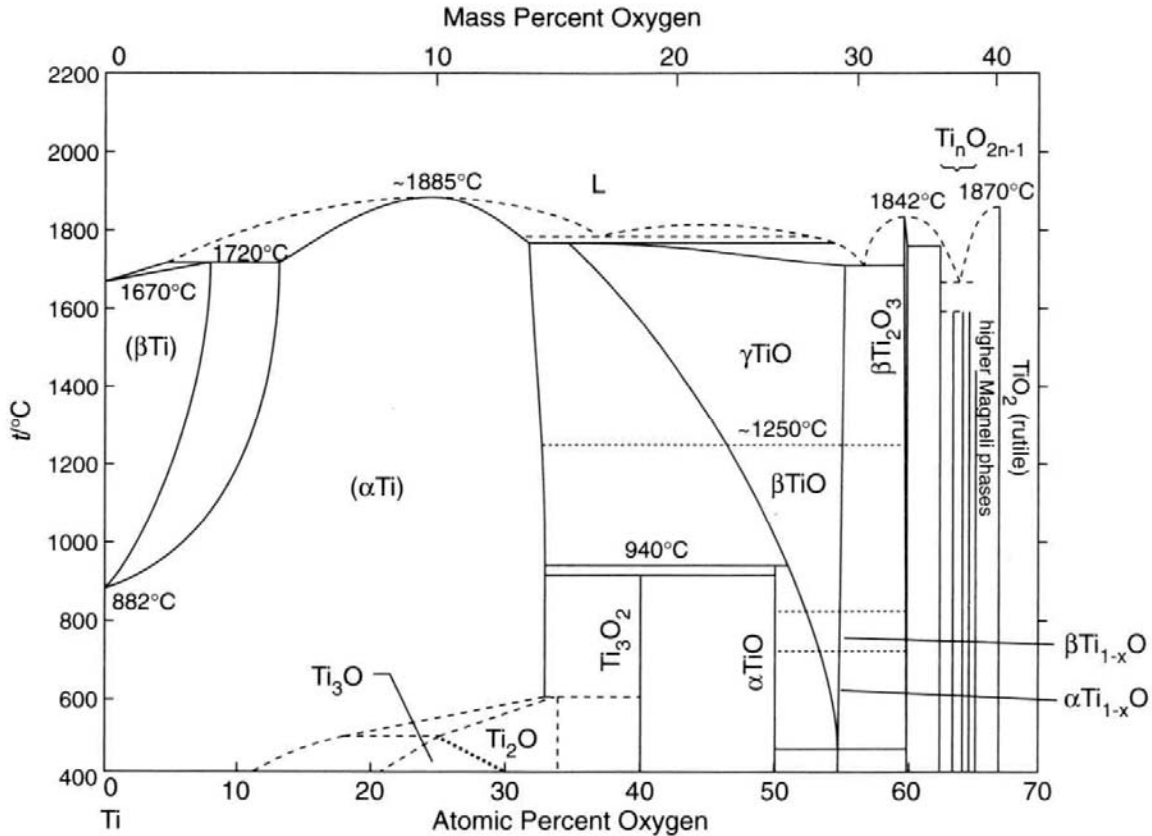


Figure 4.2: Phase diagram for the system 'titanium / oxygen' (reproduced from reference [192]).

The following list gives an overview of the different Ti_mO_n species and their properties with rising oxygen to titanium ratio from top to bottom (adapted from reference [190]).

- Ti – $TiO_{0.5}$ The hexagonal close-packed arrangement of titanium atoms is preserved and oxygen dissolves in the lattice. For the compositions Ti_6O , Ti_3O and Ti_2O ordered structures appear.
- $TiO_{0.68}$ – $TiO_{0.75}$ The hexagonal close-packed arrangement of titanium is given up and the structure of tantalum nitride is observed with oxygen vacancies.
- TiO Titanium(II) oxide is a bronze-colored compound that shows metallic conductivity. It is a non-stoichiometric species with broad phase range. Below 1173 K ordered phases exist with small homogeneous areas. For higher temperatures the phase range

	broadens. At and above 1173 K a sodium chloride defect structure with 15 % statistically distributed vacancies in both fractional lattices is observed while the composition varies from $\text{TiO}_{0.75}$ to $\text{TiO}_{1.25}$.
Ti_2O_3	Titanium(III) oxide is a species of blue to black color which crystallizes in the corundum structure. It is semiconducting, shows metallic conductivity above 473 K and is generally known in a narrow phase range (TiO_x , $x = 1.49 - 1.51$).
Ti_3O_5	Ti_3O_5 is a stoichiometric phase. It is a semiconductor and shows metallic conductivity above 448 K.
$\text{Ti}_n\text{O}_{2n-1}$	<p>The titanium oxide species that follow the description $\text{Ti}_n\text{O}_{2n-1}$ with $4 \leq n \leq 36$ are called Magnéli phases. These species show complex crystal structures in which the phenomenon of "crystallographic shearing" occurs [62, 190] resulting in a lowered mol-ratio of oxygen to titanium. The Magnéli phases of titanium oxide are all semiconductors with the single exception of Ti_4O_7 which shows metallic conductivity [193].</p> <p>For $4 \leq n \leq 10$ ($\text{TiO}_{1.75} - \text{TiO}_{1.90}$) there exist seven stoichiometric phases belonging to a homologous series [190].</p> <p>For $16 \leq n \leq 36$ ($\text{TiO}_{1.94} - \text{TiO}_{1.97}$) another homologous series of these phases is known [190].</p>
TiO_2	In TiO_2 the titanium cations have the oxidation state +IV and a defined stoichiometry exists.

Titanium dioxide:

Among the multitude of titanium oxide species the most prominent and most important one is titanium dioxide (titania, TiO_2). This material is known in three different mineral forms: rutile, anatase and brookite. All of them appear in nature, whereupon rutile is the most abundant one [62, 190]. The physical and thermodynamic properties of rutile, anatase and brookite are listed in Table 4.1.

	Rutile	Anatase	Brookite
Color:	white	white	white
Melting point:	2,116 K [62]	1,833 K [62]	-
Refraction index:	2.80 [62]	2.55 [62]	-
Density:	4.27 g/cm ³ [62]	3.90 g/cm ³ [62]	4.17 g/cm ³ [62]
Hardness:	6.2 [192]	5.8 [192]	5.8 [192]
Enthalpy ΔH_f° :	-945 kJ/mol [62], -945 kJ/mol [194]	-955 kJ/mol [62], -940 kJ/mol [194]	-
Free enthalpy ΔG_f° :	-890 kJ/mol [194]	-885 kJ/mol [194]	-
Entropy ΔS_f° :	-184.5 J/(mol·K) (based on [194])	-184.5 J/(mol·K) (based on [194])	-
Entropy S° :	50.4 J/(mol·K) [194]	49.9 J/(mol·K) [194]	-
Band gap E_g :	3.0 eV [6] (413 nm)	3.2 eV [6] (387 nm)	-

Table 4.1: Physical and thermodynamic properties of the three mineral forms of titanium dioxide: rutile, anatase and brookite [6, 62, 192, 194]. The hardness is given in the Mohs' scale (1-10) and the enthalpy, free enthalpy and entropy are valid at standard conditions (1,013.25 mbar and 298.15 K).

Regarding the thermodynamic stability of the mineral forms of titanium dioxide, rutile is the thermodynamically most stable one [193, 194]. Fahmi *et al.* [194] give values for the standard molar formation enthalpy ΔH_f° and the standard molar formation free enthalpy (Gibbs energy) ΔG_f° and report that rutile is generally more stable than anatase by 5.0 – 11.7 kJ/mol. Interestingly in reference [62] a different value for ΔH_f° of anatase is found (see Table 4.1).

Upon heating, the mineral forms anatase and brookite both transform to rutile. This transformation at higher temperatures is irreversible which supports the thermodynamic data reported by Fahmi *et al.* [194] and the conclusion that rutile is thermodynamically most stable [193]. Rutile is thermally stable, melts at 2,116 K and shows an appreciable oxygen partial pressure at a temperature above 2,073 K in

vacuum [62, 190]. At a temperature of 1,173 K and higher, rutile can be reduced to oxides of the composition Ti_nO_{2n-1} (Magnéli phases, see above) with $4 \leq n \leq 9$, $TiO_{0.7-1.3}$ or $TiO_{<0.5}$ via hydrogen or titanium [62].

In all three crystal structures, i.e., rutile, anatase and brookite, the titanium ions are surrounded distorted-octahedrally by six oxygen ions and each oxygen ion is coordinated by three titanium ions. Rutile appears in a tetragonal system [6, 192] with a slightly distorted hexagonal close-packed arrangement of oxygen ions [62]. The unit cell of the rutile crystal structure is well-described in literature [62, 190] and also formed by other metal oxides and metal difluorides. While anatase appears also in a tetragonal system, the one of brookite is rhombohedral [6, 192]. In contrast to rutile, both anatase and brookite show a cubic close-packed arrangement of oxygen ions [62].

According to reference [190] titanium dioxide is an insulator at room temperature (RT) and gains n-type semiconducting properties as soon as oxygen deficiency occurs (e.g., upon heating). For the latter case, titanium(III) ions are present in the lattice which cause the improved conductivity. In contrast to this description, Imanishi *et al.* [195] assign generally semiconducting properties to titanium dioxide and report of the work function dependence of 0.05 wt % Nb-doped TiO_2 rutile on the crystal orientation ($\Phi_{av}(TiO_2(100)) = 4.13$ eV and $\Phi_{av}(TiO_2(110)) = 4.20$ eV). Also in the review articles from Diebold [6], Aprile *et al.* [196], Fujishima *et al.* [197] and Carp *et al.* [198] TiO_2 is named in general a “wide band gap semiconductor”. The band gap is 3.0 eV for rutile and 3.2 eV for anatase which corresponds to a wavelength of 413 and 387 nm [6]. For rutile, a resistivity range from 29 – 910 Ω m can be found [192]. Titanium dioxide shows a high chemical stability [15, 62] and a large dielectric constant [15]. Further, it is nonpoisonous [62], features a high refraction index and the optical transparency lies in the visible and near infrared region [15]. These properties are the basis for a large number of applications.

Applications of titanium dioxide:

There exists a large variety of applications for TiO_2 and the corresponding literature is voluminous. In this subchapter, a small overview for its use is given. Titanium dioxide is produced commercially up to the large-scale since the early twentieth century [7]. The annual production in the world lies at several million tons [6, 62]. Due to the high

refraction index and the excellent capability of staining, coloration and brightening, titanium dioxide is the most important and most often used white pigment world-wide [190]. In addition, it is the basic material for the production of colored pigments, where TiO_2 is the host lattice for chromophoric transition metal ions [62]. It is used industrially in paints, sunscreens, and pharmaceutical and cosmetic products like ointments, salves, powders and toothpaste [7]. Moreover, TiO_2 is found in varnishes, plastics, fibers, papers, building materials, enamels, ceramics, and as additive even in cigars. Predicated on the dielectric properties of titanium dioxide, also applications in electrical industry (e.g., in capacitors) are reported [62].

An important role in science has been received by titanium dioxide since 1972. In this year, Fujishima and Honda discovered the electrochemical photolysis of water at titanium dioxide electrodes upon ultraviolet (UV) light irradiation and without an external bias [199]. This was the starting point for a strong research activity concerning titania materials and brought forth a large number of promising applications. They range from photovoltaics (energy conversion via solar cells) [200-204] and photocatalysis [197, 199, 205-210] to electrochromic devices, hydrogen storage devices and sensor applications [7].

Chen and Mao [7] divide the titanium dioxide based applications into the categories “energy” and “environment” and expect TiO_2 materials to play an important role in solving serious challenges in these fields. Regarding the energy crisis, given by a consistently growing energy demand of a rising human population at limited resources, the authors assign a key role to the utilization of solar energy in photovoltaic devices or in the production of hydrogen via TiO_2 based applications. Concerning environment protection and environmental cleanup the use of titanium dioxide based photocatalysts enables the complete decomposition of organic compounds and therefore the purification of polluted air and waste water [207]. This photo-assisted degradation of organic molecules is based on the semiconducting properties of TiO_2 . By the irradiation with sunlight electron hole pairs develop and separate. The charge carriers then migrate to the particle surface and produce highly reactive radical species in reaction with adsorbing water or oxygen. These radicals react with any adsorbed organic molecule and are able to decompose it completely into carbon dioxide and water [6]. Another experimental finding, which can be assigned to the category “environment”, is the catalytic oxidation of carbon monoxide at low temperature by finely dispersed gold particles supported on TiO_2 [6, 8] (and

other reducible metal oxides). This discovery has drawn strong interest in the 'surface science community' and a lot of work is underway to clarify the underlying phenomena.

The following list gives an overview for the most prominent applications based on titanium dioxide materials and refers to further literature.

- Industrial applications as white pigment in paints (used for staining, coloration and brightening), in sunscreens and in pharmaceutical and cosmetic products (ointments, salves, powders and toothpaste) [7, 62, 190]
- Industrial use in varnishes, plastics, fibers, papers, building materials, enamels, ceramics, and as additive even in cigars [62]
- Use for electric devices, e.g., in varistors and capacitors, possibly as gate insulator in a new generation of MOSFETs, as a spacer material in magnetic spin-valve systems and in nanostructured form in Li-based batteries [6, 62]
- Use for the fabrication of ceramics [6, 62]
- Corrosion-protective coatings, optical coatings, self-cleaning coatings and antifogging coatings [6, 197]
- Application in 'thin film optical interference coatings' (antireflective coatings, dielectric mirrors for lasers, metal mirrors with enhanced reflection, filters) [6]
- Biocompatible coatings for implants in medical applications [6]
- Medical applications: Photocatalytic cancer therapy, applied successfully in animal tests, slowing or halting the development of tumor cells [6, 197]
- Photocatalytic disinfection / sterilization [6, 197]
- Photocatalytic decomposition of organic compounds and thus purification of polluted air and waste water [6, 197, 207]
- Applications in the field of photocatalysis [197, 199, 205-210]
- Applications in heterogeneous catalysis [6]
- Photovoltaic applications: energy conversion via solar cells [200-204]
- Water splitting and hydrogen production [6, 7]
- Electrochromic devices [6, 7]
- Hydrogen storage [7]
- Sensing applications for numerous gases [6, 7]

Titanium dioxide nanomaterials:

Nanotechnology has become an inherent part of present research and also titanium dioxide is included by the current trend to synthesize, characterize and study nanomaterials [6]. A large variety of impressive nanostructures could be fabricated from TiO₂ in the past, like nanorods, whiskers, wires, spheres and ordered holes. Also, the generation of periodic arrangements of these TiO₂ nanostructures was achieved. These systems exhibit highly regular dimensions (length, diameter, pore size etc.) and promising properties [6].

Numerous examples of titanium dioxide nanomaterials are given in the review article from Chen and Mao [7]. The authors give an overview of synthetic methods for TiO₂ nanostructure fabrication, discuss the properties of TiO₂ nanomaterials and report their various applications. They clearly state that downsizing the dimension of titanium dioxide based devices is beneficial in many applications. This owes to the fact that the decreasing size of structures and particles causes new physical and chemical properties and a drastic increase of the specific surface area and the surface to volume ratio. Since chemical reactions and interactions between devices and the interacting media mainly occur on the surface or at the interface, this coherence between performance and size of the building units of devices is feasible [7]. Especially on the nanometer scale this correlation becomes perceptible.

In their review article concerning titanium dioxide nanomaterials, Chen and Mao [7] present a large number of methods for the synthesis of TiO₂ nanostructures. However, the mentioned techniques only allow for the production in an arbitrary solvent or on the whole surface area of a support material as a coating. It appears that there is a lack of a technique which enables the local fabrication of titanium dioxide nanostructures at defined positions of a sample. In the work at hand, this crucial aspect was investigated to close the existing gap. The local fabrication of titanium oxide nanostructures at predefined sample positions was studied via the technique of EBID.

5 Purification of the precursor gas titanium(IV) tetraisopropoxide (TTIP)

5.1 Introduction

In this work, the metal alkoxide TTIP (see Chapter 2.8.4) was applied as precursor, which very rarely has been used in EBID up to now [16-18]. The motivation for using this compound in electron based deposition experiments is the fabrication of titanium oxide structures on surfaces and is based on its use in chemical vapor deposition (CVD). Different groups succeeded in the fabrication of titanium oxide films on surfaces via CVD with TTIP [10-15, 74, 185, 186] and the range of CVD techniques which are available to achieve this goal exceeds “simple” thermal deposition (see Chapter 4.4).

In the following, a prerequisite for the deposition of the target materials titanium and oxygen via EBID is discussed, namely the purity and composition of the dosed precursor gas. It was found that in contrast to other precursors like $\text{Fe}(\text{CO})_5$ an extended purification procedure has to be applied for TTIP. Purification is necessary because it always contains hydrocarbon species deriving from the precursor ligands which lead to the unintended deposition of carbon. The main criterion of a successful purification procedure is that the signals of titanium and oxygen containing precursor fragments can be detected via QMS in the chamber in the expected intensity.

The actual gas composition was analyzed via QMS measurements in the mass to charge range from 1 to 200 which was accessible with the applied QMS. In literature, only little information is available concerning mass spectrometry of TTIP and the fragmentation of TTIP is not known. Damo *et al.* report on desorption chemical ionization mass spectrometry (DCI-MS) data for TTIP but only specify two molecular ion signals ($[\text{M}]^-$ at $m/z = 284$ and $[\text{M}_2]^-$ at $m/z = 568$) and one closely related fragmentation product ($[\text{M}_2 - \text{O}^i\text{Pr}]^+$ at $m/z = 509$) (see Table 3 in reference [75]). Other TTIP fragments and especially the molecule fragments with low m/z ratio ($m/z = 1$ to 200), accessible via frequently used QMS instruments, are not specified in their article. Other data acquired via QMS was not found in literature.

In the following chapter, a detailed QMS study for the use of TTIP is presented. Different states of the precursor gas are analyzed and finally a reference QM

spectrum for the purified precursor TTIP is defined with characteristic TTIP signals and signal groups. This gas reference proved to be suitable for the deposition of titanium and oxygen containing deposits via EBID with TTIP which contained only a small amount of carbon (see Chapter 7). Moreover, the necessity to monitor the precursor gas before the EBID experiment, the specific requirement for extended TTIP gas purification after filling and the necessity of heating the precursor vessel to increase the vapor pressure of TTIP are demonstrated.

5.2 Purification of the precursor gas TTIP

TTIP is highly sensitive to air and in particular to water [76, 77] (see detailed information in Chapter 2.8.4). Therefore, the compound was delivered in an argon atmosphere and transferred under inert gas conditions (nitrogen atmosphere) into a stainless steel storage device (see Chapters 3.1.4 and 16.1.1), which is compatible with the UHV instrument.

Before the first use of TTIP, some cleaning cycles were performed in order to remove the inert gas residues (argon and nitrogen) from the precursor gas. The gas dosage system was repeatedly purged with gas from the TTIP storage device and then evacuated via a turbo molecular pump. Via intermittent QMS measurements the gas quality was evaluated and the expected decline of the argon and nitrogen peaks was observed [211].

In total, 11 cleaning cycles as described above and 4 cleaning cycles in which it was pumped directly into the precursor storage device for some minutes were performed. Afterwards, the precursor gas was inspected via QMS. By means of a fine dosage valve, the precursor was dosed into the preparation chamber to a background pressure of $3.0 \cdot 10^{-7}$ mbar. The QMS measurement was carried out with a QMS from Pfeiffer Vacuum (Prisma, model QMA 200). The applied standard QMS settings in this work are a cathode voltage (U_C) of $67.5 \text{ V} \pm 0.5 \text{ V}$ and a secondary electron multiplier voltage (U_{SEM}) of $2,300 \text{ V} \pm 50 \text{ V}$.

Figure 5.1 shows the corresponding QM spectrum of the degassed precursor gas TTIP which was basically freed from the inert gas residues argon and nitrogen by the cleaning procedure described above (pipe purging and pumping via a TMP). The

figure consists of three QM spectrum parts, which are depicted with different magnifications ('x 1', 'x 40' and 'x 500') to enhance the visibility of smaller signals. In the depicted QM spectrum the largest signals can be found in the m/z region between 0 and 47. Apart from small residues of water (H_2O^+ , $m/z = 18$), nitrogen / carbon monoxide ($\text{N}_2^+ / \text{CO}^+$, 28) and carbon dioxide (CO_2^+ , 44), these signals can be attributed to hydrogen (H_2^+ , 2) and diverse hydrocarbons (15, 19, 27, 29, 31, 39, 41, 43 and 45, see Table 5.1). The middle part of Figure 5.1 (magnification 'x 40') depicts some more hydrocarbon peaks in the gas at $m/z = 58, 59, 63$ and 65 and the right part (total magnification 'x 500') contains small signals at 91 and 92 with unclear origin. Furthermore, a minor contamination from previous experiments with $\text{Fe}(\text{CO})_5$ is visible (Fe^+ (56), $\text{Fe}(\text{CO})^+$ (84) and $\text{Fe}(\text{CO})_2^+$ (112)).

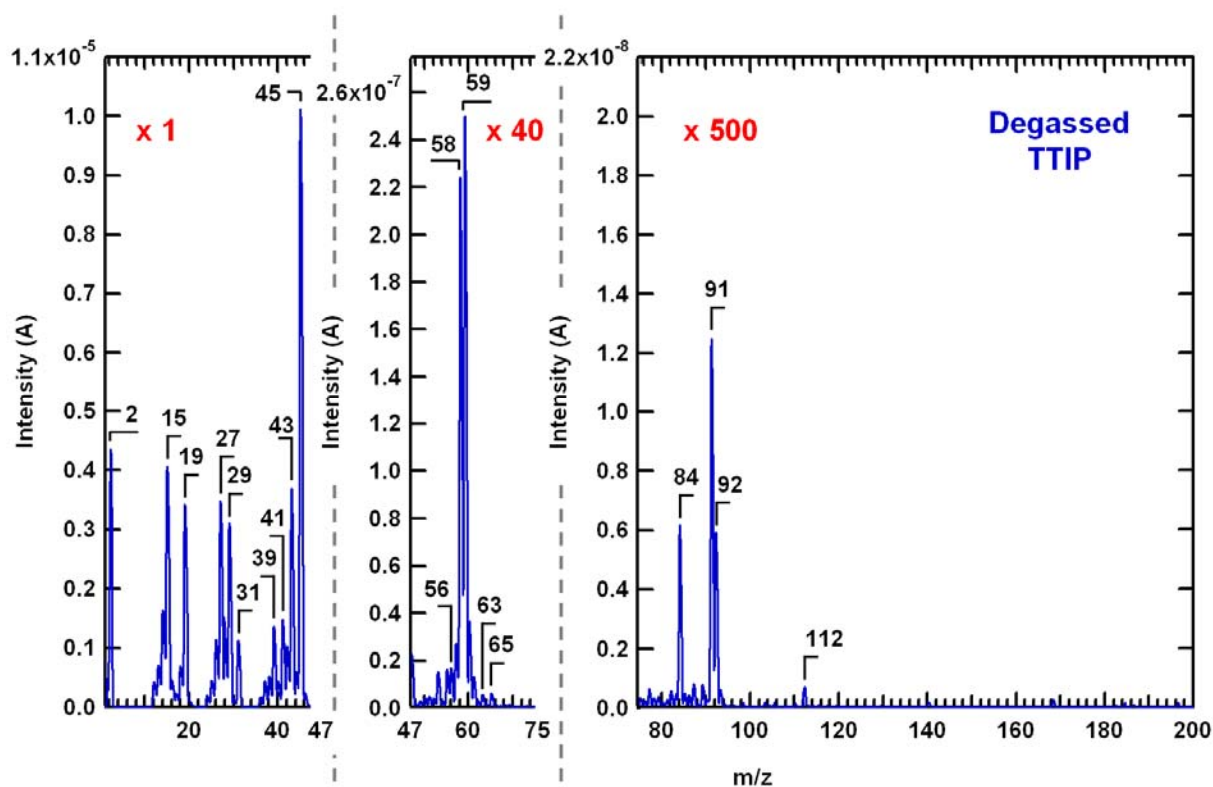


Figure 5.1: QM spectrum of the degassed TTIP precursor gas. The gas was basically freed from argon and nitrogen from delivery and filling into the container by pipe purging and pumping ($p = 3.0 \cdot 10^{-7}$ mbar).

A comparison with the residual gas spectrum of the chamber, acquired at a base pressure of $2.5 \cdot 10^{-10}$ mbar, reveals that the detected hydrocarbon signals are usually not present in the chamber. QMS measurements have further shown that

these signals also do not derive from the residual gas of the gas dosage system. Therefore, these signals can conclusively be attributed to fragments from the precursor molecule TTIP. Several signals, e.g., at $m/z = 43$, 45, 58 and 59, can unambiguously be attributed to isopropyl derivatives [51] like isopropanol or acetone. The latter becomes evident when comparing the mass spectra of the pure compounds isopropanol and acetone [51] (see Appendix, Chapter 16.2.1) in which the signals at $m/z = 43$, 45 and 58 are the dominant peaks in the spectrum.

A detailed list with the observed hydrocarbon signals in the dosed gas is given in Table 5.1. The suggested chemical structures of these hydrocarbon fragments are depicted in the Appendix (see Chapter 16.2.2).

m/z	Fragment
12	C^+
14	CH_2^+ , CO^{2+}
15	CH_3^+
27	$C_2H_3^+$
28	$C_2H_4^+$, CO^+
29	$C_2H_5^+$
31	CH_3O^+ , CH_2OH^+
39	$C_3H_3^+$
41	$C_3H_5^+$
43	$C_3H_7^+$, CH_3CO^+
45	$C_2H_5O^+$
58	$(CH_3)_2CO^+$
59	$(CH_3)_2COH^+$ / O^iPr^+

Table 5.1: Hydrocarbon fragments from the precursor TTIP.

In contrast to the observed hydrocarbon peaks, expected precursor fragment signals like Ti^+ ($m/z = 48$), TiO^+ (64), TiO_2^+ (80), $Ti(O^iPr)^+$ ($m/z = 107$) and $Ti(O^iPr)_2^+$ (166) are not visible in the QM spectrum (Figure 5.1). Above $m/z = 48$ only few and very small peaks occur which can partly be attributed to hydrocarbon signals ($m/z = 58$ and 59). For two signals of unclear origin at $m/z = 91$ and 92 it is known that they

decrease with continued purification steps, and therefore, they are also not attributed to titanium containing precursor fragment ions being characteristic for TTIP.

Additionally, titanium containing precursor fragments that appear in the QM spectrum should show a characteristic fingerprint according to the natural abundance of the titanium isotopes. The isotope pattern of titanium, depicted in Figure 5.2, is not observed in any of the signals with a m/z ratio higher than 48, which indicates the absence of titanium containing fragments in the gas.

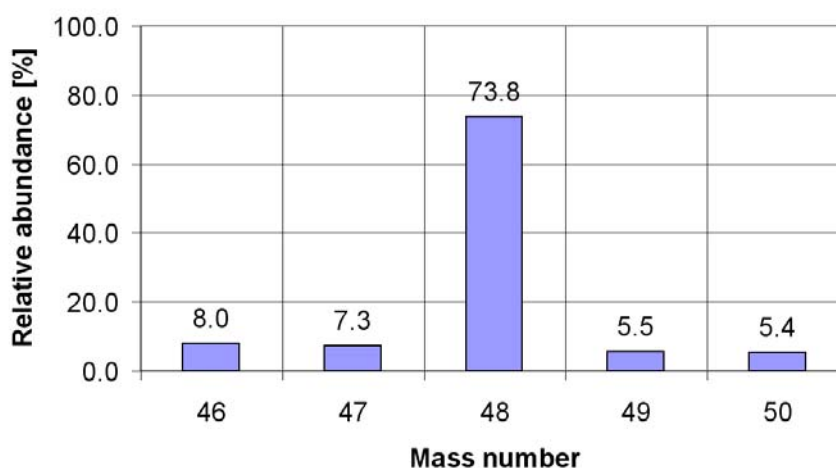


Figure 5.2: Isotope pattern of the element titanium [51].

As none of the supposed titanium containing precursor fragments can be identified in the QM spectrum, it is assumed that no or only a tiny amount of TTIP is in the applied gas. Therefore, the gas is not suitable for the deposition of titanium and oxygen containing material and further purification of the gas is necessary.

This result was confirmed by an EBID experiment on a freshly prepared Si(100) sample on which an area deposit was fabricated. The chemical characterization of this EBID deposit by means of AES revealed that it does not contain titanium and consists only of carbon and traces of oxygen [211].

During the EBID experiment the targeted background pressure of $3.0 \cdot 10^{-7}$ mbar could not be reached. The maximum pressure was $\approx 1 \cdot 10^{-7}$ mbar which corresponds to 33 % of the target value. This means that the vapor pressure of TTIP is too low at RT in the experimental setup (physical properties of TTIP see Chapter 2.8.4).

Heating of the precursor storage device was considered as a way to enhance the volatility of TTIP by increasing its vapor pressure. Therefore, the precursor vessel was heated via an external heating device (experimental details see Chapter 3.4). 413 K proved to be a suitable temperature to achieve a sufficiently high vapor pressure of TTIP that enabled to dose the gas stable at a background pressure of $3.0 \cdot 10^{-7}$ mbar.

A procedure to purify the TTIP gas was found in a combination of heating and pumping the gas with a turbo molecular pump (TMP). The procedure basically consists of three purification steps which partially were repeated for several times.

The first step is the removal of inert gas residues (argon and nitrogen, from delivery and precursor filling) and the most volatile decomposition fragments originating from the precursor (hydrocarbons: isopropanol and fragments). It was realized by purging the gas dosage system and pumping via a TMP at RT. After having repeated this process for several times, it was followed by pumping directly the precursor vessel via the TMP, also at RT. This step was usually done at the beginning of the purification directly after filling the precursor.

In the second step, the removal of less volatile decomposition products is targeted by slow heating steps of the precursor vessel to the temperatures of 333 and 373 K, respectively. During the heating process (5 – 20 min) and / or afterwards at both temperatures the precursor vessel was directly pumped via the TMP for a certain period of time (15 – 30 min).

In the last purification step it was heated to the target temperature of 413 K and the precursor vessel was directly pumped via the TMP at this temperature. This step was usually repeated for several times (cleaning cycles) and a typical heating time for one cycle at 413 K was 1 hour. In total, purification times in the range of several hours were applied.

After each step or cleaning cycle, QM spectra were recorded in the preparation chamber. By this proceeding the progress of the precursor gas quality could be monitored *in situ*. Figure 5.3 depicts QM spectra at two different preparation states of the precursor gas, both taken at a TTIP background pressure of $3.0 \cdot 10^{-7}$ mbar. This data originates from an exemplary purification of freshly filled TTIP. A detailed list of all performed purification steps and cleaning cycles can be found in the Appendix (see Table 16.4 in Chapter 16.2.3).

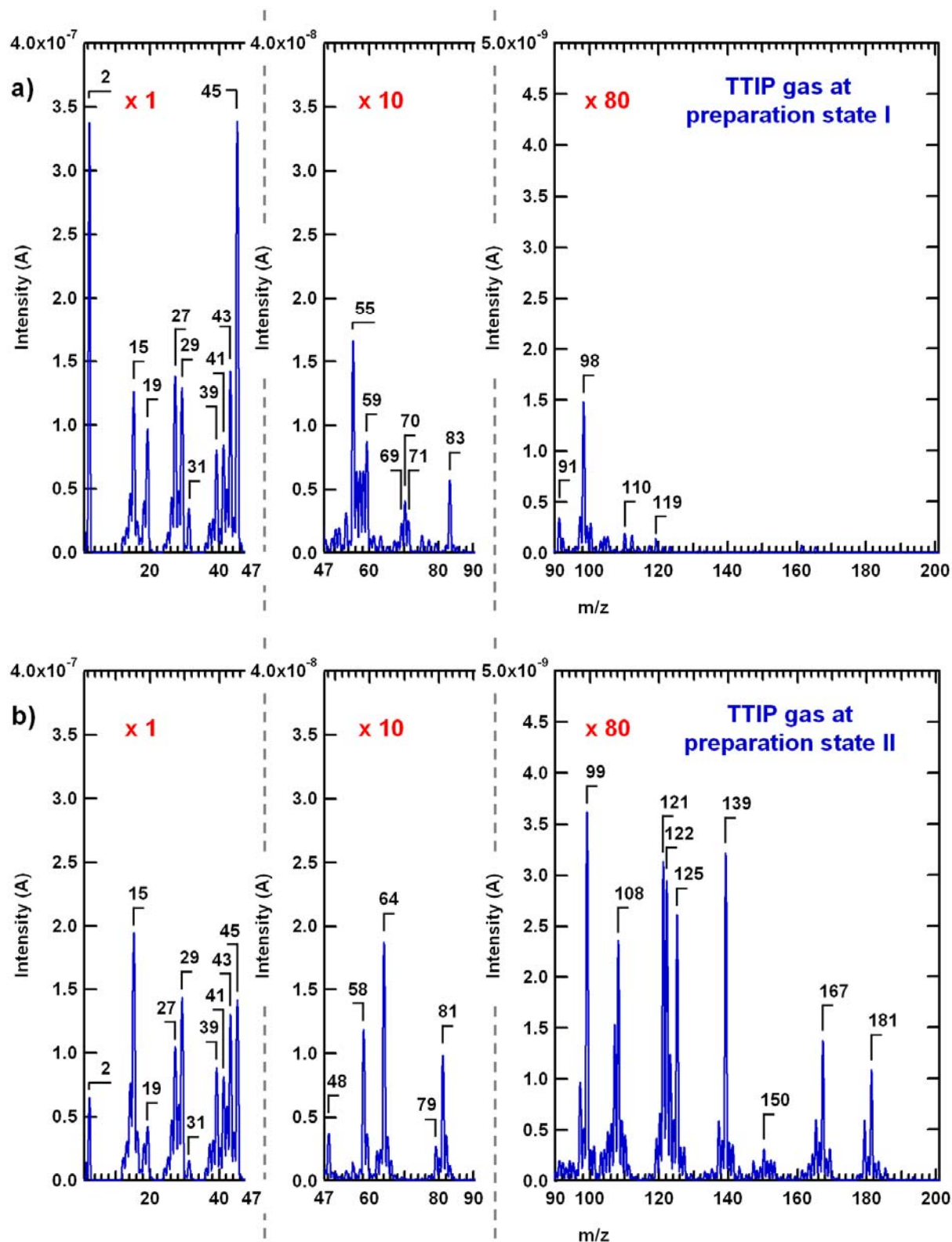


Figure 5.3: QM spectra of the TTIP precursor gas dosed from a heated vessel a) at preparation state I (at the beginning of the purification) b) at preparation state II (after four additional purification steps via heating and pumping with the TMP) ($p = 3.0 \cdot 10^{-7}$ mbar).

Preparation state I, depicted in Figure 5.3 a), is a state at the beginning of the purification process. It was reached by purging and pumping the gas dosage system five times at RT, heating the precursor storage device stepwise to the temperatures of 333 and 373 K and pumping at each temperature via the TMP directly into the vessel, followed by heating the vessel to a temperature 413 K and pumping directly into it for 30 minutes at this temperature.

The spectrum at preparation state I (Figure 5.3 a)) is dominated by hydrocarbon signals (see Table 5.1) in the m/z range between 12 and 45 (left spectrum part). These signals were also the main components of the QM spectrum when the gas was purified only by degassing via pipe purging and pumping (see Figure 5.1). In the middle (magnification 'x 10') and right part ('x 80') of the spectrum, further hydrocarbon signals ($m/z = 58$ and 59) and partly unassigned signals appear. However, no characteristic signals to be expected for TTIP (Ti^+ ($m/z = 48$), TiO^+ (64), TiO_2^+ (80), $\text{Ti}(\text{O}^i\text{Pr})^+$ (107) and $\text{Ti}(\text{O}^i\text{Pr})_2^+$ (166)) are visible in the QM spectrum and none of the signals above $m/z = 48$ shows the characteristic fingerprint according to the natural abundance of the titanium isotopes (see Figure 5.2). The performed purification process up to this preparation state, just modified by heating the precursor vessel, is not sufficient to obtain a suitable TTIP gas.

Preparation state II (see Figure 5.3 b)) is a state after four further purification steps comprising of heating the precursor vessel and pumping with the TMP. To reach this state, it was pumped directly into the storage device for in total 369 minutes at elevated temperatures (collectively 47 minutes at 333 K, 42 minutes at 373 K and 280 minutes at 413 K) and 43 minutes while the vessel was cooling down. The exact procedure, applied periods of time and adjusted temperature values are given in the Appendix (see Table 16.4 in Chapter 16.2.3).

The spectrum at preparation state II (Figure 5.3 b)) is clearly different from the spectrum at preparation state I (Figure 5.3 a)). In the left spectrum part of Figure 5.3 b) some hydrocarbon signals ($m/z = 29, 39, 41$ and 43) show only minor changes of up to $\pm 10\%$. A higher signal increase was observed for $m/z = 15$ (CH_3^+) and 58 ($(\text{CH}_3)_2\text{CO}^+$) by $+54\%$ and $+86\%$, respectively. In contrast to these signals, the ones at $m/z = 27$ (C_2H_3^+), 45 ($\text{C}_2\text{H}_5\text{O}^+$) and 59 ($(\text{CH}_3)_2\text{COH}^+ = \text{'O}^i\text{Pr}^+$) decrease significantly by -24% , -58% and -58% , respectively. Based on the mass spectrum of the pure compound isopropanol (see Appendix, Chapter 16.2.1) it is proposed that

the hydrocarbon ion $C_2H_5O^+$ (signal at $m/z = 45$) is the main decomposition product of the isopropoxy ligands and thus of the precursor molecule. Therefore, the observed signal decrease of this fragment indicates a proceeding “cleaning effect”. Moreover, a strong decrease of the hydrogen signal ($m/z = 2$) is observed.

The most important change from preparation state I to preparation state II can be observed in the middle and right spectrum part of Figure 5.3. Most of the unassigned signals in this spectrum part at preparation state I ($m/z = 55, 56, 57, 69, 70, 71, 83$ and 91) have “disappeared” at preparation state II, and the signal at $m/z = 98$ has decreased significantly. In contrast to that, a lot of new signals are visible at preparation state II which can be attributed to titanium and oxygen containing fragments of the precursor that can now be detected in the chamber. Among these signals one finds the expected TTIP signals for Ti^+ ($m/z = 48$), TiO^+ (64), TiO_2^+ (80), $Ti(O'Pr)^+$ (107) and $Ti(O'Pr)_2^+$ (166)). The latter three peaks in the spectrum ($m/z = 80, 107$ and 166) are all succeeded by a significantly larger signal one m/z unit higher ($\Delta(m/z) = + 1$). This observation is interpreted by the uptake of a hydrogen atom of the corresponding ions which generates a more stable molecule fragment. For the large number of new signals the following observations can be made: In total ten new “signal groups” appear at a mass to charge ratio of higher than 45. In this work, a “signal group” in a purified TTIP QM spectrum is defined as a group of at least five and up to nine QMS signals which appear directly next to each other ($\Delta(m/z) = \pm 1$). Each “signal group” features at least one and up to three “main signals” which show the highest intensity in the group. Additionally, the “main signals” are always preceded by at least two peaks within their “signal group” and are always succeeded by at least two peaks within the group. This observation is in line with the characteristic titanium isotope fingerprint (see Figure 5.2). A very high agreement between signal group and isotope pattern is e.g. found for the “main signals” at $m/z = 48, 64, 81, 99, 139, 167$ and 181 . Minor deviations from the isotope pattern can be explained by the superposition of signals in the spectrum. This is especially the case for the “signal group” with the “main signals” at $m/z = 121, 122$ and 125 where the signal overlap of three different molecular fragments is feasible.

In conclusion, it can be stated that the monitored gas comprises the precursor TTIP and titanium and oxygen containing fragments are detected via QMS in the instrument chamber.

Table 5.2 depicts an overview of the observed “signal groups” in the QM spectrum of the purified TTIP gas at preparation state II (Figure 5.3 b)). ‘N’ (in the left column) represents the number of the corresponding “signal group” while the respective mass to charge ratios of each group are depicted in the rows from left to right. The m/z ratios of the “main signals” are drawn in bold. Each “signal group” features exactly one “main signal”. The only exception is found for the sixth “signal group” (N = VI; $m/z = 119 - 127$) which exhibits three “main signals”.

N	m/z								
I	46	47	48	49	50				
II	62	63	64	65	66				
III	79	80	81	82	83				
IV	97	98	99	100	101				
V	105	106	107	108	109	110			
VI	119	120	121	122	123	124	125	126	127
VII	137	138	139	140	141				
VIII	147	148	149	150	151	152	153		
IX	164	165	166	167	168	169			
X	179	180	181	182	183				

Table 5.2: Ten characteristic “signal groups” in the QM spectrum of purified TTIP gas comprising titanium containing precursor fragments. ‘N’ represents the number of the corresponding “signal group”, the respective m/z ratios of each group are depicted in the rows from left to right. The m/z ratios of the “main signals” are drawn in bold.

The chemical composition of the corresponding fragments can not be unambiguously assigned. By “attaching” systematically the hydrocarbon fragments of the precursor molecule, which have actually been detected via QMS (see Table 5.1), to a titanium atom with the mass of 48, possible chemical compositions were determined for the signals depicted in Table 5.2. For this determination only singly charged ions were considered. An overview of the suggested fragment compositions for all signals in the “signal groups” is given in the Appendix (see Table 16.5). In this chapter, proposals

for the chemical composition of the “main signals” are given which show the highest intensity in their “signal group”. They are listed in Table 5.3. It has to be noted that the compositions of the titanium containing fragments in this table are suggested and thus somewhat speculative.

N	m/z	Fragment
I	48	Ti ⁺
II	64	TiO ⁺
III	81	TiO ₂ H ⁺
IV	99	TiO ₃ H ₃ ⁺
V	108	Ti(O ⁱ Pr)H ⁺ , TiOCH ₃ (C ₂ H ₅) ⁺
VI	121	TiO ₂ (C ₃ H ₅) ⁺ , Ti(O ⁱ Pr)CH ₂ ⁺ , TiO(C ₂ H ₅ O)C ⁺
VI	122	Ti(O ⁱ Pr)CH ₃ ⁺ , TiO((CH ₃) ₂ CO) ⁺ , TiOCH ₃ (C ₃ H ₇) ⁺ , TiO ₂ CH ₃ (C ₂ H ₃) ⁺
VI	125	TiO(O ⁱ Pr)H ₂ ⁺ , TiO ₂ (C ₂ H ₅ O) ⁺ , Ti(O ⁱ Pr)CH ₃ H ₃ ⁺
VII	139	TiO ₂ (O ⁱ Pr) ⁺ , TiO(O ⁱ Pr)CH ₃ H ⁺
VIII	150	TiO(O ⁱ Pr)(C ₂ H ₃) ⁺ , TiO(C ₂ H ₅ O)(C ₃ H ₅) ⁺
IX	167	Ti(O ⁱ Pr) ₂ H ⁺ , Ti ₂ (O ⁱ Pr)C ⁺ , TiO(C ₂ H ₅ O)((CH ₃) ₂ CO) ⁺
X	181	TiO(O ⁱ Pr)((CH ₃) ₂ CO) ⁺ , Ti(O ⁱ Pr) ₂ CH ₃ ⁺

Table 5.3: Possible fragment composition of the “main signals” of the ten QMS “signal groups” of purified TTIP. Note that the depicted fragments are suggested.

The *in situ* observation via QMS during precursor purification enables to analyze the development of the signal intensity of individual peaks in the QM spectra. In the following, a quantitative analysis of the signal intensity development of the most abundant hydrocarbon fragments and the “main peaks” is given as it is depicted in Figure 5.4.

In Figure 5.4 a) the development of the signal intensity of the most abundant hydrocarbon fragments (see Table 5.1) is shown. It demonstrates that most of the signals show only minor intensity fluctuations and stay rather stable upon proceeding purification (C₂H₃⁺ (m/z = 27), C₂H₅⁺ (29), C₃H₃⁺ (39), C₃H₅⁺ (41) and C₃H₇⁺ / CH₃CO⁺

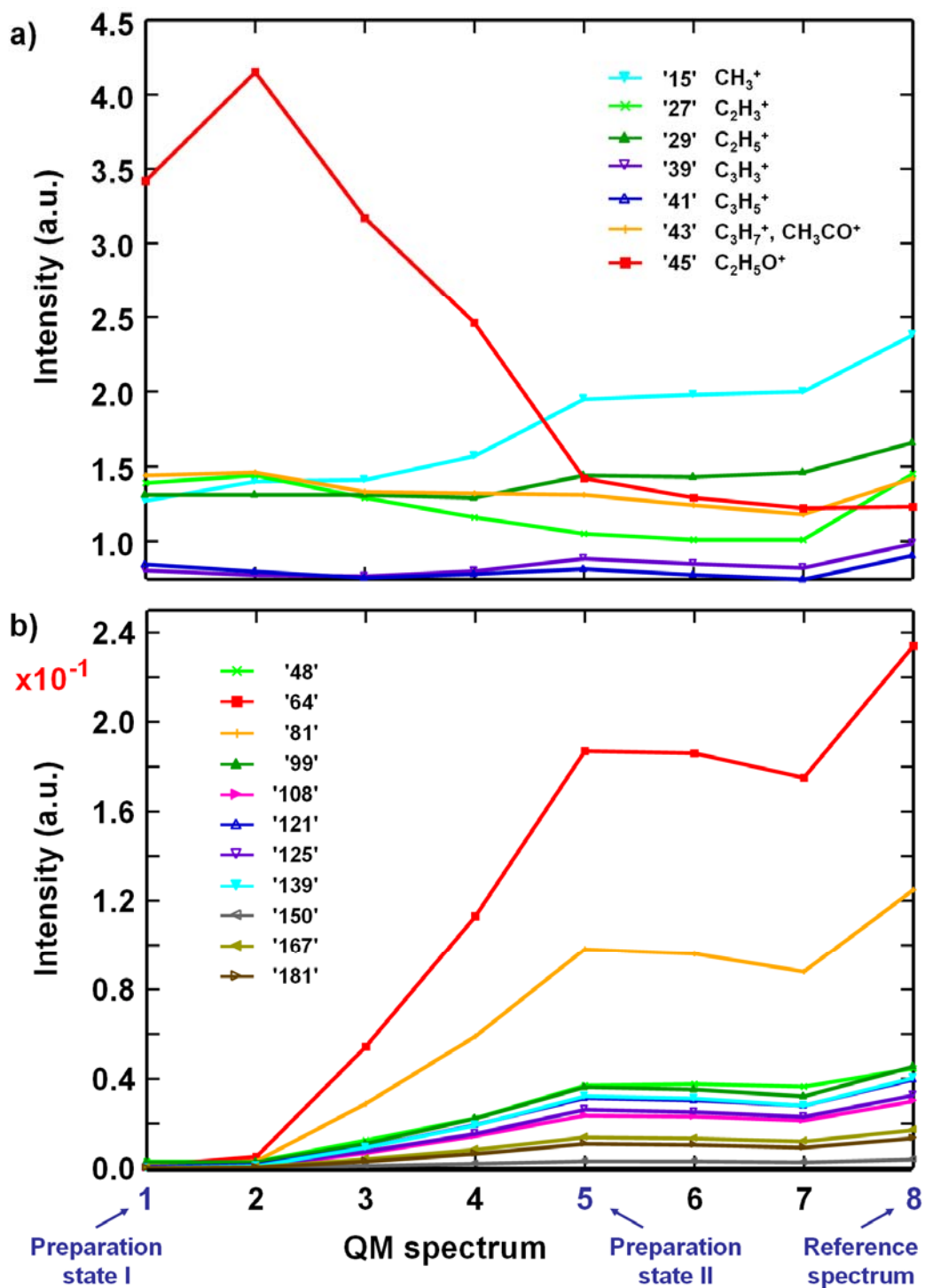


Figure 5.4: Quantitative analysis of the QMS signal intensity development of a) the most abundant hydrocarbon fragments and b) the “main peaks” of the “signal groups”. Please note that the QM spectra were not taken after equidistant time intervals. The whole purification procedure can be found in detail in the Appendix (Chapter 16.2.3). The first and fifth QM spectrum correspond to preparation state I and II in Figure 5.3 a) and b).

(43)). However, the signals at $m/z = 15$ and 45 show a stronger intensity change, i.e. an increase for the CH_3^+ (15) fragment and a decrease for $\text{C}_2\text{H}_5\text{O}^+$ (45). Based on the mass spectrum of pure isopropanol (see Appendix, Chapter 16.2.1) the hydrocarbon fragment $\text{C}_2\text{H}_5\text{O}^+$ (45) is regarded as the main decomposition product of the isopropoxy ligands and thus of the precursor molecule TTIP. It is assumed that this fragment is formed upon storage of TTIP in the precursor vessel. The observed intensity decrease of this fragment in the QM spectra upon proceeding purification indicates an ongoing “cleaning effect” for the gas.

In Figure 5.4 b) the signal intensity development of the “main peaks” in the QMS “signal groups” of purified TTIP gas is depicted. The same trend is found for all “main peaks”, i.e. upon advancing precursor gas purification all signal intensities are strongly increasing. The highest signal intensity of the “main peaks” is shown by the fragments TiO^+ ($m/z = 64$) and TiO_2H^+ (81). The trend of increasing intensity for the “main peaks” in Figure 5.4 b) indicates that the purification procedure described above leads to an increasing amount of TTIP in the dosed gas.

Based on the obtained findings one can interpret the ongoing cleaning process during the purification procedure as follows. TTIP is not stable upon storage in the stainless steel vessel. The main decomposition product is isopropanol and presumably further hydrocarbons are formed. These hydrocarbons should be of gaseous nature or should be volatile compounds with a considerably higher vapor pressure than the metal alkoxide TTIP. The vapor pressure of the main decomposition product isopropanol e.g. is 43.9 mbar at 293 K [212] and thus higher than the one of TTIP (at 303 K) by a factor of more than 160 . Due to the high volatility characteristic fragments of isopropanol ($m/z = 43$ and 45 , see Appendix, Chapter 16.2.1 [51]) and several hydrocarbon species are found in the QM spectrum of the dosed gas. Without purification no TTIP can be detected in the gas, the latter consists only of hydrocarbon species.

During the purification procedure the most volatile molecule fragments are pumped off first. These are the gaseous and highly volatile hydrocarbon species. By heating the precursor vessel the vapor pressure of TTIP is increased and upon advancing purification procedure the amount of TTIP in the gas is increased significantly. However, it has to be noted that the dosed gas can not be freed completely of hydrocarbon species. These hydrocarbons in the gas on the one hand and the

organic ligands of each dosed intact TTIP molecule on the other are the source for unintended carbon deposition in the EBID experiments (see Chapter 7).

The QM spectrum finally obtained by the above described purification procedure, i.e. spectrum number 8 in Figure 5.4, is specified as the QMS reference spectrum for purified TTIP gas in a UHV instrument measured with the applied QM spectrometer (m/z range from 1 to 200). It is depicted in Figure 5.5.

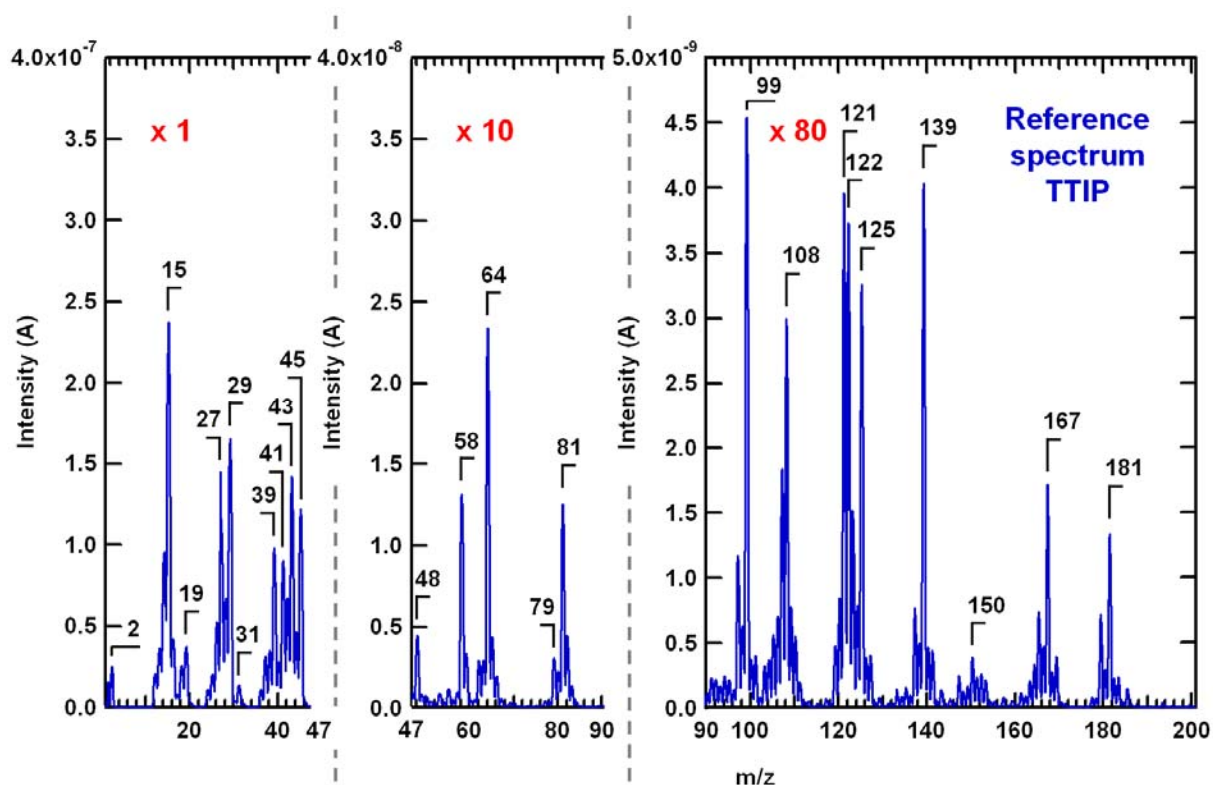


Figure 5.5: QMS reference spectrum of purified TTIP precursor gas dosed from a heated precursor storage vessel ($p = 3.0 \cdot 10^{-7}$ mbar).

For the EBID experiments presented in this work, the TTIP purification was performed until a spectrum similar to the reference in Figure 5.5 was obtained. These EBID experiments have shown that the deposition of titanium and oxygen in the deposit is achieved (see Chapter 7). Therefore, it is concluded that the above described purification procedure comprising heating the vessel and pumping via a TMP is a suitable way to purify the TTIP gas.

Finally, some significant characteristics of a purified TTIP gas are summarized. They are supposed to simplify the evaluation of a gas state in regard to an EBID experiment. A freshly filled and purified TTIP gas features the following characteristics:

- (1) The ten “signal groups” (see Table 5.2) are invariably visible in the QM spectrum of the gas. This characteristic TTIP fingerprint is the most important feature in the spectrum. It is the prerequisite for the deposition of a significant amount of titanium and oxygen via EBID with TTIP.
- (2) From all “main peaks” of these “signal groups” the ones at $m/z = 64$ (TiO^+) and $m/z = 81$ (TiO_2H^+) show the highest signal intensity in the QM spectrum.
- (3) The intensity ratio of the signal at $m/z = 64$ (TiO^+) to the one at 48 (Ti^+) and the ratios of these two signals to the most intense hydrocarbon signal of a purified TTIP gas at $m/z = 15$ (CH_3^+) should reach a certain level, respectively. As guidance, the observed intensity ratios for these fragments in the QMS reference spectrum are depicted in Table 5.4.

No.	Fragment ratio	m/z ratio	Intensity ratio
(1)	$\text{TiO}^+ / \text{Ti}^+$	'64'/'48'	5.23
(2)	$\text{Ti}^+ / \text{CH}_3^+$	'48'/'15'	0.019
(3)	$\text{TiO}^+ / \text{CH}_3^+$	'64'/'15'	0.098

Table 5.4: Intensity ratios of significant fragments in the QMS reference spectrum.

It was found that purification of the TTIP precursor is always necessary directly before an EBID experiment. When the precursor has already been purified before, the purification can usually be achieved much faster in comparison to the purification of a freshly filled TTIP. In this case, the purification effort scales with the time that passed from the previous use of the gas.

When a filled and purified TTIP gas is used for several experiments in an extended period of time, minor changes in the QM spectra after purification are observed.

Experiences were made in a period of 4 months. The overall trend is a small increase of almost all signal intensities (at the same background pressure of $3.0 \cdot 10^{-7}$ mbar). In contrast, two signals are evidently decreasing, namely the one at $m/z = 45$ ($C_2H_5O^+$) and the one at 59 ($(CH_3)_2COH^+ / O^iPr^+$).

5.3 Summary and conclusion

To summarize this chapter, one can state that purification of the precursor TTIP is mandatory before an EBID experiment as the compound tends to decompose.

After degassing, i.e. repeatedly purging the gas dosage system and evacuating the pipes by pumping via a TMP, no titanium containing precursor fragments could be detected in the dosed gas via QMS. Instead a high amount of hydrocarbon signals was found in the QM spectrum which originate from the precursor.

As the vapor pressure of TTIP is low, heating of the precursor vessel to a temperature of 413 K was found to be necessary. Thereby, the vapor pressure is increased such that the target background pressure of $3.0 \cdot 10^{-7}$ mbar in the chamber can be reached stable upon dosage.

A procedure to purify the TTIP gas was found in a combination of heating the vessel and pumping the gas with a TMP, performed in several steps. At first, the gas dosage system was repeatedly purged and evacuated via the TMP, followed by pumping directly into the precursor vessel at RT. Then, the vessel was heated to 333 and 373 K, respectively, and at each temperature the vessel was again pumped directly via the TMP. These steps target the removal of the most volatile precursor fragments, which are gaseous hydrocarbon species and hydrocarbons with a high vapor pressure (e.g. isopropanol). Finally, the precursor vessel was heated to a temperature of 413 K. Purification was achieved by repeated pumping cycles with the TMP into the vessel in the range of several hours. By this, the amount of TTIP in the gas was increased significantly.

The purification was done until a QM spectrum similar to a QMS reference spectrum from an exemplary purification was obtained. The purified TTIP gas shows distinctive features in QMS (in the detectable m/z range from 1 to 200), namely a characteristic fingerprint consisting of ten signal groups with at least one and up to three “main peaks” in the group. These signals are attributed to titanium and oxygen containing

precursor fragments. In EBID experiments the gas proved to be suitable for the deposition of titanium and oxygen. However, the QM spectrum of a purified TTIP gas still contains hydrocarbon signals. The corresponding fragments originate from the precursor molecule itself. These hydrocarbons and the carbon containing ligands of the intact TTIP molecules lead to the unintended deposition of carbon in the experiments.

The *in situ* observation of the precursor gas composition via QMS during purification enabled to follow the signal intensity development upon the applied procedure. Monitoring the gas composition via QMS directly before an EBID experiment was found to be a mandatory production step. It proved to be a significant prerequisite for the deposition of titanium and oxygen via EBID with TTIP.

5.4 Outlook

A limitation of the applied QMS in the instrument is the restricted measuring range with m/z ratios from 1 to 200. The consequence for the analysis of TTIP is that ions with higher m/z ratios than 200 are not visible in the acquired spectra. Already the molecular ion $[M]^+$ with the m/z ratio of 284 is out of the measuring range of the applied QMS. In literature, articles are found proposing a dimeric structure for the precursor [75] or even a higher degree of association [79] (see Chapter 2.8.4). Therefore, it is feasible that the vast majority of titanium containing precursor fragments, including the molecular ions $[M_n]^+$, is not accessible for the applied QMS because of the exceeded m/z ratio of 200.

As an outlook one might envisage to characterize the TTIP precursor gas at UHV conditions with a QMS providing a broader m/z range. This instrumental possibility would give further insight into the ongoing changes of the gas composition during the purification process when monitoring the gas state *in situ*.

6 Flux distribution of TTIP in the applied setup

6.1 Introduction

The gas injection system (GIS) which is used to provide the precursor molecules in the chamber is of high importance for EBID. There is no standard GIS with the consequence that each instrument and the applied gas dosage system provide a specific setup for the performance of EBID experiments.

Generally, nozzle-based gas injection systems are frequently used for gas assisted deposition and etching processes via focused electron or ion beams [19]. They consist of a precursor molecule reservoir, a tubing system which leads to the chamber and the nozzle pointing towards the sample surface (see Figure 6.1). For UHV systems the use of a leak valve between the tubing system and the nozzle is indispensable. In addition, a valve directly at the precursor reservoir is typically used.

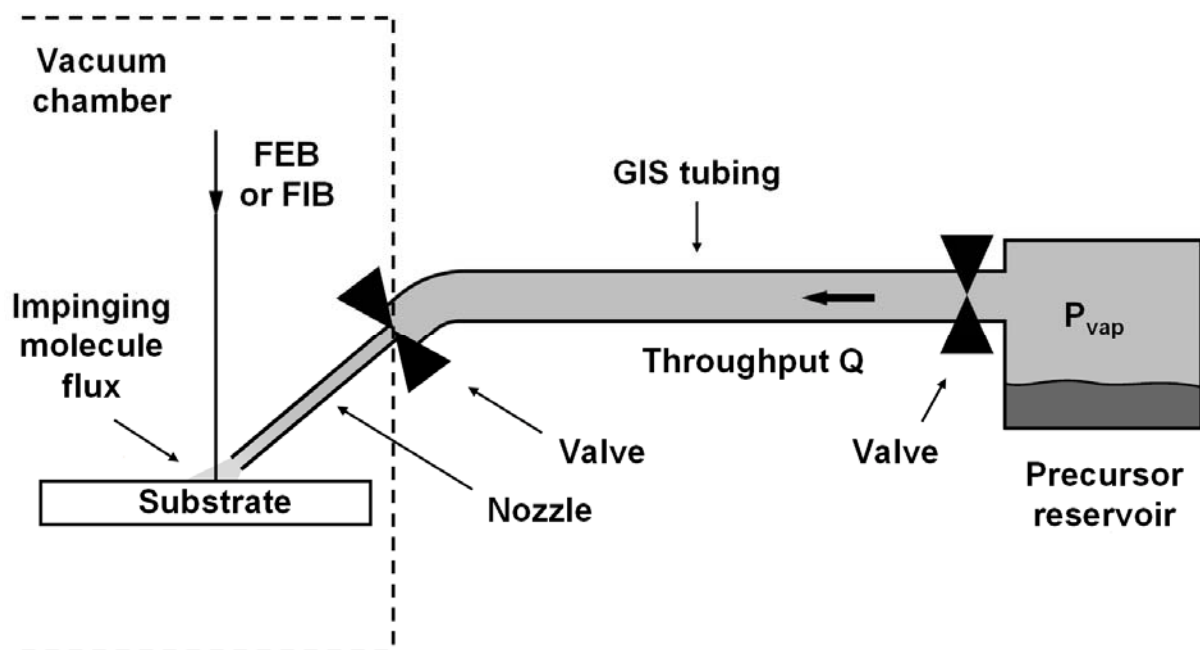


Figure 6.1: Schematic drawing of a nozzle-based GIS which is most frequently applied for FEB and FIB deposition and / or etching (image taken from reference [19] and slightly modified).

In the precursor reservoir the solid, liquid or gaseous precursor is stored. The pressure inside the vessel is determined by the vapor pressure of solid or liquid

compounds or corresponds to the pressure of a gas at the applied temperature. The advantage of nozzle-based GISs is that it is possible to realize a high local molecule flux onto the sample surface where the FEB or FIB experiment is performed. At the same time, the pressure in the chamber stays low enough for microscope operation during precursor dosage [19].

Each instrumental setup has a characteristic spatial distribution of the molecule flux on the sample surface, which depends on the nozzle geometry and the spatial arrangement of nozzle and sample. This distribution determines directly how efficiently the precursor molecules can replenish the point of beam impact after molecule dissociation and thus it defines the process regime in which deposition or etching occurs [19]. In literature it is distinguished between three different process regimes, i.e. precursor-limited, electron-limited and diffusion-enhanced regime [4, 5, 30, 117]. It is clear that the type of process regime strongly affects the result of the FEB and FIB deposition and etching experiments. It has a high impact on the process rate and the spatial resolution of the deposit or etch hole [2, 5, 213-216]. Moreover, also the chemical composition of the deposit [149, 217] and its internal structure (e.g. nanocrystal / embedded matrix structure) [144, 145] are influenced to a certain extent by the process regime [19].

Despite the frequent use of nozzle-based gas injection systems in FEB and FIB based microscopes and despite the relevance of the spatial molecule flux distribution, the latter is only rarely studied or quantified. Therefore, in most of the FEB and FIB processing literature details concerning impinging molecule flux on the sample surface and at the point where the FEB or FIB experiment is performed are not given [19]. Consequently, the interpretation of published results is hampered and, even more importantly, the reproducibility of results by other groups is difficult [19].

In the following chapter, this issue is addressed for the setup in this work. After the discussion of fundamental aspects concerning the gas flow in vacuum environments (Chapter 6.2), the precursor flux and pressure at the nozzle exit were determined based on the pumping speed S of the ion getter pump (Chapter 6.3). In order to determine flux distribution, flux and pressure directly at the sample surface, simulations were performed via a Monte Carlo software ('GIS Simulator', version 1.5, 2008) developed by Friedli and Utke [19, 218]. On the basis of the simulated results

a comparison of the pressure at the sample surface to the adjusted background pressure during EBID could be drawn (Chapter 6.4).

6.2 Fundamentals

6.2.1 Flow and rarefied gas flow

Flow is the spatial streaming or movement of a substance. The flow of gases results both from the thermal movement of individual gas particles and from macroscopic forces based on local pressure differences in the investigated system [219]. The type of gas flow is determined by compressive, inertial and frictional forces. In common, gravitational forces are very small and can thus be neglected for gases [219].

The flow regime, which appears upon streaming of a gas through a tube of arbitrary length, depends on the existing conditions. Three different flow regimes are distinguished which are molecular flow, transient flow (Knudsen flow) and viscous flow. They are labeled in the upper part of Figure 6.2.

1.) Molecular flow:

For a sufficiently small pressure the mean free path of the gas particles is very large in comparison to the lateral extension of the tube [219]. Therefore, each gas particle streams due to its thermal movement independently from the other ones through the tube [219]. Particle-particle collisions are negligible, but numerous collisions with the tube wall result in a “zigzag path” of individual gas particles. A flow described by these characteristics is also labeled ‘individual particle flow’.

2.) Viscous flow:

For a sufficiently high pressure the mean free path of the gas particles is very small in comparison to the lateral extension of the tube [219]. Therefore, the number of particle-particle collisions is very high and the particles exchange permanently energy and momentum [219]. A high number of frequently colliding gas particles can thus be treated as continuum and a flow develops due to local pressure changes [219]. A flow described by these characteristics is also labeled ‘continuum flow’.

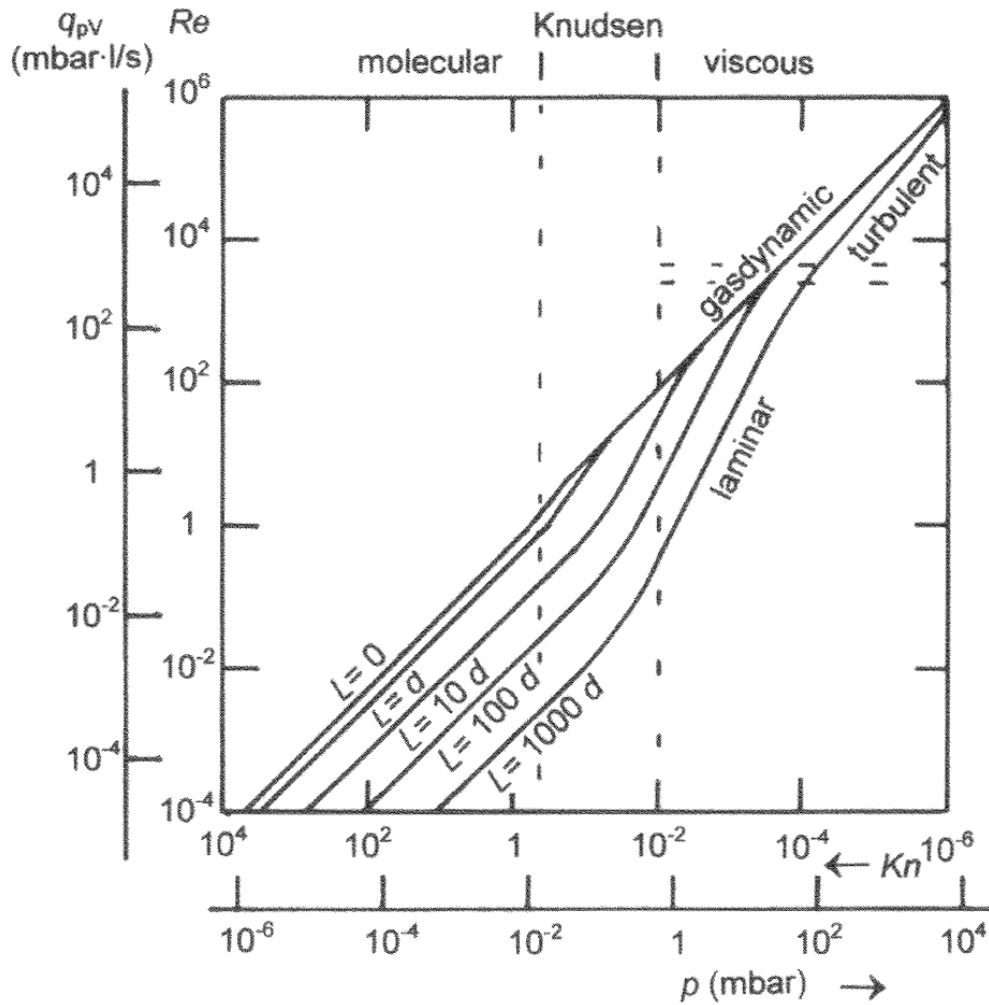


Figure 6.2: Flow regimes for pipes with a diameter of 10 mm and different tube lengths L for air at a temperature of 293 K. The pressure at the abscissa is the one at the tube entrance. The pressure at the tube exit is assumed to be negligibly small (image adapted from [219]).

3.) Transient flow (Knudsen flow):

For a medium pressure the flow is in a transient regime between molecular flow and viscous flow. In this regime, the number of particle-particle collisions is just as high as the number of gas particle collisions with the tube wall [219]. Therefore, it is labeled transient flow (or Knudsen flow).

A dimensionless characteristic number for the quantitative description of the flow regime is the so-called Knudsen number. It is defined by the ratio of the mean free

path λ to the lateral extension of the tube. For a circular cross-section of the tube, the lateral extension is simply the tube diameter d (see Equation 6.1) [19, 218, 219].

$$\text{Kn} = \frac{\lambda}{d} \quad (6.1)$$

The mean free path λ can be determined from the viscosity η according to Equation 6.2. Here, \bar{c} is the mean particle velocity, p the pressure, R the universal gas constant ($8.31451 \text{ J mol}^{-1} \text{ K}^{-1}$), T the temperature and M the molar mass of the flowing substance [219].

$$\lambda = \frac{\pi}{4} \cdot \bar{c} \cdot \eta \cdot \frac{1}{p} = \frac{\pi}{4} \cdot \sqrt{\frac{8 \cdot R \cdot T}{\pi \cdot M}} \cdot \eta \cdot \frac{1}{p} \quad (6.2)$$

An alternative expression for the mean free path λ is given by Equation 6.3 [19, 218, 219]. In this equation, k is the Boltzmann constant ($1.38 \cdot 10^{-23} \text{ J K}^{-1}$) and δ the diameter of a particle of the flowing substance. The equation is valid for a homogeneous ideal gas from which the particles are considered as hard, rigid spheres [218].

$$\lambda = \frac{k \cdot T}{\sqrt{2} \cdot \pi \cdot \delta^2 \cdot p} \quad (6.3)$$

Using Equation 6.3 a general expression for the Knudsen number can be given which illustrates the linear dependence of Kn on the temperature T and the inverse proportionality to the particle diameter δ to the power of two, the pressure p and the tube diameter d .

$$\text{Kn} = \frac{k \cdot T}{\sqrt{2} \cdot \pi \cdot \delta^2 \cdot p \cdot d} \quad (6.4)$$

The Knudsen number Kn allows to distinguish between the different flow regimes described above. In accordance with quantitative studies the following boundaries between the flow regimes are stated (see also Figure 6.2) [219, 220].

$\text{Kn} > 0.5$	Molecular flow
$0.5 > \text{Kn} > 0.01$	Transient flow (Knudsen flow)
$0.01 > \text{Kn}$	Viscous flow

At this point it should be noted that in literature also a different expression for the Knudsen number is found. Roy *et al.* [221] interpret Kn based on the ratio of the Mach number Ma and the Reynolds number Re. The authors give different boundaries for the flow regimes as stated above. The boundaries derive from continuum and molecular approaches (models) for the description of a fluid flow through microchannels. Based on this reference Friedli and Utke introduced a “rule of thumb” for the boundary between transient and molecular flow [19]. They state that molecular flow increasingly dominates for $Kn > 10$ while for $Kn < 10$ the increasingly dominating flow is of transient nature (Knudsen flow).

When applying a nozzle-based GIS (compare Figure 6.1) a pressure decay occurs along the dosing nozzle, i.e. between the valve and the nozzle exit area. For the dosed gas this means a rarefaction (dilution) which goes along with the transition between different flow regimes. In literature, the term of “rarefied gas flow” is introduced [19, 218] and the degree of rarefaction is expressed by Kn. Along the tube the pressure p and density ρ are decreasing while the mean free path λ and the Knudsen number Kn are increasing.

The tube length L and tube diameter d are characteristic parameters of the applied GIS. The importance of these parameters is illustrated in Figure 6.3. A variation of the tube length L to tube diameter d ratio strongly influences the shape of the flux that finally spreads into the vacuum chamber at the nozzle exit. For a small tube length in comparison to the tube diameter the angular distribution of the flux shows the so-called cosine distribution (see Figure 6.3 a), $L/d = 0$) [219]. When the tube length increases, the particles perform tube wall collisions. On a technical surface like the tube wall, after a collision event the direction of an emitting particle from the wall does statistically not depend on its original direction any more (diffuse tube wall reflection) [219]. This means that after tube wall collision the probability of a particle to move with or against the flow direction is roughly the same. Consequently, the number of passing particles decreases with increasing tube length L . The distance which a particle can move without tube wall collision depends on its moving direction in the tube [219]. The better the path of the particle lies in the gas flow direction, the longer is the collision-free distance the particle can move [219]. Therefore, the tube exit is mainly left by particles with a moving direction parallel to the tube walls. For the angular distribution of the emitting flux this means a more

compressed shape in comparison to the cosine distribution (see Figure 6.3 b) and c), $L/d = 1$ and 5 , respectively). The effusing particle flux is more condensed and gets a preferential direction which is parallel to the tube. The magnitude of flux compression scales with the tube length L .

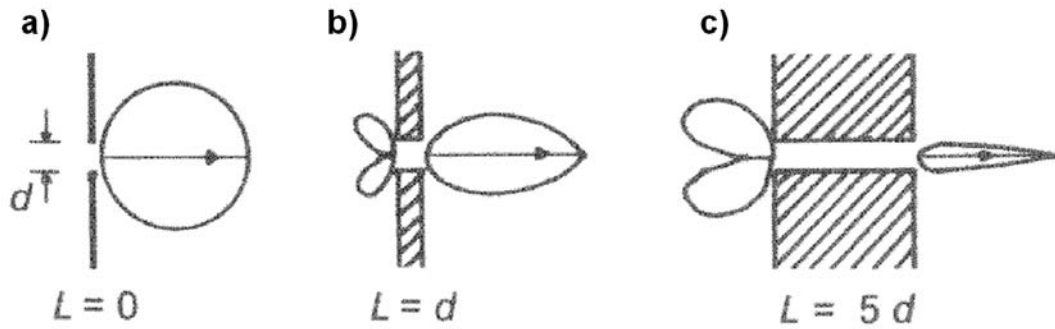


Figure 6.3: Molecular flow through a cylindrical tube. The molecules enter the tube from the left. The image shows the angular distribution of the passing and returning gas particles for three different ratios of tube length L to tube diameter d : a) $L/d = 0$ b) $L/d = 1$ and c) $L/d = 5$ [219].

6.2.2 Gas flow and throughput

When a gas is flowing through a tube, the so-called throughput q is defined by the ratio of the passing amount of gas to time [219]. As the amount of the gas can be expressed differently, there are also different expressions for the throughput q . One distinguishes between the ‘volume throughput’ q_v , the ‘mass throughput’ q_m , the ‘amount of substance throughput’ q_n and the ‘number of particles throughput’ q_N [219]. For the considerations in this work, the throughputs q_v and q_N are used. They are defined according to the Equations 6.5 and 6.6.

$$q_v = \frac{\Delta V}{\Delta t} = \dot{V} \quad [q_v] = \frac{\text{m}^3}{\text{s}} \quad (6.5)$$

$$q_N = \frac{\Delta N}{\Delta t} = \dot{N} \quad [q_N] = \frac{1}{\text{s}} \quad (6.6)$$

It should be noted that the throughput can change upon the flow through a gas tube. For example, the volume throughput q_v is different at the tube entrance and exit. As

the pressure usually decreases along the tube and thus the volume of the gas increases, q_v is higher at the exit.

A related quantity to express the throughput is the so-called 'pV-throughput', q_{pV} . This expression is the most commonly used specification for q and is defined according to Equation 6.7 [219, 220].

$$q_{pV} = p \cdot \dot{V} = p \cdot \frac{\Delta V}{\Delta t} \quad [q_{pV}] = \frac{\text{mbar} \cdot \text{l}}{\text{s}} \quad (6.7)$$

By means of the ideal gas law (Equation 6.8) and the definition of the mean particle velocity \bar{c} (Equation 6.9) a translation of the different expressions for the throughput q is possible.

$$p \cdot V = n \cdot R \cdot T = N \cdot k \cdot T \quad (6.8)$$

$$\bar{c} = \sqrt{\frac{8 \cdot R \cdot T}{\pi \cdot M}} \quad (6.9)$$

The equations for the conversion of the pV-throughput q_{pV} into the throughputs q_v and q_N are the following:

$$q_v = \frac{q_{pV}}{p} \quad (6.10)$$

$$q_N = \frac{q_{pV}}{k \cdot T} \quad (6.11)$$

6.2.3 Flux

The flux J of particles through a specific device with the cross-section A is defined according to Equation 6.12 [19, 218]. It is given in molecules per area and time.

$$J = \frac{q_N}{A} \quad [J] = \frac{1}{\text{cm}^2 \cdot \text{s}} \quad (6.12)$$

When the device, through which the particles flow, is a circular tube, the particle flux J is consequently given by Equation 6.13 [19, 218].

$$J = \frac{q_N}{r^2 \cdot \pi} = \frac{4 \cdot q_N}{d^2 \cdot \pi} \quad (6.13)$$

In this equation, r is the (inner) tube radius and d the (inner) tube diameter. Usually these parameters are given in 'cm' and thus J is typically given in the unit $\text{cm}^{-2} \text{s}^{-1}$.

6.2.4 Pumping speed and throughput of a vacuum pump

When a gas is pumped by a vacuum pump, its pumping speed S is defined by the gas volume that passes the area of the pump inlet port per time. This quantity corresponds to the volume throughput q_V at the pump inlet port, also called volume flow rate (see Equation 6.14).

$$S := \dot{V}_{\text{pump inlet port}} = q_{V \text{ pump inlet port}} \quad [S] = \frac{\text{m}^3}{\text{s}} \quad (6.14)$$

The pV-throughput at the pump inlet port is called throughput \dot{Q} of the vacuum pump. It is defined by Equation 6.15 [219].

$$\dot{Q} = q_{pV \text{ pump inlet port}} \quad [\dot{Q}] = \frac{\text{Pa} \cdot \text{m}^3}{\text{s}} = 10 \frac{\text{mbar} \cdot \text{l}}{\text{s}} \quad (6.15)$$

Applying the correlation of q_V and q_{pV} (Equation 6.10) one obtains the following relationship between the throughput \dot{Q} and the pumping speed S of the vacuum pump:

$$\dot{Q} = q_{pV \text{ pump inlet port}} = p \cdot S \quad (6.16)$$

In this equation, the pressure p is the gas pressure at the pump inlet port. When the temperature is constant, the throughput of the vacuum pump scales with the number of molecules which are pumped per time.

6.3 Determination of precursor flux and pressure at the nozzle exit

Upon normal operation of a vacuum instrument an equilibrium between the natural leak throughput (leak rate) and the throughput \dot{Q} of the vacuum pump is established. When a gas is dosed inside the instrument chamber, a deliberate throughput of particles is realized. At a constant background pressure, an equilibrium between dosing throughput and throughput \dot{Q} of the vacuum pump has adjusted. For this case, Equation 6.16 enables to calculate the throughput \dot{Q} from the pumping speed of the vacuum pump and the pressure at the pump inlet port. Due to the equilibrium

in the chamber this throughput \dot{Q} corresponds to the throughput q_{pV} of particles at the gas injection system.

The analysis chamber of the applied instrument houses an ion getter pump (Varian, Vaclon Plus 500, StarCell, type 919-1740), which is the only pump that is used during the gas dosage of an EBID experiment. The pumping speed S of this pump at the target pressure of $3.0 \cdot 10^{-7}$ mbar (background pressure adjusted during the EBID experiments) is 250 l/s for argon and 360 l/s for nitrogen (after saturation) [222]. As the precise pumping speed of the ion getter pump for the applied precursor TTIP is not known, a pumping speed in between of these two values is assumed. Therefore, in the following, all considerations are based on the averaged pumping speed of 305 l/s, assumed for TTIP.

Applying Equation 6.16, the throughput \dot{Q} and thus the throughput q_{pV} of TTIP molecules at the gas injection system can be calculated. For the applied UHV instrument (base pressure $< 2 \cdot 10^{-10}$ mbar) the natural leak throughput (leak rate) can be neglected in this consideration. The following value is obtained for the throughput q_{pV} :

$$q_{pV} = 9.2 \cdot 10^{-5} \frac{\text{mbar} \cdot \text{l}}{\text{s}} \quad (6.17)$$

For the determination of the flux J a conversion of the obtained 'pV-throughput' q_{pV} into the 'number of particles throughput' q_N is necessary. By using Equation 6.11 (with $T = 293$ K) the following value for q_N results:

$$q_N = 2.3 \cdot 10^{15} \frac{1}{\text{s}} \quad (6.18)$$

The applied GIS consists of a nozzle-based gas doser with an inner tube diameter of 3 mm (see Chapter 3.1.3). Therefore, the total particle flux J_{tot} at the nozzle exit can be calculated according to Equation 6.13. The obtained value for J_{tot} is:

$$J_{\text{tot}} = 3.2 \cdot 10^{16} \frac{1}{\text{cm}^2 \cdot \text{s}} \quad (6.19)$$

The calculated total particle flux J_{tot} at the nozzle exit can be compared to the number of molecules forming a closed layer of the unit area of 1 cm^2 . This value can be derived from the required area A for one TTIP molecule (monomer) on a surface,

which can be estimated from the volume of the molecule and thus from its molar mass M and density ρ (see Table 2.2) according to Equation 6.20.

$$A \approx V^{2/3} = \left(\frac{m}{\rho}\right)^{2/3} = \left(\frac{M \cdot n}{\rho}\right)^{2/3} = \left(\frac{M \cdot N}{\rho \cdot N_A}\right)^{2/3} = 0.63 \text{ nm}^2 \quad (6.20)$$

From the required space for one TTIP molecule (monomer) of 0.63 nm^2 the number of molecules forming a closed layer of the unit area of 1 cm^2 can be calculated to be $1.6 \cdot 10^{14} \text{ cm}^{-2}$. Consequently, for J_{tot} (Expression 6.19) one monolayer would be formed in $\approx 5 \text{ ms}$, if all molecules arrived on the sample surface.

For the determination of the pressure at the very end of the nozzle exit Friedli and Utke suggest a rough estimation from its dynamic component. According to references [19] and [218] the dynamic pressure can be calculated according to Equation 6.21:

$$p_d = J_{\text{tot}} \cdot \frac{\sqrt{2 \cdot \pi \cdot M \cdot R \cdot T}}{N_A} \quad (6.21)$$

This equation, in slightly modified form, is also specified in the reference book from Wedler [35], where it is applied to determine the number of particle collisions per time unit onto the unit area of a wall $^1Z_W (J_{\text{tot}})$ from the pressure p . Applying Equation 6.21 for the precursor molecule TTIP and calculating with $M = 284 \text{ g/mol}$ (for monomeric TTIP), $T = 293 \text{ K}$ and the above specified value for J_{tot} (Expression 6.19), one obtains the following value for the dynamic pressure p_d that exists at the nozzle exit:

$$p_d = 3.5 \cdot 10^{-4} \text{ mbar} \quad (6.22)$$

Friedli notes that the dynamic pressure p_d slightly overestimates the actual pressure in the vicinity of the nozzle exit. Moreover the author emphasizes the difficulty to correctly determine this pressure [218].

Summarizing this chapter, one can state that for the applied instrument the total flux J_{tot} at the very end of the dosing nozzle is $3.2 \cdot 10^{16} \text{ cm}^{-2} \text{ s}^{-1}$. The pressure at the nozzle exit was determined from its dynamic component and is $3.5 \cdot 10^{-4} \text{ mbar}$.

6.4 Determination of flux distribution, precursor flux and pressure directly at the sample surface

In Chapter 6.3 the total flux J_{tot} and the (dynamic) pressure p_d at the nozzle exit were determined. Two questions remain: How many molecules arrive directly at the sample surface? And what is the pressure at the sample surface at a background pressure of $3.0 \cdot 10^{-7}$ mbar (background pressure adjusted during the EBID experiments)? To answer these questions simulations with the software 'GIS Simulator' (version 1.5, 2008) were performed. By these simulations the flux distribution on the sample surface can be determined for the given experimental setup.

6.4.1 The GIS Simulator

Friedli and Utke offer a software ('GIS Simulator', version 1.5, 2008) which enables to simulate the near-field distribution of particles delivered by a nozzle-based GIS impinging on a flat sample surface [19, 218]. The software is a probabilistic simulation approach for rarefied gas flows and applicable for the molecular flow and to some extent for the transient flow regime. Calculations are performed on the basis of the so-called 'test-particle Monte Carlo' (TPMC) method which was first introduced by Davis in 1960 [223] and applied by Smith and Lewin in 1966 [224]. It takes into account the Knudsen number at the very end of the nozzle exit which describes the existing flow regime just before the particles effuse into the vacuum of the instrument chamber. By computing serially a large number of particle trajectories (typically 10^6 to 10^7) the macroscopic flow distribution of particles on the sample surface can be predicted [19].

In the strict sense, the 'test-particle approach' can only be applied for the molecular flow regime. Under these flow conditions no collisions between different particles but only tube wall collisions occur and the particle trajectories are independent of one another [19]. In order to extend the applicability of the software also the transient flow regime was included. This was realized by simulating particle-particle collisions after a particle has moved a certain distance inside the tube [19].

When the particles have left the tube nozzle, an infinite Knudsen number, i.e. infinite mean free path λ , is set. By this condition a collision-free, straight trajectory of each

particle is simulated until it either hits the sample surface or is “lost in its surrounding” [19]. This is equivalent to a molecular flow regime which typically exists in the vacuum chamber.

The simulation of a particle trajectory starts at the tube entrance with a cosine angular velocity distribution [19]. In the following, the trajectory is determined by particle-particle and / or tube wall collisions depending on the flow regime. The end of a trajectory is reached when the particle leaves the tube - either at the tube entrance, which means that the particle is backscattered, or at the tube exit, which means that the particle passed the tube and effuses into the vacuum of the instrument chamber. For the latter case, the transmitted particle is spatially mapped on the sample surface [19] and by counting the number of events of impinging molecules in dependence of the lateral position the particle flux distribution on the substrate can be determined. The locally impinging flux J , normalized with respect to the total particle flux J_{tot} , can thus be specified.

In the following, fundamental characteristics and assumptions implicated in the algorithms of the software ‘GIS Simulator’ are briefly summarized [19, 218].

(1) For the scattering of particles from the inner tube walls ‘diffuse scattering’ is applied which means that particle desorption from the surface occurs randomly and the desorption direction is independent of the direction of incidence. Surface diffusion is neglected and the angular distribution is described by the cosine law [19].

(2) The loss of particles inside the tube due to chemisorption at the inner tube walls can optionally be included by adding a so-called ‘uptake coefficient’ [19]. This parameter is defined as the probability of a particle to stick forever to the inner tube wall after collision. The reduction of the flux due to particle sorption at tube walls was already described by Smith and Lewin in 1966 [224]. However, chemisorption in the order of less than 3 % (found e.g. for $\text{Co}_2(\text{CO})_8$) did not show an observable change in simulated flux profiles [19].

(3) Scattering upon particle-particle collisions is simulated according to the hard sphere model. The collision cross-section σ is assumed to be $\delta^2\pi$ where δ is the particle diameter. All particles are assumed to have a spherically symmetric geometry [19].

(4) For the simulation of transient flows it is assumed that the mean free path λ at the tube exit is valid inside the entire tube [19]. The mean free path λ is calculated according to Equation 6.3, The Knudsen number Kn according to Equation 6.4.

(5) The concept of applying a reduced tube length L_r is advisable. It significantly decreases the computation time and yields approximately the same results concerning the particle flux distribution compared to a simulation performed with a tube of full length L [19]. For molecular flow conditions the critical reduced tube length L_r was found to be $15 \cdot d$ ($= 30 \cdot r$) with d and r being the (inner) tube diameter and radius, for transient flow conditions L_r is between $3 \cdot \lambda$ and $5 \cdot \lambda$.

(6) After the last collision inside the tube, no particle-particle collisions inside the vacuum chamber are assumed (Kn is set to ∞) [19].

(7) The scattering of particles at the sample surface and the trajectory in the chamber after a scattering event are not taken into account [19].

For further details and a complete description of the 'GIS simulator' software, the interested reader is referred to the references [19, 218]. The stochastic formalisms and three-dimensional distributions can be found in the Appendix B of reference [218].

6.4.2 Simulation of flux distribution, precursor flux and pressure at the sample surface for the applied instrumental setup

Applying the software 'GIS Simulator' (version 1.5, 2008) one can determine the local impinging precursor flux J on the sample surface from the total molecule flux J_{tot} for the applied GIS and the geometrical aspects of the setup.

In the work at hand, a nozzle-based GIS was applied. For an EBID experiment, the doser was approached to a distance of 12 mm to the sample surface (see Chapter 3.1.3). The nozzle approaches parallel to the x-axis of the sample stage with an angle ϑ of 26° with respect to the specimen surface plane [30]. Figure 6.4 shows a schematic drawing of the applied GIS in the approached state and an overview of all distances and angles.

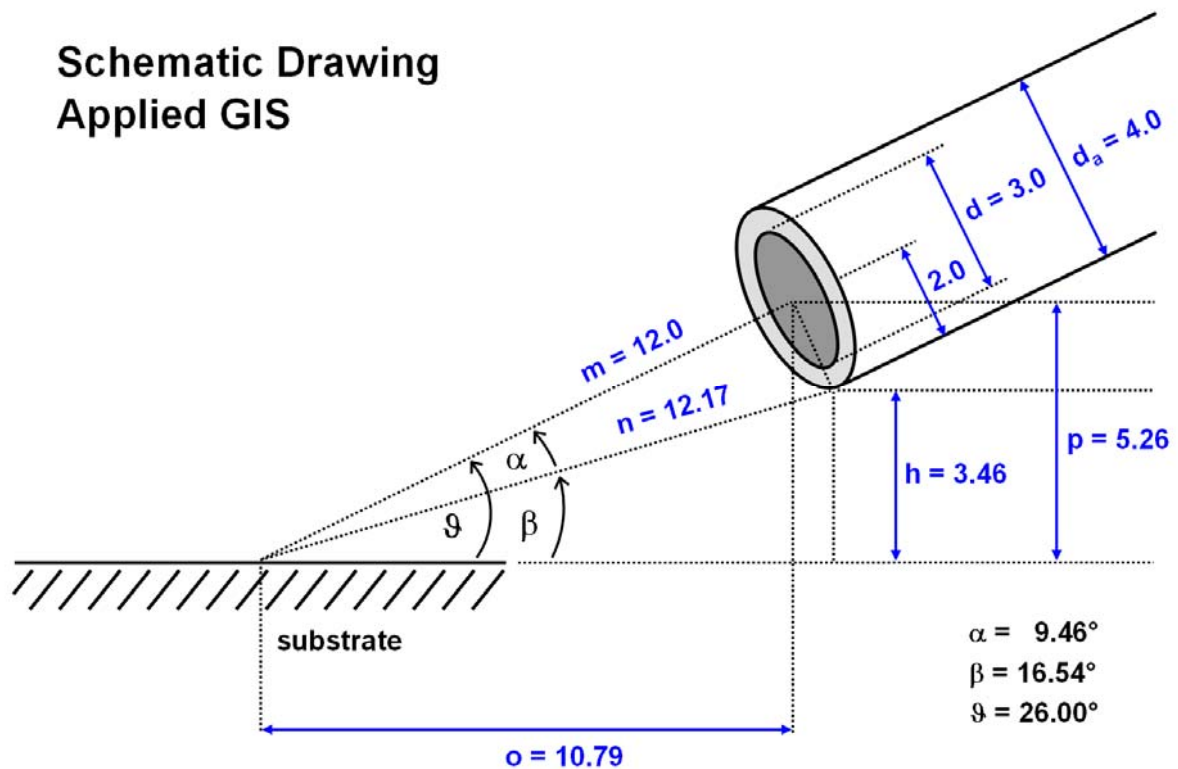


Figure 6.4: Schematic drawing of the applied GIS depicting all relevant distances and angles in the approached state of the dosing nozzle. All distances are given in mm.

For a simulation run, the flow regime simulated inside the tube has to be specified. The mean free path λ of the molecules is only to be specified if transient flow conditions are simulated.

In order to determine the flow conditions for TTIP in the applied setup, the Knudsen number Kn at the nozzle exit is calculated according to Equation 6.4. For the pressure p the determined dynamic pressure (Expression 6.22) is used, T is set to RT (293 K) and for the molecule diameter δ the value of 1 nm is applied (determination see reference [99]). The following value is obtained for the Knudsen number Kn :

$$Kn = 8.7 \quad (6.23)$$

This Kn value indicates free molecular flow conditions at the nozzle exit according to the references [219, 220]. Based on Equation 6.1 the mean free path λ of the molecules can be determined from Kn :

$$\lambda = 26.0 \text{ mm} \quad (6.24)$$

Taking into account the applied setup in this work, the following parameters were used for the run of a simulation:

Molecules contained:

Molecules #: $1 \cdot 10^6$

Tube diameter (used for absolute scaling):

Inner tube radius: 1.5 mm

Tube dimensions:

Tube length L: 320 mm

Outer tube radius r_a : 2.0 mm

Tube – substrate configuration sets:

Angle a_1 : 0°

Angle a_2 ($90^\circ - \vartheta$): 64°

Distance L_s : 12 mm

Flow regime:

Free molecular flow

Mean free path: -

Flux sampling on the substrate:

Sampling field size: 36 mm

Sampling grid points #: 128

Note that in the software input mask an absolute specification has to be given only for the inner tube radius (1.5 mm in the applied setup). All other distances have to be specified by multiples of the inner tube radius. For the tube length L the distance from the nozzle to the flange was specified (320 mm in the applied setup). This length is larger than the reduced tube length L_r for molecular flow conditions by the factor of 7.1. The simulation software runs until a certain number of molecules has transmitted through the tube (here specified: $1 \cdot 10^6$). The number of computed molecules is higher and a value for the transmission coefficient is given in the data output files.

The result of the simulation with the above specified parameters is presented in Figure 6.5. It depicts the color-coded two-dimensional isoflux contour plot (J/J_{tot}) of the impinging molecules on the sample and its surrounding. The graphic is obtained with the data output files.

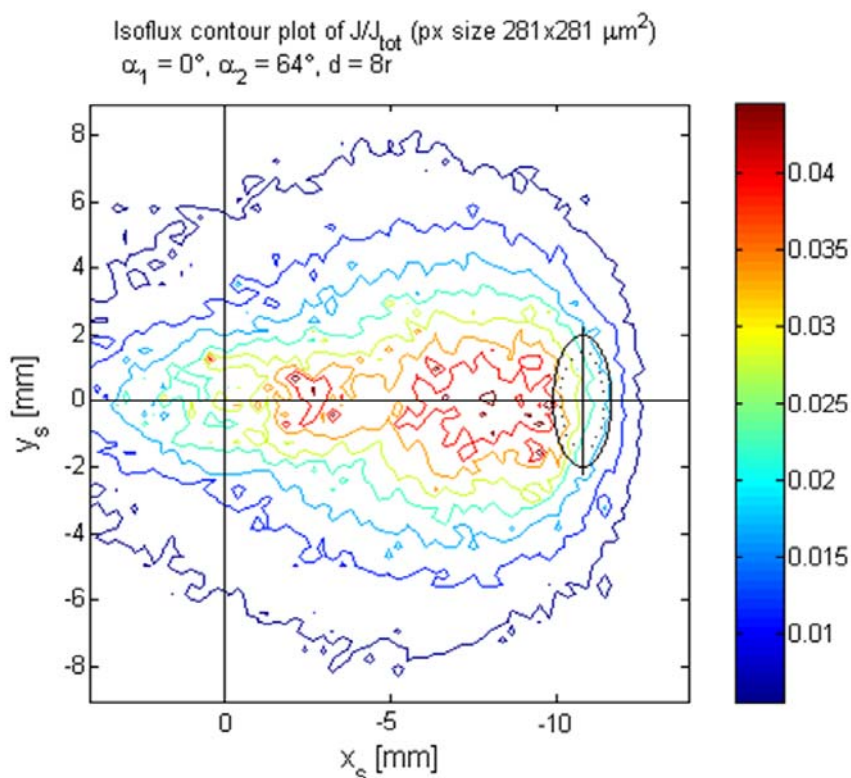


Figure 6.5: Color-coded two-dimensional isoflux contour plot (J/J_{tot}) of the impinging molecules on the sample and its surrounding, obtained from the software 'GIS Simulator' (version 1.5, 2008) [19]. The black ellipse (at $x_s = -10.79$, $y_s = 0$) symbolizes the projection of the dosing nozzle onto the xy plane. The center of the sample is at the position $x_s = y_s = 0$.

Figure 6.5 shows that for the applied GIS setup the maximum molecule flux J is obtained roughly 8 mm away from the center of the sample surface ($x_s = y_s = 0$). This can be traced back to the long distance between sample center and nozzle exit (12 mm). However, a shift of the point of maximum flux towards the sample surface can not be realized as the tube nozzle can not be approached closer to the sample due to the given instrumental setup. The right side of the sample stage and the pole shoe of the electron column are hindering a closer approach (see Figure 3.3 b) and d)).

For an EBID experiment performed in the center of the sample surface the precursor molecule flux can be derived e.g. from the flux coefficient plot (J/J_{tot}) for $y_s = 0$ in dependence of the coordinate x_s (corresponds to the x-axis of the sample stage). This drawing is depicted in Figure 6.6.

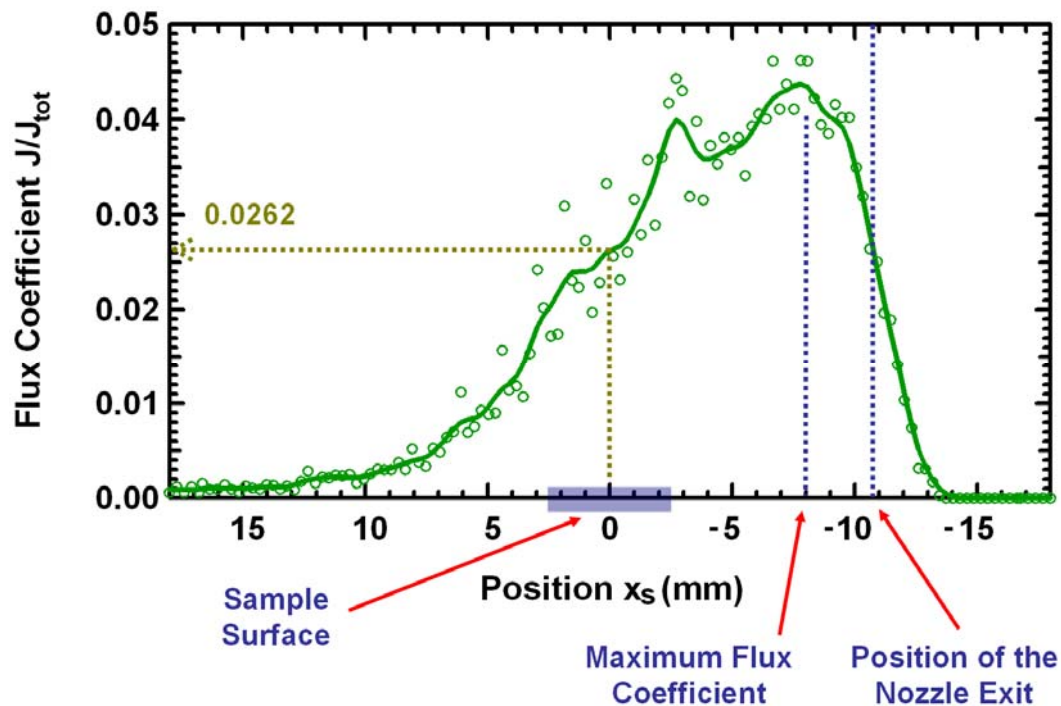


Figure 6.6: Flux coefficient plot (J/J_{tot}) for $y_s = 0$ in dependence of the coordinate x_s . The x_s -axis corresponds to the x-axis of the sample stage. The graphic is obtained from the software 'GIS Simulator' (version 1.5, 2008) [19]. The sample position is marked in light blue in the center of the abscissa, the green circles display the simulation raw data and the green line displays the smoothed graph (smoothing algorithm 'binomial smoothing' for five times).

Figure 6.6 shows that in the center of the sample surface ($x_s = y_s = 0$) the flux coefficient J/J_{tot} is about 0.026. The relative mean error according to [218], obtained from the output files, lies at $\pm 5.5\%$ at this sample position. This means that the corresponding local flux J is accurate with a mean error of $\pm 5.5\%$.

Via this result one can calculate the precursor molecule flux J impinging in the center of the sample from J_{tot} . The following value is obtained:

$$J = 8.4 \cdot 10^{14} \frac{1}{\text{cm}^2 \cdot \text{s}} \pm 5.5 \% \quad (6.25)$$

Comparing this flux to the number of TTIP molecules forming a closed layer of the unit area of 1 cm^2 , i.e. $1.6 \cdot 10^{14} \text{ cm}^{-2}$ (determination see Chapter 6.3), one can conclude that one monolayer of TTIP is formed in $\approx 190 \text{ ms}$ (in the center of the sample surface).

Analogously, the pressure directly at the sample surface is calculated leading to the following result:

$$p = 9.2 \cdot 10^{-6} \text{ mbar} \pm 5.5 \% \quad (6.26)$$

Therefore, the pressure during an EBID experiment directly at the sample surface is increased by a factor of ≈ 31 in comparison to the adjusted background pressure in the chamber, which was always $3.0 \cdot 10^{-7} \text{ mbar}$.

The setup depicted in Figure 6.4 was applied for almost all EBID experiments and results described in this work. Only for one experiment (see Chapter 9.2) the dosing nozzle was approached to a distance of $\approx 8 \text{ mm}$ to the sample surface (before modifications were made to the dosing nozzle, see Chapter 3.1.3). For this setup, the distances and angles depicted in Figure 6.4 are different: $m = 8.0 \text{ mm}$, $n = 8.3 \text{ mm}$, $o = 7.2 \text{ mm}$, $p = 3.5 \text{ mm}$, $h = 1.7 \text{ mm}$, $\alpha = 14.0^\circ$ and $\beta = 12.0^\circ$. Performing the same simulation as described above with this nozzle-sample distance yields a value of 0.044 for the flux coefficient at $x_s = y_s = 0$. This means that an increased flux and an increased pressure by the factor of + 69 % existed directly at the sample surface during this EBID experiment. Results from the latter experiment are notably specified in this work (see Chapter 9.2).

6.5 Summary and conclusions

In this chapter, an estimation was made for the precursor flux J and the pressure p directly at the sample surface for the applied instrumental setup in this work.

Based on the pumping speed S of the ion getter pump that was employed during the EBID experiments and on the background pressure, the total precursor molecule flux J_{tot} at the end of the dosing nozzle was estimated. It is $3.2 \cdot 10^{16} \text{ cm}^{-2} \text{ s}^{-1}$ for an

estimated pumping speed of 305 l/s for TTIP. From this flux value the pressure at the nozzle exit was determined. It was deduced from the dynamic pressure component, which is a rough estimation according to reference [218]. The dynamic pressure at the end of the dosing nozzle is $3.5 \cdot 10^{-4}$ mbar.

To estimate the precursor flux impinging directly on the sample surface simulations were performed with the software 'GIS Simulator' (version 1.5, 2008) provided by Friedli and Utke [19, 218]. The flux coefficient J/J_{tot} was determined in the center of the sample surface assuming free molecular flow conditions in the tube. For a nozzle-sample distance of 12 mm the flux coefficient is 0.026 with a specified accuracy for the local flux J of $\pm 5.5\%$. This results in a precursor flux of $8.4 \cdot 10^{14} \text{ cm}^{-2} \text{ s}^{-1} \pm 5.5\%$ on the sample surface.

For the pressure directly at the sample surface a value of $9.2 \cdot 10^{-6} \text{ mbar} \pm 5.5\%$ was calculated. In comparison to the adjusted background pressure during an EBID experiment ($p = 3.0 \cdot 10^{-7} \text{ mbar}$) this means an increase for the pressure at the sample surface by a factor of ≈ 31 .

Altogether, the considerations and performed quantity determinations in this chapter yield reasonable results. However, it has to be noted that the obtained results are based on several assumptions and have thus to be considered as an estimation. A summary of all assumptions is given in the Appendix of this work (see Chapter 16.3).

7 Nanostructure fabrication with TTIP

In the following chapter, EBID nanostructures fabricated with the precursor TTIP on two different substrates, namely Si(100) and Au(111), are presented and compared. On both surfaces the fabrication of structures with arbitrary shape on the nanometer scale was realized. Point, line and area deposits were generated and also arbitrarily shaped patterns. A selection of exemplary nanostructures is presented and discussed in Chapter 7.1.

One of the major questions concerning EBID with TTIP on both substrates, i.e. the chemical composition of the fabricated nanostructures, is addressed in Chapter 7.2. Chemical analysis of the deposits was performed via AES and the quantitative determination of the titanium, oxygen and carbon amount was done on the basis of reference measurements on a pure carbon layer and on a clean rutile $\text{TiO}_2(110)$ single crystal.

Finally, in Chapter 7.3 the varying contrast in SEM between deposited structure and sample material are discussed for different deposits. The fabricated nanostructures appear differently in SEM on the semiconducting Si(100) samples and the metallic Au(111) sample.

7.1 Deposition with arbitrary shape on the nanometer scale

Nanostructures were fabricated via EBID with TTIP on Si(100) samples and on a Au(111) single crystal. In order to realize the deposition of arbitrary shapes, the electron beam was controlled via the SmartSEM software (Zeiss) (see Chapter 3.2.1), the lithographic attachment ELPHY Quantum (Raith) (Chapter 3.2.2) or waveform generators (Hewlett-Packard) (Chapter 3.2.3). The Si(100) and Au(111) samples were prepared as described in Chapter 3.3. After sample preparation, the surface quality of the samples was confirmed via LEED, SEM and AES.

In Figure 7.1, selected SEM images of deposited structures are depicted. Figure 7.1 a) shows a point matrix, which was deposited on the Au(111) sample with the software ELPHY Quantum. The matrix consists of ten points arranged in three columns with three points in the left and middle one and four points in the right column. Additionally, a dot deposit is visible in the upper left corner of the SEM image, separated from the ten-point matrix. This unintended deposit is generated due

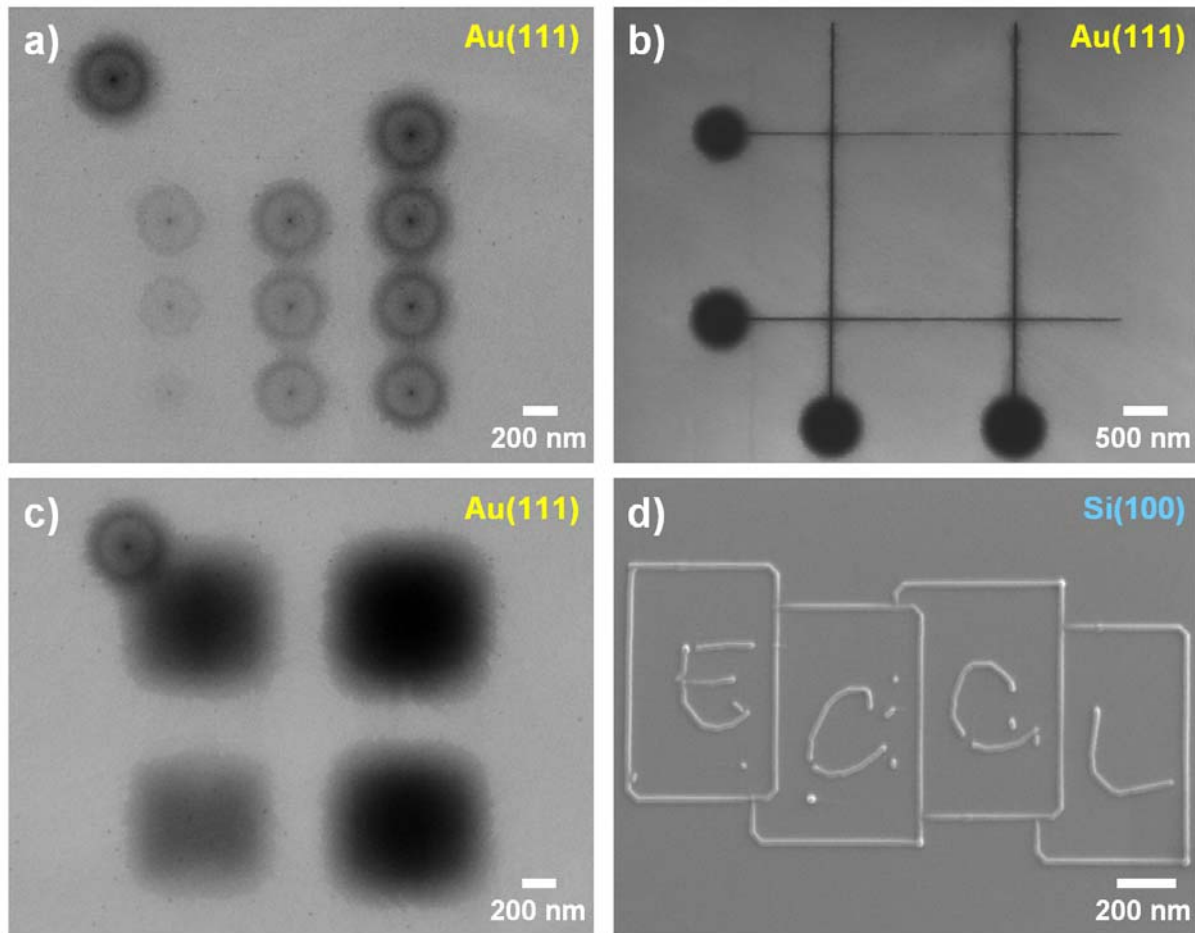


Figure 7.1: Selection of EBID deposits fabricated with TTIP on different sample materials. a) Point matrix on Au(111) consisting of ten points deposited with increasing electron dose. b) Line pattern on Au(111) with four lines of increasing electron dose oriented perpendicular to each other. c) Area deposits on Au(111) with increasing electron dose. d) ECCL logo on Si(100). Please note that in a) and c) an additional point deposit is visible in the upper left due to technical reasons; for an explanation see text.

to an unintended waiting time of the electron beam in the upper left corner of the $2\ \mu\text{m} \times 2\ \mu\text{m}$ write field. It is the ‘PT deposit’, introduced in Chapter 3.2.2. The electron dose of the point deposits in the matrix increases in each column from bottom to top and from the left to the right column. The lower left dot was fabricated with the lowest electron dose of 0.12 nC, and the electron dose is then incrementally increased by 0.12 nC per point. This results in an electron dose of 1.20 nC for the upper right dot. For rising electron dose, the dot deposits are getting darker in the

SEM image, indicating that a higher amount of material is deposited with increasing electron dose. The structure of each dot deposit obviously strongly deviates from the dot shape. Each “dot structure” consists of a point deposit in the center surrounded by a “ring” and followed by a small halo, which is fading with increasing distance from the center. The origin of this structure is addressed later in this work (see Chapter 10.1). The size of the point deposits in the center rises from $\approx 21 \pm 5$ nm for the lower left dot to $\approx 45 \pm 10$ nm for the upper right one (FWHM criterion) and the outer diameter of the halo around the dark circles is increasing with rising electron dose as well: from $\approx 233 \pm 10$ nm to $\approx 568 \pm 10$ nm (20 % criterion). Interestingly, the diameter of the dark “ring” around each dot deposit is constant and measures $\approx 350 \pm 10$ nm, which is explained later in this work (see Chapter 10.1) (lateral sizes determined via WSxM; see Chapter 3.6.8). From the measured size values one can conclude that the fabrication of structures on the nanometer scale was realized.

In Figure 7.1 b) a pattern of four lines, which are arranged perpendicular to each other, is depicted. These line structures are narrow and well-defined deposits on the Au(111) surface. All lines are $4.6 \mu\text{m}$ long and the electron dose is rising from the upper horizontal ($0.36 \mu\text{C}/\text{cm}$) to the lower horizontal line ($0.73 \mu\text{C}/\text{cm}$) and from the left vertical ($1.09 \mu\text{C}/\text{cm}$) to the right vertical one ($1.45 \mu\text{C}/\text{cm}$). Except for the line fabricated with the lowest electron dose (upper horizontal one) all lines are continuous. The large circles at the starting point of each line are the ‘WT deposit’ introduced and explained in Chapter 3.2.1. The line diameter rises with increasing electron dose from $\approx 26 \pm 3$ nm (upper horizontal line) to $\approx 33 \pm 5$ nm (lower horizontal one), $\approx 57 \pm 5$ nm (left vertical one) and $\approx 70 \pm 10$ nm (right vertical one) (measured in the middle of the line deposit with averaged 10 profile lines; all values determined via the software WSxM according to the FWHM criterion; for details see Chapter 3.6.8). The size of the lines demonstrates that structures on the low nanometer scale were generated.

Figure 7.1 c) shows the generation of area deposits on the Au(111) sample realized via ELPHY Quantum. The pattern visible in the SEM image consists of four squares which were generated by irradiating four square areas with a size of $600 \text{ nm} \times 600 \text{ nm}$. The electron dose increased from the lower left ($0.66 \text{ C}/\text{cm}^2$) to the upper left ($1.33 \text{ C}/\text{cm}^2$), lower right ($1.99 \text{ C}/\text{cm}^2$) and upper right ($2.66 \text{ C}/\text{cm}^2$). Analog to the dot deposits depicted in Figure 7.1 a), the squares appear darker with increasing

electron dose, indicating that the amount of deposited material scales with the electron dose. Again, a halo can be observed in the surrounding of the squares which is fading with increasing distance from the squares. Moreover, this pattern also exhibits the additional unintended 'PT deposit' which is visible in the upper left area of the SEM image (see Chapter 3.2.2). Via the software WSxM the actual lateral size was determined according to the 20 % criterion (for details see Chapter 3.6.8). The diameter of the squares inclusive their halos increases with rising electron dose from 900 (lower left) to 965 (upper left) to 1010 (lower right) and 1027 nm (upper right) with an estimated accuracy of ± 10 nm.

In Figure 7.1 d) the deposition of material in an arbitrary shape on a Si(100) sample is depicted. The pattern is the logo of the ESF COST Action CM0601 of "Electron Controlled Chemical Lithography" (ECCL). This logo was prepared by image conversion and patterned by using two waveform generators (see Chapter 3.2.3). The logo has a size of $1.92 \mu\text{m} \times 1.02 \mu\text{m}$ and was fabricated with a line dose of $29.1 \mu\text{C}/\text{cm}$. The dots inside the logo, located close to the letters, are 'deposition artifacts' originating from irradiation events where the synchronization between the two waveform generators was not correct (see Chapter 3.2.3). All lines of the logo in Figure 7.1 d) feature a size on the low nanometer scale. The line diameter was determined visually via WSxM and measures $\approx 29 \pm 3$ nm.

From the deposits depicted in Figure 7.1, which represent a selection of EBID structures fabricated with TTIP on the samples Au(111) and Si(100), the following conclusions can be drawn. The SEM images show that structures of arbitrary shape can be fabricated via EBID with the precursor TTIP in the applied setup. By controlling the electron beam dot, line and area structures can be generated and also the deposition of arbitrarily shaped patterns is possible. In addition, Figure 7.1 reveals that the fabrication of well-defined structures with a lateral size clearly on the nanometer scale is possible. This holds in particular for the line deposits in Figure 7.1 b) and the "ECCL" deposit in Figure 7.1 d).

Some further effects and open questions are addressed later in this work. These are e.g. the unexpected dot shape in Figure 7.1 a) (see Chapter 10.1) or the observed broadening of the area deposits in Figure 7.1 c) (see Chapter 8). The different types

of SEM contrast, responsible for the different appearance of the fabricated structures on both sample surfaces in the SEM images (bright vs. dark), are explained in Chapter 7.3.

7.2 Chemical composition of EBID deposits with TTIP

In this chapter, one of the major questions concerning EBID with the metal alkoxide precursor TTIP is addressed, i.e. the chemical composition of the deposited material on the sample surfaces Si(100) and Au(111). Moreover, the dependency of the chemical composition on the deposit structure (area, line or dot) and lithographic parameters and the oxidation state of titanium in the material are discussed.

7.2.1 Literature overview on the chemical compositions for CVD and EBID

TTIP is a well-known precursor in chemical vapor deposition (CVD) [10-15, 185, 186]. In numerous articles it is reported that the use of TTIP directly led to the formation of a TiO_2 film on the substrate surface [10-12, 14, 15, 185]. However, also the deposition of films composed of different titanium oxide species was reported, i.e. Ti_2O_3 , Ti_3O_5 and anatase and rutile TiO_2 [13, 186], depending on the applied experimental conditions. The contamination level with carbon is addressed in three of the denoted references concerning CVD. While Watanabe *et al.* report that their titanium oxide films fabricated by thermal CVD from TTIP at 523 K did not contain any traces of carbon [186], Sandell *et al.* indicate in their UHV study a small carbon contamination (0.15 ML) only in the initial stage of TiO_2 growth on Si(111) (film thickness $< 10 \text{ \AA}$ at a deposition temperature of 773 K) [10]. Interestingly, Chen *et al.* report that CVD fabricated thin TiO_2 films did not show a carbon contamination in the bulk but contained some carbonaceous species at the surface [12].

In contrast to CVD, in EBID the use of TTIP is rarely reported up to now (see Chapter 4.5) [16-18] and the same holds for specifications concerning the chemical composition of EBID deposits from this precursor. Mitchell *et al.* report of the fabrication of thin films of titanium oxide [16, 17] that clearly show a carbon contamination. Quantitative data is only specified in one reference [4] which refers to reference [18]. Under HV conditions upon applying high beam currents (10 – 250 nA)

material was deposited with the composition of 34 at. % titanium, 51 at. % oxygen and 15 at. % carbon, estimated with the volume sensitive method of energy dispersive X-ray spectroscopy (EDX).

7.2.2 Chemical composition of area structures

In this work, the chemical composition of fabricated nanostructures on Si(100) and Au(111) was analyzed via Auger electron spectroscopy (AES). In order to determine the composition quantitatively, the obtained spectra were compared with titanium dioxide and carbon reference spectra (see Chapter 3.6.8).

Figure 7.2 depicts SEM images of two area deposits fabricated via EBID with TTIP on Si(100) and on Au(111). The deposits were fabricated by scanning an area of $2.3 \mu\text{m} \times 1.7 \mu\text{m}$ for six times applying a dwell time of $204.8 \mu\text{s}$ and a total electron dose of 9.86 C/cm^2 .

On the Si(100) surface (Figure 7.2 a)) the fabricated area deposit is difficult to identify. Only the borders of the rectangular structure and a bright halo are visible with low contrast. This phenomenon is discussed in the next chapter. In contrast, the deposit on the Au(111) surface (Figure 7.2 b)) is clearly visible. Here, the deposit appears darker than the surface in the SEM image. The white dashed lines in Figure 7.2 b) indicate the irradiated area during the deposition process. Interestingly, the size of the deposit is enlarged in all lateral directions. The enlargements in the upper and lower part of the SEM image are due to proximity effects, explained in Chapter 8, while the enlargements at the left and right border are attributed to a scan artifact during the deposition process.

In order to study the chemical composition of the deposited material on both surfaces, local AES was performed. The acquired AE spectra are depicted in Figure 7.2 c) and d) (dark blue and red spectrum) and the positions where the spectra were measured are marked by the color-coded, star-shaped markers in a) and b). Additionally to the spectra on the deposits, on each sample a spectrum was taken on the unexposed, clean surface before the EBID experiments. These are the light blue spectrum for Si(100) and the orange one for Au(111), also depicted in Figure 7.2 c) and d). All spectra were measured via the 'area mode' (for details see Chapter 3.6.5).

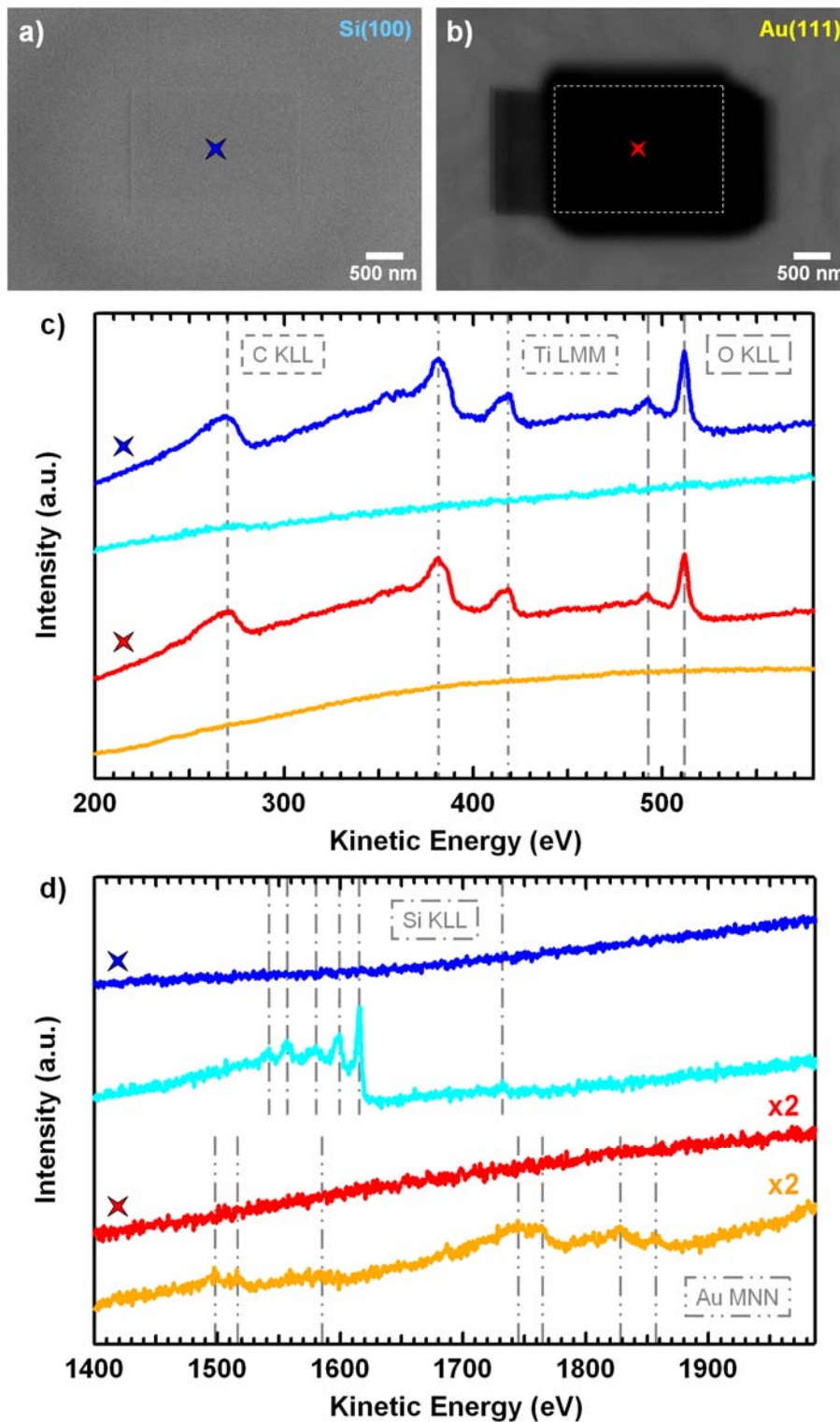


Figure 7.2: SEM images of an area deposit fabricated on a) Si(100) and b) Au(111) with corresponding AE spectra (c) and d), respectively). The dark blue and red AE spectrum were acquired in the center of the area deposits while the light blue (Si(100)) and the orange (Au(111)) AE spectrum were taken before EBID on the unexposed, clean surfaces, respectively.

Both the light blue spectrum of the unexposed, clean Si(100) surface and the orange spectrum of the unexposed, clean Au(111) surface display only the substrate Auger signals. This demonstrates that the sample surfaces were clean before the experiments. In the high kinetic energy region (Figure 7.2 d)) the light blue spectrum depicts six Auger signals at the kinetic energies of ≈ 1542 , 1557, 1580, 1598, 1615 and 1733 eV. They are assigned to Si KLL transitions [34, 40] from the Si substrate material. The orange spectrum shows seven small and broad Auger signals (Figure 7.2 d)) at the energies of ≈ 1498 , 1516, 1586, 1744, 1765, 1827 and 1859 eV, which are assigned to Au MNN transitions [34, 40] from the Au substrate material.

The dark blue and the red spectrum, which were measured in the center of the respective EBID deposit, show both complete damping of the substrate signal (see Figure 7.2 d)). This demonstrates that a thick layer was deposited in both cases, whose thickness can not be determined directly. Assuming a substrate signal which is damped to 5 % of the undamped signal of the clean surface [30] enables an estimation of the minimum layer thicknesses (details see Chapter 3.6.8). This approach yields a thickness of at least 6.1 nm on the Si(100) surface and at least 6.4 nm on the Au(111) surface.

In the low kinetic energy region (see Figure 7.2 c)) the dark blue and the red spectrum show the same spectrum shape with five pronounced Auger signals. The Auger signal at ≈ 270 eV is attributed to carbon KLL transitions, while the signals at ≈ 382 and 418 eV correspond to titanium LMM and the ones at ≈ 492 and 512 eV to oxygen KLL transitions [34, 40] (Please note that the smaller Ti LMM signals, which precede and succeed the indicated Auger signals at ≈ 382 and 418 eV, are not labeled since they show a comparably small intensity and are hardly visible). This experimental result demonstrates that EBID with the precursor TTIP leads to the deposition of titanium, oxygen and carbon on both sample materials.

In order to compare the dark blue and red spectrum in more detail and in order to determine the chemical composition of the deposited material, a quantitative analysis was performed. This analysis yields that the absolute peak areas of the normalized spectrum measured on gold (red spectrum in Figure 7.2 c)) are smaller (by 16 %) than the areas of the spectrum acquired on silicon (dark blue spectrum in Figure 7.2 c)). However, the peak area ratios of the three elements are the same in both spectra, which indicates the same chemical composition of the deposited material on

silicon and gold. Quantitative analysis of the stoichiometric composition, performed by a comparison with reference spectra (details see Chapter 3.6.8), yields a chemical composition of 21 ± 5 at. % carbon, 25 ± 5 at. % titanium and 54 ± 5 at. % oxygen for the area deposit fabricated on Si(100) and 20 ± 5 at. % carbon, 26 ± 5 at. % titanium and 54 ± 5 at. % oxygen for the one generated on Au(111). This result confirms that the deposited material has the same chemical composition on both substrates. From more experimental runs, in which the described area deposit was fabricated, an averaged chemical composition for the specified lithographic parameters of 19 ± 5 at. % carbon, 26 ± 5 at. % titanium and 55 ± 5 at. % oxygen was determined.

Concerning the carbon contamination level of the deposits, one can state the following: Despite working under UHV conditions, EBID with the precursor TTIP yields structures containing a significant amount of carbon besides the targeted elements titanium and oxygen [225]. The obtained carbon level is significantly higher than observed for EBID deposits from the precursor iron pentacarbonyl in the same UHV instrument [22, 142, 143]: In that work, applying $\text{Fe}(\text{CO})_5$ under UHV conditions enabled the fabrication of very clean deposits with a carbon and oxygen contamination level of less than 5 at. % on Si(100) and $\text{SiO}_x(300 \text{ nm}) / \text{Si}(100)$ [22, 142] and less than 12 at. % on Rh(110) [143], respectively. Considering the ultra clean UHV conditions during the experiments one can clearly rule out that carbon derives from the residual gas or from the sample surface. Since the precursor TTIP is composed of four hydrocarbon ligands bound to the central atom titanium and since a high amount of hydrocarbon species is found in the dosed TTIP gas (see QM spectra in Chapter 5), one can further conclude that the high amount of carbon in the deposits must originate from the precursor TTIP itself [225].

This unintended co-deposition of carbon in EBID experiments with precursor complexes is also addressed in literature: In their review article Utke *et al.* indicate that the deposition of pure materials via FEBID or FIBID can be achieved when the applied and released electrons (PE, BSE, SE) or ions cause a chemical reaction but do not lead to the fragmentation of the reaction products before volatile species can desorb [4]. However, for electron or ion beam induced deposition (FEBID / FIBID) the authors specify that “unspecific multiple site fragmentation of adsorbed precursor molecules” occurs and that elements, which are solids in their elementary form (like carbon or phosphorus), easily stay on the surface [4]. The consequence is that these

elements are embedded in the deposit as contamination. This appears also to apply for the precursor molecule TTIP. Obviously, the carbonaceous isopropoxy ligands are further fragmented by applied and released electrons (PE, BSE, SE) during the deposition process and the embedding of carbon and carbonaceous fragments into the deposit takes place besides the desorption of volatile species.

Comparing the carbon contamination level with the specified values in literature (15 at. % carbon, 34 at. % titanium and 51 at. % oxygen in reference [4]) one might conclude that EBID with TTIP under UHV conditions does not yield higher deposit purities compared to HV results. The average carbon content determined for the area deposits depicted in Figure 7.2 (19 at. % C) is slightly higher than specified for deposits under HV conditions. However, a direct comparison of the reported chemical composition under HV conditions in the references [4] and [18] with the composition specified in this work for UHV conditions is hampered by four aspects:

Firstly, the values in reference [4] were determined via the volume sensitive method of EDX while in the work at hand the highly surface sensitive AES technique was applied. It has to be considered the high amount of hydrocarbons in the TTIP gas during EBID and the possibility of hydrocarbon adsorption on the deposits after structure fabrication. The adsorbed hydrocarbon molecules are decomposed upon characterization via SEM and / or AES (unintended "EBID" of adsorbates during structure characterization) and result in a contamination of the deposit surface. Thus, an inhomogeneous element distribution with a higher amount of carbon in the surface layers is feasible (see also Chapters 3.6.8 and 9.1.1). This could explain the slightly higher carbon contamination level detected via AES.

Secondly, EDX strongly underestimates the content of carbon since for elements with low atomic number Z the probability of relaxation by X-ray fluorescence is significantly lower compared to that of Auger electron emission [34] (see also Figure 2.5).

Thirdly, it is known from literature that the lithographic parameters play a significant role for the final shape, size, morphology and the chemical composition of EBID deposits [5]. The lithographic parameters (like electron dose, step size, dwell time, waiting times, replenishment times, number of sweeps) applied for deposition are not specified in the references [4] and [18]. This hampers a direct comparison of the

observed chemical compositions. In addition, a higher purity obtained by other lithographic parameters might be possible upon the here applied UHV approach. Fourthly, the HV deposits fabricated with TTIP which are specified in reference [4] were generated with considerably higher beam currents, i.e. 10 – 250 nA. In comparison to the current applied for EBID in this work ($I_B = 400$ pA) the beam current was higher by a factor of 25 – 625. From literature it is known that applying higher beam currents yields deposits with increased metal content [5]. Data is given e.g. for the precursors dicobalt octacarbonyl ($\text{Co}_2(\text{CO})_8$) by Utke *et al.* [144], dimethyl gold trifluoroacetylacetonate ($\text{Me}_2\text{Au}(\text{tfac})$) by Weber *et al.* [154], cyclopentadienyl trimethyl platinum (PtCpMe_3) by Weber *et al.* [123] and Koops *et al.* [226] and molybdenum hexacarbonyl ($\text{Mo}(\text{CO})_6$) by Weber *et al.* [123, 154]. Thus, it can be concluded that the lower carbon and higher titanium content of the HV deposits reported in reference [4] might also be attributed to the significantly higher beam current used for deposition.

7.2.3 Variation of lithographic parameters

As already mentioned above the applied lithographic parameters do not only influence and determine the final shape, size and morphology of EBID deposits, but also play a role for their chemical composition [5]. In order to fabricate EBID deposits with reduced carbon content and higher purity one route thus might be to vary the lithographic parameters and study their influence on the composition. In this chapter, the chemical compositions of area deposits on Si and Au fabricated with varied lithographic parameters are discussed. The parameters that were changed are the step size s_A , the area dose d_A , the number of sweeps N_S and the dwell time t_D . In addition, an area deposit is considered that was generated on an oxidic surface, i.e. $\text{SiO}_x(300 \text{ nm}) / \text{Si}(100)$, with strongly varied parameters.

First, the influence of the area dose is investigated on silicon and gold. For this purpose, area deposits were fabricated on a Si(100) and on the Au(111) sample with identical lithographic parameters than those depicted in Figure 7.2, except for the step size and area dose. The area dose was reduced by a factor of four, i.e. from 9.86 C/cm^2 to 2.46 C/cm^2 , by scanning a rectangular area with doubled edge lengths ($4.6 \mu\text{m} \times 3.4 \mu\text{m}$). It has to be noted that by this procedure the step size is increased

by the factor of two, i.e. from 2.2 nm to 4.5 nm compared to the deposits of Figure 7.2. However, considering the size of the ‘BSE exit area’ on both substrates (see Chapter 8), this small change of the step size is assumed to be negligible.

The fabricated deposits on both surfaces are depicted in Figure 7.3. Analogous to Figure 7.2, the same contrasts appear in SEM: While the contrast between deposit and Si(100) surface is very weak and therefore the generated area structure is hardly visible (see Figure 7.3 a)), the contrast between deposit and Au(111) surface is high with the deposit appearing black on a brighter background (Figure 7.3 b)) (contrast mechanisms see Chapter 7.3).

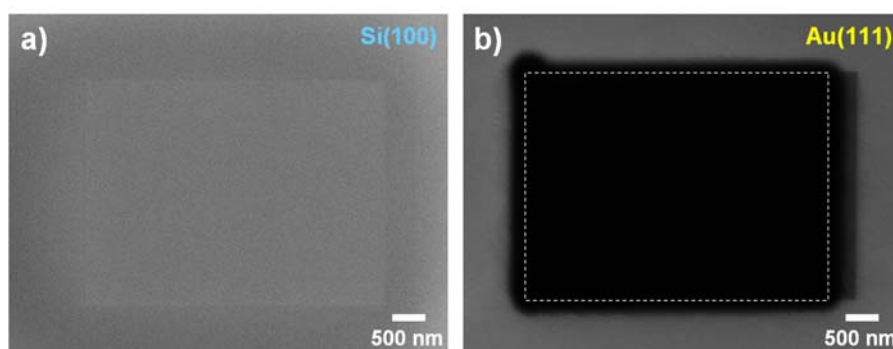


Figure 7.3: SEM images of area deposits fabricated on a) Si(100) and b) Au(111) with an electron area dose of 2.46 C/cm^2 . Compared to the area deposits depicted in Figure 7.2 a four times lower electron area dose was applied. The slightly increased step size (4.5 nm compared to 2.2 nm) is assumed to be negligible (see text).

The white dashed lines in Figure 7.3 b) indicate the irradiated area during the deposition process. Again, lateral broadening is observed in all directions due to proximity effects (see Chapter 8). The right-angled enlargement at the right deposit border is attributed to a scan artifact during the deposition process.

The quantitative chemical analysis of both structures yields a stoichiometric composition of 19 ± 5 at. % carbon, 27 ± 5 at. % titanium and 54 ± 5 at. % oxygen for the area deposit fabricated on Si(100) and 22 ± 5 at. % carbon, 28 ± 5 at. % titanium and 50 ± 5 at. % oxygen for the one generated on Au(111). With respect to the specified accuracy one can state a very similar chemical composition on both samples and in particular also a very similar chemical composition compared to the deposits discussed before (Figure 7.2). Thus, it can be concluded that for the chosen

deposition parameters a variation of the area dose from 9.86 C/cm^2 to 2.46 C/cm^2 does not change the chemical composition of the fabricated area deposits significantly.

It has to be noted that the variation of the electron dose by a factor of four is possibly too small to observe an influence on the chemical composition. A systematic study with a wide variation of the electron dose is thus advisable for future experiments. In addition, a variation of the electron dose can also be realized by changing the dwell time. Thus, also the variation of the dwell time should be included in future studies.

In order to analyze the influence of the number of sweeps during EBID, three deposits with identical lithographic parameters but varying sweep number and electron dose were fabricated on a Si(100) surface. The lithographic parameters were the same as for the deposits depicted in Figure 7.3 (scanned area of $4.6 \mu\text{m} \times 3.4 \mu\text{m}$, dwell time of $204.8 \mu\text{s}$ and step size of 4.5 nm). By varying the number of sweeps from 3 to 6 and 9 the electron doses of 1.23 C/cm^2 , 2.46 C/cm^2 and 3.70 C/cm^2 were realized. Quantitative analysis of these deposits yields a very similar chemical composition with only small deviations. For the lowest electron dose (1.23 C/cm^2) a stoichiometric composition of $17 \pm 5 \text{ at. \% C}$, $29 \pm 5 \text{ at. \% Ti}$ and $54 \pm 5 \text{ at. \% O}$ was found, for the higher doses (2.46 C/cm^2 and 3.70 C/cm^2) the composition was determined to be $19 \pm 5 \text{ at. \% C}$, $27 \pm 5 \text{ at. \% Ti}$ and $54 \pm 5 \text{ at. \% O}$. Both SEM images of the generated area deposits and the corresponding AE spectra are depicted in reference [110]. From this result it can be concluded that for the applied deposition parameters a variation of the number of sweeps from 3 to 6 and 9 does not change the chemical composition of the fabricated area deposits significantly.

It has to be noted that by varying the sweep number in the performed experiments the applied electron dose was altered simultaneously and that the sweep number variation by a factor of two and three might be too small to observe an influence on the chemical composition. Also for this lithographic parameter, a systematic study with wide variation of the number of sweeps would be interesting for future experiments. This can either be realized for a constant dwell time (then the electron dose changes with the number of sweeps, as described above) or realized for a fixed electron dose (then the dwell time would have to be adjusted for each single run).

In the framework of capping experiments, in which layered nanostructures were fabricated by successive EBID experiments with two precursors (nanostructure generation with $\text{Fe}(\text{CO})_5$, local capping with TTIP, see Chapter 13), an EBID area deposit was produced with strongly deviating lithographic parameters from the ones used for the deposits discussed above. The structure was fabricated with a significantly larger irradiated area, i.e. $32.0 \mu\text{m} \times 2.5 \mu\text{m}$, larger area step size, i.e. 31.3 nm , larger sweep number, i.e. 10,000, and a lower dwell time of $1.6 \mu\text{s}$. EBID was performed on an $\text{SiO}_x(300 \text{ nm}) / \text{Si}(100)$ sample and the electron dose for the structure was $0.67 \text{ C}/\text{cm}^2$.

The chemical analysis of this capping layer yields a stoichiometric composition of $13 \pm 5 \text{ at. \% C}$, $31 \pm 5 \text{ at. \% Ti}$ and $56 \pm 5 \text{ at. \% O}$, which means that material was deposited with a significantly lower amount of carbon. In addition, the layer thickness was determined to be 3.2 nm and in the acquired AE spectrum the substrate signals are still visible. Since the $\text{SiO}_x(300 \text{ nm}) / \text{Si}(100)$ sample was slightly contaminated with carbon before EBID (due to residues of the initial protective coating, see Chapter 3.5), the carbon content of the EBID deposit is even slightly lower than 13 at. \% C .

This result could be explained by the strong variation of the lithographic parameters in comparison to the ones described above. One can speculate that in particular the reduced dwell time (factor 128) and the significantly higher number of sweeps (factor between 1,111 and 3,333) could promote this effect. A discussion of the influence of the dwell time on the chemical composition is given in Chapter 7.2.5. However, also the use of an oxidic substrate ($\text{SiO}_x(300 \text{ nm}) / \text{Si}(100)$) might play a role. It is well-known from literature that electron stimulated desorption of oxygen takes place on silicon oxide via the Knotek-Feibelman mechanism proposed for ionic substrates [4, 227, 228]. The released oxygen atoms might react with fragments from TTIP during the EBID process, thus enhance the amount of volatile, desorbing hydrocarbon species and consequently minimize the amount of C in the deposit. More work has to be done in order to detect the origin of the acquired result (lithographic parameters, substrate induced effect or both) and to investigate this phenomenon in more detail.

Finally, an overview of different EBID area deposits from TTIP is given in Table 7.1. The table lists the applied sample surfaces, the chosen lithographic parameters and

the determined chemical compositions. In addition, the structures are listed with increasing carbon content from top to bottom.

No.	Sample	Area size [$\mu\text{m} \times \mu\text{m}$]	d_A [C/cm^2]	t_D [μs]	s_A [nm]	N_S	Composition		
							C	Ti	O
I	SiO_x	32.0 x 2.5	0.67	1.6	31.3	10,000	13	31	56
II	Si(100)	4.6 x 3.4	1.23	204.8	4.5	3	17	29	54
III	Si(100)	2.3 x 1.7	9.86	204.8	2.2	6	19	26	55
IV	Si(100)	4.6 x 3.4	2.46	204.8	4.5	6	19	26	55
V	Si(100)	4.6 x 3.4	3.70	204.8	4.5	9	19	27	54
VI	Au(111)	2.3 x 1.7	9.86	204.8	2.2	6	20	26	54
VII	Au(111)	4.6 x 3.4	2.46	204.8	4.5	6	22	28	50

Table 7.1: Determined chemical compositions of different EBID area deposits from the precursor TTIP listed with increasing carbon content from top to bottom. The denoted lithographic parameters are the area size, the area dose d_A , the dwell time t_D , the step size s_A and the number of sweeps N_S .

The chemical compositions specified in Table 7.1 support the conclusions drawn above. The variation of the area dose d_A within the range of 1.23 to 9.86 C/cm^2 (factor of 8) and the variation of the number of sweeps within the range of 3 to 9 (factor of 3) do not change the chemical composition of the corresponding area deposit significantly (see deposits II to VII). The deposit with the highest purity is the one fabricated on the $\text{SiO}_x(300 \text{ nm}) / \text{Si}(100)$ sample (capping layer, deposit I) with strongly deviating lithographic parameters from the ones described before. Based on this result one could envisage a strategy for the fabrication of deposits with reduced carbon content. It is assumed that applying a short dwell time and a high sweep number and possibly the use of an oxidic substrate could favor low carbon contents in area deposits. Moreover, Table 7.1 demonstrates that for the area deposits a mean ratio of oxygen to titanium of $\approx 2:1$ is observed.

7.2.4 Chemical composition of line and dot structures

In Chapters 7.2.2 and 7.2.3 the chemical composition of area deposits was discussed. In the following, the composition of line and dot structures fabricated via EBID with TTIP is addressed.

A line pattern consisting of three lines with a length of 4.6 μm was deposited on a Si(100) sample. The dwell time and step size were 204.8 μs and 4.5 nm, respectively, and the electron doses were 116 $\mu\text{C}/\text{cm}$ for the left vertical line, 232 $\mu\text{C}/\text{cm}$ for the horizontal line and 463 $\mu\text{C}/\text{cm}$ for the right vertical line. All lines were fabricated with multiple sweeps and the varying electron dose was realized by an increasing sweep number (632, 1,263 and 2,526 respectively). Figure 7.4 a) shows an SEM image of the line pattern.

A specific feature of each line of the line pattern is the comparably large circular structure at the starting point, this is again the ‘WT deposit’ introduced and discussed in Chapter 3.2.1 (waiting time per sweep: 27.8 ms). The doses of these “line starting points” increase with the line doses in the pattern, from 7 nC of the left vertical line to 14 nC of the horizontal one and 28 nC of the right vertical one.

In order to study the chemical composition of a line and a dot structure, local AES was performed directly on these features (‘area mode’, scan window of 20 nm x 20 nm, details see Chapter 3.6.5). Since the left vertical and horizontal line have small widths of 38 and 52 nm, respectively, the broader right vertical line (line diameter: 75 nm) was used for the chemical analysis (line widths determined visually via the software WSxM). Figure 7.4 b) shows an SEM image with high magnification of the right vertical line at the position marked in Figure 7.4 a) via the upper square in white dashed lines. Analogously, Figure 7.4 c) depicts an SEM image with high magnification of the starting point of the right vertical line (position marked in Figure 7.4 a) via the lower square in white dashed lines). The positions where local AES was done are indicated by the color-coded, star-shaped markers in Figure 7.4 a).

The red spectrum depicted in Figure 7.4 d) was acquired on the right vertical line 1 μm below the crossing point with the horizontal one and the blue spectrum was measured directly on the starting point of the right vertical line. Both spectra show in total five clearly visible Auger signals. The Auger peak at the kinetic energy of ≈ 270 eV is attributed to carbon KLL transitions, the signals at ≈ 382 and 418 eV

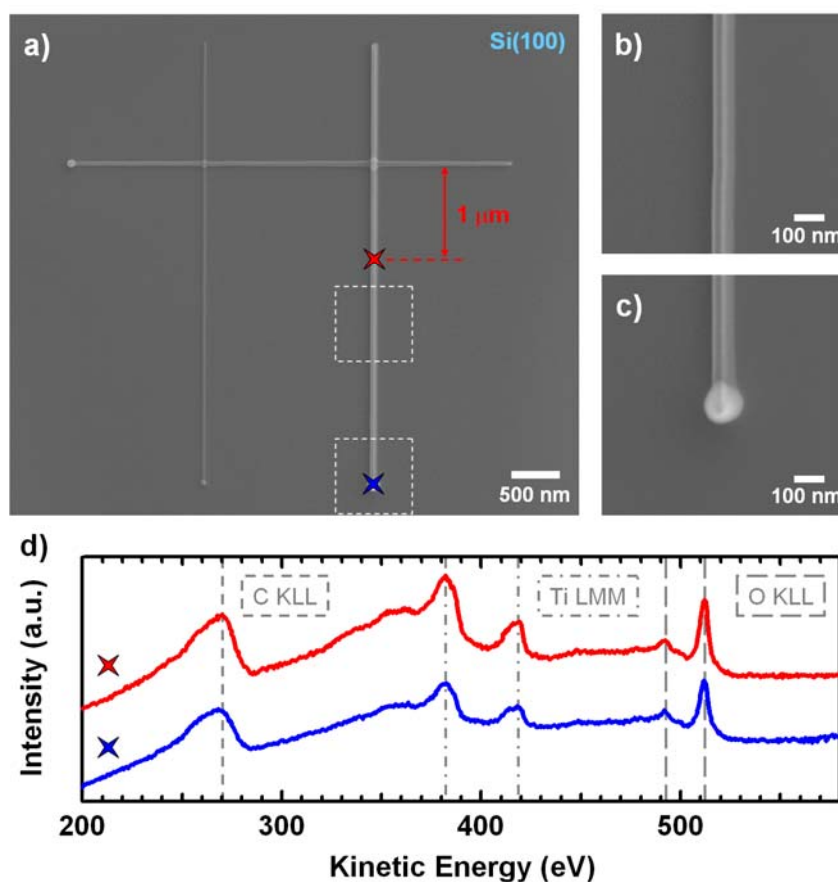


Figure 7.4: a) SEM image of a line pattern consisting of three single lines perpendicular to each other, fabricated on a Si(100) sample. b) Blow-up SEM image of the right vertical line. c) Blow-up SEM image of the starting point of the right vertical line. d) AE spectra acquired on the right vertical line (red spectrum) and its starting point (blue spectrum). The positions where the blow-up images and spectra were measured are marked in a).

correspond to titanium LMM transitions and the ones at ≈ 492 and 512 eV to oxygen KLL transitions [34, 40]. Quantitative analysis was performed with both spectra (details see Chapter 3.6.8) in order to determine the chemical composition of the structures. The analysis yields a composition of 31 ± 5 at. % carbon, 23 ± 5 at. % titanium and 46 ± 5 at. % oxygen for the line structure and 31 ± 5 at. % carbon, 17 ± 5 at. % titanium and 52 ± 5 at. % oxygen for the “dot deposit”, i.e. the starting point of the right vertical line.

Compared to the area structures investigated in Chapter 7.2.2 and Chapter 7.2.3, the carbon content of a line and dot structure is considerably larger. An average increase

of + 63 % was found for the carbon content. Moreover, a comparison of the chemical composition of the dot deposit with those of the area and line deposits yields a lowered amount of titanium in the dot deposit. Both deviations in composition can be traced back to the deposition with strongly different lithographic parameters when generating an area, line or dot deposit, respectively. Four lithographic parameters are supposed to influence strongly the chemical composition of EBID structures and are discussed in the following:

1.) The 'dwell time' (or 'pixel time') is different for the dot structures (27.8 ms) compared to the line and area structures (204.8 μ s). In multiple sweep deposition experiments the dwell time plays a significant role and determines the degree of precursor fragmentation before the beam leaves and returns.

2.) The 'replenishment time' in terms of a time elapsing until the electron beam returns to a certain point of the structure is strongly different for the structures depicted in Figure 7.4. It was 209.7 ms (i.e. the 'active line duration') for the dot deposit and 237.5 ms (i.e. the 'total line duration') for the line deposit, respectively, while for the area structures depicted in Figure 7.2 and Figure 7.3 it was 169.5 s (i.e. the 'frame duration'). During this time the replenishment with precursor molecules occurs, but also desorption and diffusion processes of volatile decomposition fragments take place which can influence the final carbon content in the deposit.

3.) When during the irradiation process the PE beam hits the surface at a certain position, also in the surrounding of this spot backscattered electrons (BSEs) and secondary electrons (SE2) are released ('BSE proximity effect', see Chapter 4.2). They escape the surface within a circular area of radius r ('BSE exit area') and trigger precursor dissociation processes as well. The shape of the structure to irradiate, i.e. dot, line or area structure, determines significantly the contribution of these lower energetic electrons to the fabrication of the corresponding deposit. The degree of additional irradiation caused by BSEs and SE2 is different in dependence of the structure shape since the overlap of the 'BSE exit area' and the structure to irradiate by the PE beam varies. It is drastically larger for an area structure compared to a line or dot structure. Consequently, a much larger amount of lower energetic BSEs and SE2 contributes to the fabrication of area deposits during the irradiation process. This might explain in particular the higher purity of area deposits compared to line and dot structures: Depending on the energy of the electrons different dissociation

mechanisms are favored [4] which are described in detail in the references [4, 5, 30, 117]. It is conceivable that the different dissociation processes influence the chemical composition of the deposit since they possibly determine which precursor fragment desorbs after electron impact [5, 117] or stays for further fragmentation and embedding into the final deposit.

4.) The 'number of sweeps' is significantly different for the above discussed dot, line and area structures. It is 2,526 for the right vertical line and its starting point ('WT deposit'), is only in the range from 3 to 9 for the area deposits on Si(100) and Au(111) and is 10,000 for the capping layer generated on SiO_x.

It is assumed that the dwell time, the replenishment time and the contribution of the lower energetic BSEs and SE2 to the precursor decomposition have the strongest impact on the chemical composition of an EBID deposit. A systematic investigation of the specific influence of these parameters on the chemical composition should be subject of further experiments. In these studies, attention should also be turned to the interplay between different lithographic parameters. In particular, the interplay between dwell time and replenishment time should be significant since these parameters determine the extent of precursor ligand fragmentation in each sweep on the one hand and the degree in which off-diffusion and desorption processes of volatile decomposition fragments take place on the other.

7.2.5 Strategies for carbon reduction in the deposits

The analysis of the chemical composition of nanostructures fabricated via EBID with TTIP under UHV conditions yields an amount of carbon in the deposits between 13 ± 5 and 31 ± 5 at. %. Separate from post-treatment procedures performed after structure generation, one might envisage strategies which enable to lower the amount of carbon in the deposit *in situ*, i.e. directly within the deposition process. As an outlook, the following two approaches are suggested in order to obtain deposits with a higher purity.

1.) In their review article Utke *et al.* report a relation between deposit purity and the extent of precursor ligand fragmentation by applied and released electrons. In order

to minimize precursor ligand fragmentation the authors suggest e.g. to apply relatively low electron densities [4]. For the metal alkoxide precursor TTIP the combination of a short dwell time and a long replenishment time, i.e. long waiting time until the primary electron beam returns to a certain position in the irradiated area, might be a promising scan strategy. The idea is that in a short dwell time a low extent of precursor fragmentation should occur causing the scission of only the weakest bonds in the molecules but avoiding the fragmentation of the organic ligands as far as possible. In this step, primarily titanium and oxygen containing fragments should be deposited. Then, when the electron beam is “off” the considered position in a long replenishment time, the carbon containing precursor fragments from the isopropoxy ligands should be able to diffuse “off” the structure or to desorb. In consequence, the amount of titanium and oxygen in the deposit could be increased while the amount of carbon might be reduced which means a higher deposit purity.

2.) The fabrication of an EBID area deposit from TTIP on an oxidic sample yielded a comparably low amount of carbon in the deposit (13 ± 5 at. %, see Chapter 7.2.3). One possible explanation for the reduced carbon content is that oxygen atoms released from the sample surface by ESD could react with carbonaceous precursor fragments and form volatile species which desorb. In consequence, one might envisage an EBID experiment with simultaneous dosage of the precursor TTIP and the reactive gas oxygen in order to decrease the amount of carbon in the deposit. The idea behind this approach is the chemical reaction of generated carbon containing precursor fragments with supplied oxygen and the possible formation of highly volatile species like CO or CO₂. The latter might readily desorb and would then not be embedded in the deposit. If this approach is not successful at RT one might further think of applying elevated temperatures during the deposition process in order to activate the above described chemical reactions [166].

7.2.6 The oxidation state of titanium in the deposited material

In the previous chapters, the focus was set to the chemical composition of the deposited structures. In addition to that, the oxidation state of titanium in the deposited material is another interesting issue of EBID with the precursor TTIP, which is investigated in the following section.

There are several possibilities concerning the oxidation state of titanium in the deposits which have to be considered. One possibility is the deposition of an amorphous material consisting of the elements carbon, titanium and oxygen in a disordered matrix. Alternatively, a titanium oxide species could be directly deposited caused by bond scissions in the TTIP molecules, primarily between the oxygen atom and the secondary carbon atom of the isopropoxy ligands. For this case, theoretically the deposition of different titanium oxide species is possible, like e.g. titanium(II) oxide (TiO), titanium(III) oxide (Ti₂O₃) or titanium(IV) oxide (TiO₂), as well as several titanium oxide species side by side. Moreover, the deposition of titanium oxide species during EBID does not rule out the simultaneous presence of an amorphous matrix into which the titanium oxide species might be embedded.

In order to address the question of the oxidation state of titanium in the deposited material a comparison was drawn between a characteristic spectrum obtained on an EBID area deposit, the measured TiO₂ reference spectrum and a spectrum for the pure metal titanium taken from literature [229]. Figure 7.5 depicts the comparison between an Auger spectrum acquired on an EBID area deposit on Si(100) and the measured TiO₂ reference spectrum. The blue spectrum in Figure 7.5 a) and b) is identical to the blue spectrum in Figure 7.2 c). The deposit has a chemical composition of 21 at. % C, 25 at. % Ti and 54 at. % O (± 5 at. %). The green spectrum is the TiO₂ reference spectrum. Both spectra were taken applying the 'area mode' with a scan window of 200 nm x 200 nm. The display region of the spectrum in a) (330 eV to 470 eV) shows the signals attributed to the Ti LMM and Ti LMV Auger transitions while the region in Figure 7.5 b) (470 eV to 550 eV) depicts the O KLL transitions. The small circles of both spectra illustrate the normalized raw data while the continuous lines represent the smoothed spectra (details see Chapter 3.6.5).

The comparison drawn in Figure 7.5 demonstrates that both spectra have a very similar shape. The same Auger signals appear and the peak positions are identical. Since also the Auger peak area ratio O KLL (512 eV) / Ti LMM (382 eV) is very similar for both spectra, i.e. 0.36 for the blue spectrum and 0.32 for the green (TiO₂ reference) spectrum, one can conclude that the deposited material is a titanium oxide species.

Considering the chemical composition of the characterized EBID deposit with an oxygen to titanium ratio of 2.16, i.e. slightly higher than 2:1 of stoichiometric TiO₂,

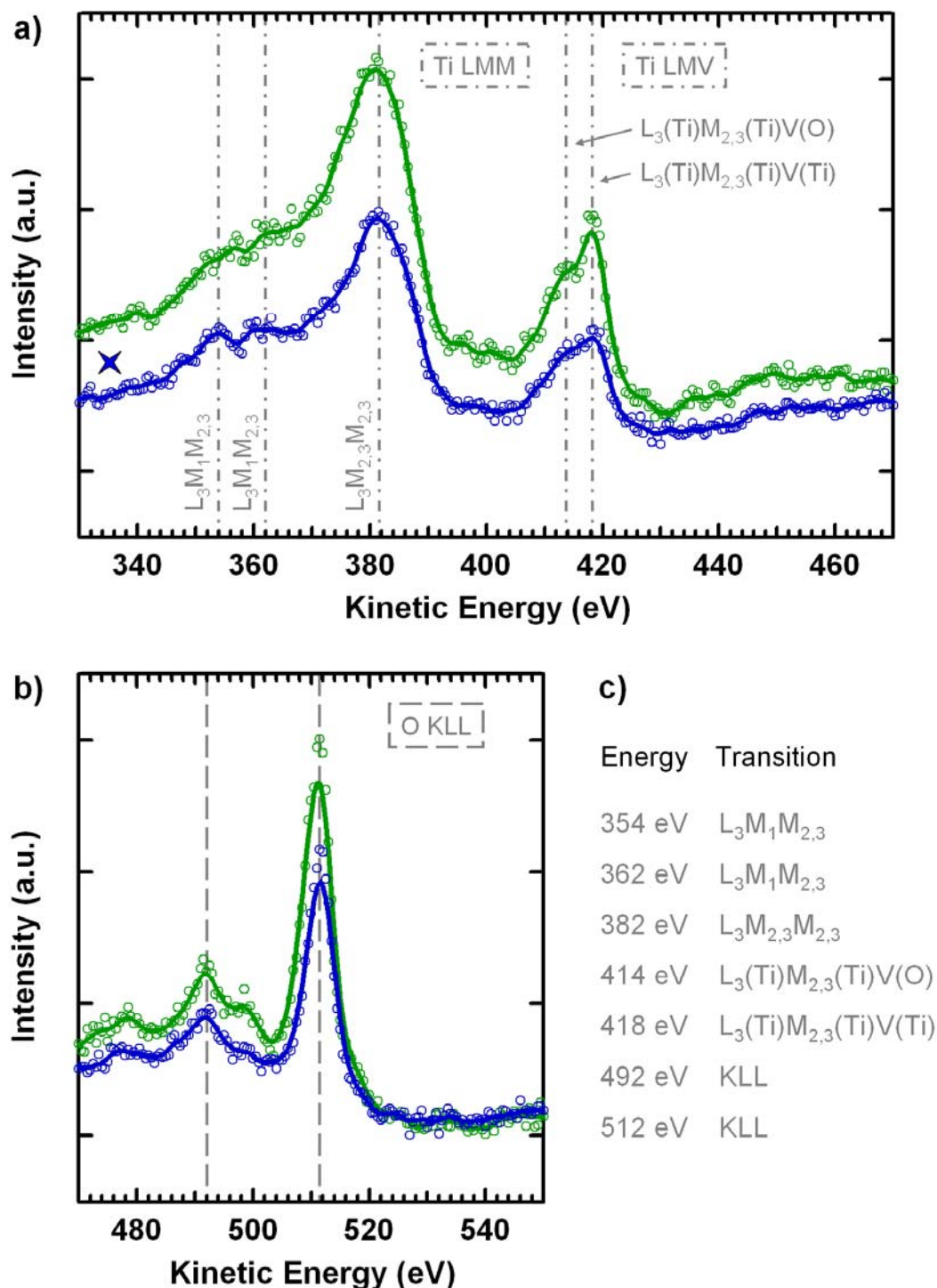


Figure 7.5: Comparison of an AE spectrum acquired on an EBID deposit on Si(100) (blue, details see text) with the measured rutile $\text{TiO}_2(110)$ reference spectrum (green). In both spectra, the small circles illustrate the normalized raw data while the continuous lines represent the smoothed data. a) Ti LMM and Ti LMV region. b) O KLL region. c) Measured kinetic energies and associated Auger transitions.

one might assume a material of a composition close to titanium dioxide, embedded into an amorphous matrix. This matrix would then be composed mainly of carbon and a small amount of oxygen. The presence of such matrixes in EBID deposits which embed nanoparticles is reported in literature for metal nanocrystals [120, 144, 145]. While Schoessler and Koops report of nanocrystalline gold single crystals embedded into a carbon containing insulating matrix [120], Utke *et al.* report of a nano-composite material with cobalt crystals embedded into an amorphous C and O rich matrix (for low beam currents) [144, 145]. In their review article van Dorp and Hagen denote the nano-composite material of reference [120] even as ‘typical EBID deposit’ [5]. Thus, a similar matrix composed of carbon and small amounts of oxygen embedding titanium oxide regions is reasonable for the deposits in the work at hand.

A detailed signal assignment in Figure 7.5 to the corresponding Auger transitions was performed according to specifications in literature. Based on references [100, 229-231] and [34] the signals at ≈ 354 and 362 eV correspond to $L_3M_1M_{2,3}$ Auger transitions, the signal at ≈ 382 eV to $L_3M_{2,3}M_{2,3}$ transitions and the two signals at ≈ 414 and 418 eV can be attributed to $L_3M_{2,3}V$ transitions (see Figure 7.5 a). Moreover, the two signals in Figure 7.5 b) at ≈ 492 and 512 eV correspond to oxygen KLL Auger transitions.

In literature, investigations of the oxidation of metallic titanium to titanium oxide [229, 232-236] and studies of various titanium oxide species [100, 105, 106, 230, 231, 237-241] via Auger electron spectroscopy and further techniques are reported. The references [53, 100, 231, 238, 241] allow a precise assignment of the $L_3M_{2,3}V$ transitions, which appear in the kinetic energy region between 400 and 430 eV (see Figure 7.5 a)). The two observed signals, which merge to a broad peak, can be attributed to inter- and intra-atomic Auger transitions including the valence band. Accordingly, the signal at 414 eV corresponds to the inter-atomic $L_3(\text{Ti})M_{2,3}(\text{Ti})V(\text{O})$ transition [53, 100, 231, 238, 241], which is expected for stoichiometric, i.e. defect-free and unreduced, titanium dioxide. Since for this material there are no valence band titanium 3d electrons available, an “inter-atomic cross transition between titanium and oxygen” [231] appears causing the emission of valence band oxygen 2p electrons. Rao and Sarma [241] justified this assignment to inter-atomic Auger transitions by the fact that the signal at 414 eV is absent in titanium metal Auger spectra and that the intensity of this peak is rising continuously with increasing

oxidation of titanium and less electrons being available in the V(Ti) level. In contrast to that, the signal at 418 eV corresponds to the intra-atomic $L_3(\text{Ti})M_{2,3}(\text{Ti})V(\text{Ti})$ transition [53, 100, 231, 238, 241] with V(Ti) being the $M_{4,5}(\text{Ti})$ level. This transition, involving only electronic states from titanium, is expected for titanium oxide species with electrons occupying the Ti 3d state [53, 100, 231, 238, 241] and for pure titanium metal [100, 229, 236, 238]. According to Rao and Sarma [241], the energy separation between both $L_3M_{2,3}V$ Auger transitions, in this work ≈ 4 eV, is close to the energy separation between Ti 3d and O 2p levels, which confirms the overall signal assignment.

Analyzing the shape of the Ti LMV signals in Figure 7.5 a), which is very sensitive to the oxidation state of titanium [100, 106, 230, 231, 234-236, 238, 241], gives further indications concerning the oxidation state of titanium in the EBID deposits from TTIP: Both spectra in Figure 7.5 a) show two Ti LMV signals merging to a broad peak, and in both cases the peak consists of a larger signal at 418 eV with the signal at 414 eV appearing as distinct shoulder. Ideally, for stoichiometric, unreduced TiO_2 only the signal at 414 eV appears because of the vacant Ti 3d level [53, 100, 230, 231]. The observation that the TiO_2 reference spectrum (green) in Figure 7.5 a) though shows a large signal at 418 eV with a shoulder at 414 eV can be traced back to the presence of Ti 3d electrons out of two reasons. First, a small number of oxygen vacancies and Ti^{3+} interstitials was formed upon UHV annealing of the reference sample [100] and secondly, in particular the measurement itself, applying a highly focused electron beam for core hole generation, produces reduced titania species [6, 104-107]. As a consequence, filling the titanium 3d level with electrons enables intra-atomic $L_3(\text{Ti})M_{2,3}(\text{Ti})V(\text{Ti})$ transitions which results in the signal at 418 eV. This signal appears even larger than the one at 414 eV in Figure 7.5 a) which can be explained by the sensitivity of the corresponding transition [53, 231]. Göpel *et al.* argue that intra-atomic Auger transitions have considerably higher transition probabilities than inter-atomic ones and that Auger transitions including d levels have a higher probability than the ones including p levels [231]. Comparing the Ti LMV peak of the blue AE spectrum and the green TiO_2 reference spectrum in Figure 7.5 a), a very similar peak shape can be found, with the 418 eV signal being slightly smaller for the spectrum measured on the EBID deposit (blue spectrum). Based on this comparison and the elucidation of the Ti LMV peak appearance in the TiO_2 reference spectrum

above one can conclude that also the EBID deposit is composed of TiO_2 or at least a material with a composition very close to titania.

Further indications concerning the oxidation state of titanium in the deposited material can be derived from analyzing an Auger spectrum of the pure titanium metal and comparing the Auger signals inclusive their positions with the ones measured on EBID deposits. Figure 7.6 depicts a section of an Auger spectrum acquired on the pure metal titanium, reproduced from reference [229]. In the display region of Figure 7.6 (330 eV to 470 eV), six signals are labeled which correspond to titanium Auger transitions. A detailed assignment of all peaks is listed in Table 7.2.

Table 7.2 reveals that the signals '1' to '3' are associated with Ti LMM transitions, signal '5' corresponds to Ti LMV transitions and signal '6' to Ti LVV transitions. Controversially discussed in literature was the origin of signal '4' [229, 230, 242, 243] which appears at $\approx 385 - 386$ eV. Finally, Bassett and Gallon [229] derived from titanium oxidation experiments that this signal is associated with $L_3M_{2,3}M_{4,5}$ transitions and a simultaneous "shake-up", i.e. excitation, of a titanium 3p electron. The authors further report that the signals '4' and '6' are characteristic for elemental titanium and demonstrate that these signals disappear upon titanium oxidation with molecular oxygen at RT [229]. Solomon and Baun [230] agree with the interpretation of signal '4', which can thus be regarded as a fingerprint for titanium metal that is absent in titanium oxide spectra.

Drawing a comparison between the signals in Figure 7.6 and the ones in Figure 7.5 a), one finds that the TiO_2 reference spectrum and the spectrum measured on the EBID deposit do clearly not show the signals labeled as '4' ($L_3M_{2,3}M_{4,5}$ and 3p electron shake-up) and '6' ($L_3M_{4,5}M_{4,5}$) which are characteristic for elemental titanium. For signal '4' ($\approx 385 - 386$ eV), this holds for all acquired AE spectra on EBID deposits fabricated from TTIP, i.e. no signal is observed. Concerning signal '6' (≈ 450 eV), it is noted that some AE spectra show a very small shoulder or signal closely above the detection limit. Since it is known that the primary electron beam in AES causes the reduction of titanium in TiO_2 materials (see discussion above), this appearance could be attributed to partial electron beam induced reduction to Ti(0) during the Auger measurement, occurring to a very low extent.

From the absence of the characteristic Ti signal '4' in all AE spectra it is concluded that the EBID deposits from TTIP initially do not contain unoxidized, metallic titanium.

Consequently, the possibility of depositing an amorphous material consisting of elemental carbon, titanium and oxygen in a disordered matrix is ruled out. This finding appears reasonable when one considers the oxidation state of titanium in the precursor molecule, which is '+IV'.

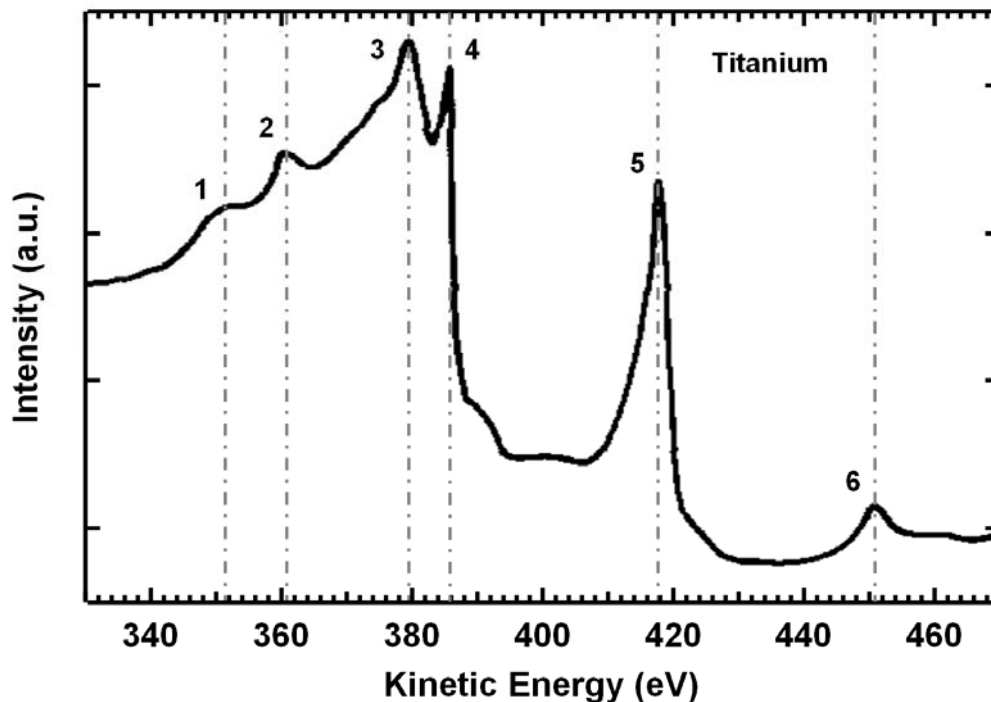


Figure 7.6: Auger spectrum in the non-derivative mode for the pure metal titanium. The spectrum is reproduced from reference [229].

No.	Auger transition
1	$L_3M_1M_{2,3} \ ^1P$
2	$L_3M_1M_{2,3} \ ^3P$
3	$L_3M_{2,3}M_{2,3}$
4	$L_3M_{2,3}M_{4,5}$ and $3p \ e^-$ shake-up
5	$L_3M_{2,3}M_{4,5}$
6	$L_3M_{4,5}M_{4,5}$

Table 7.2: Assignment of the titanium Auger signals of Figure 7.6 to the corresponding transitions according to reference [229].

Based on the results discussed in this chapter, it can be concluded that the oxidation state of titanium in the deposited material is that of titanium in a titanium oxide species. The deposit is contaminated with carbon and a small amount of additional oxygen. Concerning the contamination one can assume that titanium oxide could be embedded in a matrix composed of carbon with a small amount of oxygen.

The conclusion that a titanium oxide species with a composition very close to titanium dioxide is deposited (oxidation state '+IV') is drawn on the basis of four findings. First, quantitative analysis of the chemical composition of EBID area deposits from TTIP yields a mean oxygen to titanium ratio of $\approx 2:1$ (see Table 7.1), i.e. the same ratio as in TiO_2 . Secondly, measured Auger spectra are very similar to the TiO_2 reference spectrum with identical peak positions and very similar O KLL (512 eV) / Ti LMM (382 eV) Auger peak area ratios. Thirdly, analysis of the Ti LMV Auger transition signals indicates the initial presence of titanium(IV) ions. And fourthly, a comparison of measured Auger spectra with a reference spectrum for metallic titanium strongly indicates that the initial deposit contains no elemental titanium in the oxidation state '0'.

It has to be noted that the presence of a small amount of titanium oxide species with a lower oxidation state for titanium than '+IV' can not be completely ruled out. In addition, the high surface sensitivity of AES has to be considered which yields the chemical composition just of the topmost layers of the deposit. An inhomogeneous composition can not be ruled out (see results presented in Chapter 9.1.1). In order to study the composition of sub-surface layers of the EBID deposit one might think of depth profiling measurements. However, depth ion profiling (see Chapter 2.7) is hampered for the material titanium oxide since a high sensitivity of TiO_2 to sputter reduction is well-known from literature [107, 231, 238, 240, 244] (see Chapter 9.1.3). TEM measurements of EBID deposits fabricated on thin samples (e.g. composed of silicon oxide or silicon nitride) would be promising in order to investigate the material composition in more detail. Potentially, the elemental distribution in the deposits with varying height/depth could be addressed.

7.3 Contrast on Si(100) and Au(111)

In the previous chapters, the EBID deposits from TTIP appeared in a different contrast with respect to the substrate material in SEM images. While all fabricated structures on the Au(111) surface appear dark (black) in SEM on a bright background, the deposits on the Si(100) surface appear bright in comparison to the slightly darker sample surface. In addition, it was found on Si(100) that the contrast between deposit and surface also depends on the shape of the structure and on the electron dose. In this chapter, the contrast in SEM of EBID deposits from TTIP is addressed and its dependence on substrate material and shape of the deposit is discussed.

First, the contrast dependence on the substrate material is analyzed. Figure 7.7 depicts the EBID area deposits which have been analyzed in the previous chapters.

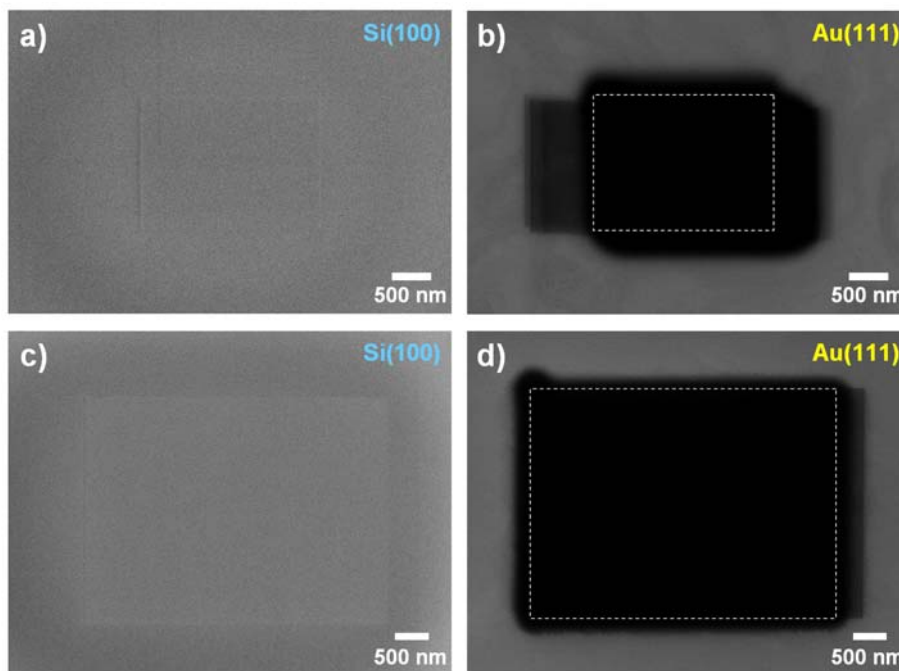


Figure 7.7: SEM images of area deposits, fabricated with TTIP on Si(100) and Au(111). The structures in a) and b) were generated with identical lithographic parameters (electron dose: 9.86 C/cm²) and the structures in c) and d) as well (2.46 C/cm²). Please note that the images in a) and b) are depicted with a slightly higher magnification than the ones in c) and d).

Obviously, the structures appear with a different contrast with respect to the Si(100) and Au(111) substrate despite the fact that they were fabricated with identical lithographic parameters in a) and b) (electron dose: 9.86 C/cm^2) and c) and d) (2.46 C/cm^2).

In order to interpret the observed contrast, one has to consider the detected signal (of the detection mode) for SEM imaging. For all SEM data in this work, the scanning electron microscope was exclusively operated with the so-called 'in-lens detector' (see Chapter 3.1.2). This detector collects the excited secondary electrons from the sample (almost exclusively SE1 and SE2 [30]); the corresponding operating mode is called 'secondary electron imaging mode' [25]. In consequence, the appearance of EBID deposits can be explained by the number of secondary electrons, which are detected from the deposited structure and the corresponding substrate surface, respectively. A low contrast between deposit and surface is attributed to a roughly equal number of detected SEs, while a high contrast indicates a strongly varying number of SEs acquired from structure and surface.

A varying amount of detected SEs can be traced back to several different types of contrast which were briefly discussed in Chapter 2.2. Since different substrate materials were applied for EBID it is feasible to attribute the varying contrast in Figure 7.7 to 'material contrast'. This contrast is naturally associated with the 'backscattered electron imaging mode' because the backscattering coefficient η is strongly depending on the atomic number Z and thus on the material [25, 28]. However, it is well-known from literature that 'material contrast' appears in the 'secondary electron imaging mode' as well when primary electron energies above 5 keV are used [25] (Note that in this work exclusively an energy of 15 keV was applied). This is based on the varying SE yields of different materials based on a different work function Φ . Additionally, the SE yield δ increases monotonically with increasing atomic number Z for high energetic primary electrons. This can be ascribed primarily to SE2 excited by BSEs on their trajectories through the surface layers ('SE2 contribution') [25]. In consequence, two quantities of the materials have to be considered in order to explain the contrasts observed in Figure 7.7. This is primarily the secondary electron yield δ , and secondly, the backscattering coefficient η .

The SE yield δ is defined according to Equation 7.1 [25].

$$\delta = \frac{I_{SE}}{I_{PE}} = \frac{I_{SE1} + I_{SE2}}{I_{PE}} = \delta_{PE} + \delta_{BSE} \quad (7.1)$$

It is equivalent to the ratio of the current caused by SEs and the PE beam current, or simply to the number of SEs produced per PE. Equation 7.1 further shows that δ has got two contributions since SEs can be produced by PEs and BSEs. Consequently, δ_{PE} is defined as the yield of SE1, i.e. SEs excited by PEs, and δ_{BSE} is defined as the yield of SE2, i.e. SEs excited by BSEs. Thus, δ is directly influenced by the number of released BSEs ('SE2 contribution') which is determined by the backscattering coefficient η . The latter is defined according to Equation 7.2 [25]:

$$\eta = \frac{I_{BSE}}{I_{PE}} \quad (7.2)$$

In analogy to δ , η is the ratio of the current caused by BSEs and the PE beam current, or simply the number of BSEs produced per PE.

For the materials applied in this work, specified values for δ and η were found in references [25] and [29]. In addition, backscattering coefficients were simulated for the pure materials and for a structure with the average chemical composition of the EBID area deposits depicted in Figure 7.7. The simulations were conducted with the software 'CASINO' (version 2.42, 2001) [20] which is explained in Chapter 8.2. The applied parameters for the simulations were adapted to the actual measurement parameters in this work ($U_B = 15$ keV, beam radius 1.5 nm). The number of primary electrons was set to 10^8 electrons.

All values for δ and η are listed in Table 7.3. It can be extracted that the SE yield for silicon ($\delta(\text{Si}) = 0.30$) is significantly smaller than the one for gold ($\delta(\text{Au}) = 0.47$). Since the SEM contrast between the fabricated area deposits and the Si(100) surface is very weak and the structures appear in SEM only marginally brighter than the surface (see Figure 7.7 a) and c)), it can be concluded that the SE yield of the deposits is very close to the one of silicon and presumably just marginally higher. This explains the contrast between EBID area deposits and the Au(111) surface. Due to the significantly larger SE yield for gold, the Au(111) surface appears bright in SEM while the EBID structures appear dark (see Figure 7.7 b) and d)).

	Seiler [29]	Reimer [25]	'CASINO' [20]
	$E_P = 20 \text{ keV}$		
$\delta(\text{Si})$	0.30	-	-
$\delta(\text{Au})$	0.47	-	-
$\delta(\text{Ti})$	0.22	-	-
$\delta(\text{C})$	0.28	-	-
	$E_P > 10 \text{ keV}$	$E_P = 15 \text{ keV}$	$E_P = 15 \text{ keV}$
$\eta(\text{Si})$	0.22	0.18	0.17
$\eta(\text{Au})$	0.45	0.49	0.47
$\eta(\text{Ti})$	0.30	-	0.26
$\eta(\text{C})$	0.10	-	0.05
$\eta(\text{C}_{19}\text{Ti}_{26}\text{O}_{55})$	-	-	0.17

Table 7.3: Secondary electron yields δ and backscattering coefficients η specified in references [25, 29] and simulated with the software 'CASINO' (version 2.42, 2001) [20].

Analyzing the backscattering coefficients η and the associated 'SE2 contribution' to δ , one finds the same tendency for the values for silicon and gold. In references [25, 29] the coefficients of 0.18 and 0.22 are found for silicon and $\eta = 0.49$ and $\eta = 0.45$ for gold. These values have been confirmed by MC simulations performed in this thesis yielding $\eta = 0.17$ for silicon and $\eta = 0.47$ for gold. This means that in gold a significantly larger number of BSEs is produced as compared to silicon, consequently causing a higher number of SE2s. This effectively explains the above discussed values for $\delta(\text{Au})$ and $\delta(\text{Si})$ ('SE2 contribution').

The backscattering coefficient η was also simulated for a material with the averaged chemical composition of the deposits depicted in Figure 7.7, i.e. 19 ± 5 at. % C, 26 ± 5 at. % Ti and 55 ± 5 at. % O. The obtained coefficient $\eta = 0.17$ is identical to the simulated one for silicon. This appears reasonable since the averaged atomic number of the deposit (11.3) is close to the one of silicon ($Z = 14$). It indicates an

equal 'SE2 contribution' to δ for both materials, thus confirms the drawn conclusion that δ of the depicted EBID area deposits and $\delta(\text{Si})$ are close to each other and finally explains the weak contrast between both materials in SEM.

In summary, it can be concluded that the different appearance in SEM of the EBID area deposits on both surfaces can be clearly traced back to 'material contrast'.

Additionally to the varying contrast on different substrate materials, a contrast dependence on the actual structure shape and applied electron dose was found, which is discussed in the following. Figure 7.8 shows two line patterns fabricated with TTIP on a Si(100) and a Au(111) surface, respectively. Both structures consist of perpendicular lines with a length of $4.6 \mu\text{m}$ and were generated with equal dwell time ($1.6 \mu\text{s}$) and step size (4.5 nm). The electron dose was varied from $5.4 \mu\text{C/cm}$ (left vertical line) to $10.9 \mu\text{C/cm}$ (horizontal line) and $21.8 \mu\text{C/cm}$ (right vertical line) in Figure 7.8 a) and from $0.36 \mu\text{C/cm}$ (upper horizontal line) to $0.73 \mu\text{C/cm}$ (lower horizontal line), $1.09 \mu\text{C/cm}$ (left vertical line) and $1.45 \mu\text{C/cm}$ (right vertical line) in Figure 7.8 b). The green numbers in Figure 7.8 label the corresponding dose factors with respect to the line fabricated with the lowest electron dose (upper horizontal line in Figure 7.8 b) with a dose of $0.36 \mu\text{C/cm}$).

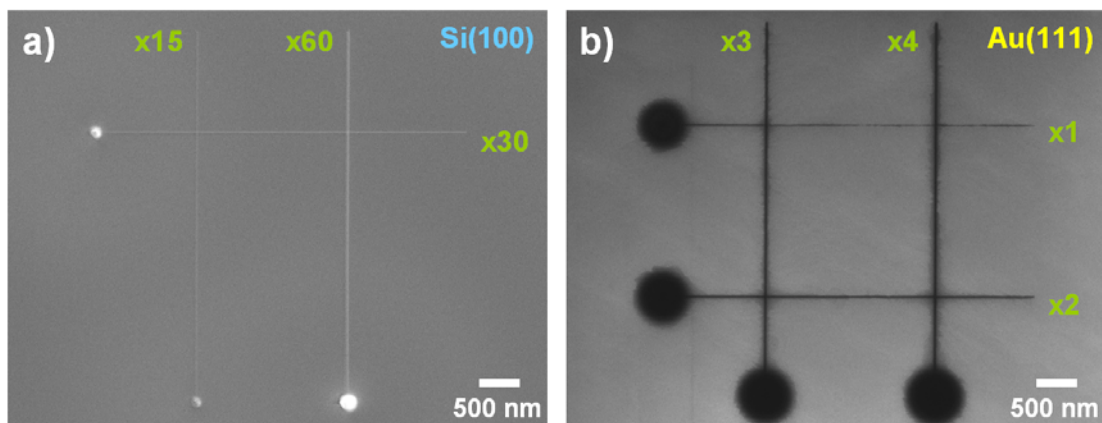


Figure 7.8: SEM images of line patterns fabricated with TTIP on a) Si(100) and b) Au(111). The green numbers label the corresponding dose factors.

The different appearance of the line deposits on the Si(100) and Au(111) surface can be attributed to 'material contrast' as described above due to the disparity in the SE yield. Again, the structures on Au(111) appear dark in SEM and the ones on Si(100) rather bright.

However, for the structures on Si(100) (Figure 7.8 a)), which were generated with higher electron doses compared to the ones on gold, an increase in contrast is observed for rising electron dose. While the left vertical line (fabricated with the lowest electron dose on Si) appears in a very weak contrast with respect to the surface, which reminds of the contrast observed in Figure 7.7 a) and c), the right vertical line (generated with the highest dose) appears significantly brighter than the other two lines and in a clear contrast with respect to the surface. This effect on the Si(100) surface can be attributed to 'topographic contrast' which increases for an increasing deposit height. The increase in height of the lines is based on the rising electron dose and enhances the 'surface-tilt contrast' (see Chapter 2.2).

On the Au(111) surface in Figure 7.8 b), no 'topographic contrast' is visible. This can be attributed to two reasons. First, on this sample the dominating type of contrast is clearly the 'material contrast'. Secondly, the applied electron doses for EBID were presumably too low on this surface in order to generate sufficiently high line deposits such that 'topographic contrast' appears in the SEM images.

In conclusion, it was found that the contrast between line deposits from TTIP and the Si(100) surface is rising with increasing electron dose. This effect in SEM is based on the increasing deposit height with dose, associated with an enhanced 'topographic contrast'.

A beneficial aspect of the strong and clearly visible 'material contrast' between EBID deposits from TTIP and the Au(111) surface is that one can clearly identify the lateral expansion of the generated deposits. This issue of EBID with TTIP on gold is exploited to analyze various effects in the following chapters. On the other hand, the weak 'material contrast' between EBID deposits from TTIP and the Si(100) surface hampers strongly the identification of the lateral dimension of fabricated structures on this substrate. A detailed characterization of the spatial area, in which precursor decomposition occurs upon EBID, is given in Chapter 8.

7.4 Summary and conclusions

To summarize this chapter, one can state that EBID with the precursor TTIP enables the fabrication of well-defined structures on the nanometer scale with arbitrary shape (see Chapter 7.1).

In the EBID process a titanium oxide species is deposited with a composition very close to titanium dioxide but which is contaminated with carbon. One could assume that titanium oxide might be embedded in a matrix composed of carbon and small amounts of oxygen. An averaged chemical composition of area deposits of 19 ± 5 at. % C, 26 ± 5 at. % Ti and 55 ± 5 at. % O was determined both for EBID on Si(100) and on Au(111). This result demonstrates that obviously the goal to fabricate pure deposits with a negligible amount of carbon could not be reached with TTIP although the experiments were conducted under ultra clean conditions, i.e. UHV conditions. However, the applied 'surface science approach' to EBID enables to rule out that the carbon contamination of the deposits derives from the sample surface and / or the residual gas. The origin of the carbon contamination can thus be traced back to the carbon containing precursor itself. To gain this finding performing the experiments in UHV atmosphere was mandatory.

For the chosen lithographic parameters it was found that the variation of the area dose d_A within the range of 1.23 to 9.86 C/cm^2 (factor of 8) and the variation of the number of sweeps within the range of 3 to 9 (factor of 3) do not change the chemical composition of the corresponding area deposits significantly. However, a strong variation of the applied parameters and the use of an oxidic surface enabled the fabrication of an area deposit with a chemical composition of 13 ± 5 at. % C, 31 ± 5 at. % Ti and 56 ± 5 at. % O on SiO_x , i.e. with a significantly reduced amount of carbon. Compared to area deposits a clearly higher amount of carbon was found for line and dot structures, i.e. ≈ 31 at. %. The observed differences in the chemical composition are traced back to the differences in the applied lithographic parameters. It is assumed that the dwell time, the replenishment time and the contribution of lower energetic BSEs and SE2 caused by the 'BSE proximity effect' have the strongest impact on the composition of the deposit.

Based on the acquired results two strategies for the direct fabrication of deposits with reduced carbon content can be envisaged. It is assumed that applying a short dwell time and combining it with a long replenishment time is one suitable strategy for the

precursor TTIP. In addition, the simultaneous dosage of TTIP and molecular oxygen during EBID might be another promising route (see Chapter 7.2).

Concerning the contrast in SEM it was found that the different appearance of EBID area deposits on both surfaces can be traced back to 'material contrast'. The Au(111) surface appears brighter in SEM than the EDID deposits due to the higher SE yield of gold. In contrast, the Si(100) surface appears almost identical in SEM compared to the area deposits, which can be explained by an SE yield being very close to each other. The contrast between line deposits from TTIP and the Si(100) surface is rising with increasing line height. This effect is associated to an enhanced 'topographic contrast' for higher line structures (see Chapter 7.3).

8 Proximity effects in EBID

The unintended deposition of material in the near surrounding of generated deposits is a common and well-known drawback of EBID. This phenomenon is caused by the so-called “proximity effects” [5, 117] (see Chapter 4.2).

In the following chapter, the unintended material deposition due to proximity effects is analyzed for EBID experiments with TTIP via spatially resolved Auger spectroscopy. The effect of lateral deposit broadening is investigated on the Si(100) and on the Au(111) surface and the chemical composition of the non-irradiated surfaces after the experiments is studied. Particular attention is put on the extent of lateral structure broadening caused by the dominating proximity effect in EBID which is the ‘BSE proximity effect’. In this context, the influence of the substrate and the differences for silicon and gold are deduced.

In addition to the experimental results, simulations were performed with the Monte Carlo software ‘CASINO’ (version 2.42, 2001) [20]. Both for the silicon and for the gold substrate the radius of the ‘BSE exit area’ is estimated from these simulations and compared to the experimental results for lateral deposit broadening.

8.1 Proximity effects on silicon

In the following chapter, the impact of proximity effects on EBID nanostructures on a silicon substrate is discussed. Figure 8.1 a) shows an SEM image of a pattern consisting of three perpendicular lines with a length of 4.6 μm . The pattern was deposited on a Si(100) sample with identical lithographic parameters to the one depicted in Figure 7.4 a). The width of the three lines in Figure 8.1 a) increases with increasing electron dose from 55 ± 3 nm to 67 ± 3 nm to 72 ± 3 nm, as determined from high resolution SEM images. The three well-defined line structures show sharp edges on both sides. Therefore, one might conclude that deposition occurred only at the irradiated lines and consequently one might think of laterally restricted, confined structures deposited isolated on the Si(100) surface. However, one has to consider that the contrast in an SEM micrograph can be due to differences in the chemical and / or topographical nature of the investigated structures. It was found that there is a very weak ‘material contrast’ between EBID deposits from TTIP and silicon (see Chapter 7.3) and that the contrast in the depicted SEM image is mainly attributed to

'topographic contrast'. Thus, the deposition of material off the line structures due to proximity effects can not be excluded based on the acquired SEM image.

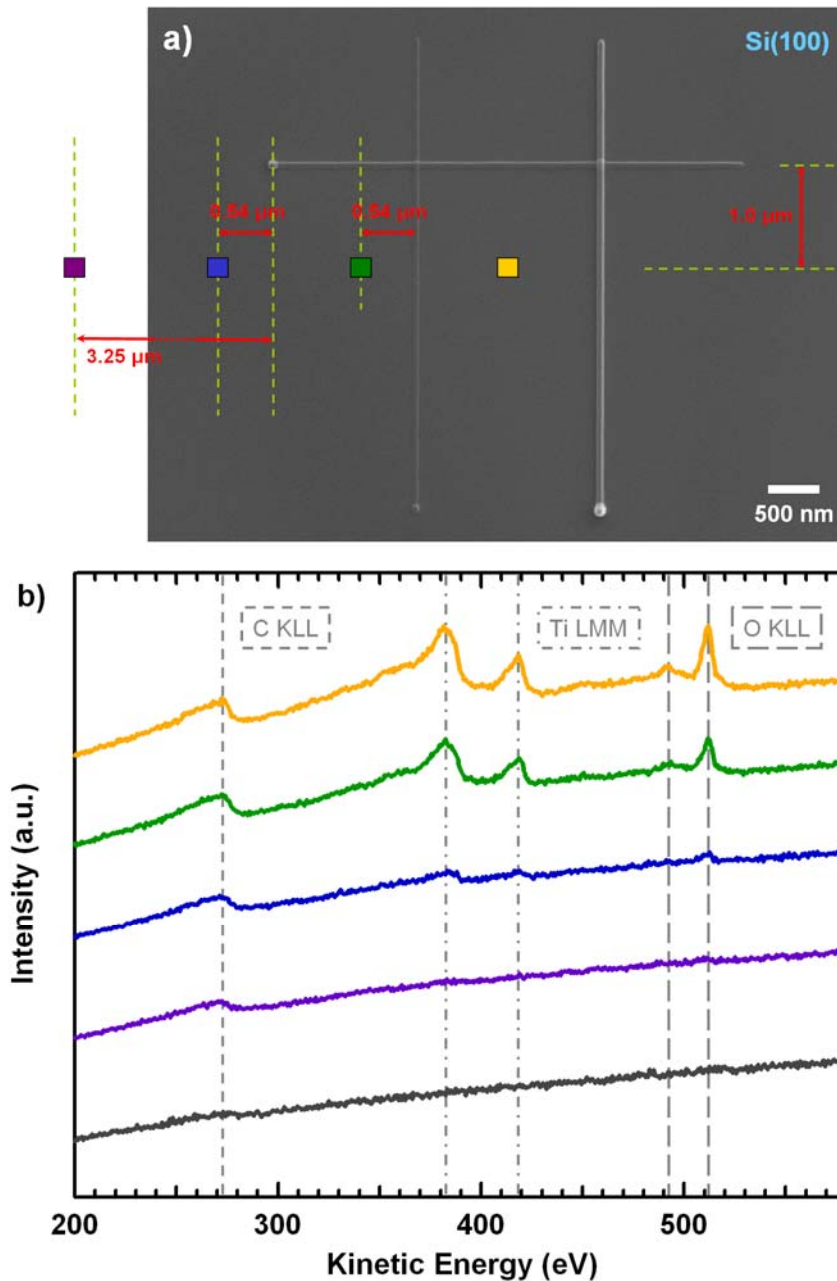


Figure 8.1: a) SEM image of a pattern consisting of three perpendicular lines fabricated with TTIP on Si(100) with electron doses of 116, 232 and 463 $\mu\text{C}/\text{cm}$. The color-coded markers denote the positions where local AES was performed. b) AE spectra acquired at the positions marked in a). The gray spectrum was acquired on the non-irradiated Si(100) surface before the EBID experiment.

In order to analyze whether material was deposited in close proximity to the lines spatially resolved AES measurements were performed at the positions labeled by the color-coded markers in Figure 8.1 a). The corresponding spectra are shown in Figure 8.1 b) using the same color code. The yellow, green, blue and purple spectra in Figure 8.1 b) represent a series of AES measurements acquired between and with increasing distance from the line pattern, while the gray spectrum was acquired on the non-irradiated Si(100) surface prior to the EBID experiment. In the yellow spectrum, acquired between the vertical lines at a distance of $1.0\ \mu\text{m}$ from the horizontal one, five Auger signals can be identified. They can be assigned to C KLL, Ti LMM and LMV and O KLL Auger transitions as indicated in Figure 8.1 b). This result clearly demonstrates that titanium, oxygen and carbon were also deposited in the surrounding of the positions directly exposed to the electron beam, which practically coincide with the lines visible in Figure 8.1 a). With increasing distance to the line pattern (green, blue and purple spectra) the intensity of the Auger peaks decreases, indicating that less material was deposited. In the purple spectrum, only a small carbon signal is visible but no signal for titanium and oxygen is found.

From the damping of the silicon AE substrate signals the thickness of the unintentionally deposited titanium oxide layers next to the line structures was determined. This analysis yields a layer thickness of $1.7 \pm 0.6\ \text{nm}$, $1.1 \pm 0.4\ \text{nm}$ and $0.4 \pm 0.2\ \text{nm}$ at the positions of the yellow, green and blue marker in Figure 8.1 a), respectively. At the position of the purple marker no significant silicon substrate signal damping is observed any more.

To obtain the height of the fabricated nanostructures, *ex situ* AFM measurements were performed under ambient conditions (details see Chapter 3.6.6). Figure 8.2 shows the corresponding AFM image to the structures depicted in Figure 8.1 a) in 2D and 3D (Figure 8.2 a) and b)) and an AFM height profile taken along the green line depicted in a) (Figure 8.2 c)). The profile shows the height of the left ($116\ \mu\text{C}/\text{cm}$) and right vertical line ($463\ \mu\text{C}/\text{cm}$) $1\ \mu\text{m}$ below the horizontal one. The determined line heights are denoted in Figure 8.2 d). It is found that the line height increases with increasing electron dose as it is to be expected, yielding values of $22 \pm 2\ \text{nm}$ for the left vertical line (electron dose $116\ \mu\text{C}/\text{cm}$), $39 \pm 2\ \text{nm}$ for the horizontal line ($232\ \mu\text{C}/\text{cm}$) and $93 \pm 2\ \text{nm}$ for the right vertical line ($463\ \mu\text{C}/\text{cm}$). By comparing the results from AFM and local AES it is found that the layer due to unintended deposition between the lines is indeed relatively thin. For example, at the position of

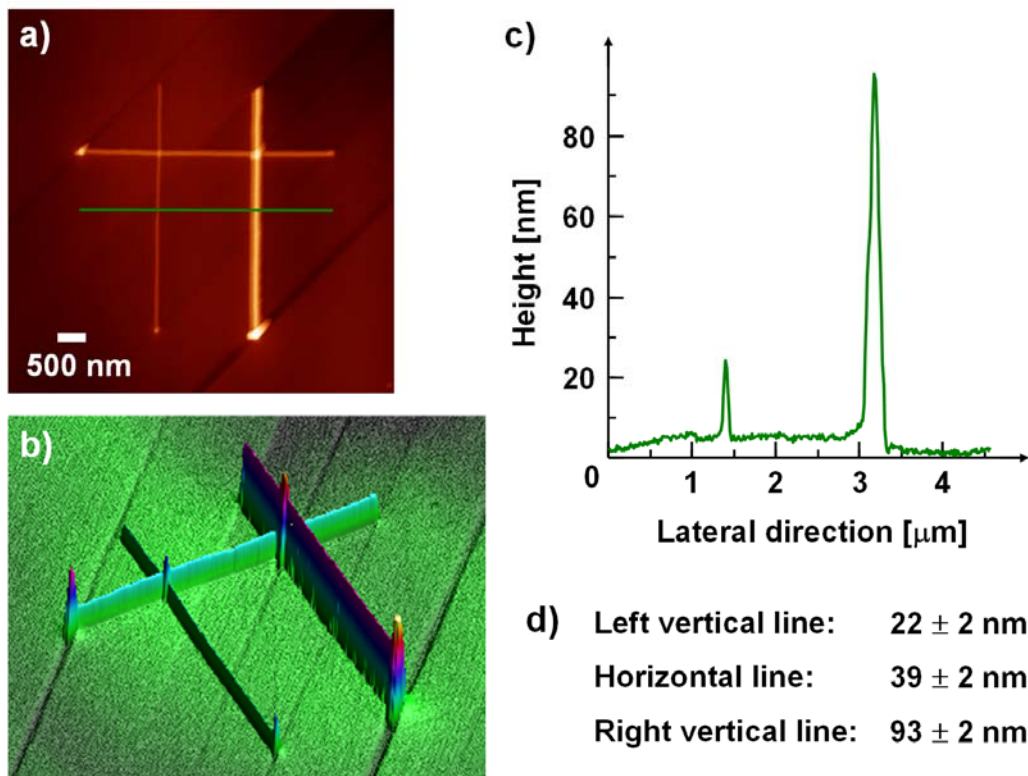


Figure 8.2: a) 2D AFM image of the line pattern depicted in Figure 8.1 a). b) Corresponding 3D AFM image (generated with the software WSxM). c) AFM height profile taken along the green line depicted in a). The profile shows the height of the left ($116 \mu\text{C}/\text{cm}$) and right vertical line ($463 \mu\text{C}/\text{cm}$) $1 \mu\text{m}$ below the horizontal one. d) Determined height values for the lines.

the yellow marker in Figure 8.1 a) the thickness is less than 2 % of the right vertical line [225].

The experimental results of local AES in close proximity to the fabricated lines clearly show material deposition in areas which were not directly irradiated by the primary electron beam. It can thus be concluded that the deposition of carbon, titanium and oxygen away from the direct impact of the PE beam is due to proximity effects. Primarily, the resulting lateral deposit broadening can be traced back to the ‘BSE proximity effect’ (see Chapter 4.2). Additionally, a contribution by the ‘FSE proximity effect’ is likely.

In addition, the findings from local AES confirm the suggested contrast in the SEM image of Figure 8.1 a). Indeed, the SEM contrast is attributed to ‘topographic contrast’ of the observed lines. Concurrently, one could be tempted to assume that

no material was deposited next to the structures due to the very weak 'material contrast' (see Chapter 7.3). In order to detect the unintended deposition, additional, spatially resolved and surface sensitive chemical analysis is mandatory. With regard to the claimed requirements local AES is an excellent tool.

Comparing the yellow spectrum in Figure 8.1 b), measured on the unintended deposit, with the spectra acquired on EBID area deposits from TTIP (see e.g. Figure 7.2 c)), one finds a lower carbon content of the unintended deposit. Quantitative analysis yields a chemical composition of 15 ± 5 at. % C, 30 ± 5 at. % Ti and 55 ± 5 at. % O for the deposit caused by proximity effects. A general difference of both deposits is that the generation of the intended deposits is dominated by the high energetic PEs while the generation of the additional, unintended deposits is dominated by lower energetic BSEs and SEs. Consequently, one can conclude that the amount of carbon in the deposits from TTIP might be reduced by "providing" electrons of lower energy for the EBID process. This can be achieved by applying a lower primary beam energy in the EBID experiment, which should be considered in future experiments targeting deposits with higher purity.

At a distance of $3.25 \mu\text{m}$ from the line pattern of Figure 8.1 a) no titanium can be detected on the non-irradiated surface (see purple spectrum). However, the purple spectrum clearly shows a small amount of carbon, which is also detected at positions with a much higher distance from the pattern, i.e. $50 \mu\text{m}$. At such distances from the position irradiated by the primary beam the release of BSEs and SEs is very rare [25]. Thus, it is concluded that no electron induced precursor decomposition occurs at these distances. It has to be noted that in other experimental runs partially very small amounts of oxygen are found as well at these distances, being close to the detection limit. Both carbon and oxygen are interpreted as a small surface contamination on silicon after EBID. Since the experiments were conducted under ultra clean UHV conditions, the origin of the contamination can be traced back to the exposure of the sample to the precursor gas. As discussed in Chapter 5, the gas contains a large amount of hydrocarbons. Thus, a reasonable explanation for the surface contamination is that these hydrocarbons adsorb on the surface and are decomposed while the AES scan for chemical analysis is performed resulting in a small carbon (and oxygen) deposit.

From Figure 8.1 the amount of unintentionally deposited material was deduced at four positions with a certain distance to the line pattern. To analyze the extent of lateral structure broadening caused by proximity effects in more detail and in order to visualize the gradient of unintended material deposition with increasing distance to one structure of the pattern, spatially resolved Auger electron line scans (AELS) were performed. These measurements were conducted across the right vertical line of the pattern depicted in Figure 8.1 a) for the elements carbon, titanium, oxygen and silicon in four separate scans. For each measurement the length of the line scan was $4.5\ \mu\text{m}$, the step size was $10\ \text{nm}$ and the dwell time was set to $1\ \text{s}$.

Figure 8.3 a) depicts an SEM image of the line pattern and the four color-coded arrows across the right vertical line indicate the positions where the AELS measurements were performed. It is well-known from literature that titanium oxide is sensitive to the bombardment with an electron beam and that processes like electron stimulated desorption (ESD) of oxygen and thus the reduction of titanium can occur [6, 104-107]. To keep the influence of these processes as low as possible, the measurement position was changed slightly for each line scan by roughly 0.3 to $0.4\ \mu\text{m}$ (Si: $1.4\ \mu\text{m}$ below the horizontal line, C: $1.7\ \mu\text{m}$, Ti: $2.0\ \mu\text{m}$, O: $2.4\ \mu\text{m}$).

The corresponding AELS data is depicted in Figure 8.3 b) using the same color code as for the arrows in a). In the following, first the line scan profiles of carbon, titanium and oxygen are discussed. Obviously, for these elements a clear peak appears in the data at the position of the right vertical line of the pattern (indicated by the dashed light green line above the zero point of the abscissa). Next to the peak, a minimum is present in the line scan profiles. These minima appear at the side of the right vertical line being opposite to the detector. Thus, released Auger electrons at this side have either momenta in the opposite direction or they “collide” with the right vertical line. In each case they do not reach the detector, which explains the intensity decrease leading to a minimum in the respective line scan profile (‘shadow effect’). With increasing distance to the right vertical line a decrease in the intensity can be observed with the intensity finally converging to a stable ground level. Since the silicon surface is slightly contaminated with carbon after the EBID experiment (see purple spectrum in Figure 8.1 b) and discussion above), the intensity decline of the carbon profile is much weaker compared to titanium and oxygen. The observed gradients demonstrate that with increasing distance to the line structure less material was deposited unintentionally due to proximity effects. From the titanium line scan

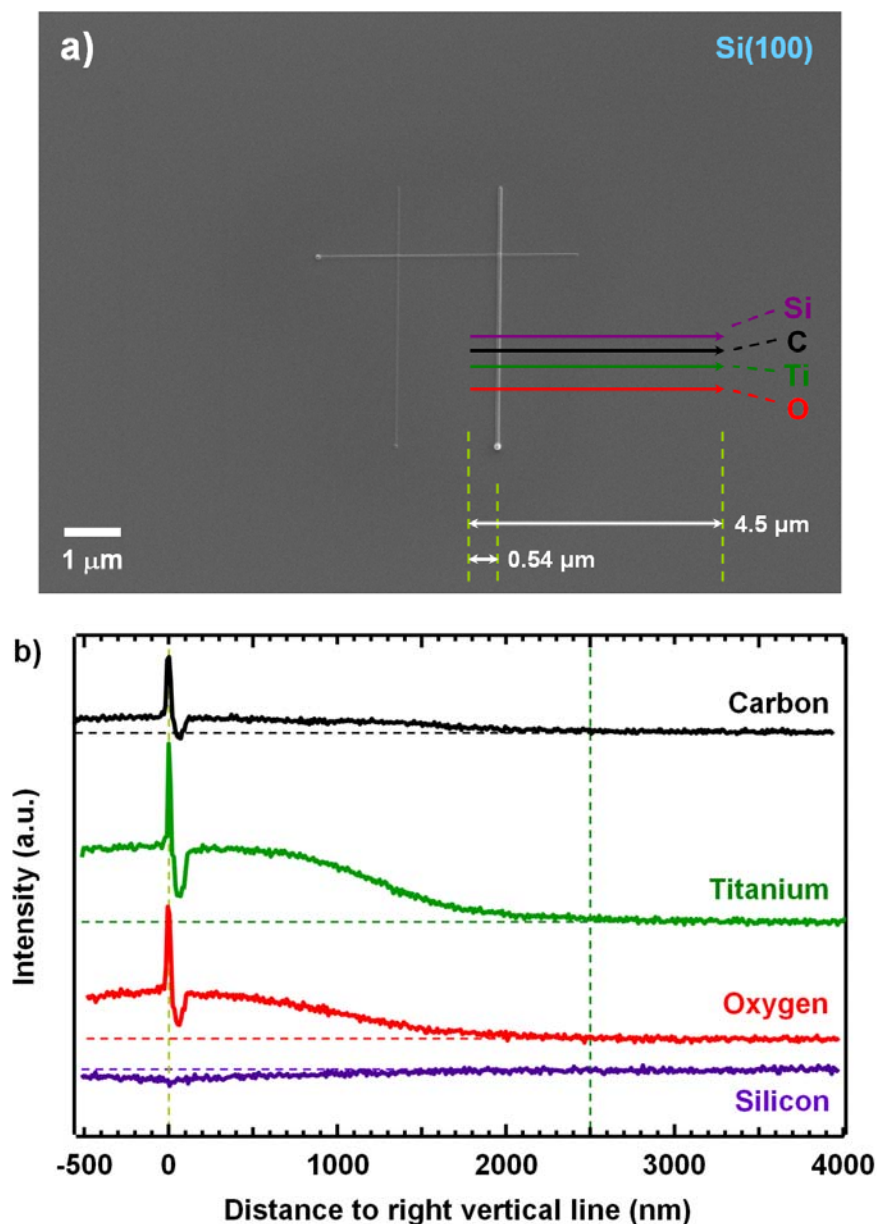


Figure 8.3: a) SEM image of the line pattern depicted in Figure 8.1 a) acquired with a lower magnification. The color-coded arrows across the right vertical line show the positions where AELS were acquired. b) Auger line scans for the elements carbon (black; $E_{Peak} = 270$ eV; $E_{Bg} = 247$ eV), titanium (green; $E_{Peak} = 382$ eV; $E_{Bg} = 400$ eV), oxygen (red; $E_{Peak} = 512$ eV; $E_{Bg} = 525$ eV) and silicon (purple; $E_{Peak} = 1615$ eV; $E_{Bg} = 1625$ eV). The length of the line scans was $4.5 \mu\text{m}$, the step size was 10 nm and the dwell time was set to 1 s. Note that the hemispherical electron energy analyzer is positioned to the left of the generated pattern which explains the ‘shadow effect’ in the line scan profiles.

(green profile) it can be extracted that with a distance of approximately 2.5 μm to the EBID structure no material deposition occurs any more. Following the expectation, the line scan for the substrate material (Si) has a completely different shape. At the position of the right vertical line a small minimum is visible in the AELS profile. With increasing distance to the line structure an intensity increase appears and the profile converges to a stable level, as well, where no substrate signal damping occurs any more.

From local AES measurements it was extracted that at a distance of 3.25 μm to the EBID structures no titanium and oxygen can be detected any more on the Si(100) surface (see Figure 8.1) and AELS measurements reveal that unintended material deposition “ends” at a distance of $\approx 2.5 \mu\text{m}$ (Figure 8.3). To evaluate these results and in order to determine the contribution of the ‘BSE proximity effect’, Monte Carlo simulations were performed, which are presented in the following chapter.

8.2 Monte Carlo simulation of the electron substrate interaction

In the previous chapter the phenomenon of unintended material deposition close to an EBID structure caused by proximity effects was discussed. Since the ‘BSE proximity effect’ plays a major role for the latter phenomenon, in this chapter the ‘electron substrate interaction’ is investigated in detail for silicon and gold. The Monte Carlo (MC) simulations were performed with the software ‘CASINO’ (version 2.42, 2001) [20].

‘CASINO’ is a program which enables the simulation of electron beam – sample interactions in a scanning electron microscope on the basis of a Monte Carlo (MC) method [20]. The software assumes a Gaussian-shaped primary electron beam and simulates complete electron trajectories via different, adjustable physical models. Applying a ‘single-scattering algorithm’ in particular low energy beam interactions in bulk and thin foil samples can be modelled. Electron deviation caused by inelastic scattering is neglected by ‘CASINO’ and instead all electron energy loss events are grouped in a ‘continuous energy loss function’ [20]. The software enables three applications, i.e. modeling BSEs, modeling X-ray emissions and simulating the

absorbed energy in the sample. The simulation of SEs is not possible via 'CASINO' and relativistic effects, which become more relevant at higher primary energies (> 50 keV), are also not considered by the program [20].

In this chapter, 'CASINO' is used to simulate the electron beam – sample interactions when the applied highly focused electron beam impinges on a silicon and gold substrate, respectively, and to visualize the released BSEs. The simulations depicted in this chapter were performed with a primary beam energy of 15 keV, a beam radius of 1.5 nm and 10^8 primary electrons. The beam energy and beam radius were adapted to the actual parameters in this work. The minimum electron energy (stop criterion for each trajectory) was set to 50 eV, which is the recommended minimum value [20].

Figure 8.4 depicts the result of a simulation performed for the substrate silicon. In Figure 8.4 a) the 'interaction volume' in the silicon sample is visible, demonstrating a penetration depth of ≈ 2.5 μm . The color code of the trajectories ranging from yellow to blue reflects the energy of the electrons which lose energy on their pathway through the bulk material. Those electrons leaving the surface after several scattering events are drawn in red. They are the backscattered electrons (BSEs), which are capable of releasing additionally secondary electrons (SE2), both being relevant for the precursor decomposition in terms of EBID.

Figure 8.4 b) shows a plot of the number of released BSEs versus the distance from the primary beam impact position. While the light blue curve depicts the number of BSEs emitted in annulus areas around the impact point (with constant increment $\Delta r = 13.2$ nm), the green curve shows the number of BSEs emitted along a line, starting at the point of PE impact (illustrated by the sketch in the upper right). The light blue curve has a maximum at a distance of ≈ 750 nm and with increasing distance it declines continuously and finally converges to zero. The green curve decreases monotonically and converges to zero, as well.

From the light blue curve in b) the total number of released BSEs can be calculated by integration. The integral is depicted in Figure 8.4 c). It demonstrates that the total number of BSEs is increasing steadily with increasing distance to the irradiation point and converges to 100 %.

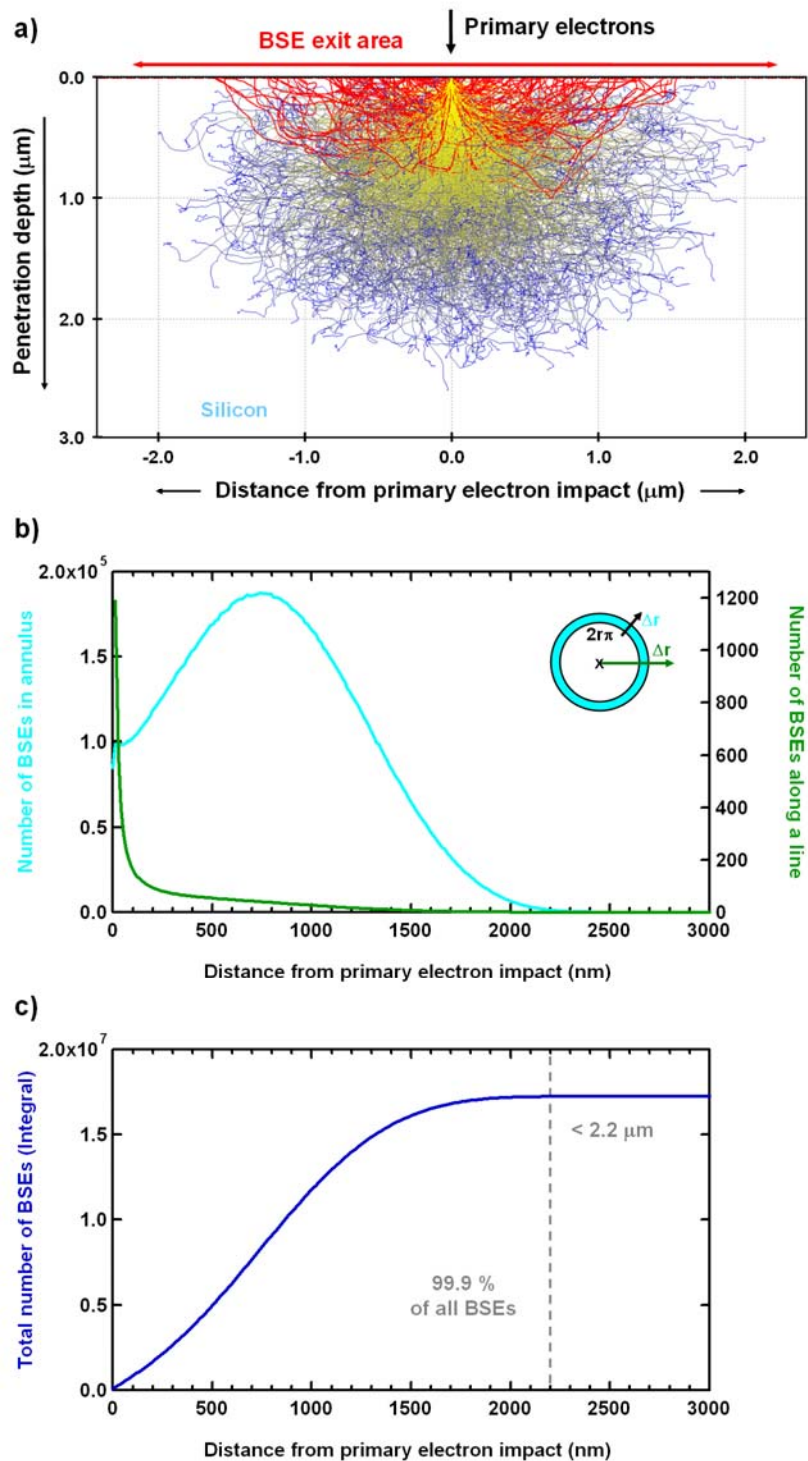


Figure 8.4: a) Monte Carlo simulation of the 'interaction volume' of a 15 keV primary electron beam in silicon conducted with 'CASINO' [20] (displayed trajectories: 1,000). b) Number of BSEs in annulus areas (light blue) and along a line (green) plotted versus the distance from the primary electron impact. c) Total number of BSEs plotted versus the distance from the primary electron impact. The curve was generated by integration of the light blue curve in b).

In an EBID experiment, deposition occurs where electrons interact with precursor molecules and cause their decomposition. Therefore, the area of the surface in which electrons are released during primary beam impact determines the lateral size of deposition. Considering the 'BSE proximity effect', the size of deposition can accordingly be estimated by the determination of the area in which BSEs (and SE2) are released. This area is denoted as 'BSE exit area' and is defined in this work by the area around the point of primary beam impact in which 99.9 % of all BSEs leave the substrate surface. In the following chapters, exclusively the radius or diameter of the 'BSE exit area' is specified.

In Figure 8.4 a) the 'BSE exit area' is indicated by the red arrow above the sample surface and the respective interaction volume in silicon. Its size can be extracted from the integral curve in Figure 8.4 c). According to the MC simulation, 99.9 % of all BSEs exit the silicon substrate surface within a radius of $\approx 2.2 \mu\text{m}$ from the PE impact point (see Figure 8.4 c)). This range is the contribution of the 'BSE proximity effect' to the phenomenon of lateral deposit broadening on silicon.

In terms of the 'BSE proximity effect' the determined value of $\approx 2.2 \mu\text{m}$ has to be considered as upper limit for unintended lateral structure broadening since the applied electron dose plays an important role. For low electron doses the extent of lateral broadening by unintended deposition is small since a minimum number of electrons is necessary to generate a detectable deposit. For increasing electron doses also the extent of structure broadening increases because the number of electrons released within the 'BSE exit area' accumulates and thus rises, as well. Finally, the deposit broadening should converge against the limiting value of $\approx 2.2 \mu\text{m}$ on silicon, which would be reached for an electron dose one can denote as 'saturation dose'.

However, this process can not be considered separately since also other effects occur during EBID. As soon as height growth appears, also forward scattering of electrons from the EBID deposit occurs. It contributes to the observed "excess" material ('FSE proximity effect') and enables a lateral deposit broadening exceeding the 'BSE exit area'. In addition, the BSEs do release SE2, which contribute to the precursor decomposition but can not be simulated by the software 'CASINO'. When these SE2 have momenta off the central deposit they can also contribute to an enlargement of the region in which unintended deposition occurs.

Considering the result of the MC simulation and the discussed effects of forward scattering and release of SE2, one can state that the simulation for silicon is in very good agreement with the experimental results discussed in the previous chapter. The found disappearance of the unintended deposit on silicon at $\approx 2.5 \mu\text{m}$ (see Figure 8.3) is very close to the BSE exit radius. Thus, the electron dose of the corresponding structure (right vertical line of the line pattern, fabricated with $463 \mu\text{C}/\text{cm}$) should also be close to the ‘saturation dose’, and the structure height ($93 \pm 2 \text{ nm}$) should be big enough that pronounced forward scattering of electrons in the EBID deposit occurs.

Two interesting questions raise at this point, namely the question for the electron beam – sample interactions in gold and in particular the question for the differences compared to the substrate silicon.

In Figure 8.5 the result of the MC simulation for the substrate gold is depicted. Figure 8.5 a) shows the ‘interaction volume’ of the beam in the bulk. While the shape is identical to the one in silicon, the overall size is drastically smaller. The penetration depth in gold is $\approx 430 \text{ nm}$, which means a roughly 5.8 times smaller value. The same holds for the ‘BSE exit area’ which is indicated in Figure 8.5 a) by the red arrow above the sample surface.

In order to determine the radius of the ‘BSE exit area’ on gold the number of released BSEs (see Figure 8.5 b)) and a corresponding integral (see Figure 8.5 c)) are plotted versus the distance from the primary beam impact position. Analogous to silicon, the orange curve in Figure 8.5 b) depicts the number of BSEs emitted in annulus areas around the impact point (with constant increment $\Delta r = 1.8 \text{ nm}$) and the green curve shows the number of BSEs emitted along a line, starting at the point of PE impact (see sketch in the upper right). Both curves have a similar shape to the corresponding ones of silicon. However, the maximum of the orange curve in Figure 8.5 b) appears already at a distance of $\approx 11 \text{ nm}$ (compared to $\approx 750 \text{ nm}$ for Si) and both curves converge much “faster” to zero with increasing distance to the impact point.

In Figure 8.5 c), the integral of the orange curve in b) is depicted, demonstrating the total number of emitted BSEs. According to the above stated definition, the radius of the ‘BSE exit area’ can be determined as $\approx 340 \text{ nm}$ for gold. This means that the radius is smaller compared to silicon by a factor of ≈ 6.5 . Again, the determined area

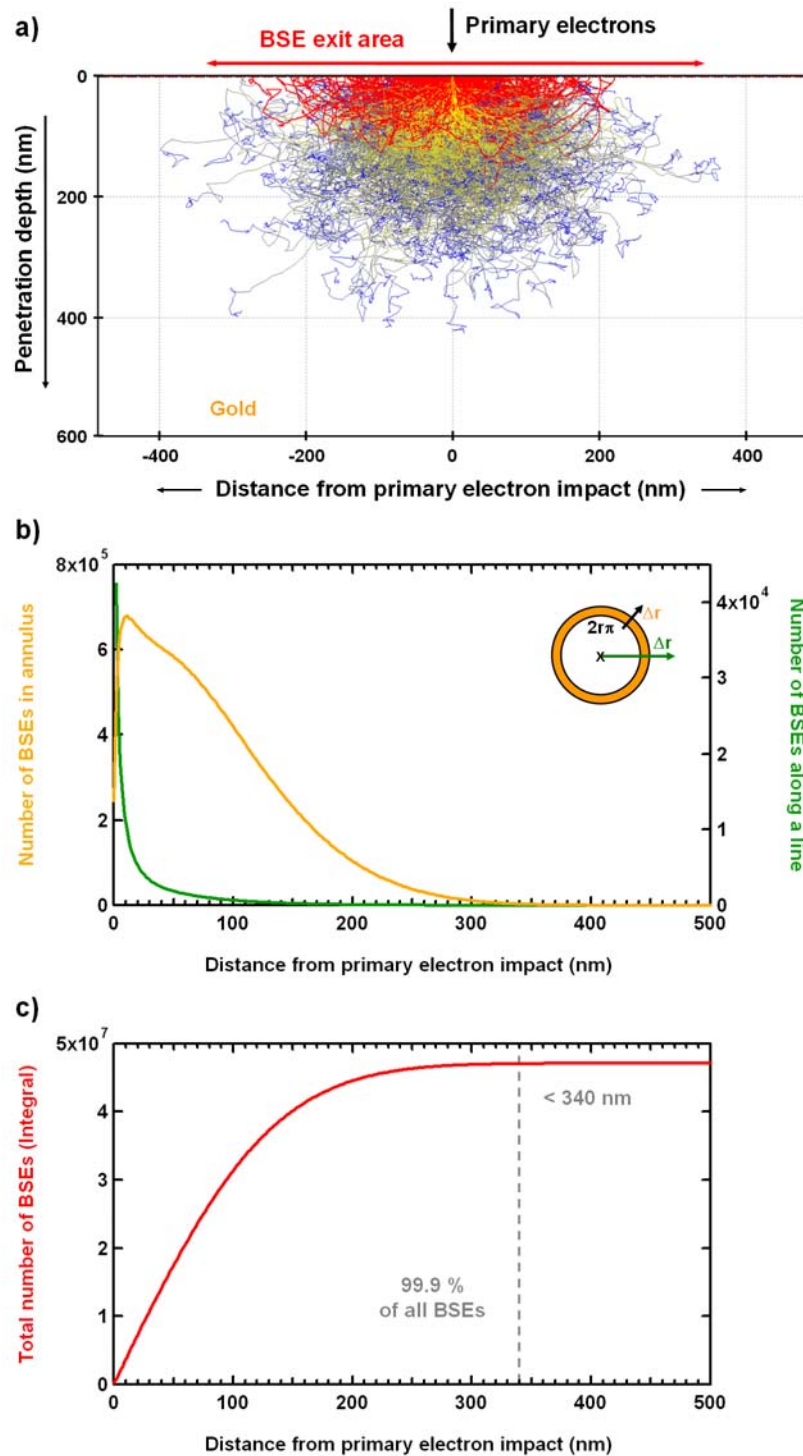


Figure 8.5: a) Monte Carlo simulation of the 'interaction volume' of a 15 keV primary electron beam in gold conducted with 'CASINO' [20] (displayed trajectories: 1,000). b) Number of BSEs in annulus areas (orange) and along a line (green) plotted versus the distance from the primary electron impact. c) Total number of BSEs plotted versus the distance from the primary electron impact. The curve was generated by integration of the orange curve in b).

specifies the contribution of the 'BSE proximity effect' to the phenomenon of lateral deposit broadening and marks the upper limit of structure broadening on gold based on this proximity effect when the 'saturation dose' is reached. In contrast, forward scattering ('FSE proximity effect') and the release of SE2 with momenta off the central deposit can occur as well and can further increase the size of the unintended deposit.

A direct comparison of the 'interaction volume' in silicon with the one in gold, both depicted with the same scale, is given in Figure 8.6.

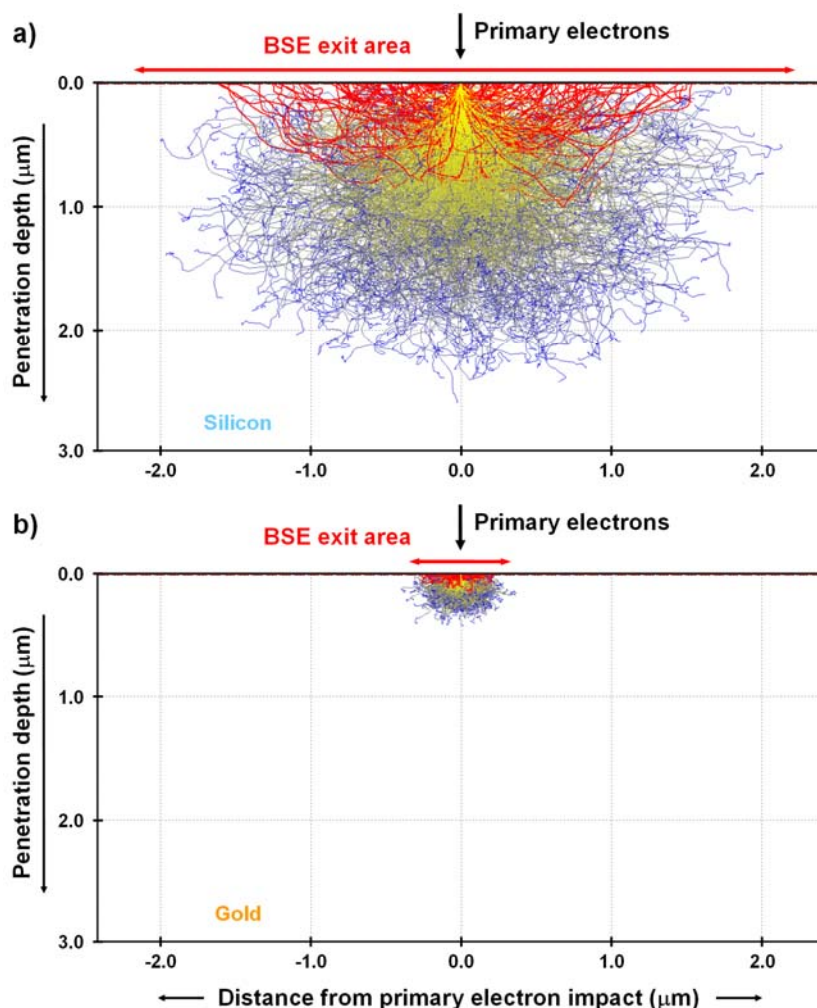


Figure 8.6: Direct comparison of the 'interaction volume' of a 15 keV PE beam in a) silicon and b) gold. Both graphics were acquired from Monte Carlo simulations with the software 'CASINO' [20].

Figure 8.6 clearly demonstrates that both the penetration depth of the primary beam and the 'BSE exit area' are significantly smaller for gold compared to silicon. This result can be attributed to the significantly higher atomic number ($Z(\text{Au}) = 79$, $Z(\text{Si}) = 14$) and the drastically higher density of gold ($\rho(\text{Au}) = 19.32 \text{ g/cm}^3$, $\rho(\text{Si}) = 2.328 \text{ g/cm}^3$ [62]).

The consequence of the ≈ 6.5 times smaller 'BSE exit area' radius on gold is that the effect of lateral deposit broadening due to the 'BSE proximity effect' is strongly reduced in EBID on this substrate material. Thus, for the fabrication of well-defined nanostructures with high resolution it is advisable to use the substrate gold or other metallic samples with high density instead of silicon.

8.3 Proximity effects on gold

Lateral deposit broadening caused by proximity effects occurs on gold as well since it is intrinsically tied to the technique of EBID. Unintended "excess" material was observed for several deposits on Au(111) presented in the previous chapters (e.g. Figure 7.1 c), Figure 7.2 b), Figure 7.3 b)), where the structure size was larger than the irradiated area. However, the simulations discussed in the previous chapter have shown that the extent of structure broadening on gold should be much smaller compared to silicon since the 'BSE exit area' radius is reduced by a factor of ≈ 6.5 .

In this chapter, the results of the simulation for gold are compared to experimental data and the feasibility of fabricating nanostructures of high resolution on the metallic gold substrate with high density is discussed.

To investigate the lateral extent of unintended deposition on gold, spatially resolved AES measurements were performed in the proximity of EBID deposits. Additionally, the chemical composition of the Au(111) surface after the exposure to the TTIP gas was studied by acquiring AE spectra at larger distance to the deposits, i.e. $\approx 10 \mu\text{m}$. Figure 8.7 a) shows an SEM image of four patterns fabricated with TTIP on the Au(111) sample. Each pattern consists of four squares and the electron dose was varied for each square and pattern. The color-coded markers indicate the positions where local AES was performed and the corresponding spectra are depicted in Figure 8.7 b). While the green AE spectrum was acquired on the square deposit with

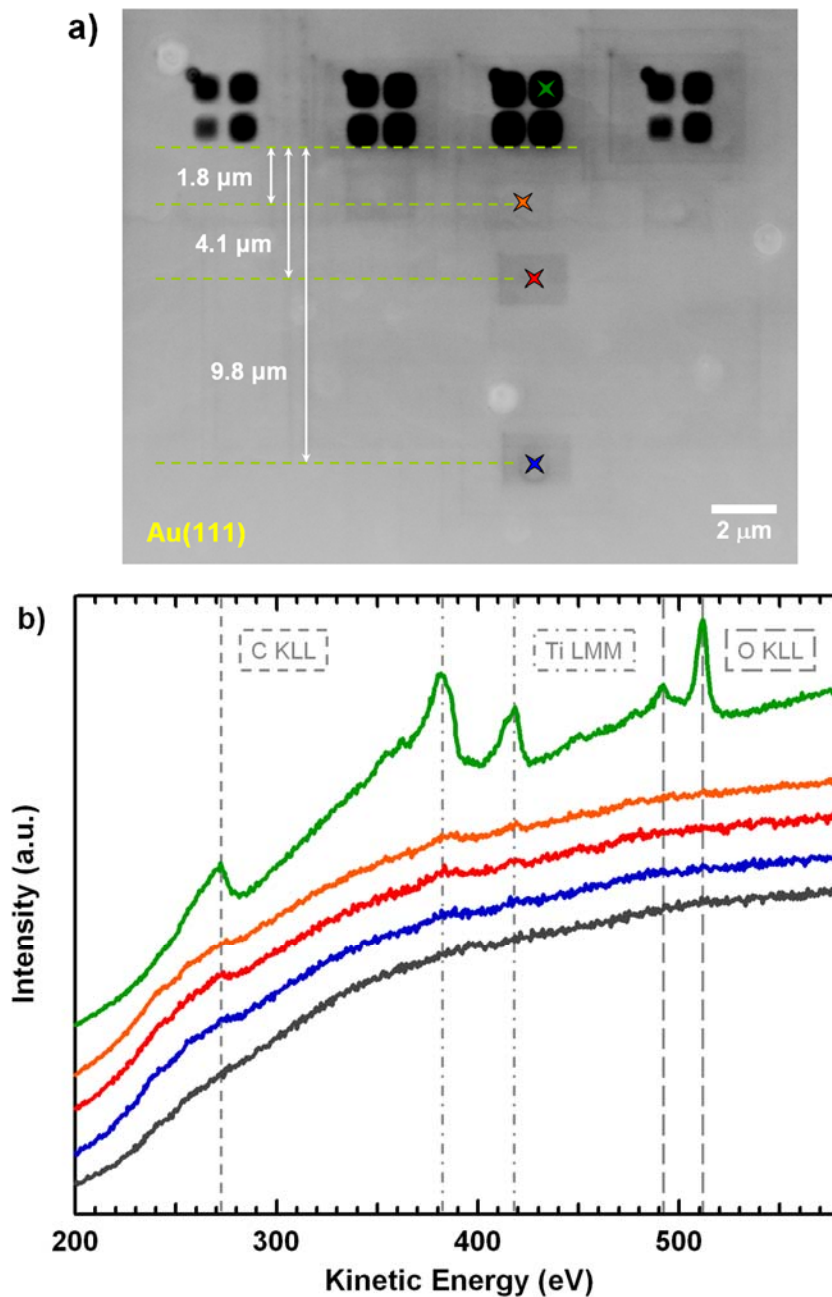


Figure 8.7: a) SEM image (15 kV, 3 nA, tilted sample) of four patterns, each composed of four square deposits, fabricated with TTIP on the Au(111) sample. The color-coded markers indicate the positions where local AES was performed. b) AE spectra acquired at the positions marked in a). The gray spectrum was acquired on the non-irradiated Au(111) surface before the EBID experiment.

the highest electron dose (7.97 C/cm^2 , one sweep), the orange, red and blue one were measured on the non-irradiated surface, each with a certain distance to the

EBID structures. In contrast to all these spectra, the gray one was acquired on the clean, unexposed Au(111) sample before the EBID experiment was performed. Please note that the SEM image in a) was acquired after the characterization via AES. Thus, the dark rectangular surroundings of the orange, red and blue marker indicate the 'scan damage' of the AES and SEM measurements on the surface.

While the green spectrum in Figure 8.7 b) depicts the expected Auger signals for an EBID deposit from TTIP at the known kinetic energies, the orange, red and blue one are very similar to the spectrum acquired on the clean, unexposed surface before the experiment (gray spectrum). At a distance of $\approx 1.8 \mu\text{m}$ (see orange spectrum) one finds that the carbon, titanium and oxygen signals are close to the detection limit. The same holds for the red and blue spectrum, which were measured in a distance of ≈ 4.1 and $\approx 9.8 \mu\text{m}$ to the EBID pattern above, respectively.

Considering the non-irradiated surface after an EBID experiment off the fabricated structures (out of the BSE range), one finds that the Au(111) surface stays clean despite the exposure to the hydrocarbon containing TTIP gas (see blue spectrum in Figure 8.7 b)). One possible explanation for this result is that hydrocarbon adsorption on the Au(111) surface takes place only to a very small extent. The conservation of a clean Au(111) surface after EBID is a clear difference to the Si(100) surfaces, which were slightly contaminated after EBID with carbon as the main contaminant.

The result of these AES measurements confirms what can be expected from the contrast of the SEM image in Figure 8.7 a). Since the dominating SEM contrast for EBID deposits from TTIP on gold is 'material contrast' (see Chapter 7.3), a direct observation of the proximity effects is possible on gold, which is in agreement with AES. Therefore, it is concluded on the basis of the contrast in Figure 8.7 a) that the "end" of unintended deposition due to proximity effects is close to the irradiated area, i.e. at the deposit border visible in SEM.

To address this in more detail a closer look is taken to the actual size of the area structures of Figure 8.7 a). Figure 8.8 depicts an SEM image of higher magnification and better resolution of the square on which the green spectrum in Figure 8.7 b) was acquired. The white dashed square indicates the area which was actually irradiated by the electron beam. Obviously, the actual size of the deposit is larger than the irradiated area due to the discussed proximity effects. Since the extent of lateral deposit broadening ($\approx 290 \text{ nm}$) for the depicted structure roughly correlates with the

determined radius of the 'BSE exit area' on gold (≈ 340 nm), one can conclude that the conducted MC simulation yields a result in good agreement with the experimental data.

The actual deposit broadening in Figure 8.8 is slightly smaller than the BSE exit radius ($\approx -15\%$). This can be explained in particular by the moderate electron dose which was applied for structure fabrication. Obviously the electron dose (7.97 C/cm², in one sweep) is smaller than the 'saturation dose' (see Chapter 8.2) that is necessary to generate a pronounced and visible deposit in the whole 'BSE exit area'. Secondly, the height of the area structure is comparably small. It was determined to be 2.3 nm from the damping of the gold substrate signals in AES (for details see Chapter 3.6.8) and indicates that forward scattering from the intended deposit ('FSE proximity effect') is very weak.

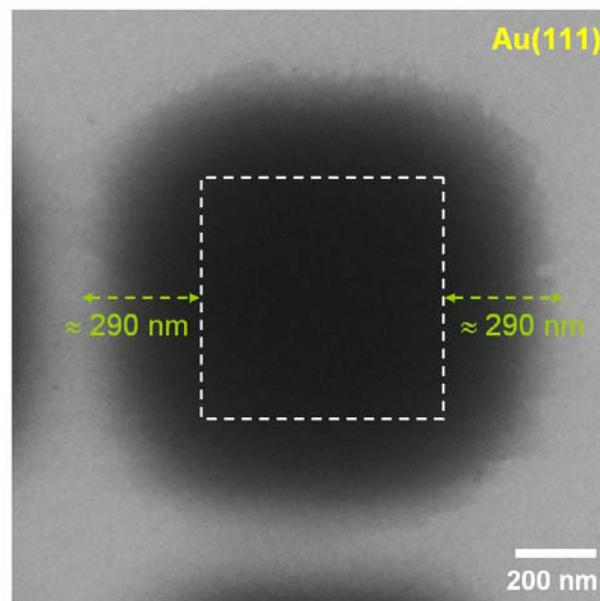


Figure 8.8: SEM image of the area deposit depicted in Figure 8.7 a) on which the green spectrum was acquired (electron dose: 7.97 C/cm², fabricated in one sweep). The white dashed square indicates the actually irradiated area while the light green dashed arrows label the phenomenon of lateral deposit broadening.

In order to investigate the extent of lateral deposit broadening on gold in more detail EBID line structures were generated with increasing electron dose (see Figure 8.9). All lines were generated with a length of 4.6 μ m and a step size of 4.5 nm. The

electron dose of these lines was varied from $1.1 \mu\text{C}/\text{cm}$ (Figure 8.9 a)) to $17.4 \mu\text{C}/\text{cm}$ (Figure 8.9 b)) and $26.2 \mu\text{C}/\text{cm}$ (Figure 8.9 c)). In addition, Figure 8.9 d) shows the ‘interaction volume’ of the applied 15 keV primary electron beam in gold (Figure 8.5 a), rotated by 90°) with identical length scale compared to the SEM images in a) – c).

The SEM images of Figure 8.9 show that the line diameter is clearly increasing with increasing electron dose, which follows the common expectation. Comparing the diameter of the line with the highest electron dose (Figure 8.9 c), $26.2 \mu\text{C}/\text{cm}$) with the lateral size of the ‘interaction volume’ in Figure 8.9 d) one finds a good agreement. Furthermore, the corresponding line diameter ($\approx 700 \text{ nm}$) is almost identical to the diameter of the ‘BSE exit area’ which was determined by simulation ($\approx 680 \text{ nm}$).

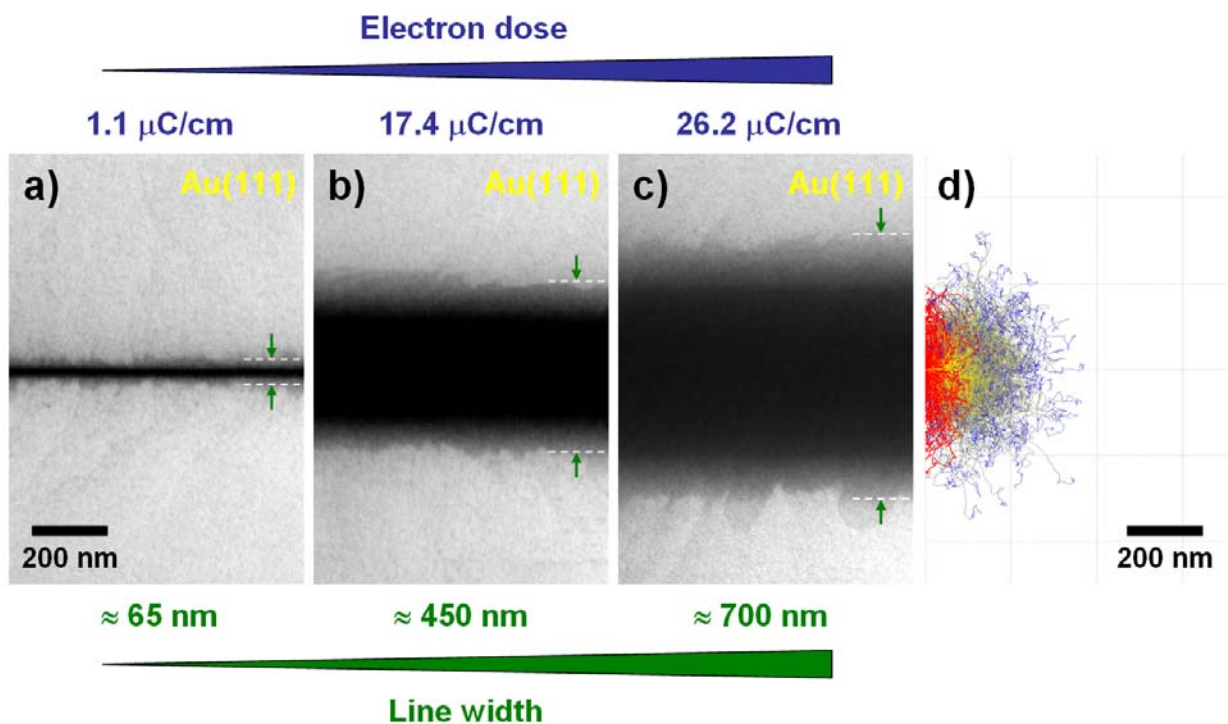


Figure 8.9: SEM images of three line deposits fabricated with TTIP on Au(111). The electron dose was increased from a) $1.1 \mu\text{C}/\text{cm}$ to b) $17.4 \mu\text{C}/\text{cm}$ and c) $26.2 \mu\text{C}/\text{cm}$, respectively. The ‘interaction volume’ of the applied 15 keV primary electron beam in gold is depicted in d) (graphic rotated by 90° and depicted with identical length scale compared to the SEM images in a) – c)).

It has to be noted that for the fabrication of the structures in Figure 8.9 different dwell times, active line durations, total line durations and numbers of sweeps were applied. However, the above drawn conclusions concerning lateral deposit broadening due to the 'BSE proximity effect' should not be affected by this variation of lithographic parameters.

Secondly, it has to be noted that for even higher electron doses than $26.2 \mu\text{C}/\text{cm}$ (not shown in this chapter, see Chapter 9.1) the line diameter is further increasing. However, for these line structures a significant height growth was observed (evidenced by sputter experiments) and thus lateral structure broadening to an extent larger than the 'BSE exit area' can be traced back to the 'FSE proximity effect'.

Finally, it can be concluded that the experimental results on gold concerning unintended deposit broadening due to proximity effects are in good agreement with the results from the conducted MC simulations. The determined radius of the 'BSE exit area' on gold of $\approx 340 \text{ nm}$ was found to be close to the extent of actually observed structure broadening. In addition, it was found that the electron dose plays an important role for the extent of lateral broadening. To observe a pronounced and clearly visible deposit in the whole 'BSE exit area' an electron dose close to a 'saturation dose' would be necessary. Structure broadening to an extent larger than the 'BSE exit area' (not shown in this chapter) can be observed for deposits with significantly higher electron doses. The latter is attributed to the occurrence of height growth and the 'FSE proximity effect'.

Since the 'BSE exit area' is significantly smaller for gold than for silicon, it is possible to fabricate nanostructures on gold with a significantly lower amount of unintended deposit in the surrounding of the intended structure. It can be concluded that applying a substrate material with high density and atomic number, such as gold, enables generally the fabrication of structures with a higher resolution and less "excess" material in the surrounding since the 'interaction volume' in the bulk is smaller.

8.4 Summary and conclusions

To summarize this chapter, one can state that in the performed EBID experiments material was deposited in areas which were not directly irradiated by the primary

electron beam. The latter was shown via spatially resolved AES and AELS measurements and can be traced back to proximity effects. For the deposits presented in this work, the 'BSE proximity effect' is the most significant one. The simulation of the electron substrate interactions with the software 'CASINO' (version 2.42, 2001) [20] allows for the quantification of lateral structure broadening based on the 'BSE proximity effect'. The 'BSE exit area', which is the upper limit for structure broadening caused by BSEs and SE2, was determined for the substrates silicon and gold. However, it was found that the electron dose plays a significant role in terms of the actual size of the unintended "excess" material. Initially, the size of deposit broadening goes along with the applied electron dose. Then, when the electron dose comes close to a 'saturation dose', the broadening approaches to the size of the 'BSE exit area'. For even higher electron doses height growth and the 'FSE proximity effect' occur, which can cause a structure broadening exceeding the 'BSE exit area'.

Both for silicon and for gold a very good agreement was found between the size of the determined 'BSE exit area' and the experimentally observed extent of lateral structure broadening. However, a comparison of both substrate materials demonstrates that the radius of the 'BSE exit area' is significantly smaller on gold, i.e. ≈ 340 nm compared to ≈ 2.2 μm . This can be attributed to the drastically smaller 'interaction volume' of the PE beam in the metal gold due to the much higher density and atomic number compared to silicon. Consequently, for the fabrication of nanostructures via EBID with a higher resolution and less "excess" material in the surrounding, the use of a metallic substrate with high density and atomic number (such as gold) is generally advisable.

It was found that the unintended deposit from TTIP on silicon has a carbon content of 15 ± 5 at. %. Thus, it has a higher purity compared to the investigated EBID area deposits on Si and Au, which showed an average value of 19 at. %. This result can be traced back to a higher number of lower energetic BSEs and SEs causing the generation of the respective unintended deposit. Consequently, the use of lower primary beam energies should be envisaged in future EBID experiments with TTIP in order to fabricate deposits with higher purity.

After the EBID experiments, a difference in the chemical composition of the non-irradiated Si(100) and the non-irradiated Au(111) surface was found. While the

Si(100) samples showed a slightly contaminated surface after EBID with carbon being the main contaminant, the purity of the Au(111) surface was conserved. This result can be attributed to a different adsorption / desorption behavior of the hydrocarbons in the TTIP gas on both surfaces. It is assumed that hydrocarbon adsorption on the Si(100) surface exceeds strongly the one on Au(111) probably due to a higher sticking coefficient or the appearance of chemisorption instead of physisorption.

9 Post-treatment procedures

In the previous chapters it was observed that EBID structures are laterally broadened due to proximity effects. The targeted deposit is usually surrounded by a thin layer of “excess” material. In addition, it was found that the deposits fabricated from TTIP are contaminated with carbon in the range of 13 ± 5 to 31 ± 5 at. %. Both lateral structure broadening due to proximity effects and the carbon contamination in the deposits are unwanted effects and generally a drawback of the EBID technique.

In this chapter, post-treatment procedures are presented to effectively reduce the consequences of the proximity effects and to generate clean nanostructures. First, sputtering is shown to be a tool for the removal of unintentionally deposited material close to generated EBID structures. Secondly, *in situ* sample heating in a low oxygen background pressure is demonstrated to be a tool for the growth of clean titanium oxide nanocrystals. A combination of these two procedures, i.e. a two-step post-treatment process after EBID, is introduced as a new pathway for the fabrication of clean localized nanostructures [225].

9.1 Sputtering

9.1.1 Sputtering as a tool for the reduction of lateral size

In Chapter 8 it is discussed that the intended EBID nanostructures are usually surrounded by a deposit which grows due to proximity effects. This “excess” material is rather flat with respect to the intended structure (see AFM data depicted in the Chapters 8 and 10), which means that significantly less material is deposited at the corresponding positions. Thus, the concept was developed to post-treat the sample by sputtering in order to ablate the top-most layers. By this approach, the thin material layer surrounding the central structure could be removed while the intended deposit remains with reduced size. The homogeneous removal of the top layers by sputtering exactly follows the concept of depth ion profiling which is a technique that is discussed later in this work (see Chapter 9.1.3). Concerning the extent of material removal a high level of control is given by the sputtering parameters, which determine the sputtering yield. These are in particular the type of the sputter gas, the gas pressure, the ion energy, the emission current and the sputtering time (see

Chapter 2.7). Figure 9.1 schematically shows the concept of sputtering for the reduction of the lateral size of nanostructures and in particular for the removal of the unintended “excess” material caused by proximity effects in EBID. It is applied to an EBID line or dot structure.

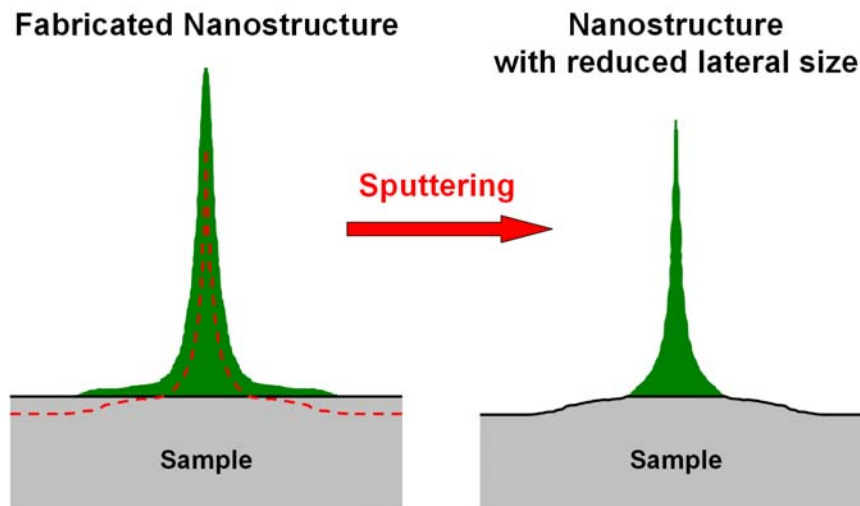


Figure 9.1: Schematic drawing which illustrates the concept of sputtering for the reduction of the lateral size of nanostructures and in particular for the removal of the unintended “excess” material caused by proximity effects in EBID.

It has to be noted that the sputtering yield additionally depends on the material to be removed and the angle of incidence, which is different for the flat surface and the nanostructure. Therefore, typically different sputtering yields result for the sample material and the deposits on the one hand and for different positions of the structure on the other (not accounted for in Figure 9.1).

To test the feasibility of this concept a line pattern was deposited on the Au(111) sample. The pattern consists of four lines with a length of $2.3\ \mu\text{m}$ which are oriented perpendicular to each other. Figure 9.2 a) shows an SEM image of the generated deposit. This SEM image is reproduced in Figure 9.2 b) with strongly increased brightness and contrast settings in order to visualize the central line structures (intended deposits) more pronounced and to be able to distinguish these structures from the rather flat “excess” material in the surrounding. A schematic drawing of the

line pattern with the applied lithographic parameters is depicted in Figure 9.2 c). Compared to the lines presented in Chapter 8.3, significantly higher line doses were used, i.e. increased by a factor of $\approx 9 - 35$.

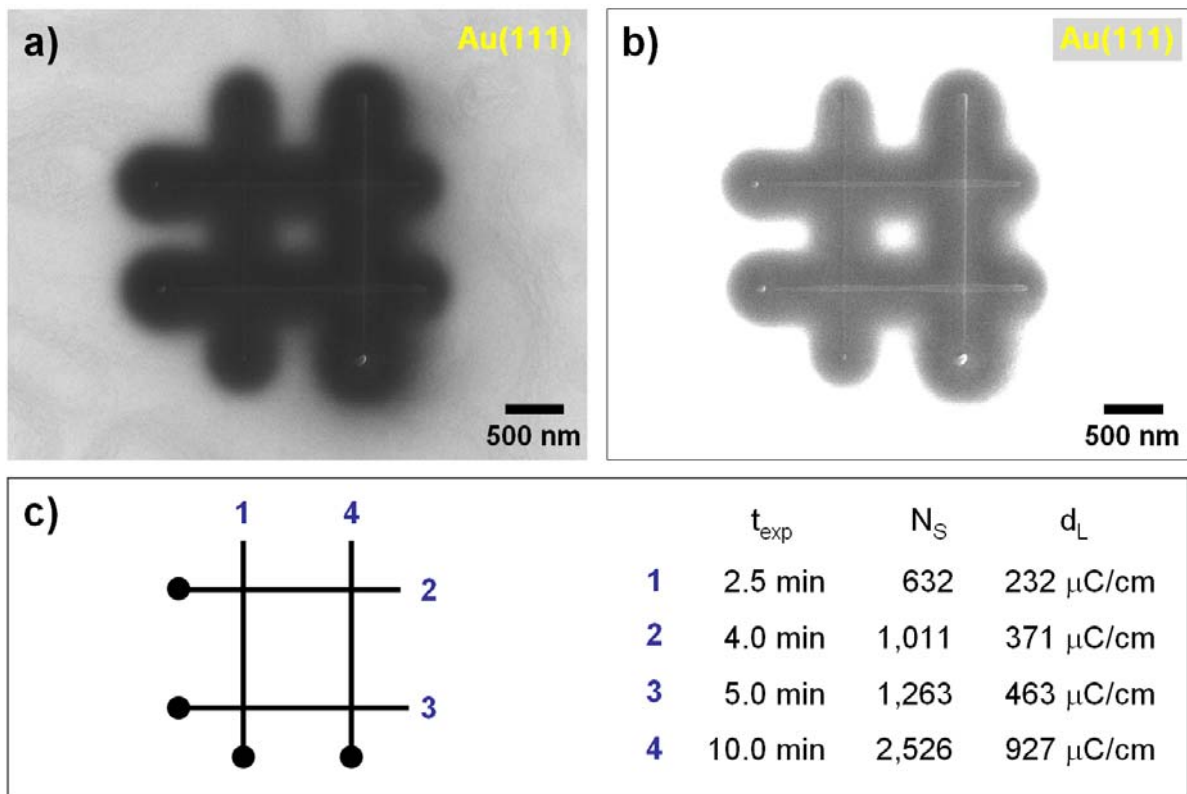


Figure 9.2: a) SEM image of a line pattern deposited via EBID with TTIP on the Au(111) sample. b) SEM image depicted in a) with strongly increased brightness and contrast settings in order to visualize the central line structures (intended deposits) and the flat “excess” material in the surrounding caused by proximity effects. c) Schematic drawing of the line pattern and specification of lithographic parameters.

To study the reduction of lateral size and the removal of unintentionally deposited material the sample was sputtered with argon ions in three steps (details see Chapter 3.6.7). Before the first sputtering step, the sample was heated while dosing oxygen (total heating time: 2 h and 40 min, maximum temperature: 705 K). This experiment was performed in order to increase the purity of the deposits. The results are shown and discussed in Chapter 9.2. In addition, the sample was annealed three

times to 875 K between the sputtering steps, which was done for sample smoothing and to remove argon atoms from the sample.

Figure 9.3 shows four SEM images of the line pattern, acquired at different times of the post-treatment procedure. The SEM image of Figure 9.3 a) was taken before applying the post-treatments while the images in b), c) and d) were acquired after successive sputtering steps. Due to the high contrast between the deposits fabricated from TTIP and the gold surface (material contrast, see Chapter 7.3) it is possible to observe the changes induced by sputtering directly via SEM. The depicted images of Figure 9.3 clearly show that the lateral size of all four lines decreases with increasing sputtering time. In addition, the edges of the lines, which appear slightly diffuse in Figure 9.3 a), become much sharper already after the first sputtering step. Considering the left vertical line of the pattern, which was fabricated with the lowest electron dose ($232 \mu\text{C}/\text{cm}$), a reduction of the lateral size (FWHM) from 580 to 28 nm can be observed after 2 h of sputtering (see a) - c)). The last sputtering step for 10 min (see c) - d)) removes the remaining thin line completely and lays open the Au support. Finally, a thin gold “bridge” is left over connecting the horizontal lines at the position where originally the line structure was deposited (see image d) and text below).

In addition, the images of b), c) and d) show edges on the Au(111) support in the direct surrounding of the line pattern. These edges are generated in the sputtering process (compare to Figure 9.1) since close to the lines first the “excess” material is removed by sputtering, while at higher distances Au from the substrate surface is ablated during the whole sputtering time. As a consequence, the remaining line deposit is finally located on a small gold plateau (see Figure 9.3 d)).

The sequence of SEM images in Figure 9.3 clearly shows that sputtering is a suitable tool to downsize the lateral dimension of the originally deposited structures. The “excess” material in the surrounding of the central line structures, which was deposited due to proximity effects (see Chapter 8), is removed continuously, while nanostructures with reduced lateral size remain on the surface.

It is noted that additionally to sputtering heating of the sample in oxygen and intermittent annealing steps were performed in the experiment described above. However, since the reduction of lateral size of nanostructures and the removal of unintentionally deposited material by sputtering were shown in several other experiments in which no heating or annealing steps were conducted, it is concluded

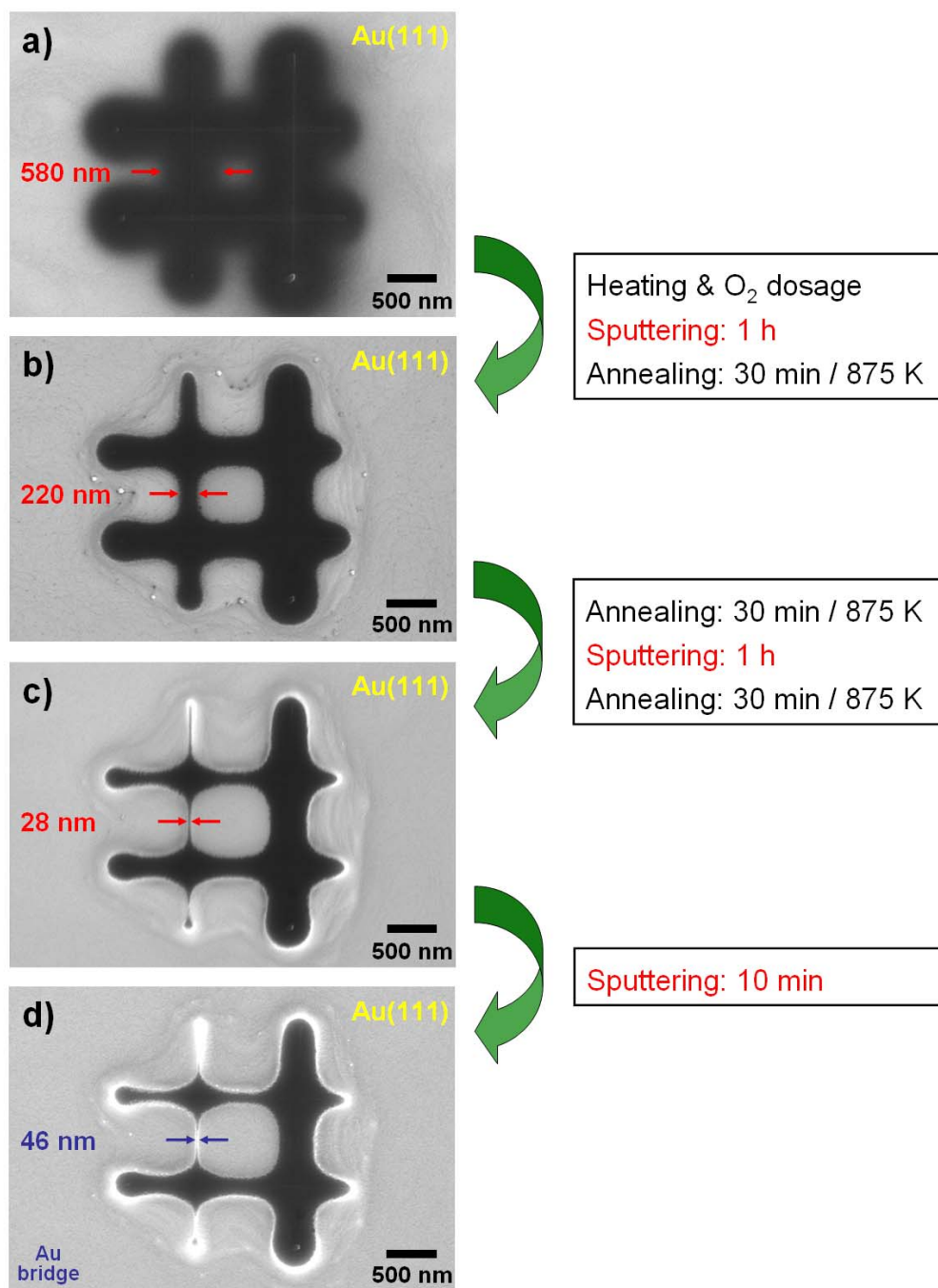


Figure 9.3: a) SEM image of the line pattern before applying the post-treatments. b) SEM image after heating in O₂ atmosphere, sputtering for 1 h and an annealing step. c) SEM image after additional sputtering for 1 h and two annealing steps. d) SEM image after additional sputtering for 10 min. The removal of the “excess” material surrounding the central lines enables to reduce the lateral structure size. The dimension of the left vertical line could be reduced from 580 to 28 nm (see a) - c)). The last sputtering step lays open the Au support (see d)).

that the described effects are clearly due to sputtering. In addition, there is no indication that heating in oxygen or annealing do influence the results presented in this chapter.

Interestingly, Figure 9.3 d) shows that only the left vertical line is removed completely after the total sputtering time of 2 h and 10 min. The latter is derived from the contrast inversion for this line from Figure 9.3 c) (dark deposit on bright sample in SEM, i.e. ‘material contrast’) to Figure 9.3 d) (very bright gold “bridge” on bright gold sample in SEM, i.e. ‘topographic contrast’), which is also confirmed by the corresponding SEM gray scale line profiles. For the other lines one finds that the lateral size after the post-treatment depends on the originally applied electron dose in the EBID process (compare to Figure 9.2 c)) and the resulting deposit thickness. This demonstrates that the sputtering time determines significantly the material removal and reduction of lateral size. It is a processing parameter which generally has to be adapted to the applied electron dose and acquired thickness of the nanostructures. In addition, it enables to adjust the final lateral size of the structures.

From a more general point of view, it can be concluded that special care has to be taken when structures with strongly varying electron dose and thus strongly varying thickness were originally generated via EBID and sputtering is used for size reduction and removal of “excess” material. For the application of low sputtering times the effects will be small for thick structures and might be insufficient (see right vertical line in Figure 9.3 d)). In contrast, long sputtering times bear the risk of removing thin structures completely (see left vertical line in Figure 9.3 d)). In this case, when long sputtering times are necessary, one might envisage covering the thin, low electron dose structures with protective capping layers (see Chapter 13) in order to avoid complete structure removal. The latter could be deposited as “sacrificial material” for the sputtering process, which would then be removed (completely) in this production step and lay open the thin, low electron dose structures again.

In the Figures 9.2 and 9.3 an example is shown in which the lateral size of high electron dose structures was reduced via sputtering. In the following, low electron dose structures are considered and the concept of sputtering in terms of size reduction and removal of “excess” material due to proximity effects is applied to these deposits.

Figure 9.4 shows the point matrix on the Au(111) sample which was already presented and discussed in detail in Chapter 7.1. It consists of ten points arranged in three columns with three points in the left and middle one and four points in the right column. The dot deposit in the upper left corner of the SEM image is the 'PT deposit' introduced in Chapter 3.2.2. The electron dose of the ten point deposits in the matrix increases in each column from bottom to top and from the left to the right column. It varies from 0.12 to 1.20 nC and is incrementally increased by 0.12 nC per point. Figure 9.4 a) depicts the ten-point matrix before the post-treatment was applied. The SEM image shows the central dot deposits (intended deposits) surrounded by

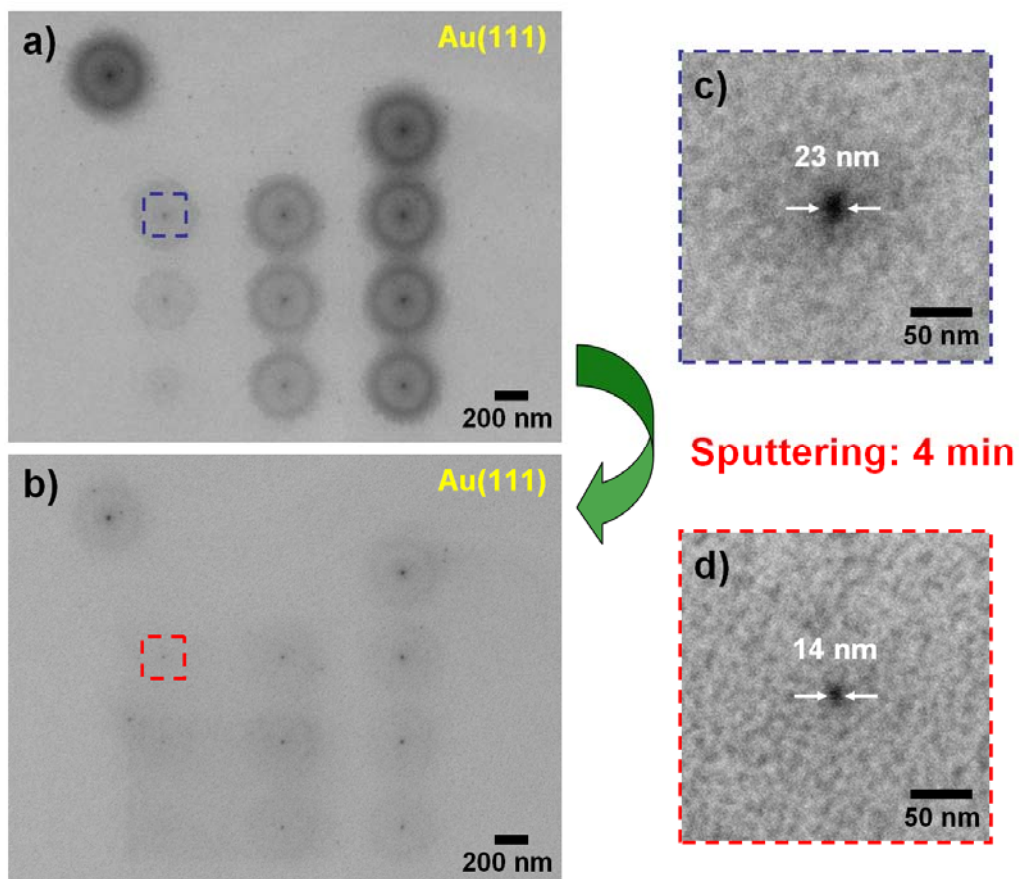


Figure 9.4: a) SEM image of a point matrix deposited on Au(111) and consisting of ten points of increasing electron dose (see text). b) SEM image of the point matrix after 4 min of sputtering. c) High magnification SEM image of the dot marked in a) (before sputtering). d) High magnification SEM image of the dot marked in b) (after 4 min of sputtering).

circular structures deposited due to the 'BSE proximity effect' (unintended deposits) (details see Chapter 8 and Chapter 10.1). Figure 9.4 b) depicts the matrix after the post-treatment procedure of sputtering for 4 min. It shows that the structures in the surrounding of the central dots were removed almost completely by the post-treatment. In addition, the size of the central dot structures was reduced. This becomes evident when high magnification SEM images of the central dots are investigated. Figure 9.4 c) and d) depict the upper dot of the left column of the matrix (dot dose: 0.36 nC) strongly magnified before and after sputtering, respectively. The images demonstrate that the size (FWHM of the gray scale line profile) of this exemplary dot was reduced from 23 to 14 nm. This corresponds to a size reduction of 39 % achieved by the post-treatment.

To summarize, one can state that sputtering is a suitable tool to reduce the lateral dimension of originally deposited structures, i.e. to remove the unwanted deposits caused by the proximity effects in EBID. It could be shown that the suggested concept of sputtering works well both for high and for low electron dose structures. A significant parameter is the sputtering time, which generally has to be adapted to the corresponding electron dose and thus thickness of the nanostructures.

To apply the post-treatment of sputtering in terms of size reduction it is significant to know the sputtering yield. Therefore, the sputtering yield for the applied experimental conditions in the instrument was determined by analyzing the data presented in the following section. In addition, this data shows the removal of unintentionally deposited material close to EBID structures, which is picked up again in Chapter 9.3, where a novel pathway for the fabrication of clean localized nanostructures is reported.

Figure 9.5 shows the line pattern generated with TTIP on Si(100) that was already discussed in previous chapters (see Figures 7.4 a) and 8.1 a)). The applied electron doses were 116 $\mu\text{C}/\text{cm}$ for the left line, 232 $\mu\text{C}/\text{cm}$ for the horizontal one and 463 $\mu\text{C}/\text{cm}$ for the right one. Figure 9.5 a) shows an SEM image of the pattern acquired after fabrication. To remove the unintentionally deposited material close to the lines, which is not visible in SEM due to the weak contrast between deposit from TTIP and silicon (see Chapter 7.3), the post-treatment of sputtering was applied in five steps with single sputtering times of 25, 15, 30, 30 and 20 min. Sputtering was

performed with Ar^+ ions, the details are specified in Chapter 3.6.7. The line pattern after the post-treatment, i.e. after a total sputtering time of 120 min, is depicted in

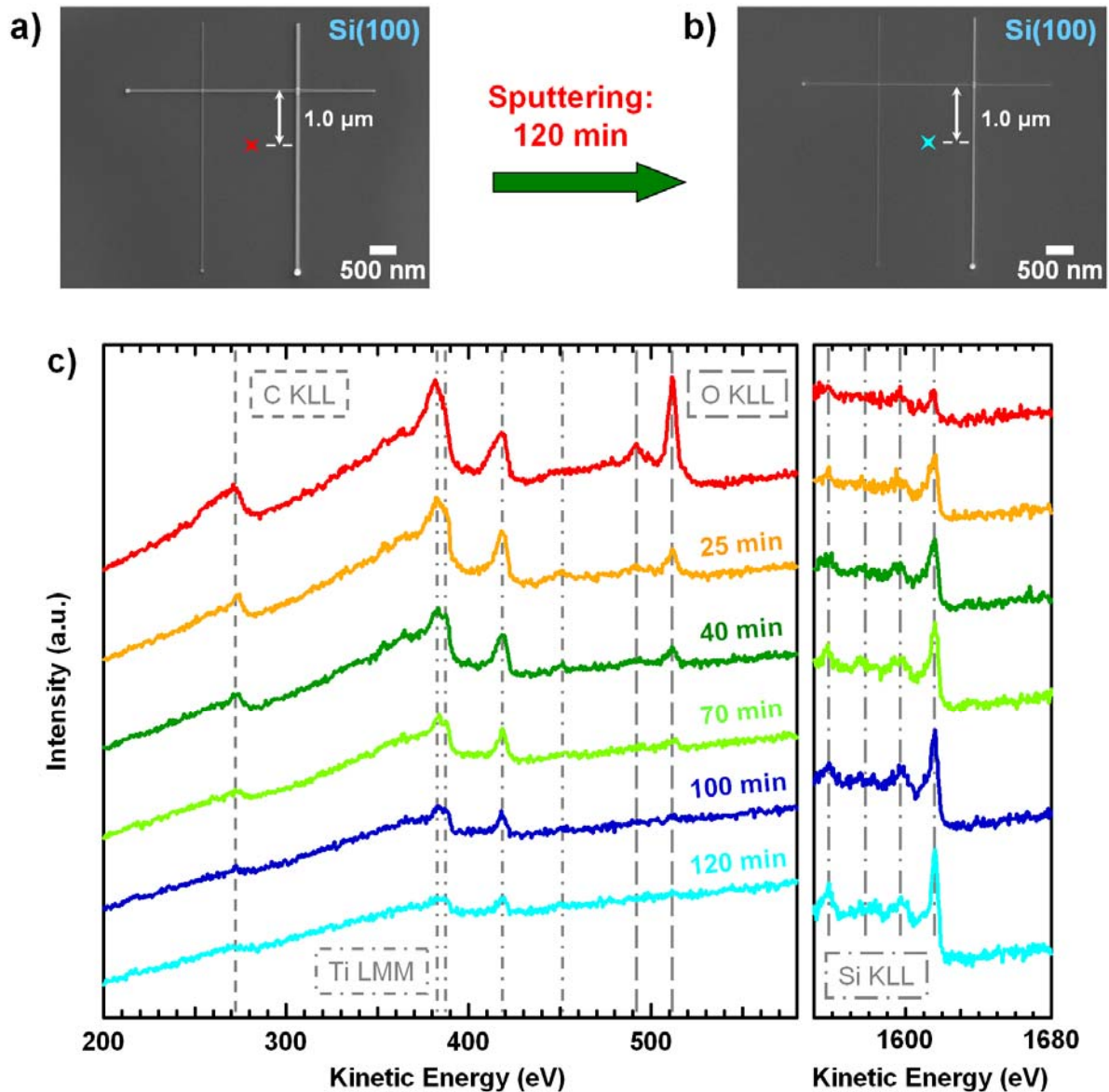


Figure 9.5: a) SEM image of a pattern consisting of three perpendicular lines fabricated with TTIP on Si(100) with electron doses of 116, 232 and 463 $\mu\text{C}/\text{cm}$ (see also Figures 7.4 a) and 8.1 a)). The red marker denotes the position where local AES was performed. b) SEM image of the pattern after 120 min of sputtering. c) AE spectra acquired at the position marked in a) and b) [225]. The red spectrum was measured before sputtering; the yellow, dark green, light green, dark blue and light blue spectra were acquired after the indicated total sputtering time.

Figure 9.5 b). It shows line structures with clearly reduced lateral size. Before sputtering and after each sputtering step, local AES was performed at the position labeled by the colored markers in Figure 9.5 a) and b). The corresponding Auger spectra are depicted in Figure 9.5 c) demonstrating the development of the peaks upon the sputtering post-treatment.

The red spectrum of Figure 9.5 c) was measured before sputtering. It shows the C KLL, Ti LMM, O KLL and Si KLL Auger peaks at the known kinetic energies. Quantitative analysis of the Auger signals yields a chemical composition of 15 ± 5 at. % carbon, 28 ± 5 at. % titanium and 57 ± 5 at. % oxygen for the deposit and a layer thickness of 2.8 nm. The chemical composition is in very good agreement with the data presented in Chapter 8.1. The other spectra in Figure 9.5 c) were acquired after the indicated color-coded total sputtering times, respectively. The AE spectra clearly evidence the removal of the material between the line structures since the carbon, titanium and oxygen Auger signals become smaller with increasing sputtering time. Correspondingly, the silicon substrate signals, which were strongly damped in the red spectrum acquired before sputtering, are growing with increasing sputtering time.

Furthermore, two conspicuous findings in the Auger spectra depicted in Figure 9.5 c) can be discussed in more detail:

Firstly, one observes that the carbon and oxygen signals decrease much faster upon sputtering in comparison to the titanium signal. For oxygen this finding is interpreted as due to a higher sputtering yield of oxygen compared to titanium. The resulting ion beam induced reduction in the metal oxide film is generally addressed as 'sputter reduction', a phenomenon which is well-known in literature [245-250]. Recently, Baer *et al.* compared sputter rates of diverse oxide films to the one of SiO₂ [245]. In this article, the authors report of the well established phenomenon that ion sputtering frequently removes oxygen preferentially compared to the metal in a metal oxide film, which decreases the oxygen to metal ratio [245]. This ion beam induced reduction of metal oxide films has been observed by many research groups and has also been described theoretically [246-250]. For titanium dioxide, the formation of highly defective, oxygen deficient surfaces upon sputtering and sputter reduction of TiO₂ to several different reduced titanium states are reported in literature [107, 231, 238, 240, 244] (for a detailed discussion see Chapter 9.1.3). In contrast to oxygen, a

different explanation is assumed for the increased removal of carbon upon sputtering. The sputtering yield for carbon is smaller than the one for titanium by a factor of ≈ 2 at the applied sputter conditions of this work (1 keV Ar^+ ions under normal incidence), i.e. 0.449 compared to 0.901 [58] (see Table 2.1, Chapter 2.7). Therefore, it is to be expected that titanium is removed faster compared to carbon upon sputtering. Since the spectra of Figure 9.5 c) demonstrate exactly the opposite behavior, i.e. an increased carbon removal upon sputtering, a possible explanation is an inhomogeneous distribution of carbon in the deposit with an increased amount of C in the topmost layers. The same result, i.e. the increased carbon removal compared to titanium upon sputtering, was recently reported by Marie-Madeleine Walz [99]. However, it is noted that more work is necessary in this field and that a detailed investigation of this effect including deposits with larger thickness should be carried out to fully clarify and explain the reported observation.

Secondly, a thorough investigation of the Ti LMM Auger signals in Figure 9.5 c) upon sputtering shows a development which gives an insight into the ongoing chemistry upon sputtering. The corresponding part of the Auger spectra from Figure 9.5 c) is depicted in Figure 9.6. It is found that after the first sputter step of 25 min the $\text{L}_3\text{M}_{2,3}\text{M}_{2,3}$ peak at ≈ 382 eV broadens due to a shoulder at the high kinetic energy side. Simultaneously, the $\text{L}_3(\text{Ti})\text{M}_{2,3}(\text{Ti})\text{V}$ peak, labeled at ≈ 418 eV in Figure 9.5 c), gets narrower and loses the shoulder at the low kinetic energy side, which is visible only in the red spectrum acquired before sputtering. Considering the Ti LMM Auger signals after 40 min of sputtering, i.e. after the second sputter step, one finds that the shoulder at the high kinetic energy side of the $\text{L}_3\text{M}_{2,3}\text{M}_{2,3}$ peak developed to a distinct signal at ≈ 388 eV. This signal also appears in the other spectra which were acquired after longer sputtering times and causes the broad appearance of the whole peak by merging with the $\text{L}_3\text{M}_{2,3}\text{M}_{2,3}$ signal at ≈ 382 eV (see blue spectra). Simultaneously, in all spectra acquired after sputtering the $\text{L}_3(\text{Ti})\text{M}_{2,3}(\text{Ti})\text{V}$ peak appears narrowed, showing a distinct signal only at ≈ 418 eV. Based on reference [229] the signal at ≈ 388 eV, which emerges upon sputtering, can be clearly associated with $\text{L}_3\text{M}_{2,3}\text{M}_{4,5}$ transitions and a simultaneous “shake-up”, i.e. excitation, of a 3p electron of metallic titanium (details see Chapter 7.2.6). In addition, the low kinetic energy side shoulder of the $\text{L}_3(\text{Ti})\text{M}_{2,3}(\text{Ti})\text{V}$ peak at ≈ 414 eV, which disappears upon sputtering, can be associated with the inter-atomic $\text{L}_3(\text{Ti})\text{M}_{2,3}(\text{Ti})\text{V}(\text{O})$ transitions, which are expected for titanium dioxide, and the remaining signal at ≈ 418 eV is attributed to intra-atomic

$L_3(\text{Ti})M_{2,3}(\text{Ti})V(\text{Ti})$ transitions being characteristic for reduced titanium oxide species and for metallic titanium [53, 100, 231, 238, 241] (details see Chapter 7.2.6). In conclusion, the development of the Ti LMM signals upon sputtering clearly demonstrates the occurrence of sputter reduction in the deposited titanium oxide material and the appearance of titanium in lower oxidation states than '+IV', which is well-known from literature [107, 231, 238, 240, 244] (see Chapter 9.1.3). The presence of the signal at ≈ 388 eV demonstrates reduction even to metallic titanium.

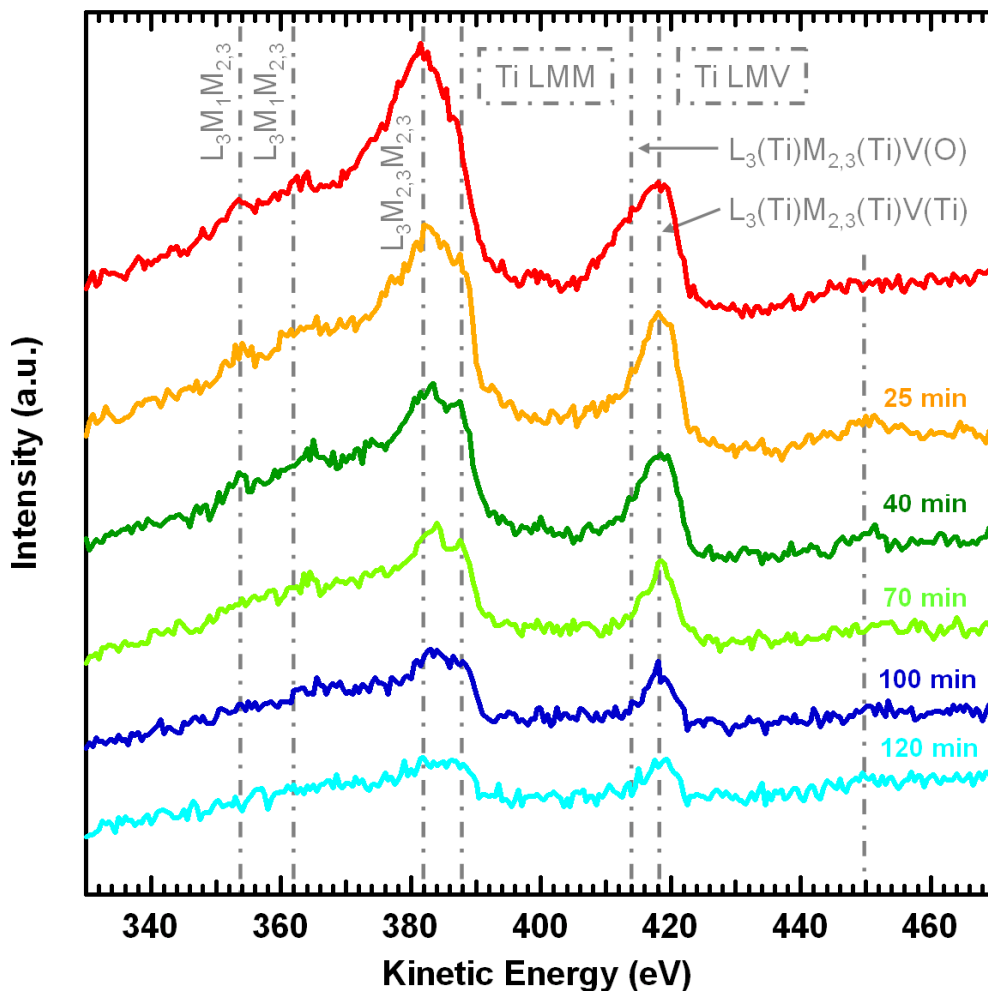


Figure 9.6: AE spectra depicted in Figure 9.5 c) with the display region from 330 to 470 eV. This region shows the Ti LMM and Ti LMV Auger signals. The red spectrum at the top was measured before sputtering; the other spectra were acquired after sputtering for the indicated total sputtering time. The signal development upon sputtering demonstrates the occurrence of sputter reduction.

To study the development of the Auger signals upon the sputtering post-treatment in more detail and to address the development of the chemical composition and the layer thickness with increasing sputtering time, quantitative analysis of the Auger data depicted in Figure 9.5 c) was performed. The results of this analysis are depicted in Figure 9.7.

Figure 9.7 a) shows the development of the normalized Ti LMM (green), C KLL (black), O KLL (red) and Si KLL (blue) Auger peak areas with increasing sputtering time. The obtained curves demonstrate material removal and evidence that carbon and oxygen are removed much faster upon sputtering compared to titanium (explanations see above). While for C and O an exponential decline is observed, a linear trend of the titanium removal is found, which is indicated by the plotted regression line. In contrast, the silicon peak area rises. In Figure 9.7 b), the corresponding chemical compositions are plotted. The graph demonstrates the already discussed changes in the material composition caused by sputter reduction (see above). The distinct depletion of oxygen is the dominating effect in this data plot. Finally, Figure 9.7 c) shows the development of the layer thickness upon sputtering. The dark blue curve corresponds to the data acquired between the lines of the pattern depicted in Figure 9.5 a) and b). In addition, material removal and the development of the corresponding layer thickness of an EBID area deposit on Si(100) was studied (see light blue curve). The corresponding deposit is depicted in Figure 7.3 a) and was generated with an electron dose of 2.46 C/cm^2 . Figure 9.7 c) demonstrates that for both deposits the decrease of the layer thickness is not linear with increasing sputtering time. After a steep decline of the layer thickness curves in the first sputtering step, a significantly lower decline is observed during the following sputtering time. This behavior is attributed to the fact that already after the first sputtering step a very thin and rough deposit is obtained. Presumably, this deposit exhibits holes with a depth down to the silicon substrate. Consequently, in the following sputter steps not only the material from the EBID deposit is ablated by sputtering but also Si from the substrate beneath the nanostructure should be removed. This could explain the decreased sputtering yield observed in both data after the first sputtering step of 25 min. In addition, also an inhomogeneous element distribution in the deposit at the surface-deposit-interface can not be ruled out, which could explain the observed behavior, as well.

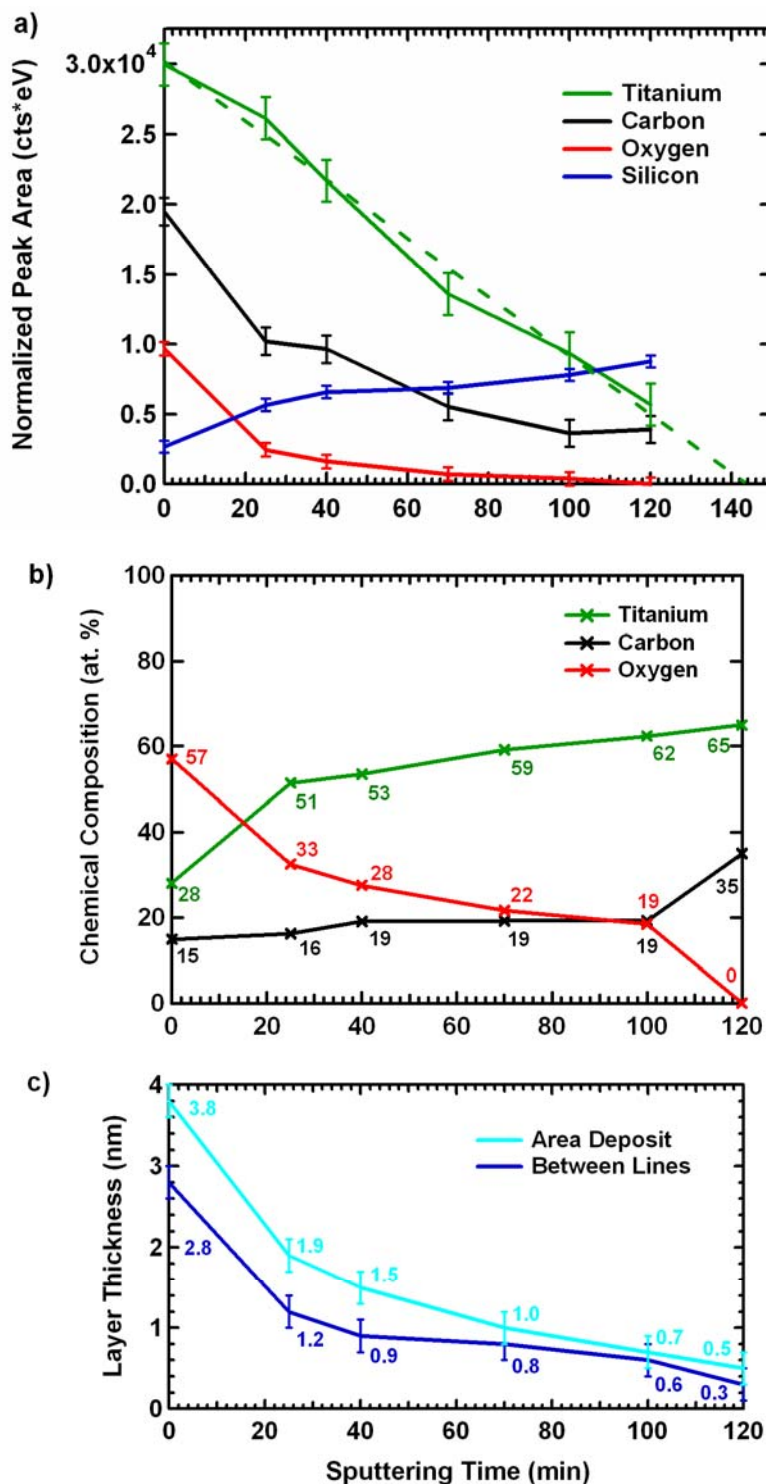


Figure 9.7: a) Normalized peak area of the Ti, C, O and Si Auger peaks in the spectra of Figure 9.5 b). b) Chemical composition of the material deposited between the lines in Figure 9.5 a). c) Layer thickness of the material deposited between the lines in Figure 9.5 a) and of an EBID area deposit on Si(100) (see Figure 7.3 a), electron dose of 2.46 C/cm^2). All quantities are drawn vs. the total sputtering time.

It is noted that this finding indicates the “difficulty” of determining the sputtering yield by the AES technique. It derives from the fact that layer thicknesses are determined from AES data by considering the substrate signal damping by the “overlayer”. However, this relies on the presence of thin deposits with incomplete substrate signal damping (in the investigated system: < 6.1 nm), in which then the above discussed phenomena are likely to occur.

For the results presented in this work, the layer thickness data of Figure 9.7 c) are interpreted as follows: Two different sputtering yields are determined being valid for material removal from “thick” deposits on the one hand and from “thin” deposits on the other. Based on the development of the layer thicknesses in the first 25 min an average sputtering yield of $\approx 4.2 \pm 0.4$ nm / h can be determined. In contrast, an average sputtering yield of $\approx 0.7 \pm 0.2$ nm / h is determined based on the development of the layer thicknesses after the first 25 min of sputtering. Both sputter rates are valid for the slightly carbon contaminated titanium oxide material which is deposited via EBID with TTIP. (Note that neglecting the distinction of cases and considering the total sputtering time of 2 h yields an average sputter rate of $\approx 1.4 \pm 0.2$ nm / h, which is specified in reference [225].)

9.1.2 Sputtering as a tool to elucidate structure morphologies

In addition to the application presented in the previous subchapter, the sputtering technique can be exploited as a valuable tool to elucidate structure morphologies. Since SEM images do not contain direct height information, sputtering can be used to ablate the deposited structures layer by layer and follow the topographic changes via SEM. By this procedure the height of structures and in particular the height of different deposit regions (e.g. central structure vs. surrounding) can be studied. In Chapter 10.2, this technique is used for the investigation of the morphology of EBID line deposits.

9.1.3 Sputtering for depth ion profiling

Apart from using sputtering for lateral size reduction of nanostructures, the removal of “excess” material caused by proximity effects and the determination of structure

morphologies one might envisage to use sputtering for depth ion profiling, which is a standard technique in surface science (see Chapter 2.7). However, it has to be noted that this technique, applied to determine the chemical composition of subsurface layers, is hampered for the material titanium oxide since it is well-known from literature that TiO_2 surfaces exhibit a high sensitivity to sputter reduction [107, 231, 238, 240, 244].

Kern *et al.* [107] report that sputtering of amorphous TiO_2 with 1 or 3 keV argon ions causes oxide reduction and the presence of titanium ions in lower oxidation states than '+IV'. The same result is described by Nishigaki [238], Göpel *et al.* [231], Pan *et al.* [244] and Vergara *et al.* [240]. Nishigaki [238] reports the easy decomposition of the TiO_2 surface layers of a $\text{TiO}_2(110)$ cleaved sample upon bombardment with 3 keV Ar^+ ions and the formation of Ti_2O_3 or TiO layers. As a reason Nishigaki refers to the disparity in sputtering yield for each element (see also Chapter 2.7) which makes the surface non-stoichiometric [238]. Göpel *et al.* [231] observed the production of intrinsic defects in a $\text{TiO}_2(110)$ surface and Pan *et al.* [244] the formation of highly oxygen deficient and highly defective $\text{TiO}_2(110)$ surfaces with several different reduced titanium states. Both groups applied 500 eV argon ion bombardment. The most comprehensive study is given by Vergara *et al.* [240] who investigated the surface changes induced by ion bombardment depth profiling. The authors observed the generation of lower titanium oxide states (TiO) and report that this effect is independent of the applied ion energy and ion density but clearly dependent on the mass of the impinging ions [240]. Thus, this study of Vergara *et al.* disagrees with the assessment of Le Mercier *et al.* who claim to avoid chemical changes on TiO_2 upon sputtering by applying Ar^+ ions of lower kinetic energy, i.e. 700 eV [251].

To summarize the results of these articles, one can state that depth ion profiling via sputtering applied on TiO_2 samples and TiO_2 based materials is hampered by the phenomenon of preferential oxygen sputtering and thus the occurrence of sputter reduction. These effects go along with a change of the chemical composition of the produced samples and materials after sputtering. One should keep in mind that the discussed effects also occur for EBID deposits fabricated with TTIP. The occurrence of sputter reduction was demonstrated in Chapter 9.1.1 (see the Figures 9.5 c), 9.6, 9.7 a) and 9.7 b)). In consequence, the technique of depth ion sputtering is not suitable to determine the chemical composition of subsurface layers of TTIP deposits.

Finally, one can conclude that for the material deposited with the precursor TTIP it is particularly valid that ‘observing means changing’ the system. This holds both for applying an electron beam (see Chapter 7.2.6) and for using an ion beam (see Chapter 9.1.1), both causing reduction of titanium in the deposit.

9.2 Annealing in oxygen

In Chapter 7.2 the chemical composition of EBID deposits with the precursor TTIP was investigated and it was found that the structures are contaminated with carbon in the range of 13 ± 5 to 31 ± 5 at. %.

Recently, Berger *et al.* [252] and Elser *et al.* [253] reported the fabrication of nanocrystalline anatase TiO_2 particles by thermal decomposition of TTIP vapor in a flow reactor system applying metal organic chemical vapor deposition (MOCVD). The authors refer to previous work by Benfer and Knözinger [254] who introduced the flow reactor apparatus and reported the fabrication of nanostructured ZrO_2 particles in this system. In order to clean the produced “raw material” from adsorbed hydrocarbons and in order to guarantee the stoichiometric composition of the targeted oxide nanoparticles, all authors describe the application of a post-treatment comprising annealing and exposing to molecular oxygen [252-254]. While Benfer and Knözinger applied a temperature of 773 K and a not further specified oxygen treatment [254], Berger *et al.* and Elser *et al.* annealed to 870 K under high vacuum conditions ($p < 10^{-6}$ mbar) for 2 h and then oxidized with 20 mbar of oxygen [252, 253].

Based on these works, the idea was developed to treat the fabricated EBID nanostructures from TTIP with a similar post-treatment comprising annealing and dosing oxygen *in situ*, in order to reduce the amount of carbon in the deposits and possibly to generate crystalline structures, as well. The idea behind this post-treatment is to oxidize carbon to volatile compounds like carbon monoxide (CO) or carbon dioxide (CO_2) and thereby to remove it from the fabricated structures. In addition, applying heat should activate the migration of all components of the EBID deposits, e.g. the migration of carbon to the surface where it can react with oxygen. In literature concerning EBID, some similar approaches have already been reported (compare reference [166] and see also Chapter 4.3). However, the novel aspects of

the post-treatments presented in this work compared to earlier approaches are (1) the ultra clean UHV environment, (2) the *in situ* processing without breaking the vacuum at any step and (3) the significantly lower applied oxygen pressure.

In the first attempt to purify EBID nanostructures from TTIP via a post-treatment procedure, the Si(100) sample was heated in the analysis chamber for 10 min at a temperature of 680 K. Simultaneously, molecular oxygen was dosed at a background pressure of $4.2 \cdot 10^{-8}$ mbar [211]. Note that the oxygen background pressure could not be further increased due to technical reasons. In this experiment, it turned out that the morphology stays unchanged by the post-treatment and that the amount of carbon detected on the deposits via local AES is slightly increased as compared to before the treatment, which is attributed to heat induced migration effects. However, the result demonstrates that the applied experimental conditions ($t = 10$ min, $T = 680$ K, $p(\text{O}_2) = 4.2 \cdot 10^{-8}$ mbar) were insufficient. Most presumably, the applied parameters were not “harsh” enough in order to achieve purification.

Therefore, in the second approach the experimental conditions were changed applying more rigorous parameters. The post-treatment time was increased to 50 min, while the Si(100) sample was heated in the preparation chamber to 1,015 K and oxygen was dosed to a background pressure of $8.0 \cdot 10^{-6}$ mbar [211]. After sample cooling the structures were investigated via SEM, SAM and local AES.

The Figures 9.8 and 9.9 show the drastic change of the deposit morphology upon the applied post-treatment procedure. Two different EBID deposits are considered. The first one is an area deposit consisting of a square and a circle, both generated with an electron dose of 39.8 C/cm^2 . Figure 9.8 a) depicts a schematic drawing of the structure and Figure 9.8 b) shows an SEM image of the corresponding deposit on the Si(100) surface. Both area structures are weakly visible in Figure 9.8 b) (for details concerning the contrast see Chapter 7.3) and are thus labeled by light blue markers. The second EBID structure is a “combined deposit” composed of two areas, two perpendicular lines and two dots. This structure was generated by scanning six times an area of $1,143 \times 858 \text{ nm}^2$ (electron dose: 39.4 C/cm^2) in horizontal direction, scanning a line of $1,143 \text{ nm}$ for 5 min (electron dose: $927 \mu\text{C/cm}$) in horizontal direction, then rotating by 90° and scanning a line of $1,143 \text{ nm}$ for 2.5 min (electron dose: $464 \mu\text{C/cm}$) in vertical direction and finally irradiating two dots statically next to

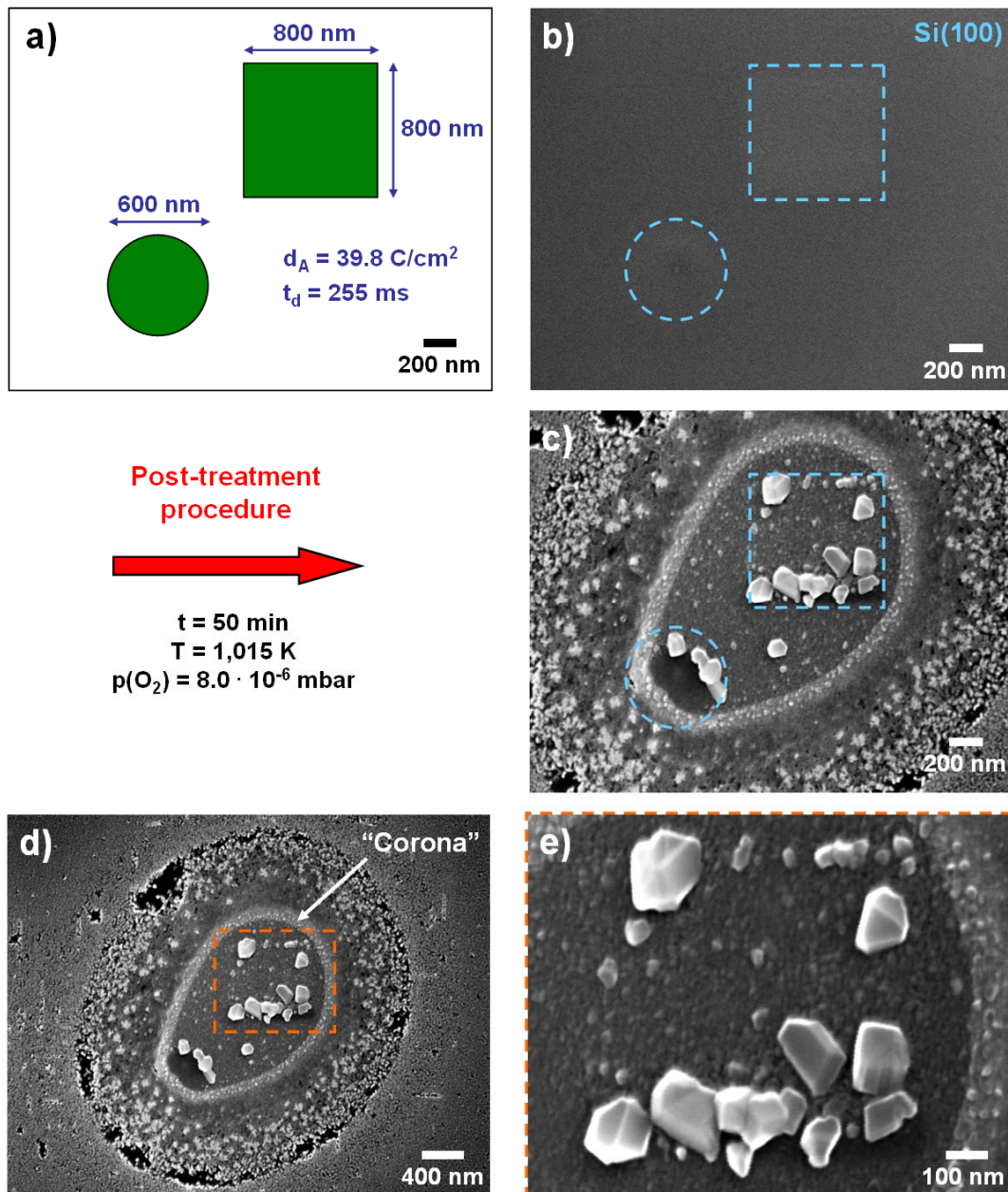


Figure 9.8: a) Schematic drawing of an EBID deposit. b) SEM image of the corresponding deposit on Si(100). c) SEM image of the grown nanostructures after the post-treatment of annealing in oxygen ($t = 50 \text{ min}$, $T = 1,015 \text{ K}$, $p(\text{O}_2) = 8.0 \cdot 10^{-6} \text{ mbar}$). d) SEM image of the grown nanostructures with reduced magnification. e) High magnification SEM image of the grown nanocrystals at the position marked in d). (Please note that all SEM images were taken with $U_B = 15 \text{ kV}$ and $I_B = 3 \text{ nA}$ on the tilted sample and that for this experiment during EBID the dosing nozzle was approached closer to the sample to a distance of $\approx 8 \text{ mm}$.)

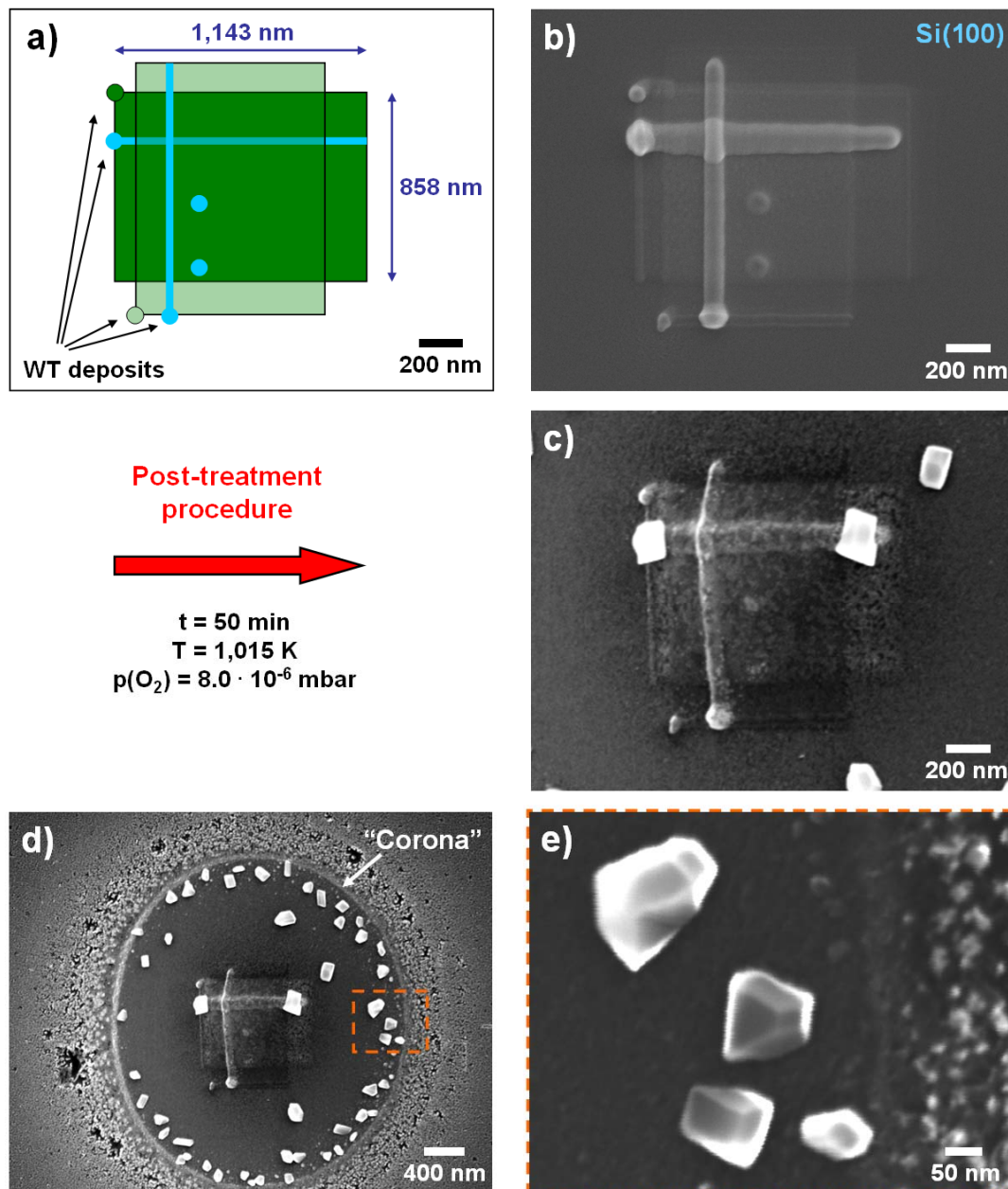


Figure 9.9: a) Schematic drawing of a combined EBID deposit. b) SEM image of the corresponding deposit on Si(100). c) SEM image of the grown nanostructures after the post-treatment of annealing in oxygen ($t = 50 \text{ min}$, $T = 1,015 \text{ K}$, $p(\text{O}_2) = 8.0 \cdot 10^{-6} \text{ mbar}$). d) SEM image of the grown nanostructures with reduced magnification. e) High magnification SEM image of the grown nanocrystals at the position marked in d). (Please note that the SEM images in c) – e) were taken with $U_B = 15 \text{ kV}$ and $I_B = 3 \text{ nA}$ on the tilted sample and that for this experiment during EBID the dosing nozzle was approached closer to the sample to a distance of $\approx 8 \text{ mm}$.)

this line for 1 min (electron dose: 24 nC), respectively. In addition, the line and dot structures were characterized via SEM *in situ*, i.e. during the experiment, by what an additional electron area dose of 6.6 C/cm^2 was applied in horizontal and 13.2 C/cm^2 in vertical direction (scanned area: $1,143 \times 858 \text{ nm}^2$). The dwell time used for the fabrication of the areas and lines of this structure was exclusively $204.8 \mu\text{s}$. Schematically, the structure is depicted in Figure 9.9 a), while an SEM image of the acquired deposit on the Si(100) surface is shown in Figure 9.9 b).

The drastic change of the deposit morphology, which was induced by the post-treatment, is visible in the SEM images of Figure 9.8 c) and Figure 9.9 c). While the area deposit consisting of a square and a circle is not visible any more (Figure 9.8 c)), the “combined deposit” appears strongly changed (Figure 9.9 c)). It appears faded and both the area and the line structures, which appear rather homogeneous in the original deposit, show numerous bright and dark areas of small size in SEM. Interestingly, for both EBID deposits many particles grew at the expense of the originally deposited nanostructures. The latter appear very bright in SEM and show pronounced facets and sharp edges and corners. This becomes more evident in the high magnification SEM images depicted in Figure 9.8 e) and Figure 9.9 e). Based on the shape of these particles it is concluded that they are of crystalline nature, i.e. that they are nanocrystals.

Where only a low amount of material was deposited via EBID (due to a low electron dose; not shown), no nanocrystals have grown. This confirms that the nanocrystals grow on the expense of the originally deposited material and indicates that a minimum amount of material is necessary for nanocrystal growth. At the corresponding positions of the low electron dose structures, large “black areas” are observed instead of nanocrystals (see reference [211]).

For the deposit consisting of a square and a circle, large nanocrystals grew at the positions where the originally fabricated structures were located (compare Figure 9.8 b) and c)). In contrast to that, only two nanocrystals grew directly on the “combined deposit” (compare Figure 9.9 b) and c)), only few in close proximity and the vast majority of nanocrystals grew “outside” in a certain distance to the structure in a circular arrangement surrounding the original deposit (see Figure 9.9 d)). (Note that the SEM images were taken on the tilted sample which explains the distorted, oval shape of the corresponding circular structure.) Furthermore, in both cases the region where the original structures were located is surrounded by a kind of “corona”

(see Figure 9.8 d) and Figure 9.9 d)), separating an inner, smoother area from the surrounding surface in the form of a thin, continuous “band” [211]. Adjacent to this “corona” another “band” occurs, in which numerous small, bright particles and a large number of “black areas” appear.

In order to study the origin of the structures in Figure 9.9 d) and to find out the chemical composition of the different nanostructures, an element specific characterization via SAM was performed (see Figure 9.10). In Figure 9.10 a) an SEM image of the nanocrystals and structures after the post-treatment of annealing in oxygen is depicted. Figure 9.10 b) and c) show the SAM images for titanium and carbon, revealing the distribution of the corresponding elements at the investigated position. In both images, bright areas indicate a high amount of the element of interest while dark areas denote a low amount. Please note that the SAM images in Figure 9.10 b) and c) are slightly distorted in the horizontal direction and thus marginally deviate from the SEM image in Figure 9.10 a). This is attributed to thermal drift effects during the measurement (measurement time of ≈ 48 min). However, the SAM images clearly show the composition of the investigated structures. The following statements can be deduced:

- (1) The vast majority of the grown nanocrystals consists of a high amount of titanium (see bright features in Figure 9.10 b)) and only a very low amount of carbon (see dark features in Figure 9.10 c)). Only the nanocrystal which grew at the starting point of the horizontal EBID line shows a significant carbon contamination.
- (2) The inner, smoother area, which is surrounded by a kind of “corona”, consists both of titanium and carbon. Interestingly, the area where the combined EBID deposit was originally fabricated is depleted of titanium and enriched of carbon although at this position the highest amount of titanium is expected. From this result, a kind of diffusion process of titanium (and oxygen) in outward direction is deduced with the “corona” as frontier line [211]. The outward diffusing material should then also be the source for the nanocrystals which have grown in a circular arrangement close to the “corona”. Since a high amount of carbon remains at the position of the original deposit, one can further speculate that the titanium atoms possibly feature a higher surface mobility than the carbon atoms [211]. In addition, the homogeneous appearance of the area within the “corona” in

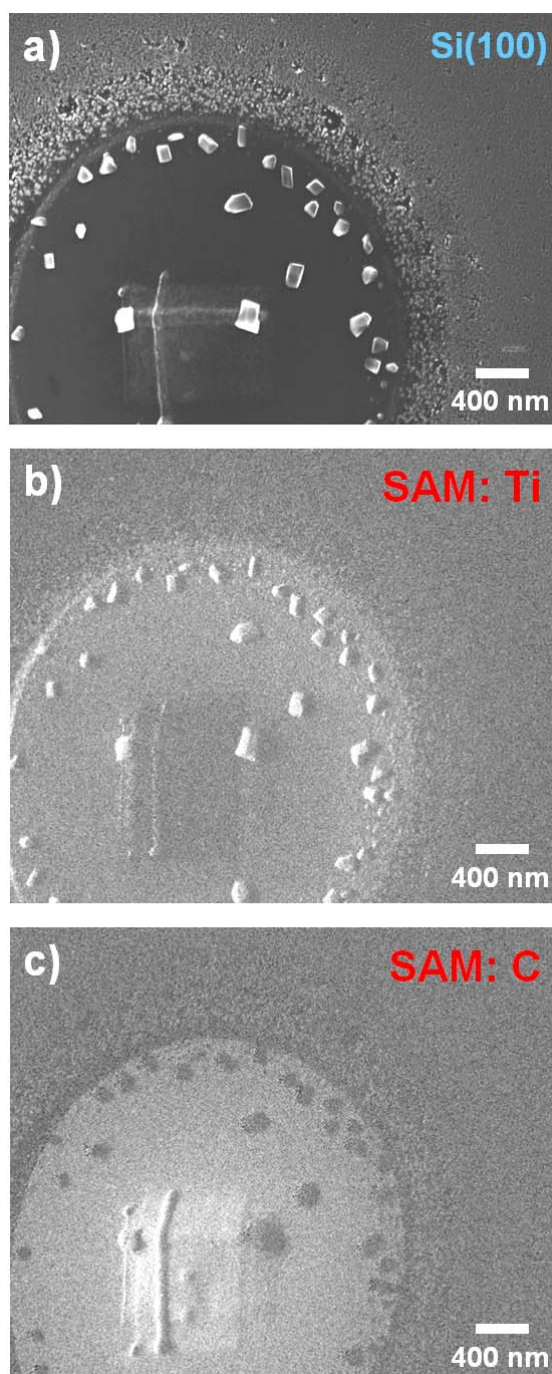


Figure 9.10: a) SEM image (15 kV, 3 nA, tilted sample) of the nanocrystals and structures depicted in Figure 9.9 d) after the post-treatment of annealing in oxygen ($t = 50$ min, $T = 1,015$ K, $p(\text{O}_2) = 8.0 \cdot 10^{-6}$ mbar). b) SAM image for the element titanium with bright areas indicating a high amount of Ti ($E_{\text{Peak}} = 381.5$ eV, $E_{\text{Bg}} = 400.5$ eV, resolution 512×384 , dwell time $t_D = 6.55$ ms). c) SAM image for the element carbon with bright areas indicating a high amount of C ($E_{\text{Peak}} = 268.0$ eV, $E_{\text{Bg}} = 290.0$ eV, resolution 512×384 , dwell time $t_D = 6.55$ ms).

both SAM images might indicate the formation of a titanium and carbon containing compound during the post-treatment-procedure [211]. The formation of a titanium carbide (TiC_x) species in this area can at least not be ruled out for the experimental conditions [255, 256].

- (3) The “corona” surrounding the inner, smooth area consists of a high amount of titanium and a low amount of carbon similar to the grown nanocrystals. This finding confirms the assumption of an outward diffusion process of titanium (and possibly oxygen) with the “corona” being the frontier line.
- (4) In the adjacent “band” outside the corona, which shows a lot of small protrusions and “black areas” in the SEM image (Figure 9.10 a)), both Ti rich and C rich structures seem to occur. However, based on the acquired SAM images it is not possible to unambiguously assign titanium rich and carbon rich structures. It can just be speculated that corresponding particles and / or areas occur close to each other.

The SAM images of Figure 9.10 provide a first hint concerning the chemical composition of the structures but the determination of the stoichiometric composition by SAM is rather difficult. Therefore, the structures were further characterized by means of local AES.

Figure 9.11 shows the result of an AES characterization of nanocrystals grown from an EBID deposit identical to the one depicted in Figure 9.8 a) and b) within the same experiment. Figure 9.11 a) shows an SEM image of the structure after the post-treatment and Figure 9.11 b) depicts the corresponding high magnification image of the nanocrystals at the position labeled in a) (orange, dashed rectangle). The local AE spectrum acquired on the central, large nanocrystal in b) (red, star-shaped marker) is shown in Figure 9.11 c). The spectrum features distinct Ti LMM and O KLL signals but shows no C KLL signal. This result demonstrates that the nanocrystals fabricated by the post-treatment procedure are indeed of high purity and confirms the SAM results. The quantitative analysis of the spectrum acquired on the nanocrystal yields a chemical composition of 34 ± 5 at. % Ti and 66 ± 5 at. % O, which means a composition of $\text{TiO}_{1.94}$ and thus a composition very close to TiO_2 . It has to be noted that the spectrum is slightly distorted in the kinetic energy region between ≈ 320 and 375 eV, which marginally hampers the quantitative analysis. However, the obtained

result demonstrates that very clean nanocrystals with a composition very close to titanium dioxide grow upon applying the post-treatment procedure of annealing in oxygen.

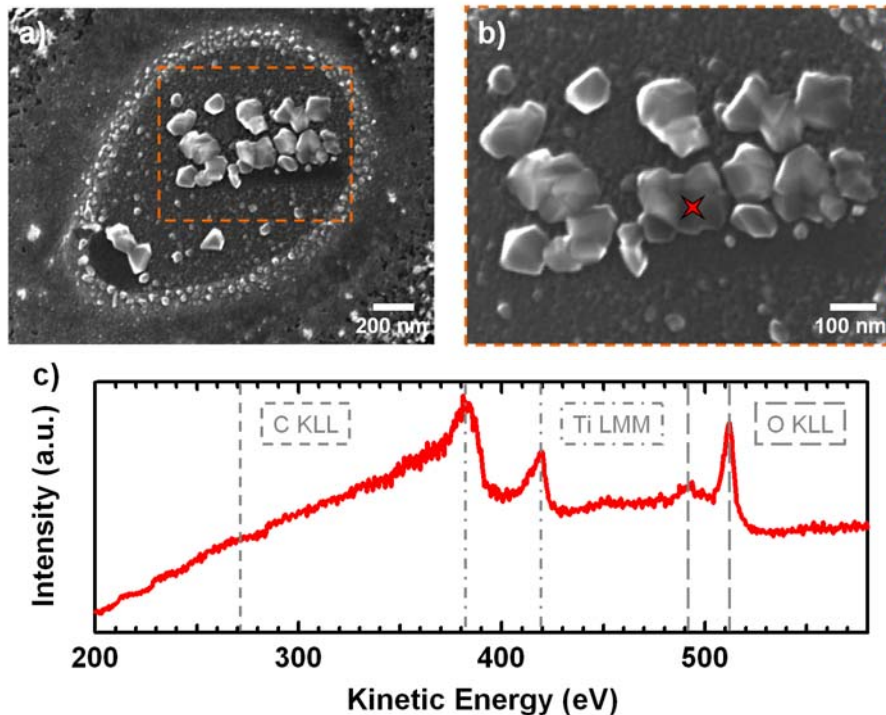


Figure 9.11: a) SEM image (15 kV, 3 nA, tilted sample) of the nanocrystals and structures grown from an EBID deposit identical to the one depicted in Figure 9.8 a) and b). b) High magnification SEM image (15 kV, 3 nA, tilted sample) of the grown nanocrystals (position marked in a) by the orange, dashed rectangle). c) Local EDS spectrum acquired on the central, large nanocrystal in b) (position indicated by the red, star-shaped marker). (Please note that for this experiment during EBID the dosing nozzle was approached closer to the sample to a distance of ≈ 8 mm.)

Concerning the origin of the structures visible in Figure 9.8 d) and Figure 9.9 d), including an inner, rather smooth area, a kind of “corona” and an adjacent “band” with a lot of small protrusions and “black areas”, it was already speculated that an outward diffusion process of titanium (and possibly oxygen) might play a role. In addition, it can be assumed that the inner, rather smooth area corresponds to the area in which initially C, Ti and O were deposited due to the ‘BSE proximity effect’.

Thus, the size of this area and the diameter of the “corona” should depend on the applied electron dose in EBID, i.e. it should increase for increasing doses. Indeed, for the structures of Figure 9.8 d) and Figure 9.11 a), which had exactly the same electron dose, the “corona” has roughly the same size. In contrast, the “corona” is significantly larger for the “combined deposit” depicted in Figure 9.9 d), which was (in total) fabricated with a considerably higher electron dose.

In order to study the morphology and the composition of the unexposed Si(100) surface after the post-treatment procedure, a characterization via SEM and local AES was performed. Figure 9.12 a) depicts the acquired SEM image. In this image, a pitted structure can be found consisting of small black regions which are partially surrounded by a bright area. The black regions seem to be “holes” in the topmost surface layers. This structure was observed at all investigated positions of the surface demonstrating that a kind of surface degradation occurred.

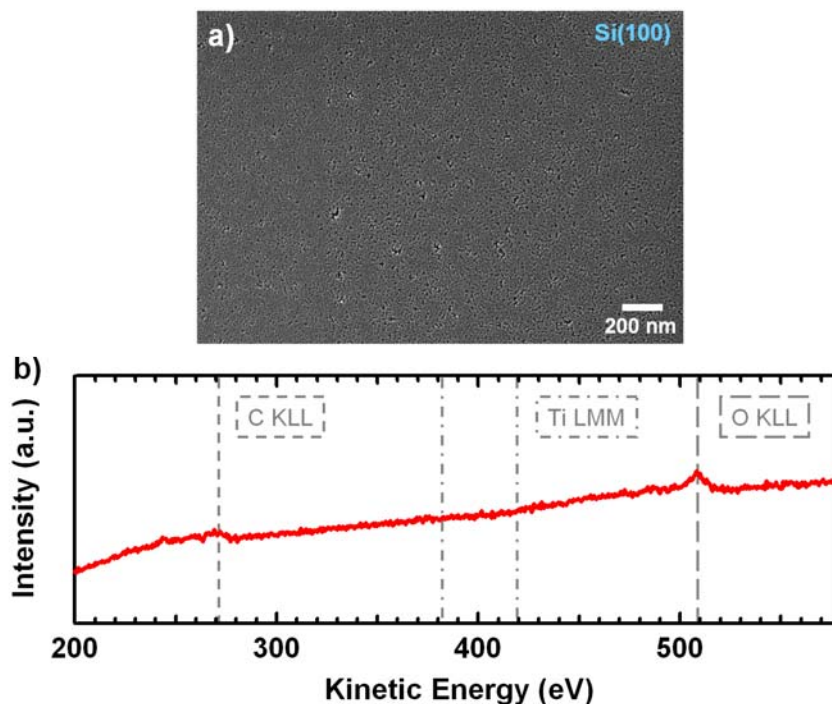


Figure 9.12: a) SEM image (15 kV, 3 nA, tilted sample) of the unexposed Si(100) surface after the post-treatment procedure. The sample shows a huge number of defects distributed homogeneously all over the surface. b) Local AE spectrum acquired directly in the center of a).

Figure 9.12 b) depicts the AE spectrum acquired directly in the center of a). The spectrum demonstrates that the unexposed surface is still slightly carbon contaminated after the treatment. In addition, a small amount of oxygen is found, which was not present before the post-treatment. Since the oxygen signal is shifted by $\approx 3 - 4$ eV to lower kinetic energies (≈ 508 eV) compared to the oxygen signal in titanium oxide (≈ 512 eV, see Chapter 7), one can conclude that the detected oxygen is of a different nature than in TiO_2 . A comparison of the kinetic energy of the O KLL Auger signal in Figure 9.12 (≈ 508 eV) to Auger data acquired on an ultra thin SiO_x film (≈ 0.5 nm) generated well-directed on a Si(100) sample in the same instrument (see reference [23], reported very recently by Marie-Madeleine Walz *et al.*) reveals a perfect agreement of the corresponding energy values. Consequently, it is concluded that a silicon oxide species has formed on top of the Si(100) surface upon the applied post-treatment procedure discussed above.

In reference [257], Starodub *et al.* distinguish between a “passive” and an “active” regime in the thermal oxidation of silicon. The authors report that for lower temperatures and higher oxygen pressures one is in the “passive” oxidation regime which leads to the formation of an amorphous silicon dioxide film on the substrate. The process follows the reaction $\text{Si (s)} + \text{O}_2 \text{ (g)} \rightarrow \text{SiO}_2 \text{ (s)}$. Instead, for higher temperatures and lower oxygen pressures one is in the “active” oxidation regime in which the volatile silicon monoxide species is formed according to the reactions $2 \text{Si (s)} + \text{O}_2 \text{ (g)} \rightarrow 2 \text{SiO (g)}$ and $\text{Si (s)} + \text{SiO}_2 \text{ (s)} \rightarrow 2 \text{SiO (g)}$. Silicon monoxide sublimates at elevated temperature into the vacuum and thus the oxide free silicon surface is maintained [257]. Considering the reported p,T-phase diagram for Si(100) oxidation [257], silicon surface oxidation in the above described post-treatment procedure occurred in the “passive” oxidation regime. Thus, the formation of a thin, amorphous silicon dioxide layer on the surface is reasonable, which is consistent with the above made assumption.

Based on the references [258-262] one can further speculate about the origin and nature of the pitted structure visible in SEM (see Figure 9.12 a)). The authors studied the thermal decomposition of thin and ultra thin silicon oxide layers on Si(100) by UHV annealing. Tromp *et al.* [258] found that the decomposition process follows a spatially inhomogeneous reaction in which initially holes exposing the clean Si surface are formed by SiO_2 removal. Then, the decomposition process occurs at the

silicon / silicon oxide boundary according to the reaction $\text{Si (s)} + \text{SiO}_2 \text{ (s)} \rightarrow 2 \text{SiO (g)}$ with silicon monoxide desorbing into the vacuum. This model was confirmed by Miyata *et al.* [259] and further studied by several other groups, see e.g. [260-262], which consistently report the formation of “voids” in the silicon oxide layer. In the applied post-treatment procedure reported above, oxygen was dosed during the whole annealing process. Despite this difference to references [258-262], very similar processes and chemical reactions are assumed to occur during the post-treatment. Thus, the small black regions in Figure 9.12 a) are interpreted as holes / voids in the formed, thin silicon oxide layer. Evidence for this interpretation is given by the AFM data presented in Chapter 9.3 (see Figure 9.19 c)).

In references [260, 261] it is further reported that the holes / voids grow significantly with time. This was observed in a different experiment from the one described above, which was performed on a Si(111)-(7x7) surface [211]. In this experiment, higher temperatures (up to 1,115 K), a lower oxygen background pressure ($3.0 \cdot 10^{-7}$ mbar) and an extended annealing time (≈ 15 h) were applied. It was found that the holes / voids (appearing black in SEM) grow in lateral direction at the expense of the surrounding silicon oxide region (appearing bright in SEM). Interestingly, on the Si(111)-(7x7) surface the holes grow along the crystallographic axes of the surface, forming star-shaped hole structures with 60° and 120° angles between the star apexes (not shown in this work, see Chapter 6.3.2.2 of reference [211]).

To address the question whether the growth of clean titanium oxide nanocrystals can also be induced on a different sample material via a similar post-treatment procedure, a line pattern deposited on Au(111) was investigated. The line pattern is the pattern that was introduced in Chapter 9.1.1 (see Figure 9.2).

In the applied post-treatment procedure, the Au(111) sample was heated in the analysis chamber slowly from RT to 705 K within 1 h and 20 min at an oxygen background pressure of $3.0 \cdot 10^{-7}$ mbar [99]. Simultaneously, SEM images were recorded to determine the onset of a possible nanocrystal growth. Then, the temperature of 705 K was held for further 1 h and 20 min at the adjusted O_2 background pressure, which means that a total heating time of 2 h and 40 min was applied.

It has to be noted that for this experiment, deviating from the other ones performed in the analysis chamber, the nozzle of the gas doser (through which O_2 was dosed) was

close to the sample stage ($x_{LT} = 85$). Thus, the local pressure of oxygen on the sample surface was higher than the adjusted background pressure of $3.0 \cdot 10^{-7}$ mbar (see Chapter 6). Moreover, the heating power and sample temperature during the experiment were limited since the sample was heated via radiative heating on the stage in the analysis chamber (for details see page 91 of reference [263]).

The result of the post-treatment procedure is displayed in Figure 9.13. While Figure 9.13 a) shows an SEM image of the line pattern before the treatment, in Figure 9.13 b) the pattern is depicted while annealing in O_2 , close to the end of the applied procedure. The SEM image in b) clearly shows that small particles grow, preferably at the edges of the deposited line pattern. It was found that the onset of nanoparticle growth occurred at a temperature of 705 K and thereafter the nanoparticles grew fractionally in size in the remaining post-treatment time of 1 h and 20 min. Image enlargements of the grown particles, generated from b), are shown in

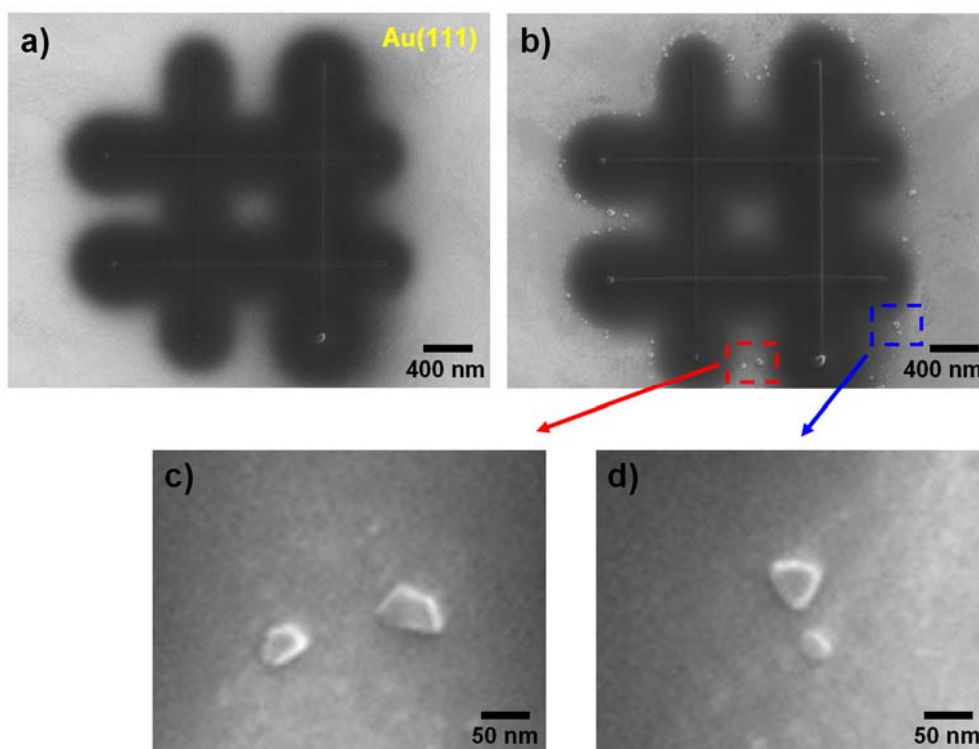


Figure 9.13: a) SEM image of a line pattern fabricated on the Au(111) sample. b) SEM image of the line pattern after the post-treatment of annealing in oxygen ($t = 2$ h 40 min, $T_{max} = 705$ K, $p(O_2) = 3.0 \cdot 10^{-7}$ mbar). c) and d) Image enlargements, generated from b), depicting the grown nanocrystals due to the post-treatment.

Figure 9.13 c) and d). They demonstrate that the grown particles show regular geometries (trapeze and triangle like) with sharp and defined edges. Since also the top sides of these particles appear flat and homogeneous in SEM, edges and top sides are assigned as facets and the particles are consequently assigned as titanium oxide nanocrystals. Since the nanocrystals grew only to a very small size upon the applied experimental parameters, no characterization via AES, Auger electron line scans (AELS) or SAM could be conducted.

As expected, the nanocrystals appear very bright in SEM (see Figure 9.13 b) to d)) and in particular much brighter than the original EBID deposits. This can be explained by different contrast mechanisms which have recently been discussed in detail by Marie-Madeleine Walz [99]. The relevant contrasts are a chemical contrast, a topographical contrast or a work function contrast, which may all contribute to the appearance in SEM.

The chemical contrast (material contrast) is based on the presumably very low carbon content of the nanocrystals. Therefore, the average atomic number of the nanocrystals should be increased compared to the original EBID deposits and thus both the backscattering coefficient η and the secondary electron yield δ should be higher [25, 28]. The latter explains an increased brightness of the nanoparticles. Topographical contrast explains the high brightness of the edges of the nanocrystals. This is due to the fact that enhanced SE emission occurs at the edges of structures due to the dependency of δ on the surface tilt (surface-tilt contrast) [25, 28]. In addition, also a kind of work function contrast can generally affect the brightness of materials in SEM. However, the work function of rutile $\text{TiO}_2(110)$ is 4.20 eV [195], the one of $\text{Au}(111)$ is 5.31 eV [264, 265] and the one of carbon is 4.8 eV in HOPG [266] and can vary between 3.2 and 5.2 eV in diamond in dependence of the grain size [267]. Therefore, work function contrast is considered to play only a minor role. It is assumed that the chemical contrast (material contrast) and in particular the topographical contrast explain the brightness of the different structures in Figure 9.13 b) to d).

Finally, two further results of the post-treatment experiment on gold are discussed. First, it was found that the nanocrystals in Figure 9.13 grew without exception at the outer edges of the line pattern while no nanocrystal growth was observed in the area

enclosed by the four lines. This result is somehow unexpected since diffusion of initially deposited material should occur in all lateral directions upon annealing [99]. One possible explanation is that a much higher amount of oxygen can be supplied to the outer edges of the pattern by diffusion of adsorbed oxygen on Au(111) from outside. Thus, the deficiency of oxygen in the center of the line pattern might be a possible reason for the experimental result.

Secondly, it was found that for a deposited area structure on Au(111) (not shown; electron dose: 9.86 C/cm^2) almost no nanocrystal growth occurred at the applied conditions. Neither on top of this deposit nor at the edges crystalline structures were observed (solely one detectable nanocrystal grew in the region of an unknown scan artifact at the left side of the deposit, see reference [99]). It is assumed that the growth of nanocrystals might possibly be induced also at this structure by a higher temperature and an extended annealing time. As an outlook, these conditions should be applied in further experiments on Au(111).

To study the growth of the nanocrystals on silicon in more detail and to observe the growth process *in situ* via SEM, an experiment was performed in which a line pattern on Si(100) was investigated during a post-treatment comprising annealing in oxygen [225]. The investigated line pattern consists of three perpendicular lines and is the one which was already analyzed in detail in previous chapters (see also Figures 7.4 a), 8.1 a) and 9.5 a)). The applied electron doses for the lines were 116, 232 and $463 \mu\text{C/cm}$, with the dose rising from the left vertical line to the horizontal one and right vertical one.

In the applied post-treatment procedure, the sample was heated *in situ* slowly up to a temperature of 1,010 K with an oxygen background pressure of $3.0 \cdot 10^{-7}$ mbar. The nozzle of the gas doser, through which molecular oxygen was dosed, was retracted from the sample stage ($x_{\text{LT}} = 55$). Thus, the local pressure of oxygen on the sample surface should correspond to the background pressure. Detailed information concerning the post-treatment procedure with all heating steps is depicted in Table 16.6 in the Appendix of this work (Chapter 16.4).

The whole post-treatment process was followed *in situ* by SEM and a corresponding time lapse movie with the full image set is given in the Supporting Information of reference [225]. Selected images showing the crossing point of the horizontal and

right vertical line are depicted in Figure 9.14 a) to d). Figure 9.14 a) was acquired prior to the post-treatment procedure. At 860 K (after 12 min of heating) the onset of the growth of small nanoparticles was observed. This can be comprehended from Figure 9.14 b), which was measured 21 min after the beginning of heating (i.e. 9 min after the onset of nanoparticle formation), still at 860 K. Particles of different sizes are observed, with the larger ones growing directly at the lines ($\approx 15 - 50$ nm at the horizontal line and $\approx 20 - 65$ nm at the vertical line) and smaller ones growing in the surroundings ($\approx 10 - 30$ nm). Upon further heating and oxygen dosage existing particles do not only grow continuously but also a large number of new particles forms, as is evident from Figure 9.14 c), which was acquired at 950 K after a heating time of 149 min. In the time span in between Figures 9.14 b) and c) individual particles easily grow 20 nm and more in diameter and most of them develop pronounced facets. This is particularly evident for the larger ones close to the lines and strongly indicates that these particles are nanocrystals, again. Finally, the SEM image of Figure 9.14 d) was acquired at 1,010 K after a total heating time of 188 min. It shows the surface morphology of the whole line pattern after the post-treatment procedure (to be compared to Figure 7.4 a), 8.1 a) or 9.5 a)). The sizes of the nanocrystals further increased, ranging now from ≈ 30 to 70 nm (horizontal line), ≈ 45 to 85 nm (right vertical line) and ≈ 15 to 40 nm (surroundings). At all times, the largest nanocrystals can be observed at the right vertical line, i.e. the line with the highest total electron exposure and thus the largest amount of deposited material. Furthermore, the image series in Figure 9.14 and the corresponding movie in the Supporting Information of reference [225] reveal that the lines thin out while the nanocrystals are growing. Obviously, the deposited material in the lines is consumed for the growth of the nanocrystals.

With increasing distance to the lines, both the number and size of the nanocrystals is decreasing steadily and at large distances the amount of deposited material is obviously too low to grow particles visible in SEM. The density of the nanocrystals close to the original lines increases with the applied electron dose, which becomes evident when one compares the left and right vertical line in Figure 9.14 d).

The composition of the observed nanocrystals cannot be directly derived from the SEM images. Even though, the crystalline appearance indicates a pure compound, i.e. a titanium oxide species. To verify this assumption, local AES measurements were performed on the nanocrystals located close to the lines. The quantitative

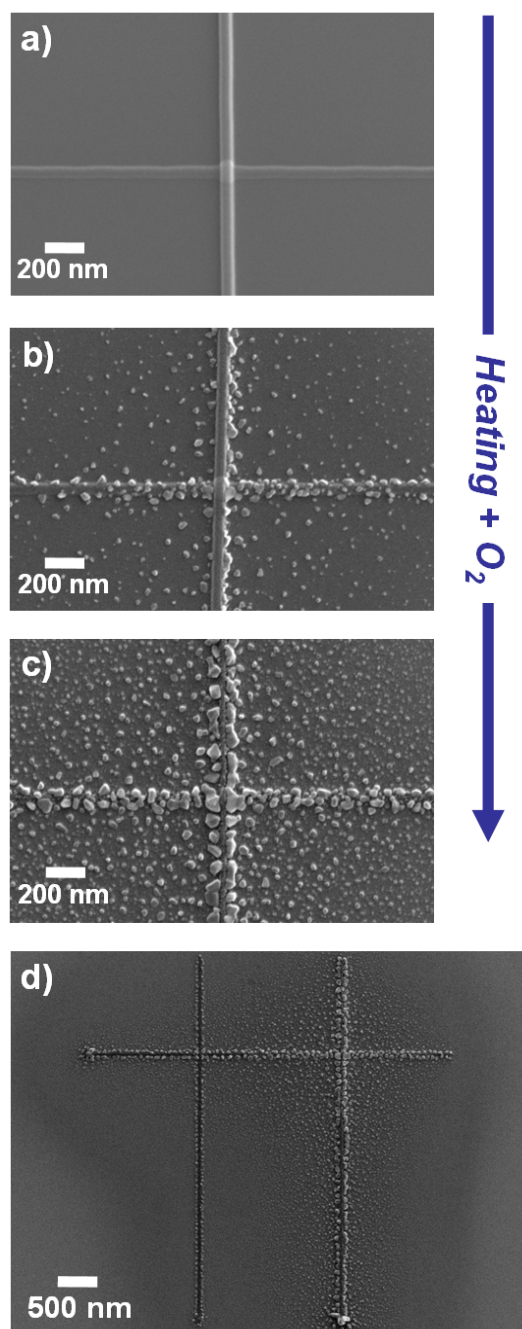


Figure 9.14: SEM images of an EBID line deposit fabricated with TTIP on a Si(100) sample. The images are selected from a movie provided in the Supporting Information of reference [225]. They were acquired during heating the as-deposited line structure slowly to $\approx 1,010$ K in an oxygen background pressure of $p(\text{O}_2) = 3.0 \cdot 10^{-7}$ mbar and depict the growth of titanium oxide nanocrystals at the line pattern and in its surroundings. a) Before heating (RT). b) After 21 min ($T = 860$ K). (c) After 149 min ($T = 950$ K). (d) After 188 min ($T = 1,010$ K).

analysis confirms that the nanocrystals show a high purity (carbon contamination level of only 6 – 8 at. %) and reveals an oxygen to titanium ratio of 1.7 – 1.9, i.e. a ratio very close to the one of titanium dioxide. It has to be noted that local AES measurements on comparably small structures are influenced by the phenomenon of ‘background contribution’ (see also Chapters 2.3 and 13.2), which is a well-known effect in the characterization of nanostructures and nanoparticles via Auger based analysis tools (AES, SAM) [36-38]. This means that Auger electrons are released also in close lateral proximity of the nanocrystals of interest due to the excitation by backscattered high energy primary electrons [36-38]. Thus, the carbon contamination level is most probably overestimated, since a contribution from the surrounding region is detected via AES, as well. This assumption is confirmed by the AES data discussed in Chapter 9.3, which demonstrates that carbon can indeed be detected in the surrounding of the nanocrystals. Moreover, the oxygen to titanium ratio in the nanocrystals, being slightly smaller than the ideal one of 2:1 in TiO_2 , can be explained by electron stimulated desorption (ESD) of oxygen [6, 104-107] caused by the *in situ* observation of the growth process via SEM.

The growth of nanocrystals occurred not only at the line pattern that is depicted in Figure 9.14, but also on other deposits of the initial EBID process which were not observed *in situ* via SEM. Nanocrystals grown with a high density on top of the initial EBID structure were found on an area deposit, which was fabricated with an electron dose of 9.86 C/cm^2 (see Figure 9.15). The initial area deposit (before the post-treatment procedure was applied) is depicted in the Figures 7.2 a) and 7.7 a). In Figure 9.15 a), the entire area deposit and its surrounding after the post-treatment procedure are depicted. In the rectangular area of the initial EBID deposit, the occurrence of large nanocrystals is found, which show facets and sharp edges. Additionally, also in the surrounding of this area the growth of nanoparticles is observed. However, these particles are clearly reduced in size, which can be traced back to the significantly lower amount of material that was deposited there solely due to proximity effects. In addition, the SEM image in Figure 9.15 a) shows the occurrence of a dark circular area surrounding the initial structure. Measured from the edges of the central, rectangular structure in outward direction to the outer edge of this dark area one finds a distance of $\approx 1.5 \mu\text{m}$, resulting in a horizontal diameter of $5.3 \mu\text{m}$ and a vertical diameter of $4.7 \mu\text{m}$. Based on the (roughly) circular shape of

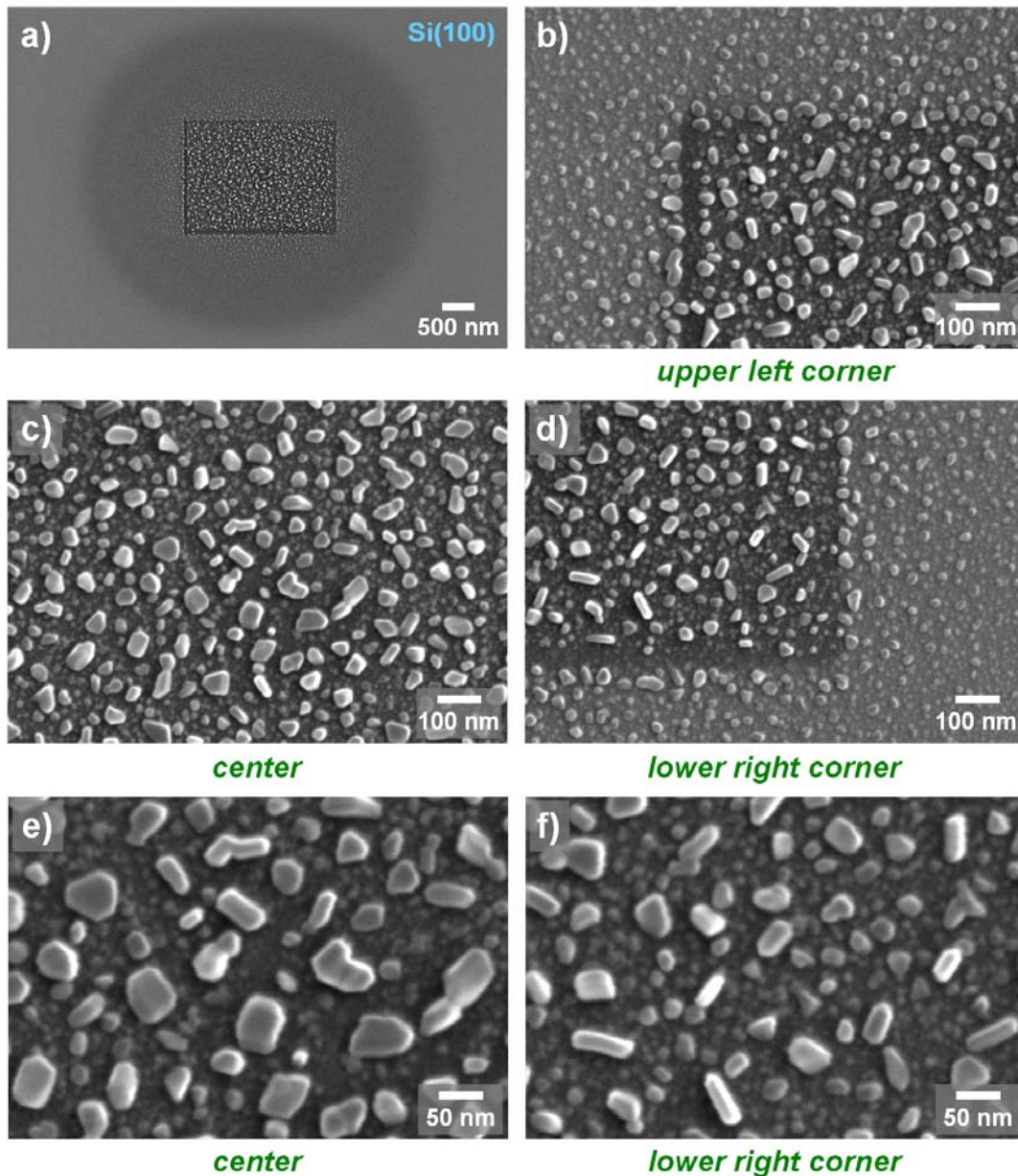


Figure 9.15: SEM images of an EBID area deposit fabricated with TTIP on a Si(100) sample with nanocrystals grown in the applied post-treatment procedure of annealing in oxygen ($t = 3\text{ h } 15\text{ min}$, $T_{max} = 1,010\text{ K}$, $p(\text{O}_2) = 3.0 \cdot 10^{-7}\text{ mbar}$). a) Entire structure inclusive the close surrounding. b) - d) Upper left corner, center and lower right corner with higher magnification. e) - f) Center and lower right corner strongly magnified.

the dark area and its lateral size it is assumed that it corresponds to the area that is influenced by the initially applied primary electron beam for structure generation and the resulting forward and backward scattered electrons (FSE and BSE) (compare

Chapter 8). Consequently, it should also correspond to the area in which material deposition occurred (during EBID) with a decreasing amount of material deposited for increasing distance to the central structure.

The different sizes of the grown nanocrystals can be observed more clearly in the SEM images acquired at higher magnification in the Figures 9.15 b) to d). Apart from the obvious size difference at the border of the initially targeted rectangular deposit one additionally finds that the nanocrystal size decreases in b) and d) with increasing distance to the latter. This observation is accordant to the assumption discussed above.

High magnification SEM images of the nanocrystals are depicted in the Figures 9.15 e) and f). Concerning the chemical composition of these nanostructures it was found that they are most probably a titanium dioxide species (see discussion above). Additionally to that, it would be highly desirable to address their mineral form. In literature, an assignment of the mineral form and of different crystal faces to titania nanoparticles was performed based on the shape of the crystals [268, 269]. However, in both references the investigated crystals are much larger in size (roughly in the range of ≈ 1 to $3 \mu\text{m}$) than the ones investigated in this work. The small size of the nanocrystals discussed here hampers the classification based on the crystal shape. (An overview of the characteristic crystal shapes for the three mineral forms rutile, anatase and brookite can be found in reference [270].)

Despite the fact that a definite assignment is not possible, one can speculate about the mineral form based on further references from literature. Diebold reports that, interestingly, TiO_2 nanostructures are almost invariably either amorphous or of the anatase form [6], although rutile is the thermodynamically most stable macrocrystalline phase. Correspondingly, Rosenthal reports that upon syntheses of nanoparticles most commonly rather anatase and brookite are formed [193] and Ranade *et al.* report that anatase and brookite are common in fine grained, nanoscale natural and synthetic samples [271]. In contrast to that, a strong size dependence of the thermodynamic phase stability of nanostructured titania was reported by Zhang and Banfield [272, 273] and it is well-known that transformations of the different mineral forms occur upon heating and concomitant coarsening [271-273]. For these phase transformations Ranade *et al.* found that the precise conditions like the particle size, the starting material, the temperature and other parameters play a significant role [271] and Zhang and Banfield report that the

surface free energy and surface stress of the grown particles are crucial, as well [272]. Based on the references [6, 193, 271] and based on the works of Berger *et al.* [252] and Elser *et al.* [253], who fabricated anatase TiO₂ nanocrystals by a similar route and post-treatment as presented in this work, it is assumed that the here shown nanocrystals are most probably of the mineral form anatase. However, further investigations should be conducted to confirm this assumption.

On a different area deposit than the one in Figure 9.15, which was fabricated with a lower electron dose (by a factor of 4), also the growth of nanocrystals was found. However, these nanocrystals are much smaller in size which confirms the assumption that the growth of the nanocrystals depends on the amount of initially deposited material and thus on the initially applied electron dose for the EBID structures.

Since nanocrystals grow also on deposits which were not observed *in situ* via SEM during the applied post-treatment procedure, one can clearly rule out that the electron beam of the SEM is the driving force for nanocrystal growth. However, a certain influence of the electron beam on the growth behavior of the nanocrystals has to be stated. This can be derived from the comparison of line structures with grown nanocrystals which were fabricated with identical electron dose in EBID but from which only one line structure was followed *in situ* via SEM while the other one was not observed during the post-treatment procedure. It was found that the nanocrystals grown directly at the lines depict morphological differences for both line structures. The nanocrystals which have grown at the *in situ* watched line structure are rather separated from each other. In contrast to this, the nanocrystals grown at the not *in situ* observed line structure seem to merge and grow together. Thus, one can speculate that prolonged electron beam irradiation via the SEM during the post-treatment procedure might induce the separated growth of single nanocrystals next to each other. An explanation for this possibly is a slight negative charging of the nanocrystals upon electron exposure. Consequently, slight electrostatic repulsion of the nanocrystals would diminish their growth in lateral direction, would rather enforce the growth in height and thus induce the growth of rather separated nanocrystals. In contrast, the omitted *in situ* observation via SEM might enable the nanocrystals to grow together easily as soon as they contact each other and might enable the formation of larger, merged nanocrystals. It has to be noted however that more

experiments are necessary in this field to completely clarify the influence of the electron beam on the growth behavior of the nanostructures.

In summary, one can state that by applying a post-treatment procedure comprising annealing the sample *in situ* in the UHV instrument and simultaneously dosing molecular oxygen to a low background pressure the growth of titanium oxide nanocrystals can be induced at and on the originally generated EBID structures [225]. These nanocrystals show a high purity, which was verified by local AES and SAM measurements, and a stoichiometry very close to the one of TiO_2 . Due to the proximity effects in EBID and concomitant material deposition in close proximity to the targeted structures, the nanocrystals additionally grow also in the surrounding of these structures [225].

9.3 Two-step post-treatment procedure for clean localized nanostructures

The overview micrograph in Figure 9.14 d) (previous chapter) demonstrates that nanocrystals do not only grow in close vicinity of the lines but also widely spread around the originally irradiated area. The same result was acquired for the area deposit depicted in Figure 9.15 a). This behavior is in line with unintended material deposition during the EBID process as a result of the proximity effects (see Chapter 8). This observation obviously constitutes a serious drawback, if one targets the fabrication of TiO_x nanocrystals confined to a pre-defined position.

In the following, a novel post-treatment procedure is introduced to overcome this problem. Based on the topography (AFM) of the lines and the thickness of the unintentionally deposited layer (AES) between the lines due to proximity effects (e.g. less than 2 % for the position of the yellow marker in Figure 8.1 a) as compared to the right vertical line) it appeared feasible to remove the unintentionally deposited material via sputtering, while leaving sufficient material at the positions of the lines. The sputtering parameters have to be chosen accordingly. In this work, the parameters were chosen to obtain a comparably low sputter rate of $\approx 1.4 \text{ nm / h}$ (details see Chapters 3.6.7 and 9.1.1). This enabled to follow the process stepwise, to keep the impact on the fabricated lines very low and also to minimize damage to

the silicon surface (e.g. roughening / napping). In the following, this procedure is denoted as 'moderate sputtering', targeting primarily at the removal of unintentionally deposited material due to proximity effects while conserving the intended structures. The idea is then to combine the sputtering and thermal treatment in an oxygen atmosphere to realize a localized nanocrystal growth only at the positions of the intended structures.

This idea was tested with a line pattern identical to the one in Figure 9.14. After the EBID process, the sample was sputtered with argon ions. Sputtering was performed in two steps comprising 25 min in the first treatment and 60 min in the second one, resulting in a total sputtering time of 85 min. The SEM image in Figure 9.16 a), acquired after sputtering, shows that the lines were preserved and the contrast between lines and the remaining surface seems to be unchanged. Via AES it was confirmed that the amount of unintentionally deposited material in the surroundings of the lines indeed decreased significantly (compare Figure 9.5). Between the lines (at a position somewhat closer to both the horizontal and the right vertical line than the yellow marker in Figure 8.1 a)), the titanium signal was lowered to $\approx 32\%$ and the oxygen signals to $\approx 9\%$ of their original values. From the Si signal damping, a reduction of the layer thickness of the unintentionally deposited material from 2.7 ± 0.9 to 0.6 ± 0.3 nm, i.e. by 78 %, was determined.

In the next step, the same post-treatment procedure by heating in an oxygen atmosphere was applied that was used for the unsputtered sample (see above in Chapter 9.2; experimental details for both treatments see Table 16.6 in the Appendix of this work). Again, the process was followed *in situ* via SEM. Selected images showing the crossing point of the horizontal and right vertical line are depicted in the Figures 9.16 a) to d) and a corresponding movie file with the full image set can be found in the Supporting Information of reference [225]. Figure 9.16 a) depicts the right crossing point of the deposited and sputtered EBID structure prior to the post-treatment procedure. At a temperature of 860 K (after 15 min of heating) the onset of nanocrystal growth was observed. The image in Figure 9.16 b) was acquired 25 min after the beginning of heating (i.e. 10 min after the onset of nanocrystal formation), at a temperature of 860 K. The size of the nanoparticles roughly ranges from 10 to 65 nm. The nanocrystals at the right vertical line, which was fabricated with the highest electron dose, apparently grow faster and larger than the ones at the horizontal line (compare also the movie in the Supporting Information of reference

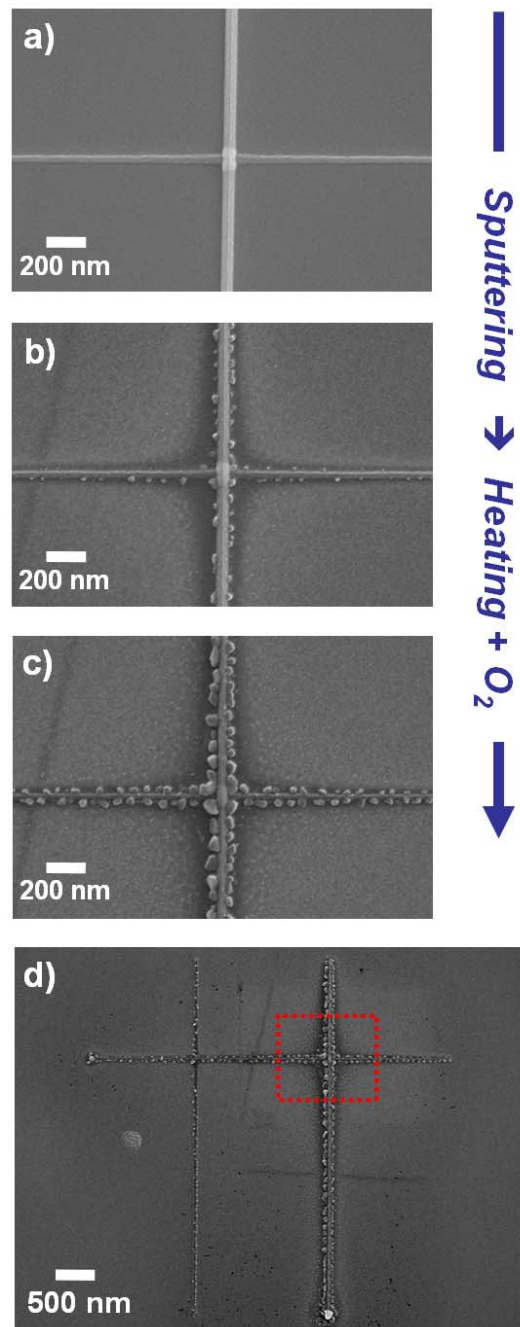


Figure 9.16: SEM images of an EBID line deposit fabricated with TTIP on a Si(100) sample. The images are selected from a movie provided in the Supporting Information of reference [225]. They were acquired during heating the deposited and afterwards moderately sputtered line structure slowly to $\approx 1,010$ K in an oxygen background pressure of $p(\text{O}_2) = 3.0 \cdot 10^{-7}$ mbar and depict the growth of titanium oxide nanocrystals only in close proximity to the lines. a) Before heating (RT). b) After 25 min ($T = 860$ K). c) After 146 min ($T = 980$ K). d) After the post-treatment procedure with a total heating time of 193 min (imaged at RT).

[225]). Figure 9.16 c) shows the surface after a total heating time of 146 min at a temperature of 980 K. Evidently, the nanocrystals again grow continuously in number and size upon prolonged heating and oxygen dosage, but this time only in close proximity to the lines, i.e. close to positions directly irradiated by the electron beam. At the horizontal line they grow rather separately, almost equidistant to each other ($\approx 25 - 60$ nm). The nanocrystals at the right vertical line are larger ($\approx 40 - 85$ nm), begin to contact each other and partially merge. Figure 9.16 d) was acquired after the post-treatment procedure was finished. It shows the surface morphology of the whole line pattern (compare to Figure 7.4 a), 8.1 a) or 9.5 a)) at RT. The crystals reach sizes in the range of 25 – 75 nm for the horizontal line and 40 – 95 nm for the right vertical line.

The direct comparison of the Figures 9.16 d) and Figure 9.14 d) shows the effect of moderate sputtering of the surface after the EBID process. The as-deposited structures in Figure 9.14 d) exhibit nanocrystal growth not only at and in the direct vicinity of the line structures but also in their surroundings, resulting from unintended material deposition due to the proximity effects. For the sputtered sample, the post-treatment procedure yields nanocrystal growth only in the direct vicinity of the line structures, as is evident from Figure 9.16 d). Thus, the applied post-treatment procedure appears as a promising tool to ‘overcome’ the limitations of EBID imposed by proximity effects.

To verify the effectiveness of the post-treatment procedure and to investigate the status of the surface in the surroundings of the deposited lines, the corresponding sample was investigated in more detail. Figure 9.17 a) shows a high resolution SEM image of the region of the top right crossing point of the fabricated line pattern (at the position indicated in Figure 9.16 d) by the red, dashed rectangle). Evidently, the nanocrystals are preferentially found next to the original lines. In the surroundings, very small bright protrusions are also visible. To determine the chemical composition, i.e. in particular to verify the purity of the nanocrystals, local AES was performed at different positions on the sample, indicated by colored markers in Figure 9.17 a). In Figure 9.17 b) the corresponding AE spectra are depicted. The red spectrum measured on the nanocrystal is clearly dominated by the large Ti peaks at 383 and 419 eV and the O peaks at 492 and 512 eV. In contrast, the carbon peak is very small, being just slightly above the detection limit. A quantitative analysis of the corresponding chemical composition yields a carbon contamination level of only

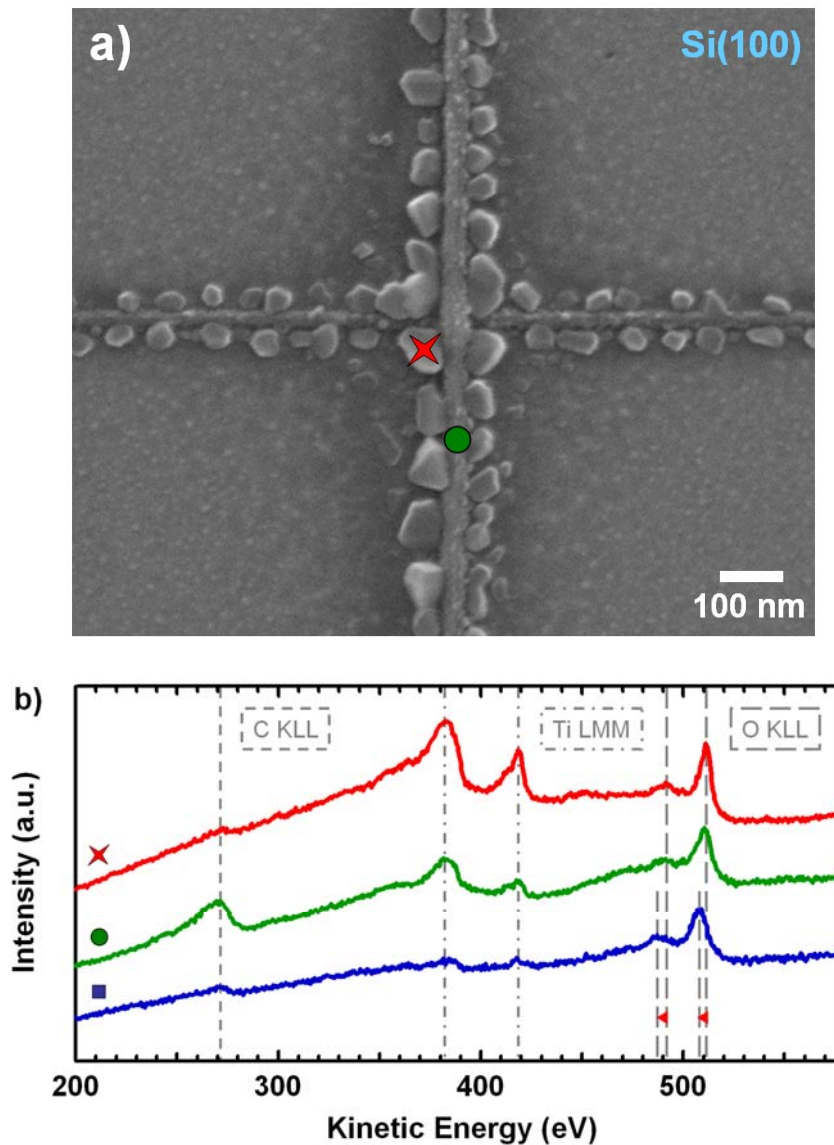


Figure 9.17: a) SEM image of the top right crossing point of the fabricated titanium oxide lines (position labeled in Figure 9.16 d)). The markers correspond to the positions where local AES was performed. b) AE spectra taken on a titanium oxide nanocrystal (red spectrum), on the residual line between the nanocrystals (green spectrum) and in the region between the lines (blue spectrum). The observed peaks correspond to the C KLL, Ti LMM, Ti LMV and O KLL transitions [225].

≈ 4 at. % and reveals an oxygen to titanium ratio of ≈ 1.8 ($\approx 34 \pm 5$ at. % Ti and $\approx 62 \pm 5$ at. % O), i.e. a ratio very close to the one of titanium dioxide. Accordingly to the data discussed in Chapter 9.2, the smaller O / Ti ratio of the nanocrystal than the

ideal one of 2:1 in TiO₂ can be explained by electron stimulated desorption (ESD) of oxygen [6, 104-107] caused by the *in situ* observation of the growth process via SEM.

The green spectrum in Figure 9.17 b), acquired directly on the residual line between the nanocrystals, does not only show the Ti and O Auger signals, but also a significant C peak at 271 eV, indicating that the remains of the initially fabricated line are still contaminated with carbon. From this chemical analysis one can unambiguously conclude that the observed nanocrystals are indeed composed of titanium oxide, and that the material deposited by EBID (the lines) serves as the resource for nanocrystal growth during the post-treatment procedure. This becomes even more evident if one considers that electron scattering events also occur during AES (phenomenon of 'background contribution' [36-38], see also Chapters 2.3, 9.2 and 13.2). Effectively, areas or features away from the point of electron beam impact can also contribute to the corresponding local Auger spectra due to the excitation by backscattered high energy primary electrons. This 'background signal contribution' due to electron backscattering is also discussed in the literature concerning the characterization of nanostructures and nanoparticles via Auger based analysis tools (AES, SAM) [36-38]. It could be considered by an effective point-spread function. Even though the corresponding function is not known in the actual case, the effect could only cause a contamination signal (e.g. a carbon signal from the residual line: see green spectrum). Consequently, the cleanliness of the investigated local nanocrystal is as indicated by the Auger spectrum or better. This means that the carbon contamination level is probably even smaller than the determined value of ≈ 4 at. %.

The blue spectrum in Figure 9.17 b) was measured at a position on the surface, which was not irradiated by the electron beam during EBID (between the lines). While the carbon and titanium signals exhibit a very low intensity, the spectrum is dominated by large oxygen peaks. The very small Ti peaks in the surrounding of the lines illustrates that, in the post-treatment by moderate sputtering, the amount of unintentionally deposited material due to the 'BSE proximity effect' was decreased significantly, but not completely. Thus, it is concluded that the small protrusions in the surroundings of the line pattern and the grown nanocrystals (see Figure 9.17 a)) are small titanium oxide nanoparticles. They did not grow to a larger size because the small amount of material at these positions (after moderate sputtering) was rapidly

consumed and, furthermore, the distance to the lines is too large such that no diffusion of titanium and oxygen seemed to occur. The analysis of the kinetic energies of the oxygen Auger peaks of Figure 9.17 b) reveals a peak shift by $\approx 3 - 4$ eV to lower kinetic energies for the blue spectrum, i.e. for the unexposed area. As the substrate is silicon and consequently the Si KLL Auger peaks at 1558, 1596 and 1615 eV were detected at a position also not directly exposed to the electron beam (not shown), the O Auger peaks in the blue spectrum can be assigned to a thin silicon oxide layer, which formed upon heating the sample in an oxygen atmosphere in the post-treatment process. This observation and interpretation is in full agreement with the data discussed in Chapter 9.2. In addition, the kinetic energy of the large O KLL Auger signal of the thin silicon oxide layer shown here (≈ 508 eV) is again in perfect agreement with the energy value very recently reported by Marie-Madeleine Walz *et al.* for an ultra thin SiO_x film on Si(001), generated and measured in the same instrument [23].

To determine the height of the grown nanocrystals, *ex situ* AFM measurements were performed on the line structures and the grown titanium oxide nanocrystals depicted in the Figures 9.16 and 9.17 (details see Chapter 3.6.6). The results of these investigations are depicted in Figure 9.18.

Figure 9.18 a) shows an AFM image of the entire line pattern visualizing the residual lines and the grown nanocrystals exclusively in their close proximity. The bright, circular structure to the left of the pattern is a particle which is also visible in Figure 9.16 d). Since it was already observed directly after the EBID process, it is assumed that it is a contamination particle of the Si(100) surface. In addition, the image shows an artifact caused by the background subtraction during the AFM measurement, namely the dark stripe to the left and right of the horizontal line. It is noted that this artifact does not affect the acquired height information when height profiles are set parallel to the scan direction (as done in Figure 9.18 c)). An AFM image of the top right crossing point acquired with higher magnification and the scan direction rotated by 45° is depicted in Figure 9.18 b). This image demonstrates that the TiO_x nanocrystals have grown to a considerable height, i.e. the ones directly at the lines roughly between 25 and 70 nm, and that the highest nanocrystals have grown directly at the top right crossing point of the line pattern. For the horizontal line of the pattern (going from top left to bottom right in b)) a range for the nanocrystal

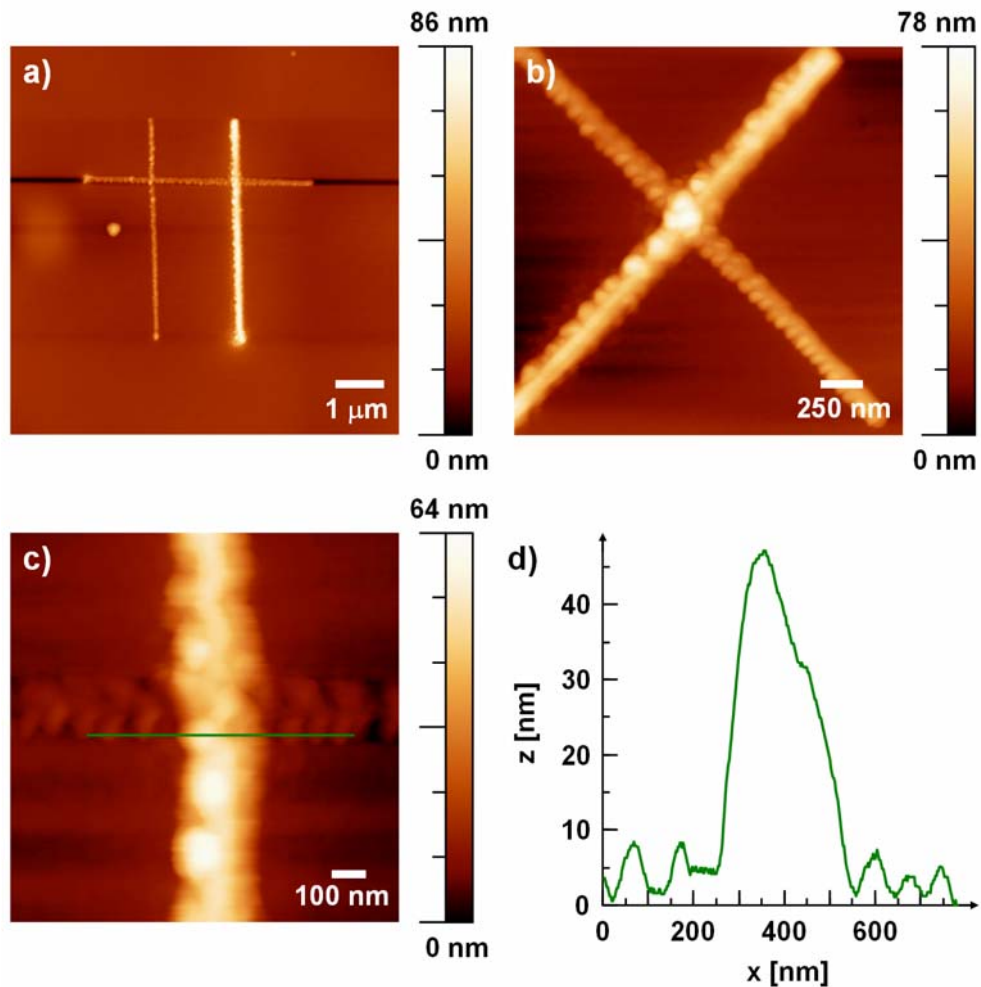


Figure 9.18: AFM data of the line pattern depicted in the Figures 9.16 and 9.17 visualizing the residual lines and the grown nanocrystals exclusively in their close proximity. a) AFM image of the entire line pattern. b) AFM image of the top right crossing point of the lines in a), with the scan direction rotated by 45° (the right vertical line of a) goes from the bottom left to the top right corner in b)). c) High magnification AFM image of the top right crossing point of a). d) Corresponding height profile to c).

height of ≈ 25 to 40 nm can be specified, while for the right vertical line (going from bottom left to top right in b)) the nanocrystal height lies between ≈ 34 and 55 nm. For the nanocrystal grown in the lower left corner of the crossing point of horizontal and right vertical line, i.e. the nanocrystal on which local AES was performed (see Figure 9.17 a), red marker), a height of ≈ 64 nm could be determined. A high magnification AFM image of the right crossing point and the latter nanocrystal is

shown in Figure 9.18 c) which is to be compared to the SEM image in Figure 9.17 a). Compared to the nanocrystals which have grown at the horizontal line in close vicinity, the nanocrystal at the crossing point has an additional height of ≈ 38 nm as demonstrated by the corresponding AFM height profile depicted in Figure 9.18 d).

In analogy to the results presented in Chapter 9.2, in the following the growth of the nanocrystals on an area deposit from TTIP is considered. For this purpose, a deposit was generated with identical lithographic parameters than the one depicted in Figure 9.15 (electron dose 9.86 C/cm^2). After moderate sputtering (see above) and applying the post-treatment of annealing in oxygen (in which the corresponding deposit was not observed *in situ* via SEM, identical to Chapter 9.2), the obtained structure was characterized via SEM and AFM. The results of this investigation are depicted in Figure 9.19.

Figure 9.19 a) shows an SEM image of the entire area deposit and the close surrounding. The image demonstrates that, in contrast to the deposit which was not treated via sputtering (see Figure 9.15), the nanocrystals have grown exclusively on the deposit and not in the surrounding of this structure. This evidences again the removal of the unintentionally deposited material due to the proximity effects in EBID by moderate sputtering. In a circular surrounding of the area structure the surface appears pitted and features small, black defects, which can be traced back to the post-treatment procedure of annealing in oxygen. These defects have also been observed in previously reported experiments (see Chapter 9.2) and are interpreted to be holes in the topmost surface layers. An evidence for this interpretation is found in the AFM image of Figure 9.19 c), which shows the area structure and its close surrounding, as well. In this AFM image, small dark regions are found at the same positions as in the SEM image. An image magnification of the corresponding structures is depicted in the inset of Figure 9.19 c) in the top right corner (position indicated by the black, rectangular marker). AFM height profiles (not shown) reveal that these structures are indeed holes of small depth in the upper surface layers, which thus evidences the interpretation given in Chapter 9.2. For the depth of the holes an average value of $\approx 1 - 2$ nm could be determined.

A high magnification SEM image of the nanocrystals grown in the center of the area deposit is depicted in Figure 9.19 b). In addition, a high magnification AFM image of these nanocrystals is shown in Figure 9.19 e). Furthermore, for both AFM images

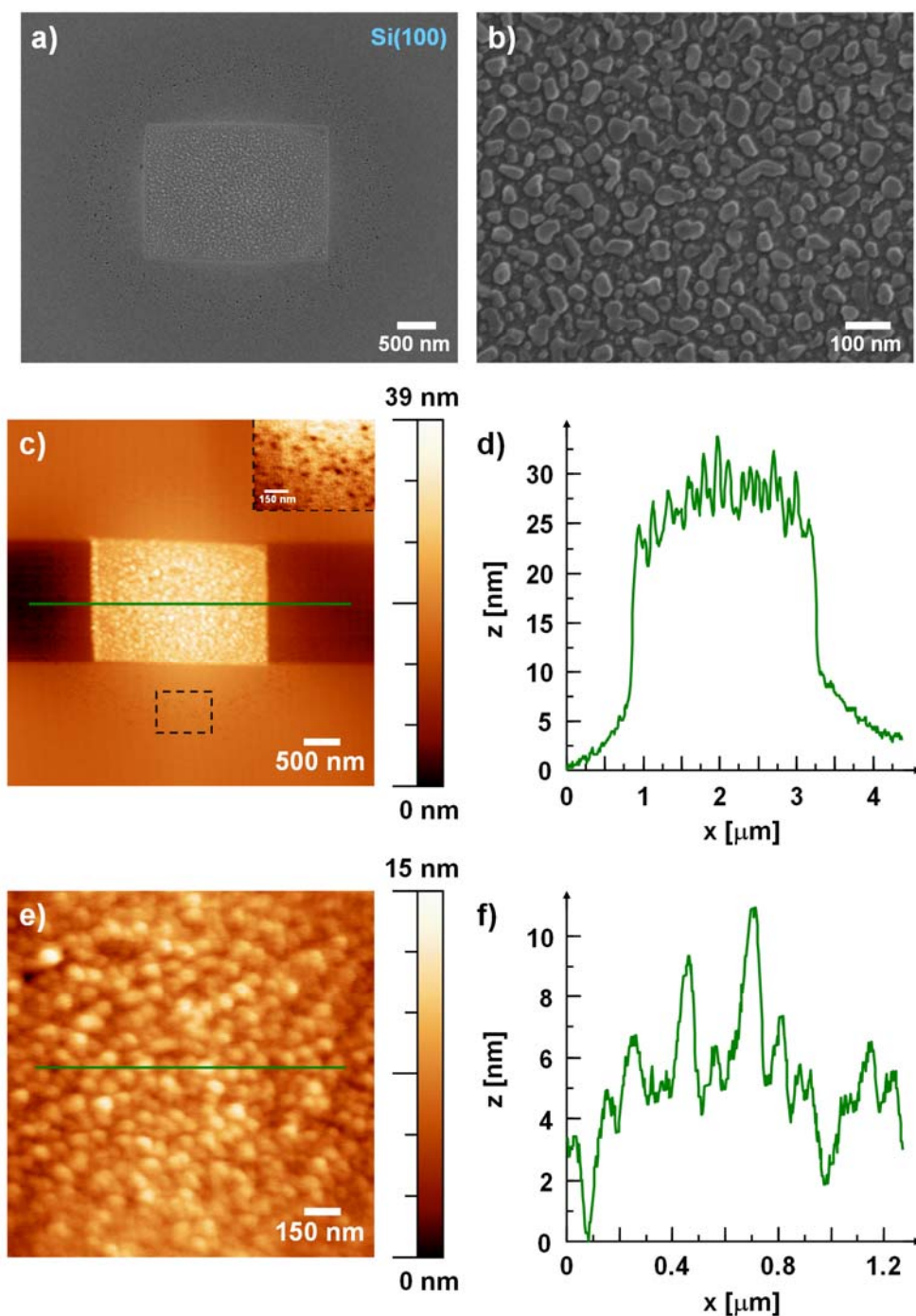


Figure 9.19: a) SEM image of an area deposit fabricated with identical parameters than the one depicted in Figure 9.15 with nanocrystals grown exclusively on the deposit after the combined post-treatments. b) High magnification SEM image of the nanocrystals grown in the center of the area deposit. c) AFM image of the area deposit and the close surrounding. d) Corresponding height profile to the green profile line positioned in c). e) High magnification AFM image of the grown nanocrystals. f) Corresponding height profile to the green profile line positioned in e).

(Figure 9.19 c) and e)) an AFM height profile is shown (see Figure 9.19 d) and f)), respectively. It can be derived that the fabricated area structure with nanocrystals on top has a maximum height of ≈ 34 nm. The height of the nanocrystals can not be determined from these data.

In summary, it can be stated that the introduced post-treatment procedure of moderate sputtering of the sample proved to effectively reduce the unintentionally deposited material next to the intended EBID structures. Applying the post-treatment of annealing in oxygen in a second step enables the localized growth of very clean titanium oxide nanocrystals exclusively on and very close to the fabricated structures [225].

9.4 Summary and conclusions

In this chapter it was shown that post-treatment procedures are a suitable tool to tune the properties of fabricated nanostructures after the deposition process. Two different post-treatment procedures are presented in this work, namely sputtering and annealing in oxygen. The combination of the latter to a two-step post-treatment process after EBID was introduced as a new pathway for the fabrication of clean localized nanostructures [225].

Sputtering was found to be a suitable tool to reduce the lateral dimension of originally deposited nanostructures and to remove the unwanted deposits caused by the proximity effects in EBID. It could be shown that for this purpose the suggested concept of sputtering works well both for high and for low electron dose structures. A significant parameter is the sputtering time, which generally has to be adapted to the thickness of the nanostructures, which is determined by the corresponding electron dose.

It was found that for EBID deposits fabricated with TTIP the phenomenon of sputter reduction occurs. The latter was evidenced via local AES measurements. In the acquired Auger spectra an increased removal of oxygen upon sputtering was found. In addition, a detailed investigation of the Ti LMM and LMV Auger signals upon sputtering shows the reduction of titanium from initially '+IV' to lower oxidation states.

Even reduction to metallic titanium (oxidation state '0') was found. Furthermore, the increased removal of carbon upon sputtering was observed, although carbon has a lower sputtering yield compared to titanium at the applied sputter conditions (by a factor of ≈ 2). This indicates an inhomogeneous distribution of carbon in the EBID deposits with C being concentrated in the topmost layers.

Two different sputtering yields were determined for the applied setup and the material deposited via EBID with TTIP. An average sputter rate of $\approx 4.2 \pm 0.4$ nm / h was determined for "thick" deposits while an average sputtering yield of $\approx 0.7 \pm 0.2$ nm / h was estimated for "thin" deposits.

The post-treatment procedure comprising annealing the sample *in situ* in the UHV instrument and simultaneously dosing molecular oxygen to a low background pressure was found to induce the growth of titanium oxide nanocrystals at and on the originally generated EBID structures [225]. These nanocrystals show a high purity, which was verified by local AES and SAM measurements, and a stoichiometry very close to the one of TiO_2 . Due to the proximity effects in EBID and concomitant unintentional material deposition in close proximity to the targeted deposits, the nanocrystals additionally grow also in the surrounding of these structures, albeit with a smaller size [225]. The growth of titanium oxide nanocrystals was found to appear both on the Si(100) and on the Au(111) surface upon applying the post-treatment comprising annealing in oxygen. Based on literature, the mineral form of the nanocrystals is assumed to be anatase.

On the unexposed Si(100) surface, the post-treatment procedure induces the generation of a thin silicon oxide layer. Depending on the applied experimental conditions the occurrence of small holes is observed in the SiO_x overlayer. In agreement with literature, these holes can be traced back to the local desorption of a volatile silicon oxide species (during the post-treatment), most probably being SiO .

To overcome the problem of unintended growth in the surrounding of targeted structures, the post-treatment by moderate sputtering of the sample is introduced [225]. It is demonstrated that the amount of unintentionally deposited material next to the structures could be significantly lowered. On such a surface, annealing in oxygen in a second post-treatment step induces nanocrystal growth exclusively on and very close to the fabricated structures. In the surrounding area no nanocrystals could be

observed by SEM. The two-step post-treatment process after EBID represents a new pathway for the fabrication of clean localized nanostructures. Moderate sputtering after the EBID process is proposed as a route to remove the unintended deposits caused by proximity effects, which are a well-known drawback of EBID. The second procedure, comprising annealing in a well-defined, low pressure oxygen atmosphere in a UHV set-up, proved then to be effective in the localized fabrication of very clean titanium oxide nanocrystals [225].

10 Morphology of EBID deposits

In the following chapter, the morphology of EBID deposits is investigated via SEM, AFM and sputtering. Depending on the experimental and system-immanent parameters a certain process regime is established during EBID, which determines the structure morphology. The process regime for the generation of dot deposits via EBID with TTIP in the UHV setup is discussed in Chapter 10.1. In addition, the deposit morphology is strongly influenced by the lithographic parameters. In Chapter 10.2, the influence of the number of sweeps and the waiting time between the sweeps (in terms of replenishment with precursor molecules) on the deposit morphology is discussed. Finally, in Chapter 10.3 a comprehensive study of the morphology of dot, line and area deposits is presented. Additionally to the characterization via SEM, the topography of these deposits was investigated *ex situ* via AFM measurements. From this complete structure characterization, comprising both the lateral size of the deposits (derived from SEM) and the vertical size (height, derived from AFM), the number of PEs is estimated which is needed to deposit one atom via EBID with TTIP for different structures.

10.1 Influence of the process regime

The process regime in EBID specifies whether deposition is limited by the number of electrons or by the number of available precursor molecules in the irradiated region [4, 5, 117]. In addition, it is connected to the way how molecule replenishment predominantly occurs [4]. The process regime depends on the applied experimental parameters on the one hand and the system-immanent parameters on the other. An overview of both types of parameters is given in Table 10.1.

Since the system-immanent parameters are often unknown, a universally valid statement concerning the process regime, being valid for all performed experiments in a specific setup, is not possible. Instead, the regime has to be determined individually for a particular experiment.

The process regime strongly determines the properties of the final deposit. On the one hand, it determines its shape including morphology and topography [274]. On the other hand, it can influence the chemical composition of the deposit and thus its

Experimental parameters	System-immanent parameters
- Substrate material	<i>I Electrons</i>
- Sample surface orientation	- Incident electron flux distribution
- Type of precursor	- Integral cross-section σ
- Precursor pressure p	<i>II Precursor</i>
- Beam voltage U_B	- Precursor molecule flux J
- Beam current I_B and current density	- Sticking probability g
- Temperature T	- Residence time τ
- Scan strategy (lithographic parameters)	- Diffusion constant D
- Pattern shape (in terms of precursor replenishment)	

Table 10.1: Experimental and system-immanent parameters, which influence the established process regime and thus the morphology, the amount of deposited material and the properties of the generated EBID deposit [4, 216]. Please note that the system-immanent parameters also depend on the experimental ones.

physical properties like density or conductivity. The latter appears reasonable when considering that the ratio of electrons per deposited molecule [5, 117] and thus the degree of fragmentation [5, 117] may be different in dependence of the process regime. In addition, the regime determines the growth rate R and thus the amount of deposited material.

In literature, three different process regimes are described. Van Dorp and Hagen presented a theoretical model disregarding surface diffusion [5, 117]. The authors consider three fundamental processes concerning the precursor molecules in EBID, namely adsorption from the gas phase, precursor molecule dissociation and desorption into the gas phase, and mathematically describe the precursor molecule coverage on the surface. Based on the obtained rate equation and a steady state consideration they determine an equation for the growth rate R. By distinction of two simplified cases they determine two different process regimes [5, 117]. In one, there is a surplus supply of precursor molecules and the growth process is thus

independent of the gas flux and limited instead by the electron current density. Consequently, this regime is referred to as the 'electron-limited regime' in EBID. In the other regime, the growth is independent of the electron current density, which means that a surplus of electrons is available, and is limited by the number of molecules which arrive at the irradiated area. This regime is referred to as the 'precursor-limited regime' in EBID [5, 117].

It has to be noted that in the model of van Dorp and Hagen the replenishment with precursor molecules in the irradiated area was considered to occur only by adsorption from the gas phase. One can assume that adsorption is the decisive way of precursor replenishment in particular under HV conditions and high precursor pressures. Consequently, in this case the suggested model is correct. However, for lower instrument and precursor pressures, e.g. under UHV conditions, surface diffusion from the surrounding region to the irradiated area should increasingly be accounted for. Thus, the latter issue was addressed e.g. by Utke *et al.* [4, 216] and by Smith, Fowlkes and Rack [215, 274]. Utke *et al.* extended the rate equation of van Dorp and Hagen by an additional term [4, 216]. The latter describes surface diffusion in dependence of the diffusion constant D and the established concentration gradient. Based on this consideration the authors found another 'molecule-limited process regime', which is characterized by molecule replenishment occurring predominantly by surface diffusion instead of adsorption from the gas phase. This regime is referred to as the 'diffusion-enhanced regime' in EBID [4, 216]. It is beam size dependent and can result in the generation of deposits with ring-like or indented morphologies when the diffusing precursor molecules already decompose at the periphery of the impinging beam (due to BSE and SE2) and do not reach the PE irradiated area [4]. The occurrence of such "ring structures" was also reported by Amman *et al.* [275], who associated their observed morphology to diffusion processes. Furthermore, the effects of surface diffusion on the growth of pillar structures were modeled by Smith, Fowlkes and Rack via three-dimensional MC simulations [215, 274].

Concerning the denotation of the process regimes many names can be found in literature. For the growth regime that is independent of the current density and limited by the number of available molecules the denotations 'precursor-limited regime' [4, 5,

117, 216], 'diffusion-enhanced regime' [4, 216], 'molecule-limited regime' [4, 216], 'mass-transport-limited regime' [274], 'vapor flux dominated growth' [215], 'diffusion dominated growth' [215] and 'diffusion mediated growth' [215] are used. For the growth regime that is independent of the gas flux and limited by the current density the denotations 'electron-limited regime' [4, 5, 117, 216] and 'reaction-rate-limited regime' [274] are found in literature. Consistently, it is reported that the highest deposition or growth rate is achieved when operating in the 'electron-limited regime' [4, 5, 117].

A reasonable classification of the process regimes in EBID is given in Figure 10.1. The classification is based on the references [4, 216] and the denotations introduced in Figure 10.1 are used consistently in this work.

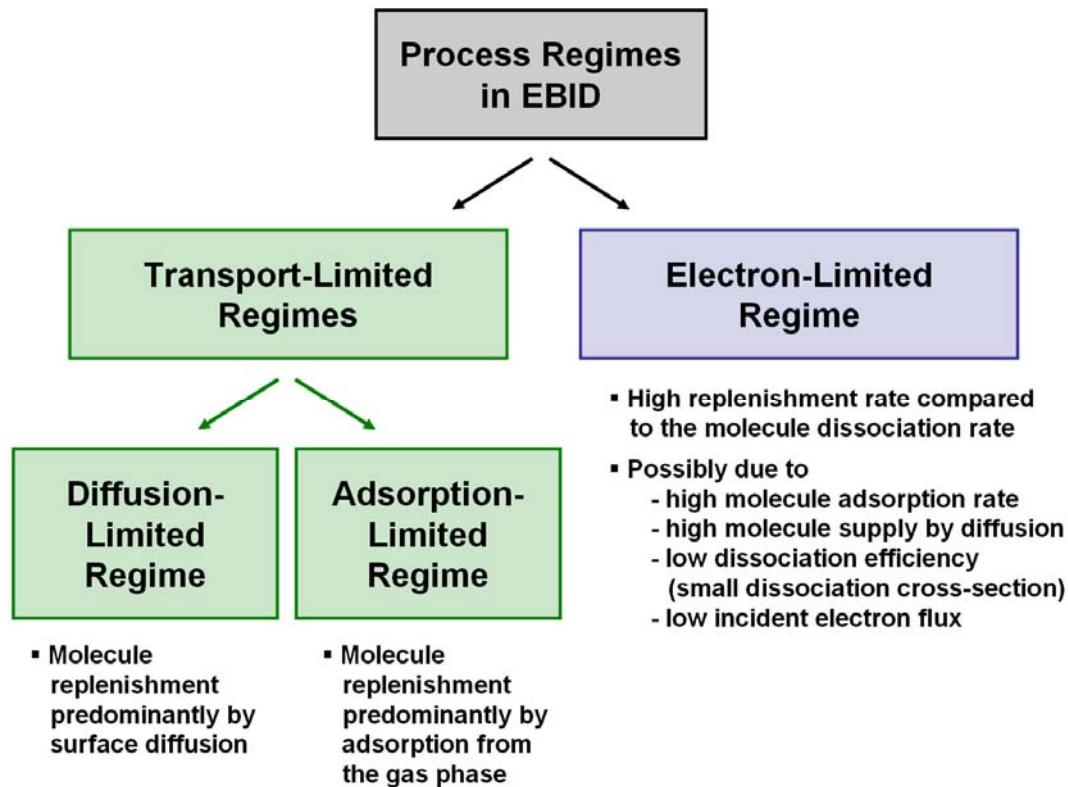


Figure 10.1: Classification of the process regimes in EBID according to literature [4, 216].

In this chapter, an assignment of the process regime for an EBID experiment with TTIP on Au(111) is given. Figure 10.2 a) shows an SEM image of ten dot deposits on the Au(111) surface, which were fabricated with varied electron dose. The

arrangement of the dots is identical to Figure 7.1 a) and Figure 9.4 a) and b) and also the electron dose is increased correspondingly. The incremental increase per point is 0.12 nC and the electron dose is increasing from the lower left dot (1.32 nC) to the upper right one (2.40 nC). Additionally, a 'PT deposit' (see Chapter 3.2.2.) is visible in the upper left corner of the SEM image, separated from the ten-point matrix. For each dot deposit the central dot is surrounded by a ring, which is followed by a halo that fades with increasing distance to the center. This becomes even more apparent in the high magnification SEM image of the lower left dot of the pattern (see red, rectangular marker), which is depicted in Figure 10.2 b).

The size of the central dot deposits is increasing (FWHM, from ≈ 44 to 56 ± 10 nm) and the dot structures appear darker in SEM with increasing electron dose (see Figure 10.2 a)) indicating that a higher amount of material is deposited by increasing the electron dose. In contrast to that, the diameter of the dark "ring" around the central deposit is constant and measures $\approx 350 \pm 10$ nm independent of the electron dose (compare also Chapter 7.1).

The occurrence of the ring structure can be explained as follows. When the primary electron beam impinges on the surface, precursor molecules are decomposed in the PE exposed area and form a deposit. In addition, precursor decomposition occurs also in the surrounding of the PE exposed area due to secondary and backscattered electrons released within the 'BSE exit area' (see Chapter 8). As a consequence of the decomposition processes, precursor molecule depletion occurs quickly in the corresponding area and the supply with "new" molecules has to occur when the process is to be sustained. In principle, two ways of precursor supply are possible, i.e. surface diffusion and adsorption from the gas phase. The fact that a ring structure is observed in the surrounding of the central dot deposits indicates that surface diffusion is a prevalent supply mechanism [4, 5, 117, 215, 216, 275, 276]. A high amount of precursor molecules, which diffuse from the outside inwards to the depleted area, is then decomposed before the molecules reach the center of the irradiated area [5, 117]. This leads to the formation of the surrounding, circular structure. The diameter of this ring depends on the number of electrons necessary to form non-volatile fragments from the precursor molecules and on the spatial distribution of the scattered electrons in the substrate. Moreover, also the diffusion constant D might influence the diameter of the ring structure. In the above described experiment a ring diameter of $\approx 350 \pm 10$ nm was found, i.e. a ring radius of

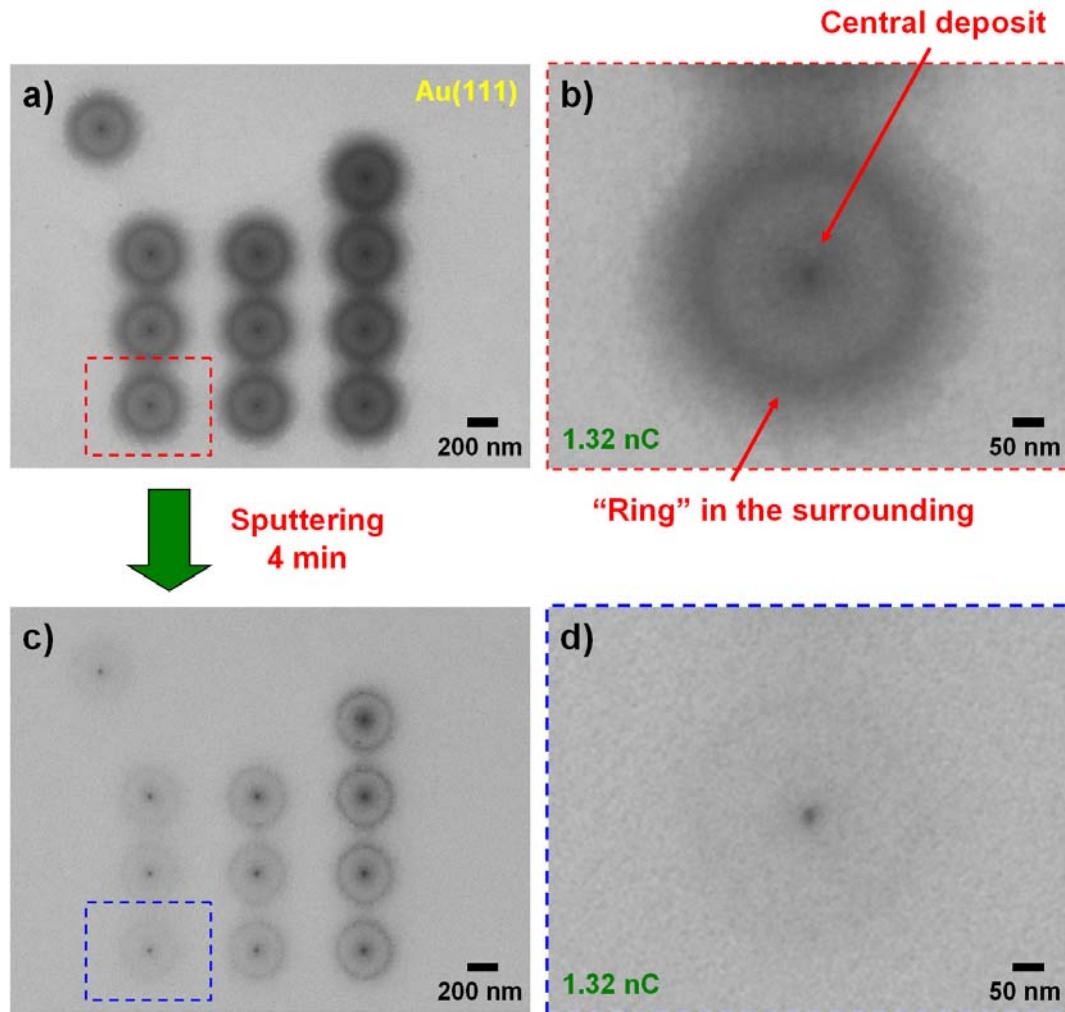


Figure 10.2: a) SEM image of dot deposits on Au(111) consisting of ten deposits fabricated with increasing electron dose. b) High magnification SEM image of the lower left dot in a) (electron dose 1.32 nC). Obviously, each structure of the pattern consists of a central dot deposit and a “ring” in the surrounding. c) SEM image of the pattern in a) after 4 min of sputtering. d) High magnification SEM image of the lower left dot in c).

≈ 175 nm. Considering the radius of the ‘BSE exit area’ on gold (≈ 340 nm, see Chapter 8.2) this means that deposition of inward diffusing molecules occurs roughly at half of the radius of the ‘BSE exit area’ (≈ 51 %).

The fact that the diameter of the surrounding ring is constant and independent of the electron dose supports that diffusion causes the formation of the ring structure. It can be assumed that laterally, at the position of the ring, the number of BSEs and SE2

and accordingly the respective current densities are just sufficient to decompose the inward diffusing molecules. Based on the MC simulations presented in Chapter 8 a BSE current density of $3.16 \cdot 10^{-2} \text{ A cm}^{-2}$ was determined at the ring radius ($\approx 175 \text{ nm}$). This BSE current density can be considered as a threshold value that is needed to generate a deposit from TTIP on gold.

To investigate the morphology of the dot deposits and the amount of deposited material in more detail the sample was sputtered for in total 4 min. Figure 10.2 c) shows the dot pattern after the sputter treatment and demonstrates that a considerable amount of material was removed in this step. It further displays that for all dot structures more material was deposited (per unit area) in the center than in the surrounding ring. Figure 10.2 d) depicts a high magnification SEM image of the lower left dot of the pattern in c) (see blue, rectangular marker), which is to be compared to Figure 10.2 b).

The fact that a ring structure is observed indicates that the process regime in EBID for the applied static irradiation conditions might be the 'diffusion-limited regime'. However, it is noted that the obtained structures show a pronounced central deposit as well and that more material was deposited (per unit area) in the center compared to the ring as derived from the sputter data. From this finding one can conclude that also adsorption from the gas phase plays a significant role and that the actual process regime might be the 'adsorption-limited regime'. Consequently, it can be stated that both surface diffusion and adsorption from the gas phase provide the precursor replenishment and that deposition occurs in between of the diffusion-limited and the adsorption-limited regime.

To illustrate the above described dot fabrication experiment, a schematic drawing is depicted in Figure 10.3. It demonstrates the dependence of the dot deposit morphology on the predominant way of replenishment in the 'transport-limited regime'.

First, the simplified sketches of the extreme cases, i.e. the diffusion-limited and the adsorption-limited process regime (Figure 10.3 a) and c)), are considered. The drawing in Figure 10.3 a) demonstrates the obtained dot morphology for surface diffusion strongly exceeding adsorption from the gas phase (diffusion-limited regime). Since a high amount of precursor molecules is decomposed at the periphery of the

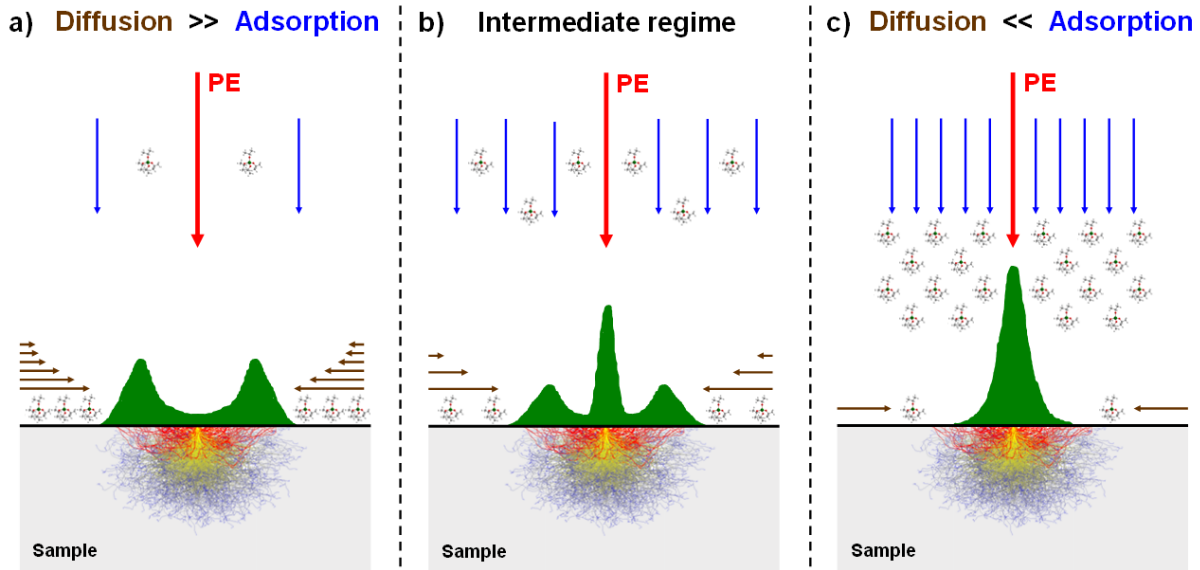


Figure 10.3: Schematic drawing illustrating the dependence of the deposit morphology on the predominant way of precursor molecule replenishment in the 'transport-limited regime'. a) EBID with surface diffusion strongly exceeding adsorption from the gas phase ('diffusion-limited regime'). b) EBID with both surface diffusion and adsorption from the gas phase. c) EBID with adsorption from the gas phase strongly exceeding surface diffusion ('adsorption-limited regime').

PE irradiated area [4], the formation of a ring structure in the surrounding of the central deposit is caused. The green structure in a) sketches the cross-sectional area of such a deposit with an arbitrarily assumed material distribution between central and exterior deposit. In contrast to that, Figure 10.3 c) shows the expected dot morphology when adsorption from the gas phase strongly exceeds surface diffusion and one is in the adsorption-limited regime. In this case, all positions in the considered surface region have an equal probability for adsorption and desorption processes [5, 117]. Thus, the amount of deposited material and the resulting structure morphology are strongly determined by the number of available electrons per unit area, i.e. by the current densities of PEs, BSEs, SEs (and by the specific cross-sections for precursor dissociation). Due to the high current density of PEs in the center and since the current density of BSEs is strongly decreasing with increasing distance to the center, deposition should predominantly occur in the center. Consequently, a "hill shaped" deposit is expected as sketched in

Figure 10.3 c). The dot deposits in Figure 10.2 feature both a large central deposit and a ring structure in the surrounding. The corresponding morphology is sketched in Figure 10.3 b). Therefore, it was reasonable to classify the established transport-limited process regime in between of the diffusion-limited and the adsorption-limited regime and to conclude that both adsorption and diffusion are essential for molecule replenishment.

The experiments were conducted in a UHV instrument at a comparably low precursor pressure ($3.0 \cdot 10^{-7}$ mbar). Therefore, a low TTIP molecule flux to the sample surface occurs and it is reasonable to assume that a rather precursor deficient deposition process establishes for static dot irradiation. The precursor molecule flux was determined to be $8.4 \cdot 10^{14} \text{ cm}^{-2} \text{ s}^{-1}$ (see Chapter 6) and the number of impinging primary electrons at a beam current of 400 pA is $2.5 \cdot 10^9 \text{ s}^{-1}$. These data allow for the determination of the ratio between impinging primary electrons and provided TTIP molecules in the established transport-limited process regime.

Considering first the 'BSE exit area' with a radius of $\approx 340 \text{ nm}$ (see Chapter 8.2), the number of provided TTIP molecules in this area is $3.1 \cdot 10^6 \text{ s}^{-1}$. This means that for the applied conditions in a static dot irradiation experiment ≈ 820 times more primary electrons impinge at the irradiated dot than TTIP molecules are provided to the 'BSE exit area' at equal time scale. Considering secondly an area as small as the PE beam spot with a radius of $\approx 1.5 \text{ nm}$ (see Chapter 3.6.3), the number of provided TTIP molecules in this area is $\approx 59 \text{ s}^{-1}$. This means that in a static dot irradiation experiment $\approx 4.2 \cdot 10^7$ times more primary electrons impinge at the irradiated dot than TTIP molecules are provided to the same area at equal time scale.

For the fabrication of the above presented dot deposits (Figure 10.2), the beam was kept statically at a defined position for irradiation. The term "statically" means that no delay time was adjusted during patterning, in which the electron beam was "deactivated" or "kept away" of this position. To confirm the above drawn conclusions, i.e. that a transport-limited process regime had established under these conditions, one might envisage experiments in which a pulsed electron beam is applied for dot irradiation. This would enable an additional, periodic replenishment of the central, PE irradiated area with "fresh" TTIP molecules during the time the beam is deactivated. Consequently, a "shift" of the process regime from the transport-

limited regime into the direction of the electron-limited regime should establish. The latter should go along with a dot morphology change from the one sketched in Figure 10.3 b) to the one sketched in Figure 10.3 c). By studying a series of dots generated with constant pulse duration and electron dose but varied 'inactive beam time' (and thus pulse frequency) one might be able to determine the diffusion constant of TTIP on the Au(111) surface. To clarify whether the electron-limited regime can even be reached further studies with varied current densities are necessary as reported by van Dorp and Hagen [5, 117].

Summarizing this chapter, an overview of the different process regimes in EBID according to literature was given. Generally, it can be distinguished between three different regimes, i.e. the diffusion-limited, the adsorption-limited and the electron-limited process regime. The diffusion-limited and the adsorption-limited regime can be subsumed in a more general transport-limited regime.

For the static fabrication of dot deposits from TTIP on Au(111), i.e. dot irradiation without providing a delay time, a definite assignment of the existent process regime can be given. The dots show a ring structure in the surrounding of a central dot deposit. It is concluded that supply and replenishment with TTIP molecules take place both via surface diffusion and adsorption from the gas phase. Further, it is deduced that deposition occurs in the transport-limited process regime, in between of the diffusion-limited and adsorption-limited regime. The ring radius was found to be constantly ≈ 175 nm on Au(111). At this distance to the center a BSE current density of $3.16 \cdot 10^{-2}$ A cm⁻² was determined for gold. The latter value can be considered as a threshold level needed for the formation of non-volatile deposits from TTIP.

To illustrate the influence of the way of precursor supply in dot fabrication experiments, i.e. predominantly by diffusion, predominantly by adsorption or by both, a scheme was considered demonstrating the corresponding dot morphologies.

10.2 Influence of lithographic parameters

In this chapter, the influence of the lithographic parameters on the morphology of EBID deposits is further investigated. For this purpose, line structures were fabricated with identical or very similar electron dose but different lithographic parameters. Due to the strong material contrast of deposits from TTIP on gold, the identification of the deposit boundaries was simplified. Sputtering was partially applied to elucidate the line morphology and to compare the amount of deposited material in EBID.

First, the line morphology was investigated in dependence of the dwell time and the number of sweeps. It is well-known from literature that these parameters can significantly influence the deposition yield and thus the structure morphology in FEBID and FIBID experiments. Extensive investigations, in which the influence of these parameters was studied for constant replenishment time and electron dose, are reported by Kohlmann-von Platen *et al.* [277], Lipp *et al.* [278], Sánchez *et al.* [279] and Beaulieu *et al.* [280] for different precursor molecules ($W(CO)_6$, $Si(OCH_3)_4$, $Si(OC_2H_5)_4 / H_2O$, $Pt(CH_3)_3(C_5H_4(CH_3))$). A detailed review of their results is also given in the articles of van Dorp and Hagen [5, 117]. In brief, Kohlmann-von Platen *et al.* and Sánchez *et al.* [277, 279] found that shorter dwell times (and thus higher numbers of sweeps) cause increased growth rates. Lipp *et al.* [278] also reported this finding, but indicate a less pronounced effect.

Figure 10.4 shows SEM images of two different line deposits fabricated with practically identical electron doses, denoted as Line A ($d_L = 17.4 \mu C/cm$) and Line B ($d_L = 17.5 \mu C/cm$). The as-deposited lines are depicted in the left SEM images of Figure 10.4 (see a) and f)) while for each line a sputter series is shown in horizontal direction with the sputtering times indicated. The number of sweeps is higher by a factor of 32 for Line A ($N_S = 380$) compared to Line B ($N_S = 12$). Consequently, the dwell time of Line B ($t_D = 1,638.4 \mu s$) is higher than the one of Line A ($t_D = 51.2 \mu s$) by the same factor to realize the same electron dose. A survey of the lithographic parameters is given in Figure 10.5.

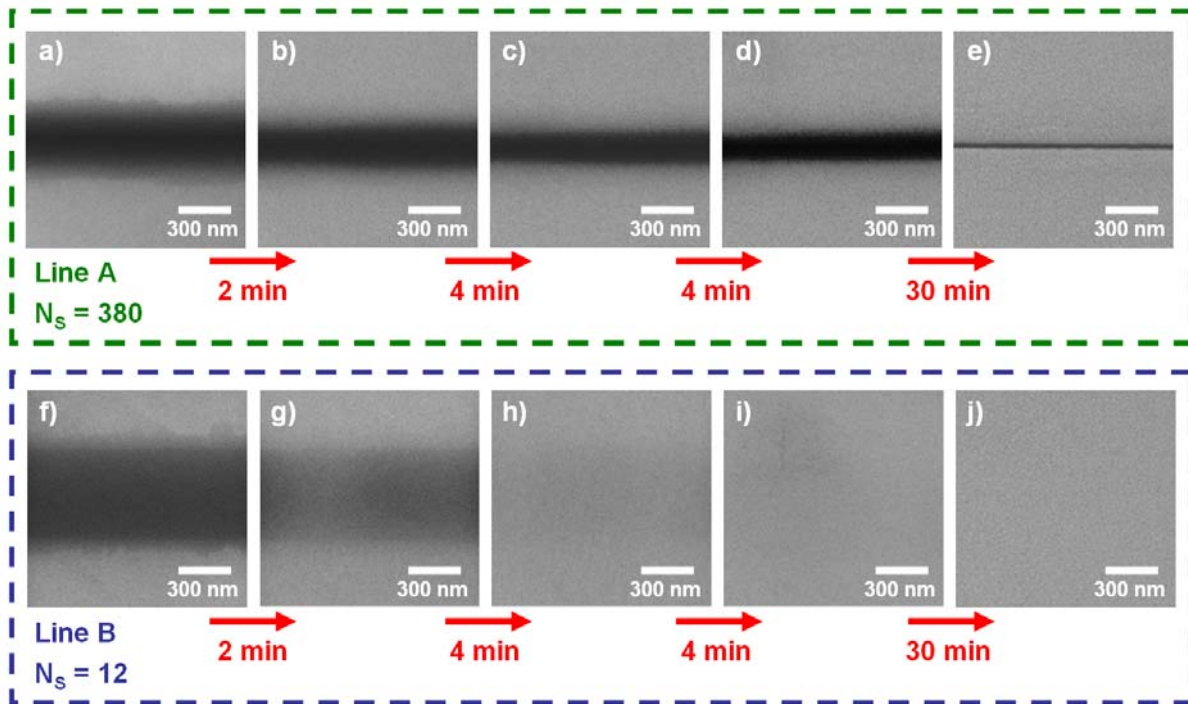


Figure 10.4: Two lines on Au(111) that were fabricated with very similar electron dose but different lithographic parameters. The number of sweeps and the dwell time of both line structures deviate by a factor of 32. SEM images of the as-deposited lines are depicted in a) and f) and sputter series are given in horizontal direction. All lithographic parameters are listed in Figure 10.5.

	t_{exp} [s]	t_{D} [μs]	t_{ALD} [ms]	t_{wait} [ms]	t_{repl} [ms]	v_{B} [cm/s]	N_{S}	d_{L} [$\mu\text{C}/\text{cm}$]
Line A	30	51.2	52.4	26.6	79	$8.7 \cdot 10^{-3}$	380	17.4
Line B	20	1,638.4	1,677.7	2.3	1,680	$2.7 \cdot 10^{-4}$	12	17.5

Figure 10.5: Lithographic parameters for the lines depicted in Figure 10.4. Both lines had a length of $4.6 \mu\text{m}$ and were generated with 1,024 points and a step size of 4.5 nm. The scheme specifies the total exposure time t_{exp} , the dwell time t_{D} , the active line duration t_{ALD} , the waiting time at the line starting point in each sweep t_{wait} , the replenishment time t_{repl} , (sum of t_{ALD} and t_{wait}), the electron beam velocity v_{B} , the number of sweeps N_{S} and the line dose d_{L} in the denoted units.

The sputtering series for Line A (see Figure 10.4 b) - e)) clearly shows a more or less continuous lateral “shrinking” of the structure until a very thin line (≈ 30 nm) remains. In contrast, the sputtering series for Line B (see Figure 10.4 g) - j)) documents a more or less homogeneous fading of the deposit till it practically vanishes after 10 min (see Figure 10.4 i); please note that the dark area in the upper left part of this image is beam damage of an AE line scan measurement). This behavior upon sputtering indicates a homogeneous and equally high deposit for Line B while in the case of Line A much more material appears to be deposited in the center. In addition, the initial diameter of Line B ($d = 570$ nm) is found to be larger than for Line A ($d = 370$ nm).

To investigate the morphology of both lines in more detail, an analysis of the line diameter within the sputtering series was performed. The result is depicted in Figure 10.6, in which the total sputtering time is plotted versus the line diameter. The plots and the sketched red profile lines indicate the cross-section of the lines. Therefore, it can be stated that Line A features a “hill shaped” structure with significantly more material deposited close to the electron beam impact position (see red profile line in Figure 10.6 a)), while Line B is a flat and homogeneous line deposit with rather constant height (see red profile line in Figure 10.6 b)).

Before further interpretation it must be noted that the sputtering yield is certainly not constant for all positions of the fabricated line structures since it also depends on other parameters, in particular the incidence angle of the impinging ions [43]. The sputtering yield increases with increasing angle between impinging ions and surface normal and reaches a maximum at $\approx 70 - 80^\circ$ [43]. Consequently, an increased sputtering yield occurs at positions which show large height differences, i.e. edges of the deposits. Since the topography of Line A and B are obviously very different, no conclusive quantitative statements can be made. However, considering the more pronounced “3D-shape” of Line A, the amount of material removed by sputtering is rather underestimated for the latter, which is in line with the drawn conclusions.

Coming back to Figure 10.4, it is obvious that both lines appear extremely broadened compared to the actual size of the electron beam. This can be traced back to proximity effects. However, the series of SEM images in Figure 10.4 and the plots in Figure 10.6 clearly demonstrate that the line morphology and the amount of

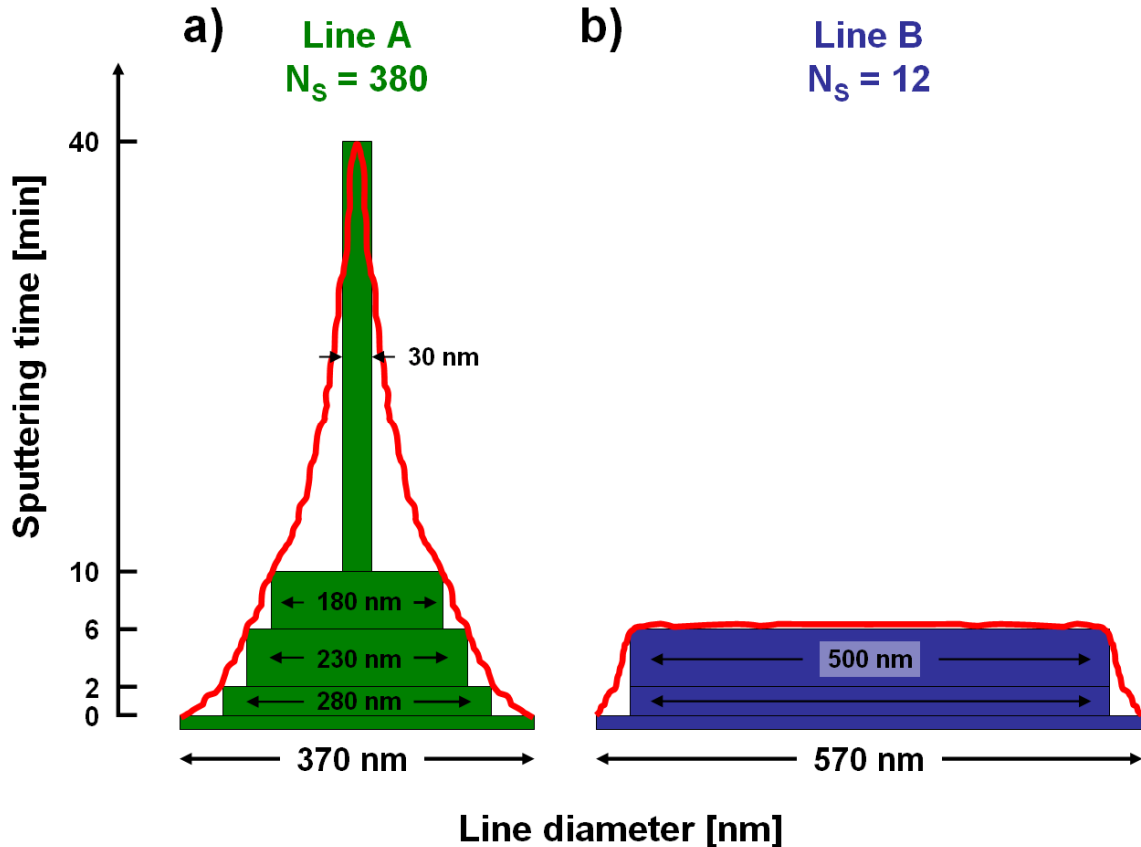


Figure 10.6: Plot of the total sputtering time vs. the diameter of Line A and B (FWHM, averaged by 10 profile lines). The plots and the sketched red profile lines indicate the actual line morphologies.

deposited material (in the central PE irradiated area and in the surrounding region) are different. Since the lines were fabricated with practically identical electron dose, the effect must be due to the variation of the lithographic parameters like dwell times and numbers of sweeps.

First, the influence of these parameters on the deposit in the center of the line structures, i.e. the area that was irradiated by the PE beam, is considered. In this area Line A shows a pronounced line deposit with significantly more material deposited compared to Line B (see Figures 10.4 and 10.6), in line with literature [277-279]. The reason for this difference is that the shorter dwell time ($t_D = 51.2 \mu\text{s}$) and the higher number of sweeps ($N_S = 380$) used for Line A enable a more effective use of the electrons. The number of impinging electrons is the same for both lines (practically identical electron dose). However, for Line A the number of electrons applied in one sweep is smaller, and thus the electrons are “dosed” in a higher

number of smaller “portions”. In contrast to that, for Line B a less effective use of the impinging electrons occurs. Due to the longer dwell time ($t_D = 1638.4 \mu\text{s}$) and the lower number of sweeps ($N_S = 12$) a higher number of electrons is applied to the line structure in one sweep. The lower amount of deposited material in the center of Line B evidences that the efficiency of the electrons is reduced compared to the one in Line A. Since the total number of electrons for both lines is practically identical, the availability of precursor molecules must be higher in the case of Line A, i.e. more TTIP molecules are effectively transported into the electron affected area. This is reasonable considering the higher number of sweeps, which also mean more replenishment events. In addition, the overall replenishment time (total exposure time) for Line A is longer (30 s compared to 20 s). In other words, this means that for Line A the lithographic parameters are such that a less transport-limited and more electron-limited process regime is established (see Chapter 10.1).

Secondly, the influence of the dwell time on the morphology of the surrounding region of the PE irradiated area is considered. It was found that the diameter of Line A (370 nm) is smaller than the one of Line B (570 nm) and that less material was deposited at a certain distance to the central, PE irradiated area for Line A (see Figures 10.4 and 10.6). The reason for the different line morphology in this region is also the different number of electrons that is applied in one sweep, caused by the dwell time. For Line A this number of electrons per sweep and thus also the numbers of BSEs and SE2 per sweep are smaller. It is assumed that at a distance larger than ≈ 200 nm to the line center the number of BSEs and SE2 is too small to decompose the TTIP molecules to generate non-volatile fragments. As to be investigated in more detail (see below), probably only partial TTIP dissociation occurs, which leads to the formation of still volatile molecule fragments which subsequently desorb or diffuse away from the line deposit. Thus, material deposition occurs only up to a distance of ≈ 200 nm to the PE irradiated line, which leads to a line diameter of ≈ 400 nm. In contrast, for Line B the number of electrons per sweep and thus also the numbers of BSEs and SE2 per sweep are higher. This leads to more material deposition in the surrounding region and to a larger diameter of Line B compared to Line A. Precursor decomposition and the formation of non-volatile fragments occur up to a distance of ≈ 300 nm from the PE irradiated line, which yields a diameter of ≈ 600 nm. Interestingly, for the lithographic parameters of Line B the amount of material deposited in the surrounding region is approximately the same than the amount of

material deposited in the directly irradiated area, i.e. a rather flat deposit is formed (see Figure 10.4 f)). Assuming an initially homogeneous TTIP coverage on the surface, this means that all precursor molecules are decomposed and the process is strongly transport-limited.

The different diameter of both lines at equal electron dose and the fact that the number of electrons applied in one sweep influences the distance up to which material deposition occurs indicate two particular properties of EBID with TTIP. First, it is assumed that a minimum number of electrons, greater than one, is necessary to generate non-volatile fragments, i.e. a deposit, from TTIP. Secondly, one can imagine that partial dissociation of TTIP, i.e. fragmentation, is possible, when the molecule interacts with a low number of electrons. In this case, the formation of volatile fragments is likely.

Amman *et al.* [275], Kohlmann-von Platen *et al.* [277], Lipp *et al.* [278] and Beaulieu *et al.* [280] investigated the influence of the replenishment time on the morphology and the deposition yield of dot, line and area structures applying a constant electron dose and constant dwell time with different precursors. Amman *et al.* [275] reported on the fabrication of “contamination structures” from residual hydrocarbons in an HV instrument, demonstrated that surface diffusion played a primary role in terms of precursor replenishment in their system and discussed in detail the dependence of line and dot morphologies on the replenishment time. The authors found that for short replenishment times the central dot and line structures are material depleted while deposition occurs predominantly in the surrounding of the structures. This result was traced back to the fact that there is insufficient time to recover the exposed region with precursor molecules between the single sweeps. In contrast, for long replenishment times the time to recover the exposed region after each sweep with molecules was found to be sufficiently long, which led to the formation of pronounced deposits in the PE irradiated regions and a low amount of material in the surrounding [275]. The influence of the replenishment time on the deposition yield of dot, line and area structures was investigated in the references [277, 278, 280]. Consistently, it is reported that the deposition yield increases with increasing replenishment time and this effect is traced back to the longer replenishment with “fresh” precursor molecules.

These results and the question of their validness for TTIP on Au(111) were the motivation for a further EBID experiment, in which the particular influence of the replenishment time on the morphology of line deposits was investigated. Additionally, the target of the experiment was to investigate if partial TTIP dissociation and the formation of volatile fragments occur when a low number of electrons interacts with the TTIP molecules in one sweep. For this purpose, a very short active line duration (and thus dwell time) was applied, i.e. the active line duration was lower by a factor of 2^9 (= 512) compared to Line A.

Figure 10.7 shows a series of SEM images of five line deposits on Au(111).

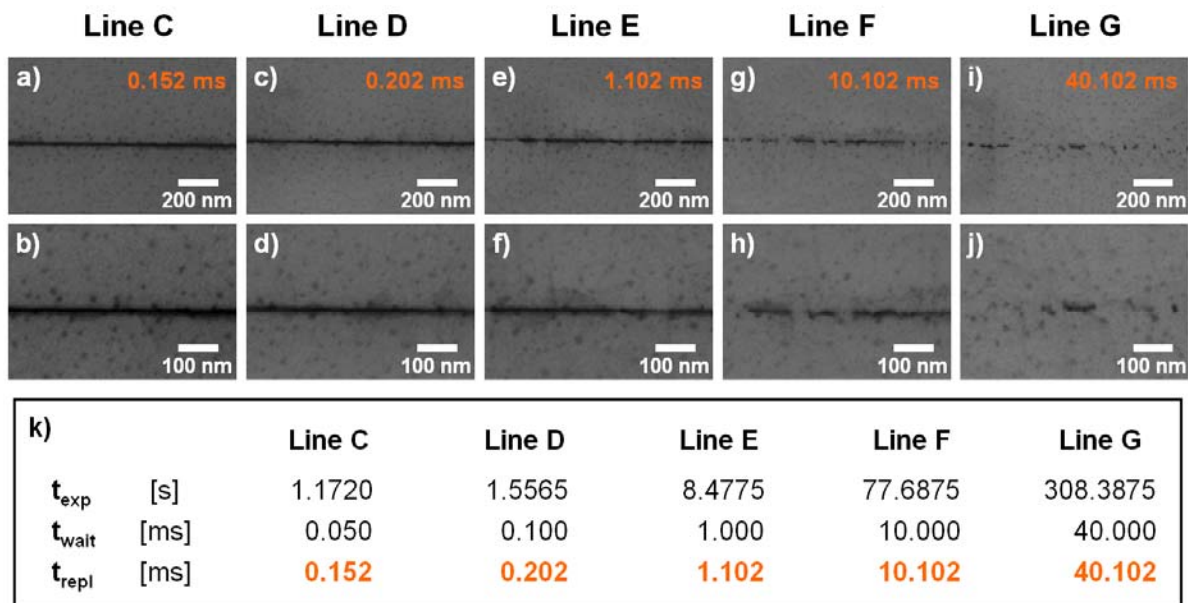


Figure 10.7: a) to j) SEM images of five line deposits on Au(111) fabricated with identical length (4,500 nm), electron dose ($0.7 \mu\text{C}/\text{cm}$), number of points (4,096), active line duration (0.102 ms), step size (1.1 nm), number of sweeps (7,690) and electron beam velocity (4.4 cm/s). Each line is depicted twice with two different magnifications. The only varied parameter is the waiting time at the line starting point after each sweep, which results in different replenishment times varying from 0.152 to 40.102 ms. All varied lithographic parameters are listed in k) including the exposure time t_{exp} , the waiting time t_{wait} and the replenishment time t_{repl} .

The lines were generated with identical length (4,500 nm), electron dose (0.7 $\mu\text{C}/\text{cm}$), number of points (4,096), active line duration (0.102 ms), step size (1.1 nm), number of sweeps (7,690) and electron beam velocity (4.4 cm/s). For each line a representative SEM image is depicted with two different magnifications. The only varied parameter is the waiting time at the line starting point between the sweeps, which results in different replenishment times. The replenishment time was varied in five steps from 0.152 ms to 40.102 ms as indicated with the orange numbers in Figure 10.7. An overview of the varied lithographic parameters is depicted in Figure 10.7 k).

While for the replenishment times of 0.152 and 0.202 ms (Line C and D) a continuous line is fabricated, for 10.102 and 40.102 ms the structure obviously is discontinuous (Line F and G). In addition, there appears to be a tendency that the lines “thin out” with increasing replenishment time. This apparent decrease of the deposition rate with increasing replenishment time is an unexpected result, which contradicts the findings of Amman *et al.* [275] and particularly the results reported in the references [277, 278, 280]. Comparable results are not reported in literature so far.

A possible explanation is given in the following. For all lines depicted in Figure 10.7 a very short active line duration is applied ($2^9 = 512$ times lower compared to Line A) and the electron beam is scanned comparably fast across the line ($v_B \approx 4.4$ cm/s). Therefore, the number of electrons applied in one sweep is significantly smaller compared to Line A. It is assumed that during the time of one single sweep bond scissions and thus TTIP decomposition occur but that partially dissociated TTIP fragments are left, which might be still mobile or even volatile. These fragments have a certain residence time τ and / or diffusion constant D on the Au(111) surface. When the electron beam is “off”, desorption and diffusion processes of these fragments occur. Under this assumption, a deposition of the fragments can only occur if they are still located in the same region when the electron beam returns, i.e. the replenishment time must be smaller than the residence time of the fragments. This means that for short replenishment times steady TTIP fragmentation and deposition occur while for long replenishment times desorption and / or diffusion processes off the electron affected region increasingly account. Obviously, replenishment times of 0.152 ms (Line C) and 0.202 ms (Line D) are suitable to fabricate a continuous line deposit. In contrast, for a replenishment time of 1.102 ms (Line E) the line already

thins out and is partially interrupted. This effect is more pronounced for increasing replenishment times, i.e. for 10.102 ms (Line F) and 40.102 ms (Line G) the line deposits are discontinuous. It is assumed that in these cases the replenishment time is longer than the (mean) local residence time τ of the fragments so that an increasing part of the volatile TTIP fragments desorbs and / or diffuses out of the PE irradiated area. Consequently, in the following sweep only a fraction of the initially generated TTIP fragments can be further fragmented and thus deposited. This fraction is getting smaller for increasing replenishment time and thus increasingly discontinuous lines are generated.

The acquired results enable a rough estimation of a (mean) diffusion constant D of the TTIP fragments. It was found that the (mean) local residence time τ of the fragments must be between ≈ 0.2 and ≈ 1.1 ms since the line generated with a replenishment time of 1.102 ms (Line E) is the first line (in Figure 10.7) that is interrupted and thus discontinuous. The average diameter of Line C, D and E is determined to ≈ 23 nm (FWHM). Consequently, in a time between ≈ 0.2 and ≈ 1.1 ms the TTIP fragments are able to leave a (circular) surface area with a diameter of ≈ 23 nm by desorption and or off-diffusion. Assigning the way of fragment removal to surface diffusion, this corresponds to a (mean) diffusion constant D between $\approx 4 \cdot 10^{-9}$ and $\approx 2 \cdot 10^{-8}$ cm² s⁻¹ for the fragments from TTIP.

In the articles [16, 17] Mitchell and Hu report that the precursor TTIP is very sensitive to electron irradiation. The authors base this statement on the “very high” [17] deposition rate which they determined from their experiments. Consequently, one can imagine that the results presented in Figure 10.7 can only be obtained when a very short active line duration and high electron beam velocity are applied (0.102 ms and ≈ 4.4 cm/s for the lines depicted in Figure 10.7). For a longer active line duration, the TTIP molecules might be increasingly decomposed already in one sweep and a considerably higher amount of material should be deposited even when a long replenishment time would be applied.

To summarize the results of this chapter, one can state that the morphology of EBID deposits and the amount of deposited material are not only determined by the electron dose and thus the applied number of primary electrons. Instead, they also strongly depend on the other lithographic parameters, like dwell time, active line

duration, number of sweeps and replenishment time, and the interplay of all of these parameters. This is the key message derived from the experiments discussed in this chapter.

First, the influence of the dwell time and the number of sweeps was investigated. It was found that the extent of how effective the applied electrons (PE, BSE and SE) can be used for precursor decomposition determines both the structure morphology and the amount of deposited material. For a short dwell time and a high number of sweeps, i.e. an “offering” of the electrons in a high number of small “portions”, a more effective use of the electrons was observed, which caused the deposition of more material in the PE irradiated area (see Line A). It is assumed that in this case predominantly an electron-limited process regime is established. Instead, for a long dwell time and a low number of sweeps predominantly a transport-limited regime is established with the occurrence of precursor depletion and a surplus of electrons. Consequently, a lower amount of material was deposited in the PE irradiated area (see Line B). Since the numbers of BSEs and SE2 released due to proximity effects accumulate, it is the dwell time that determines the distance from the PE impact point up to which precursor decomposition takes place. Accordingly, it was found that a longer dwell time causes an increased line diameter (see Line B).

Secondly, in another experiment line deposits fabricated with a very short active line duration and varying replenishment time were investigated. The replenishment time was varied by changing the waiting time at the line starting point between the sweeps. The acquired line deposits feature different morphologies and different amounts of deposited material. Interestingly, the deposition rate decreases with increasing replenishment time although an identical electron dose and sweep number was applied (see Figure 10.7), which even caused discontinuous line structures (see Line E, F and G). This result indicates the occurrence of partial TTIP dissociation and the formation of still volatile TTIP fragments, when a low number of electrons is applied in one sweep. Consequently, for long replenishment times desorption and off-diffusion of partially dissociated, volatile fragments from the PE irradiated area increasingly take place. The latter can occur when the replenishment time is longer than the (mean) local residence time τ of the TTIP fragments. These are then no longer available for further fragmentation and deposition in the next sweep. This model appears reasonable when one considers that TTIP, consisting of a central titanium atom bound to four organic ligands, is a comparably “large”

precursor molecule. In this regard, one can speculate that the decomposition of TTIP is a process for which multiple electrons are needed. The acquired results further enable a rough estimation of a (mean) diffusion constant D of TTIP fragments on Au(111). The diffusion constant is in the range of $\approx 4 \cdot 10^{-9}$ and $\approx 2 \cdot 10^{-8} \text{ cm}^2 \text{ s}^{-1}$.

10.3 Topography of EBID deposits

In this chapter, a comprehensive study of the morphology of dot, line and area deposits on a Si(100) sample is presented. The deposits were characterized via SEM to determine their lateral size and via *ex situ* AFM measurements to determine their height. From this structure characterization, the number of primary electrons is estimated which is necessary to deposit one atom via EBID with TTIP on silicon for different structures.

10.3.1 Topography investigation of dot deposits

To study the topography of dot deposits from TTIP on Si(100) two series of seven dots were fabricated using the same parameters. All dots were irradiated statically, i.e. without a delay time, and the electron dose was increased from 2 to 128 nC by doubling the dot dose from deposit to deposit.

First, the dots were characterized via SEM and it was found that the two series showed no noteworthy discrepancy concerning their morphology. Figure 10.8 depicts SEM images of one of the two series. The dots fabricated with the lowest electron dose, i.e. 2 nC and 4 nC, are only barely visible, which can be traced back to the weak material contrast between deposits from TTIP and silicon (see Chapter 7.3). All dot deposits exhibit a “volcanic crater” appearance. From a dot dose of 8 nC on (see Figure 10.8 c)), the edge inside the “crater” is getting increasingly sharper, while the edge outside the “crater” becomes first shallower and then, from a dot dose of 64 nC on (see Figure 10.8 f)), brighter in SEM, which indicates a higher volume. In addition, for the electron doses of 8, 16 and 32 nC (Figure 10.8 c) to e)) a deposit in the center of the “crater” is visible. This central deposit might be present in the dots of the electron doses of 64 and 128 nC as well, but possibly it is covered by the narrowing “cone end” of the “volcanos”. Interestingly, for the dot generated with the highest

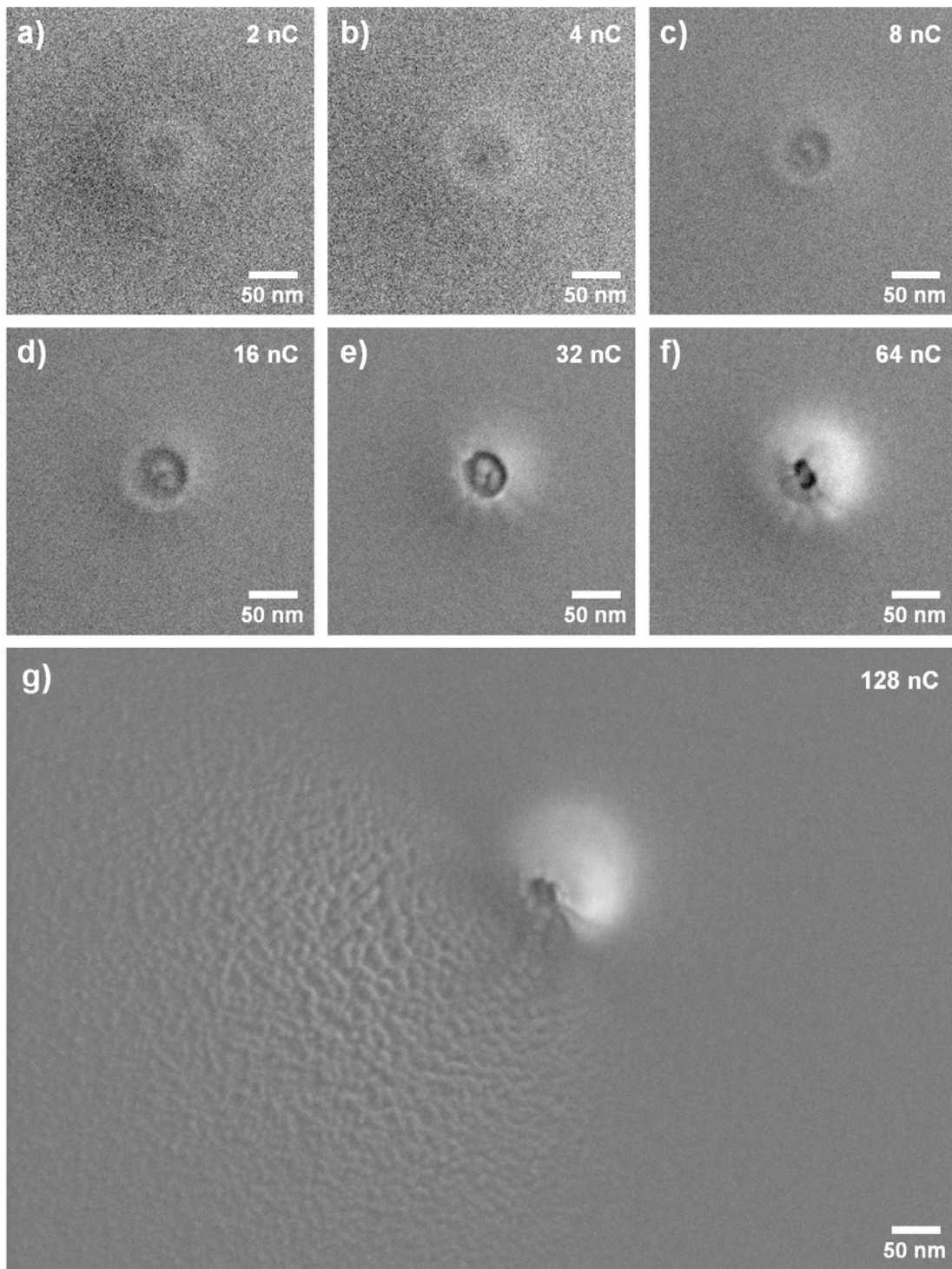


Figure 10.8: SEM images of seven dot deposits fabricated with an increasing electron dose on Si(100). The applied dot dose is denoted in the upper right of each image. Interestingly, for the dot generated with the highest electron dose (see g)) a rough structure is visible to the lower left of the dot deposit. Note that brightness and contrast of the images were adjusted significantly to enhance the visibility of the dot deposits.

electron dose (Figure 10.8 g)) a rough structure is visible to the lower left of the dot deposit. The possible origin of this structure is discussed below.

Due to the weak contrast and the shallow decline of the intensity in the depicted SEM images the visual determination of the dot width is difficult. Thus, for lateral size determination a slightly modified '20 % criterion' was applied, which is introduced and explained in Chapter 3.6.8. Further details and an example for dot width determination are given in Chapter 3.6.8, as well, and in reference [110]. For the dot deposits with the two lowest electron doses the structure diameter could not be determined in the described way, since the signal-to-noise ratio was too low in the corresponding SEM images. For the dots of higher electron dose the dot diameter was determined and the result is depicted graphically in Figure 10.9. It is found that for the electron doses of 8, 16 and 32 nC the diameter is scattered around a mean value of ≈ 122 nm. Only for the higher electron doses of 64 and 128 nC the diameter increases with dose.

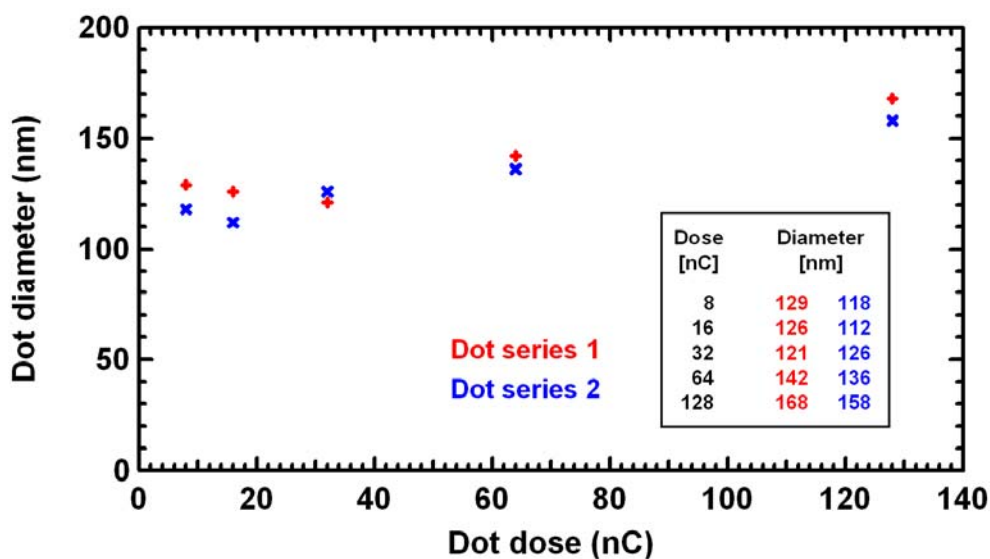


Figure 10.9: Dot diameters, determined from high magnification SEM images, in dependence of the electron dose. The diameters were determined according to the slightly modified '20 % criterion' by averaging over 5 profile lines (see Chapter 3.6.8). The red and blue colors indicate the corresponding dot series.

To investigate the height of these dot structures, the sample was transferred out of the UHV instrument and the structures were studied by means of AFM, performed *ex situ* at ambient conditions (details see Chapter 3.6.6). Figure 10.10 shows a direct comparison of acquired SEM and AFM data for one exemplary dot deposit, which was fabricated with an electron dose of 64 nC. Two findings can be made from Figure 10.10. First, the lateral resolution in the acquired AFM image is considerably lower than in the SEM image. Thus, the dot structures appear broadened by an average factor of ≈ 2 . Secondly, the AFM image in Figure 10.10 b) shows that the central structure of the dot deposit, which was interpreted as a cavity based on the acquired high resolution SEM image, can also not be resolved in the AFM measurement.

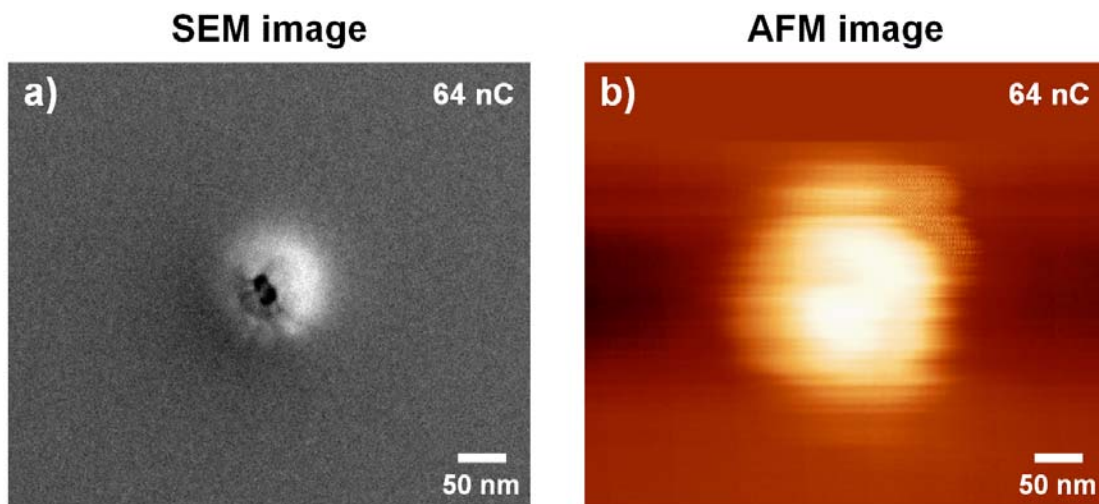


Figure 10.10: Direct comparison of SEM and AFM data of one exemplary dot deposit, which was fabricated with an electron dose of 64 nC.

The SEM image in Figure 10.8 g) shows a rough structure at the lower left of the dot deposit. Based on the appearance in SEM it can be assumed that it is a deposit generated during the fabrication of the dot structure. The acquired AFM images of the 128 nC dots confirm this idea since in both images a pronounced structure is observed. The latter was found to have a maximum height of ≈ 20 nm (compared to the smooth dot surrounding) with decreasing height for an increasing distance to the dot structure. In element specific Auger electron line scan (AELS) measurements for

C, Ti, O and Si, which were measured diagonally across one of the 128 nC dots and across the adjacent rough structure, the same chemical composition could be detected for the rough structure and the smoother area in the dot surrounding. It was found that both regions contain carbon, titanium and oxygen and that the silicon substrate signal is damped correspondingly. This result, which is also described in reference [110], can be traced back to material deposition in the surrounding of the central dot structure due to the BSE proximity effect (see Chapter 8) and considerable material deposition at the position of the rough structure. Thus, no considerable difference could be detected in AELS between the rough structure and the “smooth” dot surrounding.

Concerning the origin of the rough structure the scattering of FSE would be one probable explanation, which was also proposed by Achim Sandmann [110] and Florian Vollnhals [211]. An observation supporting this theory is that the rough structure was only observed for the dots generated with the highest electron dose, i.e. 128 nC ($t_{\text{exp}} = 320$ s), for which also the largest dot height was obtained (see results shown below). However, this can not be the only effect because scattering of FSE should occur in radial symmetry in the surrounding of the dot deposit and consequently a homogeneously thick structure would be expected. For the asymmetric appearance of the rough structure only at the lower left dot side two possible explanations can be given. First, it could be due to the position of the dosing nozzle relative to the generated dot. The nozzle was positioned on the right side of the sample (see Chapters 3.1.3 and 6), i.e. also on the right side of the dot structures. The principle possibility that the precursor gas flux influences the deposit morphology is reported e.g. by Friedli and Utke [19, 218], who describe the occurrence of “shadow effects”. Furthermore, in reference [145] Utke *et al.* report the dependence of the rotational symmetry, the high aspect ratio and the occurrence of internal structural inhomogeneities of pillar structures on the effectiveness of molecule replenishment, which also depends on the direction and strength of the precursor flux. In conclusion, an influence of the position of the dosing nozzle on the generation of the observed rough structure is feasible. Secondly, the occurrence of the rough structure at one side of the dot could be explained by drift of the sample during dot fabrication, which causes an inhomogeneous dot structure growth. Consequently, an inhomogeneous scattering of FSE in the deposit could be assumed. An enhanced scattering of FSE into one direction could then possibly

cause the growth of an additional deposit only in that direction relative to the central dot structure.

From the acquired AFM images of both dot series the heights of the dot structures were determined. Figure 10.11 shows a graphic representation of the dot height in dependence of the electron dose. The heights of the corresponding dot series are depicted in red and blue color while the mean heights of the dots are drawn in green. It is found that the dot height is linearly dependent on the electron dose, starting with a height of 2 nm (for $d_D = 2$ nC) up to 89 nm (for $d_D = 128$ nC) [110]. This means that the growth of statically irradiated dots occurs with an average growth rate of ≈ 0.7 nm / nC. Accounting for the applied beam current for structure generation, i.e. 400 pA, the latter value corresponds to a growth rate of ≈ 0.3 nm / s.

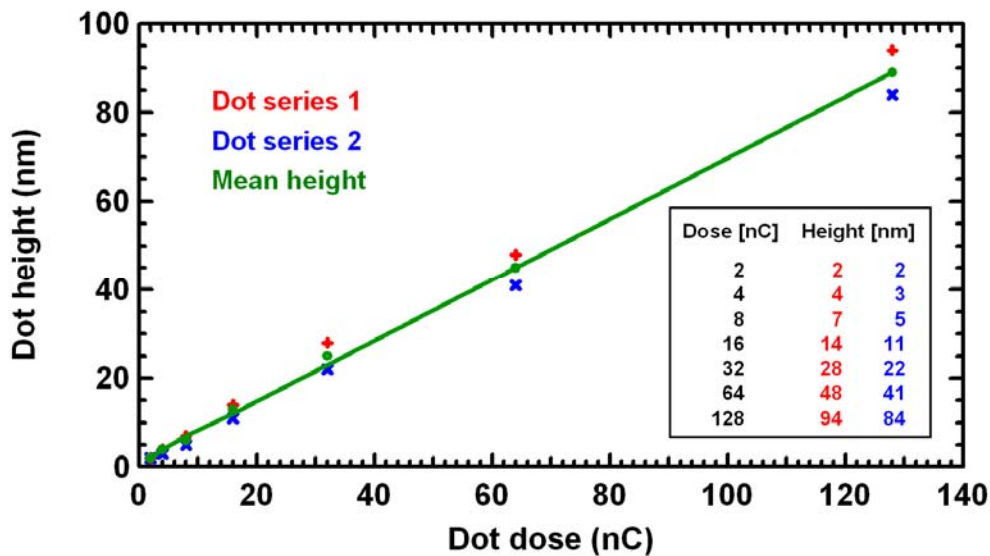


Figure 10.11: Dot heights, determined from high magnification AFM images, in dependence of the electron dose. The heights were determined by averaging over 10 profile lines. The colors red and blue indicate the corresponding dot series, the green color indicates the average values.

Based on the performed structure characterization, comprising both the lateral and vertical dot size, it is possible to roughly estimate the number of PEs which is necessary to deposit one atom, valid for EBID at the given experimental parameters.

First, an estimation of the dot volume is necessary, which is hampered by the “volcanic crater” like morphology. The minimum volume might be estimated by the volume of a cone and the maximum volume by the volume of a cylinder. It is assumed that the actual deposit volume is closest to the one of a truncated cone [110] (see Figure 16.6 b) in the Appendix). Based on this assumption the volumes of the dot deposits depicted in Figure 10.8 can be determined. Table 10.2 shows an overview of the applied lithographic parameters, the measured dot sizes and the calculated truncated cone dot volumes.

t_{exp} [s]	d_D [nC]	N(PE) -	Diameter [nm]	Height [nm]	Volume [cm ³]
5	2	$1.2 \cdot 10^{10}$	-	2	-
10	4	$2.5 \cdot 10^{10}$	-	4	-
20	8	$5.0 \cdot 10^{10}$	124	6	$4.2 \cdot 10^{-17}$
40	16	$1.0 \cdot 10^{11}$	119	13	$8.4 \cdot 10^{-17}$
80	32	$2.0 \cdot 10^{11}$	124	25	$1.8 \cdot 10^{-16}$
160	64	$4.0 \cdot 10^{11}$	139	45	$4.0 \cdot 10^{-16}$
320	128	$8.0 \cdot 10^{11}$	163	89	$1.1 \cdot 10^{-15}$

Table 10.2: Overview of the applied lithographic parameters (exposure time t_{exp} , dot dose d_D and number of primary electrons $N(\text{PE})$), the measured dot sizes and the calculated dot volumes (assuming a truncated cone shape of the deposits).

To determine the number of deposited atoms in the dots the following equation is applied:

$$N = n \cdot N_A = \frac{m}{M} \cdot N_A = \frac{\rho \cdot V}{M} \cdot N_A = V \cdot \frac{\rho \cdot N_A}{M} \quad (10.1)$$

The quantity that is to multiply with the volume V , i.e. $(\rho \cdot N_A) / M$, is a material specific number, which is addressed as ‘atom density’ in the following. For the deposited material the latter quantity can be roughly estimated from Table 16.7 of the Appendix, which depicts the densities ρ [62], molar masses M [62] and calculated

atom densities N/V of relevant materials for EBID with TTIP. To estimate the atom density of the deposits it is necessary to know their chemical composition, which was studied in Chapter 7.2. Although the chemical composition differs for dot, line and area structures and generally depends on the lithographic parameters, it was found that its influence on the atom density is marginal (see Table 16.7 of the Appendix). Thus, for simplicity and uniformity reasons for all following estimations a chemical composition of the investigated structures of 25 % carbon and 75 % TiO_2 is assumed. Using the specific data of graphitic carbon and the averaged data of titania, both specified in Table 16.7 of the Appendix, the atom density of the deposited material can be calculated to $3.5 \cdot 10^{22} \text{ cm}^{-3}$. The error that is made by estimating the chemical composition lies at $\approx \pm 3 \%$. Nevertheless, it is noted that this atom density is only an approximation because the precise density ρ of the deposits is not known. It is possible that an amorphous material was deposited via EBID with a reduced density compared to the ones of the TiO_2 species rutile, anatase and brookite. The error caused by the uncertainty of the density is considered to preponderate.

Using the estimated atom density of the deposits of $3.5 \cdot 10^{22} \text{ cm}^{-3}$, the number of deposited atoms can be calculated according to Equation 10.1. It ranges between $1.5 \cdot 10^6$ for $d_D = 8 \text{ nC}$ and $3.8 \cdot 10^7$ atoms for $d_D = 128 \text{ nC}$. This corresponds to an estimated number of primary electrons between $\approx 21,100$ and $33,900$ that is needed to deposit one atom for the statically irradiated dots. Considering the assumed chemical composition of 25 % carbon and 75 % TiO_2 this means that each fourth atom in the deposit is a titanium atom. Consequently, one needs four times as many primary electrons per TTIP molecule to generate a deposit, which corresponds to the range of $\approx 84,400$ and $135,600$.

10.3.2 Topography investigation of line deposits

To study the topography of line deposits from TTIP on Si(100) three line patterns were fabricated. The line dose was doubled (clockwise) from line to line in each pattern and additionally from pattern to pattern, ranging in total from 58 to $927 \mu\text{C}/\text{cm}$.

First, the line deposits were characterized via SEM. The Figures 10.12 a) to c) depict the acquired images with the corresponding line doses labeled close to each line. All

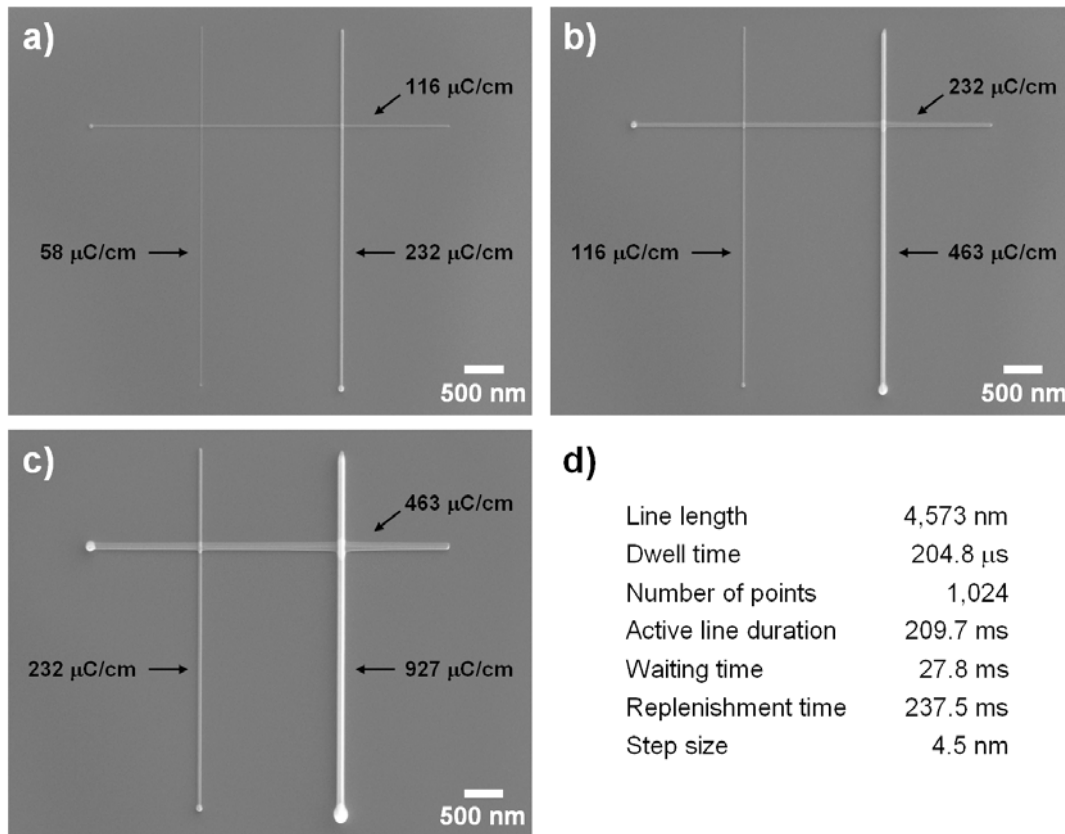


Figure 10.12: SEM images of line patterns on Si(100), each one consisting of three perpendicularly arranged line structures. The applied line dose is labeled close to each line structure. It was doubled (clockwise) from line to line in each pattern. Additionally, the line dose was doubled from the pattern in a) to the ones in b) and c), ranging in total from 58 to 927 μ C/cm. In d) the lithographic parameters are specified.

lithographic parameters are specified in Figure 10.12 d). The dot-shaped deposits at one line end are ‘WT deposits’ explained in Chapter 3.2.1. With increasing electron dose the intensity of the lines increases. This indicates that the lines are growing larger with increasing dose. The same holds for the line starting points.

To quantify the growth of the structures, the lateral size of the lines and line starting points was determined from high magnification SEM images. Figure 10.13 and Figure 10.14 show a graphic representation of the development of the diameter of both structures with increasing electron dose. It is found that both for the vertical lines (drawn in red) and for the horizontal lines (drawn in blue) the diameter of the lines and the corresponding line starting points increases linearly with dose. In addition, it

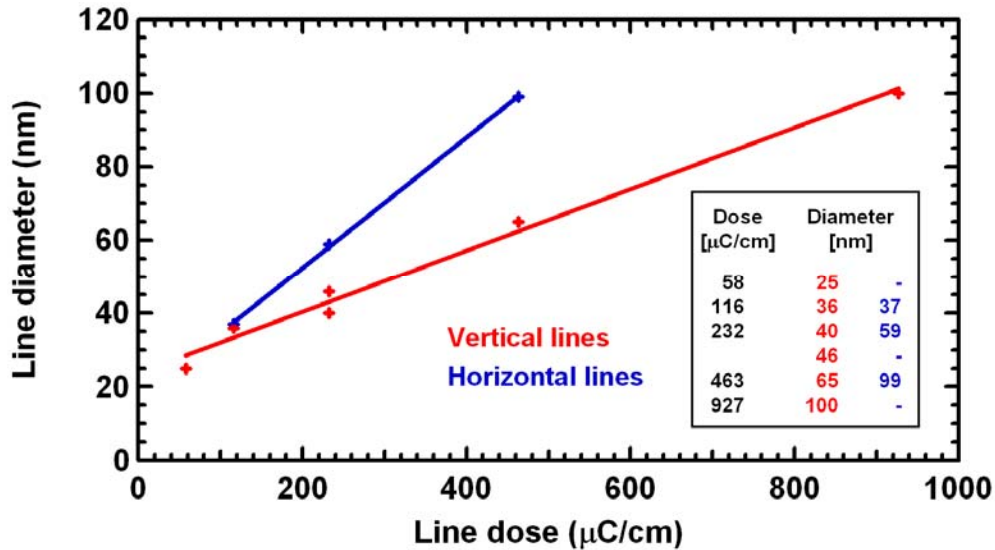


Figure 10.13: Line diameters, determined from high magnification SEM images, in dependence of the electron dose. The diameters were determined visually in WSxM by averaging over 10 profile lines. The red data labels the vertical lines while the blue data marks the horizontal ones.

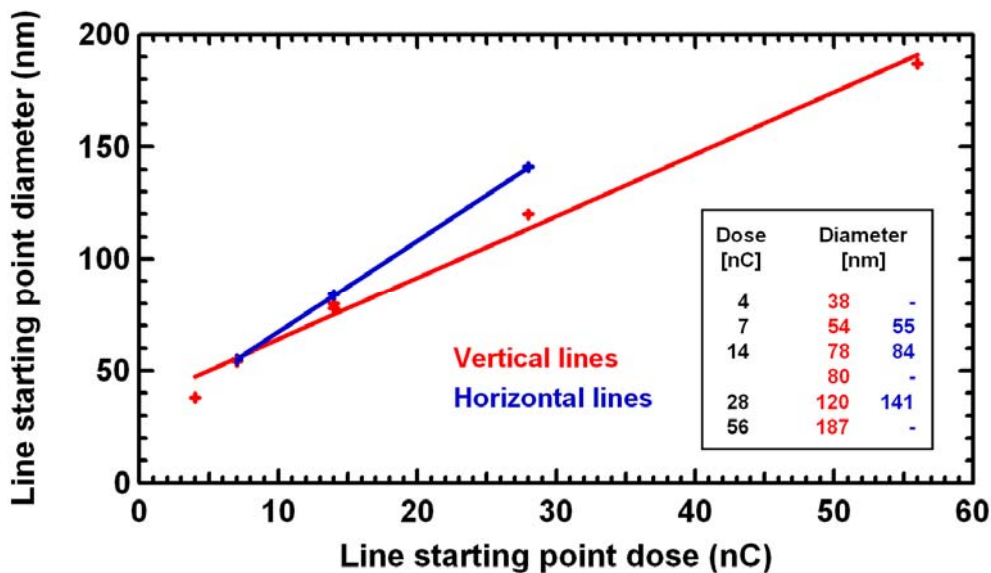


Figure 10.14: Line starting point diameters, determined from high magnification SEM images, in dependence of the electron dose. The diameters were determined visually in WSxM by averaging over 10 profile lines. The red data labels the vertical line starting points while the blue data marks the horizontal ones.

is found that the horizontal lines and also the corresponding line starting points are broader compared to the structures of equal electron dose fabricated in vertical direction. For this finding two possible explanations can be assumed, which were also considered in Chapter 10.3.1. First, a slight vertical drift of the sample during EBID would be a conclusive explanation. Secondly, also an influence of the position of the dosing nozzle and thus of the precursor molecule flux can not be ruled out. The nozzle was positioned right to the line patterns (in Figure 10.12). Consequently, the TTIP molecule flux was directed parallel to the horizontal lines and perpendicular to the vertical ones.

From Figure 10.13 it can be derived that the diameter of the horizontal lines increases per line dose in average by $\approx 0.2 \text{ nm} / (\mu\text{C}/\text{cm})$ and the diameter of the vertical lines by $\approx 0.1 \text{ nm} / (\mu\text{C}/\text{cm})$. For the line starting points the increase of the diameter per line starting point dose can be determined from Figure 10.14. It is found that the diameter of the starting points of the horizontal lines increases with a growth rate of in average $\approx 4.1 \text{ nm} / \text{nC}$, i.e. $\approx 1.6 \text{ nm} / \text{s}$, and the diameter of the vertical ones by $\approx 2.8 \text{ nm} / \text{nC}$, i.e. $\approx 1.1 \text{ nm} / \text{s}$. Comparing these growth rates with the rate of the static dot deposits ($\approx 0.7 \text{ nm} / \text{nC}$), which were discussed in Chapter 10.3.1, one finds a larger value for the line starting points by a factor of $\approx 4 - 6$. This observation completely follows the expectation since the line starting points are influenced by the adjacent line structures. They can additionally grow by the exposure with BSE and SE2 during the line irradiation. This finding emphasizes once more the significance of the lithographic parameters and of the scan strategy.

To investigate the height of the lines, the sample was transferred out of the UHV instrument and the structures were studied by means of ambient AFM (details see Chapter 3.6.6). Figure 10.15 shows the AFM images of the line patterns depicted in Figure 10.12. The images were taken by scanning the AFM tip in an angle of 45° with respect to the lines to minimize baseline distortions (details see reference [110]). In addition, for these measurements a z scale was adjusted by which all line starting points and all crossing points of the lines could be resolved [110]. The images in Figure 10.15 a), c) and e) (with increasing electron dose from top to bottom) are the acquired 2D AFM images which correspond to the SEM images in Figure 10.12 a), b) and c). The depicted images to the right (Figure 10.15 b), d) and f)) are the corresponding 3D AFM images. In the latter, the z scale was adjusted via the height

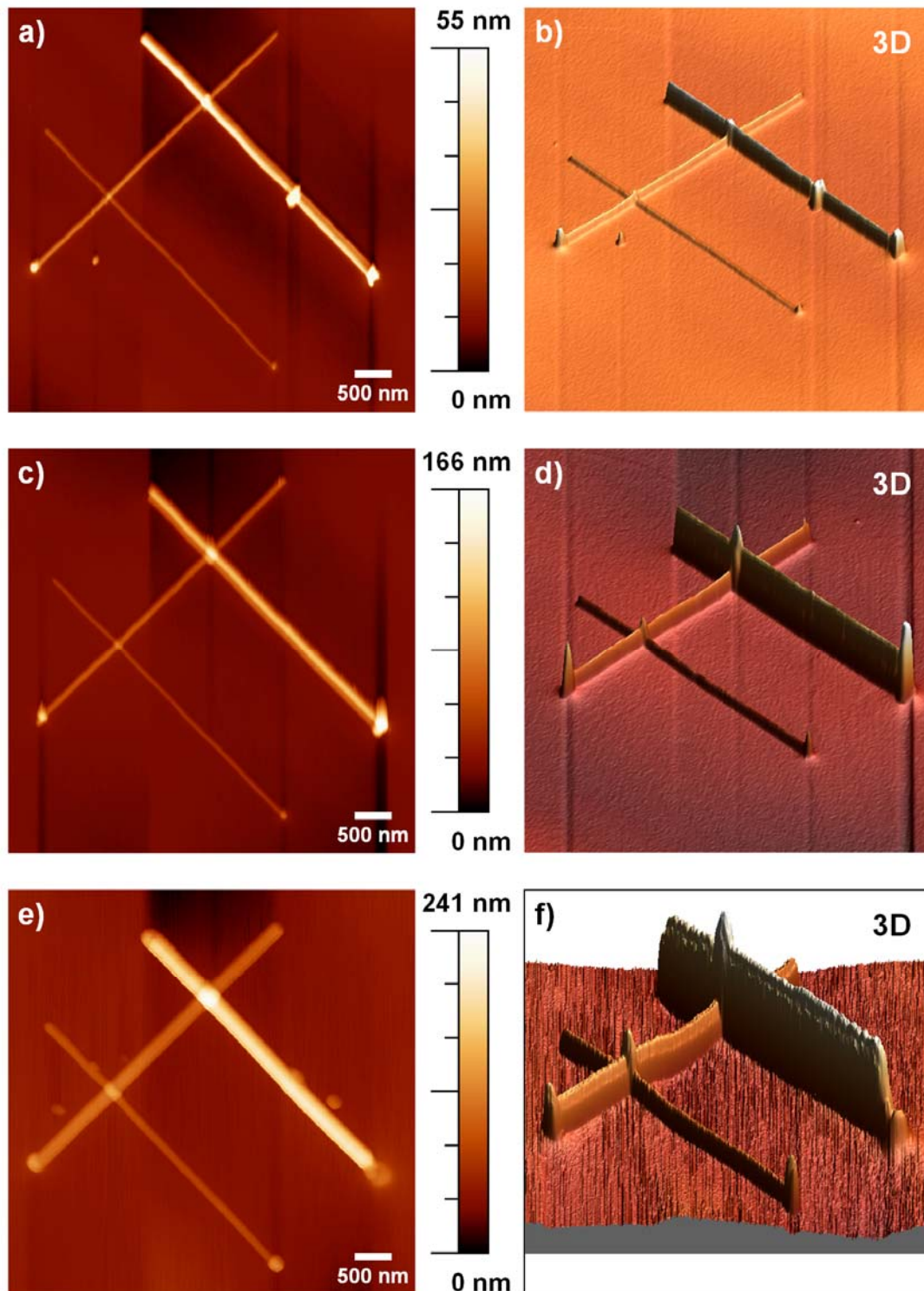


Figure 10.15: a), c) and e) AFM images of the line patterns depicted in Figure 10.12. The line doses increase from a) to c) and e). The images to the right (b), d) and f)) are the corresponding 3D AFM images. In the latter, the z scale was adjusted via the height of the right vertical line of each pattern.

of the right vertical line of each pattern. The images in Figure 10.15 indicate that the height of the lines is increasing with electron dose.

To quantify the line growth in z direction high magnification AFM images of the vertical lines were measured 1 μm below the crossing point with the horizontal line. In Figure 10.16 the line height is plotted graphically versus the electron dose. It is found that the height of the vertical lines is increasing linearly with the applied dose. A vertical growth rate of $\approx 0.2 \text{ nm} / (\mu\text{C}/\text{cm})$ can be determined.

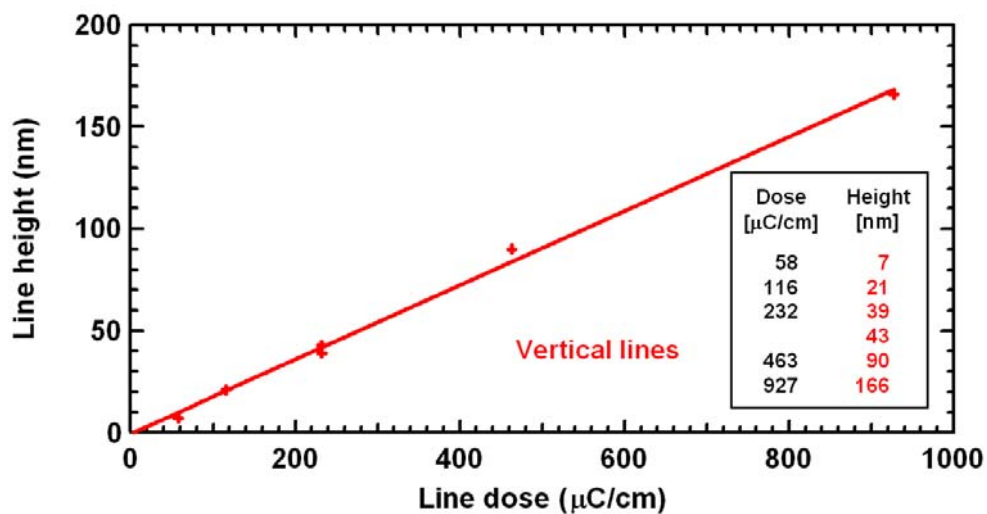


Figure 10.16: Height of the vertical lines, determined from high magnification AFM images, in dependence of the line dose. The heights were determined in WSxM by averaging over 10 profile lines.

Analogous to the statically irradiated dot structures (Chapter 10.3.1), the lateral and vertical size of the line deposits can be used to roughly estimate the number of PEs which is necessary to deposit one atom. The acquired result is valid for EBID with TTIP on Si(100) at the applied experimental parameters.

First, an estimation of the line volume is to be performed. The minimum volume might be estimated by the volume of a structure with triangular cross-section, while the maximum volume should be the one of a cuboid structure with rectangular cross-section (see Figure 16.6 d) and f) in the Appendix). It is assumed that the actual line volume is closest to the mean of these limits which can then be estimated by a structure with trapezoidal cross-section (see Figure 16.6 e) in the Appendix) [110].

Based on this assumption the volumes of the vertical line deposits depicted in Figure 10.12 were determined. Table 10.3 shows an overview of the lithographic parameters, the measured sizes of the vertical lines and the calculated line volumes. The number of deposited atoms in the lines can then be estimated by Equation 10.1 (see Chapter 10.3.1) and multiplying the calculated volumes with the suggested atom density of the deposited material. Consistent to Chapter 10.3.1, a chemical composition of 25 % carbon and 75 % TiO₂ is assumed and the atom density of the deposited material is estimated by the value of $3.5 \cdot 10^{22} \text{ cm}^{-3}$ (details see Chapter 10.3.1).

t_{exp} [min]	d_L [$\mu\text{C}/\text{cm}$]	$N(\text{PE})$ -	Diameter [nm]	Height [nm]	Volume [cm^3]
1.25	58	$1.7 \cdot 10^{11}$	25	7	$6.0 \cdot 10^{-16}$
2.5	116	$3.3 \cdot 10^{11}$	36	21	$2.6 \cdot 10^{-15}$
5	232	$6.6 \cdot 10^{11}$	40	39	$5.4 \cdot 10^{-15}$
5	232	$6.6 \cdot 10^{11}$	46	43	$6.8 \cdot 10^{-15}$
10	463	$1.3 \cdot 10^{12}$	65	90	$2.0 \cdot 10^{-14}$
20	927	$2.6 \cdot 10^{12}$	100	166	$5.7 \cdot 10^{-14}$

Table 10.3: Overview of lithographic parameters (exposure time t_{exp} , line dose d_L and number of primary electrons $N(\text{PE})$), the measured vertical line sizes and the calculated line volumes (assuming a line structure with trapezoidal cross-section).

Using the estimated atom density of $3.5 \cdot 10^{22} \text{ cm}^{-3}$, the number of deposited atoms in the vertical lines was calculated. It ranges between $2.1 \cdot 10^7$ for $d_L = 58 \mu\text{C}/\text{cm}$ and $2.0 \cdot 10^9$ atoms for $d_L = 927 \mu\text{C}/\text{cm}$. This corresponds to an estimated number of primary electrons between $\approx 1,300$ and $7,900$ that is needed to deposit one atom for the vertical line deposits. Considering the assumed chemical composition of 25 % carbon and 75 % TiO₂ this means that each fourth atom in the deposit is a titanium atom. Consequently, one needs four times as many primary electrons per TTIP molecule to generate a deposit, which corresponds to the range of $\approx 5,200$ and $31,600$.

When one compares the required number of primary electrons to deposit one atom of the vertical lines ($\approx 1,300 - 7,900$ PEs) with the one of the statically irradiated dots ($\approx 21,100 - 33,900$ PEs), one finds a strong difference. The latter could be explained by the process regime during EBID. For the fabrication of the dots no delay time for additional precursor replenishment was provided. Thus, only those molecules could be dissociated which could diffuse to the irradiated area and adsorb from the gas phase during the irradiation time. Consequently, one can assume that deposition occurred rather in the transport-limited regime (see also discussion in Chapter 10.1). In contrast to that, the lines were generated by a scanning electron beam and each dot of the line structure had a replenishment time of 237.5 ms, in which additional precursor molecules could diffuse into the irradiated area [110] and adsorb from the gas phase. It is therefore assumed that the process regime during line fabrication is closer to the electron-limited regime. Concerning the above considered numbers of primary electrons to deposit one atom this means that the number for the statically irradiated dots is most probably overestimated (since there is rather a surplus of electrons and a lack of TTIP molecules), while the number for the line structures is closer to the actually needed number.

10.3.3 Topography investigation of area deposits

To study the topography of area deposits from TTIP on Si(100) three structures of rectangular shape and varying electron dose were fabricated. The irradiated areas had a size of $4.6 \mu\text{m} \times 3.4 \mu\text{m}$ and the area doses were 1.23, 2.46 and 3.70 C/cm^2 . The area deposits were characterized via SEM and AFM. Figure 10.17 depicts a direct comparison. In the AFM images all area structures feature a pronounced, dot-shaped deposit in the upper left corner, which is a 'WT deposit' explained in Chapter 3.2.1. In addition, also the left vertical edges of the area deposits are enhanced, which are 'WT deposits', as well. The other high features in the AFM images are most presumably dust particles which contaminated the sample surface after exposure to air for the ambient AFM measurements. Obviously, the AFM images indicate that more material is deposited with increasing electron dose.

To quantify the growth of the area structures, their lateral and vertical sizes were determined. Analysis of the SEM data showed that the lateral size of all three area

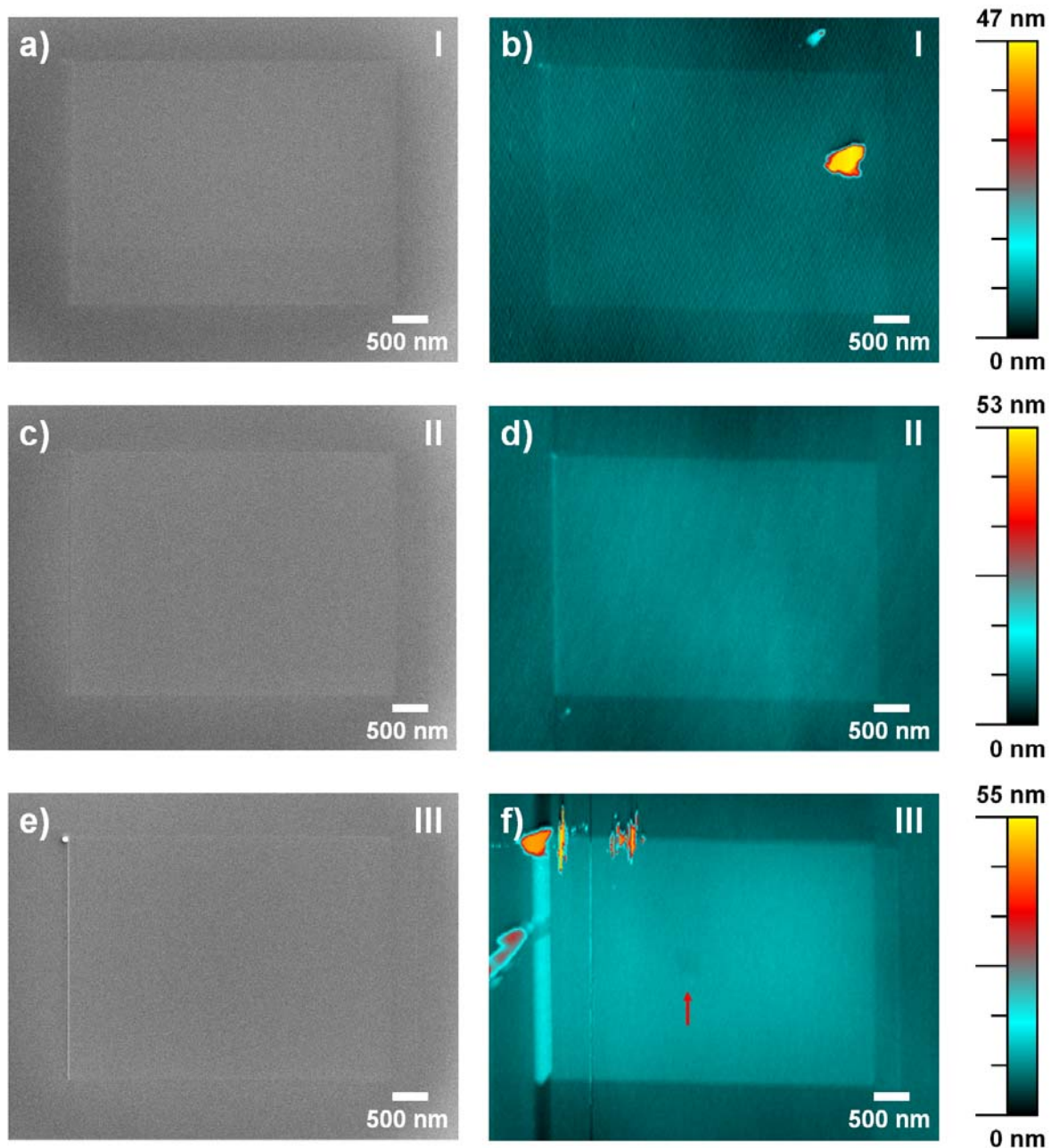


Figure 10.17: Direct comparison of SEM (left side) and AFM images (right side) of area deposits on Si(100). The electron dose of the area structures increases from deposit I (a) and b)) to deposit II (c) and d)) and deposit III (e) and f)) from 1.23 to 2.46 and 3.70 C/cm². The red arrow in f) labels the “scan damage” from an AES measurement (see text).

deposits corresponds well to the irradiated area of 4.6 μm x 3.4 μm (\pm 50 nm). From the AFM images the height of the area structures could be determined to be \approx 2 nm for area deposit I, \approx 5 nm for area deposit II and \approx 7 nm for area deposit III. Since the

area deposits were also characterized by means of AES (in UHV), a determination of the structure height was also possible via the Si substrate signal damping. From this analysis a height of 1.8 nm was determined for area deposit I, a height of 3.9 nm for area deposit II and a height bigger than 6.1 nm for area deposit III (due to complete substrate signal damping in the latter case). Table 10.4 shows a direct comparison of the heights derived from both techniques. A high agreement between both data is found. This confirms the reliability of the method of determining structure heights via the substrate signal damping in AES.

Deposit	d_A [C/cm ²]	Height from AFM [nm]	Height from AES [nm]	Deviation -
Area I	1.23	2	1.8	- 10 %
Area II	2.46	5	3.9	- 22 %
Area III	3.70	7	> 6.1	-

Table 10.4: Direct comparison of heights of area deposits determined from AFM and AES data.

An important issue of structure characterization via AES is the influence of the electron beam on the investigated material. For titanium dioxide, the significant influence of an electron beam is well-known from literature, and effects like electron stimulated desorption (ESD) of oxygen are reported [6, 104-107]. Kern *et al.* even demonstrate that electron beam exposure of amorphous TiO₂ films leads to a well-defined volume loss primarily limited to the PE irradiated area (with $U_B = 20$ kV) [107]. The authors attribute this phenomenon mainly to oxygen desorption but also describe the possibility of local crystallization into anatase [107].

Based on these reports it was pointed out already in the previous chapters that the electron beam during AES measurements can influence also EBID structures produced from TTIP. Clear evidence for this assumption is found in the AFM image depicted in Figure 10.17 f). While the area structure appears mostly homogeneous, a dark, square area is visible slightly to the left of the center of the deposit (labeled by a red arrow). This area can be assigned to the position where local AES was

performed due to its square shape and due to its size which corresponds to the size of the AES 'scan window' ($200 \times 200 \text{ nm}^2$). A closer investigation via an AFM height profile shows a local depression with a depth of $\approx 0.5 \text{ nm}$ indicating material loss.

Analogous to the statically irradiated dots (Chapter 10.3.1) and to the vertical lines (Chapter 10.3.2), the lateral and vertical size of the area deposits can be used to roughly estimate the number of PEs needed to deposit one atom.

The volume of the area deposits is calculated assuming a cuboid shape according to Figure 16.6 g) in the Appendix. Table 10.5 shows an overview of the lithographic parameters, the measured sizes and the calculated volumes.

Deposit	d_A [C/cm ²]	N(PE) -	Area [$\mu\text{m} \times \mu\text{m}$]	Height [nm]	Volume [cm ³]
Area I	1.23	$1.2 \cdot 10^{12}$	4.6 x 3.4	2	$3.1 \cdot 10^{-14}$
Area II	2.46	$2.4 \cdot 10^{12}$	4.6 x 3.4	5	$7.8 \cdot 10^{-14}$
Area III	3.70	$3.6 \cdot 10^{12}$	4.6 x 3.4	7	$1.1 \cdot 10^{-13}$

Table 10.5: Overview of lithographic parameters (area dose d_A and number of primary electrons $N(\text{PE})$), the measured sizes and the calculated volumes (assuming a cuboid deposit shape).

Applying Equation 10.1, the number of atoms in the deposits can be estimated. Consistent to the Chapters 10.3.1 and 10.3.2, a chemical composition of 25 % carbon and 75 % TiO_2 is assumed and the atom density of the deposited material is estimated by the value of $3.5 \cdot 10^{22} \text{ cm}^{-3}$ (details see Chapter 10.3.1). With these assumptions, the number of atoms in the area deposits was calculated to range between $1.1 \cdot 10^9$ atoms for $d_A = 1.23 \text{ C/cm}^2$ and $3.8 \cdot 10^9$ atoms for $d_A = 3.70 \text{ C/cm}^2$. This corresponds to an estimated number of primary electrons between ≈ 900 and 1,100, needed to deposit one atom for the area structures. 25 % carbon and 75 % TiO_2 , one needs four times as many primary electrons per TTIP molecule to generate a deposit, which corresponds to the range of $\approx 3,600$ and 4,400 PEs.

Comparing the required number of PEs to deposit one atom for area structures ($\approx 900 - 1,100$ PEs) with the one for the line structures ($\approx 1,300 - 7,900$ PEs), a deviation is noticed. This can be explained by the shape of the irradiated structure and the used scan strategy. The irradiation of one single point always leads to the exposure of the surrounding region by BSEs and SE2, which is known as 'BSE proximity effect' [5] (see Chapter 8). Therefore, in EBID the additional deposition of material is caused in this region. For structures consisting of more than one point to be irradiated, each point is influenced by the "proximity effect" of neighboring points (unless the rather improbable case that the step size is bigger than the BSE exit radius). While for a line structure the irradiated points propagate in one dimension, for area structures they propagate in two. Consequently, for an area the influence of the 'BSE proximity effect' by neighboring points on one single point of the structure is much stronger than for a line and thus a higher amount of additionally deposited material is caused in the PE irradiated area. This leads to a lower number of PEs that is required to deposit one atom, fully explaining the finding reported above. Moreover, it is obvious that PE irradiated points in the center of an area structure are influenced much stronger by the 'BSE proximity effect' than the ones at the structure edge, since the number of points in their surrounding is simply much higher. Thus, the deposition of a slightly higher amount of material is expected in the center compared to the edges which should result in a slightly rounded top face of an area deposit.

In the following, the shape of area structures and in particular the consequences of the 'BSE proximity effect' on their shape are investigated in more detail. For this purpose, the area deposits depicted in Figure 10.17 are considered. Figure 10.18 shows AFM height profiles acquired from the corresponding high resolution AFM images. In the profiles of the area deposits III and II it is found that the top face of the area deposits is indeed not flat but has a rather round, convex shape. This observation exactly follows the expectation, which was discussed above. Furthermore, it is found that the lateral size of the deposits obviously exceeds the size of the irradiated area. This can be traced back to the 'BSE proximity effect', which causes the growth of a deposit at the edges of the intended structures. The latter deposits are labeled by gray, oval markers in Figure 10.18.

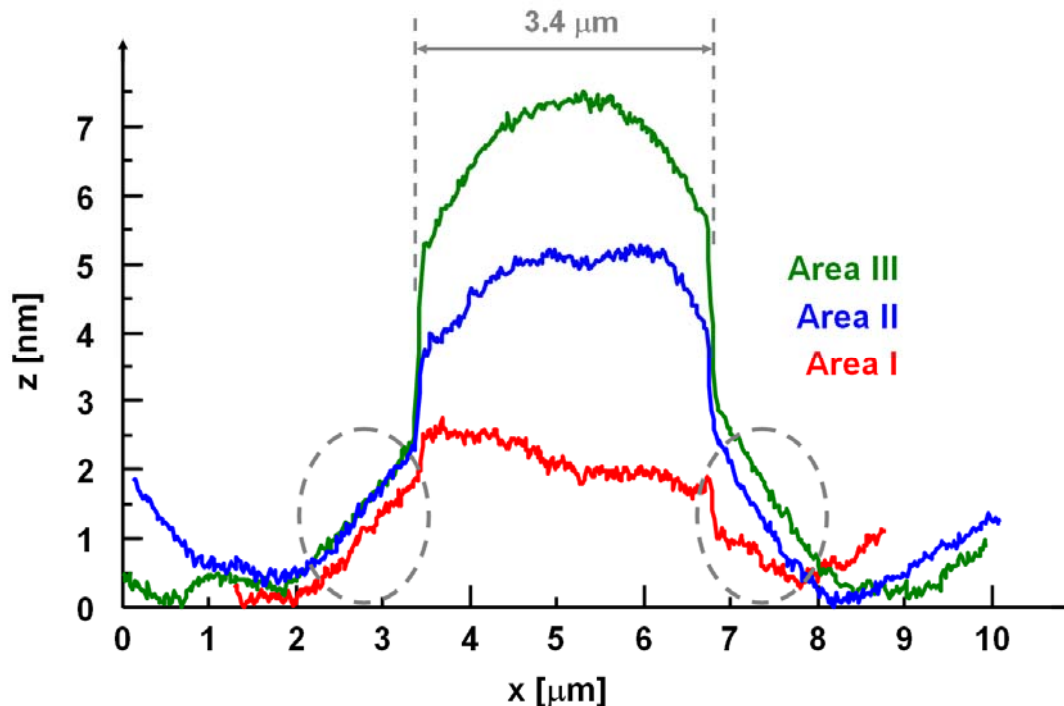


Figure 10.18: a) AFM height profiles of the area deposits I, II and III, depicted in Figure 10.17. The gray, oval markers label the deposits at the edges of the area structures which are caused by the ‘BSE proximity effect’.

Based on the latter considerations, Achim Sandmann implemented a simple model describing the distribution of the released electrons from the substrate surface, i.e. the ‘normalized number of emitted electrons’ [110]. The simplicity of the model is based on a reduction of the symmetry of the area of emitted electrons from a circular to a square shape. Figure 10.19 a) displays an assumed BSE and SE distribution for the irradiation of one spot depicted in two dimensions. The number of released electrons in the center (BSE and SE1) was set to 100 %, to only 20 % in direct proximity (BSE and SE2) and to 2 % in the further surrounding (BSE and SE2) to the end of the ‘BSE exit area’. Figure 10.19 b) displays this simplified BSE and SE distribution in 3D with the ordinate representing the ‘normalized number of emitted electrons’, which should correspond to the deposit height as a first approximation. Utilizing this approximation, which describes the irradiation of one spot on the surface, the ‘normalized number of emitted electrons’ for an area structure can be simulated. Figure 10.19 c) shows the 3D BSE and SE distribution resulting from the

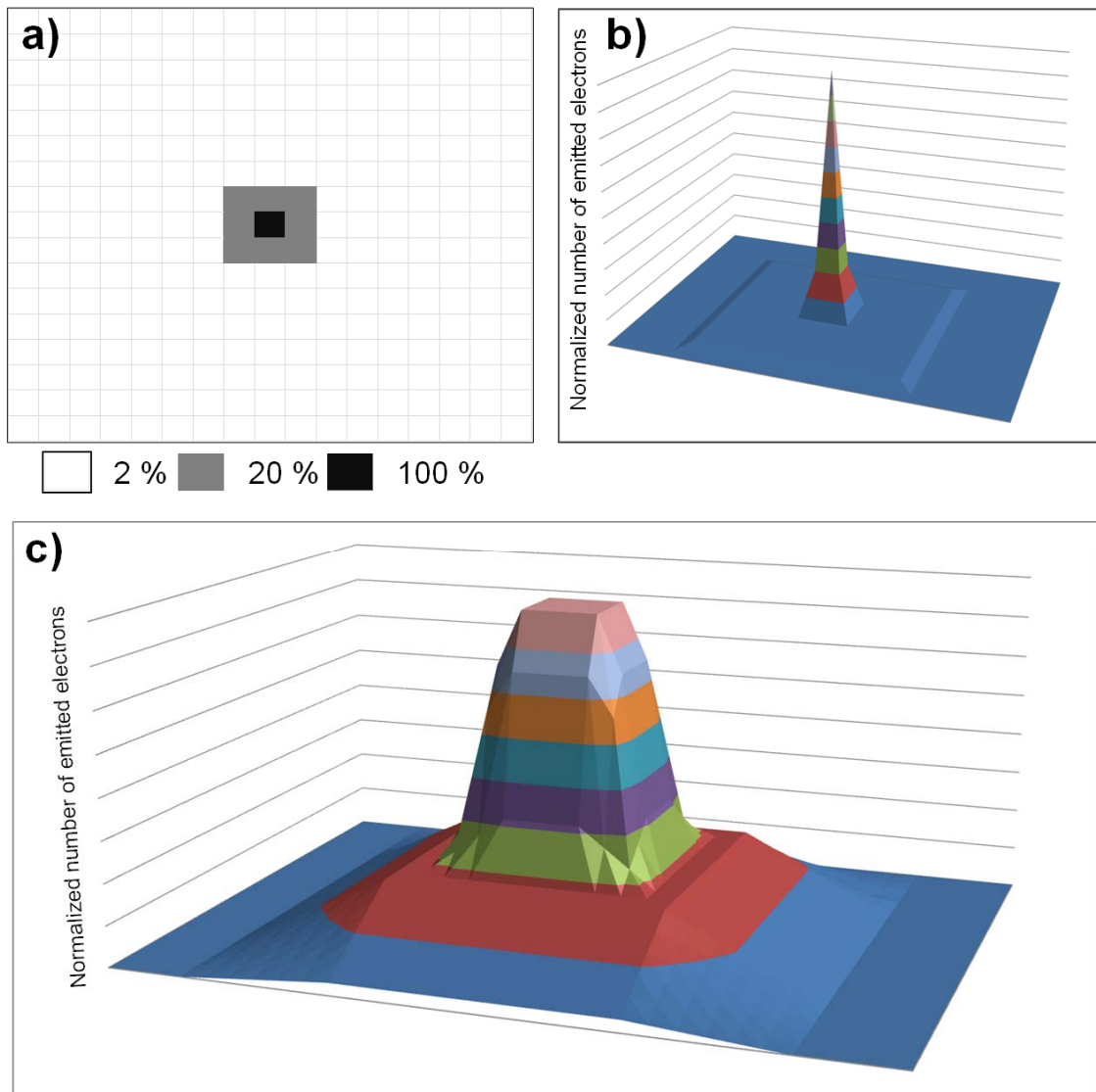


Figure 10.19: Model of the 'normalized number of emitted electrons' from the sample surface upon electron beam irradiation. a) and b) Suggested BSE and SE distribution for the irradiation of one spot, depicted in 2D (a) and 3D (b). c) Resulting BSE distribution by the overlap for a 6 by 6 square. (Please note that this model was developed by Achim Sandmann and that the figure is adapted from reference [110]).

overlap of the suggested distribution for a 6 by 6 square [110]. The acquired electron distribution strongly resembles the shape of the fabricated area structures as derived from the AFM height profiles in Figure 10.18. Both the round, convex shape of the top face of the area deposits, the steep decline at the edges and the formation of the additional deposit at the edges due to the 'BSE proximity effect' are reproduced in

Figure 10.19 c) and can thus be explained by the multiple overlap of the 'BSE exit area'.

Although the model of Achim Sandmann is strongly simplified as compared to the real electron distribution (symmetry reduction), it seems to work quite well and enables the simulation of the electron distribution in structures of arbitrary shape. It can be concluded that the final shape of a deposit is not only strongly influenced by the distribution of the primary electrons, i.e. the geometric shape of the intended structure and the scan strategy, but also by the resulting "overlap" of emitted electrons (BSEs and SE) from the substrate surface [110]. The latter is determined by the number of neighboring points to be irradiated in the EBID process.

10.3.4 Summary

In Chapter 10.3 a comprehensive investigation of the morphology of EBID deposits on Si(100) was described. Both the lateral and the vertical sizes of dot, line and area structures were studied in dependence of the electron dose. A quantitative analysis was performed using SEM and AFM data. Linear dependencies on the electron dose were found for the height growth of dot and line deposits and for the lateral growth of lines and line starting points. By comparing the deposit shapes with basic three-dimensional geometric shapes, the volumes of the nanostructures were estimated. They were used to determine the numbers of primary electrons that are needed to deposit one atom of the corresponding deposit. It was found that for dot structures the number of PEs lies between $\approx 21,100$ and $33,900$, for line structures between $\approx 1,300$ and $7,900$ and for area structures between ≈ 900 and $1,100$. The differences can be explained by the established process regime on the one hand and by the shape of the irradiated structure and the resulting scan strategy on the other. The number of neighboring points to be irradiated, which is largest for area structures, determines the influence of the 'BSE proximity effect' on the deposit shape and on the amount of deposited material in the PE irradiated area.

The direct comparison of nanostructure heights determined by AFM and by the substrate signal damping in AES showed a high agreement of both data. This demonstrates the reliability of the AES approach to determine the height of thin layers and thin nanostructures. Interestingly, the "scan damage" of a local AES measurement on an area deposit could be observed in an AFM image. A local

depression by ≈ 0.5 nm was detected, which indicates either the “loss” of material, e.g. by the electron stimulated desorption of oxygen (or even CO or CO₂), or a structural change in the deposited material.

11 Stability of fabricated nanostructures

The stability of generated structures plays a significant role in terms of potential applications of EBID deposits. In this work, the stability of the titanium oxide nanocrystals fabricated by post-treatment procedures (Chapter 9) was analyzed after long-term storage under vacuum conditions in the UHV instrument. Secondly, the stability of EBID deposits was studied after exposure to ambient conditions.

The Si(100) sample with the titanium oxide nanocrystals fabricated by post-treatment procedures (Chapter 9) was stored under vacuum conditions in the analysis chamber of the UHV instrument. The total storage time was 890 days after nanocrystal growth. In this time period, the chamber pressure was in the low 10^{-10} mbar regime except for FEBIP experiments in which a maximum background pressure of $3.0 \cdot 10^{-7}$ mbar was adjusted for several hours, respectively. To investigate whether the nanocrystals are stable upon this long-term storage they were analyzed via SEM and AES.

The characterization via SEM shows that the nanocrystals appear identical before and after the extended storage time. Two examples of structures, which demonstrate this result, are shown in the Appendix of this work (see Chapter 16.6). AES measurements demonstrate that the whole surface shows an increased carbon content after the extended storage time in vacuum. This holds both for the titanium oxide nanocrystals and the unexposed surface of the fabricated nanostructures. The carbon contamination is attributed to the adsorption of residual gases during the storage time.

In terms of structure stability it can be stated that the titanium oxide nanocrystals are long-term stable when stored under vacuum conditions in the UHV instrument.

A further question was whether fabricated EBID deposits are stable upon the harsher ambient conditions. To answer this question, another Si(100) sample with nanostructures generated from TTIP was exposed to air for a total of 20 days. Additionally, the sample was stored for another 12 days in high vacuum atmosphere (pressure $\approx 10^{-6}$ mbar) before it was transferred back into the UHV instrument and analyzed via SEM and AES.

The characterization via SEM showed that the generated dot, line and area structures are stable upon exposure to ambient conditions. An example

demonstrating the structure stability is shown in the Appendix of this work (see Chapter 16.6). The characterization via AES shows that both the EBID structures and the Si(100) surface are covered with a contamination layer consisting mainly of carbon and a smaller amount of oxygen. Comparing the thickness of the contamination layer on the EBID structures (≈ 0.4 nm, determined from the titanium signal damping on an area structure) and the thickness on the unexposed Si(100) surface (≈ 2.5 nm, determined from the silicon substrate signal damping) one finds a significantly lower contamination level of the EBID deposits. One can speculate that this result is based on the different adsorption / desorption behavior of hydrocarbons, CO and CO₂ on the deposit and the Si(100) surface. Moreover, also a catalytic activity of the EBID deposits, which are composed of titanium oxide with a composition very close to TiO₂, might play a role.

In conclusion, one can state that the fabricated EBID deposits are stable upon exposure to ambient conditions. Since titanium dioxide is a chemically inert and stable material (see Chapter 4.6 and [62]) and the composition of the generated EBID deposits from TTIP is very close to TiO₂ (see Chapter 7), this result completely follows the expectation. After exposure to air, coverage of the structure surface with a thin carbonaceous layer is found.

12 Investigation of catalytic effects

12.1 Motivation

Thomas Lukasczyk *et al.* reported the fabrication of very clean iron nanostructures via EBID under UHV conditions applying the precursor iron pentacarbonyl [30, 142, 143]. On Si(100) surfaces a purity of higher than 95 % iron was achieved [142] and on Rh(110) the purity was higher than 88 % [143]. In addition, the phenomenon of autocatalytic growth at RT was observed for the precursor $\text{Fe}(\text{CO})_5$ which is caused by the catalytic decomposition of precursor molecules on previously deposited Fe nuclei [30, 143]. A schematic drawing demonstrating the effect of autocatalysis is depicted in Figure 12.1.

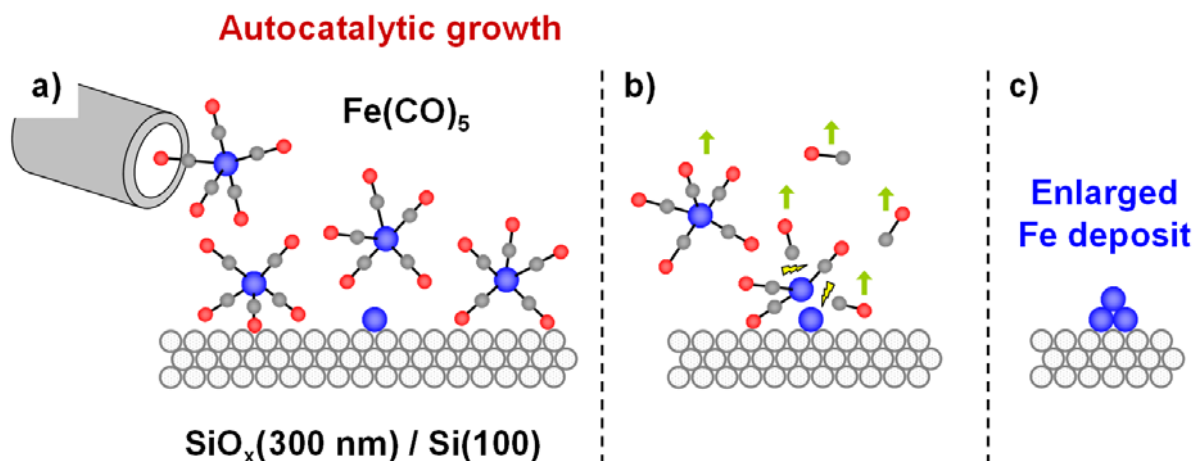


Figure 12.1: Schematic drawing illustrating the phenomenon of autocatalytic growth for the precursor iron pentacarbonyl (Scheme adapted from reference [22]). a) $\text{Fe}(\text{CO})_5$ dosage onto a surface already covered with pre-deposited Fe. b) Autocatalytic decomposition of $\text{Fe}(\text{CO})_5$ on already deposited Fe nuclei. c) Enlarged Fe deposit.

In literature, the effect of autocatalysis concerning the growth of EBID structures is only known for a few precursor molecules up to now. These are the compounds iron pentacarbonyl ($\text{Fe}(\text{CO})_5$) [136, 137, 139, 143, 281], chromium hexacarbonyl ($\text{Cr}(\text{CO})_6$) [136], dicobalt octacarbonyl ($\text{Co}_2(\text{CO})_8$) [145] and cobalt tricarbonyl nitrosyl ($\text{Co}(\text{CO})_3\text{NO}$) [119].

Recently, our group expanded the concept of EBID and reported the local activation of an oxidic surface by a focused electron beam, such that $\text{Fe}(\text{CO})_5$ is catalytically decomposed at irradiated regions at room temperature [22]. This process, denoted as electron beam induced surface activation (EBISA), was shown e.g. on an industrial standard $\text{SiO}_x(300 \text{ nm}) / \text{Si}(100)$ sample. The generation of activated nucleation sites in the first step is followed by the formation of iron nuclei when the gas is dosed in the second step. These iron seeds then grow autocatalytically upon additional $\text{Fe}(\text{CO})_5$ dosage at RT. A schematic drawing of the process of EBISA and the catalytic decomposition of $\text{Fe}(\text{CO})_5$ on electron modified silicon oxide is depicted in Figure 12.2.

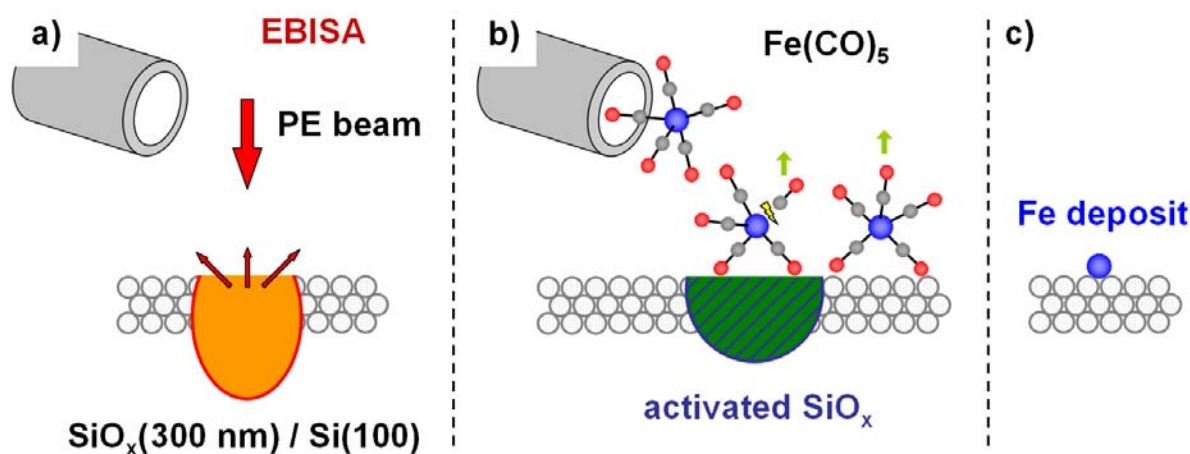


Figure 12.2: Schematic drawing of EBISA and the catalytic decomposition of $\text{Fe}(\text{CO})_5$ on electron modified, activated SiO_x (Scheme adapted from reference [22]). a) Irradiation of the SiO_x layer with the PE beam (activation process). b) Local decomposition of $\text{Fe}(\text{CO})_5$ on the activated SiO_x sample. c) Fe deposit.

The formation of nucleation sites for the autocatalytic thermal decomposition of $\text{Fe}(\text{CO})_5$ has already been reported before on silicon samples. It was achieved by local Ga^+ ion bombardment [282] or local STM induced electron stimulated desorption of surface passivating hydrogen [283]. In these works, the use of elevated temperatures was necessary for iron deposition. In contrast to that, EBISA and the growth of iron structures from $\text{Fe}(\text{CO})_5$ reported in [22] occur at RT for which the applied ultra clean UHV conditions seem to be the prerequisite [22].

In the following chapters, it is investigated whether catalytic effects do also occur for the metal alkoxide precursor TTIP.

First, it is studied whether autocatalytic growth appears in EBID experiments with TTIP (Chapter 12.2). It is important to know whether autocatalytic growth occurs since this phenomenon has a strong impact on the performed EBID experiments with the respective precursor. EBID structures are fabricated successively within one experiment, which means that each structure is exposed to the precursor gas for a different additional gas dosage time after generation. Consequently, the structures grow to a different extent autocatalytically when autocatalysis occurs. This effect can be exploited for the fabrication of well-defined nanostructures [22, 23]. However, it can also be a complication, e.g. when structures fabricated with identical lithographic parameters appear different due to varying additional gas dosage times.

Secondly, the process of EBISA followed by the potential growth of titanium oxide structures from TTIP is studied on the $\text{SiO}_x(300 \text{ nm}) / \text{Si}(100)$ sample, on which the concept worked for $\text{Fe}(\text{CO})_5$ (Chapter 12.3).

12.2 Exclusion of autocatalytic growth for TTIP at RT

In reference [22] the appearance of autocatalytic growth for $\text{Fe}(\text{CO})_5$ was shown by varying the additional gas dosage time (t_{add}) after the generation of an EBID deposit. It was found that longer additional gas dosage times go along with the deposition of more material. Therefore, in analogy to these experiments, t_{add} was varied after the fabrication of EBID structures from the precursor TTIP.

In Table 12.1 the influence of the additional gas dosage time on the height of an area deposit from TTIP is demonstrated. The investigated area structure is identical to the one depicted in Figure 7.3 a) and Figure 7.7 c). It was fabricated on Si(100) with an electron dose of 2.46 C/cm^2 . The results of four experimental runs are depicted in Table 12.1 with a variation of t_{add} for in total $\approx 2 \text{ h}$. The structure height was derived from the silicon substrate signal damping in the corresponding AE spectra.

From Table 12.1 it can be deduced that the same height ($3.8 \pm 0.2 \text{ nm}$) was acquired for the area deposit despite varying the additional gas dosage time of TTIP significantly. In addition, also in SEM all area structures appear very similar (not

shown here). From these results it can be concluded that the deposit is not affected by the variation of t_{add} which indicates that no autocatalytic growth occurs for the metal alkoxide precursor TTIP at RT.

Run	t_{add} (TTIP)	Height h [nm]
1	1 h 27 min	3.9
2	2 h 26 min	3.8
3	2 h 28 min	3.6
4	3 h 23 min	3.7

Table 12.1: Investigation of the height of an area deposit fabricated with identical lithographic parameters but varying additional gas dosage time. The area deposits were generated on Si(100) samples with an electron dose of 2.46 C/cm^2 . The structure heights were determined from the silicon substrate signal damping in the corresponding AE spectra.

Another example for EBID structures which were exposed to the TTIP gas for a different time after their fabrication is shown in Figure 12.3. It depicts SEM images of line and dot deposits on Si(100) which were generated in different experimental runs as well. The line deposit of Figure 12.3 a) to e) is the right vertical line of the line pattern depicted in Figure 7.4 a) fabricated with an electron dose of $463 \mu\text{C/cm}$. In different experimental runs a variation of t_{add} from 33 min to 4 h 14 min was realized. The dot deposit of Figure 12.3 f) to h) was generated with an electron dose of 64 nC . For this structure t_{add} was varied from 2 h 45 min to 4 h 31 min.

Figure 12.3 shows that the line deposits in a) to e) and the dot deposits in f) to h) have a very similar shape and lateral size while the additional gas dosage time was varied significantly. Only minor differences can be detected for both structures. The line deposits feature a slightly different diameter with a mean value of 71 nm (FWHM) and a standard deviation of $\pm 7 \text{ nm}$. Additionally, the bright vertical edges, indicating height growth, appear at different positions on the line structure for each experimental run. Both effects can be mainly attributed to thermal drift during the EBID process. Moreover, also minor differences in the composition of the TTIP gas and in the local pressure on the sample surface can not be completely ruled out. For

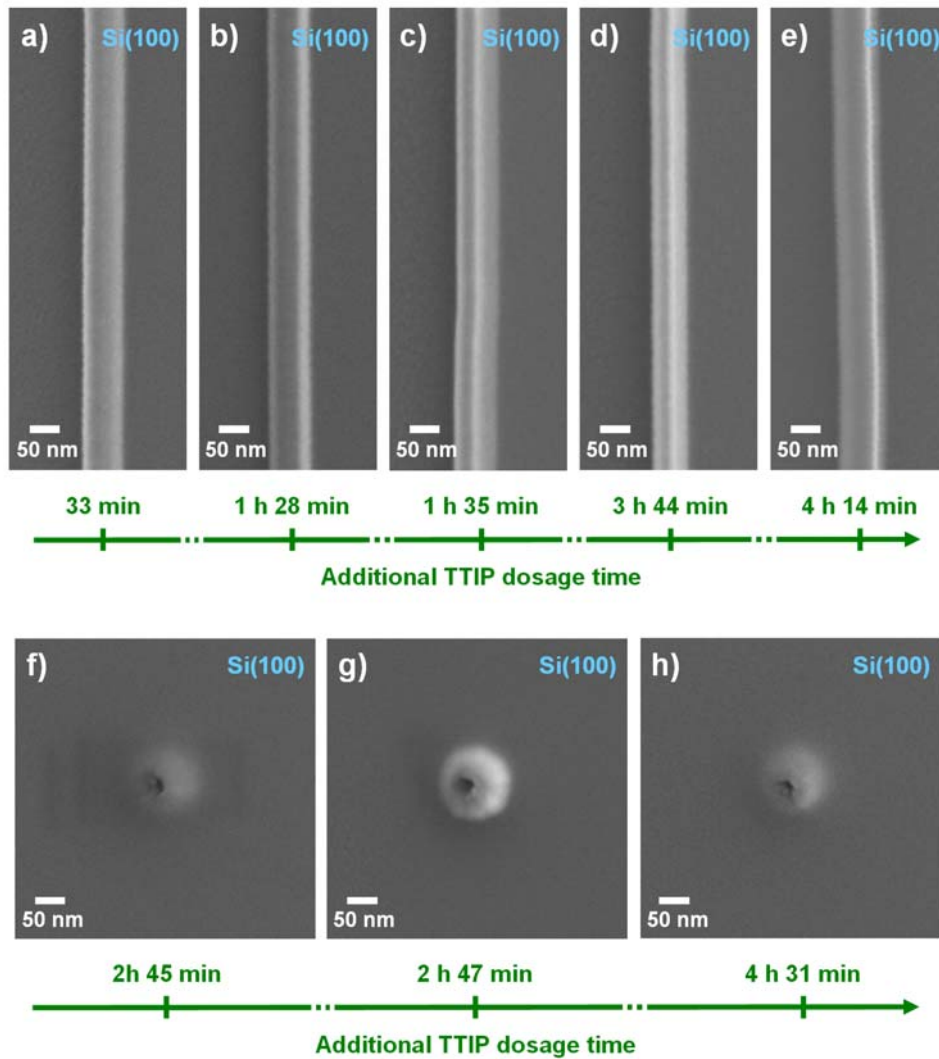


Figure 12.3: Comparison of line deposits and dot deposits from TTIP that were generated with identical lithographic parameters but varying additional gas dosage time (accuracy of all time specifications: ± 1 min). The lines from a) to e) were deposited with an electron dose of $463 \mu\text{C}/\text{cm}$, the dots from f) to h) with a dose of 64 nC .

the dot deposits it is found that one dot (Figure 12.3 g), $t_{\text{add}} = 2 \text{ h } 47 \text{ min}$) appears brighter in SEM than the others, indicating an increased height. However, all dots feature the same “volcanic” appearance with a central hole and, even more important, the deviation is not observed for the dot with the highest additional gas dosage time. Thus, the observed difference is again rather attributed to small differences in the TTIP gas and in the local surface pressure but also not to the variation of t_{add} .

One can state that no autocatalytic growth at RT is observed for the precursor TTIP. In consequence, the EBID deposits are not influenced by the additional gas dosage time when the experiment is performed at RT. This is a significant difference to the precursor iron pentacarbonyl.

12.3 Exclusion of EBISA for catalytic decomposition of TTIP

The phenomenon of local electron beam induced surface activation for the catalytic decomposition of $\text{Fe}(\text{CO})_5$ was demonstrated in reference [22]. In a two-step process the sample surface was first irradiated by the electron beam (activation) and then the precursor gas was dosed resulting in deposit growth (see Figure 12.2). In order to identify whether EBISA works in terms of catalytic decomposition of TTIP corresponding experiments were performed on an $\text{SiO}_x(300 \text{ nm}) / \text{Si}(100)$ sample.

Figure 12.4 shows the results of an EBISA and EBID experiment on an $\text{SiO}_x(300 \text{ nm}) / \text{Si}(100)$ sample. Three dots, with an electron dose of 24, 48 and 96 nC, were irradiated, once before dosing the TTIP gas, i.e. at UHV conditions ($p = 4.6 \cdot 10^{-10}$ mbar), and then while the gas was dosed. In total, the gas was offered for 2 h and 44 min.

The SEM images of Figure 12.4 a-c) show the regions of the surface which were irradiated and then exposed to the TTIP gas ('EBISA concept'). They show a dark area on the sample surface surrounding the irradiation spot. With increasing distance to the irradiation spot the dark areas are fading while their overall size is increasing with increasing electron dose. Two observations indicate the origin of the dark areas in Figure 12.4 a-c). Firstly, surface defects of the $\text{SiO}_x(300 \text{ nm}) / \text{Si}(100)$ sample are still visible in these regions as black spots (see especially in Figure 12.4 c)). And secondly, the dark areas appear identical to the darkening of the SiO_x surface when the spot irradiation is performed without TTIP gas and without dosing TTIP afterwards. Therefore, it can be concluded that TTIP dosage following the irradiation of the SiO_x surface does not lead to the growth of a pronounced and visible deposit. The generated dark areas can be attributed to the local irradiation of the oxidic surface by the electron beam ('beam damage'). It is known from literature that on

silicon oxide processes like ESD of oxygen can occur [4, 227, 228]. The resulting surface modification is assumed to strongly change the local contrast in SEM.

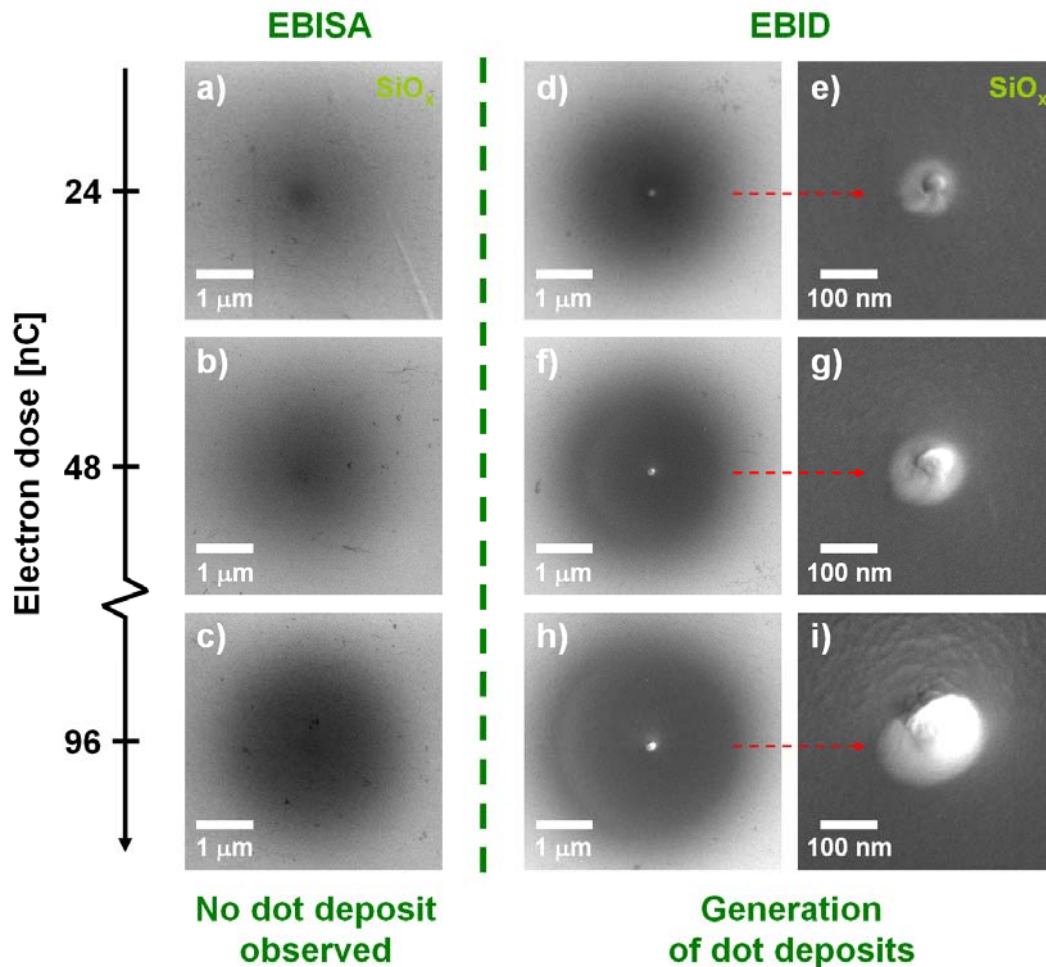


Figure 12.4: Comparison of EBISA and EBID “dot structures” generated on an $\text{SiO}_x(300 \text{ nm}) / \text{Si}(100)$ sample with identical electron dose in horizontal direction. a-c) EBISA “structures”: irradiated SiO_x surface that was exposed to the TTIP gas afterwards for 2 h 44 min. No dot deposit can be observed in the SEM images, only ‘beam damage’ is visible. d-i) EBID dot structures: fabricated by conventional EBID with simultaneous TTIP dosage. For each electron dose a central dot deposit has grown while in the surrounding material deposition due to the ‘BSE and FSE proximity effect’ is visible.

The SEM images of Figure 12.4 d-i) depict the dot structures fabricated by conventional EBID with TTIP. In contrast to the “structures” generated by EBISA, the

EBID deposits appear very different. For each electron dose a dot deposit has grown with its size depending on the applied dose. An SEM image of the central dot deposit with high magnification is shown in Figure 12.4 e), g) and i). In the surrounding of the dots, also a dark circular area is visible. However, two differences can be observed compared to the dark areas of Figure 12.4 a-c). On the one hand, the circular surroundings of the dots appear brighter in SEM compared to the EBISA “structures”. On the other, no surface defects from the $\text{SiO}_x(300 \text{ nm}) / \text{Si}(100)$ sample are visible in these regions. Thus, it is concluded that for the EBID structures material deposition occurred also in the surrounding of the central dots which can be traced back to the ‘BSE and FSE proximity effect’ (see Chapter 8).

In summary, one can state that the EBID experiment on the $\text{SiO}_x(300 \text{ nm}) / \text{Si}(100)$ sample yields the expected dot structures surrounded by a flat circular deposit due to proximity effects. In contrast, surface irradiation and dosing of TTIP in a second step (‘EBISA concept’) does not yield the growth of pronounced deposits from TTIP. In SEM only a local darkening of the surface is visible which is attributed to a local electron beam induced surface modification like ESD of oxygen [4, 227, 228].

This experimental result demonstrates that the ‘EBISA concept’ does not work on silicon oxide in terms of fabricating titanium oxide nanostructures from TTIP. It is assumed that no catalytic decomposition of TTIP occurs since no active sites selective for TTIP are produced in the irradiation process.

However, it has to be noted that the generation of active sites for catalytic TTIP decomposition can not be completely ruled out. Despite being very improbable, one could also assume that active sites are produced in the irradiation process on the silicon oxide surface, that TTIP decomposes and consequently a very thin “film” in the low sub-monolayer region forms. However, this deposit would then not grow further since no autocatalytic growth appears for TTIP at RT (see Chapter 12.2). In addition, one can assume for this scenario that hydrocarbons from the TTIP gas might “poison” the initially fabricated, hypothetical active sites by adsorption and potentially carbon deposition. This would rapidly and effectively deactivate the nucleation sites again.

12.4 Summary and conclusions

In contrast to the precursor $\text{Fe}(\text{CO})_5$ [22, 23, 30, 142, 143], for the metal alkoxide precursor TTIP no catalytic effects were observed at RT.

The appearance of autocatalytic growth of EBID structures from TTIP upon additional gas dosage can be ruled out at RT. It was found that a generated area deposit does not grow in height when the gas is offered for different additional exposure times. Moreover, area, line and dot deposits, fabricated with identical lithographic parameters, respectively, have an almost identical size and shape independently of the additional gas dosage time (see Chapter 12.2).

Furthermore, the irradiation of an $\text{SiO}_x(300 \text{ nm}) / \text{Si}(100)$ sample surface via the primary beam followed by TTIP dosage does not cause the growth of pronounced and visible deposits. This demonstrates that the 'EBISA concept' does not work on silicon oxide in terms of fabricating titanium oxide nanostructures from TTIP. It is assumed that no catalytic decomposition of TTIP occurs since no active sites selective for TTIP are produced in the irradiation process (see Chapter 12.3).

13 EBID with TTIP as a tool for local protective capping of nanostructures

In this chapter, the fabrication of layered nanostructures by successive electron beam induced deposition with two precursors is shown. In the performed experiments, the precursors $\text{Fe}(\text{CO})_5$ and TTIP were applied. First, a metallic iron line structure was fabricated from $\text{Fe}(\text{CO})_5$, which was then locally capped with a 2 - 3 nm thin titanium oxide containing film made from TTIP. The chemical composition of the deposited layers was analyzed by spatially resolved AES (see Chapter 13.2).

In addition, the protective capping of the metallic iron structures is demonstrated via spatially resolved X-ray absorption spectroscopy (XAS) at the Fe L_3 edge. It is studied whether the thin capping layer from TTIP prevents the coated iron structures from oxidation under ambient conditions, i.e., exposure to air (see Chapter 13.3).

13.1 Motivation for capping nanostructures

The starting point of the investigation was the fabrication of metallic iron nanostructures via EBID and EBISA in UHV [22, 23, 30, 142, 143]. For further studies in cooperation with external scientific groups [284] a sample transfer and thus exposure to air was inevitable. The presence of oxygen and water in this environment can lead to the oxidation of the UHV generated, metallic nanostructures, which can hamper or destroy their targeted magnetic or electronic functionalities. In addition, the presence of hydrocarbons and carbon containing molecules (e.g. CO or CO_2) can result in a carbon contamination of the structure surface (see Chapter 11). To avoid oxidation and contamination and to prevent changes in the properties of the metallic nanostructures when exposing them to lower vacuum or even ambient conditions, we developed a concept to cover the iron structures locally by an ultra thin titanium oxide containing layer via EBID [285]. This local EBID capping approach was envisaged to effectively protect the underlying structures by the capping layer and could thus also become relevant for industrial applications.

The idea of capping structures with protective layers, in order to improve their stability, to avoid oxidation, contamination and permeation and to extend their lifetime in applications, is also widely spread in other fields of science. One example is

extreme ultraviolet lithography (EUVL) [286-289] using a wavelength of 13.5 nm. Radiation of this short wavelength and high energy (92 eV) is strongly absorbed by any material [287]. Consequently, lenses typically applied in optical lithography are replaced by multilayer-coated reflective optics to increase EUV reflectivity and wavelength selectivity [287]. These so-called “multilayer mirrors” consist of 40 - 60 double layers of typically Mo (2.8 nm) and Si (4.2 nm). To avoid contamination of these optical elements, i.e. oxidation and carbon deposition in the working atmosphere of $\approx 10^{-7}$ mbar, the topmost layer of the mirrors is typically protected by a capping layer with an average thickness of ≈ 2 nm [287]. Initially having started with ruthenium as one of the first capping layer materials [288, 289], recently Bajt *et al.* found rhodium (Rh), titania (TiO₂) and zirconia (ZrO₂) to be other promising candidates [287]. For more details concerning the protection of EUVL devices by capping layers the interested reader is referred to reference [287]. In this article, Bajt *et al.* report the background, motivation, design criteria, surface chemistry considerations and fabrication and stability issues of capping layers envisaged in EUVL.

Based on the finding of Bajt *et al.* that TiO₂ is a suitable material for the protection of multilayer mirror optics in the form of thin capping layers [287] and based on the high chemical stability of TiO₂ [62], the preparation of a thin titanium oxide containing film via EBID from TTIP was envisaged to locally protect iron nanostructures. In Chapter 11, the stability of deposits from TTIP upon exposure to ambient conditions was described. Thus, it is reasonable to expect protective properties of a capping layer generated via EBID from TTIP at these conditions.

Another motivation for the work in this chapter is to expand the EBID technique, which usually applies only one precursor, in order to fabricate tailored nanostructures which are interesting for applications. Recently Bernau *et al.* presented the possibility to tailor the chemical composition of deposits by simultaneously dosing two different precursor molecules and using certain electron irradiation strategies [290]. In their approach, one precursor was Co₂(CO)₈, while hydrocarbons from the residual gas were regarded as the other precursor.

Herein, the EBID technique is expanded to the successive usage of two different, dedicated precursors with the goal of locally engineering laterally well-defined, layered nanostructures. A schematic drawing of the local capping of EBID structures is given in Figure 13.1.

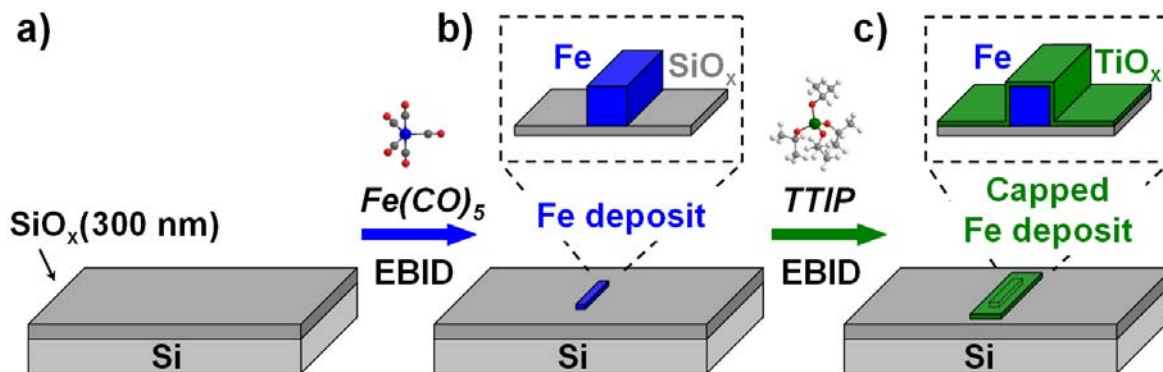


Figure 13.1: Schematic sketch of local capping of EBID structures [285]:

a) Basic substrate material, here e.g. an SiO_x(300 nm) / Si(100) sample.

b) Iron nanostructure deposited on the sample by EBID with Fe(CO)₅.

c) Titanium oxide capped iron nanostructure by EBID with TTIP.

From a more general point of view, by combining the local deposition of conducting, semiconducting and insulating materials on the nanoscale the assembly of functional components in nanoelectronic applications might be feasible.

13.2 Local capping of iron nanostructures

In Figure 13.2 the results of a capping experiment performed on an SiO_x(300 nm) / Si(100) sample are presented. In the first EBID experiment an iron line was deposited with the precursor Fe(CO)₅. The 45 μm long line was fabricated with a line dose of 1.9 μC/cm and a total exposure time of 56 s (70,000 sweeps, 300 μs active line duration, 500 μs waiting time per line). After the EBID process the precursor gas was dosed for additional 2 h and 30 min so that the line could grow autocatalytically. A scheme, which illustrates the process of autocatalytic growth for iron pentacarbonyl, is depicted in Figure 12.1. Figure 13.2 a) shows an SEM image of the Fe line illustrating its continuous character and Figure 13.2 b) an SEM image acquired at higher magnification, demonstrating the polycrystalline structure of the line deposit [22, 23, 30, 142, 143]. The width of the line is 83 nm ± 5 nm, as determined from SEM, and the height is 15 – 24 nm, as determined from *ex situ* AFM measurements (see Appendix, Chapter 16.7). The small particles in the area

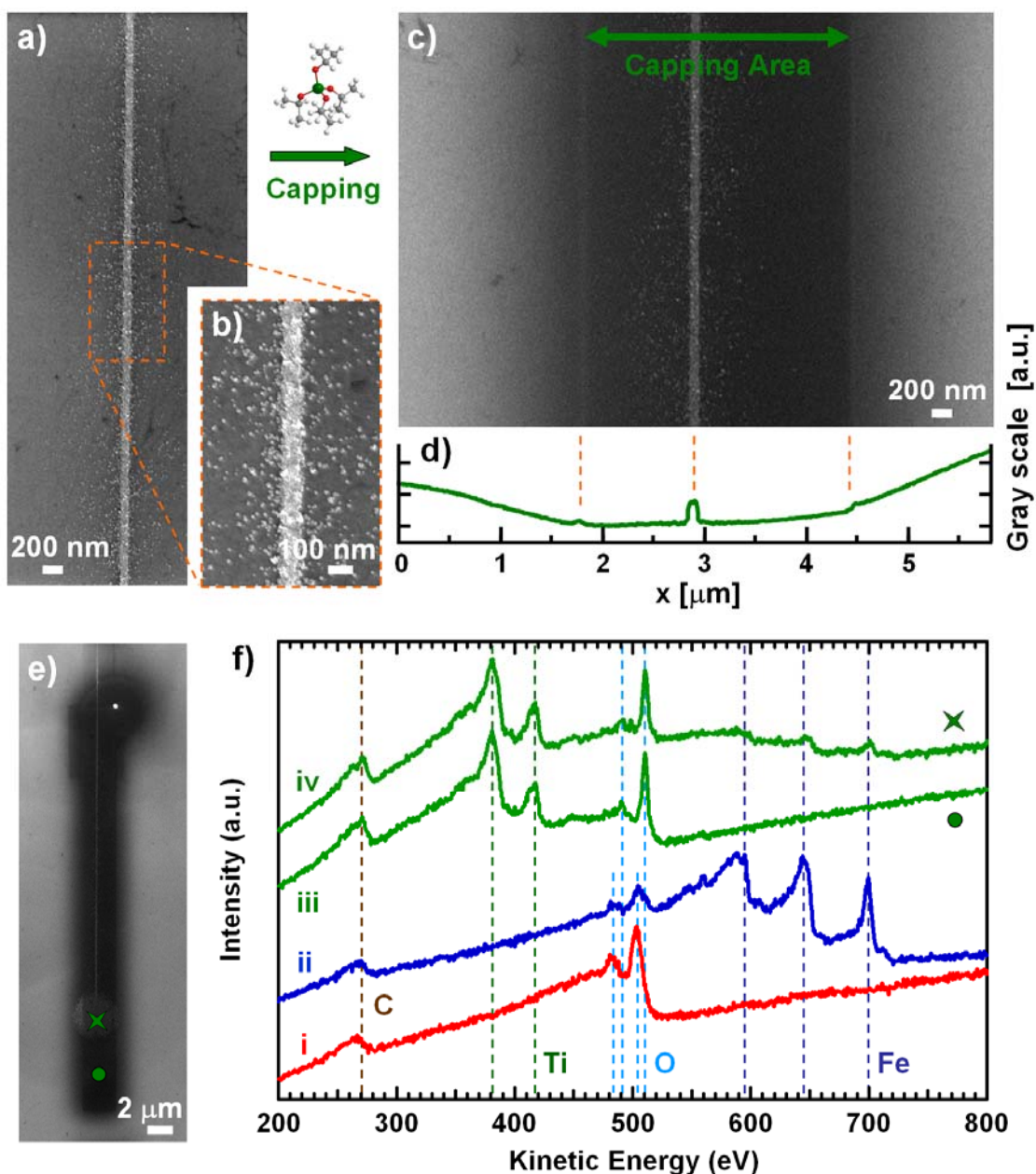


Figure 13.2: a) SEM image of the deposited Fe line from $\text{Fe}(\text{CO})_5$. b) High magnification SEM image of the center of a). c) SEM image of the capped iron line covered with a thin TiO_x containing layer from TTIP. d) Gray scale line profile in c). e) Overview SEM image depicting the capping area, covering the lower part of the Fe line and the halo around its starting point (see text). f) Spatially resolved Auger spectra taken on the surface before the experiments (i, red), on an uncapped iron line before the capping experiment (ii, blue) and on the capping area covering the silicon oxide surface (iii, see green dot marker in e)) and covering the halo around the Fe line starting point (iv, see green star-shaped marker in e)) [285].

surrounding the line are iron clusters grown as a consequence of the 'BSE proximity effect' in EBID [119, 159, 163] (see Chapters 4.2 and 8). In the second EBID process, TTIP was used as precursor to fabricate a thin capping layer on top of the iron line. For this capping process a rectangular area ($32.0\ \mu\text{m} \times 2.5\ \mu\text{m}$) was irradiated via the SEM software with an area dose of $0.67\ \text{C}/\text{cm}^2$ and a total exposure time of 30 min (10,000 frames, 134 ms active frame duration, 46 ms waiting time per frame). The result of this experiment is depicted in Figure 13.2 c) showing the previously fabricated iron line in the center, appearing still bright in SEM, and the covering titanium oxide layer, appearing dark. To illustrate the borders of the capping layer in this SEM image a 'gray scale line profile' was extracted, which is shown in Figure 13.2 d). The profile shows good agreement between the width of the irradiated area ($2.5\ \mu\text{m}$) and the obtained deposit width ($\approx 2.7\ \mu\text{m}$). Figure 13.2 e) depicts an SEM overview image, which shows the whole capping area covering the lower part of the iron line including the large halo around the Fe line starting point ('WT deposit', see Chapter 3.2.1). This feature (bright circular area deposit in the lower part of Figure 13.2 e)) is due to the waiting time of the electron beam after each sweep, which leads to the circular deposit at this position due to proximity effects [119, 159, 163]. The same applies to the capping area. Here, the electron beam dwells in the top right corner after each frame, which results in a large deposit, visible as a white spot and a dark circular surrounding in the upper part of Figure 13.2 e).

The chemical composition of the surface and of the EBID deposits was studied by AES (see Figure 13.2 f)). The red spectrum (spectrum i) was acquired on the surface of the $\text{SiO}_x(300\ \text{nm}) / \text{Si}(100)$ sample before the EBID experiments. The C KLL signal at 267 eV illustrates a minor carbon contamination, which can be attributed to residues of the initial protective coating (see Chapter 3.5). The large peaks at 484 and 504 eV correspond to the substrate oxygen KLL signals. On an iron line fabricated with similar parameters as the one depicted in Figure 13.2 a) and b) (identical lithographic parameters, but additional gas dosage time of 3 h) the blue spectrum was measured (spectrum ii, acquired before the capping experiment). The corresponding line had a diameter of $103 \pm 4\ \text{nm}$ (determined by SEM) and a height of 26 – 33 nm (determined by AFM). The AE spectrum is clearly dominated by the signals at 588, 595, 645 and 700 eV from the Fe LMM Auger transitions. In addition, it shows a small carbon signal, clearly visible oxygen substrate signals at 485 and 505 eV and a silicon substrate signal at 1605 eV (not depicted).

Considering the thickness of ≈ 30 nm of the iron line structure the signals of the underlying substrate should be completely damped. Therefore, the corresponding carbon, oxygen and silicon signals most probably derive from substrate Auger electrons in close lateral proximity to the original line excited by backscattered high energy electrons. This conclusion is supported by the observation that the kinetic energy of the oxygen Auger electrons (485 and 505 eV) is very close to the energy of the substrate oxygen KLL signals (484 and 504 eV) and deviates by ≈ -7 to -8 eV from the energy that is to be expected for oxygen in an iron deposit from $\text{Fe}(\text{CO})_5$ ($\approx 512 - 513$ eV, see e.g. references [30] and [143]). This ‘background contribution’ is a phenomenon concerning the characterization of nanostructures and nanoparticles via Auger based analysis tools (AES, SAM) that is well-known from literature [36-38]. Baer *et al.* report that in AES and SAM primary electron transmission through a nanostructure or nanoparticle and electron backscattering in the substrate contain always chemical information from a larger area than the area where the electron beam strikes [36]. This is due to the fact that Auger electrons are always produced in and detected from both where the primary electron beam hits the sample and the nearby surrounding region due to high energetic backscattered electrons [36]. Powell defines the term “analysis area” in Auger based analysis tools as the two-dimensional region of a sample surface (measured in the plane of that surface) from which the entire analytical signal or a specified percentage of that signal is detected [37]. The author finds on the basis of calculations that the radius of the analysis area can be appreciably larger than the width of the incident beam in modern instruments, i.e. by more than a factor of 100 [37]. Values for the size of the analysis area and lateral resolution of AES can be determined from an ISO standard [39].

To reduce the ‘background contribution’ in AES and SAM analysis and to increase the amount of detected Auger electrons that actually derive from the nanostructure of interest, Powell proposes to reduce the primary beam energy [37]. This would decrease both the penetration depth of the primary beam and the size of the ‘BSE exit area’ and would thus reduce the amount of Auger electrons released in the surrounding of a nanostructure. In addition, the experiments presented in Chapter 8 of this work have shown that using a substrate with high atomic number and in particular with high density causes the same effect. Therefore, reducing the primary beam energy on the one hand and using substrates with high density on the other

hand should generally be considered when characterizing nanostructures via AES or SAM in order to minimize the phenomenon of ‘background contribution’.

The generated capping layer was characterized by Auger spectra acquired at two different positions. One spectrum was taken from an area covering the silicon oxide substrate surface (spectrum iii, see green dot marker in Figure 13.2 e)), the other one on an area covering the halo of the iron line starting point (spectrum iv, see green star-shaped marker). Both spectra in Figure 13.2 f) (iii and iv) are dominated by the titanium LMM (381 and 418 eV) and oxygen KLL signals (491 and 511 eV) along with a small carbon contamination. The dominating Ti and O signals verify the effective deposition of titanium and oxygen with the precursor TTIP. Both oxygen signals in these spectra appear at 6 - 7 eV higher kinetic energy than the corresponding SiO_x substrate signals, which indicates the different chemical nature of oxygen in the capping layer. The quantitative analysis of the chemical composition of the capping layer was performed by comparing spectrum iii with a reference spectrum acquired on a rutile TiO₂(110) single crystal (details see Chapter 3.6.8). This analysis yields a composition of 13 ± 5 at. % C, 31 ± 5 at. % Ti and 56 ± 5 at. % O for the capping layer. Both spectra (iii and iv) show damped Auger signals of the material below the capping layer, i.e., a silicon signal for spectrum iii (not depicted) and three iron signals for spectrum iv. This enables to estimate the capping layer thickness (details see Chapter 3.6.8). The thicknesses of the capping layer covering the iron structure and the one covering the silicon oxide substrate were 2.4 ± 0.3 and 3.2 ± 0.3 nm, respectively. The different layer thickness on both materials can be explained by the substrate dependence of the adsorption / desorption and diffusion properties of TTIP. Moreover, it can be assumed for the applied experimental parameters, i.e. UHV conditions and a very low TTIP background pressure of $3.0 \cdot 10^{-7}$ mbar during EBID, that deposition occurs rather in the transport-limited than electron-limited regime and that diffusion is a significant mechanism for precursor supply (see Chapter 10.1). Since the Fe line with an average height of 15 – 24 nm might be a barrier for TTIP molecules supplied by diffusion, one can speculate that the lower capping layer thickness on the Fe nanostructure might be due to the possibility that less TTIP molecules “arrive” on top of this structure by diffusion and are available for EBID.

To characterize the capping layer in more detail and to verify the calculated layer thickness, the structures were analyzed via *ex situ* AFM measurements performed at ambient conditions (details see Chapter 3.6.6). Figure 13.3 shows the results of the performed AFM measurements. In Figure 13.3 a) a schematic drawing of the measurement position is depicted which corresponds to the upper part of Figure 13.2 e). The capped iron line is drawn in blue and the thin capping layer in light green while the dark green horizontal line and the dark green dot represent the 'WT deposits' of the capping layer already discussed above. Figure 13.3 b) shows the acquired AFM image at this position with all structures as indicated in Figure 13.3 a) by color code. Interestingly, the surrounding of the dot-shaped 'WT deposit' appears clearly different in the SEM image of Figure 13.2 e) and the AFM image of Figure 13.3 b). While the corresponding area appears dark in SEM (chemical information), indicating a circular deposit in the surrounding caused by proximity effects, it is not visible in the AFM image, indicating a very small height and thus a low amount of deposited material. Also hardly visible is the thin capping layer below the 'WT deposits' in Figure 13.3 b). As a guide to the eyes the latter is indicated by two white arrows and dotted lines. In contrast to that, several bright and dark regions are visible in the AFM image of Figure 13.3 b), e.g. in the upper left corner and at the left and right side of the image. These regions indicate considerable height variations of the applied SiO_x(300 nm) / Si(100) sample surface and a rough topography of the latter which was not observed in SEM. To visualize the left and right border of the capping layer the first derivative (dz / dx) of the AFM image of Figure 13.3 b) was formed (WSxM [97]), which is depicted in Figure 13.3 c). Differentiation generally demonstrates how strong a quantity changes with respect to another one. Therefore, in a first derivative AFM image with respect to one lateral direction, the edges of structures and topography changes in this direction are strongly emphasized. Indeed, in Figure 13.3. c) the left and right border of the capping layer are clearly visible which indicates the presence of edges and thus the deposition of material at the corresponding position. Apart from the edges of the capping layer also the rough topography of the thermally grown silicon oxide surface becomes visible in Figure 13.3. c). In addition to the derivative image, an AFM image with higher magnification was acquired at the position marked in b) by the white dashed square. It is depicted in Figure 13.3 d) and also shows the deposited capping layer.

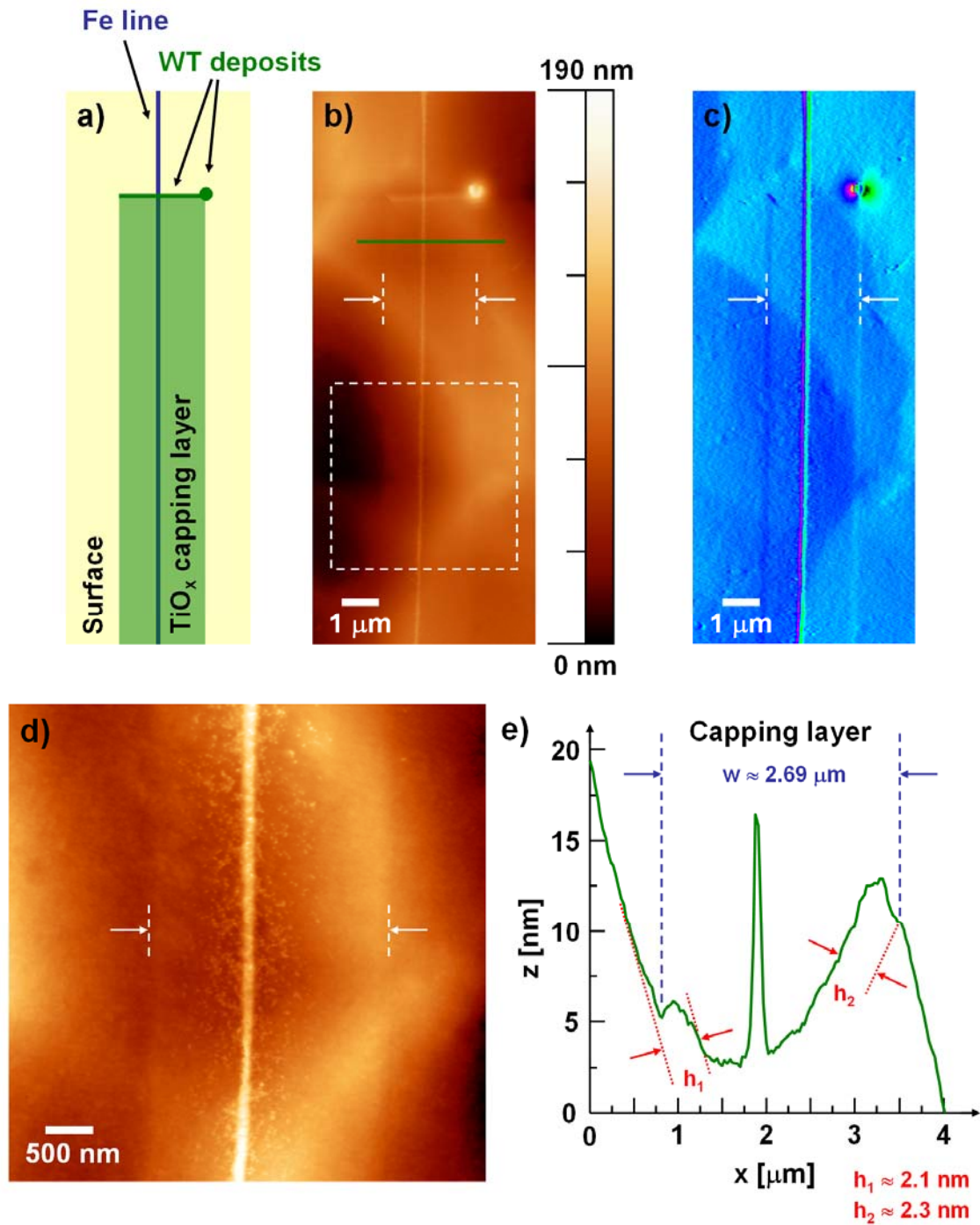


Figure 13.3: Results of the ex situ AFM measurements on the capping layer. a) Schematic drawing of the measurement position which corresponds to the upper part of Figure 13.2 e). b) AFM image at the position illustrated in a). c) First derivative (dz/dx) of the AFM image depicted in b). d) AFM image with high magnification acquired at the position labeled in b) by the white dashed square. e) AFM height profile acquired at the position labeled in b) by the green horizontal line.

To determine the height of the capping layer, an AFM height profile was taken (averaging by 5 lines) at the position labeled in b) by the green horizontal line. The profile, depicted in Figure 13.3 e), shows a height of ≈ 2.1 nm at the left edge of the capping layer and a height of ≈ 2.3 nm at the right one. It has to be noted that the considerable height variations of the thermally oxidized $\text{SiO}_x(300 \text{ nm}) / \text{Si}(100)$ surface and its rough topography hamper the height determination of the capping layer (see the shape of the height profile in e), which deviates from an ideally flat shape due to the rough topography). However, based on the AFM data an average capping layer thickness of $\approx 2 - 3$ nm can be stated, which is in good agreement with the estimation based on the Auger data. In addition, the AFM profile indicates a width of the capping layer of $\approx 2.69 \mu\text{m}$, which is in good agreement with the size observed in SEM, as well ($\approx 2.7 \mu\text{m}$, see Figure 13.2 c) and d)).

To summarize, one can state the following: The acquired SEM, AES and AFM data demonstrate that it is possible to produce an iron line structure and cover it with a thin titanium oxide containing capping layer in a two-step EBID process using successively two different precursors, namely $\text{Fe}(\text{CO})_5$ and TTIP [285].

13.3 Protection of capped iron nanostructures from oxidation upon exposure to ambient conditions

In Chapter 13.2 the local capping of an iron line with a thin titanium oxide layer by a two-step EBID process was shown. To study whether the capping layer indeed protects the nanostructures against oxidation upon exposure to ambient conditions the following experiment was performed.

Again, iron lines were fabricated in an EBID experiment with $\text{Fe}(\text{CO})_5$ and one of them was capped with a thin titanium oxide layer by EBID with TTIP, using identical parameters as for the capping experiment presented in Chapter 13.2. For the chemical analysis with X-ray photoelectron emission microscopy (X-PEEM) and X-ray absorption spectroscopy (XAS), iron lines were deposited with an increased width between 1 and 2 μm . In addition, the experiments were performed on a different sample, i.e. a GaAs / AlAs multilayer mirror with a layer of Co (≈ 1.5 nm) and a capping layer of Al_2O_3 (≈ 1 nm). This specific sample setup was used since also X-

ray standing wave photoemission experiments were performed [291, 292]. It is noted that the underlying layers did not influence the XAS measurements, which were solely aimed at investigating the Fe structures. The substrate was not further cleaned or annealed after it was introduced into UHV and before fabrication of the Fe lines. However, the chemical characterization of the iron line structures via local AES revealed a high purity of 87 ± 3 at. % iron, with 9 ± 3 at. % carbon and 4 ± 3 at. % oxygen. After the capping step, the sample was exposed to ambient conditions for three days before it was introduced into the X-PEEM chamber.

The X-ray photoelectron emission microscopy (X-PEEM) and spatially resolved X-ray absorption spectroscopy (XAS) experiments on the multilayer mirror sample were carried out at the microfocus undulator beamline UE49-PGM-a at the third generation synchrotron radiation facility BESSY II (Helmholtz-Zentrum Berlin), using the Elmitec PEEM permanently installed there. The X-rays from the undulator impinge on the surface at grazing incidence and photoelectrons are collected normal to the sample surface. The X-PEEM image shown below was taken using the secondary electron yield, which then also permits deriving spatially resolved X-ray absorption spectra by scanning the photon energy over the Fe L-edge region. For more details on the experimental setup see reference [293].

Figure 13.4 shows the data acquired at the synchrotron radiation facility BESSY II. The X-PEEM image in Figure 13.4 a) shows three different contrasts: The black parts at the lower left and the upper right stem from the alumina substrate. The gray regions are due to the titanium oxide capping layer and the light gray regions are related to the buried iron line. The wider line in the lower part of the image is due to the fact that here also the starting point of the writing process of the iron line ('WT deposit') is imaged, which is broadened due to the larger applied electron dose (irradiated area: $25,000 \times 293 \text{ nm}^2$, dwell time: $1.6 \mu\text{s}$, exposure time: 10 min, electron dose: $2,86 \text{ C/cm}^2$). In Figure 13.4 b) spatially resolved X-ray absorption spectra at the Fe L_3 edge of a capped and an uncapped iron line on the multilayer mirror sample are depicted. The spectrum of the capped line structure shows the typical line shape of metallic iron at the L_3 edge, strongly suggesting a pure and unoxidized iron structure under the titanium oxide capping layer [294]. The X-ray absorption spectrum of the uncapped iron line structure on the other hand shows an

altered peak shape. The main peak is shifted towards higher photon energies (shift by $\approx + 1.2$ eV) and only a shoulder resides at the peak position of the metallic iron line, which is typical for the formation of iron oxide [294]. This oxide formation is indeed expected for the uncoated iron deposits after exposure to air. While the peak shape is comparable to that of Fe_3O_4 [294], contributions from other Fe oxidation states cannot be ruled out from the observed line shape.

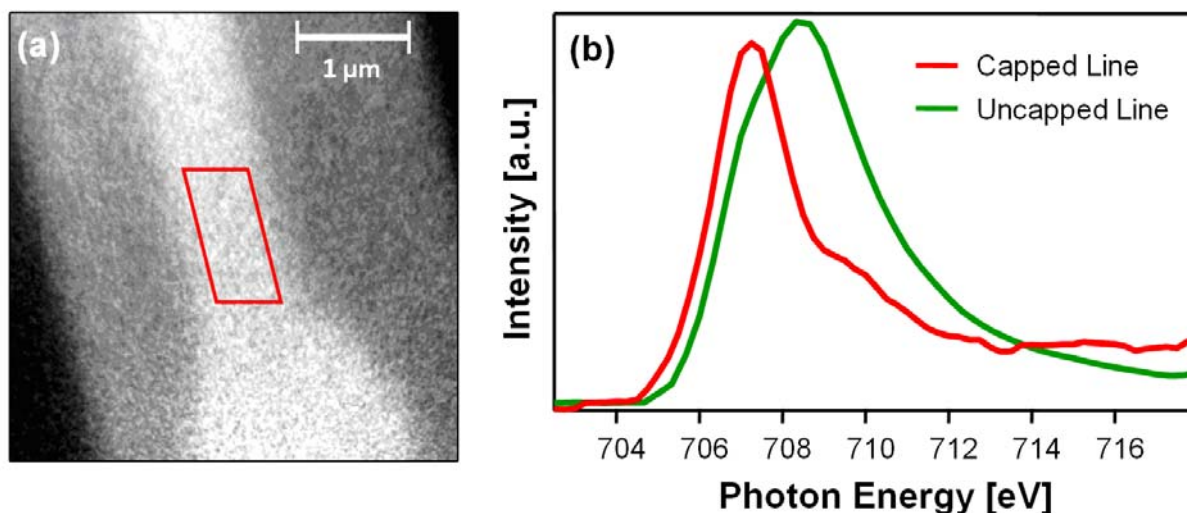


Figure 13.4: Results acquired at the third generation synchrotron radiation facility BESSY II in Berlin [285]. a) X-PEEM image ($h\nu = 708$ eV) of the capped line on the multilayer mirror sample. b) Spatially resolved X-ray absorption spectra at the Fe L_3 edge extracted from corresponding spectromicroscopic X-PEEM data. The spectrum of the capped line was acquired from the substrate area indicated in the X-PEEM image in a). The spectrum of the uncapped line was extracted in the same way (X-PEEM image not shown).

In summary, the analysis of the X-ray absorption spectra, with the characteristic metallic and oxidic line shapes for the capped and uncapped regions, respectively, clearly demonstrates that the concept of the capping procedure was indeed effective, since the oxidation of the capped iron structure was prevented [285].

13.4 Summary and conclusions

In Chapter 13 of this work, the fabrication of layered nanostructures by electron beam induced deposition (EBID) in ultra high vacuum (UHV) was demonstrated. EBID was performed in two successive steps using two different precursors. In the presented example, iron nanostructures, deposited in the first EBID experiment from $\text{Fe}(\text{CO})_5$, were locally capped with a $\approx 2 - 3$ nm thin titanium oxide layer fabricated with TTIP. By local X-ray absorption spectroscopy (XAS) at the Fe L_3 edge after exposure of the sample to ambient conditions it could be demonstrated that the thin capping layer effectively prevented the oxidation of the metallic iron structure. The stepwise application of two precursors in EBID represents an important expansion to previous works in the field and opens up a novel pathway to tailor the fabrication of nanostructures. Generally, the presented results are also the first steps towards the assembly of functional components in nanoelectronic applications, which can be realized by combining the deposition of conducting, semiconducting and insulating materials on the nanoscale.

14 Summary

In this work, the electron beam induced deposition (EBID) with the precursor titanium(IV) tetraisopropoxide (TTIP) was explored and investigated in detail. The main result is the successful local fabrication of well-defined titanium oxide nanostructures from TTIP. In EBID, a focused electron beam is used to locally decompose precursor molecules on a substrate surface and to generate a deposit from the non-volatile fragments. The precursor molecules are provided through the gas phase. By applying different scan strategies, it is possible to generate arbitrarily shaped deposits, like dot, line or area structures. Herein, two main challenges of the EBID technique were addressed, namely the control of the chemical composition of the deposits and the unintended material deposition due to proximity effects. A prerequisite in this regard was to establish well-defined and clean conditions, which allow for a reproducible process. This was achieved by a 'surface science approach', i.e. by performing EBID in an ultra clean environment under ultra high vacuum (UHV) conditions. It allowed for the preparation and maintenance of clean and well-defined sample surfaces and a negligible influence of residual gases (e.g. water and hydrocarbons) during EBID.

As a first step, a procedure was established to guarantee a reproducible precursor gas composition. For this purpose, a purification protocol comprising heating and pumping the TTIP vessel was developed. Monitoring the gas composition via quadrupole mass spectrometry (QMS) prior to the EBID process was found to be mandatory (Chapter 5). For the applied setup, i.e. dosing through a nozzle, the gas flux at the sample surface during EBID was estimated via Monte Carlo (MC) simulations with the software 'GIS Simulator' (Chapter 6).

The morphology of the EBID deposits was studied via scanning electron microscopy (SEM) and their chemical composition was investigated by means of local Auger electron spectroscopy (AES). The deposited titanium oxide species has a composition very close to TiO_2 , but is contaminated with carbon. For the investigated Si(100) and Au(111) surfaces, the average chemical composition of area deposits was determined to 19 ± 5 at. % C, 26 ± 5 at. % Ti and 55 ± 5 at. % O. For line and dot structures, a higher C content of ≈ 31 at. % was found. Since the experiments were performed under UHV, it can be ruled out that the carbon contamination of the different deposits stems from the sample surface and / or the residual gas. Its origin

was traced back to the C containing precursor itself. By varying the lithographic parameters, a reduction of the C content in area deposits to 13 ± 5 at. % was achieved on a silicon oxide surface (Chapter 7).

Using SEM, spatially resolved AES and Auger electron line scan (AELS) measurements it was shown that during EBID material was deposited also in areas which were not directly irradiated by the primary electron (PE) beam. This unintended lateral broadening of the deposits was traced back to scattered electrons, a phenomenon generally referred to as proximity effects. It was found that back-scattered electrons (BSEs) which exit the surface again are the main cause of the observed broadening ('BSE proximity effect'). The diameter of the 'BSE exit area', i.e. the area from which 99.9 % of the BSEs are emitted, was determined via MC simulations with the software 'CASINO'. For the investigated Si(100) and Au(111) substrates the diameters were obtained to 4.4 μm and 680 nm, respectively, for a 15 keV beam. On both surfaces, a very good agreement was found between 'BSE exit area' size and experimentally observed lateral structure broadening for high electron doses (Chapter 8).

Two different post-treatment procedures of the nanostructures deposited via EBID from TTIP were investigated: Sputtering of the structures after deposition enabled the removal of unwanted material in the surrounding of the intended structures caused by proximity effects and thus the reduction of their lateral dimension. Annealing the sample *in situ* in the UHV instrument and simultaneously dosing O_2 induced the growth of titanium oxide nanocrystals at the EBID structures. While the originally fabricated structures remain contaminated with carbon, the grown nanocrystals show a very high purity and a stoichiometry very close to that of TiO_2 . This was verified by local AES and scanning Auger electron microscopy (SAM). The combination of sputtering and annealing in oxygen to a two-step post-treatment process after EBID was introduced as a new pathway for the fabrication of clean localized TiO_x nanostructures (Chapter 9).

From the morphology of dot deposits fabricated from TTIP on Au(111), it was deduced that the supply and replenishment with TTIP molecules take place both via surface diffusion and adsorption from the gas phase. For the dots, deposition occurred in the transport-limited process regime, in between of the diffusion-limited and adsorption-limited regime. Furthermore, it was demonstrated that the deposit morphology and the amount of deposited material strongly depend on the

lithographic parameters, like dwell time, active line duration, number of sweeps, replenishment time, and the interplay of all of these parameters. In the course of these studies, indications were found that the decomposition of the large molecule TTIP is a multiple electron process. By a comprehensive investigation via SEM and *ex situ* atomic force microscopy (AFM), the morphology of dot, line and area deposits on a Si(100) sample was studied in dependence of the electron dose. For the height growth of dot and line deposits and for the lateral growth of lines and line starting points, linear dependencies on the dose were found. By estimating the nanostructure volumes, the numbers of PEs were determined that are required to deposit one atom of the corresponding deposit. The differences in the number of required PEs are due to the varying deposit shape and the resulting differences in scan strategy and process regime. The comparison of area deposit heights, determined by AFM and by local AES (via substrate signal damping) demonstrated the reliability of the AES approach to determine the height of thin structures (Chapter 10).

Generally, EBID deposits from TTIP were found to be stable under vacuum and also upon exposure to ambient conditions (Chapter 11). In contrast to the precursor $\text{Fe}(\text{CO})_5$, no catalytic effects were observed for TTIP at room temperature (Chapter 12).

Finally, a promising application was developed for EBID with TTIP, namely the local protective capping of nanostructures with a 2 - 3 nm thin titanium oxide containing layer, which effectively prevented the oxidation of the covered structures upon exposure to air. The latter was demonstrated by X-ray photoelectron emission microscopy (X-PEEM) and local X-ray absorption spectroscopy (XAS) measurements at the Fe L_3 edge (Chapter 13). The stepwise application of two precursors in EBID represents an important expansion to previous works in the field and opens up a novel pathway to tailor the fabrication of nanostructures. In this regard, the acquired results are a first step towards the assembly of functional devices in nanoelectronic applications consisting of conducting, semiconducting and insulating materials on the nanoscale.

15 Zusammenfassung

In der vorliegenden Arbeit wurde die elektronenstrahlinduzierte Abscheidung (engl.: electron beam induced deposition, EBID) mit dem Präkursor Titan(IV) tetraiso-propoxid (TTIP) untersucht. Ein zentrales Ergebnis ist die erfolgreiche lokale Herstellung von wohldefinierten Titanoxid-Nanostrukturen mit TTIP. In der Methode EBID wird ein fokussierter Elektronenstrahl genutzt, um lokal Präkursor-Moleküle auf einer Substratoberfläche zu zersetzen und auf diese Weise Abscheidungen zu erzeugen. Die Präkursor-Moleküle werden über die Gasphase dosiert. Durch die Wahl einer geeigneten Scanstrategie ist es möglich, Abscheidungen beliebiger Geometrie herzustellen, beispielsweise punktförmige, linienförmige oder flächige Strukturen. In dieser Arbeit wurden zwei große Herausforderungen der Methode EBID adressiert: die Kontrolle über die chemische Zusammensetzung der Abscheidungen und die unbeabsichtigte Materialabscheidung aufgrund von sogenannten „Proximity Effekten“ (engl.: proximity effects). Eine Grundvoraussetzung hierfür war das Arbeiten unter wohldefinierten und sauberen Bedingungen, um die Reproduzierbarkeit des Prozesses zu gewährleisten. Dies wurde durch einen „Surface Science“ Ansatz ermöglicht, d.h. die EBID Experimente wurden in einer extrem sauberen Umgebung unter Ultrahochvakuumbedingungen (UHV) durchgeführt. Damit gelang die Präparation und die Erhaltung von sauberen und wohldefinierten Probenoberflächen bei gleichzeitig vernachlässigbar kleinem Einfluss von Restgasen (z.B. Wasser und Kohlenwasserstoffe) während des EBID Prozesses.

Zu Beginn der Arbeit wurde zunächst eine Prozedur entwickelt, die eine reproduzierbare Zusammensetzung des Präkursor-Gases gewährleistet. Sie besteht aus mehreren Präparationsschritten, in denen der TTIP-Behälter geheizt und gepumpt wird. Die Analyse der Gaszusammensetzung mittels Quadrupolmassenspektrometrie (QMS) vor dem EBID Prozess stellte sich als unabdingbar heraus (Kapitel 5). Für den verwendeten experimentellen Aufbau, in dem das Präkursor-Gas durch eine feine Düse zugeführt wird, wurde der Gasfluss an der Probenoberfläche während des EBID Prozesses mittels Monte Carlo (MC) Simulationen mit dem Programm ‘GIS Simulator’ bestimmt (Kapitel 6).

Die Morphologie der EBID Abscheidungen wurde mittels Rasterelektronenmikroskopie (engl.: scanning electron microscopy, SEM) untersucht, und ihre chemische Zusammensetzung mittels lokaler Augerelektronenspektroskopie (engl.:

Auger electron spectroscopy, AES) bestimmt. Das abgeschiedene Titanoxid Material besitzt eine sehr ähnliche Zusammensetzung wie TiO_2 , ist jedoch mit Kohlenstoff verunreinigt. Auf den untersuchten Si(100) und Au(111) Oberflächen betrug die mittlere chemische Zusammensetzung von flächigen Abscheidungen 19 ± 5 at. % C, 26 ± 5 at. % Ti und 55 ± 5 at. % O. Für Linien und Punktstrukturen wurde mit ≈ 31 at. % ein höherer Kohlenstoffgehalt ermittelt. Da die Experimente im UHV durchgeführt wurden, kann ausgeschlossen werden, dass die Kohlenstoffverunreinigung der Abscheidungen von der Probenoberfläche und / oder aus dem Restgas stammt. Die Herkunft wird auf den kohlenstoffhaltigen Präkursor selbst zurückgeführt. Durch eine Variation der lithographischen Parameter konnte der Kohlenstoffgehalt in flächigen Abscheidungen auf einer Siliziumoxidoberfläche auf 13 ± 5 at. % reduziert werden (Kapitel 7).

Mittels SEM, lokaler AES und elementaufgelöster Auger-Linienscans (engl.: Auger electron line scan, AELS) wurde gezeigt, dass während des EBID Prozesses Material auch in Bereichen abgeschieden wurde, die nicht direkt vom Primärelektronenstrahl „belichtet“ wurden. Diese unbeabsichtigte Verbreiterung der Abscheidungen wurde auf gestreute Elektronen zurückgeführt, ein Phänomen, das allgemein unter dem Begriff „Proximity Effekte“ bekannt ist. Es wurde herausgefunden, dass rückgestreute Elektronen (engl.: backscattered electrons, BSEs), die die Probenoberfläche wieder verlassen, die Hauptursache für die beobachtete Verbreiterung sind. Dies wird als „Rückstreuelektronen Proximity Effekt“ (engl.: BSE proximity effect) bezeichnet. Der Durchmesser der Rückstreuelektronen-Austrittsfläche (engl.: BSE exit area), d.h. der Fläche, aus der 99,9 % der BSE austreten, wurde mittels MC Simulationen mit dem Programm ‘CASINO’ bestimmt. Für die untersuchten Si(100) und Au(111) Proben wurden bei einer Primärelektronenenergie von 15 keV Durchmesser von $4.4 \mu\text{m}$ und 680 nm bestimmt. Auf beiden Oberflächen stimmt die simulierte Größe der Rückstreuelektronen-Austrittsfläche mit der experimentell beobachteten lateralen Strukturverbreiterung für hohe Elektronendosen sehr gut überein (Kapitel 8).

Zwei verschiedene Nachbehandlungsverfahren (engl.: post-treatment procedures) für die mittels EBID mit TTIP hergestellten Nanostrukturen wurden untersucht: Das Sputtern der Strukturen nach dem Abscheidungsprozess ermöglichte das Abtragen von unbeabsichtigten Materialabscheidungen in der Umgebung der gewünschten Strukturen und damit eine Verkleinerung ihrer lateralen Größe. Das Heizen der

Probe bei gleichzeitiger Sauerstoffdosierung in der UHV Anlage induzierte das Wachstum von Titanoxid Nanokristallen an den EBID Strukturen. Während die ursprünglich hergestellten Strukturen weiterhin mit Kohlenstoff verunreinigt waren, zeigten die gewachsenen Nanokristalle eine sehr hohe Reinheit und eine Stöchiometrie sehr ähnlich der von TiO_2 . Dies wurde mittels lokaler AES und Raster-Augerelektronenmikroskopie (engl.: scanning Auger electron microscopy, SAM) bestimmt. Die Kombination von Sputtern und Heizen bei gleichzeitiger Sauerstoffdosierung zu einem zweistufigen Nachbehandlungsverfahren nach dem EBID Prozess wurde als neue Methode zur Herstellung von saubereren, lokalisierten TiO_x Nanokristallen eingeführt (Kapitel 9).

Basierend auf der Morphologie von Punktabscheidungen mit TTIP auf der Au(111) Oberfläche wurde festgestellt, dass die Versorgung und Wiederauffüllung mit TTIP Molekülen im Abscheidebereich sowohl über Diffusion auf der Oberfläche als auch über Adsorption aus der Gasphase erfolgt. Der Abscheidungsprozess erfolgt dabei unter transportlimitierten Prozessbedingungen, zwischen dem diffusionslimitierten und dem adsorptionslimitierten Regime. Weiterhin wurde gezeigt, dass die Morphologie der Abscheidungen und die Menge des abgeschiedenen Materials stark von den lithographischen Parametern abhängen. Zu diesen gehören die Belichtungszeit pro Punkt, die aktive Belichtungszeit pro Linie, die Zahl der Einzelbelichtungen und die Wiederauffüllzeit, sowie das Zusammenspiel aller dieser Parameter. Im Zuge dieser Untersuchungen wurden Hinweise darauf gefunden, dass die Zersetzung des großen TTIP Moleküls ein Mehrelektronenprozess ist. Durch eine umfassende Untersuchung mittels SEM und *ex situ* Rasterkraftmikroskopie (engl.: atomic force microscopy, AFM) konnte die Morphologie von Punkt-, Linien- und Flächen-Abscheidungen auf einer Si(100) Probe in Abhängigkeit von der Elektronendosis erforscht werden. Für das Höhenwachstum von Punkt- und Linien-Abscheidungen und für das laterale Wachstum von Linien und Linienstartpunkten wurde ein lineares Verhalten mit steigender Elektronendosis gefunden. Durch die Bestimmung der Volumina der Nanostrukturen wurde die Zahl der Primärelektronen bestimmt, die erforderlich ist, um ein Atom der entsprechenden Struktur abzuschneiden. Die Unterschiede in der Zahl der benötigten Primärelektronen sind in der unterschiedlichen Form der Abscheidungen und den damit verbundenen Unterschieden in der Scanstrategie und den resultierenden Prozessbedingungen begründet. Der Vergleich von Höhenwerten von flächigen Abscheidungen, die zum einen mittels AFM zum anderen mittels

lokaler AES bestimmt wurden, bestätigten die Korrektheit der Höhenbestimmung von dünnen Strukturen mittels AES über die Substratsignaldämpfung (Kapitel 10).

Als weiteres Ergebnis wurde festgestellt, dass EBID Abscheidungen mit dem Präkursor TTIP sowohl unter Vakuumbedingungen als auch bei der Exposition gegenüber Umgebungsbedingungen stabil sind (Kapitel 11). Im Gegensatz zum Präkursor $\text{Fe}(\text{CO})_5$ wurden keine katalytischen Effekte für TTIP bei Raumtemperatur beobachtet (Kapitel 12).

Abschließend wurde eine aussichtsreiche Anwendung für EBID mit TTIP entwickelt: die lokale Bedeckung von Nanostrukturen mit einer 2 - 3 nm dünnen, Titanoxid enthaltenden Schutzschicht, die die Oxidation der bedeckten Strukturen bei der Exposition gegenüber Luft verhindert. Dies wurde mittels Röntgen-Photoelektronen-emissionsmikroskopie (engl.: X-ray photoelectron emission microscopy, X-PEEM) und lokaler Röntgen-Absorptionsspektroskopie (engl.: X-ray absorption spectroscopy, XAS) an der Fe L_3 Kante (Kapitel 13) gezeigt. Die sukzessive Anwendung von zwei unterschiedlichen Präkursoren stellt eine wichtige Erweiterung zu bisherigen Arbeiten im Bereich von EBID dar und ermöglicht einen neuen Weg zur Herstellung „maßgeschneiderter“ und wohldefinierter Nanostrukturen. In diesem Sinn stellen die erhaltenen Ergebnisse auch einen ersten Schritt auf dem Weg der Herstellung von funktionellen Baugruppen für Anwendungen in der Nanoelektronik dar, die aus leitenden, halbleitenden und isolierenden Materialien auf der Nanometerskala bestehen.

16 Appendixes

16.1 Chapter 3 – Experimental

16.1.1 Precursor storage devices

For the storage of the precursor compound TTIP two different bottom parts were used, specified by “Type I” and “Type II”. A schematic drawing of both types is depicted in Figure 16.1.

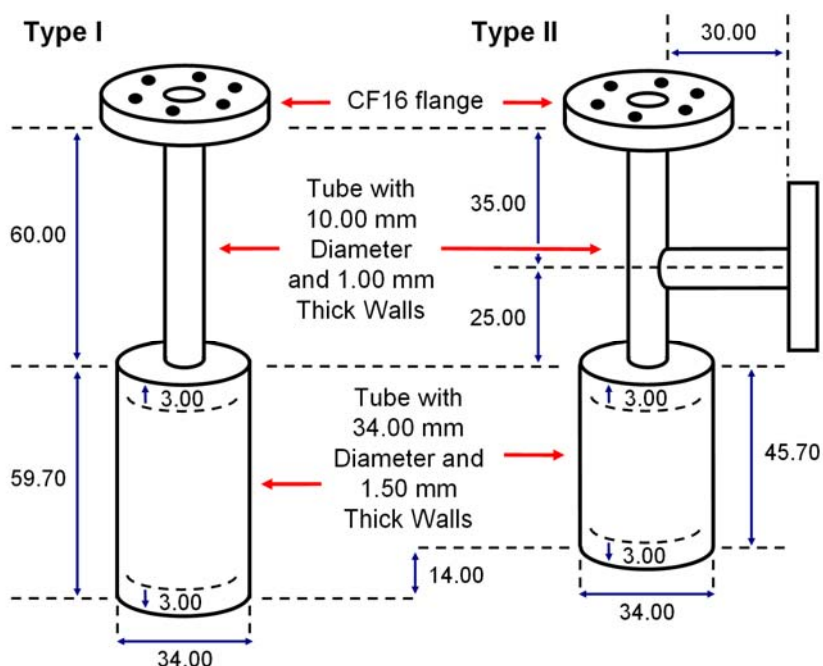


Figure 16.1: Schematic drawing of the bottom part of the precursor storage device. Two different types of bottom parts were used in the work at hand. All numbers are given in mm.

In both cases the material was stainless steel and the devices were connected to the gas dosage system via a CF16 flange and a metal valve. The storage container was fabricated from a tube with an external diameter of 34.0 mm and a wall thickness of 1.5 mm. While for the “Type I” bottom part a tube length of 59.7 mm was chosen, for “Type II” the length was decreased to 45.7 mm. The tube ends were closed by 3.0 mm thick plates which leads in both cases to a cylinder with an internal volume of 40.5 ml for “Type I” and 30.0 ml for “Type II”. To the upper plate a 60.0 mm long tube with an external diameter of 10.0 mm and a wall thickness of 1.0 mm was

concentrically attached, which was connected to a CF16 flange. For the “Type II” bottom part of the storage device a second tube with a length of 30 mm and another CF16 flange was attached perpendicularly at a height of 25 mm above the storage container. The “Type II” part was constructed to downsize the whole setup of the precursor storage device.

16.1.2 Lithographic parameters of the SmartSEM imaging software

For the fabrication of line deposits the “line scan mode” of the SmartSEM imaging software was used (see Chapter 3.2.1). An important feature of this software tool is that waiting times and thus total line durations are applied which deviate from the specified values [86] for the “full image scan mode”.

Table 16.1 lists the parameters of the “full image scan mode” for the scan speeds which are relevant for this work. Obviously, the ratio of the waiting time at the line starting point to the total line duration decreases with increasing scan speed (for two-digit scan speeds). Analogously, the ratio of the waiting time per frame to the total frame duration decreases with increasing scan speed.

Table 16.2 lists the parameters which are applied in the “line scan mode” for the scan speeds relevant for this work. The specified pixel times and active line durations are identical to the “full image scan mode”. In contrast, the waiting times and total line durations are different. The total line durations were measured with an oscilloscope (HAMEG GmbH, type HM205-3) while scanning across an STM tip introduced into the STM scanner of the instrument. The waiting times at the line starting point were calculated by subtracting the specified active line durations from the measured total line durations. The acquired time values have to be considered when determining line doses. Interestingly, the ratio of the waiting time at the line starting point to the total line duration decreases with increasing scan speed s .

All specified values in the Tables 16.1 and 16.2 are valid for a store resolution of 1024 x 768 pixels.

s	Pixel Time [μ s]	Active Line Duration [μ s]	Waiting Time (Line) [μ s]	Total Line Duration [μ s]	Waiting Time (Frame) [μ s]	Total Frame Duration [ms]
5	1.6	1,638.4	102.4	1,740.8	24,000	1,360.9344
10	51.2	52,428.8	11,000.0	63,428.8	24,000	48,737.3184
12	204.8	209,715.2	11,000.0	220,715.2	24,000	169,533.2736
15	1,638.4	1,677,721.6	11,000.0	1,688,721.6	24,000	1,296,962.1888

Table 16.1: “Full image scan mode” parameters of the “SmartSEM” imaging software (Zeiss), specified by the LEO GmbH [86]. All depicted values are valid for a store resolution of 1024 x 768 pixels. Only the scan speeds which were applied in the work at hand are denoted.

s	Pixel Time [μ s]	Active Line Duration [μ s]	Measured Total Line Duration [ms]	Calculated Waiting Time (Line) [μ s]
5	1.6	1,638.4	39.50	37,861.6
10	51.2	52,428.8	79.00	26,571.2
12	204.8	209,715.2	237.50	27,784.8
15	1,638.4	1,677,721.6	1,680.00	2,278.4

Table 16.2: “Line scan mode” parameters of the “SmartSEM” imaging software (Zeiss). The pixel times and active line durations are specified by LEO GmbH [86], the total line duration values were measured. All depicted values are valid for a store resolution of 1024 x 768 pixels. Only the scan speeds which were applied in the work at hand are denoted.

16.1.3 Experimental parameters

In the following, experimental and technical parameters are listed concerning sample mounting and heating, temperature measurements via the pyrometer and different analysis techniques.

Sample mounting and heating

The Si(100) samples were mounted on a VT sample holder designed for resistive sample heating. The sample temperature was measured via a pyrometer (see Chapter 3.6.2).

The SiO_x(300 nm) / Si(100) samples were mounted below a tantalum standard sample plate by spot-welding two stripes of a tantalum foil across the lower side of the sample. The SiO_x(300 nm) / Si(100) samples were not further cleaned in UHV.

In contrast to the silicon samples, the Au(111) single crystal was mounted on a VT sample holder with integrated pyrolytic boron nitride heater (PBN heater) configured for radiative heating. In the drill hole of the 9 x 1.3 mm² side a pair of thermocouples (type K) was mounted for temperature readout. Additionally, the temperature of the Au(111) single crystal was determined via a pyrometer (see Chapter 3.6.2).

Setup and working principle of the corresponding sample holders (VT sample holder for resistive heating, standard sample plate and VT sample holder with integrated PBN heater for radiative heating) are given in detail in reference [30] from Thomas Lukasczyk and in the references [263, 295] from Omicron NanoTechnology.

Temperature measurements via the pyrometer

Pyrometer:	Impac Elektronik GmbH / IP 120	
Sample position:	on the manipulator of the preparation chamber	
Manipulator settings:	Si(100)	Au(111)
	x = 7.855 mm	x = 6.840 mm
	y = 12.655 mm	y = 12.000 mm
	z = 30.00 mm	z = 20.00 mm
	Φ = 40.0°	Φ = 43.0°
	φ = 12.2°	φ = 12.2°
Experimental error:	± 50 K	

AES, AELS and SAM

1.) Settings for AES measurements with the software EIS:

CRR:	5 for kinetic energies between 0 and 990 eV 10 for kinetic energies between 1000 and 1987 eV
Dwell time:	0.200 s
Step size:	0.5 eV

2.) Settings for AE line scan (AELS) measurements with the software ISEM:

CRR:	5 for kinetic energies between 0 and 990 eV 10 for kinetic energies between 1000 and 1987 eV
Acquisition Method:	Point by Point
Peak Intensity Calculation:	Peak – Background

3.) Settings for SAM measurements with the software ISEM:

CRR:	5 for kinetic energies between 0 and 990 eV 10 for kinetic energies between 1000 and 1987 eV
Acquisition Method:	Line by Line
Data Schema:	Peak – Background

QMS

All QMS measurements which are depicted in this work (see Chapter 5) were performed in the preparation chamber of the instrument. The measurements were carried out with a QMS (see Chapter 3.1.1) with an accessible mass to charge range from 1 to 200. The standard settings were a cathode voltage (U_C) of $67.5 \text{ V} \pm 0.5 \text{ V}$ and a secondary electron multiplier voltage (U_{SEM}) of $2,300 \text{ V} \pm 50 \text{ V}$. During spectrum acquisition a scan speed of 0.2 s was adjusted.

The QM spectra were measured via the software 'QUADSTAR 32-bit' (version 7.02, 2004) from Pfeiffer Vacuum. They were converted to ASCII files and processed via the software 'Igor Pro' (WaveMetrics, version 5.0.2.0, 2004).

LEED

LEED measurements were performed with the sample on the manipulator of the preparation chamber oriented directly towards the LEED optics. The manipulator settings in this position were: $x = 6.500$ mm, $y = 10.350$ mm, $z = 142.00$ mm, $\Phi = 45.0^\circ$ and $\varphi = 12.2^\circ$. For the measurements a filament current of 1.678 A was adjusted, which led to an emission current in the range of 0.1 and 0.3 mA (after several minutes). The standard settings for LEED measurements were a Wehnelt voltage of -10.4 V, a suppressor voltage of -2.5 V (at a beam energy of 50.2 eV) and constant lens adjustments (lenses 1/3: Offset: 14 V, Gain: 1786 V; lens 2: Offset: 29 V, Gain: 753 V).

Sputtering

Sputtering was performed with the grounded sample on the manipulator of the preparation chamber. The manipulator position was: $x = 5.000$ mm, $y = 12.675$ mm, $z = 55.00$ mm, $\Phi = 0.0^\circ$ and $\varphi = 12.2^\circ$, which enabled sputtering under normal incidence. The focus of the ion gun was set by applying a focus energy of 787 eV and an extraction energy of 724 eV, which results in an ion beam diameter of 16 mm for a kinetic energy of 1 kV (see Chapter 3.6.7).

The sputtering current was measured to be $0.3 \mu\text{A}$. The measurement was performed with a high-precision amperemeter (Picoammeter / Voltage Source, Model 6487, Keithley) using a copper sample (length 10 mm, width 2 mm, thickness 0.5 mm) mounted on a modified VT sample holder. The latter was modified such that the copper sample was isolated at the right side of the sample holder (exchange of two metal spacers against two ceramic bushes). The obtained setup enabled the measurement of the current that flows during sputtering between the copper sample and ground at an external connector pin of the instrument. This current corresponds to the sputtering current.

16.1.4 Normalization and quantitative analysis of Auger spectra

Normalization of Auger spectra

As described in Chapter 3.6.8 the measured signal intensity in Auger spectra depends on several parameters, which are listed in the following overview:

- (1) In the used setup a high sensitivity of Auger measurements to the sample holder geometry is given due to the long distance between inlet port of the hemispherical electron energy analyzer and the sample surface ($\approx 22 - 25$ mm). Since the used samples were mounted on different sample holders (with respect to the applied heating procedure) (see Table 16.3), an influence on the intensity in AE spectra is possible.
- (2) Sample holder modifications can affect the measured signal intensities in AE spectra. The Au(111) VT sample holder was modified with tantalum stripes on top of the upper sample plate and on the inner sides of the window to shield charges on this plate. This modification was not applied to the other sample holders.
- (3) The sample geometry can influence the intensity in Auger measurements, e.g. due to shadowing effects. The used samples actually had different sizes and thus the “accessible section” of the sample below the upper sample plate was different (see Table 16.3).
- (4) The surface roughness and topography influence the acquired intensity in Auger measurements.
- (5) The position of the measurement on the sample surface was found to influence the acquired intensity in Auger measurements.
- (6) The performed Auger measurements in the experimental setup are very sensitive to perturbations like interfering electric or magnetic fields. Electric fields due to charging can not be completely ruled out.

To handle the influence of these parameters, the intensity of all Auger electron spectra shown or analyzed in this work was normalized according to the procedure described in Chapter 3.6.8. Experimental details concerning the normalization are given below.

Sample	Sample holder	Sample size	“Accessible section”
Si(100)	VT sample holder for resistive heating	10 x 1	5 x 1
Au(111)	VT sample holder with integrated PBN heater for radiative heating	9 x 2	5 x 2
C reference sample	Tantalum standard sample plate	7 x 2	5 x 2
TiO ₂ reference sample	Modified VT sample holder with integrated filament for electron beam heating	6 x 5	5 x 5

Table 16.3: The use of different sample holders with different “accessible sections” of the samples influences the performed Auger measurements. The numerical values (length x width) are given in ‘mm’. All samples were mounted below the upper sample plate.

Except for the AE spectra shown in Chapter 13, the intensity for low kinetic energies (0 – 990 eV) of all spectra of this work was normalized with respect to the intensity of a rutile TiO₂(110) reference spectrum at the kinetic energy of 530 eV (3,062 counts). The AE spectra depicted in Chapter 13 (see Figure 13.2 f)) were normalized by scaling the intensity such that it is 6,000 counts at the energy of 730 eV. Normalization by applying this higher kinetic energy, i.e. 730 instead of 530 eV, was necessary because two of the corresponding spectra depict Fe LMM Auger signals at \approx 589, 596, 645 and 701 eV, respectively, i.e. at higher kinetic energies than 530 eV. The intensity for high kinetic energies (1000 – 1987 eV) was exclusively normalized with respect to the intensity of a spectrum acquired on a clean Si(100) surface before an EBID experiment. Normalization was done by adjusting the intensity at $E_{\text{kin}} = 1950$ eV (5,812 counts).

Reference spectrum for the normalization of the intensity of AE spectra for low kinetic energies (0 – 990 eV):

Raw data file:	'110209_01_TiO2_AES.aes'
File region:	12
Sample:	Rutile TiO ₂ (110) sample
Scan window size:	200 nm x 200 nm
Reference energy:	530 eV
Reference intensity:	3,062 counts

Reference data for the normalization of the intensity of the AE spectra depicted in Chapter 13 for low kinetic energies (0 – 990 eV):

Reference energy:	730 eV
Reference intensity:	6,000 counts

Reference spectrum for the normalization of the intensity of AE spectra for high kinetic energies (1000 – 1987 eV):

Raw data file:	'100330_02_Si100_AES_Probe_26.aes'
File region:	1
Sample:	Si(100) sample
Scan window size:	200 nm x 200 nm
Reference energy:	1950 eV
Reference intensity:	5,812 counts

Quantitative analysis of Auger spectra

For the quantitative analyses of Auger spectra in this work it was found that the sum of the calculated carbon, titanium and oxygen content of EBID deposits lies below 100 %. To address this deviation, the initially calculated values were uniformly scaled such that the sum is 100 %. In the following, possible reasons are listed which can explain the initial deviation from 100 % (despite spectrum normalization).

- (1) An inhomogeneous element distribution in the EBID deposits with an increased amount of carbon at the surface (see results presented in Chapter 9.1.1) is the most probable reason for the observed deviation. This appearance depicts a

plausible error source in the performed quantitative analysis of the chemical composition since it is based on a homogeneous distribution of all elements.

- (2) The hemispherical electron energy analyzer shows an individual, instrument specific transmission function. Since the transmission function is energy dependent, it influences the intensity of AE signals appearing at different kinetic energies differently. Intensity normalization at one specific (reference) energy does not account for this effect.

16.1.5 Reference AE spectra

Reference AE spectra for pure titanium dioxide and pure carbon were used for the quantitative determination of the chemical composition of EBID deposits with TTIP (see Chapter 3.6.8). Figure 16.2 depicts the reference spectra in the kinetic energy range from 0 to 600 eV.

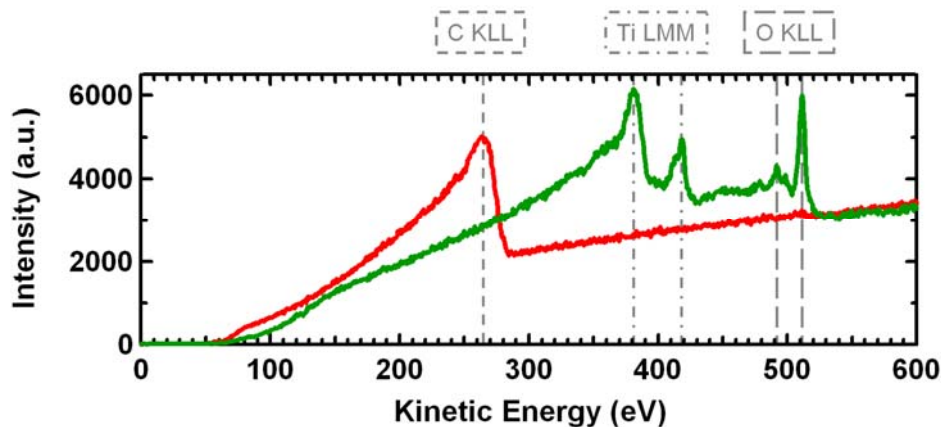


Figure 16.2: Reference AE spectra for pure titanium dioxide (green) and pure carbon (red). The intensity of the carbon spectrum was normalized with respect to the one of titanium dioxide at the kinetic energy of 530 eV.

The titanium dioxide reference AE spectrum in Figure 16.2 (green) was measured on a clean rutile $\text{TiO}_2(110)$ single crystal. The carbon reference AE spectrum in Figure 16.2 (red) was acquired on a thick carbon layer on an $\text{SiO}_x(300 \text{ nm}) / \text{Si}(100)$ sample. Both spectra were measured in the area mode (details see below).

<u>TiO₂</u> :	Raw data file:	'110209_01_TiO2_AES.aes'
	File region:	12
	Sample:	Rutile TiO ₂ (110) single crystal
	Scan window size:	200 nm x 200 nm
<u>C</u> :	Raw data file:	'081014_14_AES_Black_Specks.aes'
	File region:	11
	Sample:	Carbon on an SiO _x (300 nm) / Si(100) sample
	Scan window size:	200 nm x 200 nm

16.1.6 Attenuation lengths

Via semi-empirical equations by Cumpson and Seah [108] (see Chapter 3.6.8) the attenuation length λ_{AL} was calculated under direct consideration of the chemical composition of the deposited material. Figure 16.3 shows a plot of λ_{AL} in dependence of the kinetic energy E_{kin} for two different chemical compositions.

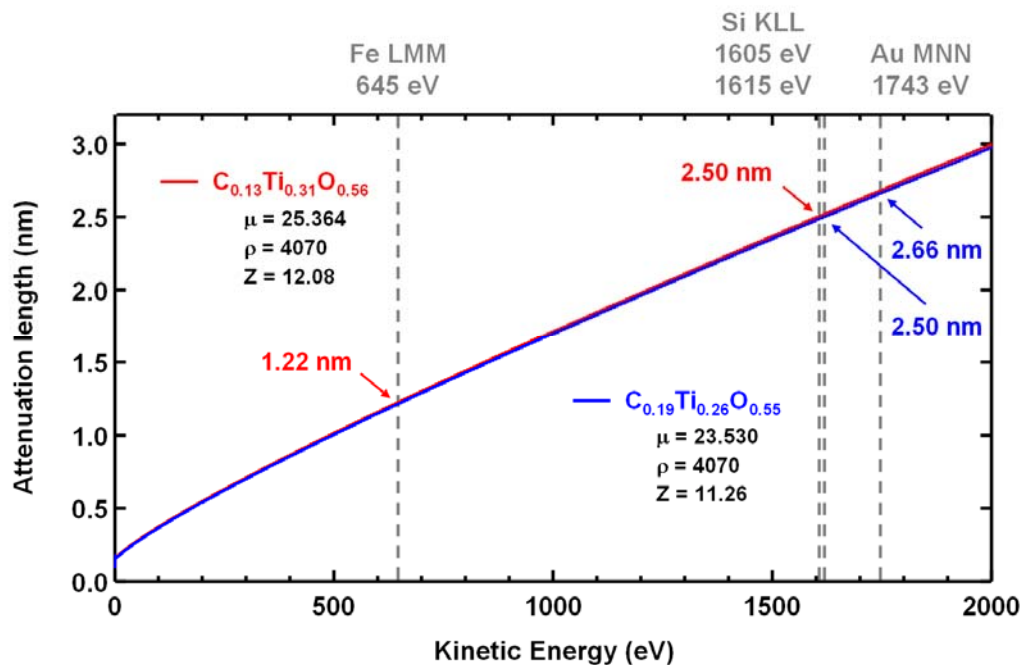


Figure 16.3: Plot of the attenuation length λ_{AL} for the deposited material in EBID area deposits against the kinetic energy E_{kin} based on semi-empirical equations given by Cumpson and Seah [108].

The two curves are nearly identical demonstrating a rather low influence of the small differences in chemical composition, which are caused by different lithographic parameters. The blue curve is the plot for area deposits fabricated on Si(100) (parameters see Chapter 7.2), the red one is valid for the deposited capping layer material (parameters see Chapter 13).

The attenuation length values used for layer thickness calculations in this work are marked color-coded in Figure 16.3 with respect to the chemical composition of the deposited material. Moreover, the parameters used for calculation (i.e. stoichiometric composition, average atomic mass per mol μ (in g), density ρ (in kg m^{-3}) and average atomic number Z) are specified.

16.2 Chapter 5 – Purification of TTIP

16.2.1 Reference mass spectra of isopropanol and acetone

Figure 16.4 shows the reference mass spectra of the two solvents isopropanol ($(\text{CH}_3)_2\text{CHOH}$) and acetone ($(\text{CH}_3)_2\text{CO}$). Both spectra are taken from reference [51].

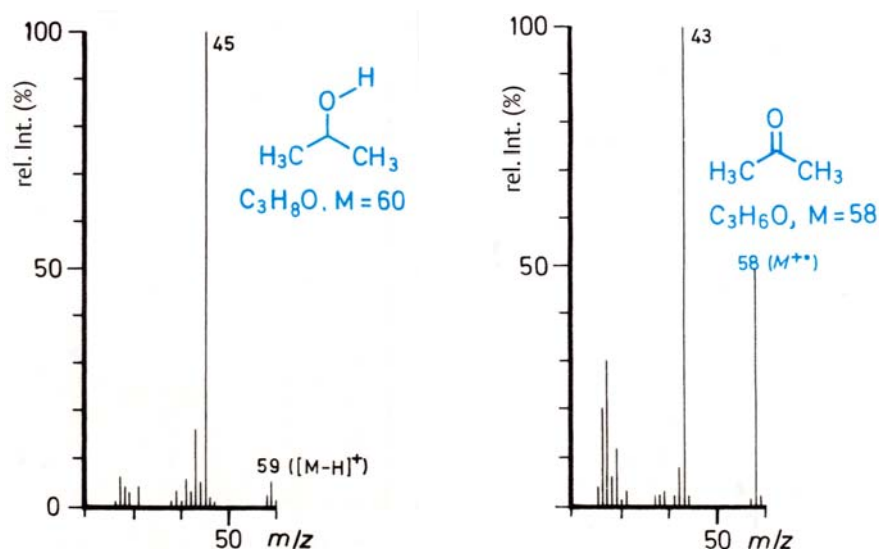


Figure 16.4: Reference mass spectra of the two solvents isopropanol ($(\text{CH}_3)_2\text{CHOH}$) and acetone ($(\text{CH}_3)_2\text{CO}$) [51].

16.2.2 Hydrocarbon precursor fragments

Figure 16.5 depicts the suggested chemical structures of the detected hydrocarbon fragments from the precursor TTIP. This figure is an extension to Table 5.1 in Chapter 5.2.

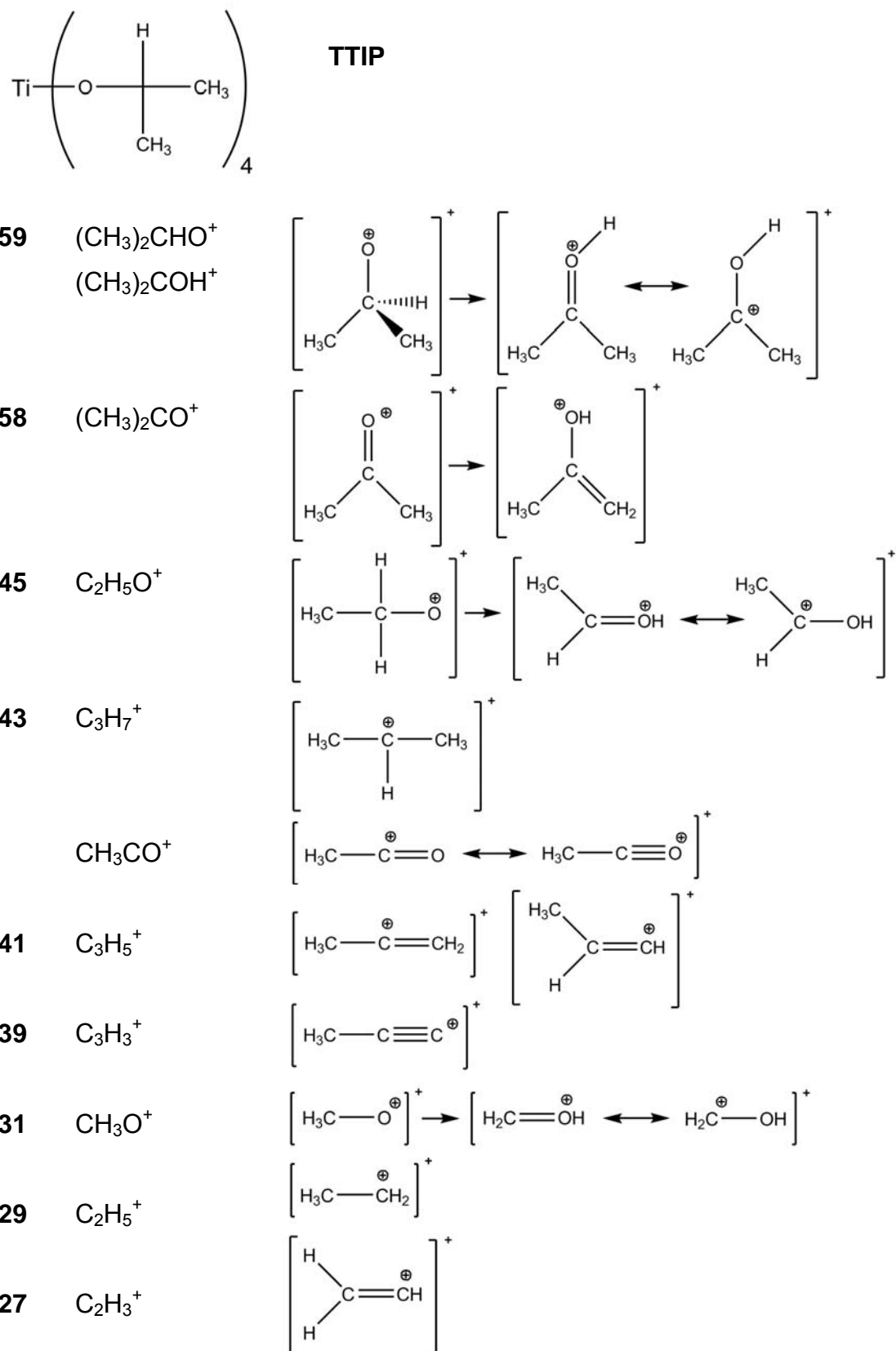


Figure 16.5: Proposed chemical structures of the detected hydrocarbon fragments from the precursor TTIP.

16.2.3 Experimental details for an exemplary precursor purification

In Chapter 5.2 the precursor purification via a combination of heating the precursor storage device and pumping via the TMP is demonstrated. Table 16.4 provides all experimental details of an exemplary precursor purification to which is referred to in the Figures 5.3, 5.4 and 5.5.

Period	Temperature	Proceeding	Pressure
5 times	RT	Degassing the vessel	-
10 min	Heating up to 333 K	-	-
	333 K	Pumping via the TMP	-
10 min	Heating up to 373 K	-	-
	373 K	Pumping via the TMP	-
	Heating up to 413 K	-	-
30 min	413 K	Pumping via the TMP	-
		QM spectrum 1	$3.0 \cdot 10^{-7}$ mbar
		= Preparation state I	
77 min	413 K	Pumping via the TMP	-
		QM spectrum 2	$3.0 \cdot 10^{-7}$ mbar
64 min	413 K	Pumping via the TMP	-
		QM spectrum 3	$3.0 \cdot 10^{-7}$ mbar
30 min	Cooling down	Pumping via the TMP	-
5 min	Heating up to 333 K	-	-
30 min	333 K	Pumping via the TMP	-
5 min	Heating up to 373 K	-	-
30 min	373 K	Pumping via the TMP	-
6 min	Heating up to 413 K	Pumping via the TMP	-
30 min	413 K	Pumping via the TMP	-
		QM spectrum 4	$3.0 \cdot 10^{-7}$ mbar

30 min	413 K	Pumping via the TMP	-
13 min	Cooling down	Pumping via the TMP	-
17 min	Heating up to 333 K	Pumping via the TMP	-
12 min	Heating up to 373 K	Pumping via the TMP	-
13 min	Heating up to 413 K	Pumping via the TMP	-
60 min	413 K	Pumping via the TMP	-
		QM spectrum 5	$3.0 \cdot 10^{-7}$ mbar
		= Preparation state II	
<hr/>			
60 min	413 K	Pumping via the TMP	-
		QM spectrum 6	$3.0 \cdot 10^{-7}$ mbar
<hr/>			
61 min	413 K	Pumping via the TMP	-
		QM spectrum 7	$3.0 \cdot 10^{-7}$ mbar
<hr/>			
	Cooling down	-	-
40 min	Heating up to 413 K	Pumping via the TMP	-
		QM spectrum 8	$3.0 \cdot 10^{-7}$ mbar
		= Reference spectrum	

Table 16.4: Experimental details of an exemplary precursor purification via a combination of heating the precursor storage device and pumping via the TMP.

16.2.4 Titanium containing precursor fragments

For the signals in the QM spectra of purified TTIP which are supposed to contain titanium, possible precursor fragments were proposed. An overview for the suggested fragment compositions is given in Table 16.5.

Note that the chemical compositions of the titanium containing precursor fragments in this table are suggested and thus somewhat speculative. The latter were determined by systematically “attaching” hydrocarbon fragments of TTIP (see Table 5.1) to a titanium atom with the mass of 48. To simplify matters, only singly charged ions were considered.

N	m/z	Fragment
I	48	Ti ⁺
II	64	TiO ⁺
	79	TiOCH ₃ ⁺
	80	TiO ₂ ⁺ , TiOHCH ₃ ⁺
III	81	TiO ₂ H ⁺
	82	TiO ₂ H ₂ ⁺
	83	-
	97	-
	98	-
IV	99	TiO ₃ H ₃ ⁺
	100	-
	101	-
	105	TiO(C ₃ H ₅) ⁺
	106	TiOCH ₃ (C ₂ H ₃) ⁺
	107	Ti(O'Pr) ⁺ , TiO ₂ (C ₂ H ₃) ⁺ , TiO ₂ CH ₃ C ⁺ , TiO(C ₃ H ₇) ⁺
V	108	Ti(O'Pr)H ⁺ , TiOCH ₃ (C ₂ H ₅) ⁺
	109	TiO(C ₂ H ₅ O) ⁺ , TiO ₂ (C ₂ H ₅) ⁺
	110	Ti(OCH ₃) ₂ ⁺ , TiOCH ₃ (CH ₃ O) ⁺ , TiO ₂ (CH ₃) ₂ ⁺
	119	TiO ₂ (C ₃ H ₃) ⁺
	120	TiOCH ₃ (C ₃ H ₅) ⁺
VI	121	TiO ₂ (C ₃ H ₅) ⁺ , Ti(O'Pr)CH ₂ ⁺ , TiO(C ₂ H ₅ O)C ⁺
VI	122	Ti(O'Pr)CH ₃ ⁺ , TiO((CH ₃) ₂ CO) ⁺ , TiOCH ₃ (C ₃ H ₇) ⁺ , TiO ₂ CH ₃ (C ₂ H ₃) ⁺
	123	TiO(O'Pr) ⁺ , TiO ₂ (C ₃ H ₇) ⁺
	124	TiO(O'Pr)H ⁺ , TiOCH ₃ (C ₂ H ₅ O) ⁺ , TiO ₂ CH ₃ (C ₂ H ₅) ⁺
VI	125	TiO(O'Pr)H ₂ ⁺ , TiO ₂ (C ₂ H ₅ O) ⁺ , Ti(O'Pr)CH ₃ H ₃ ⁺
	126	TiO ₂ CH ₃ (CH ₃ O) ⁺
	127	-
	137	TiOCH ₃ ((CH ₃) ₂ CO) ⁺ , TiO ₂ (C ₂ H ₅ O)C ⁺
	138	TiO(O'Pr)CH ₃ ⁺ , TiO ₂ ((CH ₃) ₂ CO) ⁺ , TiO ₂ CH ₃ (C ₃ H ₇) ⁺ , TiO(C ₂ H ₅ O)(C ₂ H ₅) ⁺
VII	139	TiO ₂ (O'Pr) ⁺ , TiO(O'Pr)CH ₃ H ⁺
	140	TiO(O'Pr)CH ₃ H ₂ ⁺ , TiO ₂ H(O'Pr) ⁺ , TiO ₂ CH ₃ (C ₂ H ₅ O) ⁺ , TiO(C ₂ H ₅ O)(CH ₃ O) ⁺
	141	Ti(OCH ₃) ₃ ⁺ , TiO ₃ (C ₂ H ₅ O) ⁺
	147	-
	148	TiO(C ₂ H ₅ O)(C ₃ H ₃) ⁺

	149	-
VIII	150	$\text{TiO}(\text{O}^i\text{Pr})(\text{C}_2\text{H}_3)^+$, $\text{TiO}(\text{C}_2\text{H}_5\text{O})(\text{C}_3\text{H}_5)^+$
	151	$\text{TiO}_2(\text{O}^i\text{Pr})\text{C}^+$
	152	$\text{TiO}(\text{O}^i\text{Pr})(\text{C}_2\text{H}_5)^+$, $\text{TiO}(\text{C}_2\text{H}_5\text{O})(\text{C}_3\text{H}_7)^+$, $\text{TiO}_2(\text{C}_2\text{H}_5\text{O})(\text{C}_2\text{H}_3)^+$
	153	$\text{TiO}_2\text{CH}_3((\text{CH}_3)_2\text{CO})^+$
<hr/>		
	164	$\text{TiO}(\text{O}^i\text{Pr})(\text{C}_3\text{H}_5)^+$, $\text{TiO}_2(\text{C}_2\text{H}_5\text{O})(\text{C}_3\text{H}_3)^+$
	165	$\text{Ti}(\text{O}^i\text{Pr})((\text{CH}_3)_2\text{CO})^+$
	166	$\text{Ti}(\text{O}^i\text{Pr})_2^+$, $\text{TiO}_2(\text{O}^i\text{Pr})(\text{C}_2\text{H}_3)^+$, $\text{TiO}(\text{O}^i\text{Pr})(\text{C}_3\text{H}_7)^+$, $\text{TiO}_2(\text{C}_2\text{H}_5\text{O})(\text{C}_3\text{H}_5)^+$
IX	167	$\text{Ti}(\text{O}^i\text{Pr})_2\text{H}^+$, $\text{Ti}_2(\text{O}^i\text{Pr})\text{C}^+$, $\text{TiO}(\text{C}_2\text{H}_5\text{O})((\text{CH}_3)_2\text{CO})^+$
	168	$\text{TiO}(\text{O}^i\text{Pr})(\text{C}_2\text{H}_5\text{O})^+$, $\text{TiO}_2(\text{O}^i\text{Pr})(\text{C}_2\text{H}_5)^+$, $\text{TiO}_2(\text{C}_2\text{H}_5\text{O})(\text{C}_3\text{H}_7)^+$
	169	-
<hr/>		
	179	-
	180	$\text{TiO}_2(\text{O}^i\text{Pr})(\text{C}_3\text{H}_5)^+$
X	181	$\text{TiO}(\text{O}^i\text{Pr})((\text{CH}_3)_2\text{CO})^+$, $\text{Ti}(\text{O}^i\text{Pr})_2\text{CH}_3^+$
	182	$\text{TiO}(\text{O}^i\text{Pr})_2^+$, $\text{TiO}_2(\text{O}^i\text{Pr})(\text{C}_3\text{H}_7)^+$
	183	$\text{TiO}_2(\text{C}_2\text{H}_5\text{O})((\text{CH}_3)_2\text{CO})^+$

Table 16.5: Proposed compositions for the titanium containing precursor fragments detected via QMS. 'N' describes the corresponding signal group (see Chapter 5.2) and 'm/z' the mass to charge ratio in the QM spectrum.

16.3 Chapter 6 – Flux distribution of TTIP

In Chapter 6 several assumptions were made for the determination of quantities like the precursor flux and pressure (at the nozzle exit and directly on the sample surface) and the flux distribution. Therefore, despite thorough proceeding the determination has to be considered as estimation. In the following, a summary is given for all made assumptions:

Assumptions:

I Pumping speed of the ion getter pump for TTIP:

The pumping speed S of the ion getter pump for the precursor TTIP is not known and was assumed to be in between of the pumping speeds for argon (250 l/s) and nitrogen (360 l/s). Therefore, all determined quantities are based on the assumed pumping speed of 305 l/s for TTIP.

II Nominal pumping speed:

For the pumping speed S of the ion getter pump it was assumed that it has reached a stabilized level known as 'saturation'. This pumping speed is also called 'nominal pumping speed' [222].

III Dynamic pressure:

For the determination of the pressure at the very end of the nozzle exit a rough estimation from its dynamic component was performed (via Equation 6.21). This estimation is proposed by Friedli and Utke [19, 218]. The authors note that the dynamic pressure slightly overestimates the actual pressure in the vicinity of the nozzle exit.

IV Degree of association of TTIP:

TTIP was assumed to be a monomer with the molecular mass M of 284 g/mol.

V Temperature of the precursor molecules:

The precursor vessel is heated to a temperature of 413 K during the EBID experiments. On their way to the surface the precursor molecules cool down, but the temperature distribution within the pipe system is not known. As the total distance from the vessel to the nozzle exit is roughly 3 m, it was assumed that the temperature of the molecules in the GIS (inside the UHV instrument) is at RT (293 K) again.

VI Simulation with molecular flow conditions in the tube:

The simulation with the software 'GIS Simulator' (version 1.5, 2008) was performed with the assumption of molecular flow conditions inside the tube. This assumption is based on the determined value for the Knudsen number ($Kn = 8.7$, see Chapter 6.4.2) and the specifications given in the references [219, 220] clearly indicating molecular flow. As Friedli and Utke [19] give a different boundary for molecular and transient flow ($Kn = 10$) and as the actual flow inside the tube is not known, simulations for transient flow were performed, as well. For a nozzle-sample distance of 12 mm the simulations provided a value of 0.018 for the impinging flux coefficient J/J_{tot} at the position at $x_s = y_s = 0$ on the sample surface. The obtained value is lower but basically close to the obtained one for molecular flow conditions which was 0.026. This means that for transient flow conditions in the tube the calculated quantities of molecule flux J and pressure p are lowered by an average value of - 31 %. Additionally, this result demonstrates that the findings of Chapter 6 are substantially not touched by the made assumption.

16.4 Chapter 9 – Post-treatment procedures

Table 16.6 shows the annealing steps and parameters of the applied post-treatment procedures presented in the Chapters 9.2 and 9.3. The treatments comprise heating the sample slowly to a temperature of 1,010 K within a time periods of ≈ 3 h and 15 min in an oxygen background pressure of $3.0 \cdot 10^{-7}$ mbar.

Post-treatment procedure Chapter 9.2		Post-treatment procedure Chapter 9.3	
Time in [h:min]	Temperature in [K]	Time in [h:min]	Temperature in [K]
00:00	560	00:00	560
00:01	600	00:01	600
00:02	790	00:02	790
00:12	860	00:08	860
01:38	910	00:11	910
02:11	940	00:16	860
02:22	950	00:31	880
02:29	980	01:15	910
02:49	1,010	01:48	940
03:09	980	02:05	950
03:09	950	02:16	980
03:10	910	02:38	1,010
03:11	860	02:57	980
03:12	790	02:59	950
03:13	600	03:01	910
03:14	560	03:04	860
03:15	-	03:06	790
		03:09	600
		03:11	560
		03:13	-

Total heating time: 3 h 15 min	Total heating time: 3 h 13 min
Total O ₂ dosage time: 3 h 8 min	Total O ₂ dosage time: 2 h 53 min
$p(\text{O}_2) = 3.0 \cdot 10^{-7}$ mbar	$p(\text{O}_2) = 3.0 \cdot 10^{-7}$ mbar
Sample material: Si(100)	Sample material: Si(100)

Table 16.6: Annealing steps and parameters of the applied post-treatment procedures comprising heating the sample slowly to a temperature of 1,010 K within a time period of ≈ 3 h and 15 min in an oxygen background pressure of $3.0 \cdot 10^{-7}$ mbar.

16.5 Chapter 10 – Morphology of EBID deposits

The volume of EBID deposits was estimated by comparing to basic three-dimensional geometric shapes. Figure 16.6 depicts the geometric shapes, which were considered.

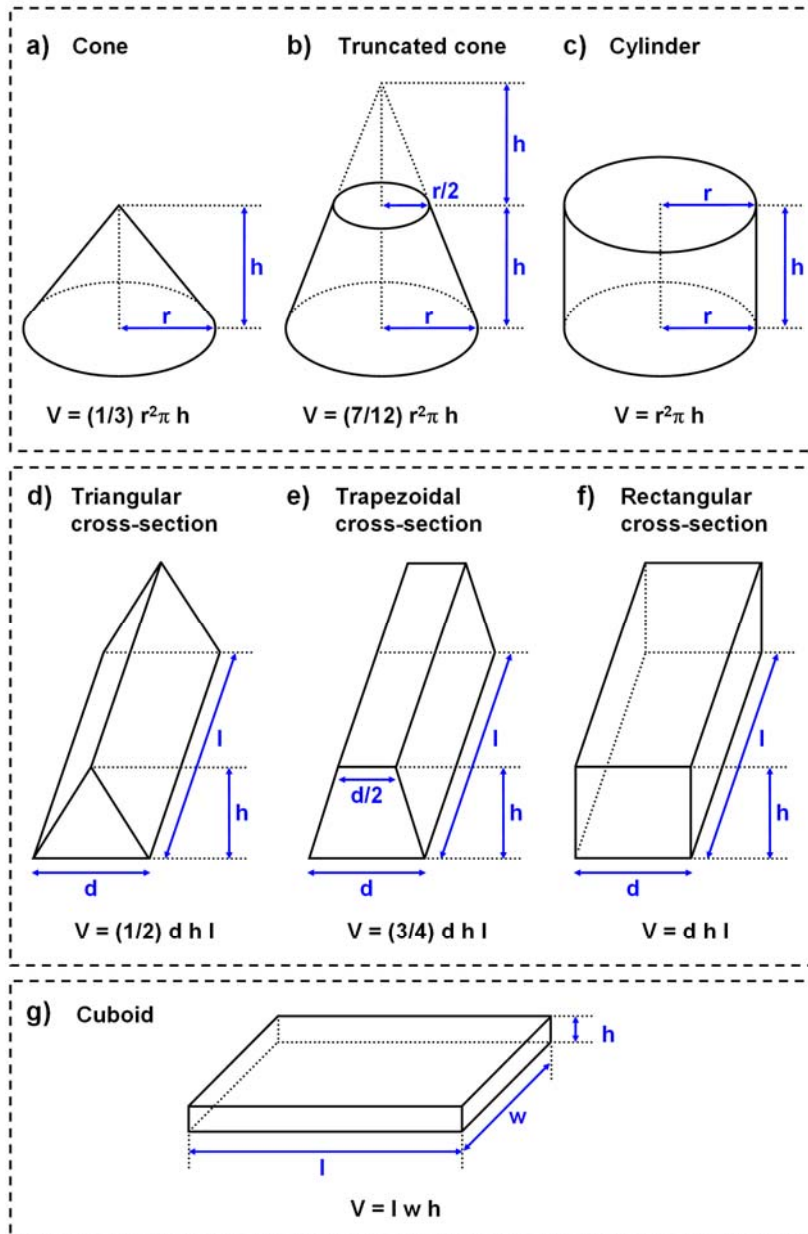


Figure 16.6: Basic three-dimensional geometric shapes considered for the estimation of the volume of EBID deposits. Actually used was the truncated cone shape (b) for dot deposits, the shape with trapezoidal cross-section (e) for line deposits and the cuboid shape (g) for area deposits.

Actually used for the calculation of the deposit volume was the truncated cone shape (b)) for dot deposits, the shape with trapezoidal cross-section (e)) for line deposits and the cuboid shape (g)) for area deposits.

To determine the number of atoms of a deposit from TTIP an estimated atom density was used in Chapter 10. Table 16.7 gives an overview of atom densities N/V of materials relevant for EBID with TTIP. They were calculated from the corresponding densities ρ [62] and molar masses M [62] according to $(\rho \cdot N_A) / M$.

Material	Symbol	ρ [g/cm ³]	M [g/mol]	N/V [cm ⁻³]
Graphite	C	2.26	12.011	$1.13 \cdot 10^{23}$
Diamond	C	3.514	12.011	$1.76 \cdot 10^{23}$
Titanium	Ti	4.506	47.880	$5.67 \cdot 10^{22}$
Rutile	TiO ₂	4.27	79.879	$3.22 \cdot 10^{22}$
Anatase	TiO ₂	3.9	79.879	$2.94 \cdot 10^{22}$
Brookite	TiO ₂	4.17	79.879	$3.14 \cdot 10^{22}$
TiO ₂ averaged	TiO ₂	4.11	79.879	$3.10 \cdot 10^{22}$
C _{0.19} (TiO ₂) _{0.81}	-	3.76	66.984	$3.38 \cdot 10^{22}$
C _{0.25} (TiO ₂) _{0.75}	-	3.65	62.912	$3.49 \cdot 10^{22}$
C _{0.30} (TiO ₂) _{0.70}	-	3.56	59.519	$3.60 \cdot 10^{22}$

Table 16.7: Densities ρ , molar masses M and atom densities N/V of materials relevant for EBID with TTIP. The values for ρ and M of graphite, diamond, titanium, rutile, anatase and brookite are taken from reference [62]. All other values are calculated.

16.6 Chapter 11 – Stability of fabricated nanostructures

In Chapter 11, the stability of generated nanostructures was discussed. Figure 16.7 shows two examples for titanium oxide nanocrystals fabricated by a post-treatment procedure from EBID deposits (Chapter 9.3). The SEM images were acquired directly after the post-treatment procedures (Figure 16.7 a) and c)) and after long-term storage under vacuum conditions in the UHV instrument (Figure 16.7 b) and d)) at exactly the same position (details see Chapter 11).

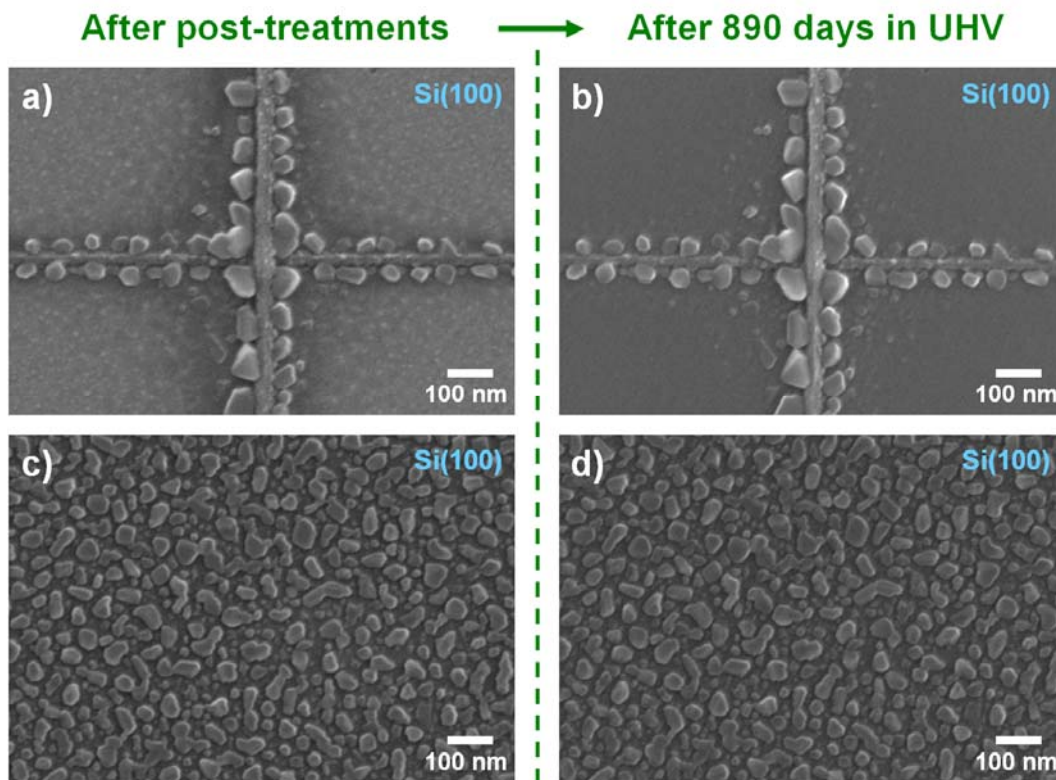


Figure 16.7: a) and c) SEM images of titanium oxide nanocrystals directly after fabrication via a post-treatment procedure (see Chapter 9.3). b) and d) SEM images of the same nanocrystals after long-term storage under vacuum conditions in the UHV instrument (details see Chapter 11).

Figure 16.7 demonstrates that the nanocrystals appear identical in SEM before and after the extended storage time in vacuum. The small and bright protrusions on the Si(100) surface in Figure 16.7 a) are not visible in Figure 16.7 b). This is attributed

rather to the different acquisition parameters for the corresponding SEM images than to an effect caused by the extended storage time.

Figure 16.8 shows an EBID line pattern fabricated with identical lithographic parameters as the line pattern depicted in Figure 7.4 a). The SEM image of Figure 16.8 a) was taken after EBID while the one of Figure 16.8 b) was acquired after exposure to ambient conditions and reintroduction into the UHV system (details see Chapter 11).

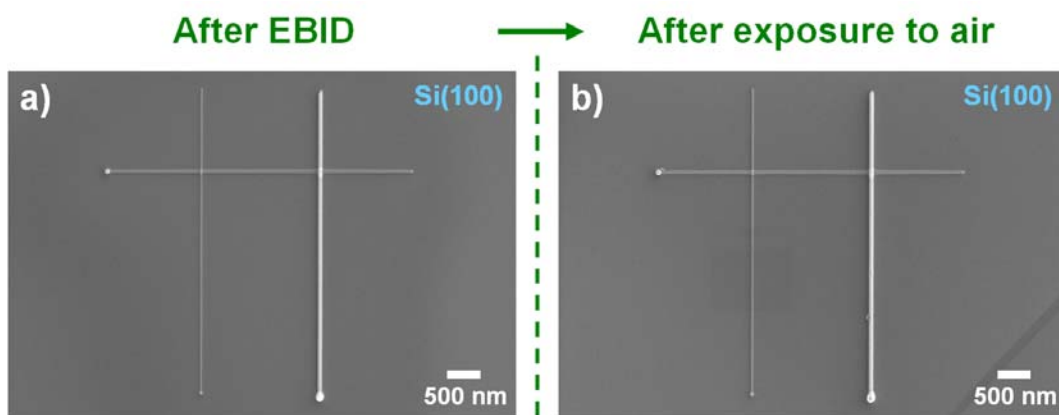


Figure 16.8: SEM images of a line pattern a) after EBID. b) after exposure to air and reintroduction into the UHV system (details see Chapter 11).

Figure 16.8 demonstrates that the fabricated EBID deposits are stable upon exposure to ambient conditions since the nanostructures appear unchanged in SEM. The small particles adjacent to the horizontal and right vertical line in Figure 16.8 b) are dust particles while the dark stripe in the lower right is most presumably a surface scratch.

16.7 Chapter 13 – Local protective capping of nanostructures

Figure 16.9 a) shows an AFM image of an uncapped region of the capped iron line depicted in Figure 13.2. An AFM height profile of this line was acquired at the position labeled in a) (green horizontal line). The corresponding profile is shown in Figure 16.9 b). The height of the polycrystalline line was determined to be $\approx 15 - 24$ nm, depending on the position where the AFM profile is taken.

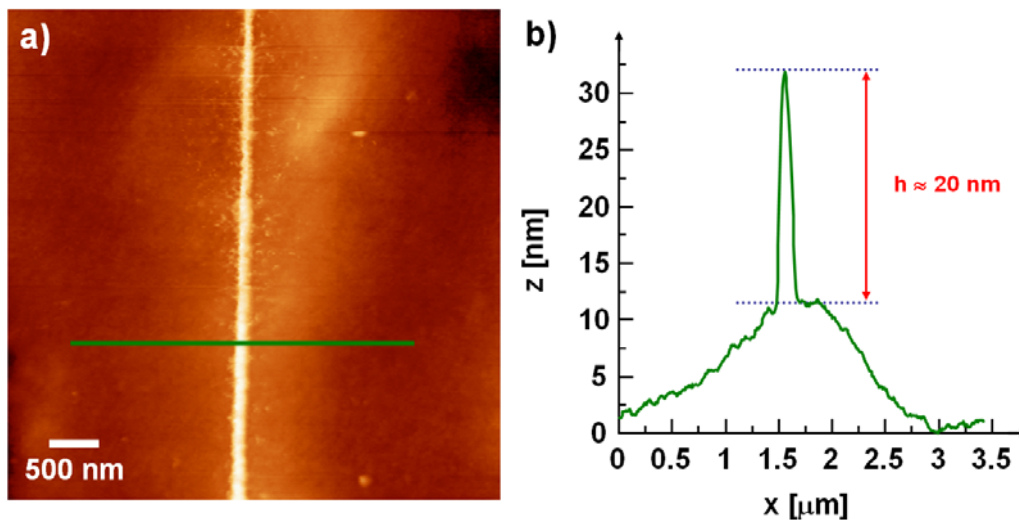


Figure 16.9: a) AFM image of an uncapped region of the capped iron line which is depicted in Figure 13.2. b) AFM height profile acquired at the position labeled in a) (averaging by 5 lines).

17 References

- [1] Rubahn, H.-G. *Basics of Nanotechnology*. 3. Edition, WILEY-VCH Verlag GmbH & Co. KGaA, Weinheim, 2008.
- [2] Randolph, S. J.; Fowlkes, J. D.; Rack, P. D.; *Critical Reviews in Solid State and Materials Sciences* **2006**, 31, 55-89.
- [3] Silvis-Cividjian, N.; Hagen, C. W.; *Advances in Imaging and Electron Physics* **2006**, 143, 1-235.
- [4] Utke, I.; Hoffmann, P.; Melngailis, J.; *Journal of Vacuum Science & Technology B* **2008**, 26, 1197-1276.
- [5] van Dorp, W. F.; Hagen, C. W.; *Journal of Applied Physics* **2008**, 104, 081301(1-42).
- [6] Diebold, U.; *Surface Science Reports* **2003**, 48, 53-229.
- [7] Chen, X.; Mao, S. S.; *Chemical Reviews* **2007**, 107, 2891-2959.
- [8] Valden, M.; Lai, X.; Goodman, D. W.; *Science* **1998**, 281, 1647-1650.
- [9] Bondzie, V. A.; Parker, S. C.; Campbell, C. T.; *Catalysis Letters* **1999**, 63, 143-151.
- [10] Sandell, A.; Anderson, M. P.; Alfredsson, Y.; Johansson, M. K.-J.; Schnadt, J.; Rensmo, H.; Siegbahn, H.; Uvdal, P.; *Journal of Applied Physics* **2002**, 92, 3381-3387.
- [11] Watanabe, A.; Tsuchiya, T.; Imai, Y.; *Thin Solid Films* **2002**, 406, 132-137.
- [12] Chen, Z.-X.; Derking, A.; *Journal of Materials Chemistry* **1993**, 3, 1137-1140.
- [13] Simcock, M. N.; *Surface and Interface Analysis* **2006**, 38, 1122-1129.
- [14] Ahn, K.-H.; Park, Y.-B.; Park, D.-W.; *Surface and Coatings Technology* **2003**, 171, 198-204.
- [15] Fictorie, C. P.; Evans, J. F.; Gladfelter, W. L.; *Journal of Vacuum Science & Technology, A* **1994**, 12, 1108-1113.
- [16] Mitchell, W. J.; Hu, E. L.; *Journal of Vacuum Science & Technology B* **1999**, 17, 1622-1626.
- [17] Mitchell, W. J.; Hu, E. L.; *Applied Physics Letters* **1999**, 74, 1916-1918.
- [18] Hoffmann, P.; Utke, I.; Perentes, A.; Bret, T.; Santschi, C.; Apostolopoulos, V. Comparison of fabrication methods of sub-100 nm nano-optical structures and

- devices. in *Proceedings of SPIE, Nanophotonic Materials and Systems II* **2005**, Bellingham, WA, 592506-1 - 592506-15.
- [19] Friedli, V.; Utke, I.; *Journal of Physics D: Applied Physics* **2009**, 42, 125305(1-11).
- [20] Drouin, D.; Couture, A. R.; Joly, D.; Tastet, X.; Aimez, V.; Gauvin, R.; *Scanning* **2007**, 29, 92-101.
- [21] Randolph, S. J.; Fowlkes, J. D.; Rack, P. D.; *Journal of Applied Physics* **2005**, 97, 124312(1-8).
- [22] Walz, M.-M.; Schirmer, M.; Vollnhals, F.; Lukasczyk, T.; Steinrück, H.-P.; Marbach, H.; *Angewandte Chemie International Edition* **2010**, 49, 4669-4673.
- [23] Walz, M.-M.; Vollnhals, F.; Schirmer, M.; Steinrück, H.-P.; Marbach, H.; *Physical Chemistry Chemical Physics* **2011**, 13, 17333-17338.
- [24] Schmidt, P. F., *Einführung in die Rasterelektronenmikroskopie*. Technische Akademie Esslingen (TAE), Seminar 'Rasterelektronenmikroskopie und Mikrobereichsanalyse', **2007**.
- [25] Reimer, L. *Scanning Electron Microscopy - Physics of Image Formation and Microanalysis*. 2. Edition, Springer-Verlag, Heidelberg, 1998.
- [26] Schmidt, P. F., *Rasterelektronenmikroskopie und Analyse von Mikrobereichen und Oberflächenschichten*. Technische Akademie Esslingen (TAE), Seminar 'Rasterelektronenmikroskopie und Mikrobereichsanalyse', **2007**.
- [27] Schmidt, P. F., *Aufbau eines Rasterelektronenmikroskops*. Technische Akademie Esslingen (TAE), Seminar 'Rasterelektronenmikroskopie und Mikrobereichsanalyse', **2007**.
- [28] Schmidt, P. F., *Kontraste in der Rasterelektronenmikroskopie*. Technische Akademie Esslingen (TAE), Seminar 'Rasterelektronenmikroskopie und Mikrobereichsanalyse', **2007**.
- [29] Seiler, H.; *Journal of Applied Physics* **1983**, 54, R1-R18.
- [30] Lukasczyk, T. *Generation of pure iron nanostructures via electron-beam induced deposition in UHV*. Doctoral thesis, Lehrstuhl für Physikalische Chemie II, Friedrich-Alexander-Universität Erlangen-Nürnberg, Erlangen, **2010**.
- [31] Meitner, L.; *Zeitschrift für Physik A Hadrons and Nuclei* **1922**, 11, 35-54.
- [32] Auger, P.; *Journal de Physique et le Radium* **1925**, 6, 205-208.
- [33] Auger, P.; *Comptes Rendus* **1925**, 180, 65-68.

- [34] Briggs, D.; Seah, M. P. *Practical Surface Analysis, Volume 1 - Auger and X-ray Photoelectron Spectroscopy*. 2. Edition, John Wiley & Sons Ltd, Chichester (England), 1990.
- [35] Wedler, G. *Lehrbuch der Physikalischen Chemie*. 5. Edition, WILEY-VCH Verlag GmbH & Co. KGaA, Weinheim, 2004.
- [36] Baer, D. R.; Gaspar, D. J.; Nachimuthu, P.; Techane, S. D.; Castner, D. G.; *Analytical and Bioanalytical Chemistry* **2010**, 396, 983-1002.
- [37] Powell, C. J.; *Applied Surface Science* **2004**, 230, 327-333.
- [38] Ecke, G.; Cimalla, V.; Tonisch, K.; Lebedev, V.; Romanus, H.; Ambacher, O.; Liday, J.; *Journal of Electrical Engineering - ISSN 1335-3632 (Bratislava, Slovakia)* **2007**, 58, 301-306.
- [39] ISO/TR 19319, *Surface chemical analysis - Auger electron spectroscopy and X-ray photoelectron spectroscopy - Determination of lateral resolution, analysis area, and sample area viewed by the analyser*. International Organization for Standards, Geneva, Switzerland, **2003**.
- [40] Davis, L. E.; MacDonald, N. C.; Palmberg, P. W.; Riach, G. E.; Weber, R. E. *Handbook of Auger Electron Spectroscopy*. 2. Edition, Physical Electronics Industries, Perkin-Elmer Corporation, Eden Prairie (Minnesota, USA), 1976.
- [41] Binnig, G.; Quate, C. F.; Gerber, C.; *Physical Review Letters* **1986**, 56, 930-933.
- [42] Binnig, G.; Rohrer, H.; Gerber, C.; Weibel, E.; *Physical Review Letters* **1982**, 49, 57-61.
- [43] Oura, K.; Lifshits, V. G.; Saranin, A. A.; Zotov, A. V.; Katayama, M. *Surface Science - An Introduction*. 1. Edition, Springer-Verlag, Berlin, 2003.
- [44] Maier, S., *Atomic Force Microscopy (AFM)*. Friedrich-Alexander-Universität Erlangen-Nürnberg, Lecture in the Graduiertenkolleg IZ-ICP, **2011**.
- [45] Kolasinski, K. W. *Surface Science - Foundations of Catalysis and Nanoscience*. 2. Edition, John Wiley & Sons Ltd, Chichester (England), 2008.
- [46] Steinrück, H.-P., *Physikalische Chemie an Oberflächen*. Friedrich-Alexander-Universität Erlangen-Nürnberg, Lecture for Physical Chemistry, **2006**.
- [47] Meyer, E.; Hug, H. J.; Bennewitz, R. *Scanning Probe Microscopy - The Lab on a Tip*. 1. Edition, Springer-Verlag, Heidelberg, 2004.
- [48] Wiesendanger, R. *Scanning Probe Microscopy and Spectroscopy - Methods and Applications*. 1. Edition, Cambridge University Press, Cambridge, 1994.

- [49] García, R.; Pérez, R.; *Surface Science Reports* **2002**, 47, 197-301.
- [50] Giessibl, F. J.; *Reviews of Modern Physics* **2003**, 75, 949-983.
- [51] Hesse, M.; Meier, H.; Zeeh, B. *Spektroskopische Methoden in der organischen Chemie*. 7. Edition, Georg Thieme Verlag, Stuttgart, 2005.
- [52] Pfeiffer Vacuum GmbH, *Massenspektrometer*. Asslar, Germany, **2005**.
- [53] Henzler, M.; Göpel, W. *Oberflächenphysik des Festkörpers*. 2. Edition, B. G. Teubner, Stuttgart, 1994.
- [54] Schneider, A., *Surface Structure and Properties: LEED and STM*. Friedrich-Alexander-Universität Erlangen-Nürnberg, Lecture in the Graduiertenkolleg IZ-ICP, **2010**.
- [55] Czanderna, A. W. *Methods of Surface Analysis*. 1. Edition, Volume 1: Methods and Phenomena, Elsevier Scientific Publishing Company, Amsterdam, 1975.
- [56] Wilson, I. H.; Todorov, S. S.; Karpuzov, D. S.; *Nuclear Instruments and Methods in Physics Research* **1983**, 209-210, 549-554.
- [57] Ziegler, J. P.; Biersack, J. P.; Littmark, U. *The Stopping Power and Range of Ions in Solids*. 1. Edition, Vol. 1, Pergamon Press, New York, 1985.
- [58] National Physical Laboratory (NPL) Surface & Nanoanalysis Group, *Sputter Yield Values*. 08.08.2011, <http://www.npl.co.uk/nanoscience/surface-nanoanalysis/products-and-services/sputter-yield-values>, **2007**.
- [59] Seah, M. P.; Clifford, C. A.; Green, F. M.; Gilmore, I. S.; *Surface and Interface Analysis* **2005**, 37, 444-458.
- [60] Seah, M. P.; *Nuclear Instruments and Methods in Physics Research Section B: Beam Interactions with Materials and Atoms* **2005**, 229, 348-358.
- [61] Seah, M. P.; *Nuclear Instruments and Methods in Physics Research Section B: Beam Interactions with Materials and Atoms* **2005**, 239, 286-287.
- [62] Holleman, A. F.; Wiberg, N. *Lehrbuch der Anorganischen Chemie*. 101. Edition, Walter de Gruyter, Berlin, 1995.
- [63] Waltenburg, H. N.; Yates, J. T.; *Chemical Reviews* **1995**, 95, 1589-1673.
- [64] Schirmer, M. *Lithographic Fabrication of Nanostructures by Means of Electron-Beam Induced Deposition (EBID)*. Master thesis, Lehrstuhl für Physikalische Chemie II, Friedrich-Alexander-Universität Erlangen-Nürnberg, Erlangen, **2006**.
- [65] Barth, J. V.; Brune, H.; Ertl, G.; Behm, R. J.; *Physical Review B* **1990**, 42, 9307-9318.

- [66] Barth, J. V.; Schuster, R.; Behm, R. J.; Ertl, G.; *Surface Science* **1996**, 348, 280-286.
- [67] Wöll, C.; Chiang, S.; Wilson, R. J.; Lippel, P. H.; *Physical Review B* **1989**, 39, 7988-7991.
- [68] van Hove, M. A.; Koestner, R. J.; Stair, P. C.; Bibérian, J. P.; Kesmodel, L. L.; Bartoš, I.; Somorjai, G. A.; *Surface Science* **1981**, 103, 189-217.
- [69] Narasimhan, S.; Vanderbilt, D.; *Physical Review Letters* **1992**, 69, 1564-1567.
- [70] Kröger, J.; Jensen, H.; Berndt, R.; *New Journal of Physics* **2007**, 9, 153(1-9).
- [71] Dovek, M. M.; Lang, C. A.; Nogami, J.; Quate, C. F.; *Physical Review B* **1989**, 40, 11973-11975.
- [72] Elschenbroich, C. *Organometallchemie*. 5. Edition, Teubner, Wiesbaden, 2005.
- [73] Bradley, D. C.; Mehrotra, R. C.; Gaur, D. P. *Metal Alkoxides*. 5. Edition, Academic Press, London, 1978.
- [74] Bradley, D. C.; *Chemical Reviews* **1989**, 89, 1317-1322.
- [75] Damo, S. M.; Lam, K.-C.; Rheingold, A.; Walters, M. A.; *Inorganic Chemistry* **2000**, 39, 1635-1638.
- [76] Alfa Aesar, *Material safety data sheet titanium tetraisopropoxide*. Karlsruhe, Germany, **2010**.
- [77] Sigma-Aldrich, *Material safety data sheet titanium tetraisopropoxide*. Steinheim, Germany, **2010**.
- [78] Babonneau, F.; Doeuff, S.; Leautic, A.; Sanchez, C.; Cartier, C.; Verdaguer, M.; *Inorganic Chemistry* **1988**, 27, 3166-3172.
- [79] Moran, P. D.; Bowmaker, G. A.; Cooney, R. P.; Finnie, K. S.; Bartlett, J. R.; Woolfrey, J. L.; *Inorganic Chemistry* **1998**, 37, 2741-2748.
- [80] Bradley, D. C.; Holloway, C. E.; *Journal of the Chemical Society A: Inorganic, Physical, Theoretical* **1968**, 1316-1319.
- [81] Hao, N.; Sayer, B. G.; Dénès, G.; Bickley, D. G.; Detellier, C.; McGlinchey, M. J.; *Journal of Magnetic Resonance (1969)* **1982**, 50, 50-63.
- [82] Sigma-Aldrich, *Material safety data sheet iron pentacarbonyl*. Steinheim, Germany, **2012**.
- [83] Strem Chemicals, *Material safety data sheet iron pentacarbonyl*. Newburyport, USA, **2011**.

- [84] Walz, M.-M. *Fabrication of Clean Iron Nanostructures on Silicon Oxide via Focused Electron Beam Induced Processing in UHV*. Doctoral thesis, Lehrstuhl für Physikalische Chemie II, Friedrich-Alexander-Universität Erlangen-Nürnberg, Erlangen, **2012**.
- [85] Omicron NanoTechnology, *3 nm UHV SEM meets Nanotechnology Applications (Advertisement flyer for Gemini column)*. Taunusstein, Germany, **2003**.
- [86] LEO GmbH, *LREM Scan Timing Firmware Version V1.4.0*. **2000**.
- [87] Raith, *Product Info ELPHY Plus, ELPHY Quantum and Laser interferometer stage*. Dortmund, **2011**.
- [88] Raith, *Software Operation Manual and Software Reference Manual, ELPHY Quantum, Version 4.0*. Dortmund, **2004**.
- [89] Hewlett-Packard Company, *Bedienerhandbuch Funktionsgenerator für beliebige Signalformen HP 33120A*. Loveland (Colorado), USA, **1994**.
- [90] Vollnhals, F. *Lithography for EBID and Electron Beam Induced Surface Activation: A look behind the scenes*. Seminar talk 08.12.2010, Lehrstuhl für Physikalische Chemie II, Friedrich-Alexander-Universität Erlangen-Nürnberg, Erlangen, **2010**.
- [91] Bernhardt, K.-H. *Vacuum Technology Compendium*. 1. Edition, Pfeiffer Vacuum GmbH, Asslar, 2010.
- [92] Marchand, P.; Marmet, L.; *Review of Scientific Instruments* **1983**, 54, 1034-1041.
- [93] HWL Scientific Instruments GmbH, *Active Vibration Isolation, TS-150, Instruction manual*. Germany, **2011**.
- [94] Newport Corporation, *Product Information, Manual Positioning, 460A Series - Low-Profile Integrated Ball Bearing Linear Stages*. **2011**.
- [95] Nanosurf AG, *easyScan DFM System - Operating Instructions, Version 1.0*. Switzerland, **2003**.
- [96] Nanosurf AG, *Basic Dynamic AFM Package*. 15.04.2011, <http://www.nanosurf.com/index.cfm?&content=04020203>, **2011**.
- [97] Horcas, I.; Fernández, R.; Gómez-Rodríguez, J. M.; Colchero, J.; Gómez-Herrero, J.; Baro, A. M.; *Review of Scientific Instruments* **2007**, 78, 013705-1 - 013705-8.

-
- [98] Kremer Vakuumphysik GmbH, *Sputtering Test Ion Source ISE 10 Data Sheets*. Pulheim, Germany, **2005**.
- [99] Walz, M.-M. *Fabrication of Titanium Oxide Nanostructures on Au(111) via Electron-Beam Induced Deposition (EBID)*. Master thesis, Lehrstuhl für Physikalische Chemie II, Friedrich-Alexander-Universität Erlangen-Nürnberg, Erlangen, **2008**.
- [100] Wu, C.; Marshall, M. S. J.; Castell, M. R.; *The Journal of Physical Chemistry C* **2011**, 115, 8643-8652.
- [101] Bowker, M.; Bennett, R. A.; *Journal of Physics: Condensed Matter* **2009**, 21, 474224(1-9).
- [102] Bennett, R. A.; Poulston, S.; Stone, P.; Bowker, M.; *Physical Review B* **1999**, 59, 10341-10346.
- [103] Bennett, R. A.; Stone, P.; Price, N. J.; Bowker, M.; *Physical Review Letters* **1999**, 82, 3831-3834.
- [104] Pang, C. L.; Bikondoa, O.; Humphrey, D. S.; Papageorgiou, A. C.; Cabailh, G.; Ithnin, R.; Chen, Q.; Muryn, C. A.; Onishi, H.; Thornton, G.; *Nanotechnology* **2006**, 17, 5397–5405.
- [105] Vergara, L. I.; Passeggi Jr., M. C. G.; Ferrón, J.; *Thin Solid Films* **2007**, 515, 8365-8370.
- [106] Brasca, R.; Vergara, L. I.; Passeggi, M. C. G.; Ferrón, J.; *Materials Research* **2007**, 10, 283-288.
- [107] Kern, P.; Müller, Y.; Patscheider, J.; Michler, J.; *The Journal of Physical Chemistry B* **2006**, 110, 23660-23668.
- [108] Cumpson, P. J.; Seah, M. P.; *Surface and Interface Analysis* **1997**, 25, 430-446.
- [109] van Dorp, W. F.; van Someren, B.; Hagen, C. W.; Kruit, P.; Crozier, P. A.; *Nano Letters* **2005**, 5, 1303-1307.
- [110] Sandmann, A. *Electron beam induced generation and characterization of titaniumoxide nanostructures*. Bachelor thesis, Lehrstuhl für Physikalische Chemie II, Friedrich-Alexander-Universität Erlangen-Nürnberg, Erlangen, **2010**.
- [111] Stewart, R. L.; *Physical Review* **1934**, 45, 488-490.
- [112] Ennos, A. E.; *British Journal of Applied Physics* **1953**, 4, 101-106.

- [113] Poole, K. M.; *Proceedings of the Physical Society. Section B* **1953**, 66, 542-547.
- [114] Christy, R. W.; *Journal of Applied Physics* **1960**, 31, 1680-1683.
- [115] Baker, A. G.; Morris, W. C.; *Review of Scientific Instruments* **1961**, 32, 458.
- [116] Koops, H. W. P.; Kretz, J.; Rudolph, M.; Weber, M.; *Journal of Vacuum Science & Technology B* **1993**, 11, 2386-2389.
- [117] van Dorp, W. F. *Sub-10 nm focused electron beam induced deposition*. Doctoral thesis, Technische Universiteit Delft, Delft, **2008**.
- [118] Hübner, B.; Koops, H. W. P.; Pagnia, H.; Sotnik, N.; Urban, J.; Weber, M.; *Ultramicroscopy* **1992**, 42-44, 1519-1525.
- [119] Lau, Y. M.; Chee, P. C.; Thong, J. T. L.; Ng, V.; *Journal of Vacuum Science & Technology A* **2002**, 20, 1295-1302.
- [120] Schoessler, C.; Koops, H. W. P.; *Journal of Vacuum Science & Technology B* **1998**, 16, 862-865.
- [121] Koops, H. W. P.; Weiel, R.; Kern, D. P.; Baum, T. H.; *Journal of Vacuum Science & Technology B* **1988**, 6, 477-481.
- [122] Matsui, S.; Mori, K.; *Journal of Vacuum Science & Technology B* **1986**, 4, 299-304.
- [123] Weber, M.; Koops, H. W. P.; Rudolph, M.; Kretz, J.; Schmidt, G.; *Journal of Vacuum Science & Technology B* **1995**, 13, 1364-1368.
- [124] Koops, H. W. P.; Schössler, C.; Kaya, A.; Weber, M.; *Journal of Vacuum Science & Technology B* **1996**, 14, 4105-4109.
- [125] Utke, I.; Hoffmann, P.; Berger, R.; Scandella, L.; *Applied Physics Letters* **2002**, 80, 4792-4794.
- [126] Cicoira, F.; Hoffmann, P.; Olsson, C. O. A.; Xanthopoulos, N.; Mathieu, H. J.; Doppelt, P.; *Applied Surface Science* **2005**, 242, 107-113.
- [127] Perentes, A.; Sinicco, G.; Boero, G.; Dwir, B.; Hoffmann, P.; *Journal of Vacuum Science & Technology B* **2007**, 25, 2228-2232.
- [128] Bret, T.; Utke, I.; Bachmann, A.; Hoffmann, P.; *Applied Physics Letters* **2003**, 83, 4005-4007.
- [129] Yavas, O.; Ochiai, C.; Takai, M.; Hosono, A.; Okuda, S.; *Applied Physics Letters* **2000**, 76, 3319-3321.
- [130] Utke, I.; Dwir, B.; Leifer, K.; Cicoira, F.; Doppelt, P.; Hoffmann, P.; Kapon, E.; *Microelectronic Engineering* **2000**, 53, 261-264.

-
- [131] Lee, K. L.; Hatzakis, M.; *Journal of Vacuum Science & Technology B* **1989**, 7, 1941-1946.
- [132] Ochiai, Y.; Fujita, J.-i.; Matsui, S.; *Journal of Vacuum Science & Technology B* **1996**, 14, 3887-3891.
- [133] Perentes, A.; Bret, T.; Utke, I.; Hoffmann, P.; Vaupel, M.; *Journal of Vacuum Science & Technology B* **2006**, 24, 587-591.
- [134] Adachi, H.; Nakane, H.; Katamoto, M.; *Applied Surface Science* **1994**, 76-77, 11-15.
- [135] Guise, O.; Marbach, H.; Levy, J.; Ahner, J.; Yates, J. T.; *Surface Science* **2004**, 571, 128-138.
- [136] Kunz, R. R.; Mayer, T. M.; *Journal of Vacuum Science & Technology B* **1988**, 6, 1557-1564.
- [137] Kunz, R. R.; Mayer, T. M.; *Applied Physics Letters* **1987**, 50, 962-964.
- [138] Zhang, W.; Shimojo, M.; Takeguchi, M.; Che, R.-C.; Furuya, K.; *Advanced Engineering Materials* **2006**, 8, 711-714.
- [139] Zhang, W.; Shimojo, M.; Takeguchi, M.; Furuya, K.; *Journal of Materials Science* **2006**, 41, 2577-2580.
- [140] Hochleitner, G.; Wanzenboeck, H. D.; Bertagnolli, E.; *Journal of Vacuum Science & Technology B* **2008**, 26, 939-944.
- [141] Shimojo, M.; Takeguchi, M.; Tanaka, M.; Mitsuishi, K.; Furuya, K.; *Applied Physics A - Materials Science & Processing* **2004**, 79, 1869-1872.
- [142] Lukasczyk, T.; Schirmer, M.; Steinrück, H.-P.; Marbach, H.; *Small* **2008**, 4, 841-846.
- [143] Lukasczyk, T.; Schirmer, M.; Steinrück, H.-P.; Marbach, H.; *Langmuir* **2009**, 25, 11930-11939.
- [144] Utke, I.; Bret, T.; Laub, D.; Buffat, P. A.; Scandella, L.; Hoffmann, P.; *Microelectronic Engineering* **2004**, 73-74, 553-558.
- [145] Utke, I.; Michler, J.; Gasser, P.; Santschi, C.; Laub, D.; Cantoni, M.; Buffat, P. A.; Jiao, C.; Hoffmann, P.; *Advanced Engineering Materials* **2005**, 7, 323-331.
- [146] Bret, T.; Utke, I.; Gaillard, C.; Hoffmann, P.; *Journal of Vacuum Science & Technology B* **2004**, 22, 2504-2510.
- [147] Cicoira, F.; Leifer, K.; Hoffmann, P.; Utke, I.; Dwir, B.; Laub, D.; Buffat, P. A.; Kapon, E.; Doppelt, P.; *Journal of Crystal Growth* **2004**, 265, 619-626.

- [148] Matsui, S.; Ichihashi, T.; Mito, M.; *Journal of Vacuum Science & Technology B* **1989**, 7, 1182-1190.
- [149] Hoyle, P. C.; Ogasawara, M.; Cleaver, J. R. A.; Ahmed, H.; *Applied Physics Letters* **1993**, 62, 3043-3045.
- [150] Li, W.; Joy, D. C.; *Journal of Vacuum Science & Technology A* **2006**, 24, 431-436.
- [151] Klein, K. L.; Randolph, S. J.; Fowlkes, J. D.; Allard, L. F.; Meyer, H. M.; Simpson, M. L.; Rack, P. D.; *Nanotechnology* **2008**, 19, 345705(1-8).
- [152] Gazzadi, G. C.; Frabboni, S.; *Journal of Vacuum Science & Technology B* **2005**, 23, L1-L3.
- [153] Gazzadi, G. C.; Frabboni, S.; Menozzi, C.; *Nanotechnology* **2007**, 18, 445709(1-7).
- [154] Weber, M.; Rudolph, M.; Kretz, J.; Koops, H. W. P.; *Journal of Vacuum Science & Technology B* **1995**, 13, 461-464.
- [155] Utke, I.; Hoffmann, P.; Dwir, B.; Leifer, K.; Kapon, E.; Doppelt, P.; *Journal of Vacuum Science & Technology B* **2000**, 18, 3168-3171.
- [156] Lee, K. L.; Abraham, D. W.; Secord, F.; Landstein, L.; *Journal of Vacuum Science & Technology B* **1991**, 9, 3562-3568.
- [157] Shimojo, M.; Takeguchi, M.; Furuya, K.; *Nanotechnology* **2006**, 17, 3637-3640.
- [158] Carl Zeiss SMS GmbH, *MeRiT® HR 32 – Takes Mask Repair to the Next Level (Advertisement Flyer)*. Jena, Germany, **2012**.
- [159] Edinger, K.; Becht, H.; Bihl, J.; Boegli, V.; Budach, M.; Hofmann, T.; Koops, H. W. P.; Kuschnerus, P.; Oster, J.; Spies, P., et al.; *Journal of Vacuum Science & Technology B* **2004**, 22, 2902-2906.
- [160] Liang, T.; Frenberg, E.; Lieberman, B.; Stivers, A.; *Journal of Vacuum Science & Technology B* **2005**, 23, 3101-3105.
- [161] Akama, Y.; Nishimura, E.; Sakai, A.; Murakami, H.; *Journal of Vacuum Science & Technology A* **1990**, 8, 429-433.
- [162] Hoyle, P. C.; Cleaver, J. R. A.; Ahmed, H.; *Journal of Vacuum Science & Technology B* **1996**, 14, 662-673.
- [163] Boero, G.; Utke, I.; Bret, T.; Quack, N.; Todorova, M.; Mouaziz, S.; Kejik, P.; Brugger, J.; Popovic, R. S.; Hoffmann, P.; *Applied Physics Letters* **2005**, 86, 042503(1-3).

- [164] Bret, T.; Utke, I.; Hoffmann, P.; Abourida, M.; Doppelt, P.; *Microelectronic Engineering* **2006**, 83, 1482-1486.
- [165] Aristov, V. V.; Kislov, N. A.; Khodos, I. I.; *Microscopy Microanalysis Microstructures* **1992**, 3, 313-322.
- [166] Botman, A.; Mulders, J. J. L.; Hagen, C. W.; *Nanotechnology* **2009**, 20, 372001(1-17).
- [167] Botman, A.; Mulders, J. J. L.; Weemaes, R.; Mentink, S.; *Nanotechnology* **2006**, 17, 3779-3785.
- [168] Wang, S.; Sun, Y.-M.; Wang, Q.; White, J. M.; *Journal of Vacuum Science & Technology B* **2004**, 22, 1803-1806.
- [169] Qiu, L.; Wang, Q.; Lin, L.; Liu, X.; Jiang, X.; Zhao, Q.; Hu, G.; Wang, R.; *Chirality* **2009**, 21, 316-323.
- [170] Li, X.; Lu, G.; Jia, X.; Wu, Y.; Chan, A. S. C.; *Chirality* **2007**, 19, 638-641.
- [171] Chi, Y.; Zhou, Y.-G.; Zhang, X.; *The Journal of Organic Chemistry* **2003**, 68, 4120-4122.
- [172] Yang, W.; Digits, C. A.; Hatada, M.; Narula, S.; Rozamus, L. W.; Huestis, C. M.; Wong, J.; Dalgarno, D.; Holt, D. A.; *Organic Letters* **1999**, 1, 2033-2035.
- [173] Zhao, S. H.; Samuel, O.; Kagan, H. B.; *Organic Syntheses* **1993**, Coll. Vol. 8, 464.
- [174] Clayden, J.; Greeves, N.; Warren, S.; Wothers, P. *Organic Chemistry*. 1. Edition, Oxford University Press, Oxford, 2001.
- [175] Horiguchi, Y.; Kodama, H.; Nakamura, M.; Yoshimura, T.; Hanezi, K.; Hamada, H.; Saitoh, T.; Sano, T.; *Chemical & Pharmaceutical Bulletin* **2002**, 50, 253-257.
- [176] Behrens, E. A.; Poojary, D. M.; Clearfield, A.; *Chemistry of Materials* **1996**, 8, 1236-1244.
- [177] Cusack, L.; Marguerettaz, X.; Rao, S. N.; Wenger, J.; Fitzmaurice, D.; *Chemistry of Materials* **1997**, 9, 1765-1772.
- [178] Guerrero, G.; Mutin, P. H.; Vioux, A.; *Chemistry of Materials* **2000**, 12, 1268-1272.
- [179] Haddow, D. B.; Kothari, S.; James, P. F.; Short, R. D.; Hatton, P. V.; van Noort, R.; *Biomaterials* **1996**, 17, 501-507.
- [180] Kokubo, T.; Ueda, T.; Kawashita, M.; Ikuhara, Y.; Takaoka, G. H.; Nakamura, T.; *Journal of Materials Science: Materials in Medicine* **2008**, 19, 695-702.

- [181] Zhang, R.; Gao, L.; Zhang, Q.; *Chemosphere* **2004**, 54, 405-411.
- [182] Iwasaki, M.; Miyamoto, Y.; Ito, S.; Furuzono, T.; Park, W.-K.; *Journal of Colloid and Interface Science* **2008**, 326, 537-540.
- [183] Guo, G.; Whitesell, J. K.; Fox, M. A.; *The Journal of Physical Chemistry B* **2005**, 109, 18781-18785.
- [184] Hass, G.; *Vacuum* **1952**, 2, 331-345.
- [185] Taylor, C. J.; Gilmer, D. C.; Colombo, D. G.; Wilk, G. D.; Campbell, S. A.; Roberts, J.; Gladfelter, W. L.; *Journal of the American Chemical Society* **1999**, 121, 5220-5229.
- [186] Watanabe, A.; Imai, Y.; *Thin Solid Films* **1999**, 348, 63-68.
- [187] Profijt, H. B.; Potts, S. E.; van de Sanden, M. C. M.; Kessels, W. M. M.; *Journal of Vacuum Science & Technology A* **2011**, 29, 050801(1-26).
- [188] Potts, S. E.; Keuning, W.; Langereis, E.; Dingemans, G.; van de Sanden, M. C. M.; Kessels, W. M. M.; *Journal of The Electrochemical Society* **2010**, 157, P66-P74.
- [189] Xie, Q.; Jiang, Y.-L.; Detavernier, C.; Deduytsche, D.; Van Meirhaeghe, R. L.; Ru, G.-P.; Li, B.-Z.; Qu, X.-P.; *Journal of Applied Physics* **2007**, 102, 083521(1-6).
- [190] Riedel, E. *Anorganische Chemie*. 3. Edition, Walter de Gruyter, Berlin, 1994.
- [191] Liborio, L.; Harrison, N.; *Physical Review B* **2008**, 77, 104104(1-10).
- [192] Lide, D. R. *CRC Handbook of Chemistry and Physics*. 86. Edition, CRC Press, Boca Raton, FL, USA, 2005.
- [193] Rosenthal, D. *Wachstum und Struktur von Titandioxid auf den Übergangsmetalloberflächen Re(10-10) und Ru(0001)*. Doctoral thesis, Freie Universität Berlin, Berlin, **2007**.
- [194] Fahmi, A.; Minot, C.; Silvi, B.; Causá, M.; *Physical Review B* **1993**, 47, 11717-11724.
- [195] Imanishi, A.; Tsuji, E.; Nakato, Y.; *The Journal of Physical Chemistry C* **2007**, 111, 2128-2132.
- [196] Aprile, C.; Corma, A.; Garcia, H.; *Physical Chemistry Chemical Physics* **2008**, 10, 769-783.
- [197] Fujishima, A.; Rao, T. N.; Tryk, D. A.; *Journal of Photochemistry and Photobiology C: Photochemistry Reviews* **2000**, 1, 1-21.

- [198] Carp, O.; Huisman, C. L.; Reller, A.; *Progress in Solid State Chemistry* **2004**, 32, 33-177.
- [199] Fujishima, A.; Honda, K.; *Nature* **1972**, 238, 37-38.
- [200] O'Regan, B.; Grätzel, M.; *Nature* **1991**, 353, 737-740.
- [201] Hagfeldt, A.; Grätzel, M.; *Chemical Reviews* **1995**, 95, 49-68.
- [202] Grätzel, M.; *Nature* **2001**, 414, 338-344.
- [203] Bisquert, J.; Cahen, D.; Hodes, G.; Rühle, S.; Zaban, A.; *The Journal of Physical Chemistry B* **2004**, 108, 8106-8118.
- [204] Watson, D. F.; Meyer, G. J.; *Annual Review of Physical Chemistry* **2005**, 56, 119-156.
- [205] Tryk, D. A.; Fujishima, A.; Honda, K.; *Electrochimica Acta* **2000**, 45, 2363-2376.
- [206] Hoffmann, M. R.; Martin, S. T.; Choi, W.; Bahnemann, D. W.; *Chemical Reviews* **1995**, 95, 69-96.
- [207] Linsebigler, A. L.; Lu, G.; Yates, J. T.; *Chemical Reviews* **1995**, 95, 735-758.
- [208] Mills, A.; Le Hunte, S.; *Journal of Photochemistry and Photobiology A: Chemistry* **1997**, 108, 1-35.
- [209] Bahnemann, D. W.; *Solar Energy* **2004**, 77, 445-459.
- [210] Thompson, T. L.; Yates, J. T. J.; *Topics in Catalysis* **2005**, 35, 197-210.
- [211] Vollnhals, F. *Titanium(IV)isopropoxide as a precursor for electron beam induced deposition (EBID)*. Bachelor thesis, Lehrstuhl für Physikalische Chemie II, Friedrich-Alexander-Universität Erlangen-Nürnberg, Erlangen, **2007**.
- [212] Alfa Aesar, *Material safety data sheet 2-propanol*. Karlsruhe, Germany, **2010**.
- [213] Lassiter, M. G.; Rack, P. D.; *Nanotechnology* **2008**, 19, 455306(1-14).
- [214] Smith, D. A.; Fowlkes, J. D.; Rack, P. D.; *Small* **2008**, 4, 1382-1389.
- [215] Smith, D. A.; Fowlkes, J. D.; Rack, P. D.; *Nanotechnology* **2008**, 19, 415704(1-11).
- [216] Utke, I.; Friedli, V.; Purrucker, M.; Michler, J.; *Journal of Vacuum Science & Technology B* **2007**, 25, 2219-2223.
- [217] Utke, I.; Friedli, V.; Michler, J.; Bret, T.; Multone, X.; Hoffmann, P.; *Applied Physics Letters* **2006**, 88, 031906(1-3).
- [218] Friedli, V. *Focused Electron- and Ion-Beam Induced Processes: In Situ Monitoring, Analysis and Modeling*. Doctoral thesis, Faculté des Sciences et

- Techniques de l'Ingénieur, École Polytechnique Fédérale de Lausanne, Lausanne, **2008**.
- [219] Jousten, K. *Wutz Handbuch Vakuumtechnik*. 10. Edition, Vieweg+Teubner, Wiesbaden, 2010.
- [220] Pantförder, J. *Photoelektronenspektroskopie im „Pressure Gap“ – Aufbau einer neuen Apparatur für Messungen im Druckbereich von 10^{-10} bis 1 mbar*. Doctoral thesis, Lehrstuhl für Physikalische Chemie II, Friedrich-Alexander-Universität Erlangen-Nürnberg, Erlangen, **2004**.
- [221] Roy, S.; Raju, R.; Chuang, H. F.; Cruden, B. A.; Meyyappan, M.; *Journal of Applied Physics* **2003**, 93, 4870-4879.
- [222] Varian vacuum technologies, *Instruction Manual - Vaclon Plus 500 pumps*. Leini, Italy, **2006**.
- [223] Davis, D. H.; *Journal of Applied Physics* **1960**, 31, 1169-1176.
- [224] Smith, C. G.; Lewin, G.; *Journal of Vacuum Science and Technology* **1966**, 3, 92-95.
- [225] Schirmer, M.; Walz, M.-M.; Vollnhals, F.; Lukasczyk, T.; Sandmann, A.; Chen, C.; Steinrück, H.-P.; Marbach, H.; *Nanotechnology* **2011**, 22, 085301(1-10).
- [226] Koops, H. W. P.; Kaya, A.; Weber, M.; *Journal of Vacuum Science & Technology B* **1995**, 13, 2400-2403.
- [227] Knotek, M. L.; Feibelman, P. J.; *Physical Review Letters* **1978**, 40, 964-967.
- [228] Feibelman, P. J.; Knotek, M. L.; *Physical Review B* **1978**, 18, 6531-6539.
- [229] Bassett, P. J.; Gallon, T. E.; *Journal of Electron Spectroscopy and Related Phenomena* **1973**, 2, 101-104.
- [230] Solomon, J. S.; Baun, W. L.; *Surface Science* **1975**, 51, 228-236.
- [231] Göpel, W.; Anderson, J. A.; Frankel, D.; Jaehnig, M.; Phillips, K.; Schäfer, J. A.; Rocker, G.; *Surface Science* **1984**, 139, 333-346.
- [232] Vaquila, I.; Passeggi Jr., M. C. G.; Ferrón, J.; *Surface Science Letters* **1993**, 292, L795-L800.
- [233] Vaquila, I.; Passeggi Jr., M. C. G.; Ferrón, J.; *Applied Surface Science* **1996**, 93, 247-253.
- [234] Vaquila, I.; Passeggi Jr., M. C. G.; Ferrón, J.; *Physical Review B* **1997**, 55, 13925-13931.
- [235] Vaquila, I.; Vergara, L. I.; Passeggi Jr., M. C. G.; Vidal, R. A.; Ferrón, J.; *Surface and Coatings Technology* **1999**, 122, 67-71.

- [236] Roman, E.; Sánchez-Avedillo, M.; Segovia, J. L.; *Applied Physics A: Materials Science & Processing* **1984**, 35, 35-40.
- [237] Knotek, M. L.; Houston, J. E.; *Physical Review B* **1977**, 15, 4580-4586.
- [238] Nishigaki, S.; *Surface Science* **1983**, 125, 762-770.
- [239] Bermudez, V. M.; *Journal of Vacuum Science and Technology* **1982**, 20, 51-57.
- [240] Vergara, L. I.; Vaquila, I.; Ferrón, J.; *Applied Surface Science* **1999**, 151, 129-138.
- [241] Rao, C. N. R.; Sarma, D. D.; *Physical Review B* **1982**, 25, 2927-2929.
- [242] Bishop, H. E.; Rivière, J. C.; Coad, J. P.; *Surface Science* **1971**, 24, 1-17.
- [243] Coad, J. P.; Rivière, J. C.; *Proceedings of the Royal Society of London. Series A, Mathematical and Physical Sciences* **1972**, 331, 403-415.
- [244] Pan, J.-M.; Maschhoff, B. L.; Diebold, U.; Madey, T. E.; *Journal of Vacuum Science & Technology A* **1992**, 10, 2470-2476.
- [245] Baer, D. R.; Engelhard, M. H.; Lea, A. S.; Nachimuthu, P.; Droubay, T. C.; Kim, J.; Lee, B.; Mathews, C.; Opila, R. L.; Saraf, L. V., et al.; *Journal of Vacuum Science & Technology A* **2010**, 28, 1060-1072.
- [246] Hofmann, S.; *Reports on Progress in Physics* **1998**, 61, 827-888.
- [247] Hofmann, S.; *High Temperature Materials and Processes* **1998**, 17, 13-28.
- [248] Mitchell, D. F.; Sproule, G. I.; Graham, M. J.; *Surface and Interface Analysis* **1990**, 15, 487-497.
- [249] Malherbe, J. B.; Hofmann, S.; Sanz, J. M.; *Applied Surface Science* **1986**, 27, 355-365.
- [250] Baretzky, B.; Möller, W.; Taglauer, E.; *Vacuum* **1992**, 43, 1207-1216.
- [251] Le Mercier, T.; Mariot, J.-M.; Goubard, F.; Quarton, M.; Fontaine, M.-F.; Hague, C. F.; *Journal of Physics and Chemistry of Solids* **1997**, 58, 679-684.
- [252] Berger, T.; Sterrer, M.; Diwald, O.; Knözinger, E.; *ChemPhysChem* **2005**, 6, 2104-2112.
- [253] Elser, M. J.; Berger, T.; Brandhuber, D.; Bernardi, J.; Diwald, O.; Knözinger, E.; *The Journal of Physical Chemistry B* **2006**, 110, 7605-7608.
- [254] Benfer, S.; Knözinger, E.; *Journal of Materials Chemistry* **1999**, 9, 1203-1209.
- [255] Miller, S.; Berning, G. L. P.; Plank, H.; Roth, J.; *Journal of Vacuum Science and Technology A* **1997**, 15, 2029-2034.
- [256] Luthin, J.; Linsmeier, C.; *Physica Scripta* **2001**, 2001, 134-137.

- [257] Starodub, D.; Gusev, E. P.; Garfunkel, E.; Gustafsson, T.; *Surface Review and Letters* **1999**, 6, 45-52.
- [258] Tromp, R.; Rubloff, G. W.; Balk, P.; LeGoues, F. K.; van Loenen, E. J.; *Physical Review Letters* **1985**, 55, 2332-2335.
- [259] Miyata, N.; Watanabe, H.; Ichikawa, M.; *Physical Review Letters* **2000**, 84, 1043-1046.
- [260] Sun, Y.-K.; Bonser, D. J.; Engel, T.; *Physical Review B* **1991**, 43, 14309-14312.
- [261] Johnson, K. E.; Wu, P. K.; Sander, M.; Engel, T.; *Surface Science* **1993**, 290, 213-231.
- [262] Wei, Y.; Wallace, R. M.; Seabaugh, A. C.; *Applied Physics Letters* **1996**, 69, 1270-1272.
- [263] Omicron NanoTechnology, *Multiscan STM VT User's Guide*. Taunusstein, Germany, **2005**.
- [264] Hüfner, S. *Photoelectron Spectroscopy - Principles and Applications*. 3. Edition, Springer-Verlag, Heidelberg, 2003.
- [265] Lecoœur, J.; Bellier, J. P.; Koehler, C.; *Electrochimica Acta* **1990**, 35, 1383-1392.
- [266] Shiraishi, M.; Ata, M.; *Carbon* **2001**, 39, 1913-1917.
- [267] Abbott, P.; Sosa, E. D.; Golden, D. E.; *Applied Physics Letters* **2001**, 79, 2835-2837.
- [268] Ohno, T.; Sarukawa, K.; Matsumura, M.; *New Journal of Chemistry* **2002**, 26, 1167-1170.
- [269] Yang, X. H.; Yang, H. G.; Li, C.; *Chemistry - A European Journal* **2011**, 17, 6615-6619.
- [270] Riedel, E.; Janiak, C. *Anorganische Chemie*. 7. Edition, Walter de Gruyter, Berlin, 2007.
- [271] Ranade, M. R.; Navrotsky, A.; Zhang, H. Z.; Banfield, J. F.; Elder, S. H.; Zaban, A.; Borse, P. H.; Kulkarni, S. K.; Doran, G. S.; Whitfield, H. J.; *Proceedings of the National Academy of Sciences of the United States of America* **2002**, 99, 6476-6481.
- [272] Zhang, H. Z.; Banfield, J. F.; *Journal of Materials Chemistry* **1998**, 8, 2073-2076.

-
- [273] Zhang, H. Z.; Banfield, J. F.; *The Journal of Physical Chemistry B* **2000**, 104, 3481-3487.
- [274] Smith, D. A.; Fowlkes, J. D.; Rack, P. D.; *Nanotechnology* **2007**, 18, 265308(1-14).
- [275] Amman, M.; Sleight, J. W.; Lombardi, D. R.; Welser, R. E.; Deshpande, M. R.; Reed, M. A.; Guido, L. J.; *Journal of Vacuum Science and Technology B* **1996**, 14, 54-62.
- [276] Reimer, L.; Wächter, M.; *Ultramicroscopy* **1978**, 3, 169-174.
- [277] Kohlmann-von Platen, K. T.; Buchmann, L.-M.; Petzold, H.-C.; Brünger, W. H.; *Journal of Vacuum Science & Technology B* **1992**, 10, 2690-2694.
- [278] Lipp, S.; Frey, L.; Lehrer, C.; Frank, B.; Demm, E.; Pauthner, S.; Ryssel, H.; *Journal of Vacuum Science & Technology B* **1996**, 14, 3920-3923.
- [279] Sánchez, E. J.; Krug II, J. T.; Xie, X. S.; *Review of Scientific Instruments* **2002**, 73, 3901-3907.
- [280] Beaulieu, D.; Ding, Y.; Wang, Z. L.; Lackey, W. J.; *Journal of Vacuum Science & Technology B* **2005**, 23, 2151-2159.
- [281] Kunz, R. R.; Allen, T. E.; Mayer, T. M.; *Journal of Vacuum Science & Technology B* **1987**, 5, 1427-1431.
- [282] Kubena, R. L.; Stratton, F. P.; Mayer, T. M.; *Journal of Vacuum Science & Technology B* **1988**, 6, 1865-1868.
- [283] Adams, D. P.; Mayer, T. M.; Swartzentruber, B. S.; *Applied Physics Letters* **1996**, 68, 2210-2212.
- [284] Porrati, F.; Sachser, R.; Walz, M.-M.; Vollnhals, F.; Steinrück, H.-P.; Marbach, H.; Huth, M.; *Journal of Physics D: Applied Physics* **2011**, 44, 425001(1-6).
- [285] Schirmer, M.; Walz, M.-M.; Papp, C.; Kronast, F.; Gray, A. X.; Balke, B.; Cramm, S.; Fadley, C. S.; Steinrück, H.-P.; Marbach, H.; *Nanotechnology* **2011**, 22, 475304(1-7).
- [286] Pelizzo, M. G.; Suman, M.; Monaco, G.; Nicolosi, P.; Windt, D. L.; *Optics Express* **2008**, 16, 15228-15237.
- [287] Bajt, S.; Edwards, N. V.; Madey, T. E.; *Surface Science Reports* **2008**, 63, 73-99.
- [288] Over, H.; He, Y. B.; Farkas, A.; Mellau, G.; Korte, C.; Knapp, M.; Chandhok, M.; Fang, M.; *Journal of Vacuum Science & Technology B* **2007**, 25, 1123-1138.

-
- [289] Singh, M.; Braat, J. J. M.; *Optics Letters* **2001**, 26, 259-261.
- [290] Bernau, L.; Gabureac, M.; Erni, R.; Utke, I.; *Angewandte Chemie International Edition* **2010**, 49, 8880-8884.
- [291] Gray, A. X.; Kronast, F.; Papp, C.; Yang, S.-H.; Cramm, S.; Krug, I. P.; Salmassi, F.; Gullikson, E. M.; Hilken, D. L.; Anderson, E. H., et al.; *Applied Physics Letters* **2010**, 97, 062503(1-3).
- [292] Yang, S.-H.; Mun, B. S.; Kay, A. W.; Kim, S.-K.; Kortright, J. B.; Underwood, J. H.; Hussain, Z.; Fadley, C. S.; *Surface Science* **2000**, 461, L557-L564.
- [293] Kronast, F.; Schlichting, J.; Radu, F.; Mishra, S. K.; Noll, T.; Dürr, H. A.; *Surface and Interface Analysis* **2010**, 42, 1532-1536.
- [294] Soriano, L.; Abbate, M.; de Groot, F. M. F.; Alders, D.; Fuggle, J. C.; Hofmann, S.; Petersen, H.; Braun, W.; *Surface and Interface Analysis* **1993**, 20, 21-26.
- [295] Omicron NanoTechnology, *Multiprobe Surface Science Systems User's Guide*. Taunusstein, Germany, **2005**.

Danksagung

Ich möchte mich an dieser Stelle bei allen bedanken, die zum Gelingen dieser Arbeit beigetragen haben.

An erster Stelle danke ich Prof. Dr. Hans-Peter Steinrück für die Möglichkeit, diese Arbeit an seinem Lehrstuhl durchzuführen. Vielen herzlichen Dank für die stets konstruktiven wissenschaftlichen Diskussionen, für Ihre stete Unterstützung, für die große Geduld während der schriftlichen Ausarbeitung dieser Dissertation und für die kollegiale, sehr angenehme Atmosphäre, die Sie in Ihrem Arbeitskreis geschaffen haben.

Weiterhin gilt mein Dank PD Dr. Hubertus Marbach für die Betreuung meiner Arbeit und die großartige Unterstützung in den vergangenen Jahren. Vielen herzlichen Dank für alle Ideen, die vielen konstruktiven Vorschläge und wissenschaftlichen Diskussionen, Deine stete Hilfe und die freundschaftliche und sehr kollegiale Atmosphäre in der Arbeitsgruppe „Microscopy and Nanolithography“.

Prof. Dr. Oliver Diwald möchte ich danken für die Übernahme der Zweitkorrektur meiner Dissertation.

Mein großer Dank gilt weiterhin dem EBID-Team, Dr. Thomas Lukasczyk, Marie-Madeleine Walz und Florian Vollnhals. Ich danke Euch herzlich für die großartige Zusammenarbeit in den vergangenen Jahren, für Eure Unterstützung und für die nicht nur kollegiale, sondern immer freundschaftliche Arbeitsatmosphäre. Vielen Dank für die schöne Zeit, die ich mit Euch verbringen durfte.

Achim Sandmann möchte ich danken für die sehr gute Zusammenarbeit während seiner Bachelorarbeit. Vor allem die *ex situ* AFM-Messungen lieferten sehr schöne und für diese Arbeit wertvolle Ergebnisse.

Weiterhin danke ich Dr. Christian Papp und seinen Kollegen für die Durchführung der X-PEEM und XAS Messungen am Helmholtz-Zentrum in Berlin und für die sehr gute Kooperation danach.

Dr. Matthias Moll und Prof. Dr. Ulrich Zenneck danke ich für ihre Hilfestellung bei der Handhabung des Eisenpentacarbonyls. Gleichzeitig danke ich Dr. Stefan Tampier und Ilona Jipa für das Abfüllen der Präkursoren unter Inertgas-Bedingungen.

Des Weiteren möchte ich mich ganz herzlich bedanken bei allen nicht-wissenschaftlichen Mitarbeitern der beiden Lehrstühle für Physikalische Chemie, die zum Gelingen dieser Arbeit beigetragen haben. Mein Dank gilt Hans-Peter Bäuml, der bei technischen Fragen und allen elektrischen und elektronischen Problemen im Labor stets ideenreich geholfen hat, Jürgen Rossa für die Hilfestellung bei der Durchführung von EBID-Experimenten und Modifikation der UHV-Anlage im Jahr 2007, Bernd Kreß für die Unterstützung bei allen vakuumtechnischen Fragestellungen im Labor, Uwe Sauer für die immer schnelle Lösung von allen PC Hardware- und Software-Problemen und Friedhold Wölfel mit allen Mitarbeitern der Mechanik-Werkstatt für die stets zügige und qualitativ ausgezeichnete Anfertigung von neuen Bauteilen für die UHV-Anlage und Durchführung von feinmechanischen Arbeiten.

Nicht vergessen zu danken möchte ich auch allen studentischen Mitarbeitern, die im Rahmen eines Praktikums zu dieser Arbeit beigetragen haben.

Allen Mitarbeitern des Arbeitskreises von Prof. Dr. Steinrück danke ich weiterhin für die sehr gute, kollegiale Zusammenarbeit in den vergangenen Jahren und für die ausgesprochen angenehme Atmosphäre am Lehrstuhl.

Schließlich möchte ich mich ganz besonders bei meiner Familie bedanken: bei meinen Eltern Hermann und Sigrid Schirmer, bei meinem Bruder Markus Schirmer und bei meinen Großeltern Jakob und Anna Drummer und Andreas und Margareta Schirmer. Ich danke Euch für Eure immer währende Unterstützung entlang meines gesamten bisherigen Lebensweges. Insbesondere meinen Eltern und meiner Oma Anna danke ich. Ohne Euch wäre diese Arbeit nicht möglich gewesen.

Abschließend möchte ich dem wichtigsten Menschen in meinem Leben danken, meiner Ehefrau Nicole. Vielen Dank für Deine liebevolle Unterstützung über all die langen Jahre hinweg, für Dein Verständnis und Deine Geduld.

Lebenslauf

Michael Schirmer

geboren am 25.11.1977 in Forchheim (Oberfranken)

UNIVERSITÄT

- 08/2006 – 05/2012 **Promotion** am Lehrstuhl für Physikalische Chemie II
der Friedrich-Alexander-Universität Erlangen-Nürnberg
Arbeitskreis von Prof. Dr. Hans-Peter Steinrück
Arbeitsgruppe „Microscopy and Nanolithography“
von PD Dr. Hubertus Marbach
- 07/2006 **Master of Science (M.Sc.)**
Master-Arbeit: „*Lithographic Fabrication of Nanostructures
by Means of Electron-Beam Induced Deposition (EBID)*“
- 10/2004 **Bachelor of Science (B.Sc.)**
Bachelor-Arbeit: „*Optimierung der elektrochemischen
Präparation von Spitzen für die Rastertunnelmikroskopie*“
- 10/2001 – 07/2006 **Studium Molecular Science**
an der Friedrich-Alexander-Universität Erlangen-Nürnberg
- 10/1998 – 09/1999 **Studium Chemie (Diplom)**
an der Friedrich-Alexander-Universität Erlangen-Nürnberg

BERUFSAUSBILDUNG

- 10/1999 – 09/2001 Ausbildung im Hause **Siemens**
zum **Industrietechnologen**
Fachrichtung Automatisierungstechnik
Schwerpunkt Prozessdatenverarbeitung

GRUNDWEHRERSATZDIENST

- 08/1997 – 08/1998 Zivildienst in der Medizinischen Uniklinik in Erlangen

SCHULE

- 09/1988 – 06/1997 Gymnasium Fränkische Schweiz in Ebermannstadt
mathematisch-naturwissenschaftlicher Zweig
Abitur und Erwerb der allgemeinen Hochschulreife
- 09/1984 – 07/1988 Grundschule Wiesenthau

Publikationsliste

I PEER-REVIEWED

(9) **Defects in Oxygen-Depleted Titanate Nanostructures**

Andrea Vittadini, **Michael Schirmer**, Marie-Madeleine Walz, Florian Vollnhals, Thomas Lukasczyk, Hans-Peter Steinrück, Hubertus Marbach, Alexander Riss, Michael J. Elser, Benedikt Schürer, and Oliver Diwald
Langmuir **2012**, 28(20), 7851–7858.

(8) **Thin Membranes versus Bulk Substrates: Investigation of Proximity Effects in Focused Electron Beam-Induced Processing**

Marie-Madeleine Walz, Florian Vollnhals, Florian Rietzler, **Michael Schirmer**, Andreas Kunzmann, Hans-Peter Steinrück, and Hubertus Marbach
Journal of Physics D: Applied Physics **2012**, 45(22), 225306 (8pp).

(7) **Investigation of Proximity Effects in Electron Microscopy and Lithography**

Marie-Madeleine Walz, Florian Vollnhals, Florian Rietzler, **Michael Schirmer**, Hans-Peter Steinrück, and Hubertus Marbach
Applied Physics Letters **2012**, 100(5), 053118 (4pp).

(6) **Fabrication of Layered Nanostructures by Successive Electron Beam Induced Deposition with two Precursors: Protective Capping of Metallic Iron Structures**

Michael Schirmer, Marie-Madeleine Walz, Christian Papp, Florian Kronast, Alexander X. Gray, Benjamin Balke, Stefan Cramm, Charles S. Fadley, Hans-Peter Steinrück and Hubertus Marbach
Nanotechnology **2011**, 22(47), 475304 (7pp).

(5) **Generation of Clean Iron Nanocrystals on an Ultra-Thin SiO_x Film on Si(001)**

Marie-Madeleine Walz, Florian Vollnhals, **Michael Schirmer**, Hans-Peter Steinrück, and Hubertus Marbach
Physical Chemistry Chemical Physics **2011**, 13(38), 17333–17338.

-
- (4) **Electron-Beam-Induced Deposition and Post-Treatment Processes to Locally Generate Clean Titanium Oxide Nanostructures on Si(100)**
Michael Schirmer, Marie-Madeleine Walz, Florian Vollnhals, Thomas Lukasczyk, Achim Sandmann, Chen Chen, Hans-Peter Steinrück and Hubertus Marbach
Nanotechnology **2011**, 22(8), 085301 (10pp).
- (3) a) **Electrons as “Invisible Ink”: Fabrication of Nanostructures by Local Electron Beam Induced Activation of SiO_x**
Marie-Madeleine Walz, **Michael Schirmer**, Florian Vollnhals, Thomas Lukasczyk, Hans-Peter Steinrück, and Hubertus Marbach
Angewandte Chemie International Edition **2010**, 49(27), 4669–4673 (VIP).
- b) **Elektronen als „unsichtbare Tinte“: Herstellung von Nanostrukturen durch lokale elektronenstrahlinduzierte Aktivierung von SiO_x**
Marie-Madeleine Walz, **Michael Schirmer**, Florian Vollnhals, Thomas Lukasczyk, Hans-Peter Steinrück, and Hubertus Marbach
Angewandte Chemie **2010**, 122(27), 4774–4778 (VIP).
- (2) **Generation of Clean Iron Structures by Electron-Beam-Induced Deposition and Selective Catalytic Decomposition of Iron Pentacarbonyl on Rh(110)**
Thomas Lukasczyk, **Michael Schirmer**, Hans-Peter Steinrück, and Hubertus Marbach
Langmuir **2009**, 25(19), 11930–11939.
- (1) **Electron-Beam-Induced Deposition in Ultrahigh Vacuum: Lithographic Fabrication of Clean Iron Nanostructures**
Thomas Lukasczyk, **Michael Schirmer**, Hans-Peter Steinrück, and Hubertus Marbach
Small **2008**, 4(6), 841–846.

II SONSTIGE

(1) An Alternative to FIB - Direct Writing with an Electron-Beam in UHV:**Lithographic Fabrication of Clean Iron Nanostructures**

Thomas Lukasczyk, **Michael Schirmer**, Marie-Madeleine Walz, Florian Vollnhals,
Hans-Peter Steinrück and Hubertus Marbach

Pico - The Omicron NanoTechnology Newsletter **2008**, 12(2), 6–8.

